

Ioan Doroftei · Cezar Oprisan  
Doina Pisla · Erwin Christian Lovasz  
*Editors*

# New Advances in Mechanism and Machine Science

Proceedings of The 12th IFToMM  
International Symposium on  
Science of Mechanisms and  
Machines (SYROM 2017)

# **Mechanisms and Machine Science**

Volume 57

## **Series editor**

Marco Ceccarelli

LARM: Laboratory of Robotics and Mechatronics

DICeM: University of Cassino and South Latium

Via Di Biasio 43, 03043 Cassino (Fr), Italy

e-mail: [ceccarelli@unicas.it](mailto:ceccarelli@unicas.it)

## **Advisory Editors**

Burkhard Corves

Institut für Getriebetechnik, Maschinendynamik und Robotik

RWTH Aachen University

Aachen

Nordrhein-Westfalen

Germany

Yukio Takeda

Department of Mechanical Engineering

Tokyo Institute of Technology

Tokyo

Japan

More information about this series at <http://www.springer.com/series/8779>

Ioan Doroftei · Cezar Oprisan  
Doina Pisla · Erwin Christian Lovasz  
Editors

# New Advances in Mechanism and Machine Science

Proceedings of The 12th IFToMM  
International Symposium on Science  
of Mechanisms and Machines (SYROM 2017)

 Springer

*Editors*

Ioan Doroftei  
Mechanical Engineering,  
Mechatronics and Robotics Department,  
Mechanical Engineering Faculty  
“Gheorghe Asachi” Technical  
University of Iași  
Iași  
Romania

Doina Pisla  
Mechanical Systems Engineering  
Department, Machine Building  
Faculty, Research Center for Industrial  
Robots Simulation and Testing  
Technical University of Cluj-Napoca  
Cluj-Napoca  
Romania

Cezar Oprisan  
Mechanical Engineering,  
Mechatronics and Robotics Department,  
Mechanical Engineering Faculty  
“Gheorghe Asachi” Technical  
University of Iași  
Iași  
Romania

Erwin Christian Lovasz  
Mechatronics Department,  
Mechanical Engineering Faculty  
Politehnica University of Timisoara  
Timisoara  
Romania

ISSN 2211-0984

ISSN 2211-0992 (electronic)

Mechanisms and Machine Science

ISBN 978-3-319-79110-4

ISBN 978-3-319-79111-1 (eBook)

<https://doi.org/10.1007/978-3-319-79111-1>

Library of Congress Control Number: 2018937335

© Springer International Publishing AG, part of Springer Nature 2018, corrected publication June 2018

This work is subject to copyright. All rights are reserved by the Publisher, whether the whole or part of the material is concerned, specifically the rights of translation, reprinting, reuse of illustrations, recitation, broadcasting, reproduction on microfilms or in any other physical way, and transmission or information storage and retrieval, electronic adaptation, computer software, or by similar or dissimilar methodology now known or hereafter developed.

The use of general descriptive names, registered names, trademarks, service marks, etc. in this publication does not imply, even in the absence of a specific statement, that such names are exempt from the relevant protective laws and regulations and therefore free for general use.

The publisher, the authors and the editors are safe to assume that the advice and information in this book are believed to be true and accurate at the date of publication. Neither the publisher nor the authors or the editors give a warranty, express or implied, with respect to the material contained herein or for any errors or omissions that may have been made. The publisher remains neutral with regard to jurisdictional claims in published maps and institutional affiliations.

Printed on acid-free paper

This Springer imprint is published by the registered company Springer International Publishing AG part of Springer Nature

The registered company address is: Gewerbestrasse 11, 6330 Cham, Switzerland

# Preface

The 12th IFToMM International Symposium on Science of Mechanisms and Machines, SYROM2017, is organized by Romanian Association for the Science of Mechanisms and Machines—ARoTMM, and Mechanical Engineering, Mechatronics and Robotics Department at the Mechanical Engineering Faculty, “Gheorghe Asachi” Technical University of Iasi, Romania, with the support of the International Federation for the Promotion of Mechanism and Machine Science—IFToMM.

The aim of the symposium is to bring together researchers, scientists, industry experts, and Ph.D. students to provide a general forum for researchers, engineers, and Ph.D. students involved in the general area of mechanisms and machines, and their applications, to disseminate their latest research results and exchange views on the future research directions of these fields.

The topics of the symposium are related to mechanisms within aspects of theory, design, practice, and applications in engineering, including but not limited to: Theoretical kinematics, Computational kinematics, Mechanism design, Experimental mechanics, Mechanics of robots, Dynamics of machinery, Dynamics of multi-body systems, Control issues of mechanical systems, Mechanisms for biomechanics, Novel designs, Mechanical transmissions, Linkages and manipulators, Micro-mechanisms, Teaching methods, History of mechanism science, and Industrial and non-industrial applications.

We would like to express grateful thanks to IFToMM International Federation for the Promotion of Mechanism and Machine Science, to the Romanian IFToMM National Committee ARoTMM, and to the members of the International Scientific Committee of SYROM 2017.

We appreciate the effort of the reviewers gathered in the International Scientific Committee of SYROM 2017. They spent time for a serious work of evaluation and improvement guidance, meant to assure a high quality of all papers.

We thank the authors who contributed valuable papers on different subjects, covering a wide scientific area of Mechanisms and Machine Science.

We thank the “Gheorghe Asachi” Technical University of Iasi, the Mechanical Engineering Faculty, and the Mechanical Engineering, Mechatronics and Robotics Department for hosting the scientific event and supporting all associated activities. The 12th IFToMM International Symposium on Science of Mechanisms and Machines, SYROM2017 became a real event due to a hard-working local organizing team: Cezar Oprisan, Virgil Atanasiu, Dumitru Leohchi, Emil Budescu, Florentin Buium, and Eugen Merticaru.

Last but not least, we are grateful to the staff at Springer Publishers for their excellent technical and editorial support.

Iași, Romania  
September 2017

Ioan Doroftei  
Cezar Oprisan  
Doina Pislă  
Erwin Christian Lovasz

# **Committees**

## **Conference Chairman**

Ioan Doroftei, Chair of ARoTMM, Romania

## **Conference Co-Chairmen**

Doina Pîslă, Romania

Erwin Christian Lovasz, Romania

## **International Scientific Committee**

Catalin Alexandru, Romania

Paun Antonescu, Romania

Virgil Atanasiu, Romania

Ioan Ardelean, Romania

Karsten Berns, Germany

Ion Bostan, Republic of Moldova

Tobias Bruckmann, Germany

Marco Ceccarelli, Italy

Burkhard Corves, Germany

Giuseppe Carbone, Italy

Ioan Doroftei, Romania

Cezar Duca, Romania

Valeriu Dulgheru, Republic of Moldova

Jean-Christophe Fauroux, France

Paulo Flores, Portugal

Grigore Gogu, France

Shuo Hung Chang, Taiwan



Manfred Husty, Austria  
Zhao Jun, China  
Codruta Jaliu, Romania  
Dirk Lefeber, Belgium  
Erwin Christian Lovasz, Romania  
Dan Mandru, Romania  
Vistrian Maties, Romania  
Vasile Merticaru, Romania  
Karl-Heinz Modler, Germany  
Mircea Neagoe, Romania  
Cezar Oprisan, Romania  
Nicolae Orlandea, USA  
Victor Petuya, Spain  
Doina Pisla, Romania  
Annika Raatz, Germany  
Alexandru Rus, Romania  
Stefan Staicu, Romania  
Daniela Tarnita, Romania  
Bram Vanderborght, Belgium  
Ion Visa, Romania  
Philippe Wenger, France  
Teresa Zielinska, Poland

### **Organizing Committee Chairman**

Cezar Oprisan, Romania

### **Organizing Committee**

Virgil Atanasiu, Romania  
Dumitru Leohchi, Romania  
Emil Budescu, Romania  
Florentin Buium, Romania  
Eugen Merticaru, Romania

### **With the Support of**

International Federation for the Promotion of Mechanism and Machine Science,  
IFToMM

# Contents

## Part I Mechanism Design

<b>Solar Tracking Parallel Linkage Applicable for All Latitudes . . . . .</b>	<b>3</b>
I. Visa, M. Neagoe, M. Moldovan and M. Comsit	
<b>On the Design of the Gravity Balancer Using Scotch Yoke Derivative Mechanism . . . . .</b>	<b>13</b>
Hong-Nguyen Nguyen and Win-Bin Shieh	
<b>Structural Synthesis of Planar 10-Link 1-DOF Kinematic Chains with up to Pentagonal Links with All Possible Multiple Joint Assortments for Mechanism Design . . . . .</b>	<b>27</b>
V. Pozhbelko and E. Kuts	
<b>Kinematic-Dynamic Analysis of the Cam-Worm Mechanism for Humanoid Robots Shrug . . . . .</b>	<b>37</b>
M. Penčić, M. Čavić, M. Rackov, B. Borovac and Z. Lu	
<b>Drive System of the Robot Eyeballs and Eyelids with 8 DOFs . . . . .</b>	<b>47</b>
M. Penčić, M. Čavić, M. Rackov, B. Borovac and Z. Lu	
<b>Method for the Kinetostatic Analysis of the Road Vehicles Axle Suspensions . . . . .</b>	<b>57</b>
C. Alexandru	
<b>Forces Transmission at Structural Group 0/4/2 . . . . .</b>	<b>67</b>
C. Duca and Fl. Buium	
<b>Topological Structure of the Actuating Mechanisms of the Urban Buses Doors . . . . .</b>	<b>75</b>
D. Antonescu, C. Brezeanu and O. Antonescu	
<b>Geometric Synthesis of the Actuating Mechanisms of Urban Bus Doors . . . . .</b>	<b>87</b>
D. Antonescu, I. Popescu and O. Antonescu	

<b>Synthesis of the Mechanisms Used to Actuate the Cabinet Doors</b> . . . . .	99
D. Antonescu, F. Gaspar and P. Antonescu	
<b>Design of a Class of Novel 3T1R Parallel Mechanisms with Low Coupling Degree</b> . . . . .	113
Huiping Shen, Hengcun Qiang, Yunyu Shen and Ting-li Yang	
<b>Part II Biomechanics and Rehabilitation</b>	
<b>Design and Finite Element Analysis of a New Spherical Prosthesis-Elbow Joint Assembly</b> . . . . .	127
D. Tarnita, C. Boborelu, D. Popa and D.-N. Tarnita	
<b>Experimental Method for Dynamic Evaluation of Spinal Column Deformation Exercises</b> . . . . .	137
A.-M. Vutan, V. Ciupe, C. M. Gruescu and E.-C. Lovasz	
<b>Kinematic Design of a Parallel Robot for Elbow and Wrist Rehabilitation</b> . . . . .	147
B. Gherman, G. Carbone, N. Plitea, M. Ceccarelli, A. Banica and D. Pisla	
<b>Preliminary Design for a Spherical Parallel Robot for Shoulder Rehabilitation</b> . . . . .	155
C. Vaida, G. Carbone, N. Plitea, I. Ulinici and D. Pisla	
<b>Study on the Effects of Rotation Axis Misalignment in an Exoskeleton-Human Hip Joint</b> . . . . .	165
C. Moldovan, I. Maniu, E. C. Lovasz and Ana-Maria Stoian	
<b>Children Locomotion Rehabilitation Test Bed Designed from Kinematic Considerations</b> . . . . .	171
C. Copilusi, N. Dumitru and A. Margine	
<b>Design and Simulation of an Underactuated Mechanism for Leg Exoskeleton</b> . . . . .	181
Shuangji Yao and Marco Ceccarelli	
<b>Design, Numerical Simulation and Manufacturing of a Powered Wheelchair</b> . . . . .	191
I. Geonea, N. Dumitru, A. Rosca and A. Didu	
<b>Methodology for Determining the Positions of the Human Spine Vertebrae</b> . . . . .	201
S. Butnariu and C. Antonya	
<b>Neurorobotic Investigation into the Control of Artificial Eye Movements</b> . . . . .	211
A. Mussina, M. Ceccarelli and G. Balbayev	

**New Concepts of Ankle Rehabilitation Devices—Part I:**  
**Theoretical Aspects** . . . . . 223  
 C. M. Racu (Cazacu) and I. Doroftei

**New Concepts of Ankle Rehabilitation Devices—Part II:**  
**Design and Simulation** . . . . . 233  
 C. M. Racu (Cazacu) and I. Doroftei

**Part III Mobile Robots**

**Service Robots for Cultural Heritage Applications** . . . . . 243  
 G. Carbone

**Dimensional Synthesis of a Robotic Arm for Mobile Manipulator  
 Using an Interactive Geo-metric Software** . . . . . 253  
 S. Maraje, J. C. Fauroux, B. C. Bouzgarrou and L. Adouane

**Design and Simulation of a Snake like Robot** . . . . . 263  
 L. Ciurezu-Gherghe, N. Dumitru and C. Copilusi

**Single DOF Leg Mechanisms Analysis Using GIM Software** . . . . . 273  
 F. Pop, C. Pop, E.-C. Lovasz, S. M. Grigorescu and I. Cărăbaș

**Design and Simulation of a Novel Hybrid Leg Mechanism  
 for Walking Machines** . . . . . 283  
 M. Demirel, G. Carbone, M. Ceccarelli and G. Kiper

**Modular Reconfigurable Robots** . . . . . 291  
 M. O. Tătar and C. I. Cirebea

**Velocity Variation Analysis of an Autonomous Vehicle  
 in Narrow Environment** . . . . . 301  
 T. M. Girbacia and G. L. Mogan

**Part IV Mechanism Theory**

**Charts of Relative and Absolute Velocities of Chosen Parts  
 of Plane Biplanetary Gear** . . . . . 311  
 J. Drewniak, J. Kopeć, J. Marszałek, K. Stańco and S. Zawiślak

**Modelling of the Static Response of a Wind/Hydro Turbine  
 with Two Rotors and a 1DOF Speed Increaser** . . . . . 321  
 R. Saulescu, M. Neagoe and C. Jaliu

**Higher-Order Cayley Transforms for SE(3)** . . . . . 331  
 D. Condurache and I.-A. Ciureanu

**Kinetostatic of Knife Edge Translating Follower Under  
 Dry Friction Conditions** . . . . . 341  
 S. Alaci, F.-C. Ciornei, E.-V. Alexandru and C. Filote

<b>Tetrapod Coupling</b> .....	349
S. Alaci, F. Buium, F.-C. Ciornei and D.-I. Dobincă	
<b>Some Mechanisms Using Internal Gears with Small Difference in Numbers of Teeth</b> .....	357
O. Crivoi and I. Doroftei	
<b>Mechanical System for Determining the Shot Force at Football</b> .....	367
E. Merticaru, R. M. Iacob and E. Budescu	
<b>Part V Manipulators</b>	
<b>Design and Simulation of a Parallel-Serial LARMBot Arm</b> .....	379
Matteo Russo and Marco Ceccarelli	
<b>Kinematically Redundant Octahedral Motion Platform for Virtual Reality Simulations</b> .....	387
G. Nawratil and A. Rasoulzadeh	
<b>Kinematic Analysis of a 3-RRPS Manipulator</b> .....	401
S. M. Grigorescu, E.-C. Lovasz and C. Pop	
<b>Dynamic Modeling and Simulation of Sliding Mode Control for a Cable Driven Parallel Robot</b> .....	413
F. Inel, Z. Mansouri, M. Ceccarelli and G. Carbone	
<b>Optimization of a Spatial 2 DOF Parallel Mechanism Used for Orientation</b> .....	427
C. Boanta, S. Besoiu and C. Brisan	
<b>Tensioned Carbon Fiber Winding on a Collaborative Robots Cell. Part 1 (System)</b> .....	437
M. P. Sbanca and G. L. Mogan	
<b>Tensioned Carbon Fiber Winding on a Collaborative Robots Cell. Part 2 (Tests)</b> .....	445
M. P. Sbanca and G. L. Mogan	
<b>An IKP-DKP Approach Emphasizing Singularities of 9R (3-RRR) Mechanisms</b> .....	455
Fl. Buium, D. Leohchi and C. D. Duca	
<b>Part VI Experimental Mechanics</b>	
<b>Use of Hypocycloidal Motion in the Study of Rolling Friction</b> .....	467
S. T. Siretean, I. Muscă, S. Alaci and F.-C. Ciornei	
<b>Experimental Bench for Spur Gears Efficiency Measurement</b> .....	477
N. Dumitru, E. Dragut, N. Craciunoiu and I. Geonea	

**Design, Development and Testing of a Dynamometer for Drill Force Measurement** . . . . . 487  
 I. Geonea, A. Rosca and P. Rinderu

**Frictional Contact Study of the Chain Link/Polyamide Contact**. . . . . 497  
 M.-T. Lateş, C. C. Gavrilă and R. Papuc

**Influence of Number of Teeth and Centrifugal Force on Forces Distribution on Silent Chain Transmissions** . . . . . 507  
 L. Jurj and R. Velicu

**Influence of Chain Pitch Increase on Bush-Sprocket Contact for Bush Chain Drives** . . . . . 515  
 R. Velicu, R. Saulescu and L. Jurj

**Increasing the Resistance of Scuffing for HCR External Helical Gearing** . . . . . 523  
 M. Rackov, M. Čavić, M. Penčić and M. Vereš

**Erratum to: Increasing the Resistance of Scuffing for HCR External Helical Gearing** . . . . . E1  
 M. Rackov, M. Čavić, M. Penčić and M. Vereš

**Author Index**. . . . . 533

**Part I**  
**Mechanism Design**

# Solar Tracking Parallel Linkage Applicable for All Latitudes



I. Visa, M. Neagoe, M. Moldovan and M. Comsit

**Abstract** In the paper a new concept of a pseudo-equatorial type 2DOF solar tracking mechanism is described. The mechanism is of parallel linkage type based on two kinematic constraints revolute-sphere (RS) which determine an 1 DOF planar loop RSSR with a passive rotation of the coupler. Two translational actuators directly linked to the frame are used to drive independently the planar loop motion and, respectively, the coupler passive rotation. By their independent motions, the elevation and diurnal angles of the solar active surface fixed on the coupler are independently modified. Tracking performances during the year and on different latitudes are analysed in the paper. In any case the daily tracking efficiency in receiving the direct solar irradiance is higher than 93%.

**Keywords** Solar tracking · Two degrees of freedom · Parallel linkage  
Tracking efficiency

## 1 Introduction

Solar tracking mechanisms are used to increase the received solar radiation on the active surfaces of the photovoltaic (PV) modules or solar thermal collectors (ST) during the day. By tracking, the amount of received solar radiation increases

---

I. Visa · M. Neagoe (✉) · M. Moldovan · M. Comsit  
Transilvania University of Brasov, Braşov, Romania  
e-mail: mneagoe@unitbv.ro

I. Visa  
e-mail: visaion@unitbv.ro

M. Moldovan  
e-mail: macedon.moldovan@unitbv.ro

M. Comsit  
e-mail: comsit@unitbv.ro



and, as result, the output energy increases up to 30–40% comparing with fixed optimally tilted active surfaces [1].

To receive the maximum solar radiation (100%), a continuous orientation of the active surface is required, such that the incidence angle between the solar beam (direct solar radiation) and the normal to the active surface to be zero. Practically, the orientation is stepwise (transmission ratio reasons), case in which there is a variable incidence angle and the received solar radiation decreases with some percent, usually between 1 and 5%.

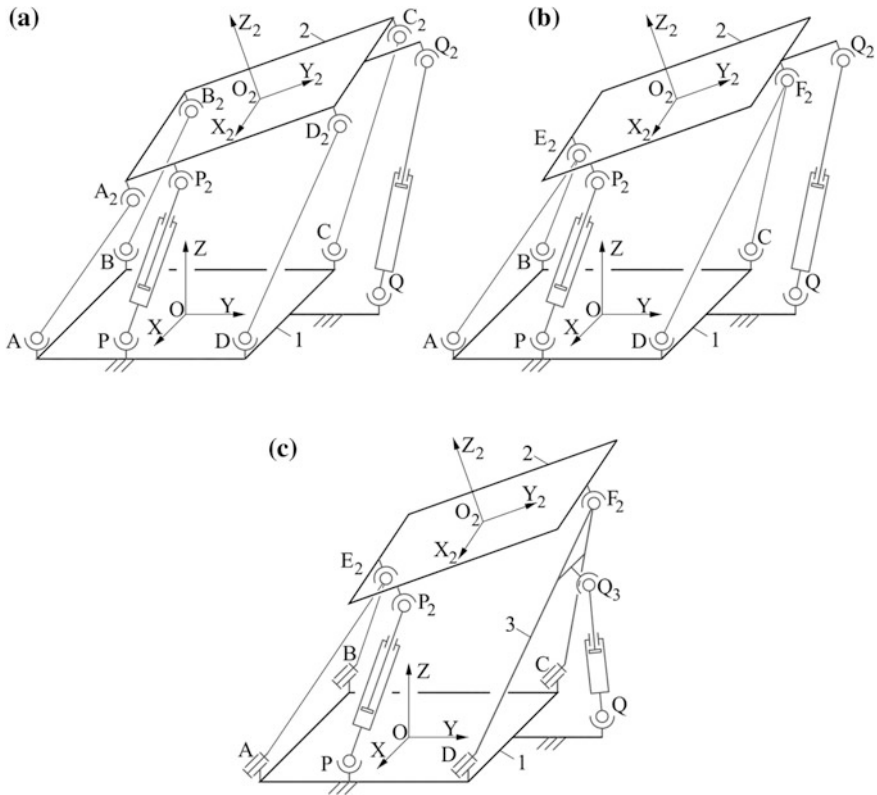
The Sun apparent position relative to a given location is defined in the local reference frame OXYZ by the altitude (elevation) angle ( $\alpha$ ) and azimuthal (diurnal) angle ( $\psi$ ). The active surface orientation could be described by four types of pairs of angles that means that four types of tracking mechanisms can be defined: equatorial, pseudo-equatorial, azimuthal and pseudo-azimuthal [1]. All of them are designed for a given latitude and the active surface is usually guided by: serial chains formed of two perpendicular rotational joints with driving motions in each joint [1]; two serial independent mechanisms [2]; parallel linkages [3–6]. Their installation on different latitudes or on transportation means (e.g. ships) which travel across different latitudes, is a barrier. Additionally, driving motions, acting simultaneous or separately, are used both for the active surface orientation. In the case of serial chains and serial mechanisms one of the actuator is not directly linked to the frame and as result the mechanism stiffness is reduced.

By this paper, a new concept of a pseudo-equatorial type 2DOF solar tracking parallel mechanism is described, having both actuators directly connected to the frame (increased stiffness) and acting separately, one of the actuator is used to adjust the elevation of the active surface according to the latitude ( $\varphi$ ) and declination angle ( $\delta$ ), and the other actuator for the daily orientation of the active surface.

## 2 Concept Description

The starting point is the 2DOF parallel tracking linkage described in [5], presented in Fig. 1a, in which the active surface 2 (mobile platform) is guided by four sphere-sphere (SS) links and the two driving motions (translational actuators) are connected between the mobile platform (2) and the frame (1). As multibody system with two bodies (frame and mobile platform) it has four kinematic constraints of SS type, that means a total number of constraints  $\sum c_{ij} = 1 + 1 + 1 + 1 = 4$ , and two driving constraints. By synthesis for an appropriate geometry it can assure the motion of the mobile platform for optimal solar radiation receiving. It does not have the flexibility to be used for different latitudes and both actuators have to act simultaneously.

By geometric particularities  $A_2 \equiv B_2 \rightarrow E_2$  and  $C_2 \equiv D_2 \rightarrow F_2$  (Fig. 1b) the kinematic constraints of the mobile platform 2 become of sphere-revolute (SR) type and a rotation axis  $E_2F_2$  is obtained. Considering  $AB \parallel CD$ , a planar loop RSSR



**Fig. 1** Parallel solar tracking mechanism: **a** general structural scheme, **b** particular structural scheme, **c** motion decoupling

( $AB - E_2 - F_2 - CD$ ) is obtained in which the mobile platform rotation around  $E_2F_2$  becomes a passive rotation.

The planar loop has 1 DOF and replacing the actuator  $QQ_2$  from the Fig. 1b by the actuator  $QQ_3$  connected to the body 3 ( $CD F_2$ ) in the spherical joint  $Q_3$  (Fig. 1c), the motion of the coupler  $E_2F_2$  is determined.

The joint  $P_2$ , as a point of the coupler  $E_2F_2$  in the planar loop, describes a coupler curve. If the coupler curve could be approximated by an arc of circle and the point  $P$  is located in the centre of the circle, the two rotations of the mobile platform 2 (as coupler in the planar loop with passive rotation) become independent. As result, the two actuators can act independently.

As multibody system, the linkage from Fig. 1c has three bodies and kinematic constraints of RS type between bodies 1 and 2, S between bodies 2 and 3, and R type between bodies 1 and 3. The driving constraints are connected between bodies 1 and 2 ( $PP_2$ ) and between bodies 1 and 3 ( $QQ_3$ ).

### 3 Tracking Motions

As we know, the Earth has two motions: a revolution around the Sun, which defines the North-South Ecliptic Earth axis perpendicular on the Sun Ray direction, and a rotation around the Earth's Polar axis (Fig. 2).

The angle  $\delta$  between the Sun ray and the equatorial plane represents the solar declination angle which depends of the day in a year, being zero at equinoxes, maximum ( $23.45^\circ$ ) at summer solstice and minimum ( $-23.45^\circ$ ) at winter solstice [1].

For a latitude  $\varphi$ , the planar loop of the tracking mechanism is disposed perpendicular to the E-W local axis of the observer horizontal plane, and the angle between the coupler and the horizontal plane (elevation angle) is  $\varphi - \delta$  (Fig. 2) also called tilt angle  $\chi$  in Fig. 3, where the active surface rotation around the coupler  $E_2F_2$  is used for the diurnal rotation ( $\beta$ ) to follow the daily Sun apparent motion. The reference position is when the active surface is south oriented. By the actuator  $QQ_3$  all the latitudes between the arctic circles could be covered. By the translational actuator  $PP_2$ , a limited diurnal motion of  $120^\circ \dots 130^\circ$  can be developed (Fig. 3).

Two configurations of the planar loop with uncrossed and crossed links which can assure the necessary elevation for northern/southern hemisphere and equator are presented in Fig. 4 and Fig. 5 respectively.

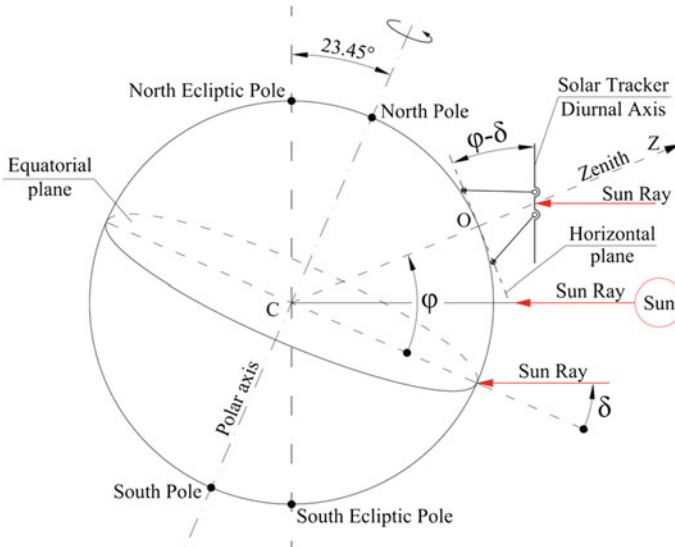


Fig. 2 Earth—Sun geometry at Summer Solstice

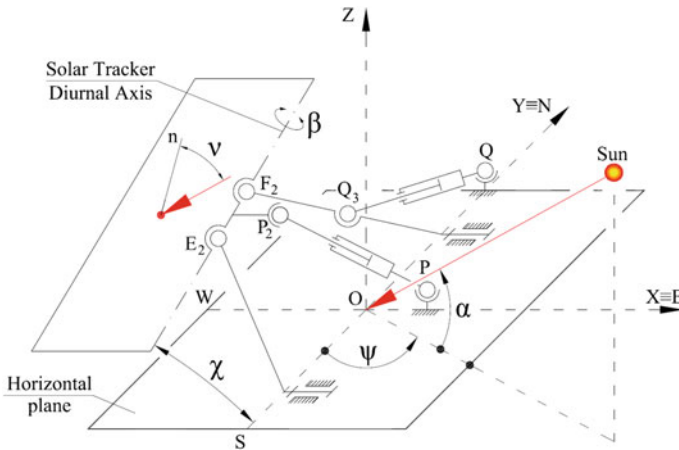


Fig. 3 Solar tracking system's position in northern hemisphere

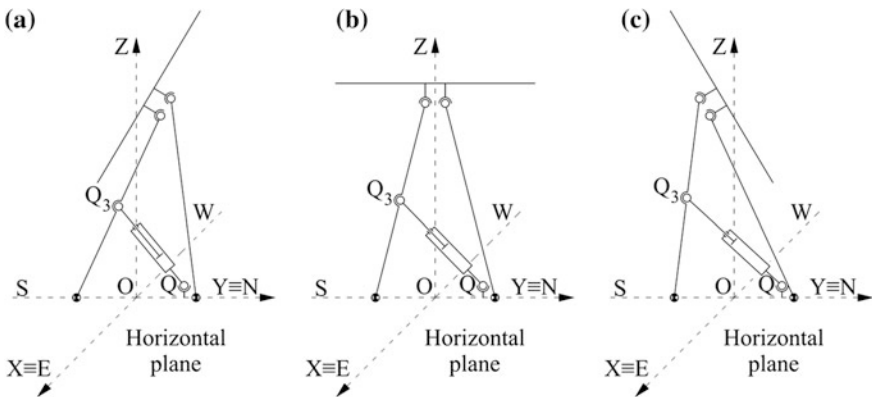
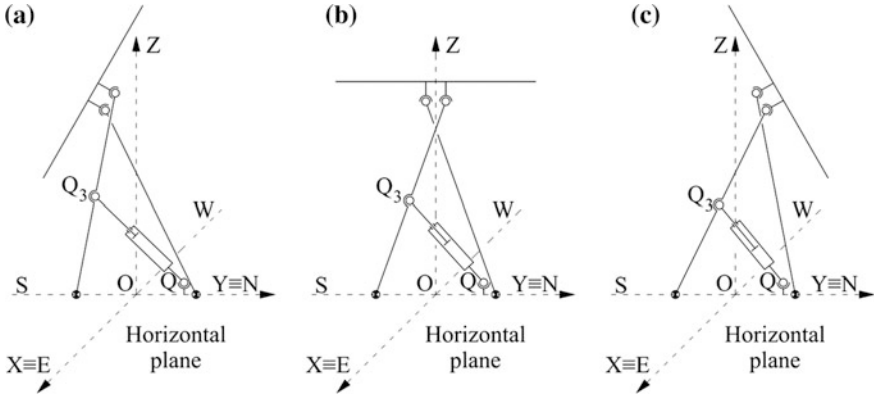


Fig. 4 Solar tracking mechanism with uncrossed links positioned in: **a** northern hemisphere, **b** equator and **c** southern hemisphere

### 4 Tracking Efficiency

Aiming at identifying the performances of the proposed pseudo-equatorial tracking mechanism in receiving the solar energy, the daily tracking efficiency [1] is investigated in this study considering two scenarios in the following assumptions:

- the solar irradiance is modelled for several relevant days (summer and winter solstices, spring equinox) in clear sky hypothesis (sunny days), and neglecting the diffuse solar radiation; thus, only direct solar irradiance is modelled for different locations and implicitly the daily tracking efficiency of receiving the direct solar irradiance ( $\eta_B = \int B_n dt / \int B dt$ ) is used as performance indicator;



**Fig. 5** Solar tracking mechanism with crossed links positioned in: **a** northern hemisphere, **b** equator and **c** southern hemisphere

- the diurnal motion stroke is limited to  $\Delta\beta = 130^\circ (\pm 65^\circ)$  due to maximum allowed value of  $65^\circ$  for the pressure angle in the mechanism based on linear actuator [1].
- for functional and constructive reasons, the elevation motion stroke is limited to  $\pm(60^\circ \dots 70^\circ)$ ;
- in order to simplify the control systems, in a specific location and day (or over a specified range of days) the tilt angle  $\chi$  is maintained fixed, while the diurnal motion  $\beta$  is performed with limited stroke according to the solar angles ( $\alpha$ ,  $\Psi$ ) variation using an one hour stepwise algorithm [7].

Without reducing the generality of the conclusions, in the first scenario a middle latitude location ( $45^\circ\text{N}$ ,  $25^\circ\text{E}$ ) in the northern hemisphere is considered for the three relevant days and two values of the tilt angle ( $\chi = \varphi$  and  $\chi = \varphi - \delta$ ); in the second scenario the tracking mechanism installed on two different locations with latitude of  $60^\circ\text{N}$  and  $0^\circ$ , and placed on the meridian  $25^\circ\text{E}$  is investigated for the summer solstice considering a fixed tilt angle  $\chi = \varphi - \delta$ .

Both the available  $B$  and received  $B_n$  direct solar irradiance are modelled based on the Meliss approach in clear sky assumption [8]:

$$B = 1367 \cdot [1 + 0.0334 \cdot \cos(0.9856^\circ \cdot N - 2.72^\circ)] \cdot \exp\left(-\frac{T_L}{0.9 + 9.4 \cdot \sin \alpha}\right) \quad (1)$$

$$B_n = B \cdot \cos \nu = B(\cos \alpha \sin \Psi \sin \beta + \cos \alpha \cos \Psi \cos \beta \sin \chi + \sin \alpha \cos \beta \cos \chi) \quad (2)$$

where  $N$  is the day number of the year,  $T_L$ —Linke turbidity factor;  $\alpha$ —solar elevation (altitude) angle;  $\psi$ —solar diurnal (azimuth) angle;  $\chi$ —tilt angle of the

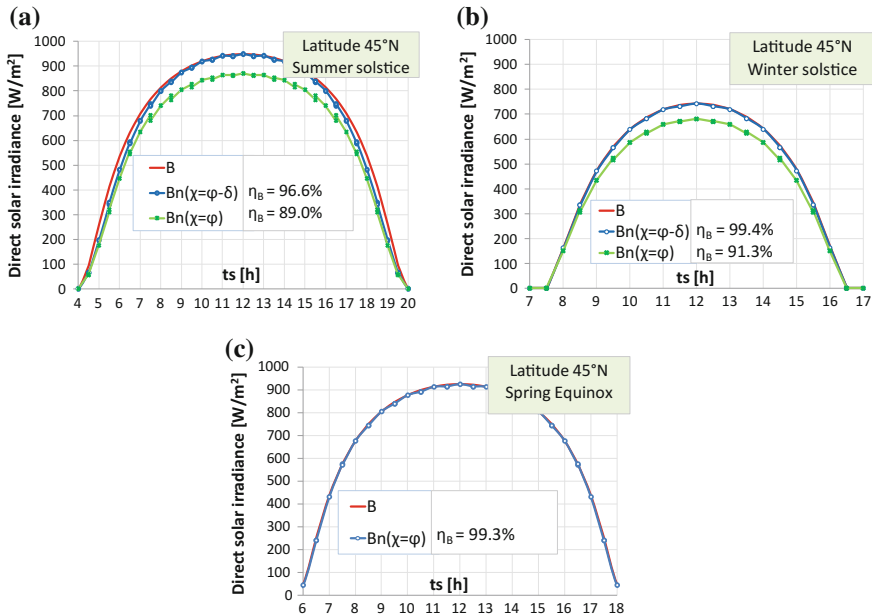
active surface;  $\beta$ —active surface diurnal angle;  $\nu$ —incidence angle. The solar angles ( $\alpha$ ,  $\psi$ ) and the active surface angles ( $\chi$ ,  $\beta$ ) are defined according to [1], and the  $T_L$  factor is obtained from the SoDa online database [9].

## 5 Results and Discussions

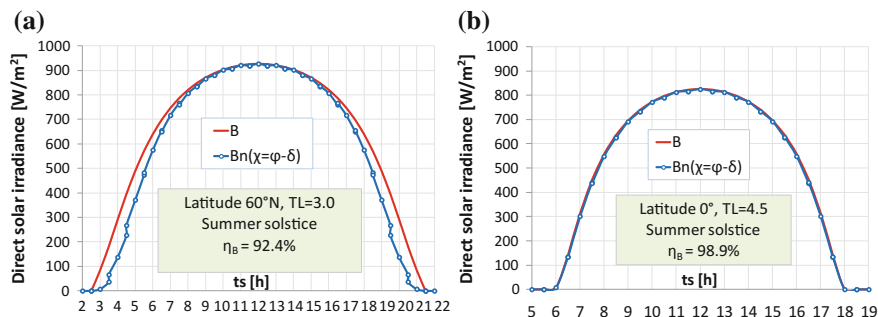
The results obtained in the first scenario, Fig. 6, highlight that:

- for a constant tilt angle  $\chi = \varphi = 45^\circ$ , the tracking efficiency is decreasing from 99.3% at equinoxes to a minimum 89% in the summer solstice;
- a significant increase of the tracking efficiency during the solstices is obtained by modifying the tilt angle  $\chi$  to  $\varphi - \delta$ , i.e.  $\eta_B > 96\%$ ;
- as the tilt angle should be changed between equinoxes and solstices for ensuring high tracking efficiencies, an optimal constant tilt angle can be identified for any given range of days;
- the actuator for the elevation motion is operated only once on a range of days for changing the tilt angle and as a result a low energy consumption is involved.

The second scenario results, Fig. 7, obtained for the summer solstice and  $\chi = -\delta$ , show that the variation of the latitude from equator to polar circle is



**Fig. 6** The available  $B$  and received  $B_n$  direct solar irradiance: **a** summer solstice ( $T_L = 3.2$ ), **b** winter solstice ( $T_L = 2.8$ ), and **c** spring equinox ( $T_L = 3$ ), ( $ts$ —solar time)



**Fig. 7** The available B and received  $B_n$  direct solar irradiance at summer solstice, for fixed tilt angles  $\chi = \varphi - \delta$  and latitudes: **a**  $60^\circ\text{N}$ ; **b**  $0^\circ$ —the equator (ts—solar time)

accompanied by a tracking efficiency decrease of about 6.5%. An insignificant loss of the direct solar radiation during tracking is registered at low latitudes, i.e. about 1% solar energy loss for the  $0^\circ$  location, Fig. 7b.

## 6 Conclusions

The novel solar tracking parallel linkage proposed in the paper can be used for all latitudes between the Arctic Circles.

The two driving motions are decoupled, that means a simplified control.

For a range of days the elevation angle can be kept constant. The optimum tilt angle for each range of days should be investigated.

The proposed tracking mechanism ensures high values of the daily tracking efficiency at all latitudes (over 93%), even a simplified control (fixed tilt angle over an appropriate range of days) and limited diurnal stroke ( $\Delta\beta \leq 130^\circ$ ) are considered.

**Acknowledgements** This work was supported by a grant of the Romanian National Authority for Scientific Research and Innovation, CNCS/CCCDI-UEFISCDI, project number PN-III-P2-2.1-PED-2016-0338, within PNCDI III.

## References

1. Visa I et al (2015) The role of mechanisms in sustainable energy systems. Transilvania University of Brasov Publishing House
2. Quaglia G, Maurino SL (2016) A new solar-tracking mechanism based on four-bar linkages. Proc Inst Mech Eng Part C J Mech Eng Sci. <https://doi.org/10.1177/0954406216641454>
3. Cammarata A (2015) Optimized design of a large-workspace 2-DOF parallel robot for solar tracking systems. Mech Mach Theory 83:175–186

4. Neagoe M, Visa I, Cretescu N, Moldovan M (2014) On a new parallel tracking system for accurate orientation of concentrated solar convertors. *Appl Mech Mater* 658:105–110
5. Visa I, Cotorcea A, Moldovan M, Neagoe M (2016) Two degrees of freedom parallel linkage to track solar thermal platforms installed on ships. *IOP Conf Ser Mat Sci Eng* 147(1):012071
6. Visa I, Neagoe M, Moldovan M, Comsit M (2014) Structural synthesis of parallel linkages by multibody systems method. *Appl Mech Mater* 658:153–160
7. Moldovan M, Visa I, Neagoe M (2015) Optimising the strokes and loads of the linear actuators in a two degrees of freedom linkage used in solar tracking systems. In: *Proceedings of the 14th IFToMM world congress*, Taipei, Taiwan. <https://doi.org/10.6567/iftomm.14th.wc.os16.009>
8. Meliss M (1997) *Regenerative Energiequellen—Praktikum*. Springer
9. Linke turbidity factor. [www.soda-pro.com](http://www.soda-pro.com). Accessed 1 May 2017



# On the Design of the Gravity Balancer Using Scotch Yoke Derivative Mechanism



Hong-Nguyen Nguyen and Win-Bin Shieh

**Abstract** Design of the gravity balancer prototypes based on the modified Scotch yoke type spring mechanism is presented. Followed by the brief description of the conceptual design and validation of the method, design of a one degree-of-freedom (dof) rotary system is proposed. In the 1st generation prototype model, the spring-gravity system is designed as a whole, while, in the 2nd generation model, the gravity balancer is designed as a modular unit for easy adjustment and simple replacement. The friction force due to the prismatic joints of a Scotch yoke derivative mechanism for the latter model has been greatly reduced by using a bushing bearing along with a guidance pole. As a consequence, by showing the equilibrium of the rotary system being sensitive to the fine-tuned position of the end-effector payload, the 2nd prototype model successfully demonstrates the gravity balancing capability of the entire system at all configurations within its range of motion. The issues related to the design of the one-dof gravity balancer are discussed, and the potential use of such balancers in the multiple-dof system is also proposed.

**Keywords** Spring balancing • Gravity balancer • Potential energy  
Scotch yoke mechanism • Zero-free-length spring

## 1 Introduction

A gravity balancing mechanism can be moved to any configuration with only a little or no actuation force/torque just as operated in a gravity-free environment. Because of such an energy-efficiency feature, gravity balancing designs have been employed

---

H.-N. Nguyen  
The University of Danang, University of Science and Technology,  
Da Nang, Vietnam  
e-mail: nhnguyen@dut.udn.vn

W.-B. Shieh (✉)  
Ming Chi University of Technology, New Taipei, Taiwan  
e-mail: wbshieh@mail.mcut.edu.tw

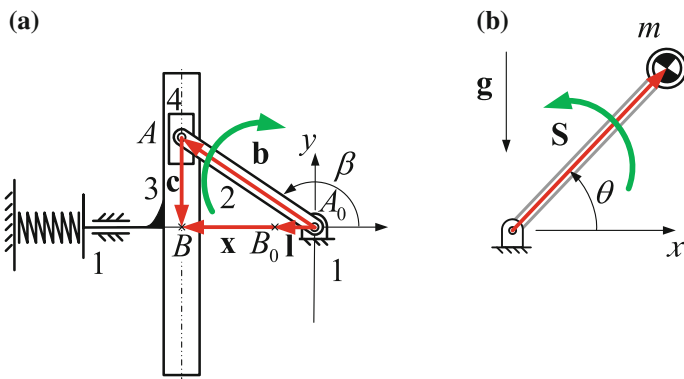
in many applications, such as robot arms [1, 7, 10], limb orthosis [3], musculoskeletal structure [5], arm support [6], parallel mechanisms [16], etc. Among them, the two most frequently applied approaches for the gravity balancing of a system are the counterweight [16] and spring balancing methods [2, 8, 9, 11, 15]. Because of the merits of lightweight and low inertia, gravity balancing designs using springs had been extensively studied.

Based on the theory of conservation of potential energy, perfect equilibrium of a spring-gravity system throughout the entire range of motion can be fulfilled by the equal exchange between the gravitational and elastic potential energy. Among the spring balancing methods, except for few designs using torsion springs [9], normal springs [15] or elastic rubber [11], zero-free-length springs are commonly proposed in the designs of most spring-gravity systems. Practically, a spring with no free length is difficult to manufacture and not readily available. Thus, many alternative devices functionally equivalent to ideal springs are proposed [2, 4, 10, 14], where wires, pulleys and linear springs are used. However, crossover of wires and additional components in those devices may complicate the system and probably interfere with the range of motion of the system. Moreover, the wire and extension spring are not reliable in terms of life span and use of the ideal spring devices may induce a small and uncertain balancing error due to misarrangement of wires and pulleys [2]. Therefore, a new type of gravity balancer which is considered practical, reliable, and simple in structure was designed by Shieh and Chou in 2015 [12] in which a Scotch yoke type mechanism and a regular compression spring are employed to get the static balance of a gravity system.

This paper focuses on the practical design issues regarding the Scotch yoke type gravity balancer proposed in [12]. Layout of the paper is as follows: a brief description about the Scotch yoke type balancing mechanism is presented in Sect. 2; a practical design of a single degree of freedom (dof) model is presented in Sect. 3; issues related to the proposed gravity balancer and possible application of such a gravity balancer in a spatial multiple-dof system are discussed in Sect. 4.

## 2 Scotch Yoke Type Balancing Mechanism

Since the gravitational potential energy of a single-dof rotary system in a vertical plane is a harmonic function of the rotary angle, the elastic potential energy of the system has to be a harmonic function and compensatory to the change of the gravitational potential energy in order to achieve the static equilibrium of the system at all configurations. Therefore, the well-known harmonic motion generator-Scotch yoke mechanism is proposed to generate the required harmonic function of the elastic potential energy.



**Fig. 1** a Scotch yoke mechanism with a compression spring **b** single-dof rotary system

## 2.1 Conceptual Design

Referring to the Scotch yoke mechanism balancer as shown in Fig. 1a, link 1 is the ground, link 2 is the crank, link 3 is a slotted link which translates along the  $x$ -axis direction, and link 4 is a slider inside the slot of link 3. A compression spring of  $k$  is placed to the left of link 3. The crank angle  $\beta$  is measured counterclockwise from the positive  $x$ -axis direction to link 2. An imaginary point  $B$  is defined as the intersecting point of the  $x$ -axis and the center line of the slot.  $B_0$  is the position of  $B$  while the compression spring of  $k$  is in its uncompressed status. For the vector system of the mechanism,  $\mathbf{b}$ ,  $\mathbf{c}$ ,  $\mathbf{l}$ , and  $\mathbf{x}$  is the position vector from  $A_0$  to  $A$ ,  $A$  to  $B$ ,  $A_0$  to  $B$ , and  $B_0$  to  $B$ , respectively. Here, position vector  $\mathbf{x}$  is considered as the displacement vector of the compression spring. Referring to the mechanism in Fig. 1a, vector  $\mathbf{b}$  and  $\mathbf{c}$  can be respectively written as

$$\mathbf{b} = b \cos \beta \mathbf{i} + b \sin \beta \mathbf{j} \quad (1)$$

$$\mathbf{c} = -b \sin \beta \mathbf{j} \quad (2)$$

By the use of  $\mathbf{l} = -l \mathbf{i}$  and based on Eqs. (1) and (2), vector  $\mathbf{x}$  can be derived as

$$\mathbf{x} = \mathbf{b} + \mathbf{c} - \mathbf{l} = (b \cos \beta + l) \mathbf{i} \quad (3)$$

With the spring constant of  $k$ , the elastic potential energy  $U_E$  of the system is expressed as

$$U_E = \frac{1}{2} k |\mathbf{x}|^2 = \frac{1}{2} k [b^2 \cos^2 \beta + 2bl \cos \beta + l^2] \quad (4)$$

For simplicity and without loss of generality,  $l$  can be zero, i.e., it is assumed that point  $B_0$  coincides with  $A_0$  while the spring is not compressed. Using double angle formula to further simplify Eq. (4) yields

$$U_E = \frac{1}{4}kb^2(1 + \cos 2\beta) \quad (5)$$

Referring to the 1-dof rotary system with  $m$  as the mass,  $\mathbf{S}$  as the position vector of the mass center, and  $\theta$  as the rotary angle, as shown in Fig. 1b, the total potential energy of the combined 1-dof spring-gravity system as shown in Fig. 1 can be obtained as

$$U = U_E + U_G = \frac{1}{4}kb^2 + (mgS \sin \theta + \frac{1}{4}kb^2 \cos 2\beta) \quad (6)$$

## 2.2 Balancing Conditions

In order for the potential energy of the spring-gravity system to be invariant, all coefficients of both sine and cosine functions in Eq. (6) have to be zero or summation of all the trigonometric terms inside the braces have to be zero. Hence, a nontrivial solution of Eq. (6) can be obtained if and only if the following requirements are satisfied simultaneously:

$$R1: \quad mgS = \frac{1}{4}kb^2 \quad (7)$$

$$R2: \quad \sin \theta = -\cos 2\beta \quad (8)$$

R1 requires that the spring constant  $k$ , the crank radius  $b$  have to be selected according to the given parameter  $m$  and  $S$  of the specified system. With the condition R2,  $\theta$  must be related to the crank angle  $\beta$  as

$$R2': \quad \theta = \frac{3\pi}{2} \mp 2\beta + 2j\pi, \quad j=0, \pm 1, \pm 2, \dots \quad (9)$$

Requirement R2' in Eq. (9) can be further classified into two subcases:

$$R2-1: \quad \theta = -2\beta + \theta_s \quad (10)$$

$$R2-2: \quad \theta = 2\beta + \theta_s \quad (11)$$

where

$$\theta_s = \dots, -\frac{5\pi}{2}, -\frac{\pi}{2}, \frac{3\pi}{2}, \frac{7\pi}{2}, \dots$$

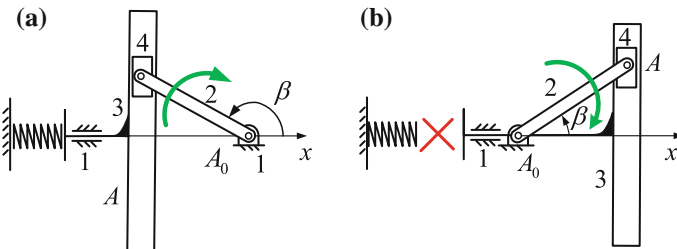
Requirement R2-1 implies that  $\theta$  of the rotary link is two times larger than the crank angle  $\beta$  with a constant phase angle shift  $\theta_s$  and the rotations of the two angles

are always in the opposite direction as shown in Fig. 1. Therefore, an external spur gear pair with a gear ratio of 1:2 can be employed to achieve the gravity balancing of the system. Similarly, for requirement *R2-2*, the rotation angle  $\theta$  of the mass link is also two times larger than the crank angle  $\beta$  of link 2 with a constant phase shift  $\theta_s$ . However, the rotations of the two angles are in the same direction, for which an internal gearing pair can be applied for the compliance of *R2-2*.

### 2.3 Design of the Failure-Proof Mechanism

Referring to the gravity balancer as shown in Fig. 1, if the angle of the single-dof rotary system is  $\theta = -90^\circ$ , the gravitational potential energy of the system is at its minimum value. In order for the combined spring-gravity system to be in a static equilibrium state at all configurations, the elastic potential energy of the spring-gravity system should have the maximum value, i.e., the spring should be in its most compressed status. At this configuration, the crank angle is  $\beta = 180^\circ$  and the shift angle is  $\theta_s = 270^\circ$ , which is complied with the condition *R2-1*. Consider the mass link of the system rotate counterclockwise from this specific position, the gravitational potential energy of the system will be increased and the elastic energy should be decreased due to the clockwise rotation of the crank link of the Scotch yoke mechanism as shown in Fig. 2a. According to *R2-1*, while the rotary mass link angle  $\theta$  reaches  $90^\circ$ , the crank  $\beta$  also reaches  $90^\circ$ . At this specific configuration, the gravitational potential energy has the maximum value and the elastic potential energy is zero. As the rotary mass link continues to rotate to beyond  $90^\circ$ , point A of the crank link would rotate to the right-hand side of joint  $A_0$ , i.e.,  $\beta < 90^\circ$ . As a result, slider 3 would lose contact with the compression spring as shown in Fig. 2b. Under this circumstance, the spring-gravity system loses its all elastic potential energy, i.e., the mechanism fails to fight against the gravity.

Therefore, with the current design, the gravity balancer can only be applied for the mass link angle within the range of  $\theta \in [-90^\circ, 90^\circ]$ . To resolve this problem, a new Scotch yoke derivative mechanism is proposed as shown in Fig. 3a as follows:



**Fig. 2** Relative position of the slider 3 and the spring during operation of the mechanism: **a** remained in contact; **b** lost contact

slotted slider (link 3) in Fig. 2 is redesigned as a cylindrical component with a flat plane; slider 4 is modified into a pair of pin  $A$  and its axis-symmetric pin  $A'$ . Using this structural modification, either pin  $A$  or  $A'$  would always be in contact with the flat plane of the cylindrical component, pushing the compression spring to the left regardless of the orientation of the rotary link of  $m$ . Such a design modification enables a rotary gravity system to be statically balanced by the spring at all angles.

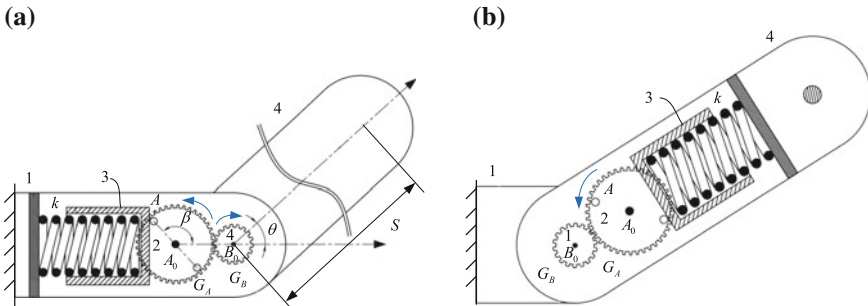
### 2.4 Installation of the Gravity Balancer

The Scotch yoke type spring balancer can be installed either in the ground or rotary link as shown in Fig. 3a or 3b, respectively. Referring to system as shown in Fig. 3a, gear  $G_A$  can freely rotate about joint  $A_0$  of link 1; gear  $G_B$  with its center at  $B_0$  is fixed on link 4 and meshes with gear  $G_A$ ; link 4 rotates with respect to link 1 about joint  $B_0$ . Hence, as link 4 rotates clockwise to lower the mass center, the compression spring will be pushed to the left due to motion of pin  $A$  (or  $A'$ ) of gear  $G_A$ . The gear system used in this installation is an ordinary gear system with

$$T_A : T_B = 2 : 1 \tag{12}$$

where  $T_A$  and  $T_B$  are the tooth number of gear  $G_A$  and  $G_B$ , respectively.

Contrarily, referring to the installation as shown in Fig. 3b, gear  $G_A$  can freely rotate about joint  $A_0$  of link 4; gear  $G_B$  with its center at  $B_0$  is fixed on link 1 and meshes with gear  $G_A$ ; link 4 can rotate with respect to link 1 about joint  $B_0$ . In this installation, the gear system becomes a planetary gear system, where  $G_B$ (link 1),  $G_A$ (link 2) and link 4 are respectively the sun gear (and also ground), planet gear, and the carrier. Therefore, the angular relation of the planetary system is obtained as



**Fig. 3** Installation of the Scotch yoke type spring balancer with an external gearing pair in: **a** ground link; **b** rotary link

$$T_A(\theta_2 - \theta_4) = -T_B(\theta_1 - \theta_4) \quad (13)$$

Since link 1 is the ground and  $\theta_4$  is the rotation angle  $\theta$  of the rotary link with respect to link 1, substituting  $\theta_1 = 0$  and  $\theta_4 = \theta$  into Eq. (13) yields

$$\frac{\theta}{\theta_2 - \theta} = \frac{T_A}{T_B} \quad (14)$$

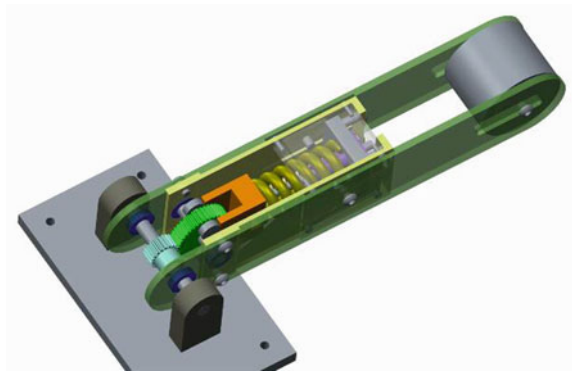
The angle  $\theta_2 - \theta$  in Eq. (14) is the relative rotation angle of  $G_A$  with respect to link 4. This in turn can be referred to the crank angle  $\beta$  as shown in Fig. 1. Hence, in order for the system to be balanced, according to Eq. (10), the two angles must maintain a relation of  $\theta: (\theta_2 - \theta) = 2: 1$ . Hence,  $T_A: T_B = 2: 1$ .

### 3 Design of Single-DOF Model

#### 3.1 Modeling and Simulation

Based on the design in Sect. 2, a numerical model is setup to illustrate the gravity balancing of a rotary system. The parameters  $m$  and  $S$  of the given system as shown in Fig. 4 is tabulated in Table 1, where the crank arm length  $b$  of the gear  $G_A$  and the spring constant  $k$  are determined according to requirement R1 specified in Eq. (7). Practically, spring constant is usually selected prior to the determination of  $b$  because of the availability in the market. Using the parameters specified in Table 1, the gravitational ( $U_G$ ), elastic ( $U_E$ ), and the total potential energy ( $U$ ) of

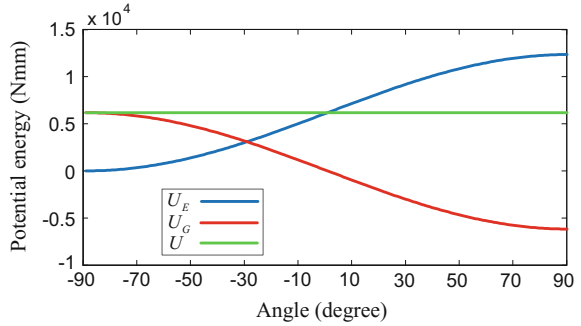
**Fig. 4** Numerical model of the Scotch yoke type gravity balancer



**Table 1** Design parameters with a given system with specified  $m$  and  $S$

$m$	$S$	$k$	$b$
2 kg	191.27 mm	68.53 N/mm	14.8 mm

**Fig. 5** Gravitational, elastic and total potential energy curves of the given system



the system verse angle  $\theta$ , ranged from  $-90^\circ$  to  $90^\circ$ , are plotted as shown in Fig. 5. In the figure, the  $U$  curve is a perfect, flat line, indicating that the gravitational potential energy can be fully balanced by the elastic potential energy at all  $\theta$ .

### 3.2 Prototyping

For the realization of the Scotch yoke type gravity balancer, two prototype models are constructed based on the specified parameters in Table 1. The overall mass of the rotary system includes the end-effector payload, the link mass and the spring mass. The mass center distance between the joint and the mass center is estimated using the commercial software Pro/E Creo. The spring is a coil compression spring with rectangular cross-section purchased from MITSUMI. The module of the gear is 1 and the tooth number of  $G_A$  and  $G_B$  are 40 and 20, respectively. These gears are also purchased from MITSUMI. The 1st generation model is built according to Fig. 3b, while a 2nd generation prototype model is manufactured as shown in Fig. 6a. In the 1st generation prototype model, the spring-gravity system is designed as a whole, while, in the 2nd generation model, the gravity balancer is designed as a modular unit. Figure 6b shows that the  $G_A$  gear (big gear), the spring, and the Scotch yoke derivative mechanism are designed as a module unit. Such a modularized design makes the assembly easy and allows the replacement of the spring of different free length, in case of the end-effector payload has been changed. Figure 6c shows that the location of the fixed end of the spring can be fine-tuned by relocating the wall against the spring through the adjustment of the 4 screws, such that an uncompressed spring can be guaranteed during the assembly procedure. Figure 6d shows a bushing bearing with the guidance pole for the reduction of the friction force between the cylindrical component and the link body.



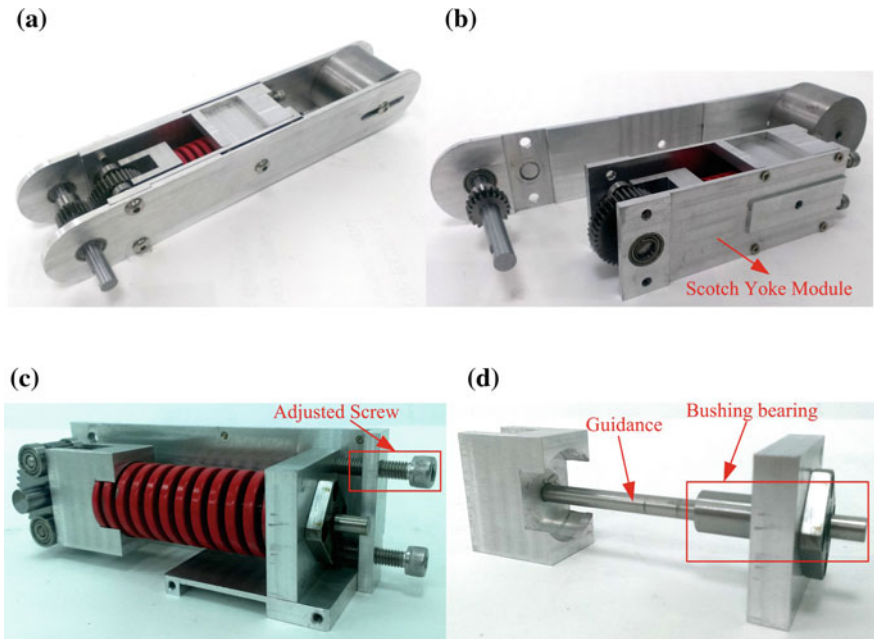


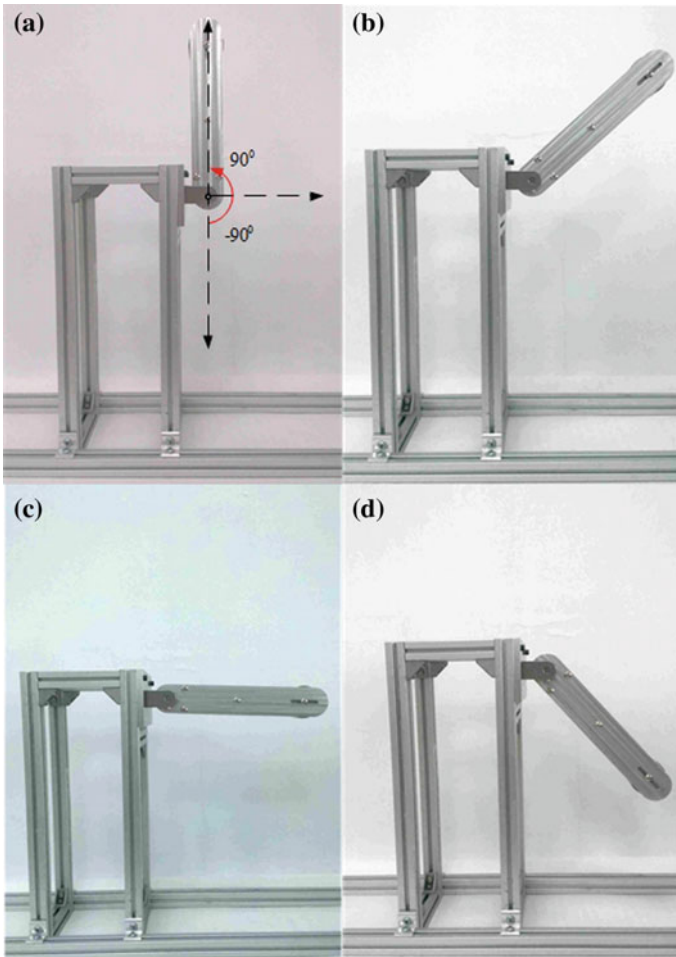
Fig. 6 Prototyping mockup of the Scotch yoke type spring balancer

### 3.3 Assembly and Testing

Figure 7a shows the range of motion of the prototype model. Figures 7b–d indicate that the model can be self-sustained at the postures of various angles. Practically, such a gravity balancing model is able to be moved to any angle with only little actuating force and can be held statically at all configurations.

## 4 Discussions and Future Works

According to the preliminary results of the experiments performed in Fig. 7, the gravity balancing of this mockup model can be successfully achieved at all positions within the specified range of motion. However, the stationary posture of the single-dof mass link at each configuration may be due to the combined effects of the desired spring force and the unexpected friction force of the model. The friction force may be attributed to two major sources: one is due to the meshing of the gear pair; the other is due to the two prismatic joints of the Scotch yoke mechanism. Normally, the friction force induced by the Scotch yoke mechanism is much larger than the gear friction. In this design, since the slider is replaced by two axis-symmetric pins and a roller bearing is mounted on each pin to prevent direct

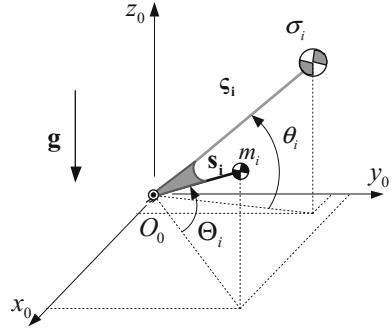


**Fig. 7** Gravity balancing of the model: **a** range of motion; **b-d** at different configurations

sliding with the flat plane, the friction force due to this prismatic joint can be eliminated. Referring to the mechanism in Fig. 3b, the other major friction force of this model comes from the prismatic joint between link 3 and 4. In order to reduce the friction force, a bushing bearing along with a guidance pole is used in the 2nd generation model. As a result, the overall friction force of the model is greatly reduced, because the equilibrium status of the rotary system can be easily altered through the fine-tuning of the payload location.

Another issue regarding the design of the Scotch yoke type gravity balancer is the drifting effects of the mass center during the operation of the model, especially while the gravity balancer is mounted in a rotary link. Referring to the balancer in Fig. 3b, as the spring is compressed; the spring and the cylindrical component 3 would move toward the distal side of the rotary link. Consequently the resulting

**Fig. 8** Angular orientation between primary link and virtual link  $i$



mass center of the rotary link would be shifted away from its original position. This problem may be insignificant if the maximum compression of the embedded spring is small or if the movable parts (slider and spring) are lightweight. Although most studies for the designs of the gravity balancing mechanisms do not take the spring mass into account, practically, the fully balancing of a gravity system cannot be fulfilled without considering the spring mass.

Finally, the applicability of this proposed gravity balancer into a gravity balancing multiple-dof system is discussed. Based on the formulation derived by Shieh and Chou [13], the gravitational potential energy of a generalized,  $n$ -link, spatial articulated manipulator can be derived as sum of the gravitational potential energy due to the  $n$  virtual link as follows:

$$U_G = \mathbf{g}^T \sum_{i=1}^n (\mu_i \mathbf{I} - m_i \mathbf{T}_i) \mathbf{r}_i = \mathbf{g}^T \sum_{i=1}^n \sigma_i \boldsymbol{\zeta}_i \tag{15}$$

where  $\sigma_i$  and  $\boldsymbol{\zeta}_i$  are the equivalent mass and the mass center position vector of virtual link  $i$ . The equivalent mass  $\sigma_i$  composes of all the link masses on the distal side of link  $i - 1$ . The position vector of the virtual link  $\boldsymbol{\zeta}_i$  can be considered to be fixed onto the real link  $i$ , and hence the virtual link  $i$  always maintain a constant angle difference with respect to real link  $i$  as indicated in Fig. 8. Because the angular orientation of real link  $i$  can be at any angle in  $[0^\circ, 360^\circ]$ , the virtual link  $i$  can be also at any angular orientation. Therefore, since the Scotch yoke type gravity balancer is capable of balancing a rotary system with all angles, the gravity balancing of such an  $n$ -link system can be achieved with all its  $n$  associate gravity balancer modules. Detailed design of a gravity-balancing, spatial, articulated manipulator using the proposed gravity balancer is currently under construction.

## 5 Conclusions

Following the conceptual design and the 1st generation prototype model of Scotch yoke type gravity balancer proposed by Shieh and Chow [12], a 2nd generation model with a modular gravity balancer is built. Because of the modular design, the replacement of a different spring and assembly/disassembly of the system can be further simplified. Although the friction could be substantial in a conventional Scotch yoke mechanism, this gravity balancer model uses the Scotch yoke derivative mechanism to resolves the friction issue by employing a bushing bearing along with a guidance pole into the model. With such design improvements, the 2nd generation model displays the perfect balance of the single-dof rotary system. Although the change of the mass center position may only have little impact on the gravity balancing of the system, further evaluation on the drifting effects due to the movable components (sliders and springs) in a multiple-dof system is required.

## References

1. Agrawal SK, Fattah A (2004) Gravity-balancing of spatial robotic manipulator. *Mech Mach Theory* 39(12):1331–1344
2. Barents R, Schenk M, Van Dorsser WD, Wisse BM, Herder JL (2011) Spring-to-spring balancing as energy-free adjustment method in gravity equilibrators. *ASME J Mech Des* 133(6):061010(1–10)
3. Fattah A, Agrawal SK, Catlin G, Hamnett J (2006) Design of a passive gravity-balanced assistive device for sit-to-stand tasks. *Trans ASME J Mech Des* 128(5):1122–1129
4. Herder JL (1998) Design of spring force compensation systems. *Mech Mach Theory* 33(1):151–161
5. Lee JH et al (2012) Adjustable spring mechanisms inspired by human musculoskeletal structure. *Mech Mach Theory* 54:76–98
6. Lenzo B, Fontana M, Marcheschi S, Salsedo F, Frisoli A, Bergamasco M (2016) Trackhold: a novel passive arm-support device. *J Mech Rob* 8(9):021007
7. Lin PY, Shieh WB, Chen DZ (2009) Design of a gravity-balanced general spatial serial-type manipulator. *ASME J Mech Rob* 2(3):031003
8. Nathan RH (1985) A constant force generation mechanism. *ASME J Mech Transm Autom Des* 107(4):508–512
9. Radaelli G, Gallego JA, Herder JL (2010) An energy approach to static balancing of systems with torsion stiffness. In: *Proceedings of the ASME design engineering technical conferences & computers and information in engineering conference, Montreal, Canada, 15–18 Aug 2010, DETC2010-28071*
10. Rahman T, Ramanathan R, Seliktar R, Harwin W (1995) A simple technique to passively gravity-balance articulated mechanisms. *Trans ASME J Mech Des* 117(4):655–658
11. Rahman T, Sample W, Seliktar R, Scavina MT, Clark AL, Moran K, Alexander MA (2007) Design and testing of a functional arm orthosis in patients with neuromuscular diseases. *IEEE Trans Neural Syst Rehabil Eng* 15(2):244–251
12. Shieh WB, Chou BS (2015) A novel spring balancing device on the basis of a scotch yoke mechanism. In: *14th World congress in mechanism and machine science, Taipei, Taiwan*

13. Shieh WB, Chou BS (2015) Gravity Balancing of a spatial articulated manipulator based on a new spring mechanism. In: Proceedings of the ASME 2015 International design engineering technical conference & computers and information in engineering conference IDETC/CIE 2015, Boston Massachusetts, USA
14. Streit DA, Gilmore BJ (1989) Perfect equilibrators for rotatable bodies. *ASME J Mech Transm Auto Des* 111(4):451–458
15. Ulrich N et al (1991) Passive mechanical gravity compensation for robot manipulator. In: Proceedings of the 1991 IEEE international conference on robotics and automation, sacramento, pp 1536–1541
16. Wang J, Gosselin CM (1999) Static balancing of spatial three-degree-of-freedom parallel mechanisms. *Mech Mach Theory* 34(4):437–452

# Structural Synthesis of Planar 10-Link 1-DOF Kinematic Chains with up to Pentagonal Links with All Possible Multiple Joint Assortments for Mechanism Design



V. Pozhbelko and E. Kuts

**Abstract** In this paper, a new method is proposed for structural synthesis of planar closed kinematic chains with all the possible kinds of multiple joints according to given number  $K$ -independent loops up to maximum multiple joint factor  $V_{\max}(K)$ . At first, the new procedure for structural synthesis of non-fractionated and fractionated multiple joint kinematic chains based on the combination of corresponding simple and multiple joints is presented. Then the atlas database with all the possible kinds of multiple joints containing various 24 (case  $K = 4$ ) multiple joint non-fractionated and fractionated structures is established and illustrated. Next, all the possible multiple joint assortments ([M.J.A.]) for non-fractionated as well as fractionated 10-link 1-DOF multiple joint kinematic chains with up to pentagonal links with  $K = 4$  and up to  $V_{\max} = 6$  are synthesized and separated for the first time. Finally, the complete structural analysis of multiple joint kinematic chains for industrial application in 10-link manipulators designed from the atlas of synthesized multiple joint kinematic chains is conducted.

**Keywords** Synthesis • Multiple-jointed kinematic chains • Manipulators

## 1 Introduction

Structural synthesis of various mechanical systems is the first and one of the most important stages in the creative design of mechanisms, completely predetermining the effectiveness of their application in mechanisms and machine theory [1–15].

---

V. Pozhbelko (✉) · E. Kuts

South Ural State University (National Research University), Chelyabinsk, Russia  
e-mail: vipox@inbox.ru

E. Kuts

e-mail: ekaterina.n.kuts@gmail.com

The various synthesis methods use Assur groups, contracted graphs, canonical adjacency and incidence matrices [3, 6, 7, 10]. It should be noted that beside simple joints [1, 3, 10] the various mechanical hinged systems also can include multiple joint (MJ) kinematic chains (KCs), that provides more simple construction and minimizes the space requirement and weight. However, when the number of links and multiple joints moves considerably, structural synthesis of multiple joint kinematic chains becomes more complex and accordingly difficult [2, 4, 11, 12, 14].

The various existing works based on graph theory contain the number structural synthesis methods of planar multiple joint kinematic chains with one multiple joint only [4] or with two multiple joints only [7] for generation of closed-loop non-fractionated kinematic chains with binary and ternary links.

In this paper, we propose structural synthesis method for non-fractionated as well as fractionated multiple joint kinematic chains up to maximum value of total multiple joint factor  $V_{\max}$  with given  $K$ -independent loops. It can be used for design of mechanisms with all possible multiple joint assortments and up to pentagonal links.

In our paper a new notation “Multiple Joint Assortment” is proposed. “Multiple Joint Assortment” ([M.J.A.]) is expressed as [M.J.A.] =  $[\nu_2 \cdot \nu_3 \cdot \nu_4 \cdot \dots \cdot \nu_j]$ , where  $\nu_2 \cdot \nu_3 \cdot \nu_4 \cdot \dots \cdot \nu_j$  are the numbers of two-pin joints ( $j_2$ ), three-pin joints ( $j_3$ ), four-pin joints ( $j_4$ ), ...,  $j$ -pin joints ( $j = j_{\max}$ ). It is necessary to form the multiple joint kinematic chains. These can be non-fractionated kinematic chains (the chains can not be separated) or fractionated kinematic chains, which otherwise can be separated in two independent kinematic chains.

Examples of the creation and complete analysis of various pin-joint and straight-line 10-link 1-DOF manipulators designed from the atlas of synthesized multiple joint kinematic chains are provided for the first time.

#### *Abbreviations, notations and symbols*

- $\tilde{n}$  total number of links in the kinematic chains:  $\tilde{n} = n_1 + n_2 + n_3 + n_4 + \dots + n_i$ ;
- $n_i$  the number of links having  $i$  joints with other links in the KC;
- $n_1$  the number of singular links;
- $n_2$  the number of binary links;
- $n_3$  the number of ternary links;
- $\nu_j$  the number of multiple joints;
- $\nu_2$  the number of two-pin joints (denoted by sign “ $j_2$ ”);
- $\nu_3$  the number of three-pin joints (denoted by sign “ $j_3$ ”);
- $\nu_4$  the number of four-pin joints (denoted by sign “ $j_4$ ”);
- $V$  resulted number of multiple joints ( $V = \sum(j - 1) \nu_j$ );
- $V$  total multiple joint factor,  $V = 0$  – simple joint kinematic chains,  $V > 0$  – multiple joint kinematic chains;
- $V_{\max}$  the max value of resulted number of multiple joints;
- $K$  the number of independent closed loops in kinematic chains;
- $F$  the number of degrees of freedom of mechanical system with the fixed link ( $DOF = F$ );
- $L_i$  independent closed loop (denoted by  $L_1, L_2, L_3$ )

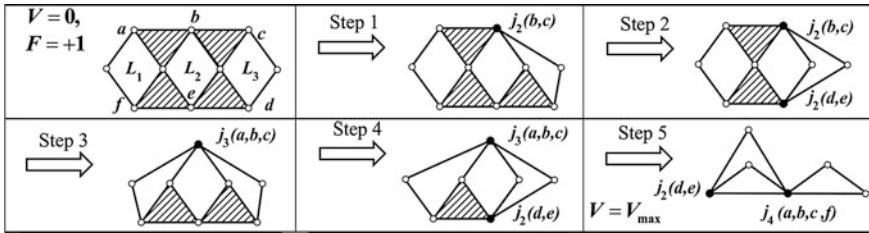


Fig. 1 The process to form multiple joint KCs with given  $K$ -independent loops (case  $F = 1$ )

## 2 Synthesis Algorithm of Multiloop Multiple-Jointed Kinematic Chains

In this paper we introduce the synthesis algorithm of multiple joint kinematic chains with all the possible kinds of multiple joints and with corresponding multiple joint assortments [M.J.A.] up to maximum total multiple joint factor  $V$ . Presented in this paper synthesis method of multiple joint kinematic chains with given number  $K$ -independent loops based on the combination of corresponding simple and multiple joints.

A new proposed algorithm for structural synthesis of multiple joint kinematic chains up to maximum total multiple joint factor ( $V_{max}$ ) is unified for non-fractionated kinematic chains (Step 1, 2, 3 and 4) as well as fractionated kinematic chains (Step 5) and contains next steps (shown in Fig. 1).

**Step 1.** Combining together simple joints ( $b$ ) and ( $c$ ) we obtain the first multiple joint  $j_2(b, c)$ ;

**Step 2.** Combining together simple joints ( $d$ ) and ( $e$ ) we obtain the second multiple joint  $j_2(d, e)$ ;

**Step 3.** Combining together simple joints ( $a$ ), ( $b$ ) and ( $c$ ) we obtain the multiple joint  $j_3(a, b, c)$ ;

**Step 4.** Combining together simple joints ( $a$ ), ( $b$ ), ( $c$ ), ( $d$ ) and ( $e$ ) we obtain the multiple joints  $j_2(d, e)$  and  $j_3(a, b, c)$ ;

**Step 5.** Combining the various simple joints we obtain the multiple joints  $j_2(d, e)$  and  $j_4(a, b, c, f)$  up to  $V = V_{max}$ .

## 3 Synthesis Results of 10-Link 1-DOF Multiple-Jointed Kinematic Chains

According to proposed algorithm of structural synthesis for multiloop multiple-jointed kinematic chains we have got the next results.



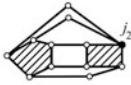
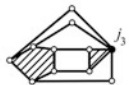
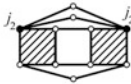

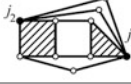
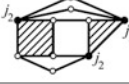
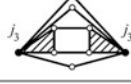
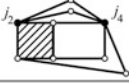
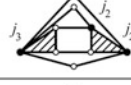
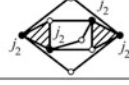
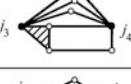
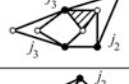
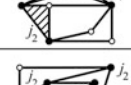





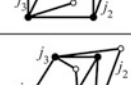
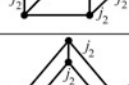
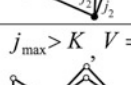
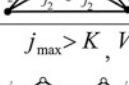
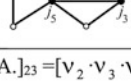
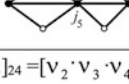
Multiple Joint Assortment ( $K = 4$ )		$[M.J.A.] = [v_2 \cdot v_3 \cdot v_4]$	
Total multiple joint factor		$V = \sum (j-1)v_j = v_2 + 2v_3 + 3v_4$	
1) 	$[1 \cdot 0 \cdot 0]$ $V = 1$	2) 	$[0 \cdot 1 \cdot 0]$ $V = 2$
3) 	$[2 \cdot 0 \cdot 0]$ $V = 2$	4) 	$[0 \cdot 0 \cdot 1]$ $V = 3$
5) 	$[1 \cdot 1 \cdot 0]$ $V = 3$	6) 	$[3 \cdot 0 \cdot 0]$ $V = 3$
7) 	$[0 \cdot 2 \cdot 0]$ $V = 4$	8) 	$[1 \cdot 0 \cdot 1]$ $V = 4$
9) 	$[2 \cdot 1 \cdot 0]$ $V = 4$	10) 	$[4 \cdot 0 \cdot 0]$ $V = 4$
11) 	$[0 \cdot 1 \cdot 1]$ $V = 5$	12) 	$[1 \cdot 2 \cdot 0]$ $V = 5$
13) 	$[2 \cdot 0 \cdot 1]$ $V = 5$	14) 	$[3 \cdot 1 \cdot 0]$ $V = 5$
15) 	$[5 \cdot 0 \cdot 0]$ $V = 5$	16) 	$[0 \cdot 0 \cdot 2]$ $V = 6$
17) 	$[0 \cdot 3 \cdot 0]$ $V = 6$	18) 	$[1 \cdot 1 \cdot 1]$ $V = 6$
19) 	$[2 \cdot 2 \cdot 0]$ $V = 6$	20) 	$[3 \cdot 0 \cdot 1]$ $V = 6$
21) 	$[4 \cdot 1 \cdot 0]$ $V = 6$	22) 	$[6 \cdot 0 \cdot 0]$ $V = 6$
23) $j_{\max} > K, V = V_{\max}$ 		24) $j_{\max} > K, V = V_{\max}$ 	
$[M.J.A.]_{23} = [v_2 \cdot v_3 \cdot v_4 \cdot v_5] = [0 \cdot 1 \cdot 0 \cdot 1];$ $V = 2v_3 + 4v_5 = 6$		$[M.J.A.]_{24} = [v_2 \cdot v_3 \cdot v_4 \cdot v_5] = [2 \cdot 0 \cdot 0 \cdot 1];$ $V = v_2 + 4v_5 = 6$	

Fig. 2 Atlas of 24 types of 4-independent loops 10-link 1-DOF multiple joint KCs ( $V_{\max} = 6$ )

**Table 1** Multiple joint assortment array of 4-independent loops non-fractionated 1-DOF and 10-link kinematic chains

No., V	M.J. assortment
(1), 1	[1 · 0 · 0]
(2), 2	[0 · 1 · 0]
(3), 3	[2 · 0 · 0]
(4), 3	[0 · 0 · 1]
(5), 3	[1 · 1 · 0]
(6), 3	[3 · 0 · 0]
(7), 4	[0 · 2 · 0]
(8), 4	[1 · 0 · 1]
(9), 4	[2 · 1 · 0]
(10), 4	[4 · 0 · 0]
(11), 5	[0 · 1 · 1]
(12), 5	[1 · 2 · 0]
(13), 5	[2 · 0 · 1]
(14), 5	[3 · 1 · 0]
(15), 5	[5 · 0 · 0]
(16), 6	[0 · 0 · 2]
(17), 6	[0 · 3 · 0]
(18), 6	[1 · 1 · 1]
(19), 6	[2 · 2 · 0]
(20), 6	[3 · 0 · 1]
(21), 6	[4 · 1 · 0]
(22), 6	[6 · 0 · 0]

Figure 2 shows the synthesized 24 types of 4-independent loop 10-link 1-DOF multiple-jointed kinematic chains with all the possible sets of various kinds of multiple joints up to maximum total multiple joint factor  $V_{max} = 6$ .

The atlas of synthesized MJ KCs (Fig. 2) contains 22 types of non-fractionated KCs (No. (1)–(22)) and 2 types of fractionated KCs (No. (23) and (24)) with up to six multiple joints (No. (22)) and up to pentagonal links (No. (1), (2) and (4)).

Table 1 presents multiple joint assortment array for structural analysis and synthesis of planar non-fractionated closed kinematic chains with 4-independent loops with 1-DOF and with total multiple joint factor from  $V = 1$  to  $V = 6$ .

Table 2 presents multiple joint assortment array for structural analysis and synthesis of planar fractionated closed kinematic chains with 4-independent loops with 1-DOF and with total multiple joint factor from  $V = 1$  to  $V = 6$ .

**Table 2** Multiple joint assortment array of 4-independent loops fractionated 1-DOF and 10-link kinematic chains

No., V	M.J. assortment
(23), 6	[0 · 1 · 0 · 1]
(24), 6	[2 · 0 · 0 · 1]

Presented in Tables 1 and 2 multiple joint assortment arrays can be used for synthesis and creation (on base any acceptable kinds of multiple joints) of the atlas database of all the possible multiloop multiple-jointed non-fractionated and fractionated kinematic chains with up to 6 multiple joints ( $[M.J.A.] = [6 \cdot 0 \cdot 0]$ ).

For example ( $K = 4$ ) all 24 non-fractionated and fractionated closed kinematic chains up to total multiple joint factor  $V_{\max} = 6$  with any kinds of multiple joints can be synthesized from the corresponding “Multiple joint assortment array” (including 24 [M.J.A.] shown in Tables 1, 2 and Fig. 2).

This algorithm (proposed in Fig. 1) has advantageous feature that distinguishes it from other algorithms: we can find different multiple joint assortments up to maximum total multiple joint factor ( $V_{\max} = 6$ ). Thus, based on this algorithm we can obtain all the possible combinations of various kinds of multiple joints up to maximum total multiple joint factor  $V_{\max}$ .

The present paper provides a complete list of multiple joint assortment arrays for planar closed non-fractionated and fractionated 10-link kinematic chains with 4-independent loops, and  $V_{\max} = 6$  for the first time.

## 4 Directed Structural Analysis of Kinematic Chains with Maximum Total Multiple Joint Factor

We use the following four unified generalized equations proposed by Pozhbelko [12] for structural analysis of planar kinematic chains:

- (1) Total multiple joint factor of a kinematic chain ( $V$ )

$$V = \sum (j-1)\nu_j \leq n_1 + 2(K-1) \Rightarrow V_{\max} = n_1 + 2(K-1) \quad (1)$$

- (2) Degree of freedom (DOF) of a kinematic chain ( $F$ )

$$F = [\sum (3-i)n_i] - V - 3, \quad (2)$$

- (3) Number of independent loops of a kinematic chain ( $K$ )

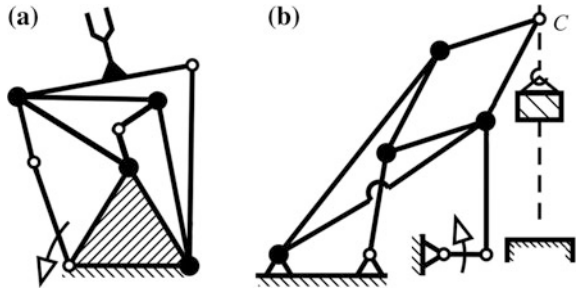
$$K = 1 + 0,5[V + \sum (i-2)n_i], \quad (3)$$

- (4) Assembly criterion of a valid kinematic chain

$$\sum (i-2)n_i = 2(K-1) - V. \quad (4)$$

On base of proposed Eqs. (1)–(4) we can carry out structural analysis of all closed multiloop non-fractionated and fractionated kinematic chains with maximum total multiple joint factor  $V = V_{\max}(K)$  shown in Fig. 2.

**Fig. 3** Industrial application of multiple-jointed kinematic chains: **a** pin-joint manipulator; **b** straight-line heavy load manipulator



**Case 1.** For 10-link closed non-fractionated kinematic chain shown in Fig. 2 No. 22), where  $n_2 = 10$ ,  $\nu_2 = 6$ ,  $\nu_3 = 0$ , the Eqs. (1)–(4) yield:

(1)  $V = 6$ ; (2)  $F = +1$ ; (3)  $K = 4$ ; (4)  $0 = 0$ ; (5)  $V_{\max} = 6$ .

**Case 2.** For 10-link closed fractionated kinematic chain shown in Fig. 2 No. (24), where  $n_2 = 10$ ,  $\nu_2 = 1$ ,  $\nu_5 = 1$ , the Eqs. (1)–(4) yield:

(1)  $V = 6$ ; (2)  $F = +1$ ; (3)  $K = 4$ ; (4)  $0 = 0$ ; (5)  $V_{\max} = 6$ .

## 5 Industrial Application of Synthesized Multiloop Kinematic Chains in Manipulators

Synthesized 10-link 1-DOF multiple-jointed kinematic chains, shown in Fig. 2, can be used in various fields of mechanical engineering, for example, in various manipulators, shown in Fig. 3 and created from the multiple joint KC (Fig. 2, No. 14)) with  $[M.J.A.] = [\nu_2 \cdot \nu_3 \cdot \nu_4] = [3 \cdot 0 \cdot 1]$ .

Based on proposed unified Eqs. (1)–(4) we can carry out structural analysis of manipulators shown in Fig. 3.

For both manipulators (10-link closed KCs) shown in Fig. 3a, b, where  $n_2 = 9$ ,  $n_3 = 1$ ,  $\nu_2 = 3$ ,  $\nu_3 = 1$ , the Eqs. (1)–(4) yield:

(1) Total multiple joint factor  $V = 5$ ; (2) Degree of freedom  $F = +1$ ; (3) Number of independent loops  $K = 4$ ; (4) Assembly verification of a valid kinematic chain:  $1 = 1$ ; (5) Maximum total multiple joint factor  $V_{\max} = 6$ .

## 6 Conclusions

In this paper, we have proposed structural synthesis method based on the combination of corresponding simple and multiple joints. By this synthesis algorithm, any structures of planar simple and multiple joint KCs with specified independent  $K$ -loops and with various total multiple joint factors  $V$  can be synthesized.

The atlas database containing all the valid multiple joints with up to pentagonal links in closed planar KCs with 4-independent loops 10-link up to total multiple joint factor  $V_{\max} = 6$  is synthesized and illustrated. Further corresponding all possible multiple joint assortments are obtained and listed in the tables. Then, examples of structure analysis of multiple joint non-fractionated and fractionated KCs with maximum total multiple joint factor are presented. At last, based on the proposed unified equations, the structural analysis of multiple joint kinematic chains applied to 10-link manipulators is performed.

The methodology of structural synthesis and analysis developed in this paper can be useful for practicing engineers for creating of complete catalog of multiple-jointed non-fractionated as well as fractionated multiloop closed kinematic chains in the process of the creative design of mechanisms.

**Acknowledgements** The work was supported by Act 211 Government of the Russian Federation, contract № 02.A03.21.0011.

## References

1. Butcher EA, Hartman C (2005) Efficient enumeration and hierarchical classification of planar simple-jointed kinematic chains: application to 12- and 14-bar single degree-of-freedom chains. *Mech Mach Theory* 40:1030–1050
2. Chu I, Cao W (1998) Systemics of Assur groups with multiple joints. *Mech Mach Theory* 33:1127–1133
3. Ding H et al (2011) Synthesis of a complete set of contracted graphs for planar non-fractionated simple-jointed kinematic chains with all possible DOFs. *Mech Mach Theory* 46:1588–1600
4. Ding H et al (2013) Automatic structural synthesis of planar multiple joint kinematic chains. *ASME J Mech Des* 135(9):091007
5. Ding H et al (2013) The whole family of kinematic structures for planar 2- and 3-DOF fractionated kinematic chains. *Mech Mach Theory* 7:74–90
6. Ding H, Huang Z (2007) A unique representation of the kinematic chain and the atlas database. *Mech Mach Theory* 42:637–651
7. Ding H, Zhao J, Huang Z (2010) Unified structural synthesis of planar simple and multiple joint kinematic chains. *Mech Mach Theory* 45:555–568
8. Erdman AG, Sandor G (1984) *Mechanism design: analysis and synthesis*. Prentice-Hall
9. Hunt KH (1978) *Kinematic geometry of mechanisms*. Oxford University Press
10. Hwang WM, Hwang YW (1992) Computer-aided structural synthesis of planar kinematic chains with simple joints. *Mech Mach Theory* 27:189–199
11. Pozhbelko V, Ermoshina E (2015) Number structural synthesis and enumeration process of all possible sets of multiple joints for 1-DOF up to 5-loop 12-link mechanisms on base of new mobility equation. *Mech Mach Theory* 90:108–127
12. Pozhbelko V (2016) A unified structure theory of multibody open, closed loop and mixed mechanical systems with simple and multiple joint kinematic chains. *Mech Mach Theory* 100:1–16
13. Yan HS (1998) *Creative design of mechanical devices*. Springer

14. Yan HS, Hsu CH (1988) Contracted graphs of kinematic chains with multiple joints. *Math Comput Model* 10:681–695
15. Yan HS, Hwang YW (1990) Number synthesis of kinematic chains based on permutation groups. *Math Comput Model* 13:29–42

# Kinematic-Dynamic Analysis of the Cam-Worm Mechanism for Humanoid Robots Shrug



M. Penčić, M. Čavić, M. Rackov, B. Borovac and Z. Lu

**Abstract** Having in mind that humans use non-verbal communication extensively is very important to enable social robots with this capacity. There are two basic ways how it can be expressed. First one is by facial expressions by appropriate moving face parts, like eyebrows, eyeballs, eyelids, lips, either as manufactured real parts or by presenting them on screen—combining them is also possible. The second way of non-verbal communication is by gestures. This paper presents the kinematic-dynamic analysis of shrug mechanism for humanoid robots. Based on the set requirements, the cam-worm mechanism that has 1 DOF and enables the simultaneous shrug of both shoulders is proposed. It consists of a worm which is meshed with two worm gears whose directions of rotation are opposite and the two cam mechanisms whose input links—cams, are rigidly attached to the worm gears. Within the kinematic-dynamic analysis, the cam profile and the worm parameters are defined and the torque on the cam/worm gear and the driving torque of the complete cam-worm mechanism are determined. The cam mechanism has a high efficiency in all positions because the values of the pressure angle are within the prescribed ones during the entire movement. Worm mechanism enables a

---

M. Penčić (✉) · M. Čavić · M. Rackov · B. Borovac  
Faculty of Technical Sciences, University of Novi Sad, Novi Sad, Serbia  
e-mail: mpencic@uns.ac.rs

M. Čavić  
e-mail: scomaja@uns.ac.rs

M. Rackov  
e-mail: racmil@uns.ac.rs

B. Borovac  
e-mail: borovac@uns.ac.rs

Z. Lu  
School of Electrical Engineering and Automation, Changshu Institute of Technology,  
Changshu, China  
e-mail: zhenlilu@cslg.cn

Z. Lu  
State Key Laboratory of Robotics, Shenyang Institute of Automation,  
Chinese Academy of Sciences, Shenyang, China

significant reduction of the driving torque and has acceptable efficiency. The rotation range of worm gear/cam is small and the movement of mechanism is very fast wherefore the shrug speed is large, which was one of the main requirement for realization.

**Keywords** Kinematic-dynamic analysis • Cam-worm mechanism  
Robot shrug • Non-verbal communication

## 1 Introduction

To be able to coexist with humans in close proximity in dynamic and non-structured environment, robots should adapt to both—to humans and to environment. To achieve coexistence interaction of humans and robots is inevitable. Besides of safety regarding both, humans and environment—there is not compromise in this issue, from robots has been expected to perform non-verbal communication in intuitive and transparent way [2]. Non-verbal communication is exceptionally powerful way to transfer large number of information in a short time [22]. According to [9] even 55% interpersonal communication belongs to non-verbal, 38% belongs to intonation—para-verbal, while just 7% belongs to verbal communication where content of the message have to be understood. Para-verbal and non-verbal communication sends crystal clear messages regardless of the meaning of spoken words [5]. Today, researchers are working intensively on improving interaction capabilities of robots.

Shrugging is one of the most obvious way of non-verbal communication, and in this paper has been presented kinematic and dynamic analysis of cam-worm shrugging mechanism. This research has been performed within project where social humanoid robot SARA with female appearance has been developed. Robot will be able to perform both way of communication—verbal and non-verbal. In case robot do not understand question or do not know the answer, it will shrug the shoulders. In addition, biologically inspired eyes with eyelids having 8 DOFs has been developing. SARA will have two anthropomorphic arms with 14 DOFs, and 3 DOFs neck [13] and 7 DOFs multi-segment lumbar spine [14].

## 2 State of the Art

A number of robots capable of non-verbal expression that is both transparent and intuitive exists. A few examples of robots able to do this, using primarily their head, are Kismet [3], iCat [23], Flobi [8], EDDIE [20] etc. Their emotional range includes positive emotions like happiness, surprise, interest and tranquility, as well as other, more negative ones, including sadness, disgust and anger. These emotions are shown by articulating facial features, most notably the lips, eyebrows and eyes.



Robots that can express non-verbal communications by using both, face and body, are Nexi [6], iCub [10], Probo [19], R1 [7], BERT2 [1], Albert HUBO [12], KOBIAN [24] etc. The emotions in this case are expressed by either articulating facial features, displaying these features on a display screen in place of the face, or a combination of both. Gesture is realized by moving the head and arms.

Reviewing the available literature, there are two robots that are able to express non-verbal communication by shrug. The first example is the WE-4RII [4], which has a mechanism with 4 DOFs that allows the shoulders motion in two directions, allowing the robot to, among other things, shrug. The other example is BARTHOC [21], with a mechanism positioned above the shoulders allowing the shrugging motion.

### 3 Kinematic-Dynamic Analysis

Shrug is relatively fast action and therefore the duration of the movement should be as short as possible. The mass and dimensions of the shrug mechanism both need to be as low as possible, to avoid overloading the spine. Also, the driving torque should be kept minimal, while also maintain as high an efficiency as possible in all positions of the shrug. Previously three shrug mechanisms were considered—two lever mechanisms [15, 16] and one worm-lever mechanism [17], which by size and power correspond to the requirements. All mechanisms have 1 DOF and enable simultaneous shrug.

A cam-worm mechanism is proposed—Fig. 1, since it has the potential to fulfill the set requirements, has 1 DOF and can be used to articulate the concurrent shrugging of both shoulders. It consists of a worm mechanism and two cam mechanisms. The worm part of the mechanism is made up of a worm meshed with two worm gears rotating in different directions—the worm being the driving element and the two worm gears coinciding with a shoulder each. Input links of cam mechanism—cams, are rigidly attached to the worm gears wherefore the torques on worm gears and torques on the cams are equal  $M_{WG} = M_C$ . Output links of cam mechanisms—followers, perform an oscillating rotational motion and enable lifting/lowering of the shoulders. Since the cams also perform an oscillatory rotational motion, cam pitch curve is not a closed curve, so the dimensions of the cams can be reduced. Given that high speed of shrug is required, the contact between the cam and the roller is ensured by form closure—grooved cam. Since shrug mechanism is symmetrical, only one-half of the mechanism is considered.

The head, neck and arms of the robot are connected to the shrug mechanism which is located on the lumbar spine. Having in mind the available space for incorporation of mechanism—the chest part of the robot, the following parameters are adopted: coordinates of the immobile points are  $O_1(50,60)$  mm and  $O_2(10,150)$  mm, length of follower  $O_2M$  is 120 mm, length of stroke of the shoulders endpoint—vertical stroke of the point M is  $h_{Mmax} = 50$  mm, and during shrug the worm gear and the cam perform a rotation of  $\pm 35^\circ$  ( $\beta = 35^\circ$ ).

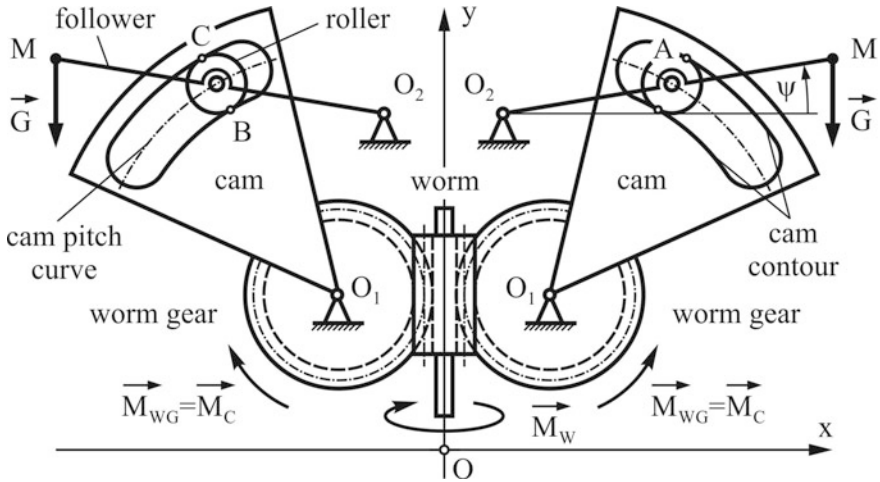


Fig. 1 Kinematic scheme of the cam-worm mechanism for shoulder shrug

By kinematic-dynamic analysis, the cam profile and worm parameters are defined and dynamic efficiency of the cam mechanism, the efficiency of the worm mechanism, the torque on the cam/worm gear and the driving torque of the complete cam-worm mechanism are determined. At first, by kinematic inversion the cam profile is defined. Coordinates of cam pitch curve are:

$$\begin{aligned} x_A &= x_{O1} + L \cos(\psi_0 - \psi) + r \cos((\psi_0 - \psi) + \pi + (\varphi_0 - \varphi)) \\ y_A &= y_{O1} + L \sin(\psi_0 - \psi) + r \sin((\psi_0 - \psi) + \pi + (\varphi_0 - \varphi)) \end{aligned} \quad (1)$$

where:  $L$ —the distance between points  $O_1$  and  $O_2$ ,  $\psi_0$ —angle between  $O_1O_2$  and follower in the start position,  $r = 60 \text{ mm}$ —adopted lever length  $O_2A$ ,  $\psi$ —follower rotation angle,  $\varphi_0$ —angle between  $O_1O_2$  and horizontal axis, and  $\varphi$ —cam shaft angle. According to the cycloidal law, the motion of the follower is defined as:

$$\psi = \psi_{\max} \beta^{-1} \varphi - \psi_{\max} (2\pi)^{-1} \sin(2\pi \beta^{-1} \varphi) \quad (2)$$

where:  $\psi_{\max}$ —angle at which the height of shrug is maximal—vertical stroke of the point  $M$ . Coordinates of points  $B$  and  $C$  on the cam contour are:

$$x_B = x_A + r_R \cos \gamma, \quad y_B = y_A + r_R \sin \gamma \quad (3)$$

$$x_C = x_A - r_R \cos \gamma, \quad y_C = y_A - r_R \sin \gamma \quad (4)$$

where:  $r_R = 15 \text{ mm}$ —adopted roller radius. Angle  $\gamma$  is determined according to:

$$\gamma = 0.5\pi + \arctan\left(\frac{L \sin(\psi_0 - \psi) + r \sin((\psi_0 - \psi) + \pi + (\varphi_0 - \varphi))}{L \cos(\psi_0 - \psi) + r \cos((\psi_0 - \psi) + \pi + (\varphi_0 - \varphi))}\right) \quad (5)$$

The dynamic efficiency of the cam mechanism is defined by the pressure angle  $\alpha$  which must be under  $45^\circ$ . By decreasing the pressure angle most of the power is used for overcoming workload, and less for internal loads, so the mechanism is more efficient. The pressure angle of the cam mechanism is determined according to:

$$\alpha = \gamma - 0.5\pi - ((\psi_0 - \psi) + (\varphi_0 - \varphi)) \quad (6)$$

Kinetostatic equations are formed within the dynamic analysis and by solving them, the reactions in the joints and driving torque on the cam are determined:

$$M_C = G \cos \psi \overline{O_1 D} (x_A \sin \gamma - y_A \cos \gamma) (r(\cos \psi \sin \gamma - \sin \psi \cos \gamma))^{-1} \quad (7)$$

where:  $G$  is a workload by which mass of the arm amounts the total of  $m = 5$  kg. Driving torque  $M_W$  on the input link—worm is:

$$M_W = 2M_C (i \cdot \eta)^{-1} \quad (8)$$

where:  $\eta$ —coefficient of efficiency of the worm pair which can be determined as:

$$\eta = \tan \gamma_m (\tan(\gamma_m + \rho))^{-1} \quad (9)$$

where:  $\gamma_m$ —lead angle and  $\rho$ —friction angle for worm pair. Friction angle is  $\rho \cong 6^\circ$ , because shrug movement is a fast one and it is not performed frequently, so the dry lubricant can be used [11]. Lead angle  $\gamma_m$  of the worm is calculated from:

$$\gamma_m = \arctan(z_W q^{-1}) \quad (10)$$

where:  $z_W$ —number of leads on the worm and  $q$ —diametral quotient of worm.

High-speed worm pair with diametral quotient of worm  $q = 7 \div 10$  has to be used, because fast movement of the mechanism is needed. In order to increase efficiency of the worm pair, multi-lead worm has to be used  $z_W > 1$ . Center distance is prescribed to be  $a = 50$  mm due to the design reasons, so using equation:

$$a = 0.5 m (q + z_{WG}) \quad (11)$$

where:  $m$ —module of worm gearing and  $z_{WG}$ —number of teeth on worm gear. Following values of parameters are obtained:  $q = 8$ ,  $z_W = 3$ ,  $m = 2$  mm. From equation:

$$i = (2a - mq)(m \cdot z_w)^{-1} \tag{12}$$

transmission ratio  $i$  of the worm pair is calculated and has value  $i = 14$ . Such transmission ratio ensures high reduction of the torque as well as increased number of the teeth in the mesh thus having positive effect on the minimization of the backlash which is essential for motion control [18]. Using Eq. (9), coefficient of efficiency of the worm pair is  $\eta = 0.75$ .

Figure 2 shows a cam-worm mechanism in the initial and the final position. To complete the full stroke of the shrug  $h_{Mmax} = 50$  mm, the worm and its corresponding cam complete the same angle  $\beta = |\varphi_{START} - \varphi_{END}| = 35^\circ$ . Given to the small range of rotation, a small number of teeth of the worm gear is in use, so it is possible to reduce both the dimensions and mass, which is one of the requirements. The overall dimensions of the shrug mechanism are  $280 \times 180$  mm.

Figure 3 shows the change of the torque on the input link and the change of the pressure angle, respectively. Maximum torque on the cam is  $M_C = 7.6$  Nm. After taking all of these parameters into account, the driving torque of the cam-worm mechanism is calculated and amounts to  $M_W = 1.45$  Nm. The pressure angle has a maximum value of  $\alpha = 32.1^\circ$ , less than the prescribed maximum of  $45^\circ$ , meaning that the cam mechanism is highly efficient throughout the entire movement, which was one of the requirements.

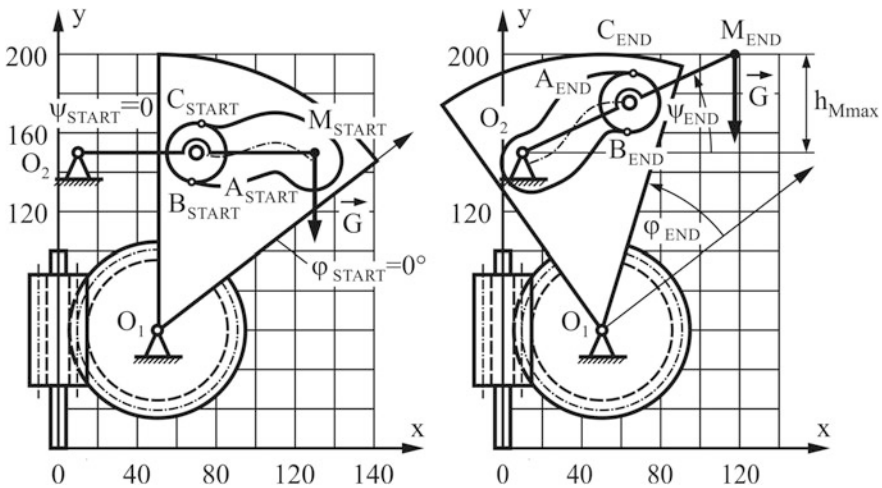


Fig. 2 Cam-worm mechanism: the initial position (left) and the end position (right)

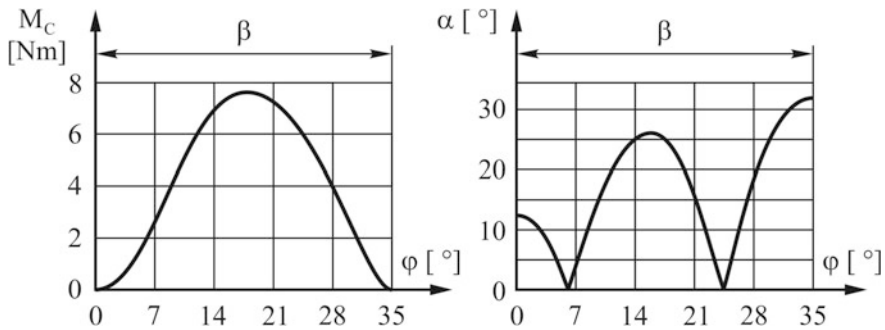


Fig. 3 Torque on the cam (left) and pressure angle during the whole movement (right)

## 4 Conclusions

This paper presents a kinematic and dynamic analysis of the cam-worm mechanism for humanoid robots shrug as a form of non-verbal communication. The proposed mechanism allows this robot complete a shrugging motion that appears natural, while maintaining simplicity by having only 1 DOF. It consists of a worm meshed with a pair of worm gears with contrary directions of rotation, and a pair of cam mechanisms with input links bound to the worm gears, one cam input link to each gear. This mechanism was chosen due to the fact that its characteristics fulfill the following set requirements—high shrug speed, high efficiency in all positions and low driving torque. After adopting the mechanism structure, a kinematic-dynamic analysis was carried out. The cam profile and worm parameters are defined and torque on the input link of the cam mechanism—torque on the worm gear and the driving torque of complete cam-worm mechanism are determined. Output links of the cam mechanisms—followers, perform an oscillatory rotational motion and enable lifting/lowering of the shoulders. The cam also performs an oscillatory rotational motion therefore the cam pitch curve is not a closed curve. Contact between the cam and the roller is ensured by form closure—grooved cam. Since the pressure angle has a value below the prescribed maximum during the entirety of the movement, the efficiency of the cam mechanism is high. The worm part of the mechanism has acceptable efficiency, if somewhat lower than the cam mechanism, but allows a significant reduction of the driving torque. Finally, since the rotation range of the worm gear-cam pairing is quite small, the final output movement is very quick, which was one of the basic set requirements. Further work will explore the possibilities for an additional reduction of torque and higher efficiency, which requires an optimal synthesis.

**Acknowledgements** This research was funded by the Ministry of Education, Science and Technological Development of the Republic of Serbia under the contract III44008 and by the Provincial Secretariat for Higher Education and Scientific Research of AP Vojvodina under the

contract 114-451-2116/2011. It is also supported by the National Science Foundation of China under the contract 61473283 and by the Chinese State Key Laboratory of Robotics under the contract 2014-O08.

## References

1. Bazo D et al (2010) Design and testing of a hybrid expressive face for a humanoid robot. In: Proceedings of the IEEE/RSJ international conference on intelligent robots and systems (IROS), Taipei, pp 5317–5322
2. Breazeal C (2013) Toward sociable robots. *Robot Auton Syst* 42(3–4):167–175
3. Breazeal C (2003) Emotion and sociable humanoid robots. *Int J Hum Comput Stud* 59(1–2): 119–155
4. Itoh K et al (2006) Mechanical design of emotion expression humanoid robot WE-4RII. In: Zielinska T et al (eds) ROMANSY 16: robot design, dynamics and control, vol 487. CISM, Springer, pp 255–262
5. Knapp ML et al (2014) Nonverbal communication in human interaction. Cengage Learning, Boston, MA
6. Knox WB et al (2013) Training a robot via human feedback: a case study. In: Herrmann G et al. (eds.) Social robotics: ICSR 2013, vol 8239. LNCS, Springer, pp 460–470
7. Lehmann H et al (2016) Head and face design for a new humanoid service robot. In: Agah A et al (eds) Social robotics: ICSR 2016, vol 9979. LNCS, Springer, pp 382–391
8. Lutkebohle I et al (2010) The bielefeld anthropomorphic robot head “Flobi”. In: Proceedings of the IEEE international conference on robotics and automation (ICRA), Anchorage, pp 3384–3391
9. Mehrabian A (1981) Silent messages: implicit communication of emotions and attitudes. Wadsworth, Belmont, CA
10. Metta G et al (2010) The iCub humanoid robot: an open-systems platform for research in cognitive development. *Neural Netw* 23(8–9):1125–1134
11. Miltenović, V (2009) Machine elements—forms, calculation and application (in Serbian), University of Niš, Faculty of Mechanical Engineering, Niš
12. Park I-W et al (2008) Control hardware integration of a biped humanoid robot with an android head. *Robot Auton Syst* 56(1):95–103
13. Penčić M et al (2016) Analysis of mechanisms for achieving different ways of power transmission and motion of the anthropomorphic robots upper body. In: Proceedings of the international conference on power transmission (BAPT), Ohrid, pp 115–122
14. Penčić M et al (2016) Development of the multi-segment lumbar spine for humanoid robots. *Therm Sci* 20(Suppl. 2):S581–S590
15. Penčić M et al (2016) Comparative analysis of the shrug mechanisms for humanoid robots. In: Proceedings of the international conference on electrical, electronic and computing engineering (IcETRAN), Zlatibor, pp ROI1.3-1–ROI1.3-5
16. Penčić M et al (2016) Comparative synthesis of the shrug mechanisms for humanoid robots. In Proceedings of the international research/expert conference on trends in the development of machinery and associated technology (TMT), Mediterranean Sea Cruising, pp 249–252
17. Penčić M et al (2017) Optimal synthesis of the worm-lever mechanism for humanoid robots shrug. *Serb J Electr Eng* 14(2):245–256
18. Penčić M et al (2017) Development of the low backlash planetary gearbox for humanoid robots. *FME Trans* 45(1):122–129
19. Saldien J et al (2010) Expressing emotions with the social robot Probo. *Int J Soc Robot* 2(4): 377–389

20. Sosnowski S et al (2006) Design and evaluation of emotion-display EDDIE. In: Proceedings of the IEEE/RSJ international conference on intelligent robots and systems (IROS), Beijing, pp 3113–3118
21. Spexard TP et al (2007) Human-oriented interaction with an anthropomorphic robot. *IEEE Trans Rob* 23(5):852–862
22. Trovato G et al (2013) Generation of humanoid robot's facial expressions for context-aware communication. *Int J Humanoid Robot* 10(1):1350013-1–1350013-23
23. van Breemen AJN (2004) Animation engine for believable interactive user-interface robots. In: Proceedings of the IEEE/RSJ international conference on intelligent robots and systems (IROS), Sendai, pp 2873–2878
24. Zecca M et al (2009) Whole body emotion expressions for KOBIAN humanoid robot—preliminary experiments with different emotional patterns. In: Proceedings of the IEEE International Symposium on Robot and Human Interactive Communication (RO-MAN), Toyama, pp 381–386

# Drive System of the Robot Eyeballs and Eyelids with 8 DOFs



M. Penčić, M. Čavić, M. Rackov, B. Borovac and Z. Lu

**Abstract** Significant aspect of the socially interactive robots are eyes which present the most expressive part of the face, especially when it is rigid as is the case with majority of the robots. For this reason to the design and realization of the eyes a particular attention should be dedicated. This paper presents the drive system of the robot eyeballs and eyelids with 8 DOFs. Eyeballs drive system has 4 DOFs and consists of two symmetrical planar mechanisms that enable independent motion of the eyeballs about the yaw axis—abduction/adduction movements and two identical spatial mechanisms that enable independent motion of the eyeballs about the pitch axis—elevation/depression movements. Eyelids drive system has 4 DOFs and consists of four structurally equal spatial mechanisms that enable independent motion of each eyelid—mechanisms for driving the upper and lower eyelids, respectively, are symmetrical. Based on the kinematic analysis, motion simulation of eyeball and upper/lower eyelid is performed. Velocities of the eyeball/eyelids movements are within the parameters of the human eye. The structure of the eyeballs drive system is such that enables inserting the camera directly into the

---

M. Penčić (✉) · M. Čavić · M. Rackov · B. Borovac  
Faculty of Technical Sciences, University of Novi Sad, Novi Sad, Serbia  
e-mail: mpencic@uns.ac.rs

M. Čavić  
e-mail: scomaja@uns.ac.rs

M. Rackov  
e-mail: racmil@uns.ac.rs

B. Borovac  
e-mail: borovac@uns.ac.rs

Z. Lu  
School of Electrical Engineering and Automation, Changshu Institute of Technology,  
Changshu, China  
e-mail: zhenlilu@cslg.cn

Z. Lu  
State Key Laboratory of Robotics, Shenyang Institute of Automation,  
Chinese Academy of Sciences, Shenyang, China



eyeballs. In this way it is possible to achieve some of the functions of robots artificial vision such as recognizing objects, distance estimation etc.

**Keywords** Drive system • Robot eye mechanism • Planar linkage mechanism  
Spatial linkage mechanism

## 1 Introduction

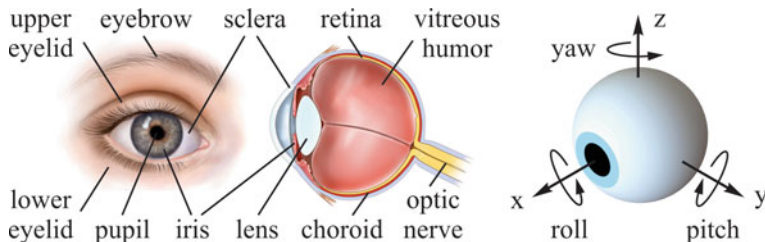
Active and natural eyes are extreme important for social robots. For example, following face in front of it robot gives an impression of attention and focus, while blinking gives the impression of naturalness. Besides, the intensity of openness and the position of the eyelids enable the expression of various emotions such as surprise, fatigue, sadness, etc. All this gets additional importance if the rest of the face is rigid and immobile, as it is the case with most robots. Therefore, special attention should be paid to the design and realization of the eyes. Also, if the cameras are inserted into the eyeballs, it is possible to achieve some of the artificial vision capabilities, such as the detection of a person in front of a robot, estimation of the distance from the robot, etc.

This paper presents the drive system of robot eyeballs and eyelids with 8 DOFs. The research was done in the framework of the project in which the social humanoid robot Sara—a mobile anthropomorphic platform for researching the social behavior of robots, has been developing. Some of the advanced capabilities of this robot are described in [15–17].

### 1.1 *Human Eye and Its Mobility*

The eye is a pair organ that consists of the eyeball, optic nerve and supporting structures—Fig. 1. The eyeball enables the reception of visual impressions thanks to the transparent structure of its media, the diopter system and the presence of neuroepithelial elements in the retina. Visual paths are connect the eyeball respectively the nerve membrane—retina with the visual centers in the brain, and thus the visual stimulus created on the retina is transmitted in the corresponding centers of the brain cortex, where they are interpreted [4, 11].

The eyeball has 3 DOFs enables rotation about the z axis—abduction/adduction movements, rotation about the y axis—elevation/depression movements and rotation about the x axis—excyclotorsion/incyclotorsion movements. Mobility is the largest about the yaw axis—approximate to  $89 \pm 13^\circ$ , then about the pitch axis—approximate to  $75 \pm 15^\circ$  [21], and at least about the roll axis.



**Fig. 1** Anatomy of human eye (left) and eyeball movements (right)

## 2 State of the Art

There are two basic groups of robots which can move the eyeballs and/or the eyelids independently from the face. The first group of the robot—Kismet [2], Domo [5], Flobi [8], iCub [13], Melvin [20], Probo [7], Twente [19], Muecas [3], EDDIE [22], KOBAN [23] etc., has eyeballs with 3 DOFs that enable the movements about the pitch axis and independent motion of the eyeballs about the yaw axis. The second group of robots—Robotinho [6], EveR-2 [1], Romeo [14], ROMAN [9], HUBO [12], KIBO [10] etc., has eyeballs with 4 DOFs that enable independent movements about the pitch and yaw axes.

Upper eyelids can be actuated together with the eyeballs or independently—it is possible to move each eyelid individually or both together, while the lower eyelids are usually immovable. Power transmission and motion from the actuators to the eyeballs and eyelids is usually performed by belt mechanisms, lever mechanisms and low backlash gear mechanisms that provide high positioning accuracy and repeatability of movements.

## 3 Robot Eyes Drive System

Figure 2 shows the face of social humanoid robot Sara that is rigid, while the eyes are movable. The eyeballs have 4 DOFs and enable independent motion about the pitch and yaw axes, while the eyelids have 4 DOFs and enable independent motion of all four eyelids about the pitch axis. An important requirement during the formation of eyes drive system was to emphasize the feminine characteristics of the eye, because the eyes are the most expressive part of the face. Therefore, the eyelids are rotated in two planes—about the  $z$  axis for the angle  $\alpha$ , and then about the  $x_L$  axis for an angle  $\beta$ . In addition, the upper eyelids have striking eyelashes.

Figure 3 shows the kinematic scheme of eyelids drive system that has 4 DOFs and enables independent motion of the upper/lower left eyelids about the  $y_L$  axis—angles  $\psi_{UL}$  and  $\psi_{LL}$  as well as independent movement of upper/lower right eyelids

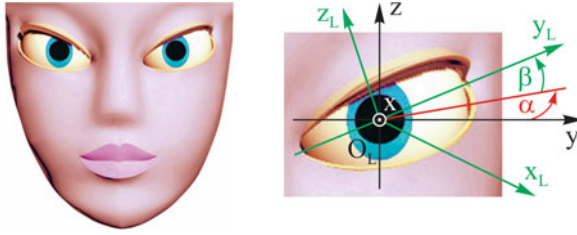


Fig. 2 Face of social humanoid robot Sara

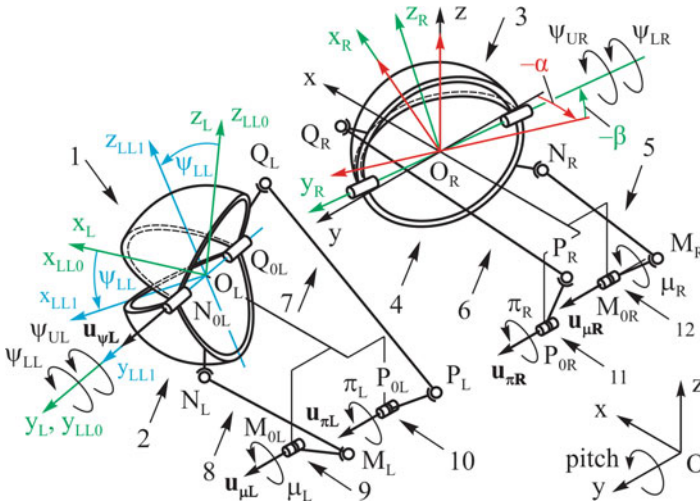


Fig. 3 Kinematic scheme of the eyelids drive system: 1 and 3—upper left and right eyelid, 2 and 4—lower left and right eyelid, 5, 6, 7 and 8—spatial mechanisms, 9 and 12—motors for driving lower eyelids, and 10 and 11—motors for driving upper eyelids

about the  $y_R$  axis—angles  $\psi_{UR}$  and  $\psi_{LR}$ . The immovable coordinate system  $O_Lx_Ly_Lz_L$  is rotated, relative to the global immovable system  $Oxyz$ , by angle  $\alpha$  about the  $z$  axis, and then by angle  $\beta$  about the  $x_L$  axis. The immovable coordinate system  $O_Rx_Ry_Rz_R$  is rotated, relative to the global immovable system  $Oxyz$ , by angle  $-\alpha$  about the  $z$  axis, and then by angle  $-\beta$  about the  $x_R$  axis. The eyelids drive system consists of four spatial mechanisms 5, 6, 7 and 8 which are actuated by motors 9, 10, 11 and 12—joints  $M_{OL}$ ,  $P_{OL}$ ,  $M_{OR}$  and  $P_{OR}$ . The upper/lower left eyelids 1 and 2, and upper/lower right eyelids 3 and 4 are spherical shells of thickness  $t$  with the centers in  $O_L$  and  $O_R$ , respectively. The mechanisms for driving the upper and lower eyelids are symmetrical and structurally equal and therefore only one eye—the left one is considered.

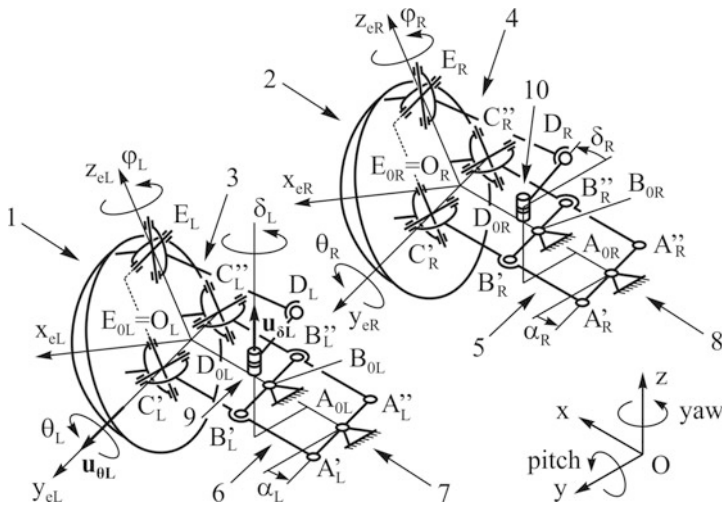
The spatial mechanism for driving the lower eyelid consists of input link  $M_{OL}M_L$ , floating link  $M_LN_L$  and output link—lower eyelid. Lever  $N_{OL}N_L$  will be considered the output link. The mechanism is of the RSSR type. The connection between the immovable link and the input link  $M_{OL}M_L$  is cylindrical joint in point  $M_{OL}$  enabling the rotation of one link relative to the other about an axis whose unit vector is  $\mathbf{u}_{\mu L}$ . The connection between the input link  $M_{OL}M_L$  and floating link  $M_LN_L$  is the spherical joint in the point  $M_L$ . The connection between the floating link  $M_LN_L$  and output link  $N_{OL}N_L$  is a spherical joint in the point  $N_L$ . The connection between the output link and the immovable link is the cylindrical joint in the point  $N_{OL}$  with rotation axis defined by unit vector  $\mathbf{u}_{\psi L}$ .

The spatial mechanism for driving the upper eyelid consists of input link  $P_{OL}P_L$ , floating link  $P_LQ_L$  and output link—upper eyelid. Lever  $Q_{OL}Q_L$  is considered the output link. The connection between the immovable link and the input link  $P_{OL}P_L$  is the cylindrical joint in point  $P_{OL}$  whose unit vector is  $\mathbf{u}_{\pi L}$ . The connection between the input link  $P_{OL}P_L$  and floating link  $P_LQ_L$  is the spherical joint in point  $P_L$ . The connection between the floating link  $P_LQ_L$  and output link  $Q_{OL}Q_L$  is a spherical joint in point  $Q_L$ . The connection between the output link and the immovable link is the cylindrical joint in point  $Q_{OL}$  with rotation axis defined by unit vector  $\mathbf{u}_{\psi L}$ .

Figure 4 shows the kinematic scheme of the eyeballs drive system that has 4 DOFs and enables independent motion of the eyeballs about the pitch and yaw axis—angles  $\theta_L$  and  $\theta_R$ , and  $\varphi_L$  and  $\varphi_R$ , respectively. Eyeballs 1 and 2 are spheres of radius  $r$  with a center in points  $O_L$  and  $O_R$ , respectively. Eyeball movements about the pitch axis are enabled by two identical spatial mechanisms 3 and 4 which are actuated by motors 9 and 10—joints  $D_{OL}$  and  $D_{OR}$ . Eyeball movements about the yaw axis are enabled by two identical planar mechanisms 5 and 6 which are actuated by motors 7 and 8—the joints  $A_{OL}$  and  $A_{OR}$ . Given that mechanisms 3 and 4, and 5 and 6 are identical, only one eyeball is considered, the left one, and the indices L—left and R—right, can be neglected. Due to the structure of the links, the mechanisms can function independently. Local coordinate system with the center in point O and axes  $x_e$ ,  $y_e$ ,  $z_e$  is fixed to the eyeball and in the initial position, axes  $x_e$ ,  $y_e$ ,  $z_e$  are parallel with the axes of global coordinate system Oxyz.

The planar mechanism consists of two four-bar linkages  $A_0A'B'B_0$  and  $A_0A''B''B_0$ . Points A', A<sub>0</sub>, and A'', as well as points B', B<sub>0</sub>, and B'' are located on the same lever. Angle  $\alpha$  is an input parameter and represents the rotation of lever A'A'' about point A<sub>0</sub>. Four-bar linkages are of the parallelogram configurations so  $A_0A' = B'B_0$  and  $A_0A'' = B''B_0$ . In addition  $A_0A' = A_0A''$ ,  $B'B_0 = B''B_0$ ,  $A'B' = A''B''$  and  $C'B' = C''B''$ . Links between the eyeballs and the mechanisms—points C' and C'', are of the second order and enable two rotations whereby the axes of rotation are mutually perpendicular. One axis is parallel to the y axis, and the other with the z<sub>e</sub> axis. Centers of the links—points C' and C'' are on the y<sub>e</sub> axis.

The spatial mechanism represents a four-bar linkage of RSCR configuration. The input link is lever  $D_0D$  which is by a cylindrical joint connected to an immovable link in the point  $D_0$ . Lever  $D_0D$  performs a rotation by angle  $\delta$  about an axis whose unit vector is  $\mathbf{u}_\delta$ . Lever  $D_0D$  is connected by spherical joint to the floating link DE in point D. Link DE is connected to the output link—eyeball at point E with a



**Fig. 4** Kinematic scheme of the eyeballs drive system: 1 and 2—left and right eyeball, 3 and 4—spatial mechanisms, 5 and 6—planar mechanisms, 7 and 8—motors for abduction/adduction movements, 9 and 10—motors for elevation/depression movements

second order connection, which is on the  $z_e$  axis. The rotation axes are mutually perpendicular—one axis is parallel to the  $y_e$  axis, and the other is at the initial position parallel to the  $z$  axis.

## 4 Motion Simulation—Results

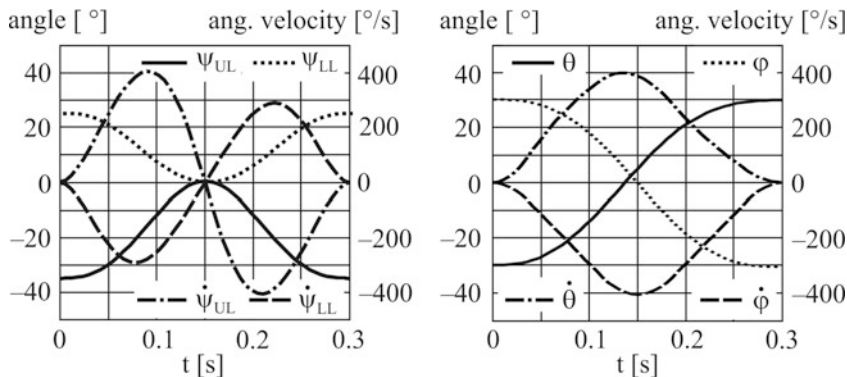
The motion simulation is performed based on the equations that are shown in [18], using MATLAB software. Adopted law of the input link displacement is a fifth degree polynomial. For the known geometric and input kinematic parameters of the eyeball and eyelids—Table 1, the output kinematic parameters of the eyeballs  $\varphi(t), \dot{\varphi}(t)$  and  $\theta(t), \dot{\theta}(t)$  as well as those of the upper/lower eyelid  $\psi_{LL}(t), \dot{\psi}_{LL}(t)$  and  $\psi_{UL}(t), \dot{\psi}_{UL}(t)$  are determined, which is shown in Fig. 5.

The upper eyelid performs a movement from  $0^\circ$  to  $35^\circ$  – closing the eyelid and from  $35^\circ$  to  $0^\circ$  – opening the eyelid, total duration is 0.3 s. In the initial position, the upper eyelid is opened and is rotated by  $-35^\circ$  about the  $y_L$ , i.e. the eyelid is in the upper end position. The maximum value of angular velocity is  $400^\circ/s$ .

The lower eyelid performs a movement from  $0^\circ$  to  $25^\circ$ —closing the eyelid and from  $25^\circ$  to  $0^\circ$ —opening the eyelid, total duration is 0.3 s. In the initial position the lower eyelid is opened and is rotated by  $25^\circ$  about the  $y_L$  axis, i.e. the eyelid is in the lower end position. The maximum value of angular velocity is  $300^\circ/s$ .

**Table 1** Input geometric and kinematic parameters of the eyeball and lower/upper eyelid; notation:  $\mathbf{p}_{0L}$ —position vector of immovable point  $P_{0L}$ ,  $\mathbf{p}_{sL}$ —position vector of point  $P_L$  in initial position ( $\pi L=0$ ) and  $\mathbf{u}_{\pi L}$ —unit vector of axis  $\pi L$

Upper eyelid		Lower eyelid			Eyeball						
Vector	Coordinates [mm]			Vector	Coordinates [mm]			Vector	Coordinates [mm]		
	x	y	z		x	y	z		x	y	z
$\mathbf{p}_{0L}$	-120	45	-12	-120	-45	-30	$\mathbf{d}_{0L}$	-100	10	25	
$\mathbf{p}_{sL}$	-109.43	45	10.66	-117.82	-45	-54.90	$\mathbf{d}_{sL}$	-100	-15	25	
$\mathbf{u}_{\pi L}$	0	1	0	0	1	0	$\mathbf{u}_{\delta L}$	0	0	1	
$\mathbf{q}_{0L}$	-11.24	25.85	10.26	-11.24	25.85	10.26	$\mathbf{e}_{0L}$	0	0	0	
$\mathbf{q}_{sL}$	-24.34	16.14	-27.33	-10.44	-30.04	-24.25	$\mathbf{e}_{sL}$	-12.04	0	17.20	
$\mathbf{u}_{\varphi L}$	-0.37	0.86	0.34	-0.37	0.86	0.34	$\mathbf{u}_{\theta L}$	0	1	0	



**Fig. 5** Motion simulation: upper/lower eyelids movements (left) and eyeball movements (right)

Eyeball movement in the direction of elevation/depression is  $60^\circ$ . In the initial position the eyeball is rotated about the y axis by  $-30^\circ$ . The duration of the movement is 0.3 s. The maximum value of angular velocity is  $400^\circ/\text{s}$ .

Eyeball movement in the direction of abduction/adduction is  $60^\circ$ . In the initial position the eyeball is rotated about the z axis by  $30^\circ$ . The duration of the movement is 0.3 s. Maximal value of angular velocity is  $400^\circ/\text{s}$ .

## 5 Conclusions

This paper presents the drive system of the robot eyeballs and eyelids with 8 DOFs. The eyeballs drive system has 4 DOFs and consists of two symmetrical planar mechanisms that enable independent motion of the eyeballs about the yaw axis—abduction/adduction movements and two identical spatial mechanisms that enable independent motion of the eyeballs about the pitch axis—elevation/depression movements. The eyelids drive system has 4 DOFs and consists of four structurally equal spatial mechanisms that enable independent motion of each eyelid—the mechanisms for driving the upper and lower eyelids, respectively, are symmetrical. Based on the kinematic analysis, the motion simulation of eyeball and upper/lower eyelid is performed. Velocities of eyeball/eyelids movements are within the parameters of the human eye. The proposed solution enables the inserting the camera directly into the eyeball enabling the artificial vision function of the robot. In addition, eyelids are rotated in two planes—see Fig. 2, thus mimicking the appearance of female eye. Further research will examine the impact of geometrical parameters on the kinematic characteristics in order to increase the velocity of movement of the eyelids and the eyeball, which require an optimal synthesis.

**Acknowledgements** This research was funded by the Ministry of Education, Science and Technological Development of the Republic of Serbia under the contract III44008 and by the Provincial Secretariat for Higher Education and Scientific Research of AP Vojvodina under the contract 114-451-2116/2011. It is also supported by the National Science Foundation of China under the contract 61473283 and by the Chinese State Key Laboratory of Robotics under the contract 2014-O08.

## References

1. Ahn HS et al (2011) Development of an android for singing with facial expression. In: Proceedings of the IEEE industrial electronics society (IECON), Melbourne, pp 104–109
2. Breazeal C (2003) Emotion and sociable humanoid robots. *Int J Hum Comput Stud* 59(1–2): 119–155
3. Cid F et al (2014) Muecas: a multi-sensor robotic head for affective human robot interaction and imitation. *Sensors* 14(5):7711–7737
4. Cvetković D et al (2010) Ophthalmology for medical students (in Serbian). University of Belgrade, Faculty of Medicine, Belgrade
5. Edsinger-Gonzales A et al (2004) Domo: a force sensing humanoid robot for manipulation research. In: Proceedings of the IEEE-RAS international conference on humanoid robots (Humanoids), Santa Monica, pp 273–291
6. Faber F et al (2009) The humanoid museum tour guide Robotinho. In: Proceedings of the IEEE international symposium on robot and human interactive communication (RO-MAN), Toyama, pp 891–896
7. Goris K et al (2011) Mechanical design of the huggable robot Probo. *Int J Hum Rob* 8(3): 481–511
8. Hegel F et al (2010) The social robot ‘Flobi’: key concepts of industrial design. In: Proceedings of the IEEE international symposium in robot and human interactive communication (RO-MAN), Viareggio, pp 107–112
9. Hirth J et al (2007) Emotional architecture for the humanoid robot head ROMAN. In: Proceedings of the IEEE international conference on robotics and automation (ICRA), Roma, pp 2150–2155
10. Lee S et al (2013) Development and walking control of emotional humanoid robot, KIBO. *Int J Hum Rob* 10(4):1350024-1–1350024-35
11. Litričin O et al (2004) Ophthalmology (in Serbian). *Elit Medica*, Belgrade
12. Park I-W et al (2007) Mechanical design of the humanoid robot platform, HUBO. *Adv Rob* 21(11):1305–1322
13. Parmiggiani A et al (2011) The design of the iCub humanoid robot. *Int J Hum Rob* 9(4): 1250027-1–1250027-24
14. Pateromichelakis N et al (2014) Head-eyes system and gaze analysis of the humanoid robot Romeo. In: Proceedings of the IEEE/RSJ international conference on intelligent robots and systems (IROS), Chicago, pp 1374–1379
15. Penčić M et al (2017) Optimal synthesis of the worm-lever mechanism for humanoid robots shrug. *Serb J Electr Eng* 14(2):245–256
16. Penčić M et al (2016) Analysis of mechanisms for achieving different ways of power transmission and motion of the anthropomorphic robots upper body. In: Proceedings of the international conference on power transmission (BAPT), Ohrid, pp 115–122
17. Penčić M et al (2016) Development of the multi-segment lumbar spine for humanoid robots. *Thermal Sci* 20(Suppl. 2):S581–S590
18. Penčić M et al (2017) Kinematic analysis of the robot eyes drive system with 7 DOFs. In: Proceedings of the PSU-UNS international conference on engineering and technology (ICET), Novi Sad, pp PS-1.14-1–PS-1.14-5



19. Reilink R et al (2011) Mechatronic design of the Twente humanoid head. *Intell Serv Robot* 4(2):107–118
20. Shayganfar M et al (2012) A design methodology for expressing emotion on robot faces. In: *Proceedings of the IEEE/RSJ international conference on intelligent robots and systems (IROS)*, Vilamoura, pp 4577–4583
21. Shin Y et al (2016) Normal range of eye movement and its relationship to age. *Acta Ophthalmol* 94(suppl. 256), n/a–n/a
22. Sosnowski S et al (2006) Design and evaluation of emotion-display EDDIE. In: *Proceedings of the IEEE/RSJ international conference on intelligent robots and systems (IROS)*, Beijing, pp 3113–3118
23. Zecca M et al (2008) Design of the humanoid robot KOBIAN—preliminary analysis of facial and whole body emotion expression capabilities. In: *Proceedings of the IEEE-RAS international conference on humanoid robots (Humanoids)*, Daejeon, pp 487–492

# Method for the Kinetostatic Analysis of the Road Vehicles Axle Suspensions



C. Alexandru

**Abstract** The purpose of the research is to develop a numerical method for the kinetostatic analysis of linkages that guide the rear beam axle of some road vehicles (mainly, commercial and off-road vehicles). The study is performed in two distinctive stages, which are then integrated in an unitary numerical algorithm, with the aim to evaluate the way in which the suspension system behaves under various loading states. For beginning, the static equilibrium of the suspension mechanism is expressed by considering the external loads and the reactions that occur in the force generating elements of the suspension system, depending on the linear and angular deformations of these flexible (compliant) elements. In the second stage, the kinematics of the suspension mechanism is performed by an original analytical algorithm, with the aim to establish the variations of the global coordinates of the design points that are used to express the linear and angular deformations of the compliant elements. Then, the two algorithms are coupled in an optimization problem that intend to determine the value(s) of the independent kinematic parameter(s) for which the minimum value of the static equation is reached.

**Keywords** Kinetostatic analysis • Linkage • Road vehicles • Beam axle  
Compliant elements

## 1 Introduction

The suspension system has a crucial role for the handling and stability performance of the road vehicles, the quality of the suspension being also reflected in the comfort performance [3, 4, 6]. For the vehicles with two axles (front—rear), the design of the front suspension is different from that of the rear suspension, having in view the available mounting space and the loading regime on axles, the study developed in this paper being focused on the rear suspension system.

---

C. Alexandru (✉)  
Transilvania University of Braşov, Braşov, Romania  
e-mail: calex@unitbv.ro

The guidance of the rear wheels of the road vehicles can be achieved independently (each wheel being equipped with its own suspension mechanism), or with a dependent suspension design, in which the wheels are connected laterally by a beam axle, whose motion relative to the vehicle chassis is constrained by a set on guiding bars, disposed in various configurations.

For the nowadays road vehicles, the independent suspension design is used mostly at light (passenger) cars, while the beam axle suspension design is frequently implemented on the commercial and off-road vehicles, due to their specific operating requirements. The main benefits of the beam axle come from its simplicity, which is reflected in a space-efficient solution, and a better durability.

The arms of the axle suspension linkage are usually connected to the adjacent elements (axle and chassis) by bushings (compliant joints), which are subject to linear and angular deformations, thus generating elastic reaction forces and torques. The study of the influence of these deformations on the kinematic and dynamic behavior of the suspension system is a key subject for the beam axle design [7, 8, 12]. Based on the study performed in [13], the influence of the linear deformations on the guiding accuracy of the beam axle is not a significant one, much more important being the angular capability of the bushings.

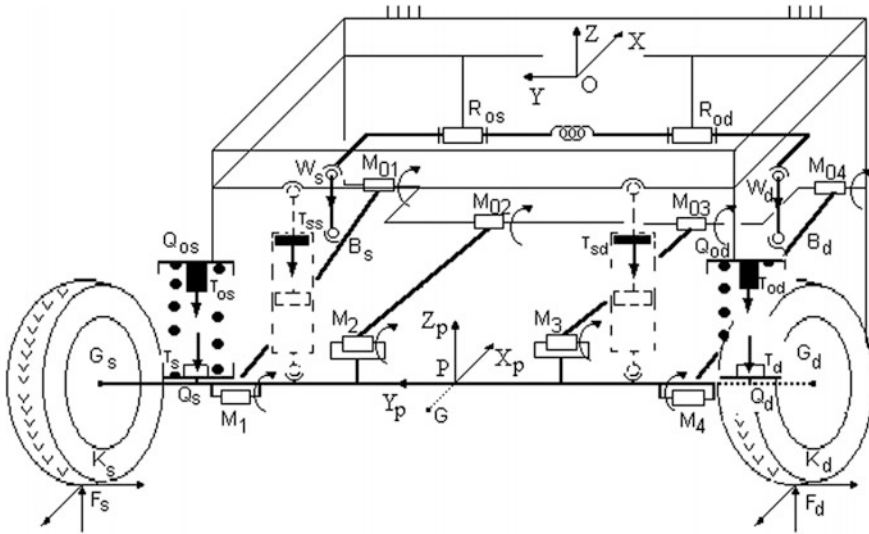
Thus, for the study developed in this work, the bushings have been modeled as compliant spherical (ball) joints, whose travel is defined as the angular displacement between the two connected parts (guiding arm—axle, and respectively guiding arm—chassis), quantifying in fact the amount of swing angle of the ball stud relative to the ball housing. In these terms, axle suspension linkages with low number of degrees of mobility ( $DOM = 1$ , and  $DOM = 2$ ) are obtained, a detailed systematization based on the ball joint supposition being presented in [1].

The scientific literature show several methods/approaches for determining the equilibrium state of the vehicle suspension systems, with application for the front or rear wheels/axle [9–11]. Usually, these methods are developed—applied for a specific suspension mechanism, being difficult to understand how they could be adapted (transposed) for any suspension design.

Under these terms, in this work, the kinetostatic analysis of the beam axle suspension system is approached with the aim of developing a general numerical algorithm to find the equilibrium configuration, which to be applicable to most existing suspension systems. In the numerical function by which the equilibrium configuration is modeled, there are considered the external loads and the reactions that occur in the elastic elements of the suspension system (springs, bump-stops, antiroll bar, bushings), depending on their linear and angular deformations.

## 2 Defining the Static Equilibrium

In order to define the static model of the beam axle suspension, there have been considered/defined two types of reference coordinate systems, as shown in Fig. 1: the global coordinate system (OXYZ), connected to the vehicle chassis, which is



**Fig. 1** Beam axle suspension system

the fixed part of the model (this being one of the simplified assumptions used in the static analysis); the local coordinate systems ( $PX_P Y_P Z_P$  and/or  $M_i X_{M_i} Y_{M_i} Z_{M_i}$ ), connected to the beam axle of the vehicle, and respectively to the specific links (bars) of the axle guiding linkage. The locations of the specific design points are expressed in the two types of the reference coordinate systems, in terms of global and local Cartesian coordinates.

The center  $O$  of the vehicle reference coordinate system belongs to a technological frame, defined by the manufacturer, the global axes  $XYZ$  being oriented in the following way: the longitudinal axis  $X$  points backward (from the front to the back), the transversal axis  $Y$  is directed to the right, while the vertical axis  $Z$  upwards, thus obtaining a right-handed coordinate system. The centers of the local reference coordinate systems are located at the middle of the beam axle ( $P$ ), and respectively of the compliant joint used to connect the specific link (bar) to the beam axle ( $M_i$ ). In the initial (modeling) configuration of the suspension system, at the beginning of the analysis, all the local reference coordinate systems are parallel to the global one, the way in which the relative position and orientation of the local systems towards the global system is established during the simulation being approached in the 3rd section of the paper (in terms of kinematic behavior).

Under the action of the reaction forces occurring in the contacts between the vehicle tires and the driveway, the axle guiding linkage (including the beam axle) changes its configuration, in terms of spatial position and orientation relative to the global reference coordinate system, thus deforming the compliant/elastic components of the suspension (helical springs, bump-stops, anti-roll bar) and generating the corresponding elastic reactions.

In the static analysis, the contact forces on tires ( $F_{s,d}$ , which are applied in  $K_{s,d}$ —see Fig. 1) are known input data, which can be obtained from the general dynamics of the vehicle, while the reaction forces in the compliant components can be determined in accordance with the numerical algorithm for the positional analysis presented in the 3rd section of the paper, which allow to establish the corresponding deformations of the compliant components (from the spatial position and orientation of the axle guiding linkage relative to the vehicle chassis), and the procedure described in [2], by which the correlations between the elastic deformations and reactions are defined.

By considering the two structural groups of axle guiding linkages—with one or two degrees of mobility (in accordance with those presented in the 1st section of the paper), the balance configuration of the suspension system (where the applied and reaction forces/torques reach the equilibrium) can be expressed in terms of global vertical coordinates (in OXYZ) of the wheel(s) centre(s), meaning  $Z_{Gs}$  for the mono-mobile axle guiding linkages, and respectively  $Z_{Gs}$  and  $Z_{Gd}$  for the bi-mobile guiding linkages. These vertical global coordinates are the independent motion parameters for the positional (kinematic) analysis, which is approached in the next section of the work.

In accordance with those shown Fig. 1, the following notations for the reaction forces/torques in the compliant components of the suspension are used in the numerical algorithm presented below:  $F_{as,d}$ —for the helical springs,  $F_{ts,d}$ —for the bump-stops,  $F_{ws,d}$ —for the anti-roll bar,  $M_f$ —for the compliant joints by which the guiding links are connected on axle and chassis.

In these terms, the following equation can be used to express the static balance state of the beam axle suspension system (i.e. the configuration in which the forces and torques acting upon the suspension system is zero), in terms of virtual works:

$$\begin{aligned} F_s \cdot \delta r_{Ks} + F_d \cdot \delta r_{Kd} + F_{as} \cdot \delta r_{Qs} + F_{ad} \cdot \delta r_{Qd} + F_{ts} \cdot \delta r_{Ts} + F_{td} \cdot \delta r_{Td} \\ + F_{ws} \cdot \delta r_{Ws} + F_{wd} \cdot \delta r_{Wd} + \sum_{i=1}^n (M_f \cdot \delta \varphi_f)_i = 0 \end{aligned} \quad (1)$$

where  $n$  represents the number of compliant joints (connections) from the multi-link axle guiding mechanism, while  $\delta r/\delta \varphi$  are the virtual displacements/rotations, which are expressed in correlation with the independent motion parameters ( $Z_{Gs}$ , respectively  $Z_{Gs}$  and  $Z_{Gd}$ —depending on the number of degrees of mobility). By replacing the virtual displacements and rotations in the virtual works Eq. (1), the following functions are obtained:

$$\begin{aligned} F(Z_{Gs}) = F_s \cdot \frac{\partial r_{Ks}}{\partial Z_{Gs}} + F_d \cdot \frac{\partial r_{Kd}}{\partial Z_{Gs}} + F_{as} \cdot \frac{\partial r_{Qs}}{\partial Z_{Gs}} + F_{ad} \cdot \frac{\partial r_{Qd}}{\partial Z_{Gs}} + F_{ts} \cdot \frac{\partial r_{Ts}}{\partial Z_{Gs}} \\ + F_{td} \cdot \frac{\partial r_{Td}}{\partial Z_{Gs}} + F_{ws} \cdot \frac{\partial r_{Ws}}{\partial Z_{Gs}} + F_{wd} \cdot \frac{\partial r_{Wd}}{\partial Z_{Gs}} + \sum_{i=1}^n \left( M_f \cdot \frac{\partial \varphi_f}{\partial Z_{Gs}} \right)_i = 0 \end{aligned} \quad (2)$$

$$\begin{aligned}
F(Z_{Gs}, Z_{Gd}) = & F_s \cdot \frac{\partial r_{Ks}}{\partial Z_{Gs,d}} + F_d \cdot \frac{\partial r_{Kd}}{\partial Z_{Gs,d}} + F_{as} \cdot \frac{\partial r_{Qs}}{\partial Z_{Gs,d}} + F_{ad} \cdot \frac{\partial r_{Qd}}{\partial Z_{Gs,d}} + F_{ts} \cdot \frac{\partial r_{Ts}}{\partial Z_{Gs,d}} \\
& + F_{td} \cdot \frac{\partial r_{Td}}{\partial Z_{Gs,d}} + F_{ws} \cdot \frac{\partial r_{Ws}}{\partial Z_{Gs,d}} + F_{wd} \cdot \frac{\partial r_{Wd}}{\partial Z_{Gs,d}} + \sum_{i=1}^n \left( M_f \cdot \frac{\partial \varphi_f}{\partial Z_{Gs,d}} \right)_i = 0
\end{aligned} \tag{3}$$

where Eq. (2) corresponds to the beam axle suspension systems based on mono-mobile guiding linkages, while Eq. (3) is specific for bi-mobile linkages.

In this way, the static balance position/configuration is that in which the function (2) or (3) reaches the minimum, and it is defined by the corresponding value(s) of the specific independent motion parameter(s)  $Z_{Gs}/Z_{Gs}$  and  $Z_{Gd}$  (the design variable (s) in the optimal design process).

Considering a particular set of values for the applied forces on tires  $F_{s,d}$  (in correlation with the specific regime, e.g. traction, braking, stationary), the up-down motion range of the wheels (which is determined by the extreme limits  $Z_{Gs/d \min}$ ,  $Z_{Gs/d \max}$ ) is splitted in a list of discrete values, by considering the increment  $\Delta Z_{Gs/d}$ . In the first iteration, the value(s) of the independent motion parameter(s) will be the very minimum value(s)  $Z_{Gs/d \min}$ , while a particular iteration  $k$  from the wheel motion range is defined by  $Z_{Gs/d}^k = Z_{Gs/d}^{k-1} + \Delta Z_{Gs/d}$ , the iterative process being repeated until  $Z_{Gs/d} = Z_{Gs/d \max}$ .

For each iteration defined in this way, there are performed the followings operations (steps):

- establishing the global coordinates of the mounting points of the compliant components of the suspension (e.g.  $X_{Qs,d}$  for the helical springs) by the positional (kinematic) analysis of the multi-link axle guiding mechanism, which is approached in the next section of the paper;
- establishing the deformations and elastic reactions of the compliant components (e.g.  $F_{as,d}$  for the helical springs), in correlation with those presented in [2];
- determining the corresponding value of the design objective function (2) or (3).

In the end, from the so obtained set of values, the optimal design is selected, corresponding to the minimum value of the design objective function  $F(Z_{Gs})$ , and respectively  $F(Z_{Gs}, Z_{Gd})$ , which defines the static balance state (configuration) of the beam axle suspension system.

### 3 Kinematics of the Axle Suspension Mechanisms

As presented in the previous section of the work, the kinematic analysis of the axle guiding linkages is a part of the general algorithm for the static analysis, with the purpose to determine the spatial positioning (position and orientation) of the guiding linkage, having as central element the beam axle, relative to the vehicle chassis (which is the fixed/reference part of the system). The scientific literature in

the field shows several methods for performing the kinematic analysis of the multi-link axle/wheel guiding mechanisms, a detailed discussion on some representative methods being presented in [4].

In this work, the kinematic analysis of the multi-link axle guiding mechanism is carried out by an original numerical algorithm, which proved to have unitary and general character while also avoiding some known issues of other existing methods. By reference to the algorithm presented in [5], significant improvements are brought by the method described below, mainly related to the accuracy of the initial solution, and the convergence of the system.

In the concept of the proposed method, the kinematic behavior (i.e. the spatial position and orientation) of the multi-link axle guiding mechanisms is analytically described by a non-linear system that include the constraint equations of the guiding points of the axle (depending on the structural variant of mechanism, in accordance with the systematization presented in [1]), to which the rigid body equations for the rear axle are added. For example, the kinematics of the 4-link guiding axle mechanism shown in Fig. 1 (with  $DOM = 2$ ) is defined by the following set of 7 equations:

$$(X_{M_i} - X_{M_{0i}})^2 + (Y_{M_i} - Y_{M_{0i}})^2 + (Z_{M_i} - Z_{M_{0i}})^2 - M_i M_{0i}^2 = 0, \quad i = 1 \dots 4 \quad (4)$$

$$\begin{aligned} (X_G - X_{G_d})^2 + (Y_G - Y_{G_d})^2 + (Z_G - Z_{G_d})^2 - GG_d^2 &= 0 \\ (X_G - X_{G_s})^2 + (Y_G - Y_{G_s})^2 + (Z_G - Z_{G_s})^2 - GG_s^2 &= 0 \\ (X_{G_s} - X_{G_d})^2 + (Y_{G_s} - Y_{G_d})^2 + (Z_{G_s} - Z_{G_d})^2 - G_s G_d^2 &= 0 \end{aligned} \quad (5)$$

where Eq. (4) define the geometric constraints, in this case 4 constant distance conditions between pairs of points located on axle ( $M_i$ ) and chassis ( $M_{0i}$ ), while Eq. (5) are used to model the rigid body feature of the axle. The three specific points whose global coordinates define the rigid body conditions (5) are the centers of the left and right wheels ( $G_s$  and  $G_d$ ), in other words the extremities of the axle, to which a third point ( $G$ ) from the axle plane is added (see Fig. 1).

Each guiding point  $M_i$  of the axle can be expressed in correlation with the three specific points  $G_s$ ,  $G_d$  and  $G$ , under the form:

$$\begin{aligned} (X_{M_i} - X_{G_s})^2 + (Y_{M_i} - Y_{G_s})^2 + (Z_{M_i} - Z_{G_s})^2 - M_i G_s^2 &= 0, \\ (X_{M_i} - X_{G_d})^2 + (Y_{M_i} - Y_{G_d})^2 + (Z_{M_i} - Z_{G_d})^2 - M_i G_d^2 &= 0, \\ (X_{M_i} - X_G)^2 + (Y_{M_i} - Y_G)^2 + (Z_{M_i} - Z_G)^2 - M_i G^2 &= 0. \end{aligned} \quad (6)$$

The 3-equation non-linear system (6) was solved by subtracting the first equation from the other two, resulting two linear equations in  $X_{M_i}$  and  $Y_{M_i}$  as functions of  $Z_{M_i}$ . These functions are replaced in the first equation of the system, resulting in this way a quadratic equation in  $Z_{M_i}$  with the well-known solution, which is then used to determine the other two global coordinates  $X_{M_i}$  and  $Y_{M_i}$ .

In the next stage, the general non-linear system formed by Eqs. (4) and (5) is solved by using the Newton-Kantorovich iterative method, the initial solution of the system (in the first iteration) being accurately established in correlation with the initial position of the axle coordinate system, which is expressed by the set of global coordinates  $\{X_P, Y_P, Z_P\}^0$ , and the local coordinates of the three specific points in  $PX_P Y_P Z_P \{X_{G_s, G_d, G}, Y_{G_s, G_d, G}, Z_{G_s, G_d, G}\}^P$  (all these coordinates being known input data).

The iterative algorithm is repeated until the entire up-down motion travel of the wheel(s) is covered, in a particular position (configuration)  $k$ , the solution obtained in the previous position  $k - 1$  acting as initial solution. In this way, the kinematic behavior of the multi-link guiding mechanism is determined, the results of the positional analysis being then used for establishing the deformations and the corresponding reaction forces in the elastic components of the suspension, thus allowing the evaluation/computation of the static function (2) or (3).

## 4 Results and Conclusions

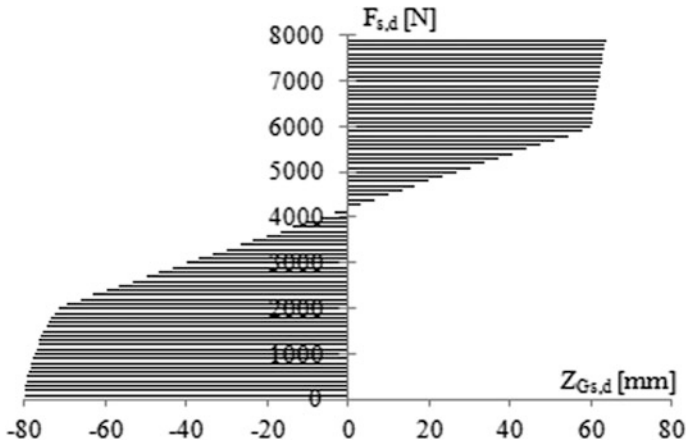
The numerical algorithm was transposed in computer code by using the programming language C++. Several variants of suspension systems (based on multi-link guiding mechanisms with  $DOM = 1$  and  $DOM = 2$ ) have been analyzed by running the in-house made application, by considering some representative static cases, such as stationary, traction or braking, which are reflected in the set of values for the applied forces on tires as result of the contact with the road surface (driveway).

For this paper, the kinetostatic analysis was performed for a suspension system based on bi-mobile guiding linkage, which is similar (equivalent) to the solution shown in Fig. 1. The suspension system was tested by considering the stationary static regime, which is materialized by a set of vertical forces applied on wheels, in the variation domain  $F_{s,d} \in [0, 8000]$  N. The results of the analysis, in terms of equilibrium position (which is expressed by the vertical coordinates  $Z_{G_s, d}$  of the wheels centers) are shown in Fig. 2. In the stationary empty position ( $F_{s,d} \approx 4200$  N), the equilibrium state is defined by  $Z_{G_s, d} \approx 0$ , this being in good correlation with the value on the real vehicle, which demonstrates the viability of the method.

By reference to other methods from literature, the numerical algorithm proposed in this work brings several important benefits for the kinetostatic analysis of the beam axle suspension systems, such as the degree of applicability (the method can be implemented for most known axle suspension systems, in unitary way), the fast convergence of the non-linear system used to model the kinematic behavior of the axle guiding mechanisms, the accurate selection of the initial solution from which is going to solve the system.

The mode in which the deformations of the compliant components are defined in correlation with the spatial positioning of the mounting points, through an original kinematic approach, allows the facile integration with the computing algorithm of the force equilibrium state, which is conducted as an optimal design process, aiming





**Fig. 2** Results of the kinetostatic analysis

the minimization of the static function. For a further work, the author intends to adapt the method for the kinetostatic analysis of the independent wheels suspensions, which are frequently used in nowadays passenger cars.

## References

1. Alexandru C (2009) The kinematic optimization of the multi-link suspension mechanisms used for the rear axle of the motor vehicles. *Proc Rom Acad* 10(3):244–253
2. Alexandru C, Barbu I (2010) The modeling of the elastic and damping elements from the suspension system of the cars axle. In: *Proceedings of 8th symposium on mechanisms and mechanical transmission*, pp 33–38
3. Alexandru C, Alexandru P (2011) A comparative analysis between the vehicles' passive and active suspensions. *Int J Mech* 5(4):371–378
4. Alexandru C, Țoțu V (2016) Method for the multi-criteria optimization of car wheel suspension mechanisms. *Ing e Investig* 36(2):60–67
5. Alexandru C (2016) Analytical method for determining the static equilibrium position of the rear axles guiding mechanisms of the motor vehicles. *Appl Mech Mater* 841:59–64
6. Alexandru P, Macaveiu D, Alexandru C (2012) Design and simulation of a steering gearbox with variable transmission ratio. *Proc Inst Mech Eng—Part C J Mech Eng Sci* 226(10):2538–2548
7. Ambrosio J, Verissimo P (2009) Sensitivity of a vehicle ride to the suspension bushing characteristics. *J Mech Sci Technol* 23(4):1075–1082
8. Knapczyk J, Maniowski M (2002) Selected effects of bushings characteristics on five-link suspension elastokinematics. *Mob Veh Mech* 3(2):107–121
9. Knapczyk J, Maniowski M (2006) Elastokinematic modeling and study of five-rod suspension with subframe. *Mech Mach Theory* 41(9):1031–1047
10. Livermore DF (1987) The determination of the equilibrium configurations of spring restrained mechanisms using 4x4 matrix method. *J Eng Ind*, 87–91

11. Stroe I, Staicu Ş (2010) Calculus of joint forces using Lagrange equations and principle of virtual work. *Proc Rom Acad—Ser A* 11(3):253–260
12. Țoțu V, Alexandru C (2013) Study concerning the effect of the bushings' deformability on the static behavior of the rear axle guiding linkages. *Appl Mech Mater* 245, 132–137
13. Verissimo P, Ambrosio J (2006) Improved bushing models for vehicle dynamics. In: *Proceedings of 3rd European conference on computational mechanics*, pp 1–20

# Forces Transmission at Structural Group 0/4/2



C. Duca and Fl. Buium

**Abstract** The paper uses as forces transmission quality index the coefficient's determinant of the system serving to static analysis without friction. Then it does the connection between this determinants value and the configuration parameter, expressing the length between exterior joints centres. Aided this length, the conditions for a favourable transmission regime, it formulates. It formulates also the driving link rotatability condition for the simplest mechanism, containing the 0/4/2 structural group.

**Keywords** Forces transmission index · 042 structural group · Configuration parameter · Singularity · Mechanism self-locking

## 1 Introduction

The 0/4/2 structural group (0—degree of freedom, 4—class, 2—order), has a relative reduced usage in mechanism's practice, but its behavior analysis is however useful. This paper deals with the variant containing revolute pairs only, Fig. 1, as being the most used in practice. As we showed in a series of previous papers [5–12], singularities, self-blocking and forces transmission are connected each other phenomena and have specified characteristics for each structural group, as it will result from this paper too. We mention that general meaning of specialists, the essential index of forces transmission quality is the transmission angle (or the pressure angle) [1–4]. But, this index can be applied to simple mechanisms only—four-bar linkage and slider-crank) because these contain only one structural group. The attempts to extend pressure angle usage for the 6 link mechanisms did not lead to favorable results, in our opinion. Starting from the essential idea that

---

C. Duca · Fl. Buium (✉)

“Gheorghe Asachi” Technical University of Iasi, Iasi, Romania  
e-mail: fbuium@gmail.com

C. Duca

e-mail: cdduca@hotmail.com

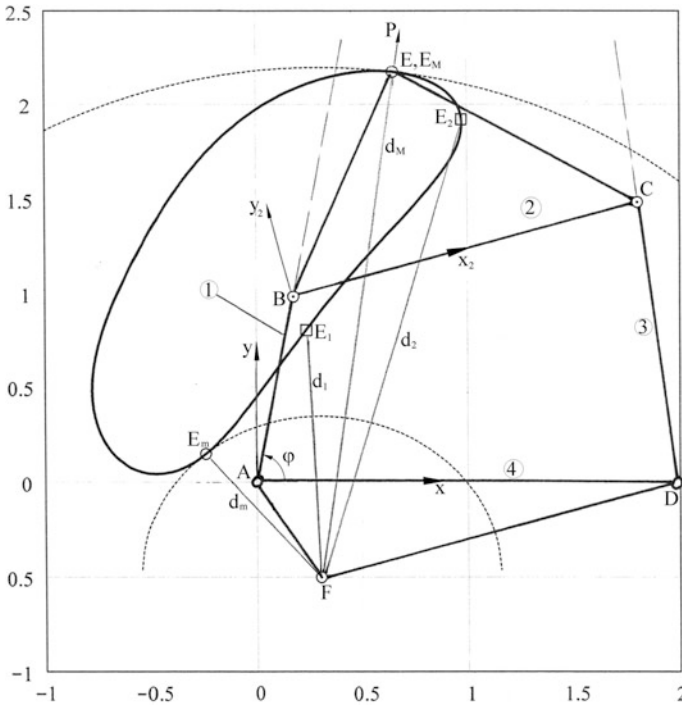


Fig. 1 The structural group 0/4/2. Numbers on the axes represent relative lengths

forces transmission quality index is a specific characteristic of each structural group and not of the mechanism as a whole, in a series of our papers [5–12] we analyzed 0/2/2 and 0/3/3 structural groups. Naturally, structural group completing the usual domain is 0/4/2, that we treat in present paper. In scientific literature we did not find such an approach of above mentioned problem, no for the group itself, nor for mechanisms containing structural group 0/4/2.

In [9–11], we legitimately proposed usage as quality index of forces transmission, the absolute value of the nonlinear equation system Jacobian, deserving position analysis. This determinant is proportional to the coefficient’s determinant associated to the linear system intervening in velocities analysis and to the coefficients determinant from the static analysis without frictions, so any from this three can be used.

## 2 The Forces Transmission Index

Afterwards we adopt as forces transmission index  $T(\varphi)$ , the absolute value of the determinant from the static analysis without friction (written  $\Delta$ ). Thus, it was taken into consideration the loads (resultant torsors consisting of forces and torques) on

each of four elements. Then it was written the equilibrium (d'Alembert) equations neglecting frictions. In result it obtained a linear system with 12 equations and 12 unknowns (all reactions components in those 6 kinematic pairs). After certain substitutions, this linear system reduces to a system with 8 equations and 8 unknowns. The coefficients of this system forms the determinant  $\Delta$ ). Because of space limitations, this paper does not indicate explicitly the equations of this system. The value of this determinant depends on the group configuration (the group position related to one of its elements). In the case of this group, the configuration is determined by one parameter only because the internal degree of freedom, obtained by external pairs elimination, equals one. So, we adopted the  $\varphi$  angle, Fig. 1, and the configuration reports to a referential system associated to the link 1. In such conditions, the  $T(\varphi)$  index has expression:

$$T(\varphi) = |\Delta(\varphi)| \tag{1}$$

where,  $\Delta(\varphi) =$

$$= \begin{vmatrix} y_F - y_A & -(x_F - x_A) & y_F - y_D & -(x_F - x_D) & 0 & 0 & 0 & 0 \\ 1 & 0 & 1 & 0 & 1 & 0 & 0 & 0 \\ 0 & 1 & 0 & 1 & 0 & 1 & 0 & 0 \\ -(y_E(\varphi) - y_B(\varphi)) & x_E(\varphi) - x_B(\varphi) & -(y_E(\varphi) - y_C(\varphi)) & x_E(\varphi) - x_C(\varphi) & 0 & 0 & 0 & 0 \\ -1 & 0 & -1 & 0 & 0 & 0 & 1 & 0 \\ 0 & -1 & 0 & -1 & 0 & 0 & 0 & 1 \\ y_A - y_B(\varphi) & -(x_A - x_B(\varphi)) & 0 & 0 & 0 & 0 & 0 & 0 \\ 0 & 0 & y_D - y_C(\varphi) & -(x_D - x_C(\varphi)) & 0 & 0 & 0 & 0 \end{vmatrix}$$

However, the geometric natural parameter determining the configuration is  $d = FE$ , because this parameter is imposed by connecting the structural group into mechanism, consequently it makes the connection between the group and the mechanism.

Between  $d$  and  $\varphi$  it can be established the expression  $d(\varphi)$  obtained from the  $ABCD$  four bar linkage, Fig. 1. Finally it results a correspondence between  $T$  and  $d$ , by intermediary  $\varphi$  parameter. This fact allows to adopt a running zone, for  $d$ , inside where the forces transmission does properly. We will illustrate the working mode aided by a concrete example.

Let consider a structural group with following relative lengths:  $AB = 1, BC = 1.7, CD = 1.5, AD = 2, x_F = 0.3, y_F = -0.5, x_{2E} = 0.8, y_{2E} = 1$ , Fig. 1.

It computes  $T$  and  $d$  using Eq. (1) and also the positions analysis of the  $ABCD$  four bar linkage with basis 2 and, it performs, considering the independent variable  $\varphi \in [0, 2\pi]$ .

In Fig. 1, the trajectory of the point  $E$  is traced, reported to the referential system  $Oxy$ . It results diagrams from Fig. 2.

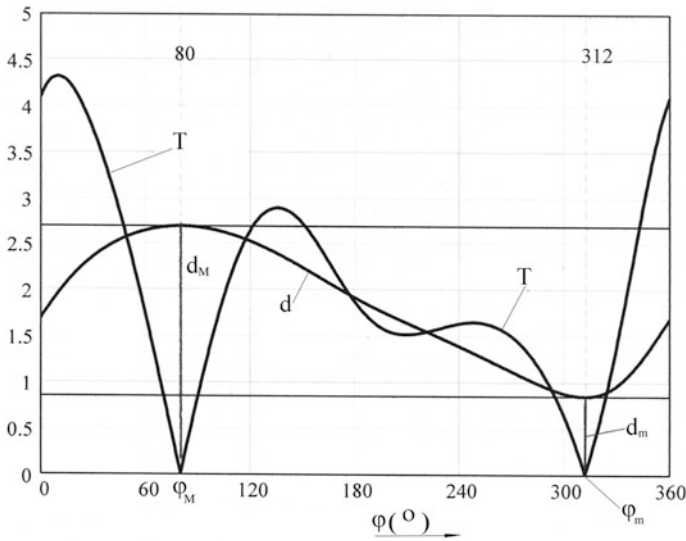


Fig. 2 Diagrams of  $T$  and  $d$ . Numbers on the vertical axis represents relative lengths

### 3 Discussions and Interpretations

These diagrams study points out certain important observations. Thus, the function  $T$  passes two time through zero, at  $\varphi_M = 80^\circ$  and at  $\varphi_m = 312^\circ$ . In these points it notices two singular configurations, characterized by fact that points  $E, F$  and  $P$  (placed at the intersection of the lines  $AB$  and  $CD$ ), are collinear [6]. In Fig. 1, the group is shown in singular position corresponding to point  $\varphi_M$ . This geometric property can be noticed also, from diagrams of  $\varphi_E(\varphi)$  and  $\varphi_F(\varphi)$  angles, made by lines  $FE$  and  $FP$  with  $Ox$  axis, Fig. 3.

The two curves are exactly intersected at points  $\varphi_M$  and  $\varphi_m$ . In singular positions, the length  $d$  receives the extreme values  $d_m = FE_m = 0.851$  and  $d_M = FE_M = 2.698$ , as it results from Figs. 1 and 2. This situation explains itself by fact that singularities separates an interval of variable  $d$ ,  $[d_m, d_M]$  [10], where positions problem has real solutions. Outside this interval, the solutions are complex and, consequently the group cannot be built. By graphical substitution of variable  $\varphi$  between functions  $T(\varphi)$  and  $d(\varphi)$  it obtains diagram  $T(d)$ , Fig. 4. The graphic presents two branches, separated by the two singular configurations, which are evidenced also in Fig. 2. The upper branch on Fig. 4 corresponds to interval  $[\varphi_m, \varphi_M]$  from Fig. 2, and the lower branch corresponds to interval  $[\varphi_M, \varphi_m]$ .

Interesting for us is the upper branch, that present bigger values for  $T$ . Running on one or another branch is determined by the assembling mode at group building. In order to assure the forces transmission quality, we have to impose a lower, admissible limit for the parameter  $T$ , written  $T_a$ . On this purpose, we define a relative index  $T_r = T/T_{max}$ , and in order to adopt an admissible value  $T_{ra}$ , we make

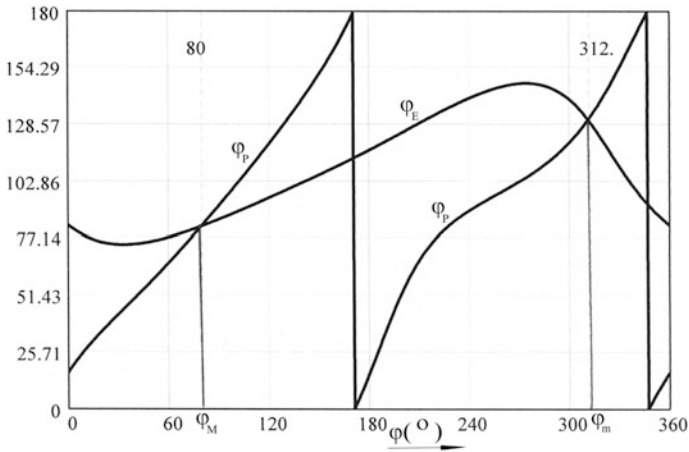


Fig. 3 Diagrams of  $\varphi_P$  and  $\varphi_E$ . Numbers on the axes represents hexadecimal degrees

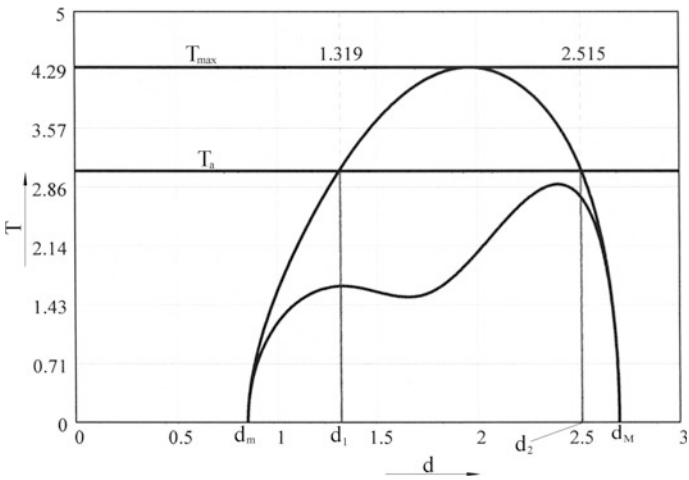
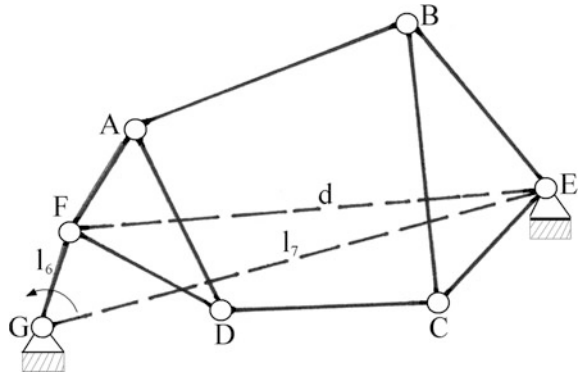


Fig. 4 Diagrams of  $T_{max}$  and  $T_a$  as functions of relative length  $d$

an analogy with *RRR* structural group or with four bar linkage. To this mechanism it recommends as admissible value for the transmission angle  $\gamma_a = 45^\circ$  that leads to an admissible value  $T_{ra} = \sin 45^\circ \cong 0.707$  [7, 8]. Taking  $T_{max} = 4.323$  from Fig. 4, it calculates  $T_a = T_{ra} \cdot T_{max} = 3.056$ .

The same diagram allows now to define an interval  $[d_1, d_2]$  with  $d_1 = 1.319$  and  $d_2 = 2.515$ , located inside the interval  $[d_m, d_M]$ . In order to put in relief the usefulness of these values let consider the most simple mechanism that contains this group and comes from Stephenson kinematic chain, Fig. 5.

**Fig. 5** The simplest mechanism built with 0/4/2 structural group



Length  $d$  is computed from  $EFG$  triangle and then is transferred to the group  $FABECD$ . Its extreme values are  $d_{\min} = |l_6 - l_7|$  and  $d_{\max} = l_6 + l_7$ . In order to the element 6 admits a full rotation in mechanism, it is necessary that interval  $[d_{\min}, d_{\max}]$  does be located entirely inside the  $[d_m, d_M]$  interval, i.e. it must respect the following condition:

$$\begin{aligned} d_{\min} &= |l_6 - l_7| \geq d_m \\ d_{\max} &= l_6 + l_7 \leq d_M \end{aligned} \quad (2)$$

Finally, to ensure the forces transmission quality ( $T_r \geq T_{ra}$ ) it is necessary that interval  $[d_{\min}, d_{\max}]$  must be located inside the  $[d_1, d_2]$  interval, respecting the following conditions:

$$\begin{aligned} d_{\min} &= |l_6 - l_7| \geq d_1 \\ d_{\max} &= l_6 + l_7 \leq d_2 \end{aligned} \quad (3)$$

Of course, conditions (3) are most restrictive than (2), so that respecting its ensure the respect of (2) conditions. Adopting  $l=0.5$  and  $l=1.9$ , it can be noticed that both conditions are satisfied.

## 4 Conclusions

Conditions (3), together with computing procedure of intervening parameters allow the evaluation of forces transmission regime for structural group 0/4/2.

Conditions (2) allow driving link rotatability verification of the simplest mechanism containing this group.

These conditions are useful both: for mechanism analysis and for synthesis of mechanisms where the 0/4/2 group intervenes.



**Acknowledgements** The SYROM'2017 Organizing Committee wants to acknowledge the support received from the previous organizers of SYROM.

## References

1. Bandyopandhyay S, Ghosal A (2004) Analysis of configuration space singularities of closed-loop mechanisms and parallel manipulators. *Mech Mach Theory* 39:519–594
2. Buium FI, Duca C, Leohchi D (2014) Problems regarding singularities analysis of a 3 RRR parallel mechanism. *Appl Mech Mater* 658:569–574
3. Duca C, Buium F (2001) Determination of mechanism precision aided by structural groups. *Bul. Inst Pol Din Iasi, Tom XLVII(LI), Supl., Sectia Constructii de Masini*, pp 289–298
4. Duca C, Buium FI, Paraoaru G Critical positions and mechanism self-blocking (I), (II), PRASIC'02, vol I, pp 113–126
5. Duca C, Buium FI (2006) Critical configurations of the structural groups, *Bul. Inst Pol Iași, Tom. LII(LVI), Fasc. 7A*, pp 241–2416
6. Duca C, Buium FI (2008) A critical position regarding the critical positions of mechanisms, *Bul. Inst Pol Iași, Tom.LIV(LVIII), Fasc.1*, pp 481–486
7. Duca C, Buium FI (2010) Questions about self-blocking of mechanisms, *Bul. Inst Pol Iași, Tom LVI(LX), Fasc 4A*, pp 248–254
8. Duca C, Buium FI (2013) Forces transmission in the 0/3/3 structural group, *Bul. Inst Pol Iași, Tom LIX(LXIII), Fasc. 1*, pp 17–22
9. Duca C, Buium FI (2014) Singularities classification for structural groups of dyad type. *Appl Mech Mater* 658:47–54
10. Duca C, Buium FI (2014) Transmission indices adoption for 6R structural group. *Appl Mech Mater* 658:55
11. Lin Chen-Chou, Chang Wen-Tung (2002) The force transmissivity index of planar linkage mechanisms. *Mech Mach Theory* 37:1465–1485
12. Shrinivas SB, Satish C (2002) Transmission angle in mechanisms (Triangle in Mech). *Mech Mach Theory* 37:175–195

# Topological Structure of the Actuating Mechanisms of the Urban Buses Doors



D. Antonescu, C. Brezeanu and O. Antonescu

**Abstract** The paper analyzes the structural and geometric-kinematic aspects of the articulated bar mechanisms used to actuate the doors of urban buses. A mechanism of this kind consists of two main parts: the control mechanism mounted under or above the door, and the crank-slider final mechanism which actuates the folding doors. The analyzed mechanisms have in their structure simple dyad chains or complex chains of triad type. For these types of planar linkages that are equipping the urban buses, the topological and geometric structure is analyzed in order to find solutions to minimize the swept volume of them.

**Keywords** Urban bus • Folding door-part • Articulated planar mechanism  
Topological structure

## 1 Introduction

Urban transport by buses (Fig. 1), trolleybuses, trams must, unlike other vehicles, make several stops at the same time for boarding and lowering passengers at the stations on the route. Therefore, the bus door mechanisms have a high number of operating cycles which require a very good reliability.

In Sect. 2 the most well known types of urban bus doors are presented. Two types of doors are commonly used on today buses:

---

D. Antonescu  
“Iuliu Maniu” High School, Bucharest, Romania  
e-mail: daniela.mihalache@yahoo.com

C. Brezeanu  
Tenaris Group, Zalau-Calarasi, Romania  
e-mail: br79@yahoo.com

O. Antonescu (✉)  
Politehnica University of Bucharest, Bucharest, Romania  
e-mail: oval33@hotmail.com



**Fig. 1** Photos [13] of two models of buses

- with circular sliding motion [1, 3];
- with rotational-sliding motion [3, 4].

In Sect. 3 a comparing analysis of the actuated mechanisms of the urban and trolley buses doors is performed [4, 13]. First, the bus type TV-20 uses two fixed longitudinal opposed cylinders for the control mechanism. Then the trolleybus type TV use only one fixed longitudinal cylinder for the control linkage. Next, the bus type Ikarus uses a rotational cylinder as the actuator. Finally, the bus type Skoda uses only one fixed oblique cylinder for the control linkage [13].

For the first three types, a detailed topological analysis is performed, including the displaying of the structural and the kinematic chain schemes [3, 5, 8]. The goal of the paper is to identify the optimum design solution of the door mechanism regarding the swept volume of it. The smaller swept volume is generated by the door linkage, the higher saved space inside the bus is obtained. As it can be observed, the type Ikarus of the door mechanism is the most compact of the presented models.

Starting from this structural analysis, a general method of geometrical synthesis of these planar mechanisms with articulated bars can be elaborated on the basis of relative-associated positions [3, 4, 8, 9].

Based on the presented topological analysis of the bus door mechanisms, new control and/or final linkages, whose kinematic schemes are simpler, performing higher transmission angles [4, 10, 17] and therefore having a better operating behavior, can be achieved.

## 2 Types of Mechanisms for Bus Doors

### 2.1 *Swinging Door (Conventional) with Hinge Joint*

In the case of classical design buses (Fig. 2a), but also to the most vans (Fig. 2b), the doors are opened by a swinging movement around a vertical axis by means of a hinge [14].

### 2.2 *Door with Circular Sliding Motion*

In some modern buses the movement of doors is circular sliding [1, 3], being done by means of an articulated parallelogram mechanism (Fig. 3).

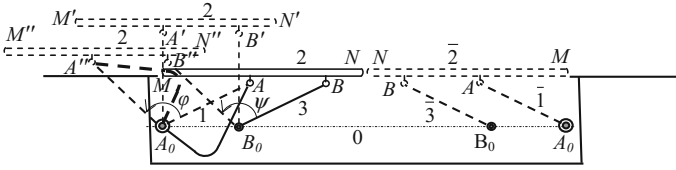
The kinematic scheme of the articulated parallelogram mechanism (Fig. 4) shows that the vehicle door (represented by the MN segment) is rigid connected with the coupler AB. In the practical case of bus doors, the positioning of the fixed joints  $A_0$  and  $B_0$  is made inside the body 0, in the area of the stairway.



Fig. 2 Swinging doors in horizontal plane (conventional doors)



Fig. 3 Folding door (circular sliding movement) outside the bus



**Fig. 4** The kinematic scheme of the double symmetrical parallelogram mechanism

Each of the two door-parts is rigidly connected with the coupler 2 of the parallelogram  $A_0ABB_0$  in the closed position of the door with width  $MN$ . In the open position of the door  $M''N''$ , the parallelogram mechanism is  $A_0A''B''B_0$ . Note that the bar 1 cannot be in a straight line as it would interfere with the bus body, so that the shape of it is curved and it does not collide with the vehicle body.

The kinematic scheme of the parallelogram mechanism was drawn in three positions: two extreme positions (closed and open) and an intermediate position  $M'N'$  at the maximum distance of the body (Fig. 4).

A parallelogram mechanism is corresponding for each of the two door-part, whose kinematic schemes are symmetrically represented.

Due to the fact that the bar 1 ( $A_0A$ ) is the driving kinematic element, it has a much larger cross-section than the bar 3, having primarily a geometric role.

Note that for the right part, the parallelogram mechanism was represented only in the closed position.

### 2.3 Door with Planar Rotational-Sliding Motion

The door of the bus can be made of two parts articulated each other, of which one of the parts performs a horizontal rotation and the other one performs a rotational-sliding motion.

The most commonly used solution is the one in which the door is made of a single part having a horizontal planar movement (rotational-sliding). When the door is open, the door-part is fully folded (Fig. 5a) or partially folded (Fig. 5b) inside the bus.

In an intermediate position of the bus door (Fig. 6) the door-part being rigidly connected to the coupler of a crank-coupler planar mechanism (Fig. 7) can be observed.

The control and actuation mechanism of the door is usually located at the top of the bus body.



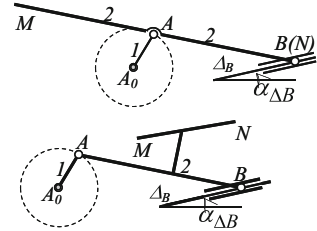
(a) Fully folding doors inside the bus      (b) Partially folding doors inside the bus

**Fig. 5** a Fully folding doors inside the bus. b Partially folding doors inside the bus

**Fig. 6** Doors with one-part inside folding



**Fig. 7** The scheme of the crank-coupler mechanism



### 3 Topological Structure of Bus-Door Actuation Mechanisms

#### 3.1 The Door Mechanism of a Bus Type TV-20

This planar mechanism (Fig. 8) is consisting of two series-connected kinematic chains [3, 6, 8, 13]: the “control” mechanism MC (1<sub>a</sub>, 2<sub>a</sub>, 3, 1<sub>b</sub>, 2<sub>b</sub>, 3) and the “final” mechanism ME (3, 4, 5, 6, 7).

Observing that the joint of A is double, the degree of mobility of the mechanism results [3, 4]:

$$M_3 = 3n - 2C_5 - C_4 = 3 \cdot 9 - 2 \cdot 13 = 1 \tag{1}$$

The structural scheme (Fig. 8a) matches the analytically determined degree of mobility (1) and indicates that the mechanism is simple (class II), regardless of which of the elements 1<sub>a</sub>, 1<sub>b</sub> is the driving component.

The “motor mechanism” (Fig. 8b) has the same structural class regardless of the driving element 1<sub>a</sub> or 1<sub>b</sub>, the kinematic chain from which it originates being symmetrical [4, 10, 12].

The actuating agent of the mechanism is pressurized air, acting alternately on the pistons 1<sub>a</sub> and 1<sub>b</sub>.

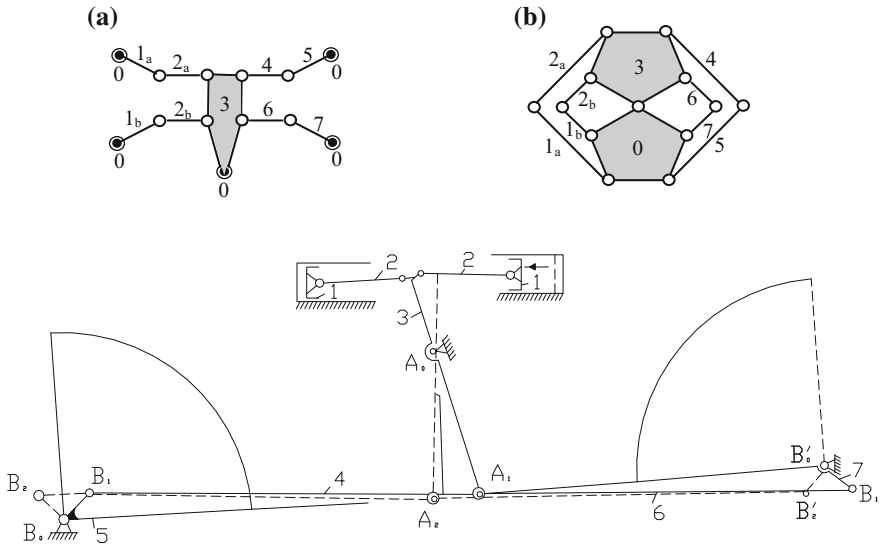
In fact, due to the small displacements of the pistons, instead of the piston cylinders, there are used pneumatic chambers with elastic diaphragms to which the connecting rods 2<sub>a</sub> and 2<sub>b</sub> are fixed.

Both parallel-connected mechanisms (3, 4, 5), (3, 6, 7) operate as a double rocker [6–8] because the rotation of the elements 5, 7 is limited to 90° (Fig. 8).

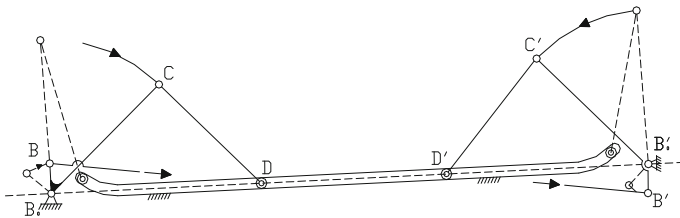
The ME (3, 4, 5, 6, 7) transmit the oscillation movement of the central rocker 3 to the left and right rockers (5, 7) linked in parallel.

They form a common body with the single doors or with the main parts of the folding doors, which are made as crank-coupler mechanisms with curved guide near the fixed joint B<sub>0</sub> (Fig. 9).

Transmission functions of the zero order, accomplished by the two mechanisms, are equal and have opposite signs:



**Fig. 8** The kinematic scheme of the planar mechanism with bars; the structural topological scheme (a) and the kinematic chain (b)



**Fig. 9** The kinematic scheme of the door mechanism with curved guide

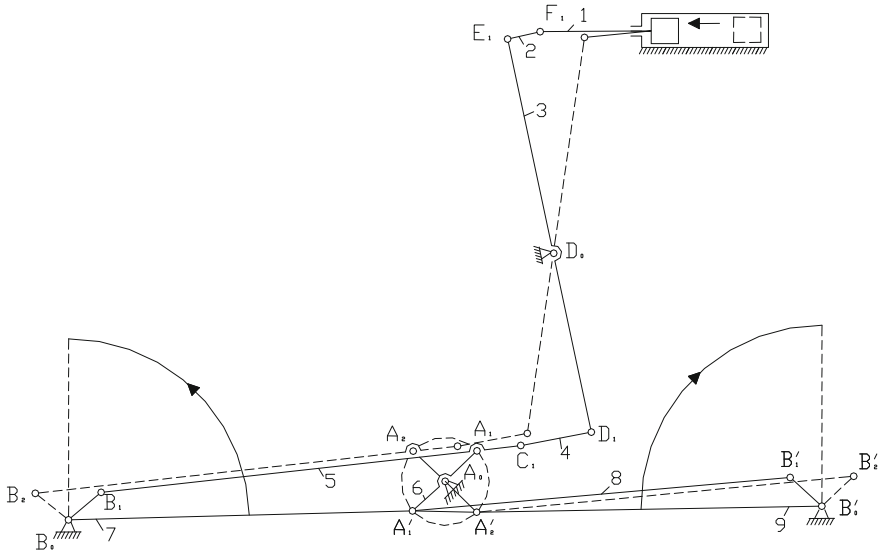
$$i_{35} = -i_{37} = \frac{\varphi_{12}}{\psi_{12}} \cong \frac{1}{4} \tag{2}$$

where:  $\varphi_{12} = 23^\circ$ ;  $\psi_{12} = \psi'_{12} = 90^\circ$ .

### 3.2 The Door Mechanism of a Trolleybus Type TV

This type of mechanism (Fig. 10) consists of three series-connected mechanisms: MC (1, 2, 3) and ME (3, 4, 5, 6, 7); (6, 8, 9), having the same number of kinematic elements [13] as in the previous case.





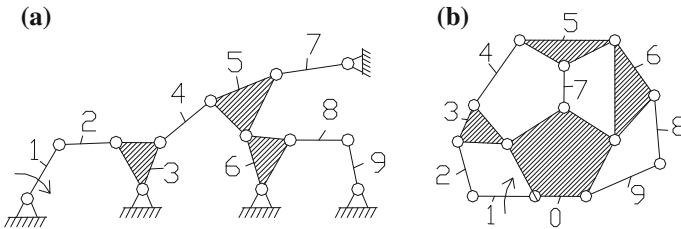
**Fig. 10** The kinematic scheme of the planar mechanism with triadic chain

By means of the formula (1), the degree of mobility ( $M_3 = 1$ ) is verified, which can also be observed on the structural scheme (Fig. 11a) showing in addition that the “motor mechanism” (Fig. 10) is a complex planar mechanism (3rd class).

The structural scheme is asymmetric by observing the kinematic chain (Fig. 11b), from which the analyzed “motor-mechanism” was obtained.

The final mechanism consists of a parallelogram (5, 6, 7) and an anti-parallelogram (6, 8, 9) so that the transmission ratio is achieved between the driven elements 7 and 9:

$$i_{79} = i_{76} \cdot i_{69} = -1 \tag{3}$$



**Fig. 11** The structural scheme (a) and the planar kinematic chain (b)

The piston 1 operates with double effect, the compressed air acting on both sides, and by means of the connecting rod 2 the linear sliding motion is turned into a rotational motion, swinging the rocker 3.

Further, the movement is transmitted, by the coupler 4, to the parallelogram (5, 6, 7) and then, via the element 6, to the anti-parallelogram (6, 8, 9) (Fig. 9).

The doors or the main parts of the folding doors are fixed to the driven elements 7 and 9 (having limited rotation of 90°), according to the kinematic scheme (Fig. 10) or the structural scheme (Fig. 11a).

### 3.3 The Door Mechanism of a Bus Type Ikarus

This type of mechanism (Fig. 12) consists of MC (1, 2, 3) with oscillating cylinder and ME (3, 4, 5, 6, 7) formed by the parallelogram (0, 3, 4, 5) and the anti-parallelogram (0, 3, 6, 7) obtained by extending the MC [4, 13]. ME (3, 4, 5, 6, 7) is similar to that used on the TV trolley (Fig. 10).

The doors or the main parts of the folding doors are fixed to the driven elements 5 and 7, made as crank-coupler mechanisms with curved guide (Fig. 12).

The structural scheme (Fig. 13a) is made taking into consideration that the articulation A is double, the analytically-determined degree of mobility being [3]:

$$M_3 = 3n - 2C_5 = 3 \cdot 7 - 2 \cdot 10 = 1 \tag{4}$$

The “motor mechanism” (Fig. 13a) has a simple structure (class II), being obtained from the 8-element kinematic chain (Fig. 13b).

Compared with the other two analyzed mechanisms (Figs. 8 and 10), this mechanism (Fig. 13) is made of fewer elements and the swept volume of it is smaller, the pneumatic cylinder being mounted at a minimum distance in respect of direction B<sub>0</sub>B’.

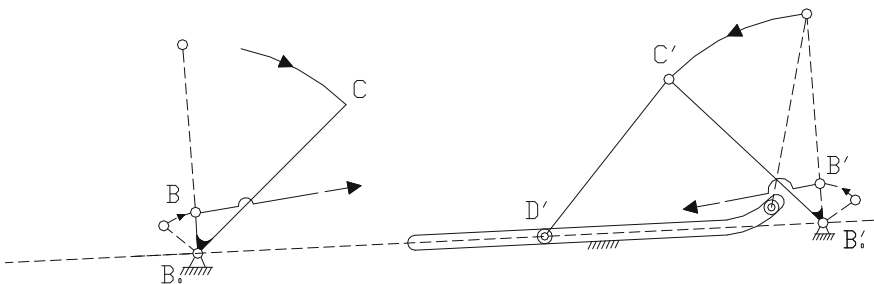


Fig. 12 The kinematic scheme of the door mechanism with the curved guide

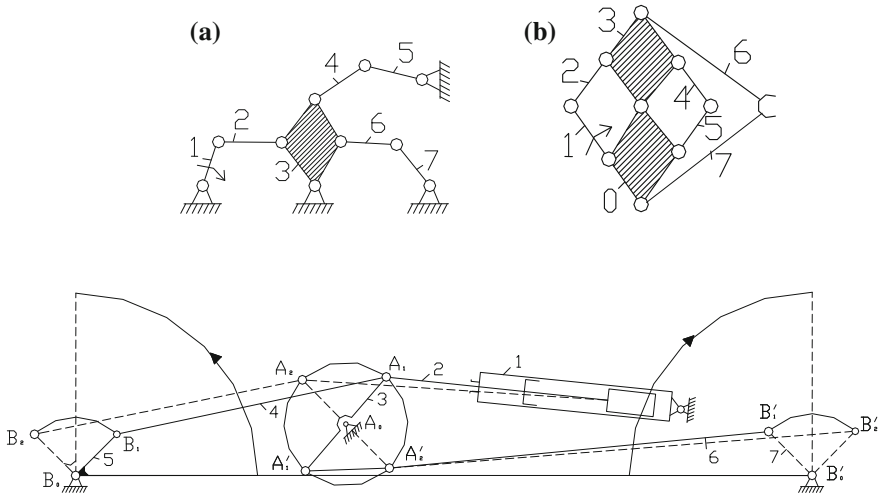


Fig. 13 The kinematic scheme of the articulated planar mechanism

### 3.4 The Door Mechanism of a Bus Type Skoda

This type of mechanism (Fig. 15) has the same number of kinematic elements [13] as the precedent (Fig. 14), the kinematic schemes being similar, and the structural scheme obtained from the same kinematic chain (Fig. 13b).

In this mechanism, the pneumatic cylinder is fixed (Fig. 15), all the kinematic joints are simple and the fixed joint  $A_0$  is located at a greater distance with respect to  $B_0B'$ , which implies a larger swept volume.

The doors are made of a single part connected to the coupler CD of the crank-slider mechanism (Fig. 16).

Note that the essential difference among the four studied mechanisms is the way of designing the control mechanism, while the final mechanisms are similar.

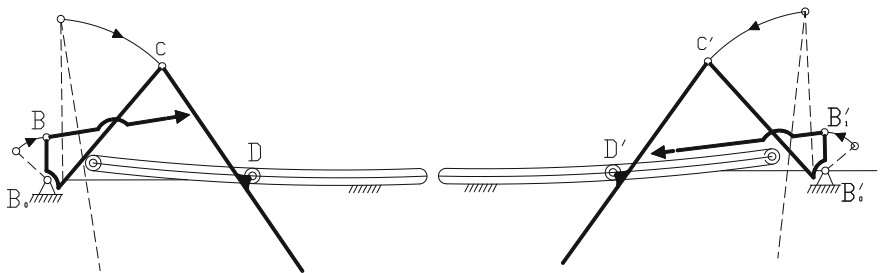


Fig. 14 The kinematic scheme of the planar mechanism with curved guide

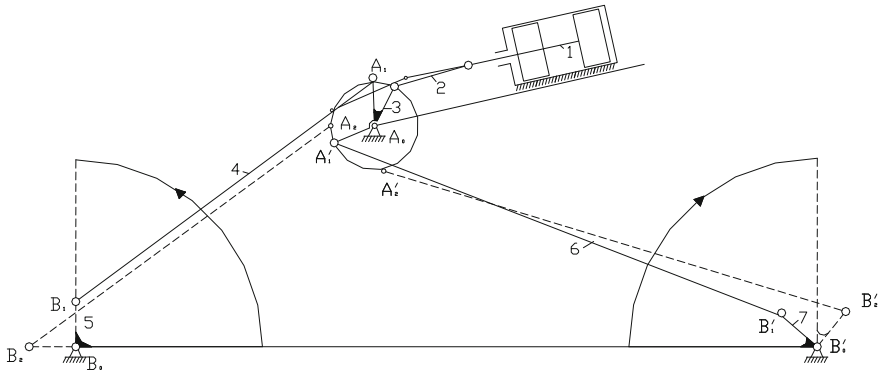


Fig. 15 The kinematic scheme of the planar linkage in the extreme positions

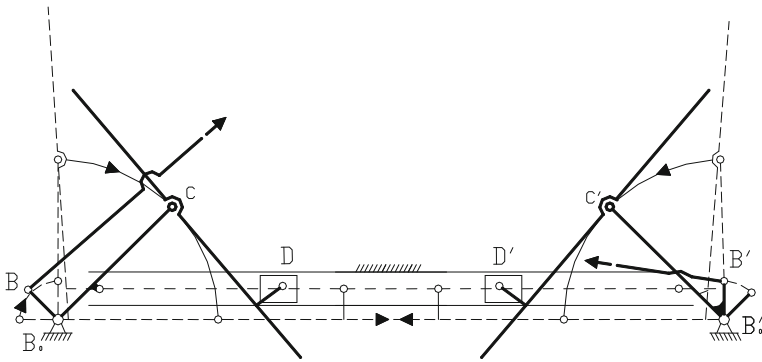


Fig. 16 The kinematic scheme of the final mechanism equipped with sliders

## 4 Conclusions

In the paper the structural and geometric-kinematic aspects of the articulated bars mechanisms for actuating the doors of the urban buses were analyzed.

It is emphasized that all the studied mechanisms have a common part, both the execution mechanism and the control mechanism being made up of a quadrilateral (parallelogram) and an anti-quadrilateral (anti-parallelogram).

Knowing the topological structure, these planar bus-door mechanisms with articulated bars can be redesigned in order to improve the operating and to achieve a smaller swept volume.

Also, comparing the bus doors with circular sliding motion to those with rotational-sliding movement, the main advantage of the first type is the offering of a greater comfort the passengers since the doors do not occupy any space inside the bus.

This topological-structural analysis represents a base for a future work on design of a new actuating mechanism for bus doors.

## References

1. Antonescu D, Veliscu V (2012) Analysis and synthesis of planar mechanisms used for generating curve line translation motion. *Mech Manip J* 11(2)
2. Antonescu E, Antonescu P, Fratila Gh (1972) Synthesis of the mechanisms for actuating the urban bus doors (in Romanian). *Simp de Mecanisme si transmisii mec, Resita*
3. Antonescu O, Antonescu P (2016) Mechanism and machine science—coursebook. Politehnica Press, Bucharest
4. Antonescu P (1970) Synthesis for relative-associated positions, the particular case of the positional synthesis (in Romanian). In: *A II-a Conferinta de Mecanica tehnica*, vol 11
5. Copilus C, Veliscu V (2014) An approach regarding windshield wiper mechanism design. In: *Congres International SMAT, Craiova*
6. Hartenberg R, Denavit D (1968) *Kinematics Synthesis of Linkages*. New York
7. Kovacs Fr et al (1971) On the synthesis of a function-generator mechanism on the basis of imposed precision conditions (in Romanian). *Revista Constructii de masini* 12
8. Lichtenheldt W (1970) *Konstruktionslehre der Getriebe*. Berlin
9. Manolescu NI, Antonescu P (1970) Systemizing of the tri-positioning synthesis of the planar mechanisms with 4 elements of diverse design types (in Romanian). In: *A II-a Conf. de mecanica tehnica*, vol II
10. Veliscu V, Antonescu D, Mesarici D (2015) Mechanisms used for driving windows of car side doors. In: *8th symposium on durability and reliability of mechanical systems, Symech*
11. Veliscu V, Antonescu O, Brezeanu C (2015) Main types of mechanisms used as windshield wipers. In: *8th symposium on durability and reliability of mechanical systems, Symech*
12. Veliscu, V, Mesarici, D, Antonescu P (2015) Topological structure and mobility of mechanisms used in car mechanical jacks. In: *8th symposium on durability and reliability of mechanical systems, Symech*
13. Technical documentation of buses TV-20, Skoda, Ikarus-180 and trolleybus TV
14. [www.autoline-eu.ro](http://www.autoline-eu.ro)
15. [www.slideshare.net/WaleedAlyafie/automatic-door-of-bus-door](http://www.slideshare.net/WaleedAlyafie/automatic-door-of-bus-door)
16. www Automatic bus door mechanisms
17. www US Patent: school bus door operator US 6264267 B1

# Geometric Synthesis of the Actuating Mechanisms of Urban Bus Doors



D. Antonescu, I. Popescu and O. Antonescu

**Abstract** The paper presents the method of geometrical synthesis of two new kinematic schemes of articulated planar mechanisms used to actuate the urban bus doors. The stages of solving geometrical synthesis for the two and three relative-associated positions of the bars articulated to the body are performed. In order to optimize the geometric synthesis and to avoid the mechanism stalling, the limiting of the pressure angle is required. One of the two proposed mechanisms has kinematic chains of dyad type in its structure, and the other mechanism also includes a triad-type kinematic chain. The new solutions have a smaller swept volume regarding the control mechanism.

**Keywords** Urban bus door • Articulated mechanism • Kinematic scheme  
Geometric synthesis

## 1 Introduction

For a high frequency of stops and a high number of passengers getting on and off, as well as for ensuring the safety of the passengers on boarding and during the journey, the urban vehicles are equipped with doors [11–14, 16] consisting of two or more folding parts, pneumatically or electrically controlled (Fig. 1).

A mechanism for actuating the city bus doors is generally composed [1, 4] of two main parts:

---

D. Antonescu · I. Popescu  
“Iuliu Maniu” High School, Bucharest, Romania  
e-mail: daniela.mihalache@yahoo.com

I. Popescu  
e-mail: ioana.popescu@yahoo.com

O. Antonescu (✉)  
Politehnica University of Bucharest, Bucharest, Romania  
e-mail: oval33@hotmail.com



Fig. 1 Photos [15] of urban buses

- the control mechanism, mounted either under the stairs or above the door (Fig. 1);
- the crank-slider final mechanisms to which either the crank and the coupler or only the couplers or the cranks are rigidly linked to one part of the folding door.

The structure and kinematics of the mechanisms used to actuate the urban bus doors [6] highlight the unitary character of the control mechanisms.

The paper presents the method of geometric synthesis of the control mechanisms, based on the relative-associated positions [2, 5] corresponding to both the extreme positions of the bus doors (open-closed), as well as in their intermediate positions.

A general method of geometrical synthesis of these planar mechanisms with articulated bars was developed based on the relative-associated positions [2, 4, 5].

On this basis, two new control mechanisms have been designed whose kinematic scheme is simpler, achieves higher transmission angles [6, 8], thus having a better efficiency.

## 2 Synthesis of New Kinematic Schemes for the Door Actuating Mechanism

### 2.1 Geometric Synthesis of the Four-Bar Mechanism Type Anti-parallelogram

The planar linkages type anti-quadrilateral and, especially, the anti-parallelogram, have the following transmission ratio between the cranks [10]:

$$i_{13} = \frac{\varphi_{12}}{\psi_{12}} = \frac{\omega_{1m}}{\omega_{3m}} = -1 \quad (1)$$

This ratio allows swinging, in opposite directions, the double doors between closed or open positions.

By imposing the  $A_0B_0$  distance (Fig. 2), corresponding to the double door opening, as well as the rotation of the main parts of the folding doors, it is possible to synthesize the anti-quadrilateral mechanism for a number of relative-associated positions [5] of the oscillating cranks (rigid connected to the main parts of the doors).

Therefore, knowing the rotation angles of the main door-parts, equal to  $90^\circ$ , two relative-associated positions can be considered.

The relative rotation pole  $R_{12}$ , located on the segment mediator  $A_0B_0$ , is obtained, since

$$\overrightarrow{\varphi}_{12} = \overleftarrow{\psi}_{12} = 90^\circ \tag{2}$$

By conveniently choosing the position  $A_1$  of the mobile articulation A, results the angle  $\beta_{12} = \sphericalangle A_0R_{12}A_1$ , which is being drawn in the same direction to the segment  $R_{12}B_0$ , obtaining the direction  $U_{12}$  as the geometric spot for the position  $B_1$  of the other movable articulation B (Fig. 2).

The limited swept volume outside the vehicle (corresponding to the space below  $A_0B_0$ ) requires the choosing of  $B_1$  at the minimum distance to  $B_0$ .

For three relative-associated positions, the following angles are imposed (Fig. 3):

$$\overrightarrow{\varphi}_{12} = \overrightarrow{\varphi}_{23} = 45^\circ; \quad \overleftarrow{\psi}_{12} = \overleftarrow{\psi}_{23} = 45^\circ \tag{3}$$

Thus, three poles of rotation are resulting, of which  $R_{12}$ ,  $R_{13}$  are used and both are located on the mediator of  $A_0B_0$ .

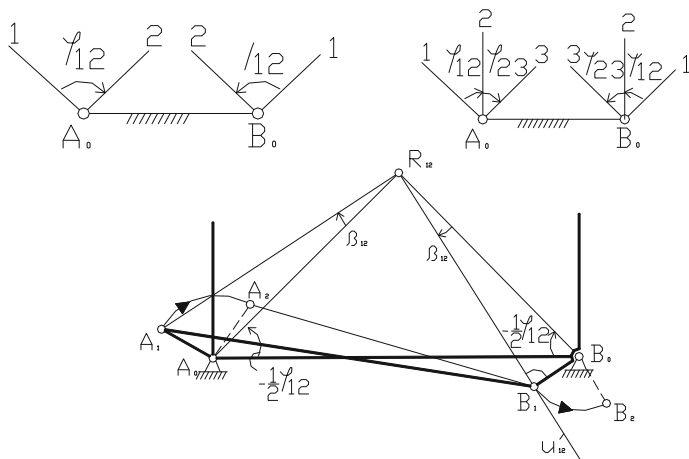
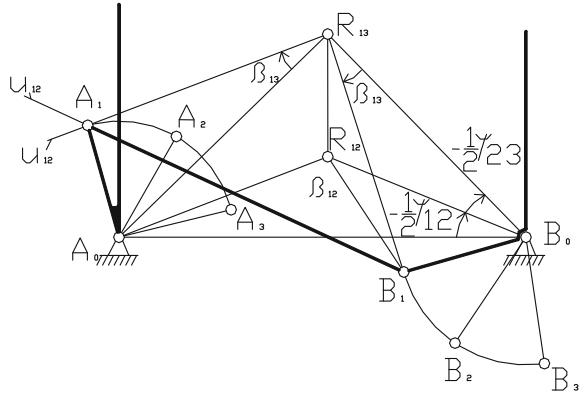


Fig. 2 Two relative positions of the mechanism [3]



**Fig. 3** Three relative positions of the mechanism [3]



If the position of \$B\_1\$ is selected and, implicitly, the length \$B\_0B\$ of the crank, the angles result:

$$\beta_{12} = \sphericalangle B_0R_{12}B_1; \quad \beta_{13} = \sphericalangle B_0R_{13}B_1 \tag{4}$$

These angles, measured in the same direction in respect of \$A\_0R\_{12}\$ and respectively \$A\_0R\_{13}\$, determine the directions \$U\_{12}, U\_{13}\$ whose point of intersection represents the position \$A\_1\$ of the mobile articulation \$A\$.

The passing of the anti-quadrilateral mechanism \$A\_0ABB\_0\$ through the three imposed positions, checks the solution found graphically (Fig. 3).

Considering the case of the anti-parallelogram mechanism and limiting the transmission angle [6] to the value \$\mu\_{min}\$, in the extreme positions, the solutions found in the synthesis of the mechanism for two relative-associated positions can be diminished (Fig. 2).

Therefore, knowing \$\varphi\_{12} = \psi\_{12} = 90^\circ\$ \$O\_1\$ and \$O\_2\$ are obtained symmetrically to \$A\_0B\_0\$, representing the centers of the orthogonal circles \$(C\_1), (C\_2)\$, measuring the angles:

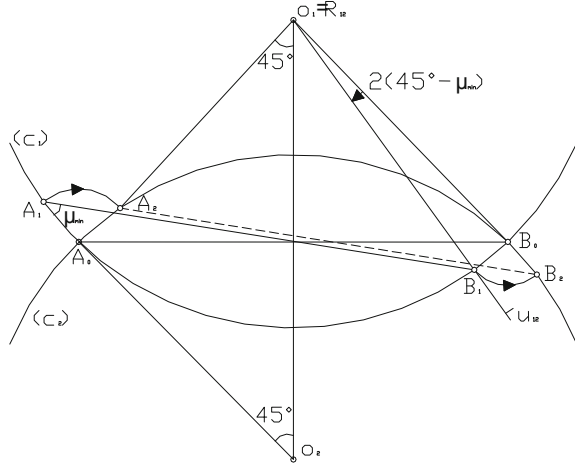
$$\sphericalangle A_0O_1B_0 = \sphericalangle AO_2B_0 = 90^\circ \tag{5}$$

Observing that \$O\_1 = R\_{12}\$ is drawn with respect to \$O\_1B\_0\$, the angle is equal to \$2(45^\circ - \mu\_{min})\$ where \$B\_1 = (C\_1) \cap U\_{12}\$.

Regardless of the position of \$A\_1 \in (C\_1)\$ above the \$A\_0B\_0\$, the following condition is fulfilled:

$$\sphericalangle A_0A_1B_1 = \mu_{min} \tag{6}$$

**Fig. 4** Geometrical synthesis of the articulated anti-quadrilateral



In the case of actuating the final mechanism via the coupler AB, it is necessary to obtain the angle  $\mu_{\min}$  at both oscillating cranks, i.e.

$$\sphericalangle AA_1B_1 = \sphericalangle B_0B_2A_2 = \mu_{\min} \tag{7}$$

In conclusion, the condition (7) is fulfilled by the anti-quadrilateral mechanism in which the positions  $A_1, B_1 \in (C_1)$ , and  $A_2, B_2 \in (C_2)$ , so that (Fig. 4):

$$\varphi_{12} = \sphericalangle A_1A_0A_2 = 90^\circ; \quad \psi_{12} = \sphericalangle B_1B_0B_2 = 90^\circ \tag{8}$$

### 2.2 New Kinematic Schemes of the Actuating Mechanisms of the Urban Bus Doors

Using the geometrical method of synthesis, two kinematic schemes (Figs. 5 and 6) have been designed with a small number of elements, which can be accomplished as pneumatic mechanisms for actuating the urban bus doors.

The first proposed kinematic scheme (Fig. 5) is a complex “motor mechanism” (class III—Fig. 5a) derived from an 8-element kinematic chain (Fig. 5b).

The second proposed kinematic scheme (Fig. 7) is a complex “motor mechanism” (class III—Fig. 6a) derived from another 8-element kinematic chain (Fig. 6b) [7].

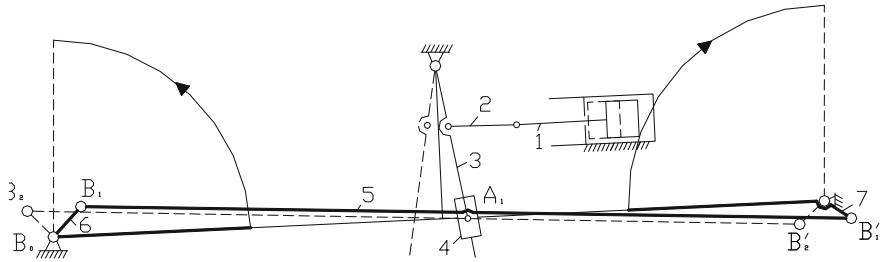
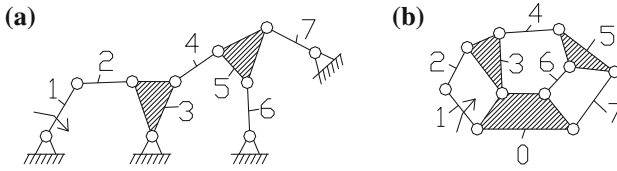


Fig. 5 Triadic kinematic scheme of the door actuating mechanism

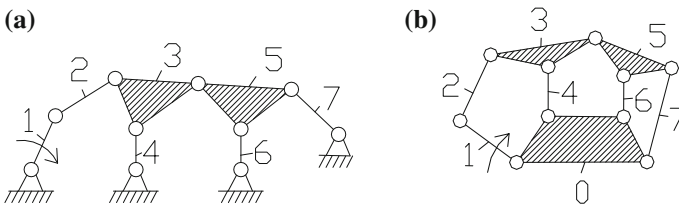


Fig. 6 The structural scheme (a) and the kinematic chain of the door actuating mechanism (b)

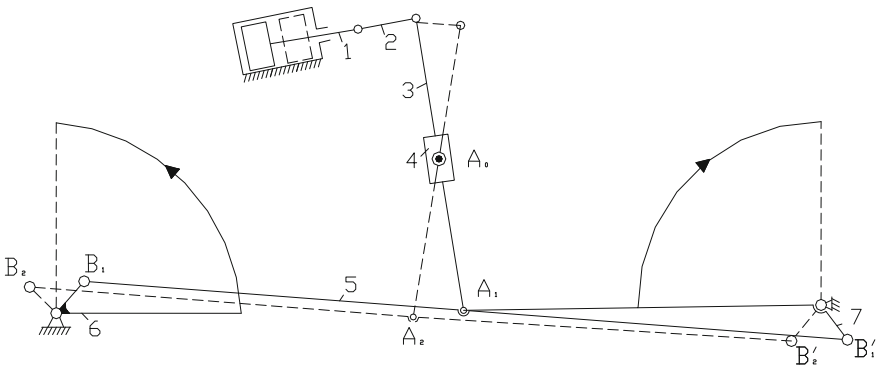


Fig. 7 Double-triad kinematic scheme of the door actuating mechanism

### 3 Synthesis of Planar Mechanisms with Six Kinematic Elements (Quadrilateral + Anti-quadrilateral)

The problem of the synthesis of 6-element mechanisms, type quadrilateral (four-bar) and anti-quadrilateral, is related to the fact that the majority of the existing mechanisms have the final mechanism made up of two elementary mechanisms (quadrilateral + anti-quadrilateral) connected in series.

Typically, the mechanisms used in this field consist of specific mechanisms type parallelogram and anti-parallelogram.

Furthermore, a more general case of mechanisms consisting of quadrilateral and anti-quadrilateral connected in series has been considered. Through the design project the distance  $B_0B_0'$  (opening of the double door) is imposed and the position of the third fixed joint  $A_0$  (Fig. 8) is conveniently chosen.

Three relative-associated positions of the driven elements are selected, positions drawn in  $B_0$ , respectively  $B'$ , and indicated by the angles:

$$\psi_{12} = \psi_{23} = 45^\circ; \quad \psi'_{12} = \psi'_{12} = 45^\circ \tag{9}$$

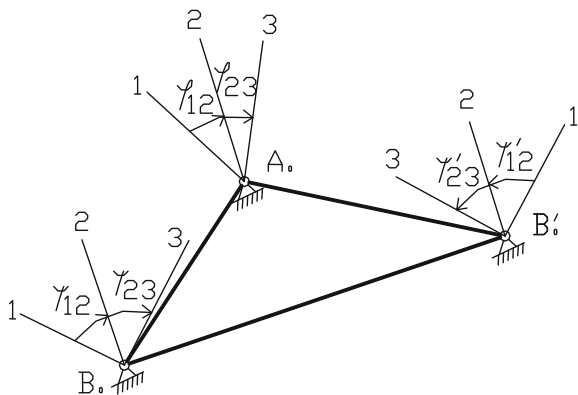
According to the imposed transmission ratio ( $i < 1$ ), from the driving element (central) to each of the two driven elements, the three positions of the driving element are selected, positions drawn in  $A_0$  by measuring the angles:

$$\varphi_{12} = \varphi_{23} = \frac{\pi}{4} i \tag{10}$$

For the synthesis of the quadrilateral mechanism, the direction  $A_0B_0$  is considered, in respect of which the relative rotation poles  $R_{12}, R_{13}$  are drawn, and for the synthesis of the anti-quadrilateral mechanism the relative poles  $R'_{12}, R'_{13}$  are drawn with respect to the direction  $A_0B'_0$  (Fig. 9).

If the  $B_1$  position of the B joint is conveniently selected, the following angles are obtained (Fig. 9):

**Fig. 8** Three relative-associated positions of the quadrilateral and anti-quadrilateral mechanism



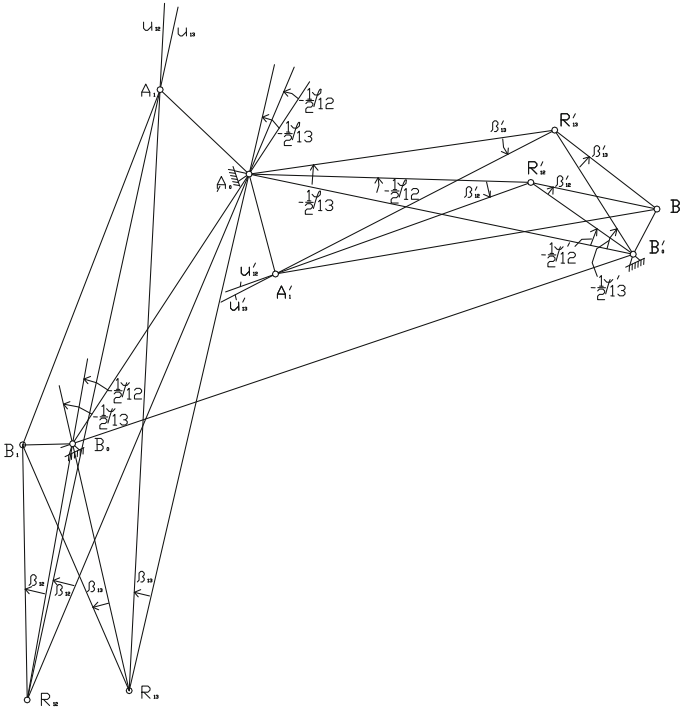


Fig. 9 Geometrical synthesis for three relative-associated positions [3]

$$\beta_{12} = \sphericalangle B_1R_{12}B_0; \quad \beta_{13} = \sphericalangle B_1R_1B_0 \tag{11}$$

These angles are drawn in the same direction about the directions  $A_0R_{12}$ , respectively  $A_0R_{13}$ , resulting in the directions  $U_{12}$ ,  $U_{13}$  and the position of the mobile articulation  $A: A_1 = U_{12} \cap U_{13}$ . By analogy,  $B'_1$  is selected and the angles are:

$$\beta'_{12} = \sphericalangle B'_1R'_{12}B'_0; \quad \beta'_{13} = \sphericalangle B'_1R'_{13}B'_0; \tag{12}$$

If these angles are drawn in the same direction about the directions  $A_0R'_{12}$ ,  $A_0R'_{13}$ , the directions  $U'_{12}$ ,  $U'_{13}$  are obtained and therefore  $A'_1 = U'_{12} \cap U'_{13}$ , the position of the mobile joint  $A'$  (Fig. 9).

The points  $A$  and  $A'$  belong to the same kinematic element which, by a rotation of  $\varphi_{13} = \varphi_{12} + \varphi_{23}$ , determines the simultaneous rotations in opposite directions of the oscillating cranks  $B_0B$ ,  $B'_0B'$  with the angles:

$$\overrightarrow{\psi}_{13} = \overrightarrow{\psi}_{12} + \overrightarrow{\psi}_{23}; \quad \overleftarrow{\psi}'_{13} = \overleftarrow{\psi}'_{12} + \overleftarrow{\psi}'_{23} \tag{13}$$

After designing the final/control mechanism, the position of the driving element is determined in order to efficiently transmit the force developed in the pneumatic cylinder or the electric motor torque.

### 4 Synthesis of the Parallelogram Mechanism with Electric Actuation

The kinematic scheme of the parallelogram mechanism (Fig. 10) is designed for actuating a single part of the bus door.

In the real case (Fig. 11), the parallelogram mechanism must allow the rotation of both bars 1 and 3 at the same angle  $\varphi = \psi$ . In order to achieve this, bar 1 is designed in “L” shape, which will allow it to be rotated in the position  $A_0A''$  of the door opening (represented by the segment  $M''N''$ ).

The actuation of the two symmetrical parallelograms can be achieved by means of bars 1 and  $\bar{1}$  with two electric motors, one for each articulated parallelogram mechanism. Another solution, more practically, for the actuating of the two articulated parallelograms is by using a single electric motor placed either in the lower part of the chassis under the stairs or, more commonly, above the doors (Fig. 12). This will avoid the synchronizing issue between the two doors.

Note that from the closed position ( $M_1N_1$ ) to the open position ( $M_2N_2$ ) the rotation angle of the bar 1 is an obtuse angle  $\angle(A_1A_0A_2) = \varphi_{max}$ . By means of the

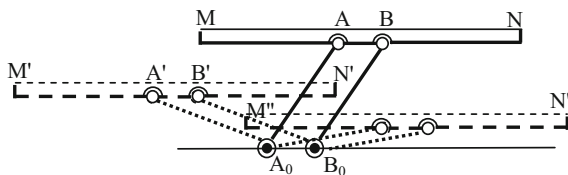


Fig. 10 The kinematic scheme of the parallelogram mechanism

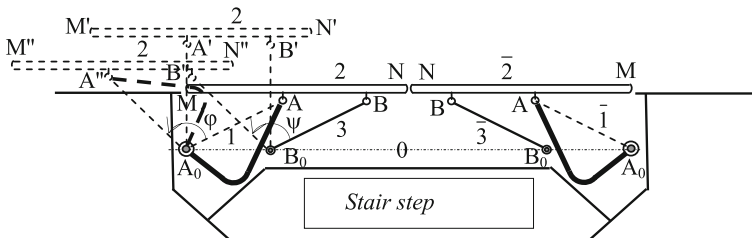
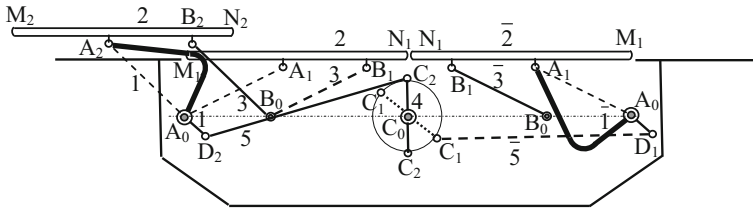
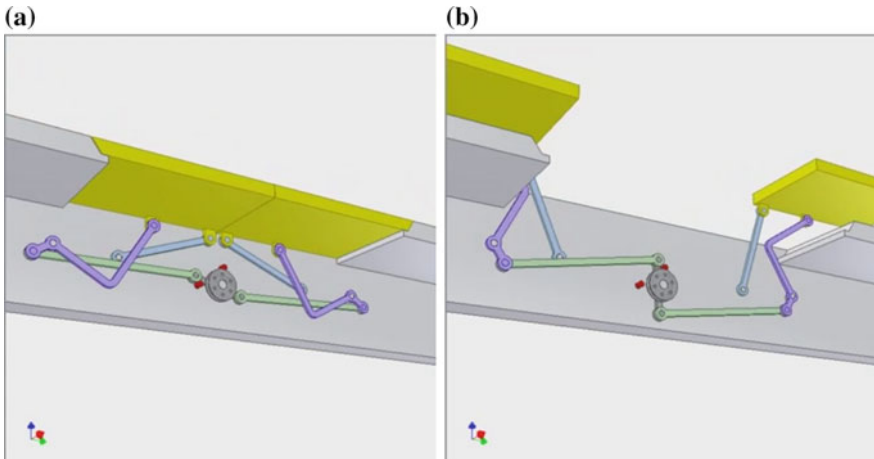


Fig. 11 The kinematic scheme of the double symmetrical parallelogram mechanism



**Fig. 12** The kinematic scheme of the left-right control mechanism



**Fig. 13** Simulation of the bus doors in the extreme positions: closed (a) and open (b)

dyad chain LD (4, 5), the angle  $\varphi_{max}$ , through the rotation of the bar 5 about the fixed joint  $C_0$ , is obtained (Fig. 12).

The geometrical synthesis of the quadrilateral mechanism  $0145(A_0DCC_0)$  is achieved on the condition that at the same rotation of the bar 5, the two left and right parallelograms to rotate at the same angle.

Using modeling software, the simulation of the mechanism in closed and open positions has been accomplished (Fig. 13).

## 5 Conclusions

Knowing the extreme positions occupied by the driven elements, the paper presents the method of synthesis for relative-associated positions of the mechanisms with four elements type anti-quadrilateral and the mechanisms with six elements made of serial connecting of the elementary quadrilateral and anti-quadrilateral mechanisms.

By means of this method, two new kinematic schemes have been designed in order to actuate more efficiently the urban bus doors.

Also, the presented method in the paper allows redesigning the existing pneumatic door mechanisms on urban buses in order to improve the operation and to achieve a smaller swept volume. Therefore, the comfort of the passengers will increase substantially due to the fact that almost all urban door linkages are positioned above the door.

## References

1. Alyafie W (2012) Automatic door system—conceptual design for MECH N450. Higler College of Tehnology. [www.slideshare.net/WaleedAlyafie/automatic-door-of-bus-door](http://www.slideshare.net/WaleedAlyafie/automatic-door-of-bus-door)
2. Antonescu E, Antonescu P, Fratila Gh (1972) Synthesis of the mechanisms for actuating the urban bus doors (in Romanian). Simp. de Mecanisme si transmisii mecanice, Resita
3. Antonescu O, Antonescu P (2016) Mechanism and machine science—coursebook. Politehnica Press, Bucharest
4. Antonescu P (1970) Synthesis for relative-associated positions, the particular case of the positional synthesis (in Romanian). In: A II-a Conferinta de Mecanica tehnica, vol 11
5. Kovacs Fr et al (1971) On the synthesis of a function-generator mechanism on the basis of imposed precision conditions (in Romanian). In: Revista Constructii de masini, 12
6. Lichtenheldt W (1970) Konstruktionslehre der Getriebe. Berlin
7. Manolescu NI et al (1963) Exercise book of mechanism and machine theory (in Romanian), vol I, Bucharest
8. Manolescu NI, Antonescu P (1970) Systemizing of the tri-positioning synthesis of the planar mechanisms with 4 elements of diverse design types (in Romanian). In: A II-a Conf. de mecanica tehnica, vol II
9. Manolescu NI, Erceanu I, Antonescu P (1962) Domain of applicability of kinematic research of articulated planar mechanisms (in Romanian). In: S.C.M.A., no 6
10. Technical documents of buses TV-20, Skoda, Ikarus-180 and trolleybus TV
11. School bus door operator, US 6264267 B1
12. Method and apparatus for attaching a door to a passenger vehicle, US 20040256882 A1
13. Emergency release mechanism for electrical bus door, EP 1256683
14. Bus with floor and door mechanism, EP 0610822 A1
15. [www.autoline-eu.ro](http://www.autoline-eu.ro)
16. [www.google.ro/search?q=door+mechanism+for+bus&safe=active&client=opera&hs=HHI&tbn](http://www.google.ro/search?q=door+mechanism+for+bus&safe=active&client=opera&hs=HHI&tbn)



# Synthesis of the Mechanisms Used to Actuate the Cabinet Doors



D. Antonescu, F. Gaspar and P. Antonescu

**Abstract** The paper presents three kinematic schemes of planar mechanisms with bars used to open/close a cabinet (buffet). The mechanisms are mounted on the left and right walls of the cabinet, working in parallel, in a vertical plane. Both mechanisms are hinged to a single door that swings  $90^\circ$  in a vertical plane from a vertical position (closed) to a horizontal position (open). The three kinematic schemes proposed for door actuation have in their structure either only revolute joints (RRRR) or revolute and prismatic joints in the variants RRTR and RRRT. To each of the three kinematic schemes of mechanisms, an analytical method of geometric synthesis for two and three associated positions has been presented.

**Keywords** Mechanism • Geometric synthesis • Cabinet • Door  
Kinematic scheme • Transmission angle

## 1 Introduction

The mechanism for vertically opening/closing the doors of the agglomerated wood furniture, pallet furniture or aluminum frame doors is a more modern version of the famous scissor mechanism used in the past for furniture that also has a built-in bar and its door opens up and serves as bottle holder and serving glasses [5].

For a bar cabinet furniture [3], the door opens automatically and closes by braking (Fig. 1).

---

D. Antonescu • F. Gaspar  
“Iuliu Maniu” High School, Bucharest, Romania  
e-mail: daniela.mihalache@yahoo.com

F. Gaspar  
e-mail: florentina\_gaspar@yahoo.com

P. Antonescu (✉)  
Politehnica University of Bucharest, Bucharest, Romania  
e-mail: panton38@hotmail.com

**Fig. 1** The mechanism of a bar door [3]



These mechanisms are the most well-known and used accessories in the custom-made furniture industry and agglomerated wood furniture.

They are used in the residential area, for the doors of agglomerated wood and pallet kitchen furniture (Fig. 2), as well as in the cabinets of the living rooms, children rooms, bathrooms, cabinets, bedrooms, hotel rooms, restaurants, institutions, schools, etc.

**Fig. 2** The vertical mechanism for a cabinet door [3]



In the first variant (Fig. 1), the mechanism has only one articulated bar to the vertical wall, the other fixed revolute joint (not displayed in the figure) is that of the door that performs a vertical rotation.

In the case of the second variant (Fig. 2), the mechanism is a parallelogram which has both fixed revolute joints very closed to each other, located on the vertical wall of the cabinet, and the cabinet door performs a circular sliding movement in the vertical plane.

## 2 The Three Specific Kinematic Schemes

The kinematic scheme of the articulated bar mechanism [5, 7] is drawn in the two extreme (open/closed) positions of the cabinet door. The mechanism is an articulated planar four-bar linkage (Fig. 3), where the extreme position (open door) corresponds to the horizontal position of the rocker 1, which is rigidly connected with the cabinet door (with rotation motion in the vertical plane).

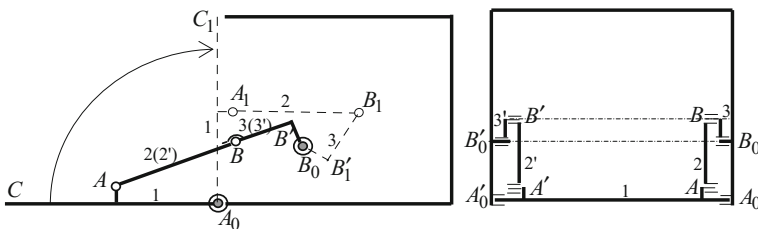
The mechanism has two kinematic chains type dyads LD (2, 3) and LD (2', 3') that are mounted and operate in parallel. The two couplers 2 and 2' are articulated in points A and A' at the same element 1, representing the door of the bar cabinet.

The horizontal position of the segment A<sub>0</sub>C in the plane of element 1 (Fig. 3) allows the use of the open door as a table to “serving” beverages.

In the open position of the cabinet, the bars 2 and 3 are stiffened, so that points B', B and A are collinear. The solution with the points A, B, and B<sub>0</sub> being collinear was avoided, because in this case the transmission angle would be zero, which would not allow easy action through the bar 1 of the four-bar linkage [2].

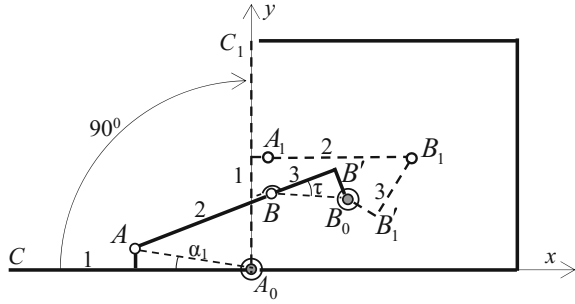
In the situation used in practice (Fig. 4), the angle of transmission (measured at the driven element 3) is formed by the directions B<sub>0</sub>B and AB, i.e. the sharp angle  $\angle(B_0BB') = \tau$  is different from zero [2\_3, 4\_5, 6\_7] with a minimum value greater than the critical value ( $\tau_{min} > \tau_{cr}$ ).

The characteristic dimensions of the mechanism can have the following numerical values:



**Fig. 3** The kinematic scheme of the door mechanism of a bar cabinet

**Fig. 4** Graphic revealing of the transmission angle



$$\begin{aligned}
 x_{B_0} &= 50 - 60 \text{ mm}; y_{B_0} = 85 - 95 \text{ mm}; \\
 AA_0 &= 80 - 100 \text{ mm}; AB = 90 - 100 \text{ mm}; \\
 CA_0 &= 290 - 310 \text{ mm}; \angle(AA_0C) = \alpha_1 = 10^\circ - 15^\circ; \\
 B_0B' &= 10 - 20 \text{ mm}; BB' = 60 - 80 \text{ mm}; \angle(BB'B_0) = 90^\circ.
 \end{aligned}$$

In order to have a stall mechanism in the horizontal position of the bar 1 (Fig. 5), an extension of the segment  $BB'$  (to direction of the articulation B) which limits the relative rotation, has been performed.

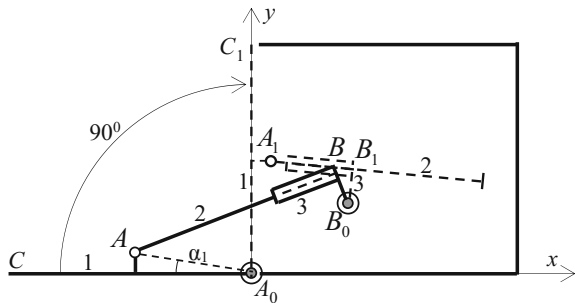
A variant of the four-bar mechanism [1, 2] is obtained if, instead of the joint B (2, 3), a kinematic prismatic joint (Fig. 5) is used, having a rotary movable guide.

In this case (Fig. 5), a dyadic chain LD (2, 3) type RTR is highlighted, on which the transmission angle is optimal,  $\angle(ABB_0) = \tau = 90^\circ$ , which implies a better operation of the system both in opening and closing phases.

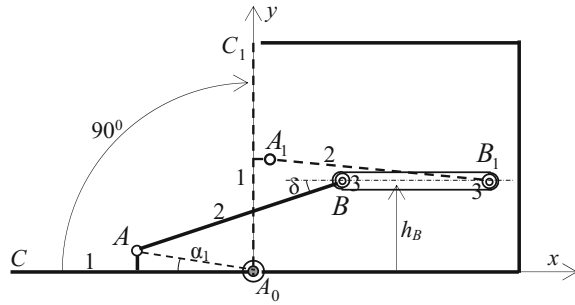
The blocking of the dyadic chain (2, 3) in the open position (when the bar 1 is horizontal) is obtained by mounting a limiter device to the free end of the bar 2 (Fig. 5).

To avoid jamming of the bar 2 into the guide of the element 3, the length of this guide must be long enough.

**Fig. 5** The kinematic scheme of the mechanism with dyad chain type RTR [2]



**Fig. 6** The kinematic scheme of the mechanism with dyadic chain type RRT [2]



Another variant of the mechanism is the one that uses a dyadic chain type RRT (Fig. 6), on which the fixed guide is horizontal, being at the height  $h_B = 100\text{--}110$  mm.

In fact, in the new version (Fig. 6), an equivalent dyadic chain has been used, in which a kinematic element (slider 3) was replaced by a kinematic rotational-sliding joint (4th class). To reduce the sliding friction, a roll 3 is used, this being guided between two parallel surfaces against which the rolling friction occurs.

The positioning and fixing of the rectilinear guide is such that the left end of this guide corresponds to the horizontal position of bar 1. Thus, for a  $90^\circ$  rotation of the  $A_0C$  bar, the point B (the center of the roller 3) must go through the distance  $BB_1$ .

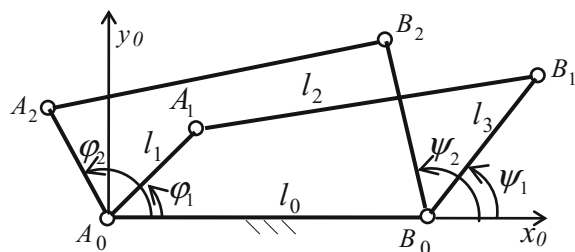
The geometrical condition for a proper operation of this fixed-guide mechanism consists in keeping the pressure angle  $\delta$  at as low as possible, below a critical value of  $30^\circ$ .

### 3 Synthesis of the RRRR Four-Bar Mechanism for Associated Positions

#### 3.1 The Case of Two Imposed Associated Positions

The positions of the fixed joints  $A_0$  and  $B_0$  ( $A_0B_0 = l_0$ ) of the planar four-bar mechanism (Fig. 7) are considered known.

**Fig. 7** The planar four-bar mechanism in two associated positions



The two associated positions of the articulated four-bar linkage are defined (Fig. 7) by the contours  $A_0A_1B_1B_0$  and  $A_0A_2B_2B_0$  that have the fixed element  $A_0B_0$ .

Therefore, when rotating the kinematic input element (driving) with the angle  $\Delta\varphi_{12} = \varphi_2 - \varphi_1$ , the kinematic output element (driven) rotates with the angle  $\Delta\psi_{12} = \psi_2 - \psi_1$ .

In the case of a geometric synthesis application of the mechanism, the relative rotation angles  $\Delta\varphi_{12}$  and  $\Delta\psi_{12}$  are imposed, the lengths  $A_0A = l_1$  and  $B_0B = l_3$  to be determined by analytical calculation, as well as the angles  $\varphi_1$  and  $\psi_1$ .

An analytical solution is obtained by solving the system formed by two non-linear equations, called the Freudenstein synthesis equations, written for the two required positions. Freudenstein's equation can be written as:

$$l_0l_1(\cos\varphi_2 - \cos\varphi_1) - l_0l_3(\cos\psi_2 - \cos\psi_1) + l_1l_3[\cos(\psi_2 - \varphi_2) - \cos(\psi_1 - \varphi_1)] = 0 \quad (1)$$

In the more general case, when the base  $A_0B_0$  of the four-bar linkage is inclined with the angle  $\alpha_0$  (Fig. 8), Eq. (1) has the expression:

$$l_0l_1[\cos(\varphi_2 - \alpha_0) - \cos(\varphi_1 - \alpha_0)] - l_0l_3[\cos(\psi_2 - \alpha_0) - \cos(\psi_1 - \alpha_0)] + l_1l_3[\cos(\psi_2 - \varphi_2) - \cos(\psi_1 - \varphi_1)] = 0 \quad (2)$$

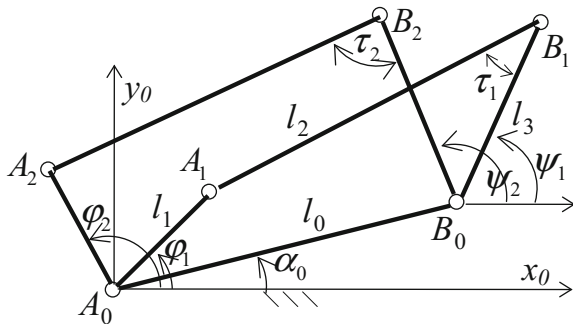
In each of the two positions of the four-bar mechanism (Fig. 8), with the bar 1 as the driving element, the transmission angle (measured in the movable joint of the driven element 3) must be greater than a critical limit value  $\tau_c = 20^\circ$ .

Therefore, from the triangles  $A_0A_1B_0$  and  $A_0A_2B_0$ , the distances  $A_1B_0$  and  $A_2B_0$  are deduced:

$$A_1B_0 = \sqrt{l_1^2 + l_0^2 - 2l_1l_0\cos(\varphi_1 - \alpha_0)} \quad \text{and} \quad A_2B_0 = \sqrt{l_1^2 + l_0^2 - 2l_1l_0\cos(\varphi_2 - \alpha_0)} \quad (3)$$

The transmission angles [2, 4] in the two positions of the four-bar mechanism have the expressions:

**Fig. 8** The more general case when the base is inclined with the angle  $\alpha_0$



$$\cos \tau_1 = (l_2^2 + l_3^2 - A_1B_0^2)/2l_2l_3 \text{ and } \cos \tau_2 = (l_2^2 + l_3^2 - A_2B_0^2)/2l_2l_3 \quad (4)$$

For the transmission angles, values in the ranges  $\tau_1 = 25^\circ - 40^\circ$  and  $\tau_2 = 75^\circ - 90^\circ$ , for example,  $\tau_1 = 30^\circ$  and  $\tau_2 = 80^\circ$ , are chosen. If the angles  $\varphi_1, \varphi_2$  and  $\psi_1, \psi_2$  are imposed, then the lengths  $l_0, l_1, l_2$  and  $l_3$  of the sides of the articulated quadrant remain unknown.

For practical reasons, the length  $A_0A = l_1$  is chosen and the length of the base  $A_0B_0 = l_0$  is chosen equal to the unit ( $l_0 = 1$ ). So, for average values of the transmission angles  $\tau_1$  and  $\tau_2$ , from the nonlinear Eq. (2–4), the parameters  $l_2, l_3$  (as reduced lengths) and  $\alpha_0$  are calculated. If the angle  $\alpha_0$  is imposed, the linear parameters  $l_1, l_2$  and  $l_3$  (as reduced lengths) can be deduced from the three nonlinear Eq. (2–4).

For this variant, the system of three scalar equations to be solved is expressed as follows:

$$l_1[\cos(\varphi_2 - \alpha_0) - \cos(\varphi_1 - \alpha_0)] - l_3[\cos(\psi_2 - \alpha_0) - \cos(\psi_1 - \alpha_0)] + l_1l_3[\cos(\psi_2 - \varphi_2) - \cos(\psi_1 - \varphi_1)] = 0 \quad (5)$$

$$l_2^2 + l_3^2 - l_1^2 - 1 + 2l_1 \cos(\varphi_1 - \alpha_0) - 2l_2l_3 \cos \tau_1 = 0 \quad (6)$$

$$l_2^2 + l_3^2 - l_1^2 - 1 + 2l_1 \cos(\varphi_2 - \alpha_0) - 2l_2l_3 \cos \tau_2 = 0 \quad (7)$$

For example, if:  $\alpha_0 = 45^\circ; \varphi_1 = 90^\circ; \varphi_2 = 180^\circ; \psi_1 = 30^\circ; \psi_2 = 135^\circ;$

$$\tau_1 = 30^\circ; \tau_2 = 80^\circ,$$

the previous equations become:

$$l_1(\cos 135^\circ - \cos 45^\circ) - l_3(\cos 90^\circ - \cos 15^\circ) + l_1l_3(\cos 45^\circ - \cos 60^\circ) = 0 \quad (5')$$

$$l_2^2 + l_3^2 - l_1^2 - 1 + 2l_1 \cos 45^\circ - 2l_2l_3 \cos 30^\circ = 0 \quad (6')$$

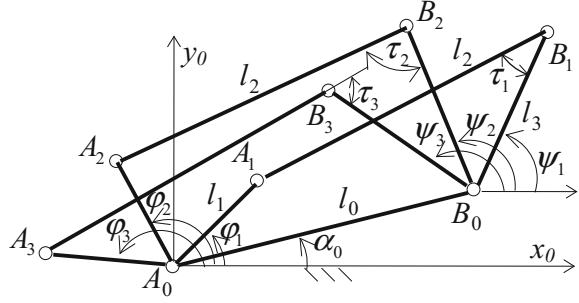
$$l_2^2 + l_3^2 - l_1^2 - 1 + 2l_1 \cos 135^\circ - 2l_2l_3 \cos 75^\circ = 0 \quad (7')$$

### 3.2 The Case of Three Imposed Associated Positions

Let's consider the general case of the articulated four-bar mechanism when the base  $A_0B_0$  is inclined with the angle  $\alpha_0$  (Fig. 9).

The three associated positions [2, 7] of the articulated four-bar linkage are given by the pairs of angles:  $\varphi_1, \psi_1; \varphi_2, \psi_2; \varphi_3, \psi_3$ .

**Fig. 9** The four-bar mechanism in three associated positions



In this case, two Freudenstein equations [5, 8] can be written:

$$l_1 [\cos(\varphi_2 - \alpha_0) - \cos(\varphi_1 - \alpha_0)] - l_3 [\cos(\psi_2 - \alpha_0) - \cos(\psi_1 - \alpha_0)] + l_1 l_3 [\cos(\psi_2 - \varphi_2) - \cos(\psi_1 - \varphi_1)] = 0 \quad (8)$$

$$l_1 [\cos(\varphi_3 - \alpha_0) - \cos(\varphi_2 - \alpha_0)] - l_3 [\cos(\psi_3 - \alpha_0) - \cos(\psi_2 - \alpha_0)] + l_1 l_3 [\cos(\psi_3 - \varphi_3) - \cos(\psi_2 - \varphi_2)] = 0 \quad (9)$$

From the condition imposed on the transmission angle in the three positions (Fig. 9), the following equations are deduced:

$$l_2^2 + l_3^2 - l_1^2 - 1 + 2l_1 \cos(\varphi_1 - \alpha_0) - 2l_2 l_3 \cos \tau_1 = 0 \quad (10)$$

$$l_2^2 + l_3^2 - l_1^2 - 1 + 2l_1 \cos(\varphi_2 - \alpha_0) - 2l_2 l_3 \cos \tau_2 = 0 \quad (11)$$

$$l_2^2 + l_3^2 - l_1^2 - 1 + 2l_1 \cos(\varphi_3 - \alpha_0) + 2l_2 l_3 \cos \tau_3 = 0 \quad (12)$$

For the transmission angles, numerical values are chosen within the ranges:

$$\tau_1 = 20^\circ - 35^\circ; \tau_2 = 75^\circ - 90^\circ; \tau_3 = 45^\circ - 60^\circ.$$

If the linear parameter  $l_1$  and the angles  $\varphi_1, \varphi_2, \varphi_3$  and  $\alpha_0$  are imposed, the lengths  $l_2, l_3$  and angles  $\psi_1, \psi_2, \psi_3$  can be calculated from the system formed by the five nonlinear Eq. (8–12).

For example, for the imposed parameters the following numerical values are considered (Fig. 9):  $l_1 = 0.9; \varphi_1 = 90^\circ; \varphi_2 = 45^\circ; \varphi_3 = 180^\circ; \alpha_0 = 60^\circ$ .

With these numerical data, the synthesis equations are written:

$$0,9[\cos(135^\circ - 60^\circ) - \cos(90^\circ - 60^\circ)] - X_5[\cos(X_2 - 60^\circ) - \cos(X_1 - 60^\circ)] + 0,9X_5[\cos(X_2 - 135^\circ) - \cos(X_1 - 90^\circ)] = 0 \quad (8')$$

$$0,9[\cos(180^\circ - 60^\circ) - \cos(135^\circ - 60^\circ)] - X_5[\cos(X_3 - 60^\circ) - \cos(X_2 - 60^\circ)] + 0,9X_5[\cos(X_3 - 180^\circ) - \cos(X_2 - 135^\circ)] = 0 \quad (9')$$



$$X_4^2 + X_5^2 - 0,9^2 - 1 + 1.8 \cos(90^\circ - 60^\circ) - 2X_4X_5 \cos 25^\circ = 0 \quad (10')$$

$$X_4^2 + X_5^2 - 0,9^2 - 1 + 1.8 \cos(135^\circ - 60^\circ) - 2X_4X_5 \cos 80^\circ = 0 \quad (11')$$

$$X_4^2 + X_5^2 - 0,9^2 - 1 + 1.8 \cos(180^\circ - 60^\circ) + 2X_4X_5 \cos 50^\circ = 0 \quad (12')$$

## 4 Synthesis of the RRTR Crank-Slider Mechanism for Associated Positions

### 4.1 The Case of Two Imposed Associated Positions

The kinematic scheme of the RRTR mechanism (Fig. 10) is considered in two absolutely associated positions, on which the bar 2 is guided in a rectilinear way by the oscillating slider-support about the point  $B_0$ .

The length  $AB = s_2$  of bar 2 is variable and the length  $BB_0 = l_3$  (perpendicular to  $AB$ ) is constant (Fig. 10), the limit being zero. The fixed bar  $A_0B_0 = l_0$  (of constant length) is inclined to the constant angle  $\angle x_0A_0B_0 = \alpha_0$  in respect of the horizontal (axis  $A_0x_0$ ). The positioning angles of the bars 1 ( $A_0A = l_1$ ) and 3 ( $BB_0 = l_3$ ) are  $\varphi_1, \varphi_2$  and  $\psi_1, \psi_2$ , being measured in a positive direction about axis  $A_0x_0$ .

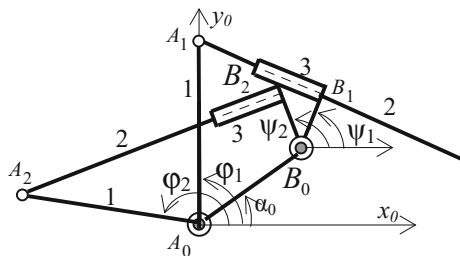
If the closed contour  $A_0ABB_0A_0$  is projected on the direction  $BB_0$  (Fig. 10), for the two positions, the following equations are obtained:

$$l_1 \cos(\varphi_1 - \psi_1) - l_0 \cos(\psi_1 - \alpha_0) - l_3 = 0 \quad (13)$$

$$l_1 \cos(\varphi_2 - \psi_2) - l_0 \cos(\psi_2 - \alpha_0) - l_3 = 0 \quad (14)$$

For the geometrical synthesis of the mechanism, the unitary length of the base  $l_0 = 1$  and the numerical values of the positioning angles  $\varphi_1, \psi_1; \varphi_2, \psi_2$  and  $\alpha_0$ , are imposed. The unknowns of the problem are the reduced lengths  $l_1 = X_1$  and  $l_3 = X_2$ , their numerical value being calculated from the system of two linear Eq. (13–14).

**Fig. 10** The kinematic scheme of the RRTR mechanism in two positions



For this purpose the following equations are written:

$$X_1 \cdot \cos(\varphi_1 - \psi_1) - X_2 = \cos(\psi_1 - \alpha_0) \quad (13')$$

$$X_1 \cdot \cos(\varphi_2 - \psi_2) - X_2 = \cos(\psi_2 - \alpha_0) \quad (14')$$

If the lengths  $l_0 = 1, l_1$  and the position angles  $\varphi_1, \psi_1; \varphi_2, \psi_2$ , are imposed, then the length  $l_3 = X_1$  and angle  $\alpha_0 = X_2$  can be obtained from the system of two non-linear Eq. (13–14).

## 4.2 The Case of Three Imposed Associated Positions

If three absolutely associated positions are required, three equations of closing the kinematic contour have been written:

$$l_1 \cos(\varphi_1 - \psi_1) - l_0 \cos(\psi_1 - \alpha_0) - l_3 = 0 \quad (14)$$

$$l_1 \cos(\varphi_2 - \psi_2) - l_0 \cos(\psi_2 - \alpha_0) - l_3 = 0 \quad (15)$$

$$l_1 \cos(\varphi_3 - \psi_3) - l_0 \cos(\psi_3 - \alpha_0) - l_3 = 0 \quad (16)$$

In the hypothesis of imposing the associated position angles, by means of the three equations we can calculate  $l_1, l_3$  and  $\alpha_0$ .

## 5 Geometrical Synthesis of the RRRT Mechanism for Associated Positions

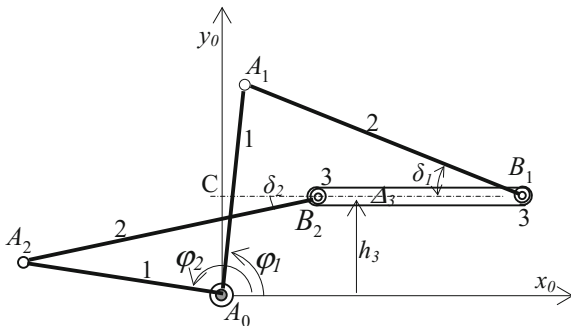
### 5.1 Synthesis for Two Associated Positions

Let's consider the kinematic scheme of the planar sliding mechanism with roller in a fixed horizontal guide (Fig. 11).

In this case the pressure angle  $\delta$ , which is formed by the coupler 2 ( $AB = l_2$ ) with the line  $\Delta_3$  along which the point B (the center of the roller 3) moves, is outlined.

This pressure angle (complement of the transmission angle) must be as small as possible, the optimal value being  $\delta = 0$ . The maximum admissible value of the pressure angle is  $\delta_{max} = 50^\circ$ , so that in the two imposed positions (Fig. 11) the pressure angles are limited:  $\delta_2 < \delta_1 < 50^\circ$ . This is a requirement for avoiding the linkage stall [2].

**Fig. 11** Kinematic scheme of the mechanism with rectilinear guided roller



Observing the closed contour  $A_0ABCA_0$  (Fig. 11), in each of the two absolutely associated positions, the length of bar 2 is expressed according to the coordinates of points A and B:

$$AB^2 = (x_B - x_A)^2 + (y_B - y_A)^2 \tag{17}$$

In the two associated positions, the coordinates of points A and B are:

$$x_{A_1} = l_1 \cos \varphi_1; y_{A_1} = l_1 \sin \varphi_1; x_{A_2} = l_1 \cos \varphi_2; y_{A_2} = l_1 \sin \varphi_2; \tag{18}$$

$$x_{B_1} = CB_1 = s_1; y_{B_1} = A_0C = h_3; x_{B_2} = CB_2 = s_2; y_{B_2} = A_0C = h_3. \tag{19}$$

After substituting these coordinates in Eq. (17), the following equations are deduced:

$$(s_1 - l_1 \cos \varphi_1)^2 + (y_3 - l_1 \sin \varphi_1)^2 = l_2^2; \tag{20}$$

$$(s_2 - l_1 \cos \varphi_2)^2 + (y_3 - l_1 \sin \varphi_2)^2 = l_2^2. \tag{21}$$

For the synthesis of the mechanism, the following parameters are imposed: the length  $l_1$ , the angles  $\varphi_1, \varphi_2$  ( $\varphi_1 < \varphi_2$ ) and the segments  $s_1, s_2$  ( $s_1 > s_2$ ).

In the system formed by the nonlinear Eqs. (20) and (21) we denote  $l_2 = X_1; y_3 = X_2$  representing the two unknowns. Therefore, the system is written in the following form:

$$X_1^2 - (X_2 - l_1 \sin \varphi_1)^2 = (s_1 - l_1 \cos \varphi_1)^2 \tag{22}$$

$$X_1^2 - (X_2 - l_1 \sin \varphi_2)^2 = (s_2 - l_1 \cos \varphi_2)^2 \tag{23}$$

## 5.2 Synthesis for Three Associated Positions

In this case three positions of the mechanism are imposed, i.e. the angular  $\varphi_1, \varphi_2, \varphi_3$  and the linear  $s_1, s_2, s_3$  displacements. Three nonlinear scalar equations are written in which the unknowns can be  $l_1 = X_1; l_2 = X_2; y_3 = X_3$ :

$$(s_1 - X_1 \cos \varphi_1)^2 + (X_3 - X_1 \sin \varphi_1)^2 - X_2^2 = 0; \quad (24)$$

$$(s_2 - X_1 \cos \varphi_2)^2 + (X_3 - X_1 \sin \varphi_2)^2 - X_2^2 = 0; \quad (25)$$

$$(s_3 - X_1 \cos \varphi_3)^2 + (X_3 - X_1 \sin \varphi_3)^2 - X_2^2 = 0. \quad (26)$$

## 6 Conclusions

The paper analyzes the kinematic schemes of the planar bar mechanisms used to open/close the door of a cabinet (buffet). For the case of a door which rotates vertically, an analytical method of geometric synthesis of the RRRR, RRTR and RRRT mechanisms is applied.

The mechanisms are double structures, being mounted in parallel in the vertical plane. In the vertical position, the door closes the cabinet, and in the horizontal position, it opens the cabinet, being ready to “serve”.

The geometric synthesis is solved for two and three associated positions imposed on the two kinematic elements linked to the base. In determining the solutions, the limitation imposed by the transmission/pressure angle is taken into account. The contribution is represented by the synthesis of three associated positions of the three researched linkages, i.e. two extreme positions and one middle position.

## References

1. Antonescu O, Antonescu P (2006) Mechanisms and manipulators (in Romanian). Ed. Printech, Bucharest
2. Antonescu P, Antonescu O (2005) Mechanisms and machines dynamics—coursebook (in Romanian). Ed. Printech, Bucharest
3. Gustav S (2011) Furniture for the entire household (in Romanian). Ed. MAST
4. Lichtenheldt W (1970) Konstruktionslehre der Getriebe. Berlin
5. Popescu I (2014) Opening/closing mechanisms used at doors, windows and cabinets (in Romanian). PhD Report no. 2
6. Sandor GN, Erdman AG (1997) Advanced mechanism design. Prentice Hall, Englewood Cliffs, New Jersey

7. Stoilov Todorov T (1998) Synthesis of four-bar mechanisms by Freudenstein–Chebyshev. *Mech Mach Theory* J 33
8. Zamfir V, Virgolici H, Stoicuta O (2011) Further notes on the interpolation method at the synthesis of mechanisms. *J Mech Manip* 10(1):33–38

# Design of a Class of Novel 3T1R Parallel Mechanisms with Low Coupling Degree



Huiping Shen, Hengcun Qiang, Yunyu Shen and Ting-li Yang

**Abstract** Comparing with three-translation Delta Parallel Mechanisms (PM), 4-DOF three-translation and one-rotation (3T1R) PMs have complex topological structures, which result in complex forward kinematics and inverse dynamics solutions. Therefore, the investigation of novel 3T1R PMs with simple forward kinematics and dynamics solutions is still not completed yet. Coupling degree reduction of a PM can directly reduce its complexity of forward kinematics and dynamics. By using coupling-reducing methods proposed by authors, five original 3T1R PMs with coupling degree 2 are analyzed, which lead to ten novel 3T1R PMs with coupling degree 1 while their basic function, such as DOF and output motion type of the moving platform, stay same. Thus, the forward kinematics and inverse dynamics solutions of the ten 3T1R PMs can be easily obtained by using one dimensional search method or by solving a one-variable polynomial equation.

**Keywords** Coupling-reducing · Topological structure optimization  
Coupling degree · Position and orientation characteristics · Forward kinematics

---

H. Shen (✉) · H. Qiang · T. Yang  
Changzhou University, Changzhou, China  
e-mail: shp65@126.com

H. Qiang  
e-mail: 574656458@qq.com

T. Yang  
e-mail: yangtl@126.com

Y. Shen  
Northeast University, Shenyang, China  
e-mail: 919304858@qq.com

## 1 Introduction

The SCARA (Selective Compliance Assembly Robot Arm) serial robot was invented in 1978. It generates X, Y and Z translations, and a rotation about Z axis, which especially suitable for assembly and has been widely used in various applications [1]. Later, the ABB Company developed FlexPicker in 1999, a SCARA parallel robot. The parallel robot is based on three-translation Delta (1985, Clavel) robot [2, 3] and also has been widely used. The 4-DOF H4(1999), I4(2003), Par4 (2005) SCARA parallel robots were invented by Pierrot's team and they implemented lots of good industrial applications [4–6].

Zhao and Huang put forward a 4-URU type 3T1R parallel robot in 2000 [7]. Yang et al. [8] proposed a class of 3T1R parallel robots by using Single-Open-Chain (SOC) theory in 2001. Huang invented a 4-DOF (3T1R) Cross-IV high-speed handling robots with two or three moving platforms in 2010 [9]. In 2012, Liu developed a prototype of X4 parallel robot with one moving platform [10].

On the other hand, solution for forward position is one of the most important issues in the investigation of PMs since it directly influences the error analysis, singularity analysis and dynamic analysis. Forward position solutions are related to coupling degree  $\kappa$  of a PM [11, 12]. The coupling degree  $\kappa$  reflects the dependency of the kinematic and dynamic parameters among independent loops of a mechanism, which reflects the complexity of solving the kinematics and dynamics of a mechanism. It is proved that the greater coupling degree  $\kappa$  is, the more complex the forward kinematics and inverse dynamics solutions are [12, 13]. However, how to reduce coupling degree  $\kappa$  is less studied so far.

From the perspective of the topological structure of branched chains and topological arrangement of branched chains between the base and moving platforms, three structural Coupling-Reducing Design (denoted as CRD) methods are proposed [13] that could be regarded as one of the most important issues of topological structure optimization [13, 14].

Recently, thirteen SCARA (3T1R) PMs with potential application prospects were proposed by the authors [15]. Among them, ten are original PMs, but their coupling degree are large and 2 [15], which is caused by their own relatively complex topological structure. Further, it will lead to complicate kinematics and dynamics calculations. Therefore, how to reduce their coupling degree is important to design and application of these new 3T1R PMs.

This paper completes the structure coupling-reducing of the five new PMs according to the CRD methods [13, 14]. This work results in five coupling-reducing PMs whose moving platform has three connected points and another five coupling-reducing PMs whose moving platform has two connected points. While the coupling degree of the ten PMs is only one, their basic functions, such as DOF and Position and Orientation Characteristics (POC) of the moving platform, remain unchanged. Thus, the forward kinematics and inverse dynamic solutions of the ten

PMs can easily achieve stable numerical solutions by one dimensional search method or by a high order algebra equation with only one unknown variable [14]. This is good for real control of these manipulators.

## 2 Coupling-Reducing Design Method

### 2.1 Coupling Degree

According to the mechanism composition principle based on the ordered single-open-chains (SOC) units, any PM can be decomposed into a series of SOCs, while a series of SOCs can be further grouped into several Assur Kinematic Chain (AKC). The constraint degree  $\Delta_j$  of the  $j$ th SOC is defined as [12]

$$\Delta_j = \sum_{i=1}^{m_j} f_i - I_j - \xi_{L_j} = \begin{cases} \Delta_j^- = -5, -4, -3, -2, -1 \\ \Delta_j^0 = 0 \\ \Delta_j^+ = +1, +2, +3 \dots \end{cases} \quad (1)$$

The physical meanings of  $\Delta_j^-$ ,  $\Delta_j^0$  and  $\Delta_j^+$  are:

- $\Delta_j^-$  represents a SOC with negative constraint degree, which means it reduces the DOF of a mechanism by  $|\Delta_j^-|$  or applies  $|\Delta_j^-|$  constraints to the mechanism. Therefore,  $|\Delta_j^-|$  constraint equations should be established.
- The  $\Delta_j^0$  represents a SOC with zero constraint degree, which means it does not affect the DOF of the PM and its motion is self-deterministic. In other words, the position of the SOC can be solved independently.
- The  $\Delta_j^+$  represents a SOC with positive constraint degree, which means it increases the degree of freedom of the mechanism by  $\Delta_j^+$ . Further  $\Delta_j^+$  virtual variables should be assigned on the SOC to determine the position of the SOC.

For an AKC, there is always the following equation

$$\sum_{j=1}^{\nu} \Delta_j = 0 \quad (2)$$

Therefore, coupling degree of an Assur Kinematic Chain (AKC) is defined by

$$\kappa = |\Delta_j^-| = \Delta_j^+ \quad \text{or} \quad \kappa = \frac{1}{2} \min \left\{ \sum_{j=1}^{\nu} |\Delta_j| \right\} \quad (3)$$



**Table 1** Ten novel 3T1R PMs obtained from coupling-reducing design (CRD)

No	High coupling degree before CRD ( $\kappa=2$ )	Low coupling degree after CRD ( $\kappa=1$ )	
	A. The original PM	B. Platform with three connected points	C. Platform with two connected points
1			
2			
3			
4			
5			

where operator  $\min.\{\bullet\}$  means that there are many methods for an AKC to be divided into  $\nu$   $SOC(\Delta_j)$ , the one with the least  $\sum |\Delta_j|$  is selected. The coupling degree  $k$  is the maximum among all AKCs.

By the way, the general formula of degree of freedom (DOF) used in the following section was proposed by authors of this paper [12], which is given as

$$F = \sum_{i=1}^m f_i - \sum_{j=1}^{\nu} \xi_{L_j} \quad (4)$$

$$\xi_{L_j} = \dim.\left\{\left(\bigcap_{j=1}^j M_{b_j}\right) \cup M_{b_{(j+1)}}\right\} \quad (5)$$

where operator  $\dim\{\dots\}$  refers to the union operations between the sub-PM's POC which consists of the previous  $j$  chains and the last  $(j + 1)$  chain end's POC.

## 2.2 Coupling-Reducing Design Method

So-called structural coupling-reducing design (shortly, CRD) of a PM is to reduce coupling degree of the PM. Three CRD methods are introduced in [13, 14], i.e., the hybrid branch chain design method, kinematic joints combination method and characteristic branch chain driving method. Since the five new 3T1R PMs, i.e., No. 1–No. 5 listed in the first column of Table 1, are made up of only rotational and spherical joints, kinematic joints combination method is utilized in this paper.

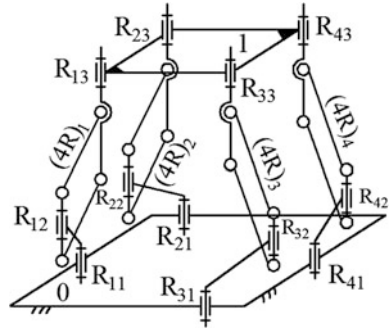
According to Eqs. (1) and (3), the coupling degree  $\kappa$  of an AKC depends on the constraint degree  $(\Delta_j)$  of each member SOC. Accordingly, constraint degree reduction of the SOC can reduce the coupling degree  $\kappa$  of the PM [13], in this way, CRD of these five new 3T1R PMs can be achieved.

## 3 Coupling-Reducing Design for 3T1R PMs

### 3.1 Design of Original 3T1R PM

We take No. 1 original 3T1R PM [15, 16] in Table 1 as an example to illustrate CRD and coupling degree analysis. The 3T1R PM, shown in Fig. 1, is made up of moving platform 1, base platform 0, and four identical hybrid branch chains. There are four connected points, i.e. joints  $R_{13}$ ,  $R_{23}$ ,  $R_{33}$ , and  $R_{43}$  on the moving platform 1. Each branch chain contains one planar 4R parallel quadrilateral linkage which can be expressed as  $R_{i1} \parallel R_{i2} (-\diamond(4R)_i -) \parallel R_{i3}$  ( $i = 1, 2, 3, 4$ ) where, symbol  $\parallel$  stands for parallel, while  $\diamond$  means parallel quadrilateral. The axes of  $R_{13}$ ,  $R_{23}$ ,  $R_{33}$ ,  $R_{43}$

**Fig. 1** No. 1 3T1R PM

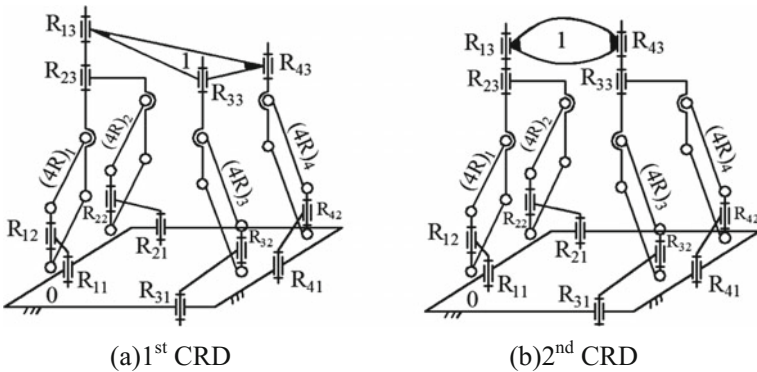


are perpendicular to the moving platform 1, and parallel to the axes of four pairs  $R_{11}$ ,  $R_{21}$ ,  $R_{31}$ ,  $R_{41}$  on the base platform 0.

It is easy to know that when  $R_{11}$ ,  $R_{21}$ ,  $R_{31}$ , and  $R_{41}$  are the actuated pairs, moving platform 1 can achieve three-translation and one-rotation output about the normal of the moving platform 1. This PM is made up of only one AKC and its coupling degree is  $\kappa = 2$  [15]. Therefore, the forward kinematics solutions and dynamic solutions of this PM are more complicate.

### 3.2 CRD for No. 1 3T1R PM

According to kinematic joints combination method [13, 14], if we combine the axes of  $R_{13}$  and  $R_{23}$  in Fig. 1, then a low coupling degree PM is obtained, as in Fig. 2a [17]. We call it the first CRD. At this moment, the moving platform 1 has three connected points, i.e., joints  $R_{13}$ ,  $R_{33}$ , and  $R_{43}$ . The coupling degree  $\kappa$  and POC analysis for this coupling reduced PM are calculated as below.



**Fig. 2** CRD for No. 1 3T1R PM

(1) The topological structure of the PM

Four branch chains can be denoted as  $\{-R_{i1}||R_{i2}(-\diamond(4R)_i) - ||R_{i3}\}$  ( $i = 1, 2, 3, 4$ )

(2) Determine POC generated by the end of each branch chain

$$M_{bi} = \begin{bmatrix} t^1(\perp R_{i1}) \\ r^1(//R_{i1}) \end{bmatrix} \cup \begin{bmatrix} t^1(\perp R_{i2}) \\ r^1(//R_{i2}) \end{bmatrix} \cup \begin{bmatrix} t^1(\diamond abcd) \\ r^0 \end{bmatrix} \cup \begin{bmatrix} t^1(\perp R_{i3}) \\ r^1(//R_{i3}) \end{bmatrix} = \begin{bmatrix} t^3 \\ r^1(//R_{i1}) \end{bmatrix}, (i = 1, 2, 3, 4)$$

(3) Determine the number of independent displacement equations of the first loop  $\xi_{L_1}$ .

(a) The first loop is formed by the 1st, 2nd branch

$$SOC_1 \{-R_{11}||R_{12}(-\diamond(4R)_1) - ||R_{13}||R_{23}||(-\diamond(4R)_2 - )R_{22}||R_{21} - \}$$

$$\xi_{L_1} = \dim. \left\{ \begin{bmatrix} t^3 \\ r^1(//R_{11}) \end{bmatrix} \cup \begin{bmatrix} t^3 \\ r^1(//R_{21}) \end{bmatrix} \right\} = \dim. \left\{ \begin{bmatrix} t^3 \\ r^1(//R_{11}) \end{bmatrix} \right\} = 4$$

Where  $t^3$  represents three translations

$r^1(//R_{11})$  represents one rotation about the axis of joint  $R_{11}$

(b) The DOF and POC of this sub-PM formed are

$$F_{(1-2)} = \sum_{i=1}^m f_i - \sum_{j=1}^1 \xi_{L_1} = 7 - 4 = 4$$

$$M_{pa(1-2)} = \begin{bmatrix} t^3 \\ r^1(//R_{11}) \end{bmatrix} \cap \begin{bmatrix} t^3 \\ r^1(//R_{21}) \end{bmatrix} = \begin{bmatrix} t^3 \\ r^1(//R_{11}) \end{bmatrix}$$

(4) Determine the number of independent displacement equations of the 2nd loop  $\xi_{L_2}$ .

(a) The second loop is composed of the 3rd branch

$$SOC_2 \{-R_{31}||R_{32}(-\diamond(4R)_3 - ||R_{33}\}$$

$$\xi_{L_2} = \dim. (M_{pa(1-2)} \cup M_{b3}) = \dim. \left\{ \begin{bmatrix} t^3 \\ r^1(//R_{11}) \end{bmatrix} \cup \begin{bmatrix} t^3 \\ r^1(//R_{31}) \end{bmatrix} \right\} = 4$$

(b) The DOF and POC of the 2nd sub-PM formed by the 1st sub-PM and 3rd branch chains are

$$F_{(1-2-3)} = \sum_{i=1}^m f_i - \sum_{j=1}^2 \xi_{L_j} = (7+5) - (4+4) = 4$$

$$M_{pa(1-2-3)} = \left[ \begin{array}{c} t^3 \\ r^1(//R_{11}) \end{array} \right] \cup \left[ \begin{array}{c} t^3 \\ r^1(//R_{31}) \end{array} \right] = \left[ \begin{array}{c} t^3 \\ r^1(//R_{11}) \end{array} \right]$$

- (5) Determine the number of independent displacement equations of the 3rd loop  $\xi_{L_3}$ .

The third loop is composed of the 4th branch

$$SOC_3 \{ -R_{41} \| R_{42} ( - \diamond (4R) )_4 - \| R_{43} \}$$

$$\xi_{L_3} = \dim. (M_{pa(1-2-3)} \cup M_{b_4}) = \dim. \left( \left[ \begin{array}{c} t^3 \\ r^1(//R_{11}) \end{array} \right] \cup \left[ \begin{array}{c} t^3 \\ r^1(//R_{41}) \end{array} \right] \right) = \dim. \left\{ \left[ \begin{array}{c} t^3 \\ r^1(//R_{11}) \end{array} \right] \right\} = 4$$

- (6) Determine DOF of the PM

$$F = \sum_{i=1}^m f_i - \sum_{j=1}^3 \xi_{L_j} = (7+5+4) - (4+4+4) = 4$$

- (7) Determine the POC of the moving platform of the PM

$$M_{pa} = M_{pa(1-3)} \cap M_{b_4} = \left[ \begin{array}{c} t^3 \\ r^1(//R_{11}) \end{array} \right] \cap \left[ \begin{array}{c} t^3 \\ r^1(//R_{41}) \end{array} \right] = \left[ \begin{array}{c} t^3 \\ r^1(//R_{11}) \end{array} \right]$$

Therefore, DOF = 4. When the pairs  $R_{11}$ ,  $R_{21}$ ,  $R_{31}$  and  $R_{41}$  on the base platform 0 are actuated, the moving platform 1 can achieve three translations and one rotational output around the normal of the moving platform 1.

- (8) Determine coupling degree  $\kappa$

Once we have obtained the number of independent displacement equations of each loop such that  $\xi_{L_1} = \xi_{L_2} = \xi_{L_3} = 4$ .

We have from Eq. (1)

$$\Delta_1 = \sum_{i=1}^{m_1} f_i - I_1 - \xi_{L_1} = 7 - 2 - 4 = 1$$

$$\Delta_2 = \sum_{i=1}^{m_1} f_i - I_2 - \xi_{L_2} = 5 - 1 - 4 = 0$$

$$\Delta_3 = \sum_{i=1}^{m_1} f_i - I_3 - \xi_{L_3} = 4 - 1 - 4 = -1$$

By using Eq. (3), the coupling degree  $\kappa$  of the PM is

$$\kappa = \frac{1}{2} \sum_{j=1}^{\nu} |\Delta_j| = \frac{1}{2} (1 + |-1|) = 1$$

Further, if the axes of  $R_{33}$  and  $R_{43}$  on the moving platform 1 shown in Fig. 2a are further combined together, which results in another new PM with low coupling degree that has two connected points [18] as shown in Fig. 2b. We call this case as the 2nd CRD. While analyzing its coupling degree, selection of three loops is the same as above. Therefore, the constraint degrees  $\Delta_j$  ( $j = 1-3$ ) are the same. Thus, the coupling degree of the PM is still 1.

In this way, the basic functions, such as DOF and POC which are important topological features, remain unchanged. However, the forward kinematics and inverse dynamic solutions of two PMs become simpler since  $\kappa = 1$ . The difference is that the moving platforms have three or two connected points respectively, which affect work flexibility and the workspace of the moving platform 1. It is still under further investigations.

### 3.3 CRD for Other 3T1R PMs

Similarly, we have conducted CRD for other four 3T1R PMs, such as No. 2–No. 5 PM shown in Table 1[19–21], and performed coupling degree  $\kappa$  and POC analysis. Their results are listed in columns B, C of Table 1.

In Table 1, column A has five original PMs before CRD whose coupling degrees are 2. While columns B and C have ten PMs with low coupling degree  $\kappa = 1$  after CRD, the moving platform of which has respectively three or two connected points. Therefore, the forward kinematics and inverse dynamic solution of these ten new low coupling degree PMs can be found by one dimensional search method [22] or by an one-variable high order algebraic equation.

It is noted that the five PMs in column A of Table 1 are synthesized by using topological structure synthesis theory for PM based on POC equation [12, 15]. Of course, these PMs could also be synthesized by using screw method, displacement subgroups or other methods. However, it is difficult to use those methods to synthesize these ten low coupling degree PMs directly, shown in the columns B and C of Table 1. It means that by using CRD method we can obtain new PMs for which the basic functions remain unchanged, but the coupling degree  $\kappa$  is low. Therefore, CRD can not only be regarded as one of the strategies of the topology optimization of the existing PMs, but also can be regarded as a new practical method which could design PMs with low coupling degree.

The ten 3T1R PMs with low coupling degree ( $\kappa = 1$ ) have simpler forward kinematics and inverse dynamics solutions, which will be further investigated.

## 4 Conclusions

The coupling degree  $\kappa$  describes the topology complexity of a PM and it reflects complexity of solving forward kinematics and inverse dynamics. The greater the  $\kappa$  value is, the more complicate kinematics and dynamics solutions is. Structure CRD not only can be regarded as one of the strategies of the topology optimization of the existing PMs, but also can be as a new practical design method to design PMs with low coupling degree.

The coupling degree of the PMs can be reduced by kinematic joints combination of the rotating or spherical pairs on the moving platform.

The forward kinematics and inverse dynamic solution of ten PMs with coupling degree  $\kappa = 1$  can be easily solved by one dimensional search method or by a one-variable high order algebraic equation. These PMs also have practical development values.

**Acknowledgements** This research is sponsored by the NSFC (Grant No. 51375062 and 51475050) and Jiangsu Key Development Project (No. BE2015043) and Jiangsu Scientific and Technology Transformation Fund Project (No. BA2015098).

## References

1. Shan Y (2005) SCARA robot-still fast and reliable. *Robot Tech Appl* 5:31–33
2. Clavel R. Device for the movement and positioning of an element in space: US, 4976582, 11 Dec 1990
3. ABB. IRB 360 Flexpicker[EB/OL]. <http://www.new.abb.com/products/robotics/industrial-robots/irb-360>. Accessed 06 May 2015
4. Pierrot F (1999) COMPANY O. H4: a new family of 4-dof parallel robots. In: 1999 Proceedings of the IEEE/ASME international conference on advanced intelligent mechatronics, 19–23 Sept 1999. IEEE, Atlanta. New York, pp 508–513
5. Krut S, Company O et al (2003) I4: A new parallel mechanism for SCARA motions. In: Proceedings of the IEEE international conference on robotics and automation, 14–19 Sept 2003. IEEE, Taiwan, China, pp 1875–1880
6. Nabat V, Company O et al (2005) Par4: very high speed parallel robot for pick-and-place. In: Proceedings of the IEEE/RSJ international conference on intelligent robots and systems, 2–6 Aug 2005. IEEE, Alberta, New York, pp 1202–1207
7. Tieshi Z, Zhen H (2000) Theory and application of selecting actuating components of spatial parallel mechanisms. *Chin J Mech Eng* 36(10):81–85
8. Yang T-L, Jin Q, Liu A-X, Yao F-H, Luo Y-F (2001) Structure synthesis of 4-dof (3-translation and 1-rotation)parallel robot mechanisms based on the units of single-opened-Chain. In: Proceedings of the ASME 2001 Design engineering technical conference and computers and information in engineering conference, Paper no. DETC2001/DAC-21152
9. Huang T, Liu H, Meng LI (2005) The robot with five degree of freedom: China, CN1709657, 11 July 2005
10. Liu X, Xie F, Wang L et al (2012) A four freedom of degree parallel mechanism with single moving platform which can achieve SCARA move:China, 201210435375.1, 02 Nov 2012

11. Yang TL (1983) Structural analysis and number synthesis of spatial mechanisms. In: Proceedings of the 6th world congress on the theory of machines and mechanisms, New Delhi, vol 1, pp 280–283
12. Tingli Y, Anxin L, Yufeng L et al (2012) Theory and application of robot mechanism topology. China science press, Beijing
13. Shen HP, Yang L-J, Meng Q-M, Yin H (2015) Topological structure coupling-reducing of parallel mechanisms. In: IFToMM World Congress, 25–30 Oct 2015, Taipei, Taiwan. <https://doi.org/10.6567/iftomm.14th.wc.os13.120>
14. Shen H, Zhu X, Yin H et al (2016) The principle and design method for structure coupling-reducing of parallel mechanisms. *J Mech Eng* 52(23)
15. Yang T, Liu A, Shen H, Hang L (2016) Topological structure synthesis of 3T1R parallel mechanism based on POC equations. In: Proceedings of 9th international conference on intelligent robotics and applications, ICIRA 2016, Lecture notes in computer science, v9834, pp 147–161. [https://doi.org/10.1007/978-3-319-43506-0\\_13](https://doi.org/10.1007/978-3-319-43506-0_13)
16. Shen H, Yang T, Li J et al (2015) A parallel robot device with three translations and one rotation: China, 201510567133.1, 8 Sept 2015
17. Shen H, Xiong K, Yang Ti et al (2016) A low coupling degree three-translation and one-rotation parallel robot device with a three-joint moving platform: China, 201610141841.3, 12 Mar 2016
18. Shen H, Zeng Q, Qiang H et al (2016) A low coupling degree three-translation and one-rotation parallel robot device with a two-joint moving platform: China, 201610141696.9 [P]. 2016-03-12
19. Shen H, Yang T, Deng J et al (2015) A parallel robot mechanism with three translations and one rotation: China, 201510566039.4, 8 Sept 2015
20. Meng Q, Shen H, Shao G et al (2016) A low coupling degree three-translation and one-rotation parallel robot device with a two-joint moving platform: China, 201610141831.X, 12 Mar 2016
21. Li J, Shen H, et al (2016) A low coupling degree three-translation and one-rotation parallel robot platform with a three-joint moving platform: China 201610141614.0, 12 Mar 2016
22. Shen HP, Ting KL, Yang TL (2000) Configuration analysis of complex multiloop linkages and manipulators. *Mech Mach Theory* 35(3):353–362



**Part II**  
**Biomechanics and Rehabilitation**

# Design and Finite Element Analysis of a New Spherical Prosthesis-Elbow Joint Assembly



D. Tarnita, C. Boborelu, D. Popa and D.-N. Tarnita

**Abstract** This study aims to present a new virtual model of an elbow prosthesis with as few components as possible, having a simpler technological approach which can be an important base for the study of the complex behavior of the elbow joint. The prosthetic system is of spherical type consisting of three parts: a part implanted in the humerus, a part implanted in the ulna bone and a third part transforms the assembly from an unconstrained prosthesis in a semi-constrained prosthesis. The kinematic simulation of the flexion-extension and pronation-supination movements of the spherical prosthesis—joint assembly was performed. The virtual model is designed in Solid Works software. By using the finite element method, the healthy elbow joint and the prosthetic elbow joint assembly were analysed and the comparative diagrams of the maximum stress in healthy elbow joint and in prosthetic elbow joint concerning the flexion-extension and pronation-supination movements were drawn and analysed.

**Keywords** Virtual model · Elbow joint · Spherical prosthesis  
Finite element method · Stress

---

D. Tarnita (✉) · D. Popa  
University of Craiova, Craiova, Romania  
e-mail: tarnita.daniela@gmail.com

C. Boborelu  
Emergency Hospital of Dolj County, Craiova, Romania  
e-mail: boboreluc@yahoo.com

D.-N. Tarnita  
University of Medicine and Pharmacy, Craiova, Romania  
e-mail: dan\_tarnita@yahoo.com

## 1 Introduction

Virtual modeling, starting from CT or MRI sectional images, as well as finite element analysis of biomechanical behavior and strains and deformations of integral human bones as well as fractured and implanted with various types of implants such as plates, fixators or centromedular rods, have been addressed in numerous studies [1–9]. The normal human joints, the affected joints by various diseases, such as osteoarthritis, and prosthetic joints have been modeled and analyzed with finite elements in order to study their biomechanical behavior. The elbow joint is a mechanical complex joint, composed by: ■ the humeroulnar joint (main joint) and the humeroradial joint (secondary joint)—which allow the flexion-extension movements; ■ the proximal radioulnar joint (the main joint) and the humeroradial joint (the secondary joint)— which allow the pronation-supination movement [1].

Prosthetic implant can be defined as a permanent device that are used in surgical implant technique aiming at the elimination of pain and improvement of the functionality in a joint [1, 10–16]. The most known types of elbow prosthesis are: 1. Radial head prosthesis; 2. Humero-ulnar prosthesis; 3. Total elbow prosthesis. The most commonly used Humero-ulnar prosthesis are: 1. Souter-Strathclyde prosthesis; 2. KUDO prosthesis; 3. GSB prosthesis (Gschwend, Scheier and Bähler); 4. Coonrad-Morrey prosthesis; 5. Ewald prosthesis (capillary-condyle); 6. Latitude prosthesis.

Total elbow arthroplasty, which can be defined as a reconstructive surgical intervention with bone sacrifice and prosthetic replacement of articular components, remains the most definitive functional procedure for patients with end-stage painful arthritis of the elbow. During the time, in the last decades, complication rates have been quite high. A good understanding of elbow anatomy and kinematics has led to advances in prosthetic design and surgical technique. Mechanical failures of the elbow prosthesis lead to the shortening of prosthesis life and of the use of arthroplasty in a younger, higher-demand patient population.

In order to be really efficient, articular endoprosthesis must fulfill specific compulsory characteristics [10, 14–16]:—biocompatibility;—low friction between the components;—efficient, solid and durable fixation;—design of components must reproduce the joint as accurately as possible and not disturb the articular architecture.

Therefore, in order to fulfill the goals proposed and to comply with the mentioned characteristics, the objectives in relation to prosthetic implant design are, regardless of the constructive version, the following [10, 14–16]:—simplicity, both in terms of design and in terms of insertion;—quality keeping, expressed as the capacity of sacrificing a minimum quantity of healthy tissue; manufacturing characteristic;—cost;—safety;—durability. Still, a series of problems that are the object of an intense research nowadays, such as: finding an optimum design for the implant; optimization of fixation techniques; improvement of the instruments used; facilitation of review surgeries are unsolved.

The method of evaluating the results of elbow arthroplasty implants has become standardized and the evaluation system has been established by Morrey et al. [16]. This system includes the use of three criteria:—Radiographic appearance;—pain;—movement. The Morrey evaluation system considers the following categories of results [16].

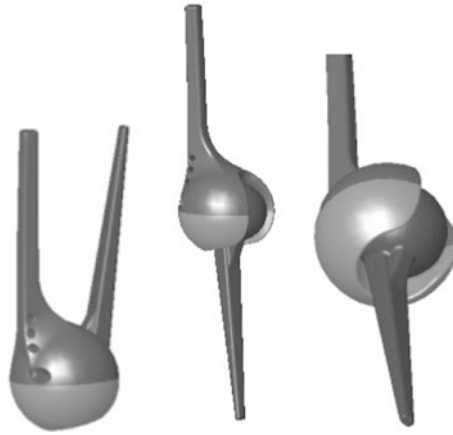
- **Good results:** No radiological changes of the bone-cement-prosthesis interface; No pain; Flexibility greater than  $90^\circ$ ; Pronation and supination of  $60^\circ$ .
- **Satisfactory results:** More than 1 mm of the bone-cement-prosthesis interface enlargement; Moderate pain; Flexion- extension between  $50$  and  $90^\circ$ ; Pronation—supination less than  $40^\circ$ .
- **Poor results:** More than 2 mm of augmentation of the bone-cement-prosthesis interface; Pain that significantly limits activity; Flexion-extension less than  $50^\circ$ ; Pronation-supination less than  $40^\circ$ ; Revision of elbow arthroplasty.

This study aims to present a new virtual model of a elbow prosthesis with as few components as possible, having a simpler technological approach which can be an important base for the study of the complex behavior of the elbow joint.

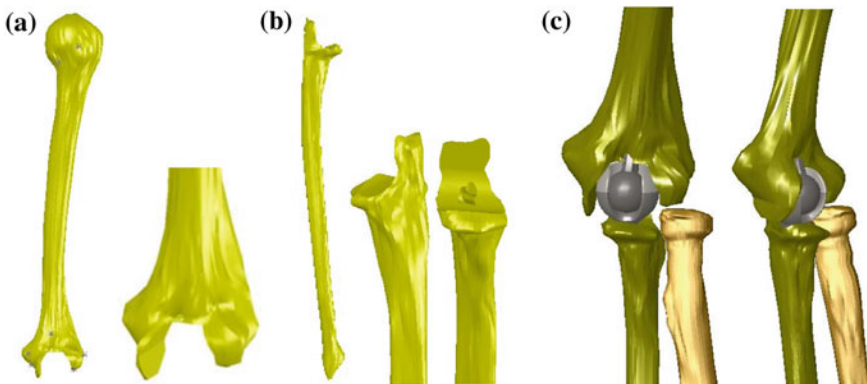
## 2 Virtual Modeling of the Spherical Prosthesis

In order to generate and design the virtual geometric model of spherical elbow prosthesis the conditions imposed by the anatomy of the elbow joint, the prosthetic surgeon techniques and the kinetic parameters analysis of the biomechanics of the normal elbow were analyzed. SolidWorks [17] software was used to parameterize the new proposed spherical prosthesis. Starting from the crossed elbow sections obtained by computer tomography the three-dimensional virtual model of healthy elbow joint, was developed in [1, 3], and, for numerical simulation and analysis of the new prosthetic joint assembly, the virtual models of the humerus, ulna and radius bone components were cut with profiles made in various planes, in order to respect the imposed requirements. The model is designed to allow dimensional changes to adapt it to patient groups using the full geometric parameterisation property. Using specific commands that remove certain degrees of freedom, the spherical elbow prosthesis model was elaborated (Fig. 1).

The humeral and ulnar bone components were subjected to different operations based on the analysis of the orthopedic-surgical methods and operations during the surgical procedure. The modified bone components and the attached stems of the spherical elbow components were loaded into the assembly module, as is shown in Fig. 2. The prosthetic system is of spherical type consisting of three parts: a part implanted in the humerus bone, a part implanted in the ulna bone and the third part which transforms the assembly from an unconstrained prosthesis into a semiconstrained prosthesis. The metallic implant is fixed through cementation in the humerus and ulna.



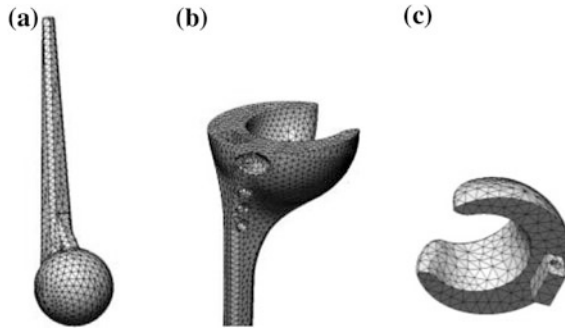
**Fig. 1** Virtual model of spherical elbow prosthesis



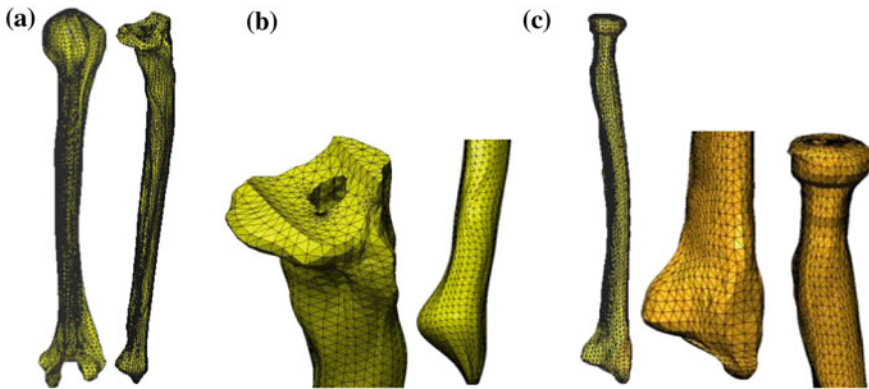
**Fig. 2** Virtual model of humerus (a) and ulna prepared for implantation (b); the spherical prosthesis-elbow joint assembly (c)

The finite element analysis method is a modern and very powerful tool used to understand the biomechanical behaviour of the healthy human joints or pathological ones, being therefore very useful, particularly for the human elbow joint [1, 5, 7]. The prosthetic components and the bones were meshed into finite elements (Figs. 3 and 4), obtaining a network of 286802 nodes and 174897 elements.

For the FEA analysis of the stress developed in the elbow-prosthesis assembly, the characteristics of materials are presented in Table 1.



**Fig. 3** Finite element network for the spherical prosthesis components: **a** humeral component; **b** ulnar component; component for semi-constrained prosthesis



**Fig. 4** Finite element network of humerus **(a)**, cubitus **(b)** and radius **(c)**

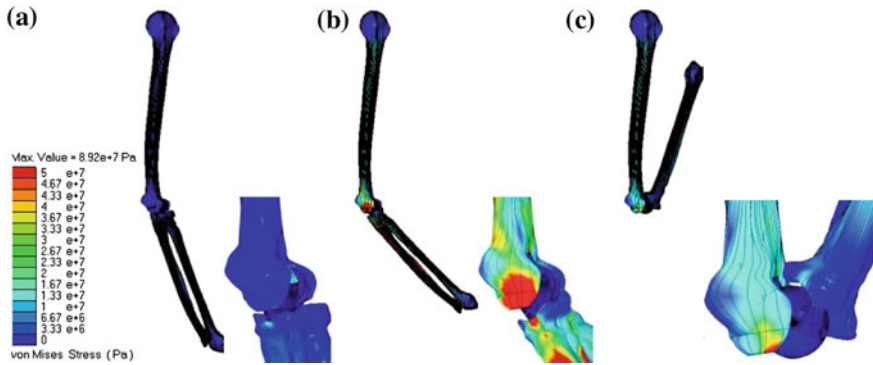
**Table 1** Characteristics of material [1]

Characteristics	Bone	Titan
Density ( kg/mm <sup>3</sup> )	1.4e - 5	4.85e - 6
Elastic modulus (Pa)	2.14e + 10	1.02e + 11
Poisson's ratio	0.5	0.3

### 3 Finite Element Analysis of the Prosthesis-Elbow Assembly

#### 3.1 Flexion-Extension

The virtual test of the spherical prosthesis-elbow assembly for flexionextension is performed in Visual Nastran software and the parameters are:



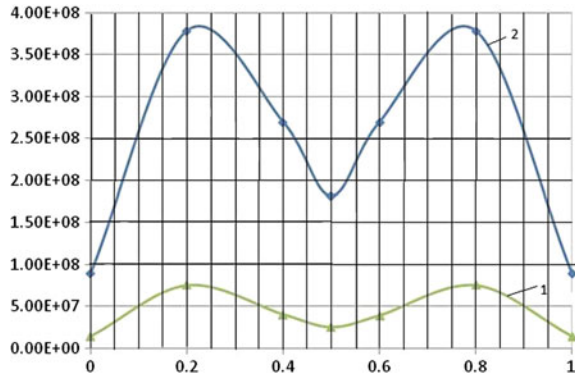
**Fig. 5** Stress map for prosthetic elbow flexion-extension: **a**  $t = 0.1$  s, **b**  $t = 0.2$  s, **c**  $t = 0.6$  s

- the total duration of flexion-extension movement is 1 s;
- the force is equal to 100 N, corresponding to the lifting and lowering of a weight by pure flexion-extension movement, it has permanent vertical action and has the point of application at the end of the ulnar stem;
- the humeral stem is fixed, other elements are considered movable or attached to fixed or moving elements;
- a motor coupler having a constant angular speed of 160 deg/s was defined between the two components forming the spherical joint;
- modeling Software: Solidworks; Virtual Testing Software: Visual Nastran [18].

3 frames of dynamic stress map for flexion-extension of elbow are shown in Fig. 5.

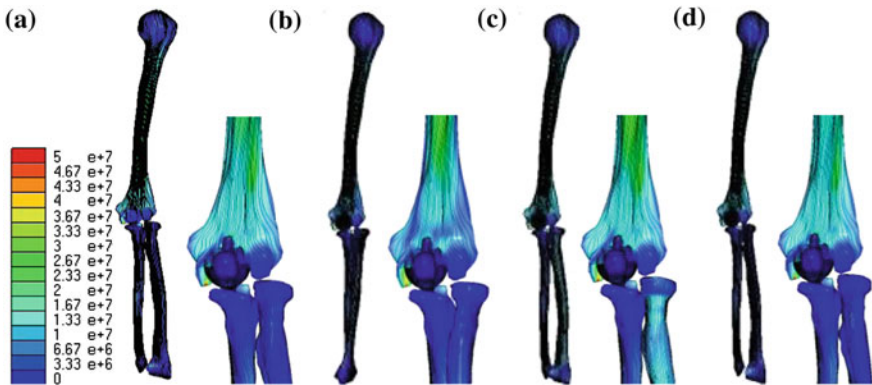
Based on the stress maps obtained for the analyzed timeframe, the diagram of maximum stress values of the spherical prosthesis-elbow joint was plotted. Figure 6 presents comparative graphs of the maximum stresses for flexion-extension in the case of a healthy elbow and the prosthetic elbow with the spherical prosthesis. From Fig. 6 it is observed that the maximum values of the elbow joint in the case of extension flexion movements are recorded for the elbow in the  $90^\circ$  position, when the bending moment is maximum due to the maximum arm of the force. Minimum stresses are recorded in the maximum extension position when the force arm tilts to 0. Small values are also recorded in the maximum flexion position when the force arm becomes very small, but not zero (due to the fact that, for anatomical reasons, the flexion can be made up to an angle of maximum  $70^\circ$  to the horizontal position). The maximum stress values of flexion-extension angle in healthy elbow are about 5 times lower than those obtained in proposed prosthesis-elbow assembly, but in the prosthetic case, the values remain within admissible material strength values.

**Fig. 6** Comparative diagram of the maximum flexion-extension stress [MPa] for: 1 healthy elbow and 2 spherical prosthesis-elbow assembly



### 3.2 Pronation-Supination

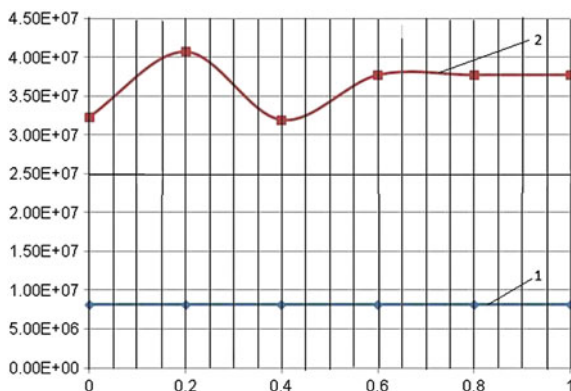
Stress maps corresponding to the pronation-supination with the supporting of a 10 kg weight (Fig. 7), were obtained using the same kinematic simulation and loading scheme as in the study of flexion-extension. Based on the stress maps obtained for the analyzed time interval, the comparative diagrams of maximum stress values for pronation-supination for the case of the healthy elbow and the elbow with spherical prosthesis are presented in Fig. 8. It is noted that the values of the stress in elbow joint in the case of pronationsupination movements remain almost constant throughout the movement because, in the vertical anatomical position of the arm, sections of the bones or prostheses are only subject to the vertical force equal to 100 N. Minimum stresses are recorded for healthy elbow, increased values (about 5 times) are present in spherical prosthesis-elbow assembly. The results were obtained taking into account the fact that, in order to perform a



**Fig. 7** Dynamic tension map of the prosthetic elbow joint in transe-supination motion for **a** t = 0 s, **b** t = 0.6 s, **c** t = 0.8 s **d** t = 1 s



**Fig. 8** Comparative diagram of maximum pronation-supination stress for: 1 healthy elbow, and 2 elbow with spherical prosthesis



finite element analysis on a very complex structure, like the one of the healthy and prosthetic elbow joint, some simplifications have been made: only the bones and metallic components were taken into account, and the action of the muscles, tendons and ligaments was disregarded.

The proposed prosthesis fulfils the main criteria in order to be considered superior to those used so far:

- **Simplicity**—the new prosthetic model, consisting of two components, fulfils the criterion of simplicity; implantation kit is simple and it does not use special tools;
- **conservation**—bone damage during implantation is low;
- **manufacturing**—the simplicity of the prosthetic components allows them to be made with classical tools with no special equipment;
- **cost**—due to the simplicity of the components, the costs are much smaller than in the case of current prostheses;
- **safety**—especially concerning the dysfunctionality and the failure of the prosthesis. A main advantage consists in the fact that it is a metal metal-type prosthesis, without other materials such as polyethylene;
- **service**—by increasing the options and reducing the technical barriers in the revision surgery of the damaged prosthetic components, the service is easy to carry out due to the very simple manner of implantation;

For future work the experimental kinematics of healthy and prosthetic elbow joint will be performed on samples of healthy subjects and patients using Biometrics, an advanced acquisition system [19, 20] and a dedicated experimental bench [21].

## References

1. Tarnita D et al (2010) The three-dimensional modeling of the complex virtual human elbow joint. *Rom J Morphol embr* 51(3):489–495
2. Rathnayaka, K., 3D Reconstruction of Long Bones Utilising Magnetic Resonance Imaging (MRI), thesis PhD, Institute of Health and Biomedical Innovation, Queensland University of Technology, Brisbane, Australia, 2011
3. Tarnita D, Berceanu C, Tarnita C (2010) The three-dimensional printing—a modern technology used for biomedical prototypes. *Materiale plastice* 47(3):328–334
4. Zhang L et al (2011) Upper limb musculo-skeletal model for biomechanical investigation of elbow fl movement. *Journal of Shanghai Jiaotong Univ. (Science)* 16(1):61–64
5. Tarnita D et al (2010) In vitro experiment of the modular orthopedic plate based on Nitinol, used for human radius bone fractures. *Rom J Morphol Embryol* 51(2):315–320
6. Rathnayaka K, Momot KI, Noser H, Volp A, Schuetz MA, Sahama T, Schmutz B (2012) Quantification of the accuracy of MRI generated 3D models of long bones compared to CT generated 3D models. *Med Eng Phys* 34(3):357–363
7. Tarnita, D., et al, Modular adaptive bone plate for humerus bone osteosynthesis, *Romanian Journal of Morphology and embryology*, Vol. 50(3), pp 447–452
8. Gelaude F, Sloten JV, Lauwers B (2006) Semi-automated segmentation and visualization of outer bone cortex from medical images. *Computer Methods in Biomechanics & Biomedical Engineering* 9(1):65–77
9. Gelaude F, Sloten JV, Lauwers B (2008) Accuracy assessment of CT-based outer surface femur meshes. *Computer Aided Surgery* 13(4):188–199
10. Cobb TK, Morrey BF (1997) Total elbow arthroplasty as primary treatment for distal humeral fractures in elderly patients. *J Bone Joint Surg Am* 79(6):826–832
11. Kamineni S, Morrey BF, Distal humeral fractures treated with noncustom total elbow replacement. *Surgical technique J Bone Joint Surg Am*. 2005 Mar; 87 Suppl 1(Pt 1):41–50
12. Gramstad GD, King GJ, O'Driscoll SW, Yamaguchi K (2005) Elbow arthroplasty using a convertible implant. *Tech Hand Up Extrem Surg*. 9(3):153–163
13. Kerboull M (1990) Arthroplastie totale de la hanche par voie transtrohanterienne-*Encycl. Med. Chir. (Editions Techniques) Orthopedie*, Paris, vol 44665, 4-1990, pp 1–12
14. Tooms RE, Harkess WJ (1992) Arthroplasty: Introduction and overview in *Campbell's operative orthopaedics (Crenshaw A.H.)-Ed, vol 1. Mosby Year Book, Boston*, pp 371–389
15. van der Lugt JC, Rozing PM (2004) Systematic review of primary total elbow prostheses used for the rheumatoid elbow. *Clin Rheumatol* 23(4):291–298
16. Morrey B, Askew I, Chao E (1050) Total elbow arthroplasty. *J Bone Joint Surg* 1981:63A
17. [www.solidworks.com](http://www.solidworks.com)
18. [www.mssoftware.com](http://www.mssoftware.com)
19. Tarnita D (2016) Wearable sensors used for human gait analysis. *Rom J Morphol Embryol* 57(2):373–382
20. Tarnita D, Tarnita DN (2016) Experimental measurement of flexion-extension movement in normal and corpse prosthetic elbow joint. *Rom J Morphol Embryol* 57(1):145–151
21. Tarnita D et al (2015) Experimental bench used to test human elbow endoprosthesis. In: *new trends in mechanism and machine sciences: from fundamentals to industrial applications*, vol 24, pp 669–677

# Experimental Method for Dynamic Evaluation of Spinal Column Deformation Exercises



A.-M. Vutan, V. Ciupe, C. M. Gruescu and E.-C. Lovasz

**Abstract** Spinal deformities appear very frequently in child or adult population. Researches in this field are widely spread and continuously developing now-days, as the current schemes of treatment are long-lasting, costly and not very effective. The authors propose an investigation method based on a set of sensors, which are accelerometers and provide data in order to generate a mathematical model of the spine, namely a high degree polynomial. Basic parameters, such as the Cobb angle are computed within the mathematical algorithm. The angles acquired by the sensors are recorded as functions of time, so that the change in shape of the spine during the exercises prescribed by the kinetotherapist is subject of study and a criterion for optimizing the nature and intensity of the exercises.

**Keywords** Spinal deformation • Accelerometer • Mathematical model of the spine

## 1 Introduction

Vertebral disorders are very common in recent years among children and adults, due to lack of physical activity [1] and long-term prolonged sitting position [2]. Spinal deviations, such as scoliosis, may occur from younger ages continuing to

---

A.-M. Vutan · V. Ciupe · C. M. Gruescu (✉) · E.-C. Lovasz  
Politehnica University of Timisoara, Timișoara, Romania  
e-mail: corina.gruescu@upt.ro

A.-M. Vutan  
e-mail: anamariavutan@yahoo.com

V. Ciupe  
e-mail: valentin.ciupe@upt.ro

E.-C. Lovasz  
e-mail: erwin.lovasz@upt.ro

aggravate in puberty and in adulthood, and can cause painful syndromes, low self-esteem, and even cardiopulmonary complication.

Among the deviations of the spine, scoliosis is the most common deformity in children and adolescents [3]. Scoliosis is a progressive disease characterized by one or more lateral curvatures of the spine, visible in the frontal plan and accompanied by the rotation of the vertebral bodies [4].

Over the last 40 years, numerous studies have been conducted on the incidence of scoliosis among children. In the literature, idiopathic scoliosis has a prevalence of 0.47–5.2% [3]. The girls are most affected and the risk of increasing the deviation is higher than for boys.

The orthopedic doctor is the one who establishes the diagnosis of scoliosis and follows the evolution in time. The follow-up protocol of scoliosis involves performing every 6 months the clinical and imaging control over the entire period of time until bone maturation is achieved. Currently, the examination can be achieved by X-ray, CT, MRI, Moiré topography, integrated shape imaging system (ISIS) and computer raster stereography. Because some of these investigations use radiations that are harmful for children [4], new approaches of investigation have been attempted in a non-invasive manner for the human body. These new devices are not widespread for use at this time: thermography, mapping the three-dimensional digital image acquisition using InSpeck system [5–8], mapping with ultrasonic digital equipment such as Zebris [9], 3D scanning and 3D reconstruction using Kinect sensor [10], a wearable monitoring system based on inertial sensors [11].

As a result of the imaging examination, the orthopedic doctor establishes the diagnosis and the magnitude of the scoliotic curvature by calculating the Cobb angle. This represents the angle formed by the intersection of the tangent line to the upper plateau of the upper vertebra of the curvature and the tangent line to the lower plateau of the lower vertebra of the curvature. Depending on the value of the Cobb angle, the treatment followed by the patient will be determined by the protocol proposed by Stagnara:

- if the Cobb angle is between  $0^\circ$  and  $30^\circ$ , physical therapy is recommended
- if the Cobb angle is between  $30^\circ$  and  $50^\circ$ , physiotherapy and orthopedic brace are recommended
- if the Cobb angle is over  $50^\circ$ , the spine surgery is indicated.

There had been done numerous studies during the last decades on the effectiveness of physical therapy treatments. The authors of [12] conducted a systematic review of the effectiveness of specific exercises used in rehabilitation of scoliosis (AIS—adolescent idiopathic scoliosis). There have been studied:

- Non-specific physical therapy exercises
- Exercises from Schroth therapy: exercises based upon fixing the pelvis, thus actively performing a trunk elongation, derotation of the ribs and flattening the ribs hump. Patients do an intensive treatment for 6–8 h a day for 4–6 weeks and after this period, they continue at home a program of specific exercises for 90 min a day [13, 14]

- Side-shift therapy (original approach by Min Mehto): auto-correction exercises for the trunk (in time, these auto-correction have to be applied in activities of everyday life) [15]
- Exercises DoboMed: symmetric position to perform active movements in closed kinematic chain in order to facilitate the active correction in between the two symmetric stable girdles and to support the consolidation of the correct postural habit
- Exercises from SEAS (Scientific Exercises Approach to Scoliosis) by ISICO (Italian Scientific Spine Institute): exercises based on auto-elongation of the former Lyon method [12]
- ISR (integrated scoliosis rehabilitation): exercises to correct the scoliotic posture by means of proprioceptive and external stimulation [16]. The patient is supervised by a team consisting of a physician, a therapist and a psychologist.

Almost all studies all over the world (Asia, USA, and Europe) have concluded that specific exercises play an important role in the evolution of scoliosis. Unfortunately, there are mentioned in the literature cases where, regardless of the method used, the Cobb angle continued to evolve. It is very difficult to calculate the percentage of progression in patients under 16 years old [17]. The progressing rate of scoliosis depends on age, magnitude of the Cobb angle, sex, the method of rehabilitation, the patient's conscious involvement. In the literature the progression values of scoliosis are based on the factors listed below, from 2.8% [16] to 11.6% [18] and even 19.5% [16].

Starting from the data presented above, this paper proposes to study the effects of the specific exercises used in the scoliosis recovery programs by analyzing the change of the Cobb angle in the course of the movement and if it is possible to choose from a given number of exercises only those that are most effective for the patient. An individual recovery program, specific to each patient, according to its particularities, is to be established.

For this purpose, a set of accelerometers is attached to the patient's trunk and provides data in order to generate a dynamic mathematical model of the spine.

## 2 Method for Dynamic Measurement of the Cobb Angle

The sensors applied on the vertebrae body provide data, consisting of three angles ( $\varphi_x, \varphi_y, \varphi_z$ ) around the axes of a reference system, attached to each bone. The shape of the spine is relevant especially within the frontal plane. The mathematical model is going to be generated as a plane curve contained in the frontal plane. In addition, the relative rotation angles between the vertebrae in the transverse plane can be easily computed from the differences between the angles  $\varphi_z$ .

The projection of the measurement points on the frontal plane consists of nine points, for which the angles  $\varphi_{xi}$  ( $i=1 \dots 9$ ) are known from the sensors. The

distances between the points  $l_i, i+1$  ( $i = 1, \dots, 8$ ) are measured directly by the operator who runs the medical investigation.

Figure 1 shows points  $M_1, \dots, M_9$ , drawn in an orthogonal reference system attached to the first lower point.

The purpose of acquiring data is the computation of the coordinates and the generation of a mathematical model of the spine. This model is intended to be a high degree polynomial (the highest degree is eight, as the number of precision points is 9). Once the analytical equation of the spine is established, it is possible to determine the inflection points of the curve, the direction of the normal lines in these points and the computation of the Cobb angle (or Cobb angles, depending on the number of inflection points). In Fig. 1 there are three inflection points and thus, there are two Cobb angles to determine.

The coordinates of the points are given by the relations:

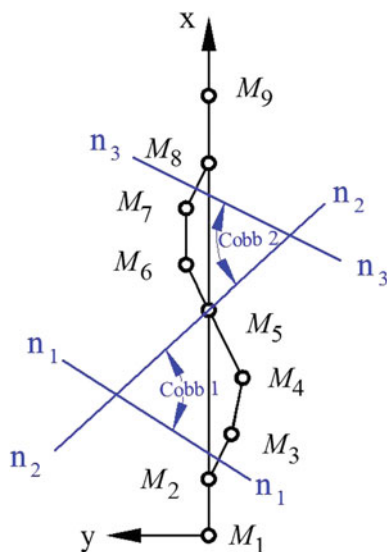
$$\begin{cases} x_{M1} = 0 \\ y_{M1} = 0 \\ x_{Mi+1} = x_{Mi} + l_i \cos \varphi_i & i = \overline{1,8} \\ y_{Mi+1} = y_{Mi} + l_i \sin \varphi_i & i = \overline{1,8} \end{cases} \quad (1)$$

The nine pairs of coordinates allow the determination of an interpolation polynomial of eighth degree. The shape of the spine will be described by the equation:

$$y = a_0x^8 + a_1x^7 + a_2x^6 + a_3x^5 + a_4x^4 + a_5x^3 + a_6x^2 + a_7x + a_8. \quad (2)$$

The roots of the second derivative of Eq. (2) and the study of the sign change of the second derivative provide the inflection points of the polynomial function.

**Fig. 1** Nine points on the deformed spine and Cobb angles



Considering the inflection points  $I_1(x_1, y_1)$ ,  $I_2(x_2, y_2)$  and  $I_3(x_3, y_3)$ , the gradient of the normal to the polynomial (2) is given by the relations:

$$m_1 = -\frac{1}{y'(x_1)}, \quad m_2 = -\frac{1}{y'(x_2)}, \quad m_3 = -\frac{1}{y'(x_3)}, \quad (3)$$

where  $y'$  is the first derivative of the polynomial (2).

The Cobb angles (Fig. 1), as angles between two normal, can be computed as follows:

$$Cobb1 = \arctan\left|\frac{m_1 - m_2}{1 - m_1m_2}\right|, \quad Cobb2 = \arctan\left|\frac{m_2 - m_3}{1 - m_2m_3}\right|. \quad (4)$$

The angles  $\varphi_x$  are recorded as functions of time and thus, it is possible to get the variation of the Cobb angles during the exercises performed by the patient under the supervision of the kinetotherapist.

### 3 Equipment for the Experimental Measurement of on-Line Spinal Deformities

In order to collect the angles of the vertebrae, an acquisition system must be set up. This consists of an assembly of 8 MEMS IMUs [19] (inertial measurement units) connected via their I<sup>2</sup>C bus to an I<sup>2</sup>C multiplexer [20] and ultimately to a microcontroller board [21] (Fig. 2a: scheme and b: experimental arrangement). The multiplexer is needed because the IMUs have two fixed bus addresses, these being the same for all 8 IMUs. Considering that the IMU boards are PCB carriers these

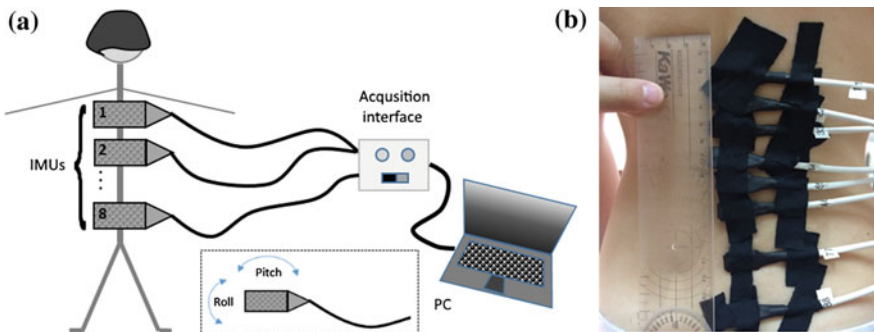


Fig. 2 Angle acquisition assembly. Scheme (a) and experimental arrangement (b)

have been protected against ingress of foreign material (adhesive, liquid droplets, finger touch) by encapsulating them in thermo-contractile tubes, which also provided for a stronger cable ending and also a flat surface ready to be applied to the patient's skin.

For the current experiments the Roll and Pitch angles are recorded and transmitted to a PC in the form of comma separated values, via a serial port. The angles are computed from the accelerometer values by considering the IMU's own coordinate reference system [22]:

$$Roll = \arctan(G_y/G_z), \quad Pitch = \arctan\left(-G_x/\sqrt{G_y^2 + G_z^2}\right) \quad (5)$$

where:  $G_x$ ,  $G_y$ ,  $G_z$  are the raw gravitational acceleration values measured in the earth's reference frame, recorded by the IMU.

Since above equations give multiple solutions in the  $0 \dots 2\pi$  region, the angles must be limited and the selected convention for this application is to limit both *Roll* and *Pitch* to  $0 \dots \pi$  in the microcontroller code and enforce the vertebrae application position to that pictured in Fig. 1. With this restriction respected, the base angles (IMUs vertical with cable to the right and flat PCB surface facing patient's skin) are both  $\pi/2$ .

The microcontroller reads all 8 IMU raw accelerometer values in a continuous loop, computes the angles and sends the values to the connected PC with a frequency of 5 Hz. Considering the nature of the therapeutic exercises that the patient must conduct (which are mostly static – assume a pose and keep it for a few seconds) the amount of angle data collected is sufficient for further analysis.

## 4 Example of Data Acquisition and Processing Results

A first set of data was acquired from a volunteer patient, who was informed and agreed with the use of data in a scientific experimental research. The patient stood in a static straight posture, which is a sequence of a prescribed exercise by the kinetherapist for the treatment of a spinal deformity. Data acquired for this position is used to test and validate different mathematical algorithms, which pursue the obtaining of an analytical shape of the spine and the computation of Cobb angles.

In order to apply the algorithm for getting the interpolation polynomial, only the angle  $\varphi_x$  and the distances  $l_i$  are necessary.

Table 1 contains the values of the acquired data and computed coordinates of the nine interpolation points in a reference system attached to the lowest vertebra, which is considered as the origin of the system.



**Table 1** Acquired data and computed coordinates

Sensor number	$\varphi_x$ [deg]	l [mm]	y [mm]	x [mm]
	0	0	0	0
1	3.5	28	1.70	27.94
2	7.91	28.5	3.91	56.13
3	12.3	28.5	6.06	83.94
4	4.58	26.9	2.14	110.78
5	-0.77	11.5	-0.15	122.32
6	-5.76	16.9	-1.69	139.15
7	-4.3	15.4	-1.15	154.50
8	1.48	14.6	0.37	169.11

The coefficients of the eighth degree polynomial described in Eq. (2) are:

$$a_0 = 1.76 \times 10^{-14}, a_1 = -1.25 \times 10^{-11}, a_2 = 3.57 \times 10^{-9}, a_3 = -5.27 \times 10^{-7}$$

$$a_4 = 4.25 \times 10^{-5}, a_5 = -1.86 \times 10^{-3}, a_6 = 4.14 \times 10^{-2}, a_7 = -0.30, a_8 = 0. \tag{6}$$

The curve is represented in Fig. 3a. The computation and graph are performed by means of an application, written in Mathcad 14.

The inflection points are found for the coordinates:

$$I_1(35.52; 2.20), I_2(110.45; 2.23), I_3(161.80; -0.61) \tag{7}$$

The last point  $I_3$  did not result on mathematical basis, but it was selected as the midpoint of the last vertebrae distance  $l_8$ .

The computation of the normals' slope in these points and applying the relations (4) provide the following Cobb angles:

$$Cobb\ 1 = 15.63^\circ, \quad Cobb\ 2 = 17.45^\circ \tag{8}$$

The correctness of the shape is confirmed by a simpler approximation, with a fourth degree polynomial:

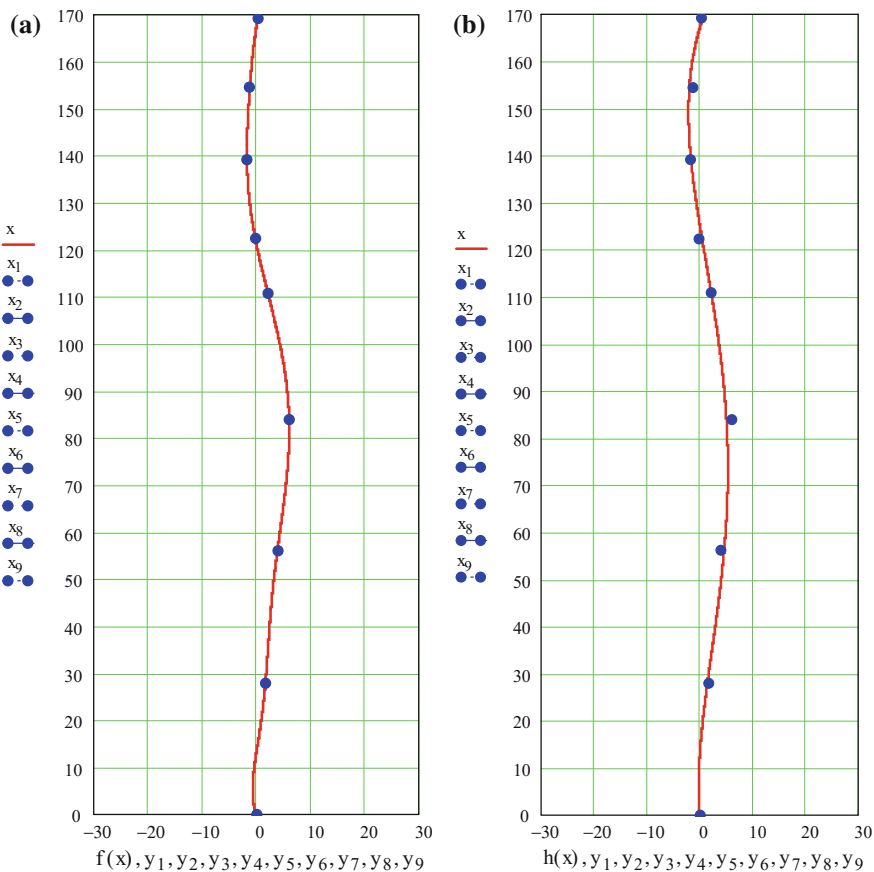
$$y = b_0x^4 + b_1x^3 + b_2x^2 + b_3x + b_4, \tag{9}$$

got in a different software application, MS Excel Office 2010, by means of the function *Trendline* applied to the graph passing through the nine precision points.

The coefficients of the fourth degree approximation polynomial are:

$$b_0 = 2.437 \times 10^{-7}, b_1 = -7.432 \times 10^{-5}, b_2 = 5.97 \times 10^{-3},$$

$$b_3 = -6.178 \times 10^{-2}, b_4 = 0 \tag{10}$$



**Fig. 3** Model of the spine—polynomial of 8th degree (a) and polynomial of 4th degree (b)

The resulting graph (also drawn in Mathcad for uniformity) is given in Fig. 3b. The inflection points of the approximation polynomial are found for the coordinates:

$$I_1(34.73; 2.30), I_2(117.57; 1.19), I_3(161.80; -1.11). \tag{11}$$

The computation of the normals' slope in these points and applying the relations (4) provide the following Cobb angles:

$$Cobb\ 1 = 15.78^\circ, \quad Cobb\ 2 = 18.25^\circ. \tag{12}$$

The curves in Fig. 3 look very similar. In addition, their inflection points are very close, so that the Cobb angles are different with less than 1 deg, i.e. the relative error is of approximately 4.3%.

The dynamic recording of data through the whole rehabilitations exercise allows the therapist to establish whether the exercise is appropriate in nature and intensity.

## 5 Conclusions

The study starts from the conclusions presented in an extensive bibliography regarding spinal deformities and the efficiency of current treatment.

The paper proposes a new investigation method, based on data provided by a set of eight accelerometers, which are stuck on the body of the vertebrae during the whole therapy exercises. The goal of the study is to develop a method to record the Cobb angles variation, which should provide in the future an evaluation of the therapy exercises.

The acquired angular data is used to compute an eighth degree polynomial as a model of the spine. The high degree of the polynomial is not very convenient because the large number of inflection points and not recommendable for automated computation. The mathematical model can be improved by using an approximated polynomial of fourth degree, which has high correlation coefficient.

Appropriate mathematical algorithm is developed in order to compute the co-ordinates, the coefficients of the polynomial and the Cobb angles.

The mathematical model, which was tested and validated using an eighth degree polynomial and a fourth degree approximation polynomial is intended to be further confronted with the results of other types of investigation, such as traditional and modern imaging.

## References

1. Juskelene V, Magnus P, Bakketeig LS, Dailidiene N (1996) Prevalence and risk factors for asymmetric posture in preschool children aged 6-7 years. *Int J Epidemiol* 5:1053-1059
2. Linton SJ, Hellsing AL, Halme T, Akerstedt K (1994) The effects of ergonomically designed school furniture on pupils' attitudes, symptoms and behavior. *Appl Ergonomics* 5:299-304
3. Balla JB, Hantiu I (2015) School screening programs of scoliosis: a meta-analysis. In: *The annals of the Oradea University, Faculty of Physical Education and Sport*, no. XXV, pp 90-98
4. Jianu M (2010) *Pediatric scoliosis*. Publishing House and Typography Pro, Bucuresti
5. Gruescu CM, Garaiman A, Lovasz EC (2015) Modeling of human spinal column and simulation of spinal deformities. *Mechanika* 21:214-219
6. Gugoasa-Garaiman, A (2010) Contribution to the implementation of advanced non-invasive techics for investigation of spine deformities, Thesis, Polytechnic University of Timisoara
7. Lovasz EC, Mateas M, Mircea M (2005) Determination of the human spine geometry with CCD-cameras. In: *Proceedings of the scientific reunion of the special program of the Alexander Von Humboldt, Timisoara*, pp 292-295
8. Mateas M, Vacarescu V, Lovasz EC, Nemes IDA, Mircea M (2007) About a new method for the 3D determination of the human spine geometry. In: *Proceedings of The 12th IFToMM International Congress, Besancon, France*, pp 300-305

9. Lovasz EC, Mateas M, Vilmos F (2003) Geometry determination of the human spine in 3D. In: Proceedings Inter-Ing. Conference, Tg-Mures, pp 131–137
10. Ciobanu O, Ciobanu G, Aiello A (2017) An application of Kinect sensor for scoliosis and kyphosis screening. In: Proceedings of the international conference on medical and biological engineering (CMBEBIH), conference paper. Springer, pp 713–717
11. Voinea G-D, Butnariu S, Mogan G (2017) Measurement and geometric modelling of human spine posture for medical rehabilitation purposes using a wearable monitoring system based on inertial sensors. *Sensors* 17(1)
12. Negrini S, Fusco C, Atanasio S, Zaina F, Romano M (2008) Exercises reduce the progression rate of adolescent idiopathic scoliosis: results of a comprehensive systematic review of the literature. *Disabil Rehabil* 772–785
13. Lehnert-Schroth C (2007) Three-dimensional treatment for scoliosis. A physiotherapeutic method for deformities of the spine. Published by The Martindale Press, Palo Alto, California
14. Weiss HR (1992) Influence of an in-patient exercise program on scoliotic curve. *Ital J Orthop Traumatol* 395–406
15. Mehta MH (1985) Active Correction by side-shift: an alternative treatment for early idiopathic scoliosis. In: Warner JO, New-York, pp 126–140
16. Weiss HR, Klein R (2006) Improving excellence in scoliosis rehabilitation: a controlled study of matched pairs. *Pediatr Rehabil* 190–200
17. Negrini S, Antonini G, Carabalona R, Minozzi S (2003) Physical exercises as a treatment for adolescent idiopathic scoliosis. A systematic review. *Pediatr Rehabil* 6:227–235
18. Rigo M et al (2008) Scoliosis intensive out-patient rehabilitation based on Schroth method. *Stud Health Technol Inform*, 208–227
19. MinIMU-9 v5 Gyro, Accelerometer, and Compass (LSM6DS33 and LIS3MDL Carrier)—product information and resources webpage. <https://www.pololu.com/product/2738>. Accessed: 03, 17
20. TCA9548A 1-to-8 I2C Multiplexer Breakout—product information and resources webpage. <https://learn.adafruit.com/adafruit-tca9548a-1-to-8-i2c-multiplexer-breakout?view=all>, Accessed 03, 17
21. A-Star 32U4 Micro—product information and resources webpage; <https://www.pololu.com/product/3101>. Accessed 03, 17
22. Pedley M. Tilt Sensing using a three-axis accelerometer—freescale semiconductor application note. [https://cache.freescale.com/files/sensors/doc/app\\_note/AN3461.pdf](https://cache.freescale.com/files/sensors/doc/app_note/AN3461.pdf). Accessed 04, 17

# Kinematic Design of a Parallel Robot for Elbow and Wrist Rehabilitation



**B. Gherman, G. Carbone, N. Plitea, M. Ceccarelli, A. Banica and D. Pisla**

**Abstract** This paper presents the kinematics of modular a parallel robot for post-stroke rehabilitation of elbow and wrist. The targeted motions for rehabilitation are: elbow flexion, pronation/supination, flexion/extension and adduction/abduction (radial/ulnar deviation) of the wrist. The kinematic structure of the robotic system is presented starting from general considerations concerning the rehabilitation protocol of the upper limb. Its kinematics is developed and simulation results are presented for a proposed training exercise.

**Keywords** Parallel robot · Elbow and wrist rehabilitation · Kinematics Modularity

---

B. Gherman · N. Plitea · A. Banica · D. Pisla (✉)  
CESTER, Technical University of Cluj-Napoca, Cluj-Napoca, Romania  
e-mail: doina.pisla@mep.utcluj.ro

B. Gherman  
e-mail: bogdan.gherman@mep.utcluj.ro

N. Plitea  
e-mail: nicolae.plitea@mep.utcluj.ro

A. Banica  
e-mail: alexandru.banica@omt.utcluj.ro

G. Carbone · M. Ceccarelli  
LARM, University of Cassino and South Latium, Cassino, Italy  
e-mail: carbone@unicas.it

M. Ceccarelli  
e-mail: ceccarelli@unicas.it

## 1 Introduction

Stroke is one of the most encountered causes of death and a main cause of chronic disability in the world [9]. Although current possibilities in the stroke treatment and prevention have reduced its impact, the ageing population phenomenon, especially in Europe will increase the incidence rate of stroke and cardiovascular diseases [18]. On the other hand, mortality rate from strokes has declined over time [12], resulting in an increased worldwide prevalence of stroke. Romania has proved to be a leading country in Europe concerning the cardiovascular diseases and especially stroke related disabilities [7]. Great advances have been achieved in the management of acute phase of post-stroke survivors, but even so the care of these patients still relies on the rehabilitation treatments. Robotic-assisted rehabilitation has proved to accelerate the recovery of lost motor functions for post-stroke survivors, enabling clinics to switch from the classical intensive-oriented training to higher repetitive technological treatment [4].

Huge effort has been made by private companies, research centers and universities to provide suitable robotic solutions for rehabilitation [13]. The developed robotic systems could be classified according the targeted are for rehabilitation (i.e. lower limb, upper limb) or by their architecture: end-effector based or exoskeletons. The first category of rehabilitation robots use a classic serial or parallel architecture in which the targeted limb is mobilized using the robot end-effector, especially designed to hold the patient's limb using a pre-determined anchor point: [3, 6, 8, 17]. Compared to end-effector robotic systems, exoskeletons provide certain advantages like: the workspace similarity in form and size, lack of singularities or the precise mapping of the joint forces [15]. The main disadvantages of exoskeletons rely in the impossibility to replicate the human kinematics because of its diversity and in their innate more complicated design. Achievements are numerous and prove that such architectures can be successfully used for training: [1, 2, 10]. Most exoskeletons have a serial architecture, since their design requires a wrapping of the human limb. Parallel structures have proven their advantages compared to serial ones, especially in terms of stiffness and dynamic performances. In [5] the authors proposed a serial-parallel exoskeleton for the rehabilitation of the upper limb. It has a high stiffness, very accurate, but has also a complicated structure, using differential mechanism of bevel gear transmission and lacks the abduction/adduction of the wrist. In [11] the authors developed a 5 DOF shoulder exoskeleton in a modular design: the first module with 3 DOF (a spherical parallel manipulator) has an active function and the second module with 2 DOF acting as a passive slip interface designed to increase the system's mobility and to prevent joint misalignment. The robotic system is designed to train only the shoulder.

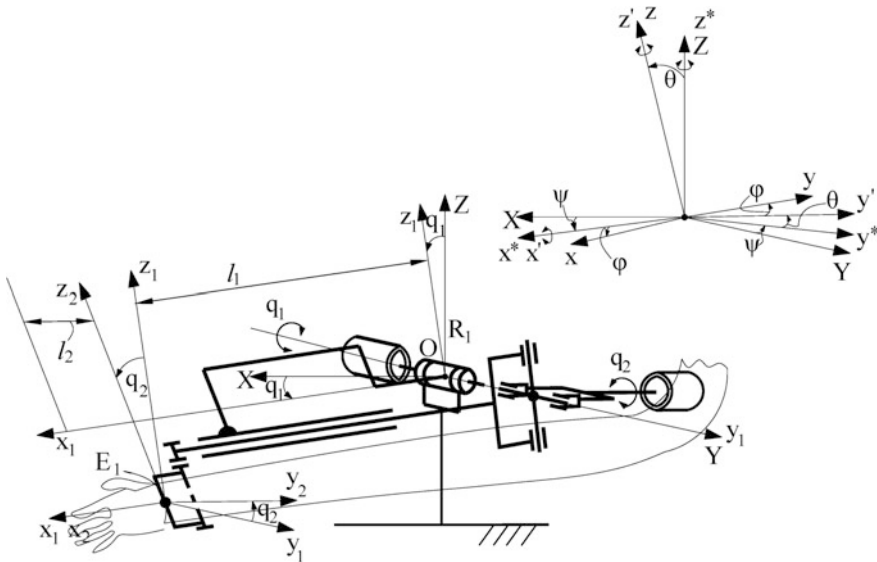
The current paper presents a modular exoskeleton robotic system, with a parallel architecture, for the training and rehabilitation of elbow and wrist, specifically the following motions: elbow flexion/extension, pronation/supination and the wrist flexion/extension and adduction/abduction. Section 2 presents the kinematics and Sect. 3 a set of training-based simulations.

## 2 A Parallel Modular Robot for Elbow and Wrist Rehabilitation

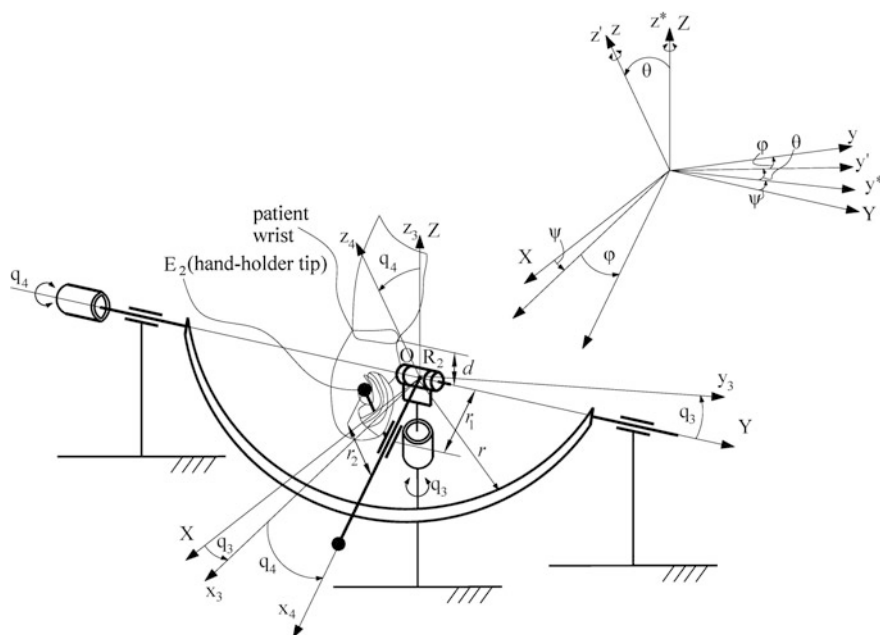
The authors have proposed and discussed in [14] the main requirements for a rehabilitation robotic system in terms of motion analysis including anchoring (active/passive), range and actuation force. The PaRReEx robotic system consists of two independent parallel modules, one for elbow rehabilitation (PaRReEx—elbow, see Fig. 1) and the other for wrist rehabilitation (PaRReEx—wrist, see Fig. 2) [16]. The PaRReEx—elbow achieves the pronation/supination motions, while the PaRReEx—wrist achieves the wrist flexion/extension and adduction/abduction.

The PaRReEx—elbow module has 2 DOF: two rotations, one around the OY axis (achieved by the  $q_1$  active joint) and the other around OX axis (achieved by the  $q_2$  active joint).  $q_1$  achieves the elbow flexion/extension while  $q_2$  achieves the pronation/supination motion, using a bevel gear mechanism. The fixed coordinate system is placed in the  $R_1$  rotation joint, the geometrical parameters being:  $l_1$  (the length of the mechanism on the OX axis) and  $l_2$  (distance from the  $R_1$  joint to the hand axis).

The PaRReEx—wrist module has 2 DOF: two rotations, one around the OZ axis (using the  $q_3$  active joint), which achieves the wrist flexion/extension and the other around the OY axis (using  $q_4$  active joint), which achieves the adduction/abduction motion. The fixed coordinate system is placed in the  $R_2$  active rotation joint, the geometrical parameters being:  $r_1$ , as the distance between the patient's wrist joint and the hand-holder (this being a human parameter used as input data into the kinematic model of the robot),  $r_2$  as the height of the hand-holder and  $d$  as the distance between the patient's wrist joint and the  $R_2$  robot joint.



**Fig. 1** The PaRReEx—elbow module of the parallel robot for elbow flexion/extension and pronation/supination rehabilitation



**Fig. 2** The PaRReEx—wrist module of the parallel robot for wrist flexion/extension and adduction/abduction rehabilitation

### 2.1 Kinematics

The forward kinematics of the PaRReEx modules requires as input data the values of the active joints  $q_1, q_2, q_3, q_4$  and the geometrical parameters ( $l_1, l_2, r_1, r_2, d$ ) while the target is to determine the end-effector coordinates  $E_1(X_{E1}, Y_{E1}, Z_{E1})$  and orientation  $\psi_1, \theta_1, \varphi_1$ —for the elbow and  $E_2(X_{E2}, Y_{E2}, Z_{E2}), \psi_2, \theta_2, \varphi_2$ —for the wrist. Relations (1) to (4) show the closed-form kinematic equations of the forward kinematics.

$$\begin{cases} X_{E1} = l_1 \cos(q_1); \\ Y_{E1} = l_2; \\ Z_{E1} = -l_1 \sin(q_1); \end{cases} \quad (1)$$

$$\begin{cases} \psi_1 = \text{atan2}(\cos(q_2) \sin(q_1), \sin(q_2)); \\ \theta_1 = \text{atan2}\left(\sqrt{1 - (\cos(q_1) \cos(q_2))^2}, \cos(q_1) \cos(q_2)\right); \\ \varphi_1 = \text{atan2}(-\sin(q_1) \cos(q_1), \sin(q_2)); \end{cases} \quad (2)$$



and:

$$\begin{cases} X_{E2} = \cos(q_3) \cos(q_4)(r_1 - d \sin(q_4)) + r_2 \cos(q_3) \sin(q_4); \\ Y_{E2} = \sin(q_3) \cos(q_4)(r_1 - d \sin(q_4)) + r_2 \sin(q_3) \sin(q_4); \\ Z_{E2} = r_2 \cos(q_4) - \sin(q_4)(r_1 - d \sin(q_4)); \end{cases} \quad (3)$$

$$\begin{cases} \psi_2 = \text{atan2}(\cos(q_3), -\sin(q_3)); \\ \theta_2 = q_4; \\ \varphi_2 = 3\frac{\pi}{2}; \end{cases} \quad (4)$$

In the case of PaRReEx—wrist, because of the  $d$  geometric parameter, the term  $r_1 - d \sin(q_4)$  has been used as a displacement on the  $OX$  axis. Figure 3 explains how it has been obtained.

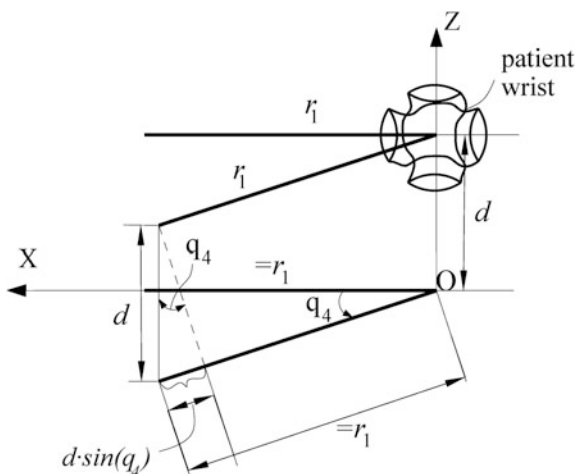
The inverse kinematics requires as input data the hand orientation (the angles  $\psi_1, \theta_1, \varphi_1$ ) to determine the active joints coordinates:  $q_1$  and  $q_2$  of the PaRReEx—elbow:

$$\begin{cases} q_1 = \text{atan2}(-\sin(\varphi) \sin(\theta), \cos(\varphi) \cos(\psi) - \cos(\theta) \sin(\varphi) \sin(\psi)); \\ q_2 = \text{atan2}(-\cos(\psi) \sin(\theta), \cos(\theta) \cos(\varphi) \cos(\psi) - \sin(\varphi) \sin(\psi)); \end{cases} \quad (5)$$

The same for the PaRReEx—wrist, where the solution of the inverse kinematics is trivial.

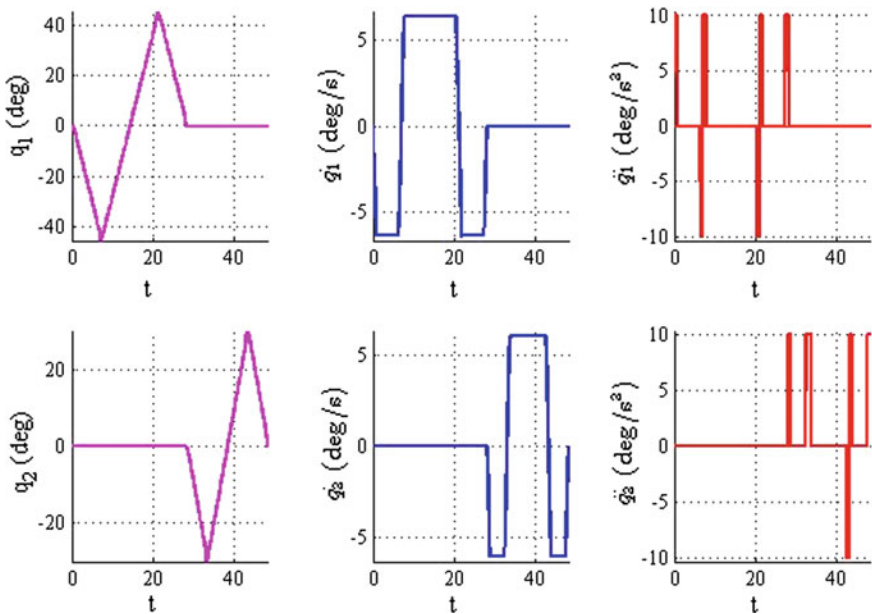
$$\begin{cases} q_3 = \psi - \frac{\pi}{2}; \\ q_4 = \theta; \end{cases} \quad (6)$$

**Fig. 3** A detail of the PaRReEx—wrist

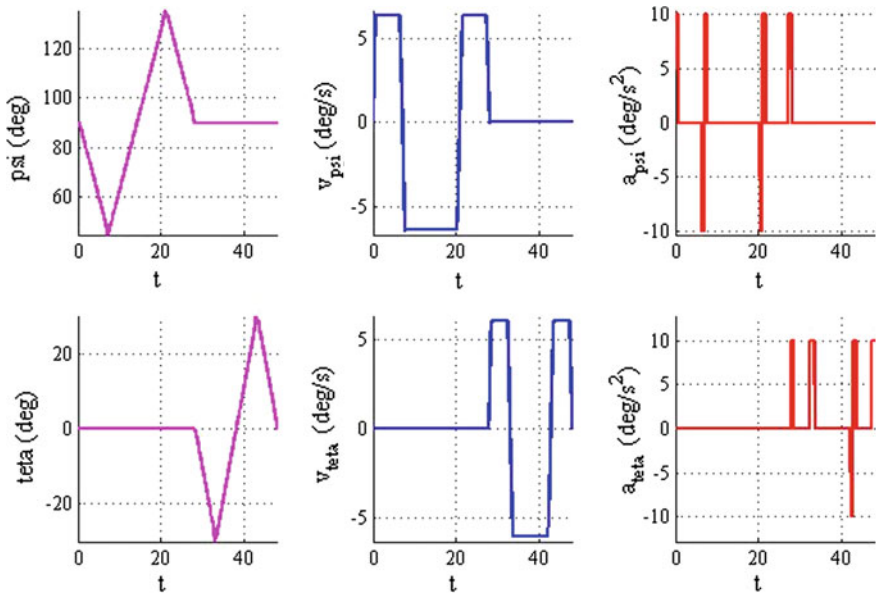


### 3 Training-Based Simulations of the PaRReEx Robotic System

A simulation exercise has been programmed using MATLAB as a proposal for the wrist rehabilitation, using the PaRReEx—wrist module. The two motions (wrist flexion/extension and adduction/abduction) are performed independently, to avoid any interference, but if necessary these could be performed also together. The current formulation of kinematic analysis, used also in this simulation, can be used for optimal design procedures and exploitation to characterize the feasibility of the proposed robotic design. The  $q_3$  active joint (which performs the flexion/extension) ranges between:  $0^\circ: -45^\circ: 0^\circ: +45^\circ: 0^\circ$ , while  $q_4$  (which performs the adduction/abduction) ranges between:  $0^\circ: -30^\circ: 0^\circ: +30^\circ: 0^\circ$ . The motion parameters, chosen based on [14] can be assumed as:  $v_{\max} = 6.5^\circ/\text{s}$  and  $\varepsilon_{\max} = 10^\circ/\text{s}^2$ . Figure 4 shows the simulation, as the computed joints motions (acting as input data) and Fig. 5 the simulation results, namely the end-effector orientation time history diagram (namely the angles  $\psi$  and  $\theta$ ).



**Fig. 4** Computed joint motions of PaRReEx—wrist for wrist flexion/extension and adduction/abduction motion: positions, velocities and accelerations of the active joints



**Fig. 5** The time history diagrams of the end-effector (orientation  $\psi$  and  $\theta$ ) velocities and accelerations for a simulated rehabilitation exercise

## 4 Conclusions

The paper presents the kinematics of a parallel modular robotic system designed for rehabilitation purposes of the upper limb. The robotic system targets the flexion/extension and the pronation/supination motions, using the PaRReEx—elbow parallel robotic module and the flexion/extension and adduction/abduction motions using the PaRReEx—elbow parallel robotic module. This proves that the proposed kinematics is suitable to perform all the motions of the upper limb starting from the elbow up to the wrist (excluding the shoulder), which is something that other systems have not entirely covered. The achieved simulations present a possible training exercise motion for a range of  $90^\circ$  for flexion/extension and  $60^\circ$  for the adduction/abduction, proving that the designed robotic system is suitable for the targeted task and the kinematics can be easily implemented into the robot control.

**Acknowledgements** The paper presents results from the research activities of the project ID 37\_215, MySMIS code 103415 “Innovative approaches regarding the rehabilitation and assistive robotics for healthy ageing” co-financed by the European Regional Development Fund through the Competitiveness Operational Programme 2014–2020, Priority Axis 1, Action 1.1.4, through the financing contract 20/01.09.2016, between the Technical University of Cluj-Napoca and ANCSI as Intermediary Organism in the name and for the Ministry of European Funds.

## References

1. Allington J, Spencer SJ, Klein J, Buell M, Reinkensmeyer DJ, Bobrow J (2011) Supinator extender (SUE): a pneumatically actuated robot for forearm/wrist rehabilitation after stroke. In: Proceedings of the Conference on IEEE Engineering in Medicine and Biology Society, pp 1579–1582
2. Carbone G et al (2017) A study of feasibility for a limb exercising device. Advances in Italian mechanism science. In: Proceedings of the first international conference of the IFToMM Italy, pp 11–21
3. Ceccarelli M (2004) Fundamentals of mechanics of robotic manipulation. Springer
4. Chan DYI, Chan CCH, Au DKS (2006) Motor relearning programme for stroke patients: a randomized controlled trial. *Clin Rehabil* 20(3):191–200
5. Chen Y, Li G, Zhu Y, Zhao J, Cai H (2014) Design of a 6-DOF upper limb rehabilitation exoskeleton with parallel actuated joints. *Bio-Med Mater Eng* 24:2527–2535
6. Colizzi L, Lidonnici A, Pignolo P (2012) Upper limb rehabilitation after stroke: ARAMIS a “robomechatronic” innovative approach and prototype. In: Proceedings of the 4th IEEE RAS & EMBS international conference on biomedical robotics and biomechatronics (BioRob), pp 1410–1414
7. Dorobantu M et al (2012) Profile of the Romanian hypertensive patient data from SEPHAR II study. *Rom J Intern Med* 50(4):285–296
8. Duret C, Courtial O, Grosmaire A, Hutin E (2015) Use of a robotic device for the rehabilitation severe upper limb paresis in subacute stroke: exploration of patient/robot interaction and the motor recovery process. *BioMed Res Int*, Article ID 482389
9. Go AS et al (2014) Heart disease and stroke statistics—2014 update: a report from the American Heart Association. *Circulation* 129(3):e28–e292
10. Ho NS et al (2011) An EMG-driven exoskeleton hand robotic training device on chronic stroke subjects: task training system for stroke rehabilitation. In: Proceedings of IEEE International Conference on Rehabilitation Robotics
11. Hunt J, Lee H, Artemiadis P (2016) A novel shoulder exoskeleton robot using parallel actuation and a passive slip interface. *J Mech Robot* 9(1)
12. Lackland DT et al (2014) Factors influencing the decline in stroke mortality. *Stroke* 45(1):315–353
13. Maciejasz P, Eschweiler J, Gerlach-Hahn K, Jansen-Troy A, Leonhardt S (2014) A survey on robotic devices for upper limb rehabilitation. *J Neuroeng Rehabil* 11(3) (2014)
14. Major KA, Major ZZ, Carbone G, Pişlă A, Vaida C, Gherman B, Pişlă D (2016) Ranges of motion as basis for robot-assisted post-stroke rehabilitation. *Int J Bioflux Soc Hum Vet Med* 8(4):192–196
15. Mihelj M, Nef T, Riener R (2007) Armin II—7 dof rehabilitation robot: mechanics and kinematics. In Proceedings of 2007 IEEE international conference on robotics and automation, pp 4120–4125
16. Plitea N et al (2017) Parallel robotic system for elbow and wrist rehabilitation. Patent pending
17. Tarnita D, Geonea I, Petcu A, Tarnita DN (2016) Experimental characterization of human walking on stairs applied to humanoid dynamics. In: Advances in robot design and intelligent control. Springer, pp 293–301
18. Veerbeek M et al (2014) What is the evidence for physical therapy poststroke? A systematic review and meta-analysis. *PLoS ONE* 9(2)

# Preliminary Design for a Spherical Parallel Robot for Shoulder Rehabilitation



C. Vaida, G. Carbone, N. Plitea, I. Ulinici and D. Pisla

**Abstract** Stroke is one of the major causes of disabilities among elderly people which have a negative effect on the life quality and independent living. Robotic assisted rehabilitation enable physical therapists to create patient oriented, individual therapies aiming to achieve high level of recovery for the motoric lost functions. However there exists no standardization in the design of such devices. This paper presents a set of critical design characteristics and constraints for rehabilitation robotics. Based on this data an innovative spherical robot for shoulder rehabilitation is presented. Its workspace modelling and trajectory simulation illustrate the robot capabilities of performing from simple to complex trajectories having a high degree of universality for the given task.

**Keywords** Robotic assisted rehabilitation · Design · Spherical robot  
Stroke

---

C. Vaida (✉) · N. Plitea · I. Ulinici · D. Pisla  
CESTER, Technical University of Cluj-Napoca, Cluj-Napoca, Romania  
e-mail: calin.vaida@mep.utcluj.ro

N. Plitea  
e-mail: nicolae.plitea@mep.utcluj.ro

I. Ulinici  
e-mail: ionut.ulnici@mep.utcluj.ro

D. Pisla  
e-mail: doina.pisla@mep.utcluj.ro

G. Carbone  
University of Cassino and South Latium, Cassino, Italy  
e-mail: carbone@unicas.it

## 1 Introduction

The recent progress in all medical related sciences contributed to a continuous increase of the average life expectancy, which started in advanced countries and then slowly expanded also between the developing ones. As clearly pointed in the strategic robotic development agenda for Europe, promoted by Eurobotics AIBSL, [14], the population aged over 65 will reach 30% of the total population by 2060 whereas 12.1% will be over 80 years old. Despite medical progresses, the elderly population is prone to a series of diseases that induce serious disabilities for survivors. The first place on this list is stroke (with its two forms: hemorrhagic and ischemic) which has a 75% survival rate one year after the incident a number that will definitely increase in time. Unfortunately 80% of the stroke survivors suffer a certain level of disability half of them being unable to support an independent living. As 80% of patients are suffering from the paresis of the upper limb, it should come as no surprise that this affliction is detrimental from societal, individual and familial perspectives [2]. As in the next decades the existing number of physical therapists will no longer be able to support all the patients requiring rehabilitation a clear need of a paradigm shift in this medical field is needed. A robotic rehabilitation device would remove several constrictions imposed on the physical therapist, such as the limited number of patients that can be attended daily, the duration of the daily rehabilitation procedures, the precision with which rehabilitative motions are reproduced and the repeatability of the said motions. Thus, the therapist would change its role from personally attending a patient towards a personalized therapy developer which, based on patient data, background, interests and personality would determine the best set of tools and interactive interfaces that would deliver maximum efficiency in the rehabilitation program along a continuous monitoring and assessment of patient progress.

Thus far, several different approaches to robotic assisted rehabilitation are readily available on the market, or in development, these can be either stationary or mobile. Stationary devices come in the form of end effector based systems (InMotion ARM, [3]), exoskeleton based (Dampace, [10]), or parallel systems (CRAMER, [9]). Mobile devices, on the other hand are mostly available in the form of exoskeleton based structures (MyoPro Motion [7]).

The paper emphasizes in Sect. 2 a set of general design rules that would lead to the development of efficient new robotic solutions and estimate the effort level that has to be put in each of these critical characteristics. Section 3 covers the design of a new robotic device for shoulder rehabilitation, its workspace and motion on a complex trajectory followed by conclusions.

## 2 Design Considerations for Robotic Rehabilitation

Based on the demographic and medical data, rehabilitation is a field where robotic systems become a necessity. However, to the current date, there is no standard to define such a system characteristics, behavior, safety conditions, a dedicated ISO under the code IEC/CD 80601-2-78 being under development.

It is necessary to specify that due to the environment where the device will be used and the fact that robots used in rehabilitation have two types of users, mainly the medical specialist and the patient (who is uninstructed in the usage of the device), several aspects need to be analyzed ranging from safety to cost-effectiveness. Therefore several design factors that are considered to be pivotal in the development of a robotic solution for rehabilitation are enunciated below.

**Integrated design:** the development team should include the expertise of mechanical/electrical engineers for the development of the robot itself, together with computer specialists that will develop the control architecture based on HRI (Human Robot Interfaces) [1, 12] all based on the specific requests from the medical experts (physicians, and occupational therapists);

**User centered design:** emphasis is put on several aspects related to the patient and medical specialist (users) that will work with the device where safety features and patient information privacy have to be achieved in a cost efficient solution that will ensure intuitive usability;

**Therapeutic functionality:** the ability of the device to provide assistive forces proportional to each patient's needs, the joint alignments between the device and the human limb must be maintained, thus ensuring the proper execution of the exercises. The positioning of the attachment points between the human and the device should be made in areas of the body with similar feature sizes among adults but relevant and useful for the motion generation, keeping in mind that these areas should also be uninterrupted by joints. An important therapeutic functionality would be muscle pain/fatigue detection, ensuring the patient's wellbeing during device usage enabling therapists to understand each patient's limits [4, 5].

**The mechanical functionalities:** the robot must have a functional workspace adapted to the motion amplitudes of the human body, ensuring smooth motions along the entire path. Due to the complexity of the human motions detailed analysis of the motion plan defined by the medical experts is needed that will define the number of DOF of the robot. In addition, due to the unique anthropometric characteristics of each patient, the robot must be able to adapt to different sizes and human positions.

**Safety standards:** In the form of hardware based safety standards, it is necessary to implement limitations on the motion ranges (which are defined in the literature a minimum, average and maximum values but are unique for each patient). Safety protocols in case of emergency or danger must also be considered, and emergency stop switches should be installed. With regards to the software which has multiple implications in the rehabilitation process, being, through the user interface the element that links the patient to the robot software it is necessary for the

rehabilitation robot to have constant information sharing between user and device [4]. With all this information sharing between user and device it should also be noted that a standard for improved patient confidentiality should be considered.

**Accessibility and sensory interactions:** the robot should have human centered forms and shapes (concave components shapes to fit human limb convexities), *Proxemics* [6], meaning that the device structure should not overwhelm the human body, adaptability to the patient anthropometric characteristics, Kinesthetics [6] (the human—robot contact should not have negative influences on the patient limb), also thermal balances as the robot should not induce any temperature variation on the human body during exercises and sensorial capabilities which, of course, must be adapted to the specific rehabilitation task [11].

Aside from the aforementioned aspects, there are several **work environment related considerations** (size, weight, portability, power requirements, actuation), and **aesthetic considerations** that would influence the patient’s mentality while approaching and using such a device (shapes, materials, colors, textures).

The successful achievement of these characteristics will lead to an efficient rehabilitation device. The next step is to evaluate exactly how much effort should be invested in each specific area. The analysis is performed using the Analytic hierarchy Process (AHP) technique to rank these design characteristics (Fig. 1). Each item is evaluated with respect to all the others using a comparative scale of importance (AHP Toplevel Matrix 1). By filling in the upper half of the matrix the

Group:	Top Level ITEMS	Output									Completed:	<input checked="" type="checkbox"/>
	AHP Toplevel Matrix 1											
	9	9,00 an order of ...	1/3	0,14 demonstrat...								
	8	8,00 absolutely ...	1/8	0,13 absolutely l...								
	7	7,00 demonstrat...	1/7	0,11 an order of ...								
	6	6,00 demonstrat...										
	5	5,00 essentially ...										
	4	4,00 essentially ...										
	3	3,00 considerabl...										
	2	2,00 twice as im...										
	+	1,50 somewhat ...										
	○	1,00 Equally imp...										
	-	0,67 somewhat l...										
	1/2	0,50 half as impo...										
	1/3	0,33 clearly less ...										
	1/4	0,25 essentially l...										
	1/5	0,20 essentially l...										
	1/6	0,17 demonstrat...										
			1	2	3	4	5	6	7	8	9	
Input	1	Integrated design		○	○	+	2	2	+	-	2	
	2	User centered design			-	○	+	+	○	○	+	
	3	Therapeutic functionality				○	2	2	+	+	3	
	4	Mechanical functionalities					○	○	○	○	+	
	5	Hardware based safety standards						○	○	-	+	
	6	Software based safety standards							○	-	+	
	7	Work environment related considerations								1/2	+	
	8	Accesibility and sensory interactions									2	
	9	Aesthetics										
											Importance in group	
											14,1%	
											11,7%	
											16,2%	
											10,3%	
											8,7%	
											8,7%	
											9,4%	
											14,4%	
											6,4%	

Fig. 1 The AHP comparison matrix



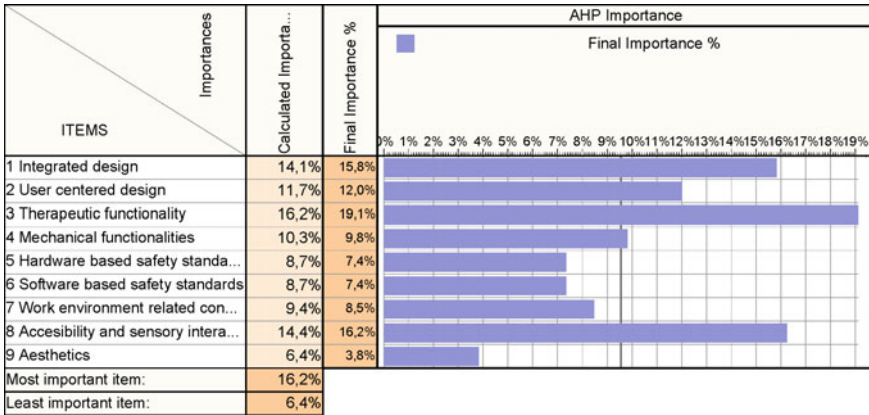


Fig. 2 The AHP final results

relative importance (out of a total of 100%) is distributed among the characteristics. The final results (Fig. 2), are calculated by imposing a scales factor of 1:5 between the most and least critical requirement. Thus, Fig. 2 expresses the amount of effort that should be integrated in each of the critical design requirements for a new rehabilitation robotic device.

### 3 A Case Study: Aspire—An Innovative Spherical Parallel Robot for Shoulder Rehabilitation

One of the current problems and technology gaps reported by several reviews [1, 12, 13] is the unbalanced number of devices developed for each upper limb joint with very few solutions for the proximal joints (shoulder). Thus, starting from a set of experimental clinical measurements [5], it resulted that for the proper rehabilitation of the upper arm segment and the shoulder joint, the abduction/adduction and flexion/extension motions are required. A simplified definition of these motions is that the abduction/adduction represents a rotation of the arm achieved in the horizontal plane while the flexion/extension is achieved in the vertical plane. However, the same reviews [1, 12, 13] illustrated that only simple motions are insufficient to achieve a proper motoric limb rehabilitation. Using the flow-chart in Fig. 3 that integrates the design prioritization results, one solution that enables the unrestricted generation of any type of motion of the arm is a spherical robot that uses the shoulder joint as its rotation center. The kinematic scheme of the new device, entitled Aspire, is presented in Fig. 4 [8]. The concept design integrates two active rotational joints that describe each of the basic (vertical and horizontal) arm motions, being able to generate, by a combined motion of the two active joints any trajectory for the patient arm.

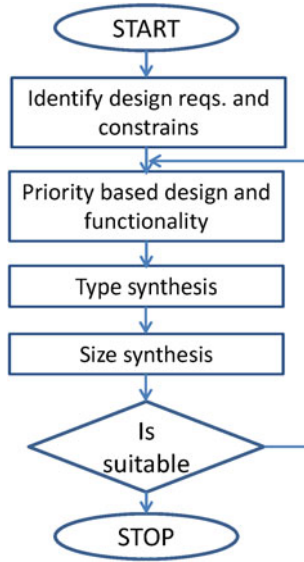


Fig. 3 Design flow-chart

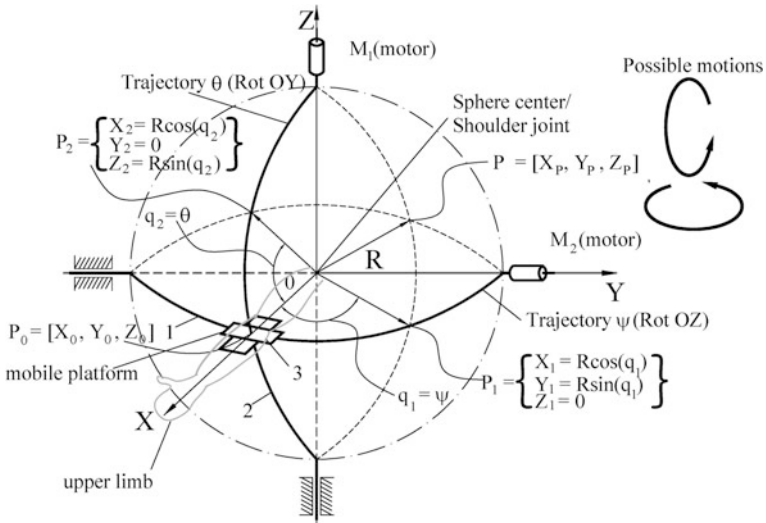
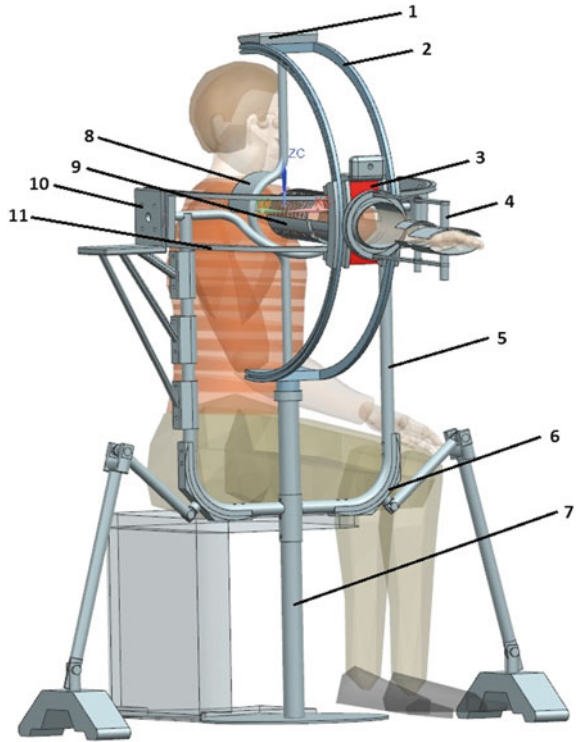


Fig. 4 Kinematic scheme of the spherical mechanism for shoulder rehabilitation

The first constructive design of Aspire is comprised of two spherical guides 2 and 10, that are actuated in turn by two motors M1 and M2 (placed on supports 1 and 9), which enable the positioning of the mobile platform 3 (that integrates the patient arm support), which execute their motion along the previously mentioned

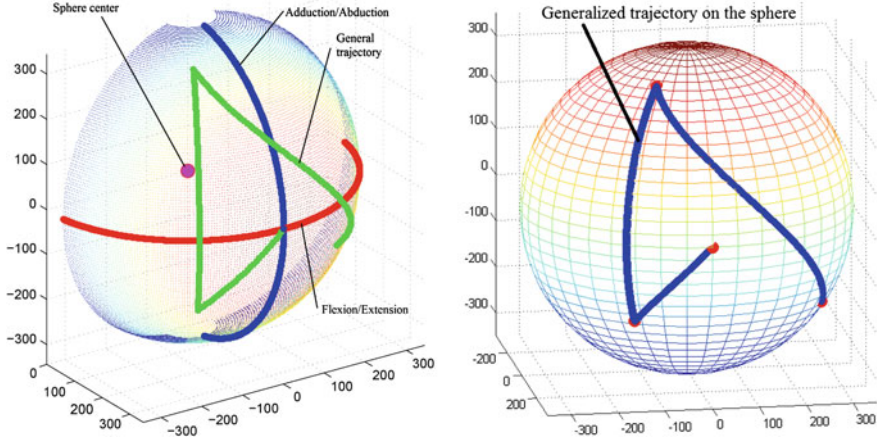
**Fig. 5** First detailed design of ASPIRE spherical robot



guides. The device contains 4 rotation joints, two of which belong to two of the 3 mobile elements in the structure. The basic motions effectuated by the mobile platform, are determined by the two guides: the first rotation is around the vertical axis (OZ), thus defining the basic horizontal motion, the second rotation occurs around the horizontal axis (OY), and it results in a basic vertical motion.

The patient’s shoulder is supported by the shoulder guard 8 while the upper arm is supported by guard 9. The forearm and the hand are kept in a proper position during exercise using the adjustable bracer 4 (connected directly to the mobile platform). The device itself is supported on three legs. The central leg 7 can be used to adjust the height of the device on the vertical axis and the two (detachable) legs 6. The bars 5 are used to support the guide responsible for vertical motions (Fig. 5).

Based on the kinematic scheme from Fig. 4, the two angles,  $\psi$  and  $\theta$  represent the input data for the inverse kinematics of ASPIRE. One geometric parameter is also introduced, namely the radius of the sphere (R), which based on the anthropometric data of the human body has a value of 350 mm. Two rotation matrices describe the robot motion, R1—rotation around OZ axis with angle  $\psi$  and R2—rotation around the OY axis with angle  $\theta$ . Considering that the sphere center has the coordinates O(0, 0, 0) and the initial position of the human arm is Based on the kinematic scheme from Fig. 4, for the inverse kinematics of the spherical robot, the



**Fig. 6** ASPIRE workspace with multiple trajectories

input data is represented by the two angles,  $\psi$  and  $\theta$ . In addition, the robot has one important geometric parameter, the radius of the sphere ( $R$ ) which, based on the anthropometric data of the human body was established at  $R = 350$  mm.

The robot motion can be described using two rotation matrices,  $R1$ —rotation around  $OZ$  axis with the angle  $\psi$  and  $R2$ —rotation around the  $OY$  axis with the angle  $\theta$ . Defining also the geometric coordinates of the sphere center  $O(0, 0, 0)$  and the initial position of the human arm is  $P_0(R, 0, 0)$ , the coordinates of point  $P$  are:

$$\begin{cases} X_P = R \cdot \cos(\psi) \cdot \cos(\theta) \\ Y_P = R \cdot \cos(\theta) \cdot \sin(\psi) \\ Z_P = -R \cdot \sin(\theta) \end{cases} \quad (1)$$

Using these simple equations the robot workspace can be computed for a range of motions of the angles  $\psi$  and  $\theta$ , considered here between  $-80^\circ$  and  $80^\circ$ .

Within the generated workspace, three trajectories are illustrated: two simple trajectories that describe the basic motions for the shoulder rehabilitation a complex one that illustrates the robot capabilities of generating any trajectory for the shoulder joint. Figure 6 illustrates the workspace and the complex trajectory on a sphere, while Fig. 7 illustrates the motion parameters of the ASPIRE robot for that particular trajectory determined based on its kinematic model.

The generalized trajectory has four control points being generated by computing the arc lengths between two consecutive points having, for each segment an angular speed  $\omega = 10^\circ/\text{s}$  and an angular acceleration of  $\varepsilon = 5^\circ/\text{s}^2$ :

$$(1): \begin{cases} \psi_1 = 0^\circ \\ \theta_1 = 0^\circ \end{cases}; (2): \begin{cases} \psi_2 = -30^\circ \\ \theta_2 = 30^\circ \end{cases}; (3): \begin{cases} \psi_3 = -30^\circ \\ \theta_3 = -60^\circ \end{cases}; (4): \begin{cases} \psi_4 = 60^\circ \\ \theta_4 = 30^\circ \end{cases} \quad (2)$$

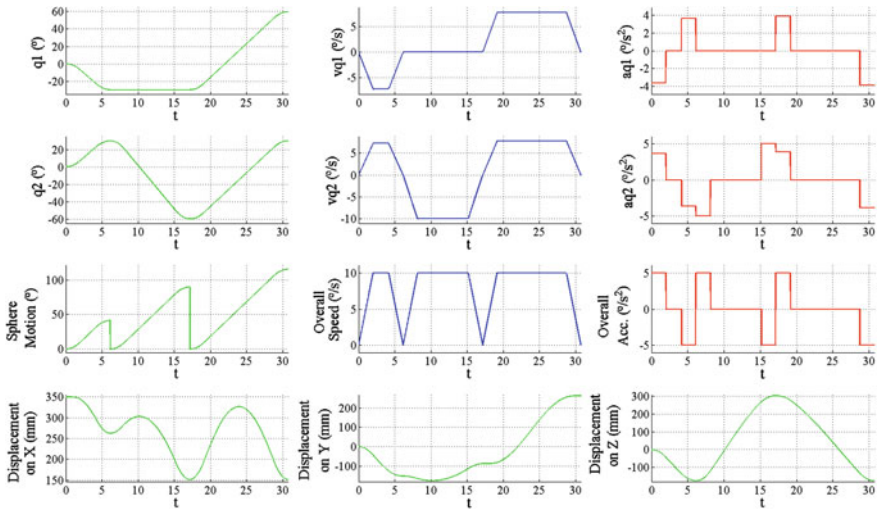


Fig. 7 Motion simulation of the Aspire robot on a complex trajectory

## 4 Conclusions

The integration of robots in the rehabilitation process represents one of the possible solutions to allow physical therapists to work with more patients in an efficient way. The paper identifies a set of critical design requirements for this type of devices. The proposed design requirements and their analysis are implemented in a case study, where a new spherical robotic device for shoulder rehabilitation, ASPIRE, was proposed. Main kinematics and path planning aspects are discussed to show the engineering feasibility of the proposed device. The robot behavior for a complex trajectory is illustrated through simulation results. Future work will include detailed payload requirements to enable efficient element sizing and actuator selection followed by the achievement a first experimental model.

**Acknowledgements** The paper presents results from the research activities of the project ID 37\_215, MySMIS code 103415 “Innovative approaches regarding the rehabilitation and assistive robotics for healthy ageing” cofinanced by the European Regional Development Fund through the Competitiveness Operational Programme 2014–2020, Priority Axis 1, Action 1.1.4, through the financing contract 20/01.09.2016, between the Technical University of Cluj-Napoca and ANCSI as Intermediary Organism in the name and for the Ministry of European Funds.

## References

1. Basteris A et al (2014) Training modalities in robot-mediated upper limb rehabilitation in stroke: a framework for classification based on a systematic review. *J NeuroEng Rehabil* 11 (111):15
2. Beebe JA, Lang CE (2009) Active range of motion predicts upper extremity function three months post-stroke. *Stroke* 40(5):1772–1779. <https://doi.org/10.1161/STROKEAHA.108.536763>
3. Krebs HI, Hogan N, Aisen ML, Volpe BT (1998) Robot-aided neurorehabilitation. *IEEE Trans Rehabil Eng* 6:75–87. <https://doi.org/10.1109/86.662623>
4. Lu E et al (2011) Development of a robotic device for upper limb stroke rehabilitation: a user-centered design approach. *Paladyn* 2(4):176–184
5. Major KA et al (2016) Ranges of motion as basis for robot-assisted post-stroke rehabilitation. *J Bioflux Soc Hum Vet Med* 8(4):192–196
6. Moore N (2010) *Nonverbal communication: studies and applications*. Oxford University Press
7. Myomo Inc. (2015) MyoPro myoelectric upper limb orthosis. <http://www.myopro.com>
8. Plitea N et al (2017) Spherical mechanism for shoulder rehabilitation. Patent pending
9. Spencer SJ et al (2008) A low cost parallel robot and trajectory optimization method for wrist and forearm rehabilitation using the Wii. In: *Proceedings of the 2nd IEEE RAS & EMBS international conference on biomedical robotics and biomechatronics*, pp 869–874
10. Stienen A et al (2009) Design of an exoskeleton for force-coordination training in upper-extremity rehabilitation. *J Med Devices* 3:031003
11. Tarnita D (2016) Wearable sensors used for human gait analysis. *Rom J Morphol Embryol* 57 (2):373–382
12. Vaida C et al (2017) On human robot interaction modalities in the upper limb rehabilitation after stroke. *Acta Teh Napoc Appl Math Mech Eng* 60(1)
13. Yadav et al (2016) Efficacy of modified constraint induced movement therapy in the treatment of hemiparetic upper limb in stroke patients: a randomized controlled trial. *J Clin Diagn Res* 10(11):YC01–YC05
14. (2016) *Robotics 2020 Multi-annual Roadmap*

# Study on the Effects of Rotation Axis Misalignment in an Exoskeleton-Human Hip Joint



C. Moldovan, I. Maniu, E. C. Lovasz and Ana-Maria Stoian

**Abstract** The paper presents research on one DOF (Degree of Freedom) hip joint of an exoskeleton regarding the possibilities and effects of rotation axis misalignment in the hip joint. By rotation axis misalignment, we understand the difference of alignment between the hip joint axis of rotation in human and exoskeleton; we also consider only parallel, not angular axis misalignments in our model. The proposed approach for the development of exoskeletons is to take into consideration inherent axis misalignments and analyze the possibilities to reduce their effects on the ergonomics of the device. The first step in this approach is the quantification of effects of rotation axis misalignments in exoskeletons and to achieve this, we developed the kinematic model which is presented in this paper. Most approaches focus on perfectly aligned axis of rotation, while this is not the case in our study, we focus on an acceptable misalignment for the user.

**Keywords** Exoskeleton · Hip joint · Misalignment · Biomechanics Kinematics

---

C. Moldovan (✉) · I. Maniu · E. C. Lovasz · A.-M. Stoian  
University Politehnica Timisoara, Timișoara, Romania  
e-mail: cristian.moldovan@upt.ro

I. Maniu  
e-mail: inocentiu.maniu@upt.ro

E. C. Lovasz  
e-mail: erwin.lovasz@upt.ro

A.-M. Stoian  
e-mail: ana.stoian@upt.ro

## 1 Introduction

For this paper we refer to an exoskeleton as a wearable mobile machine that is powered by a system of electric motors, pneumatics, levers, hydraulics, or a combination of technologies that allow for limb movement with increased strength and endurance [1].

We consider two major directions for the development of exoskeletons, namely human functions augmentation and medical assistive exoskeletons that reproduce lost functions of the human body, such as walking.

Regarding the functions augmentation of the human body, research is focused on the construction of systems that allow humans to perform better in a specific area, for instance, there are military or construction work applications where the user has to carry large weights over long periods of time. With the help of an exoskeleton, the loads on the users skeletal and muscle systems are reduced thus allowing increased performance.

Our paper addresses the second—medical assistive exoskeleton area, where reduced or lost functions of the body are compensated or replaced by the use of an exoskeleton. Further, we are concerned about the lower limb exoskeletons as case study where through some event, the human is unable to control his legs, but problems regarding axis misalignments are general and can appear at any joint level.

When considering the state of the art on walking aid exoskeletons, two main directions emerge, hybrid and automated exoskeletons. The differences between the two areas are quite significant and include aspects such as own weight support or balance. In a hybrid system, the user has to actively maintain balance using crutches repositioning them at every step in order to maintain balance. On the other hand, in an automated system the walking cycle and leg position are computed automatically with the help of sensor data such that the human user strapped in the exoskeleton maintains balance, it is a chair on legs.

There are some examples of commercial functioning hybrid exoskeleton designs in the medical area, such as ReWalk [1]—which has a price tag of 65.000 dollars; The precise fit of the ReWalk Exoskeleton is given within hardware (adjustments available up to 0.5 cm) and the software to ensure joint alignment. There is a limit in the software that limits the movement and a fixed mechanical stop that prevents excessive movements. Hip flexion is limited between  $-34$  and  $104^\circ$  relative to the torso sagittal plane. The knee flexion is limited to  $2^\circ$  extension and  $112^\circ$  flexion. The torque is limited to 125 Nm (max). Other products are Ekso [2] (also called eLEGS) developed at Berkley University—approved by USA's Food and Drug Administration to be used in medical scopes; HAL [3] (Hybrid Assistive Limb) developed by Cyberdyne, a startup from Tsukuba University or Indego [4]. The above mentioned exoskeletons can only be used by paraplegics with help of crutches, through which, the user is responsible for balance.



An automatic medical exoskeleton is REX from REX Bionics in New Zealand and, in comparison, it is not necessary for the user to assist the exoskeleton with crutches, the exoskeleton is able to walk basically by itself.

From the presented examples it can be seen that hip joint axes alignment in exoskeleton and human is very difficult to achieve, although the systems are endowed with adjusting mechanisms and misalignments are minimized, mainly because the human body is not very stiff (exception some parts, like bones), and the exoskeleton-human connection (Human Machine Interface) is made, generally, with Velcro on fat-muscle tissue.

Another problem consists in determining the hip joint centre of rotation, which is in itself extremely difficult [5, 6], it takes special procedures and is not suitable when mounting and un-mounting the exoskeleton. Proposed solutions for the problem in the community are, for example, Cempini in [7] where is presented a theoretical approach to the problem through a self-centering mechanism. The main problem with these approaches is that the solutions include a large number of joints that need to be actuated, thus increasing the device's complexity.

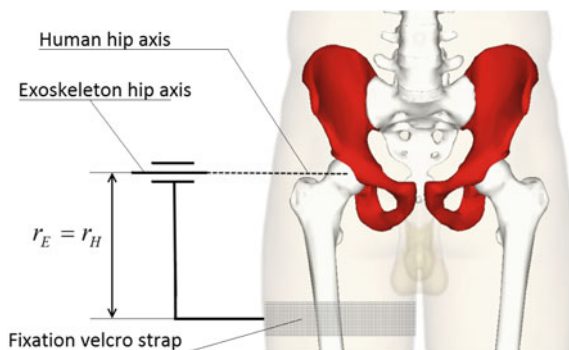
Our approach proposes, as first step, the assessment of the effects of misalignment and, if necessary, in the following steps (which are not included in the paper), the introduction of passive compliance, or actuated joints.

## 2 Analysis Method for Determination of Axis Misalignment Effects

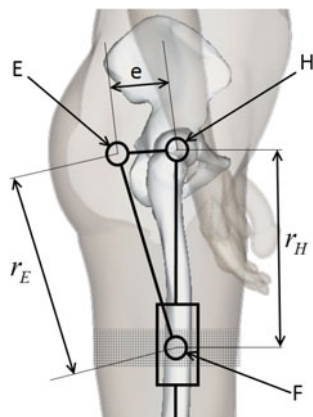
The existing exoskeleton solutions on the market offer one and two DOF hip joints. The analysis will be conducted on a one Degree of Freedom (DOF) hip joint. The used terminology is the standard terminology used for the anatomical planes of the human body.

The proposed case is presented in Fig. 1, where the axis of rotation is perpendicular to the sagittal plane at hip level and the human and exoskeleton hip rotation is aligned, thus relationship (1) can be written.

**Fig. 1** Model of a human wearing an exoskeleton where the rotation axis is aligned at hip level. Image created with help of BodyParts3D [8]



**Fig. 2** Model of a human wearing an exoskeleton where the rotation axis is misaligned at hip level. Image created with help of BodyParts3D [8]



$$r_E = r_H \quad (1)$$

where

$r_E$  is the rotation radius from exoskeleton rotation axis to Velcro strap;

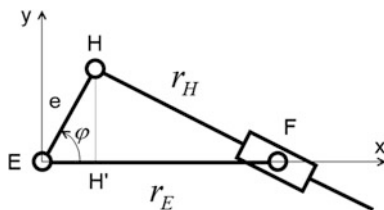
$r_H$  is the rotation radius from human hip rotation axis to Velcro strap.

The next step is the construction of a kinematic model for the hip of the human-exoskeleton system where misalignments are present. For this scenario, we consider only misalignments where rotation axes remain parallel. One parametric example for this scenario is presented in Fig. 2. We considered the modeling of the Velcro fixation between the exoskeleton and human through the slider in F.

In Fig. 3 can be seen that a crank-slider mechanism is produced, for which we can perform kinematic analysis. For the mechanism are used the following notations:

H—human hip joint; E—exoskeleton hip joint; F—fixation point; links  $r_E$  and  $r_H$  are defined at relationship (1); link  $e$ —is the eccentricity (misalignment) between human and exoskeleton hip. For the kinematic analysis, we consider link  $e$  fixed, the driving/input joint is E and output of the mechanism is the sliding displacement of point F on  $r_H$ . The derived Crank-slider mechanism is presented separately in Fig. 3.

**Fig. 3** Derived Crank-Slider mechanism



Our objective is to determine the dependency between the eccentricity  $e$ , and the displacement of point F on  $r_H$ , basically the length of  $r_H$ , when the mechanism is in motion. The motion is produced by the actuation of link  $r_E$  through actuated joint E, which we do in our model by introducing angle  $\varphi$  as parameter.

To establish a relationship between  $e$  and  $r_H$  geometrically, we project point H on  $r_E$ , resulting in point H', thus relationship (2) can be derived, in  $\Delta EHH'$ :

$$EH' = e \cos(\varphi); HH' = e \sin(\varphi) \tag{2}$$

Considering  $\Delta FHH'$  relationship (3) can be derived:

$$r_H = (H'F^2 + H'H^2)^{1/2} \tag{3}$$

where,

$$H'F = r_E - EH' \tag{4}$$

By replacing (2) and (4) in (3) results relationship (5):

$$r_H = \left( (r_E - e \cos(\varphi))^2 + (e \sin(\varphi))^2 \right)^{1/2} \tag{5}$$

Using relationship (5) we can express the dependency of eccentricity, rotation angle and displacement of the fixation on the femur. The results are presented graphically in Fig. 4, given the following initialization values:  $r_E = 25$  mm; parameter  $e$  has values of 30, 50, 70 and 100 mm respectively.

The actuated angle  $\varphi$  has values from  $-20$  to  $40^\circ$  corresponding to the motion angle of the femur with respect to the acetabulum.

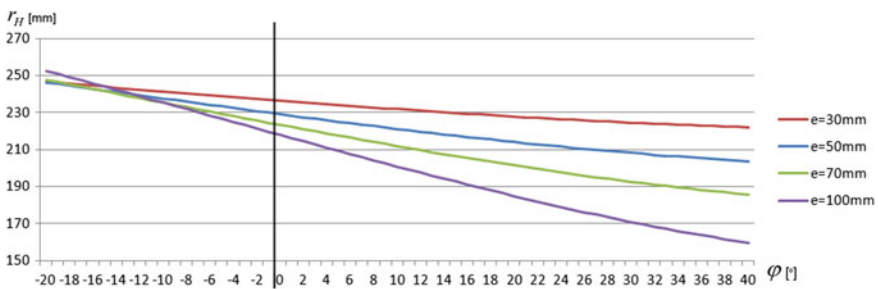


Fig. 4 Displacement of F with respect to motor angle  $\varphi$

### 3 Conclusions

Our objective was to show and quantify the effects of axis misalignment for a human-exoskeleton system at hip level. For this we constructed a kinematic model, extracted the specific equations and represented graphically the dependency of parameters.

The graphics in Fig. 5 follow the intuition, namely, that the bigger the misalignment is, the greater is the displacement of the fixation point of the exoskeleton on the thigh, but also show the amount of displacement. For future work in the area of exoskeletons HMI, there can be tested what amount of displacement can be tolerable by a human person without damage to the soft tissue of the thigh.

Also, having a relationship for the displacements and eccentricity, sensors can be mounted on the mechanism to indicate the degree of comfort of the human user. This is necessary to be done with sensors, since a paralyzed person cannot sense by himself.

Also, for future work, it is our intention to expand the model to lateral motion of the leg, constructing a 2DOF exoskeleton hip joint to assess the effects of axis misalignment.

### References

1. ReWalk Website (2017) <http://rewalk.com/>. Accessed 30 Apr 2017
2. Exobionics Website (2017) <http://eksobionics.com/>. Accessed on 30 Apr 2017
3. Cyberdyne Website (2017) <http://www.cyberdyne.jp/english/index.html> Accessed on 30 Apr 2017
4. Indego Website (2017) <http://www.indego.com/indego/en/home>. Accessed 30 Apr 2017
5. Costin S, Micu C, Mustata C, Trifan L (2013) Selection of methods for determining the rotation center of the hip articulation for the design of a custom acetabular prosthesis. In: Proceedings of the 4th international conference on automotive and transportation systems, Brasov. WSEAS—ICAT, pp 294–300
6. Schofer MD (2010) Radiological determination of the anatomic hip centre from pelvic landmarks. *Acta Orthop. Belg.* 76:479–485
7. Cempini M et al (2013) Self-alignment mechanisms for assistive wearable robots: a kinetostatic compatibility method. *IEEE Trans Rob* 29(1):236–250
8. BodyParts3D (2017) © The Database Center for Life Science licensed under CC Attribution-Share Alike 2.1 Japan. <http://lifesciencedb.jp/bp3d/>. Accessed 30 Apr 2017
9. Rex Bionics Website (2017) <http://www.rexbionics.com/>. Accessed 30 Apr 2017

# Children Locomotion Rehabilitation Test Bed Designed from Kinematic Considerations



C. Copilusi, N. Dumitru and A. Margine

**Abstract** In this paper a locomotion system kinematic analysis is presented in order to obtain the hips, knees and ankles motions equations for a child walking. With these equations an experimental test bed was especially designed and simulated for locomotion rehabilitation by using MSC Adams. The whole human locomotion system was analyzed from kinematic viewpoints. Based on the obtained results a locomotion rehabilitation test bed prototype for a 7 years old child with locomotion disabilities was fabricated.

**Keywords** Human walking · Kinematic analysis · Experimental test bed  
Lower limbs motions

## 1 Introduction

In these days there were developed different methods for human locomotion system analysis [1–4]. An usual and known method, which can be used in this research is Denavit-Hartenberg method. By considering only the walking phases, sometimes this will begin to be a close-loop kinematic chain when the both feet will be in contact with the ground.

By taking into account this important argument, in this research frame, other methods can be suitable for this kinematic analysis. Thus, it is proposed a method for this kinematic analysis which has flexible characteristics and ensures an interface for dynamic analysis especially for Finite Element Modeling (FEM) of spatial and planar mobile mechanical systems [3, 5–8]. On this purpose it will be

---

C. Copilusi (✉) · N. Dumitru · A. Margine  
University of Craiova, Craiova, Romania  
e-mail: cristache03@yahoo.co.uk

N. Dumitru  
e-mail: nicolae\_dtru@yahoo.com

A. Margine  
e-mail: fam\_margine@yahoo.com

considered a case study for a 7 years old child for obtaining the anthropometric parameters. The proposed locomotion system kinematic model will be represented through motions equations which can be numerically processed. The motion equations will be used as input data for simulating the virtual model of the proposed test bed in MSC Adams environment. Conclusions are formulated based on the obtained results for the elaborated human locomotion test bed prototype.

## 2 Human Locomotion System Kinematic Analysis

For this analysis, a kinematic linkage will be considered as it is shown in Fig. 1.

A major viewpoint is the one of considering two cases of the proposed linkage and these are: first case where both feet are in contact with the ground and second case when a foot has ground contact lost. Thus, the second case will be analyzed during one gait for right lower limb. From a structural viewpoint, the kinematic chain consists of 16 rotation joints ( $i = \overline{1, 16}$ ). For obtaining the mathematic model we considered a kinematic element realized from  $n$  solid rigid bodies connected together through  $n - 1$  kinematic pairs (Fig. 1). For these kinematic elements, we make the following notations:  $T_i(x_i, y_i, z_i)$ , represents the reference coordinate system attached to  $i$  element, having the  $\overline{W}_i(\overline{i}_i, \overline{j}_i, \overline{k}_i)$ , unit vectors base with  $i = \overline{1, 16}$ ;  $T_{0T}(x_0, y_0, z_0)$ , represents the global reference system with  $\overline{W}_0(\overline{i}_0, \overline{j}_0, \overline{k}_0)$  unit vectors base;  $\overline{\delta}_i$ , represents the relative translation vector between  $i - 1$  and  $i$  elements, depending on the  $T_{i-1}$  tried, if there exists a translation joint between  $i - 1$  and  $i$ , ( $i = \overline{1, 16}$ );  $\overline{r}_i$ , represents the position vector which depends on the  $T_{i-1}$ , reference system, with respect to the  $O_i^i$ , point, when the relative translation starts ( $i = \overline{1, 16}$ );  $\overline{S}_i$  represents the position vector of  $M_i$ , depending on  $T_i$ , attached to the  $i$  element.

The position vector of point **R**, in rapport to the global reference system is given by the Eq. (1).

$$\overline{r}_R^{TOT} = \overline{O_0 M_n} = \sum_{i=1}^n (\overline{r}_i + \overline{d}_i) + \overline{S}_n \quad (1)$$

where:

$$\overline{r}_i = \{r_i^x, r_i^y, r_i^z\}_{i-1}^T = \{r_i\}^T \cdot \{\overline{W}_{i-1}\} \quad (2)$$

$$\overline{\delta}_i = \{\delta_i^x, \delta_i^y, \delta_i^z\}_{i-1}^T = \{\delta_i\}^T \cdot \{\overline{W}_{i-1}\} \quad (3)$$

$$\overline{S}_n = \{S_n^x, S_n^y, S_n^z\}_{i-1}^T = \{S_n\}^T \cdot \{\overline{W}_n\} \quad (4)$$

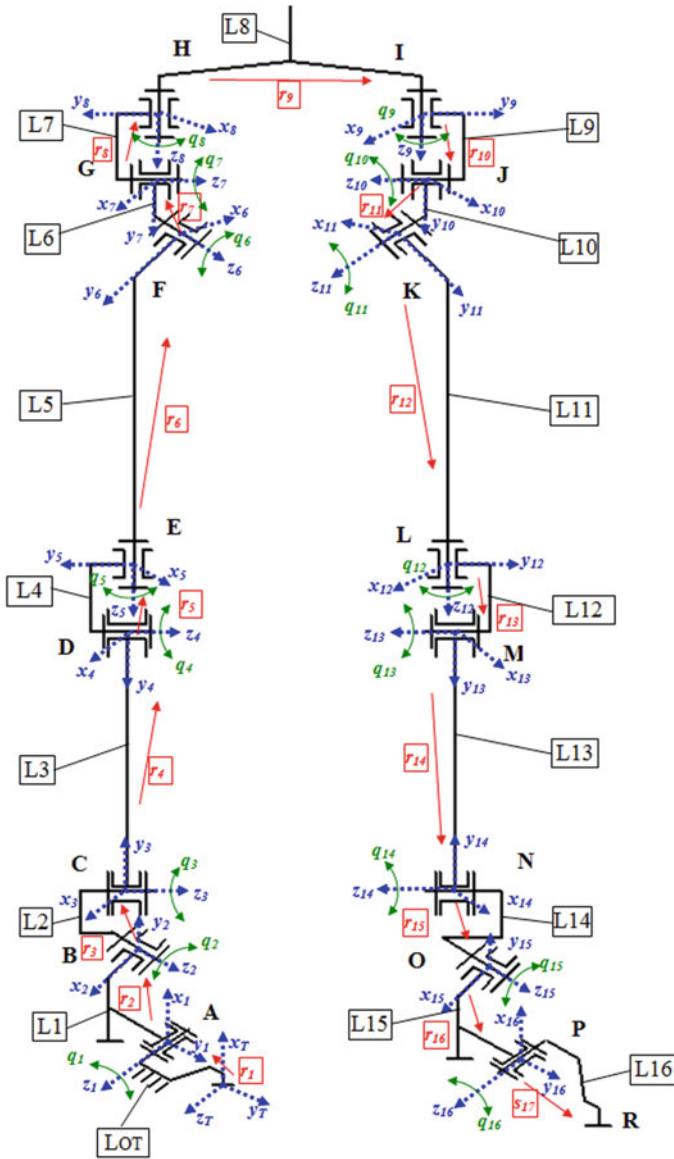


Fig. 1 Kinematic model equivalent with the proposed human locomotion system

By introducing the Eqs. (2), (3), (4) in (1), we obtain:

$$\vec{r}_R^{T0T} = \overline{O_0 M_n} = \sum_{i=1}^n ((\{r_i\}^T + \{\delta_i\}^T \cdot [A_{0,i-1}] + \{S_n\}^T \cdot [A_{0,n}])) \cdot \{\overline{W_0}\} \quad (5)$$

The speed will be obtained by differentiating Eq. (5) depending on time. Considering the coordinate transformation matrix as a quadratic:

$$[A_{0i}] \cdot [A_{0i}]^T = [I] \quad (6)$$

By differentiating Eq. (6) depending on time, we obtain:

$$\left[ \dot{[A_{0i}]} \cdot [A_{0i}] \right]^T = [A_{0i}] \cdot \dot{[A_{0i}]}^T = - \dot{[A_{0i}]} \cdot [A_{0i}]^T \quad (7)$$

We observe that  $\dot{[A_{0i}]} \cdot [A_{0i}]^T$  - is a non symmetric matrix:

$$[\tilde{\omega}_{0i}] = \left[ \dot{[A_{0i}]} \right] \cdot [A_{0i}]^T \quad (8)$$

By multiplying Eq. (8) with  $[A_{0i}]$ , we will obtain:

$$[\tilde{\omega}_{0i}] \cdot [A_{0i}] = \left[ \dot{[A_{0i}]} \right] \quad (9)$$

For each vector  $\overline{\delta_i}$ ,  $\overline{r_i}$  and  $\overline{S_i}$ , ( $i = \overline{1, 16}$ ), a non symmetric matrix can be attached. Thus, it can be written in the following form:

$$\begin{aligned} \{r_i\}^T \cdot [\tilde{\omega}_{0,i-1}] &= \{\omega_{0,i-1}\}^T \cdot [\tilde{r}_i]; \quad \{\delta_i\}^T \cdot [\tilde{\omega}_{0,i-1}] = \{\omega_{0,i-1}\}^T \cdot [\tilde{\delta}_i]; \\ \{S_n\}^T \cdot [\tilde{\omega}_{0,n}] &= \{\omega_{0,n}\}^T \cdot [\tilde{S}_n]; \quad \{\omega_{0p}\} = \left\{ \omega_p^x, \omega_p^y, \omega_p^z \right\} \end{aligned} \quad (11)$$

By applying the general Eqs. (1) to (11), the displacement for **R** point is given by Eq. (12) and differentiating this velocity and acceleration can be obtained.



$$\{\overline{r}_R^{OT}\} = \left( \begin{array}{l} \{r_1\}^T + \{r_2\}^T \cdot [A_{OT1}] + \{r_3\}^T \cdot [A_{12}] \cdot [A_{OT1}] + \{r_4\}^T \cdot [A_{23}] \cdot [A_{12}] \cdot [A_{OT1}] \\ + \{r_5\}^T \cdot [A_{34}] \cdot [A_{23}] \cdot [A_{12}] \cdot [A_{OT1}] + \{r_6\}^T \cdot [A_{45}] \cdot [A_{34}] \cdot [A_{23}] \cdot [A_{12}] \cdot [A_{OT1}] \\ + \{r_7\}^T \cdot [A_{56}] \cdot [A_{45}] \cdot [A_{34}] \cdot [A_{23}] \cdot [A_{12}] \cdot [A_{OT1}] + \{r_8\}^T \cdot [A_{67}] \\ \cdot [A_{56}] \cdot [A_{45}] \cdot [A_{34}] \cdot [A_{23}] \cdot [A_{12}] \cdot [A_{OT1}] + \{r_9\}^T \cdot [A_{78}] \cdot [A_{67}] \cdot [A_{56}] \\ \cdot [A_{45}] \cdot [A_{34}] \cdot [A_{23}] \cdot [A_{12}] \cdot [A_{OT1}] + \{r_{10}\}^T \cdot [A_{89}] \cdot [A_{78}] \cdot [A_{67}] \cdot [A_{56}] \cdot [A_{45}] \\ \cdot [A_{34}] \cdot [A_{23}] \cdot [A_{12}] \cdot [A_{OT1}] + \{r_{11}\}^T \cdot [A_{910}] \cdot [A_{89}] \cdot [A_{78}] \cdot [A_{67}] \\ \cdot [A_{56}] \cdot [A_{45}] \cdot [A_{34}] \cdot [A_{23}] \cdot [A_{12}] \cdot [A_{OT1}] + \{r_{12}\}^T \cdot [A_{1011}] \cdot [A_{910}] \cdot [A_{89}] \\ \cdot [A_{78}] \cdot [A_{67}] \cdot [A_{56}] \cdot [A_{45}] \cdot [A_{34}] \cdot [A_{23}] \cdot [A_{12}] \cdot [A_{OT1}] \\ + \{r_{13}\}^T \cdot [A_{1112}] \cdot [A_{1011}] \cdot [A_{910}] \cdot [A_{89}] \cdot [A_{78}] \cdot [A_{67}] \cdot [A_{56}] \cdot [A_{45}] \cdot [A_{34}] \cdot [A_{23}] \\ \cdot [A_{12}] \cdot [A_{OT1}] + \{r_{14}\}^T \cdot [A_{1213}] \cdot [A_{1112}] \cdot [A_{1011}] \cdot [A_{910}] \cdot [A_{89}] \cdot [A_{78}] \\ \cdot [A_{67}] \cdot [A_{56}] \cdot [A_{45}] \cdot [A_{34}] \cdot [A_{23}] \cdot [A_{12}] \cdot [A_{OT1}] + \{r_{15}\}^T \cdot [A_{1314}] \cdot [A_{1213}] \\ \cdot [A_{1112}] \cdot [A_{1011}] \cdot [A_{910}] \cdot [A_{89}] \cdot [A_{78}] \cdot [A_{67}] \cdot [A_{56}] \cdot [A_{45}] \cdot [A_{34}] \\ \cdot [A_{23}] \cdot [A_{12}] \cdot [A_{OT1}] + \{r_{16}\}^T \cdot [A_{1415}] \cdot [A_{1314}] \cdot [A_{1213}] \cdot [A_{1112}] \\ \cdot [A_{1011}] \cdot [A_{910}] \cdot [A_{89}] \cdot [A_{78}] \cdot [A_{67}] \cdot [A_{56}] \cdot [A_{45}] \cdot [A_{34}] \cdot [A_{23}] \cdot [A_{12}] \cdot [A_{OT1}] \\ + \{S_{17}\}^T \cdot [A_{1516}] \cdot [A_{1415}] \cdot [A_{1314}] \cdot [A_{1213}] \cdot [A_{1112}] \cdot [A_{1011}] \cdot [A_{910}] \\ \cdot [A_{89}] \cdot [A_{78}] \cdot [A_{67}] \cdot [A_{56}] \cdot [A_{45}] \cdot [A_{34}] \cdot [A_{23}] \cdot [A_{12}] \cdot [A_{OT1}] \end{array} \right) \cdot \{\overline{W}_{OT}\} \tag{12}$$

### 3 Numerical Processing

For kinematic analysis, an algorithm was created with MAPLE. The geometrical elements dimensions are in millimetres as:  $L_{OT} = 100$ ;  $L_1 = 90$ ;  $L_2 = 90$ ;  $L_3 = 260$ ;  $L_4 = 9$ ;  $L_5 = 275$ ;  $L_6 = 9$ ;  $L_7 = 9$ ;  $L_8 = 241$ ;  $L_9 = 9$ ;  $L_{10} = 9$ ;  $L_{11} = 275$ ;  $L_{12} = 9$ ;  $L_{13} = 260$ ;  $L_{14} = 90$ ;  $L_{15} = 90$ ;  $L_{16} = 100$ . The results after computing the algorithm were represented by the hips, knees and ankles joints motions equations and according with the kinematic linkage from Fig. 1, these are C, D, G, J, M and N joints. In the proposed case, joint motion equations were shown in Fig. 2 for right hip, knee and ankle joint, other were similar but in a mirrored form. These results will be used as further input data for numerical simulations of the proposed virtual model and these were processed only in sagittal plane.

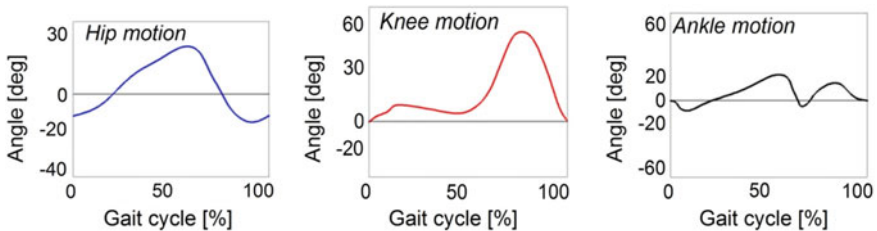


Fig. 2 Right hip, knee and ankle joints angular variations during one gait for a 7 years old child case study

## 4 Human Locomotion Test Bed Design

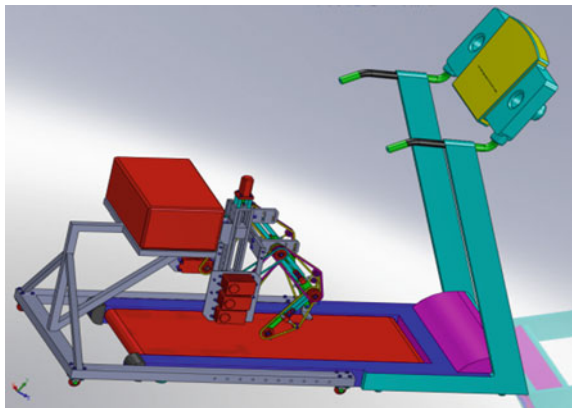
Thus, for a new human locomotion test bed mechanism there will be used a set of six servomotors and actuate each joint through a set of chain transmissions. A virtual model of the proposed test bed is shown in Fig. 3. This was designed in SolidWorks in a parameterized form and imported in MSC Adams environment.

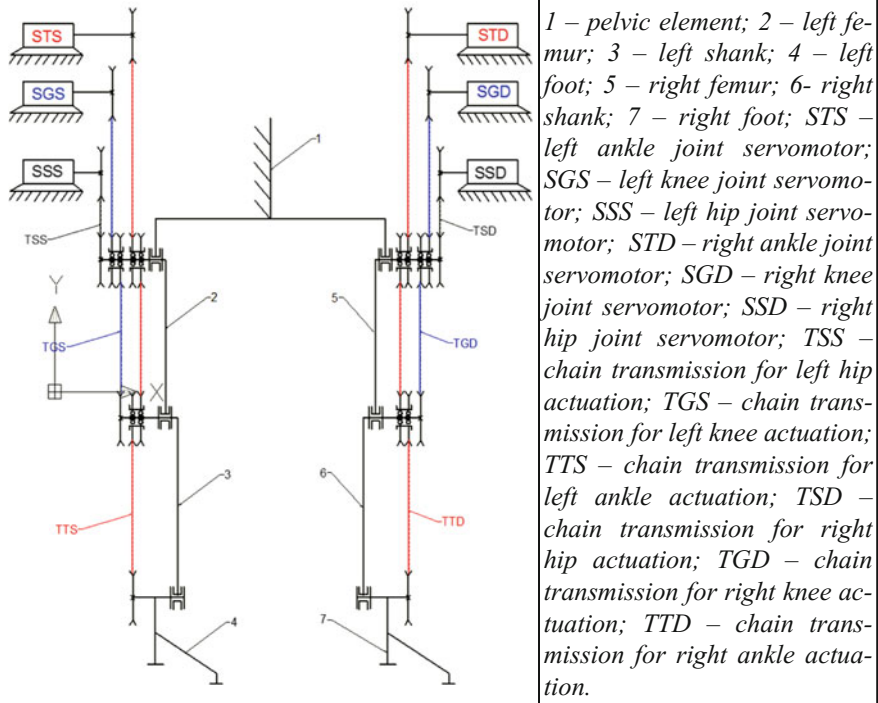
Also a structural scheme is presented in Fig. 4, in order to clarify the system functionality. For motion transmission chains transmissions was used and for this were used pairs of chain sprockets. These are placed on special shafts articulated on roller bearings.

For simulating the proposed test bed, there were defined in a parametric form the actuation chain transmission parameters on MSC Adams, a number of 12 revolute joint which include also the main hips, knees and ankle joints. MSC Adams software allows simulating in a dynamic mode the mechanism behavior, and by considering this, the whole test bed virtual model was loaded with equivalent weight of the seven years old child (23 kg). Also the ground contact between foot and treadmill was considered, but the revolute joints friction was neglected. The obtained results were represented through motion diagrams for whole virtual model, obtained as an objective for this research and these are shown in Fig. 5. The virtual simulations were done for a full gait cycle, which in MSC Adams environment corresponds to a time of 1.4 s.

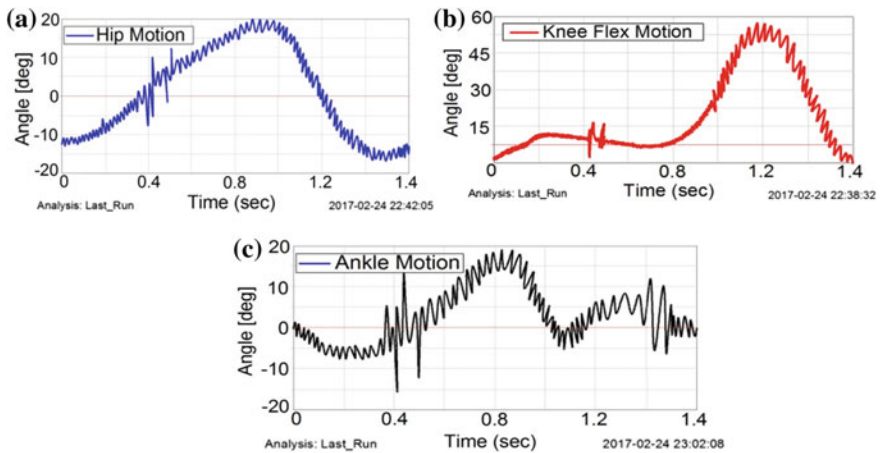
At the first look of the presented diagrams from Fig. 5 it can be observed that the curve shape and values for each joint are almost appropriate with the ones presented in Fig. 2 for the selected joints. In case of hip joint the angular variation were between a lower limit of  $-12.295^\circ$  to  $+19.897^\circ$  (around  $32.192^\circ$  angular amplitude) and according with the literature data this variation is good. By considering the knee joint, the MSC Adams results record an angular variation between 0 to

**Fig. 3** A 3D model of the proposed exoskeleton

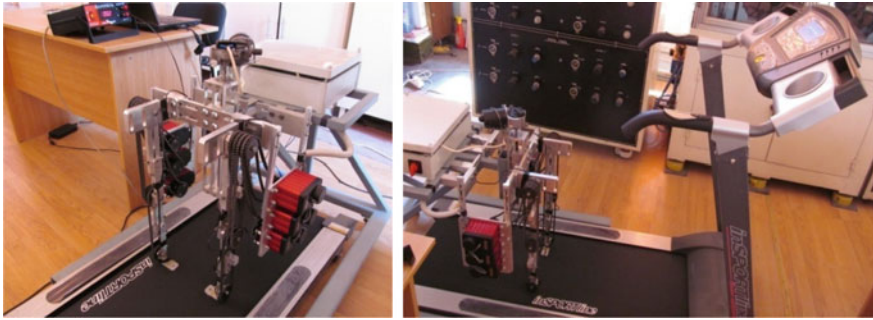




**Fig. 4** A structural scheme for a new leg exoskeleton mechanism with chain transmissions



**Fig. 5** Angular variations for the desired joints: **a** hip joint; **b** knee joint; **c** ankle joint



**Fig. 6** Children rehabilitation locomotion test bed prototype—first stage

$+54.573^\circ$  (around  $54.573^\circ$  angular amplitude) which also this is a good value according with the literature data [9].

In case of knee joint, the obtained angular variation was obtained a lower value of  $-7.698^\circ$  and a high value of  $+17.432^\circ$  (angular amplitude of  $25.13^\circ$ ). By comparing the obtained values with the existent ones from literature data, these correspond with the reality [9]. Thus a first stage prototype was elaborated and the obtained results demonstrate a proper functionality and easy-operation features. This is shown in Fig. 6.

But two negative viewpoints can be remarked on the obtained results and these are: one is the curve shapes which have a lot of spikes due to the chain and sprockets contacts during simulations and other is the contact between ground and foot which is quite noisy at the time of 0.4 s. Thus the negative remarks cannot have a bad influence of the real prototype. Firstly the noisy curvature can be eliminated by decreasing the teeth step of the chain wheels in order to have a large number of teeth on the designed chain transmissions. The contact between foot and ground has a crucial role when we refer to orientation and stability of the entire system, but in this case the obtained results are quite reasonable and validates the proposed children locomotion rehabilitation test bed to be manufactured.

## 5 Conclusions

A new design solution is proposed for a human locomotion rehabilitation test bed which is based on linkage and a mechanism structure with chain transmissions. In particular, the proposed design is evaluated by looking at previous leg mechanisms and experimental tests. The elaborated prototype is based on chain transmission solution whose design and performance are defined and evaluated by numerical results of the simulations.

A new kinematic design has been sized and characterized by using operation simulation in MSC Adams environment with suitable models for design purposes.

In the appropriate future this kinematic model will be improved and there will be developed a second prototype with special purposes on human walking rehabilitation.

## References

1. Surdilovic D, Bernhardt R (2007) STRING-MAN-Wire robot for gait rehabilitation: further development and testing. In: IEEE 10th international conference on rehabilitation robotics. Netherlands, pp 446–453
2. Hillman M (2003) Rehabilitation robotics from past to present—a historical perspective. In: Proceedings of the 8th international conference on rehabilitation and robotics ICORR, pp 1–4
3. Nef T, Mihelj M, Riener R (2007) ARMin: a robot for patient cooperative arm therapy. *Med Biol Eng Comput* 45:887–900
4. Tarnita D, Marghitu D (2013) Analysis of a hand arm system. *Robot Comput-Int Manuf* 29 (6):493–501. <http://dx.doi.org/10.1016/j.rcim.2013.06.001>
5. Copilusi C, Dumitru N, Marin M, Rusu L (2012) Children orthotics and prostheses devices designed from cinematic and dynamic considerations. *Eng Lett J* 20:301–317 (2012). Published by International Association of Engineering IAENG. ISSN 1816-0948
6. Geonea I, Ceccarelli M, Carbone G (2015) Design and analysis of an exoskeleton for people with motor disabilities. In: 14th world congress in mechanism and machine science, Taipei, Taiwan
7. Herr H, Walsh C, Valiente A, Pasch K (2011) Exoskeletons for running and walking. US Patent Application US20110040216 A1
8. Dumitrache SI, Dumitru N, Geonea I (2012) Human locomotion system design based on cam mechanisms. In: Proceedings of the world congress on engineering, vol III, pp 283–288. ISBN 978-988-19252-2-0
9. Williams M (1992) Biomechanics of human motion. In: WWB Saunders Company. London, 200 pp. ISBN 10: 0721657435

# Design and Simulation of an Underactuated Mechanism for Leg Exoskeleton



Shuangji Yao and Marco Ceccarelli

**Abstract** The paper discusses design requirements and presents a leg exoskeleton for human rehabilitation purposes. The exoskeleton is based on an underactuated mechanism to achieve a leg walking motion with desired human-like behavior. A design solution with appropriate parameters is presented with its peculiarities and the operation performances are characterized via a dynamic simulation.

**Keywords** Leg exoskeletons • Human rehabilitation • Underactuated mechanism • Simulation

## 1 Introduction

For the design and research of lower extremity exoskeleton, theoretical investigation and technical development have been worked out for decades [1, 2]. There are many devices and mechanical systems that can also be used for walking rehabilitation and exercise. Some of them are low-cost solutions and others are quite expensive [3–7]. They have actuators, sensors, and other electronic devices, that in general are controlled by computer processors. But those devices are expensive, not accessible to end-users skills, although they can fulfill most of the needs for persons with walking disabilities. One of an important feature for lower extremity exoskeleton using in rehabilitation is light-weight and energy saving, suitable for long time work. Therefore, it is recognized that use less number of drives with more degree of freedom. It is a key research purpose to improve energy utilization efficiency for the exoskeleton mechanism.

---

S. Yao (✉)  
Yanshan University, Qinhuangdao, China  
e-mail: buaayaoshuangji@163.com

M. Ceccarelli  
University of Cassino and South Latium, Cassino, Italy  
e-mail: ceccarelli@unicas.it

This paper provides a low-cost easy-operation underactuated linkage mechanism for disabled medical recovery training and exercise. Characteristics and design requirements for the underactuated exoskeleton mechanism of human walking are presented for rehabilitation purposes. Some simulation results of the underactuated mechanism with one of the parameters solution. Some kinematics performances are analyzed which will be used for the low-cost easy-operation underactuated walking exoskeleton design.

## 2 Design Requirements

Human walking represents a complex dynamic activity, due to human body major coordination. These tasks are: keeping stability, prevent injuries, avoiding obstacles and human body spatial motions. The new exoskeleton prototype is designed by considering leg mechanism solutions in [8, 9]. The exoskeleton mechanism design requirements aims to disabled medical recovery training and exercise should be matched with some elementary tasks such as simple structure, lightweight, easy to wear and to adapt to human locomotion. Some characters of the design requirements are list and discussed as:

- (1) the proposed mechanism should perform human gait cycle;
- (2) the mechanism has less actuators than degree of freedoms;
- (3) the mechanism has at least three joints: hip, knee and ankle joint;
- (4) the mechanism should perform a suitable motion space, to prevent the wearers' joints do not be injured by the leg exoskeleton.

According to [3] researchers believe that the biped walking represents a cycle which occurs on a time period between heel strike with the ground and second ground contact of the same heel. This cycle consists of two main phases: stand phase and balance phase. One of each phase is formed on a number of steps according with human gait cycle. These gait phases and their proper steps are shown in Fig. 1 in [3].

An underactuated lower limb walking can be considered as related to a walking motion that is obtained by a reduced number of actuators in the walking device comparing with DOFs. In order to achieve an underactuated walking motion, two possible approaches for mechanism structures are discussed, namely using passive joints for dynamic walking [10] or designing underactuated mechanisms.

Passive elements or flexible elements can be used to constrain the kinematics of a mechanism, such as torsional springs, linear springs, flexible joints or flexible links. A linkage mechanism with passive or flexible elements can adjust the position of links according to the contact ground. A leg exoskeleton with suitable passive mechanical elements will act human gait walking motion by means of only one motor as input actuator [11].

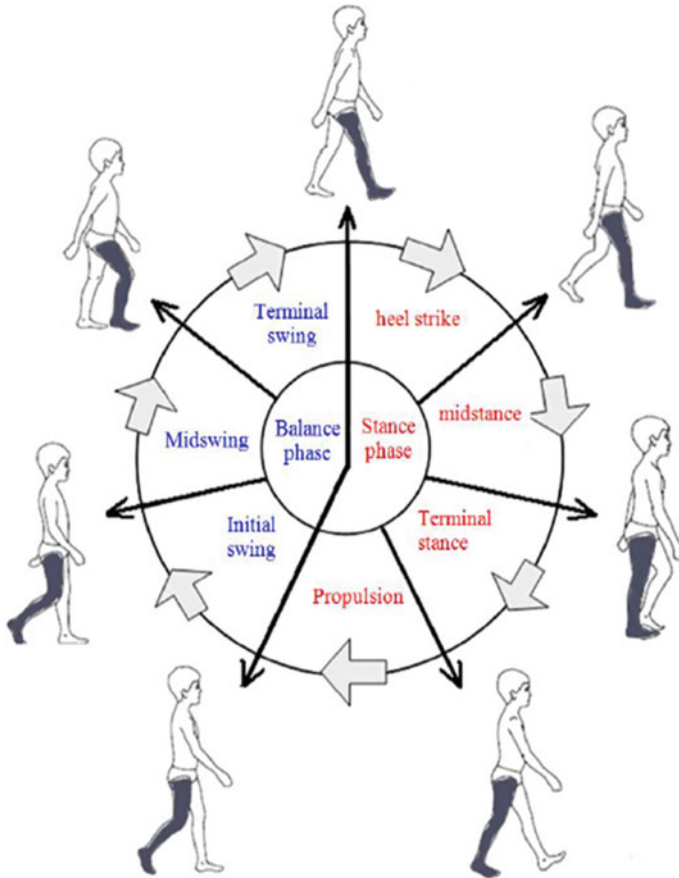
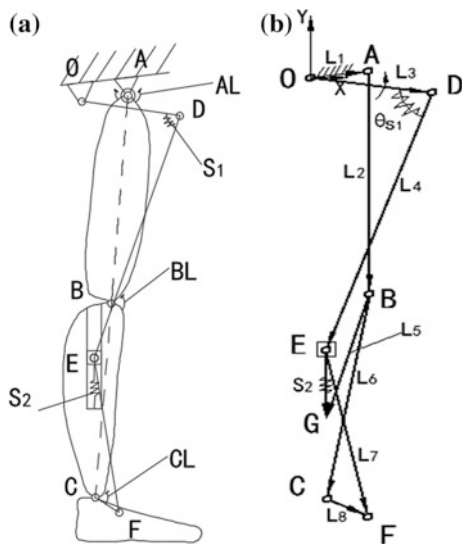


Fig. 1 Human gait phases [3]

### 3 The Underactuated Leg Exoskeleton Mechanism

The proposed underactuated leg exoskeleton mechanism in this paper is shown in Fig. 2. The mechanism is designed with only 1 actuator and 3 DOFs in hip, knee and ankle joint respectively. It contains springs elements to constrain the kinematics and three joints limitation in each joint. This kinematic design for a new underactuated leg exoskeleton is based on four-bar mechanism and linkage-slider mechanism with torsional springs and linear springs. It can perform human gait walking motion. In order to limit the rotation angle in a reasonable work space to prevent injured like human being, three joint limitations are set in each joint. There are two spring systems in this mechanism. All these elements in Fig. 2 are described as listed in Table 1.





**Fig. 2** **a** The proposed underactuated leg mechanism exoskeleton; **b** Kinematics parameters of leg exoskeleton

**Table 1** Elements description in Fig. 2

O—actuator joint (rotation joint)	AB—exoskeleton human-like thigh link
A—exoskeleton hip joint	BC—exoskeleton human-like shank link
B—exoskeleton knee joint	CF—exoskeleton human-like foot link
C—exoskeleton ankle joint	OD—actuator link for leg exoskeleton mechanism
E—linear slider	DE—middle link for leg exoskeleton mechanism
S1—torsional spring	EF—lower link for leg exoskeleton mechanism
S2—linear spring	AL— rotation limitation in hip joint
BL—rotation limitation in knee joint	CL— rotation limitation in ankle joint

This mechanism is a closed chain linkage with underactuated joints. It can only rely on the sole driving source on hip joint to drive the motion in three joints at hip, knee and ankle. Thus, the mechanism can greatly reduce the number of drivers and the weight of exoskeleton. Main characteristics for this leg exoskeleton mechanism can be considered in design process as in the following.

Firstly, the basic units of mechanical structure are joints, links and a slider, so it can be designed according to the physiological structure as human legs. Some design solutions with suitable dimension in lengths and angles can meet the requirements of the walking rehabilitation assistance treatment.

Secondly, there are joint rotation limitations in the exoskeleton joints. In the standing situation, the knee and ankle joint limitation will work. Thus, the linkage mechanism can perform high rigidity and stability when exoskeleton standing on

the ground. Therefore, the closed chain linkage mechanism can ensure the exoskeleton in the case of large load standing.

Thirdly, there are two spring elements set in the thigh and shank links, as shown in Fig. 2. In order to constrain the kinematics in underactuated joints, a torsional spring and a linear spring are designed. These torsion spring and linear spring will produce elastic deformation and damping in the spring tension and compression process. Thus, the springs can reduce the impact force and vibration on leg when the gait motion transfers from swing to standing.

### 4 Performance Analyses via Simulation

The design parameters of a new underactuated mechanism for this leg exoskeleton design solutions are shown in Fig. 2a. In order to show the relationship of each links, the mechanism link vectors closed chain are shown in Fig. 2b. The  $L_i$  ( $i = 1, \dots, 8$ ) are the length of each links in the mechanism, The  $\theta_i$  ( $i = 1, \dots, 8$ ) are the angle of each links relative to coordinate axis X.  $\theta_{S1}$  is the angle of the torsional spring,  $S_2$  is the length of the linear spring. Link sizes of the designed new leg exoskeleton mechanism are obtained by kinematics tests in 3D software and listed in Table 2.

Numerical simulation for the two legs exoskeleton mechanism walking is run in SolidWorks Motion environment. It has been computed with the input angle initial value of  $\theta_3$  as  $\theta_3(0) = 352^\circ$ , and the initial values of spring parameters are assumed as some other design parameters are:  $\theta_{S1} = 78.5^\circ$ ;  $S_2 = 135$  mm;  $\theta_{S2} = 270^\circ$ ; The value of coefficients  $k_1, k_2, c_1, c_2$  of springs and dampers in simulations have been determined with values  $k_1 = 25 \times 10^{-3}$  Nm/deg,  $k_2 = 15 \times 10^3$  N/m,  $c_1 = 20 \times 10^{-3}$  Nms/deg and  $c_2 = 5 \times 10^3$  Ns/m, respectively.

A simulated sequence of walking motion by the proposed two legs mechanism is shown in Fig. 3. The walking ground is plane and the material of contact surface between shoes and ground is set as rubber. For the disabled people rehabilitation walking exercise function, the movement of the waist in horizontal direction is restricted by two frame bars as shown in Fig. 3.

An actuated cyclic rotating motion is located at link L3, who's the input motion formulation of link L3 for left and right leg is given by

**Table 2** Lengths and angle parameters for the underactuated leg exoskeleton mechanism in Fig. 2

Design parameters	1	2	3	4	5	6	7	8
$L_i/(mm)$	122	550	260	678	283	515	413	74
$\theta_i/(^\circ)$	7.3	266.5	352	250.5	260.8	265.3	279	328

**Fig. 3** Two legs exoskeleton mechanism in a simulation environment



$$\text{Left leg: } \Delta\theta_{3L}(t) = \begin{cases} A \sin(2\pi/T)t & \text{if } \sin(2\pi/T)t \geq 0; \\ 0 & \text{if } \sin(2\pi/T)t < 0; \end{cases} \quad (1)$$

$$\text{Right leg: } \Delta\theta_{3R}(t) = \begin{cases} 0 & \text{if } \sin(2\pi/T)t \geq 0; \\ -A \sin(2\pi/T)t & \text{if } \sin(2\pi/T)t < 0; \end{cases} \quad (2)$$

where  $t$  is the time variable,  $A$  is the maximum swing rang for link L3. In order to move the linkage mechanism smoothly, sine function is selected in Eqs. (1) and (2) as the movement function with the features of cyclic and intermittent motion. The variable  $T$  in Eqs. (1) and (2) is the cyclic time for the movement.

Considering the human walking cycle time, set the cyclic time  $T = 2$  s in Eqs. (1) and (2) for this simulation. It means the exoskeleton walking process spends 1 s by a leg per step. Considering the human thigh rotated range in walking, set the maximum swing angle is  $30^\circ$  of link L3, thus  $A = 30^\circ$  in Eqs. (1) and (2). It means the input link L3 will rotates  $30^\circ$  and back in a walking cycle. The simulation continues 12 s, some input movement and simulation results are shown from Figs. 4 to 9.

The walking simulation involved gravity and the inertial force of the underactuated leg exoskeleton. The exoskeleton gait phases and their proper steps are shown in Fig. 4 like the gait defined in 3. The proposed exoskeleton mechanism can perform human-like walking gait with suitable kinematics design in Table 2. The joints' rotation in hip, knee and ankle joints in the mechanism coupled with the linkages can carry out human-like walking motions by two legs.

The joints motion of hip, knee and ankle joints in walking simulation are shown in Fig. 5a. It can be seen that the red curve in Fig. 5a described the hip joint rotated angle range. The link AB, which is thigh link of the exoskeleton, is  $190^\circ$  while it is standing. Link AB rotated about  $35^\circ$  forward in leg swing forward phase. When the leg is landing, link AB rotated about  $7^\circ$  backward for the thigh backward swing. The joint limitation in hip joint is not work in simulation. The deep blue curve in Fig. 5a described the knee joint rotated angle range. The simulation result express link BC (which is shank link of the exoskeleton) rotated angle according link AB. The knee rotated angle begins from about  $160^\circ$  while the leg is standing. Link BC rotated about  $56^\circ$  according link AB in thigh link swing forward process. When the

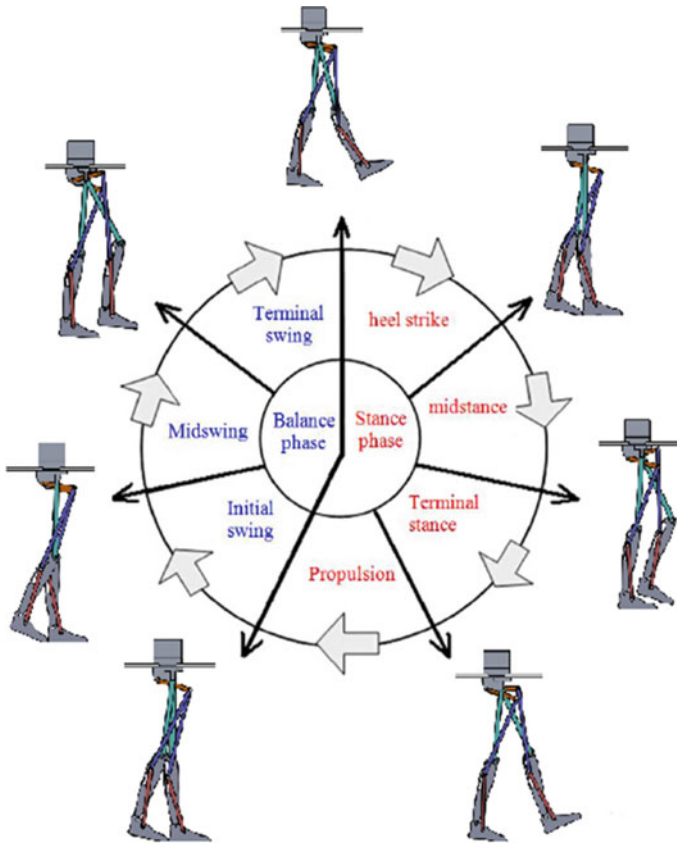


Fig. 4 Simulated result of the underactuated leg mechanism’s gait

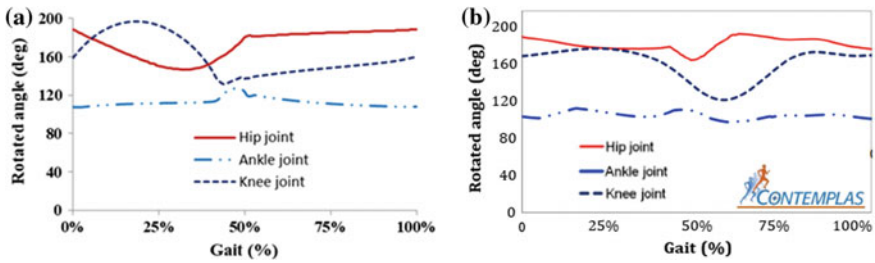
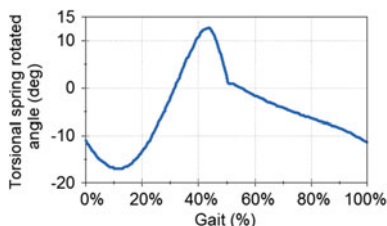


Fig. 5 Rotation angle in hip, knee and ankle joint: **a** rotated angle of the proposed leg exoskeleton; **b** rotated angle of human biological motion cited from [3]

**Fig. 6** Torsional spring rotated angle



thigh link swing backward the angle between link AB and link BC become small. The minimum angle is  $137^\circ$  before foot landing, which reached the angle limitation of knee joint. The knee joint angle increases slowly while the gait is from standing phase to back swing phase. The light blue curve in Fig. 5a described the ankle joint rotated angle range. The simulation result express link CF (foot link of the exoskeleton) rotated angle according link BC. The angle of ankle joint performs stable cyclic motion when the mechanism in walking process. The ankle joint rotated range is  $20^\circ$  totally which is from  $108^\circ$  to  $128^\circ$  in the walking cycle. The ankle joint limitation is reached when the leg is swing forward and backward.

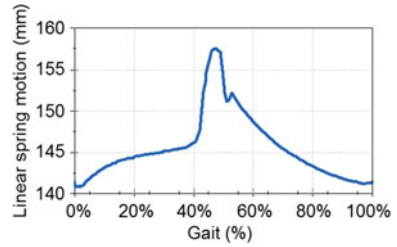
Comparing with the human biological motion in Fig. 5b, the leg mechanism is designed to reproduce the similar motion of human legs with the simulation results. It can perform approximately with the characterization of human biological motion.

Figures 6 and 7 show the motion of torsional spring and linear spring in walking cycle. Because the first step is begin from two legs standing state, the springs performance are different in the first second by comparing with their performance in other time. The torsional spring angle rotated from  $-15^\circ$  to  $13^\circ$  and the curve is smooth in Fig. 6. It means the torsional spring working in a stable state when the underactuated mechanism is walking. The initial length of linear spring is 150 mm. It is compressed to 140 mm and extended to 157 mm in walking cycle. It can be seen from in Fig. 7 that there are small disturbance in the curve of linear spring motion at the moment of foot landing on the ground. It means the contact process has some vibration between foot and ground. Thus, the linear spring parameters should be better designed by selecting suitable spring coefficient and damping.

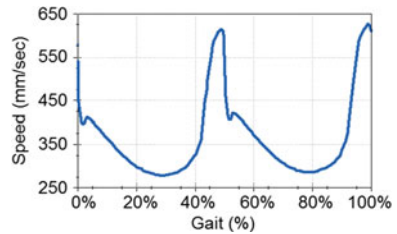
The waist part of two legs exoskeleton mechanism is limited in the horizontal bars. Figure 8 shows the moving speed of the waist part in horizontal direction. The waist moving speed becomes to a stable cycle when the walking cycle become regularly. The leg exoskeleton mechanism can walk in a constant speed in this regular cyclic process.

Figure 9 shows the reaction force on the foot by the ground. It can be seen that the contact force at the moment of foot landing is more than 1500 N. Foot landing and contact the ground is a collision process in very short time, thus the impact force is very large at that moment. The contact force is less than 100 N when the foot is standing on the ground, which is much smaller than landing process.

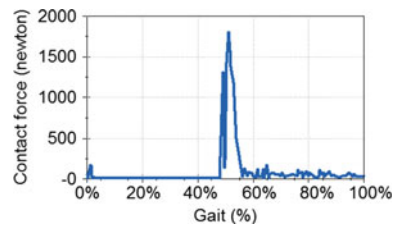
**Fig. 7** Linear spring motion



**Fig. 8** Waist speed in horizontal direction(X axis)



**Fig. 9** Contact force on the foot by the ground



## 5 Conclusions

In this paper we have discussed the design requirements for the low-cost easy operation leg exoskeleton mechanism. An underactuated mechanism of leg exoskeleton based on closed chain linkage bar is proposed. The proposed leg exoskeleton mechanism has 3 DOFs with only 1 actuator. It can simulate human hip joint, knee joint and ankle joint and the normal physiological structure of thigh, shank, foot size. The rotation range in each joint can be limited by joint limitation design. Simulation of walking is carried out to characterize the solution performance. The simulation results show the proposed underactuated leg exoskeleton mechanism can obtain feasible human like walking cycle gait with design results.

## References

1. Kazerooni H (2006) The berkeley lower extremity exoskeleton project experimental robotics IX. Springer, Berlin Heidelberg, pp 9–15
2. Phoenix. <http://www.suitx.com/phoenix.html>. Accessed 27 Mar 2017
3. Copilusi C, Ceccarelli M, Carbone G (2015) Design and numerical characterization of a new leg exoskeleton for motion assistance. *Robotica* 33(5):1–16
4. Carbone G, Ceccarelli M (2005) Legged robotic systems. *Cutting edge robotics*. InTech
5. Tao L, Ceccarelli M (2014) Design and simulated characteristics of a new biped mechanism. *Robotica* 33(7):1–21
6. Liu J, Tan M, Zhao X (2007) Legged robots—an overview. *Trans Inst Meas Control* 29(2):185–202
7. Walsh CJ, Paluska D, Pasch K et al (2006) Development of a lightweight, underactuated exoskeleton for load-carrying augmentation. In: *IEEE international conference on robotics and automation*. IEEE, pp 3485–3491
8. Lim HO, Takanishi A (2006) Mechanism and control of anthropomorphic biped robots. In: *Mobile robotics, moving intelligence*. InTech
9. Wang M, Ceccarelli M. Design and Simulation of Walking Operation of a Cassino Biped Locomotor. *New Trends in Mechanism and Machine Science*. Springer International Publishing, 2015:613–621
10. McGeer T (1990) Passive walking with knees. In: *Proceedings of the IEEE international conference on robotics and automation*, vol 3. IEEE Xplore, pp 1640–1645
11. Cherry MS, Choi DJ, Deng KJ et al (2006) Design and fabrication of an elastic knee orthosis—preliminary results. In: *ASME 2006 international design engineering technical conferences and computers and information in engineering conference*. american society of mechanical engineers, pp 565–573

# Design, Numerical Simulation and Manufacturing of a Powered Wheelchair



I. Geonea, N. Dumitru, A. Rosca and A. Didu

**Abstract** This study presents the authors research to develop a powered wheelchair for disabled people. The wheelchair is intended mainly for use in buildings area. The proposed solution for the wheelchair propulsion uses a chain transmission for each wheel and two motors. The benefits of the chain transmission, from ergonomic aspect is that they ensure the wheelchair folding for easy transportation with a vehicle and allows the motors placing in the front, thus providing better stability to access ramps and for climbs. From dynamic perspective, implementation of a chain transmission in the wheelchair propulsion, improves dynamic performances by multiplying the torque. Simulations performed in ADAMS reveal optimal performance of the wheelchair. Based on the proposed design of the wheelchair a prototype is manufactured and are presented experimental obtained results for motion analysis.

**Keywords** Wheelchair · Design · Manufacture · Dynamic study

## 1 Introduction

For disabled people the wheelchair is the most used transportation device available on the market [1, 6, 9]. Today are manufactured wheelchairs that can travel in crowded spaces, can climb stairs in areas that are not equipped with access ramps.

---

I. Geonea (✉) · N. Dumitru · A. Rosca · A. Didu  
Faculty of Mechanics, University of Craiova, Craiova, Romania  
e-mail: igeonea@yahoo.com

N. Dumitru  
e-mail: nicolae\_dtru@yahoo.com

A. Rosca  
e-mail: adrian\_sorin\_rosca@yahoo.com

A. Didu  
e-mail: ankadidu11@gmail.com



Also a great interest is pointed on the direction to develop wheelchairs for easy access in public transportation vehicles. In the last years to this research direction the novelty represents the development of intelligent wheelchairs that can recognize objects, and avoid collision with obstacles. Also another development is represented by the wheelchairs equipped with robotic arms, which are used by the human disabled patient to manipulate objects [7, 10].

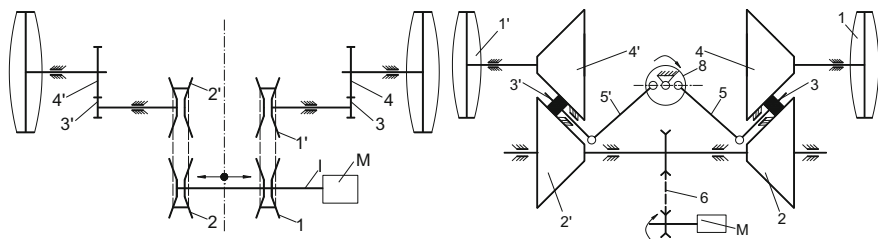
There are numerous advances in the wheelchair design and construction, represented by the progress in motors, transmission, batteries, safety, autonomy and human interface [5]. Most of the wheelchairs use two motors placed directly at the back wheels for travel and steering. In that case the motors must provide high torque especially at low speed, and because that they have a special construction and are expensive [2, 8].

Recent developments use motors equipped with worm gears reducers and also planetary gearboxes [3, 4]. This construction increases the purchase price of the wheelchair. In this research is proposed the development of a wheelchair equipped with two motors and chain transmission from motors to the back wheels. The purpose of the chain transmission is to increase the motor torque. As a future develop direction to the wheels can be used more chain pinions in order to change gears, in case of a ramp climb. Also the chain transmission simplifies the design, because the motors are mounted in the front and allows the design to be ergonomic. As a novelty the wheelchair keeps its folding capability.

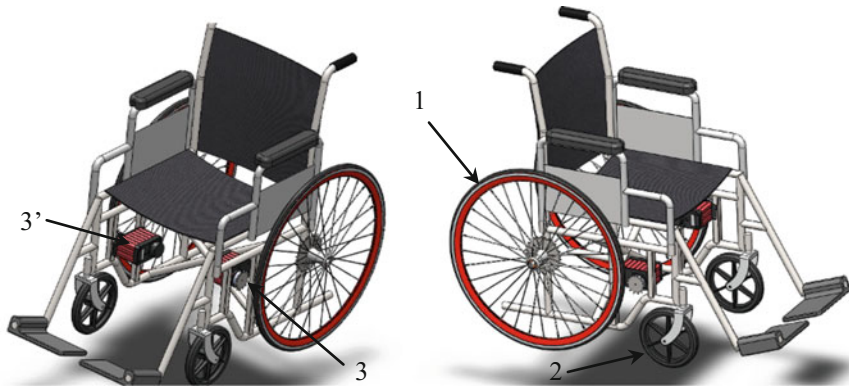
## 2 Wheelchair Design and Kinematics

The principle of wheelchair design in most of the cases, consist in using two motors. Differentiating the motors speed is realized the steering and this principle it is called differential steering. In this case it is necessary to implement a complex command and control computer architecture. In order to obtain a simplified construction are proposed in Fig. 1, two schemes that use only one motor.

The first scheme uses one motor  $M$  and two continuous variable transmissions (CVT) and also a final transmission with spur gears (3), (4). In the middle position the transmission ratio for the left and right CVT are equal. By changing the



**Fig. 1** Wheelchair transmission kinematic scheme



**Fig. 2** Wheelchair design model in solid works

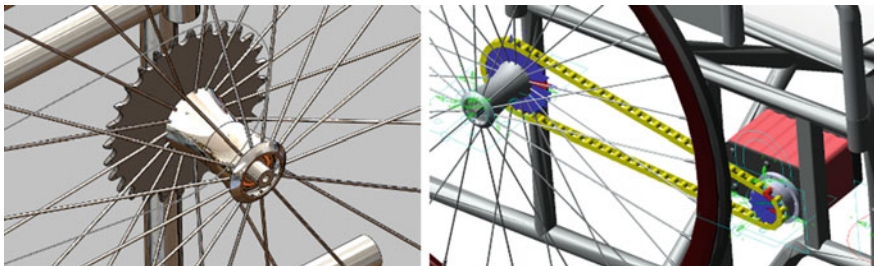
transmission ratio, the wheels speed varies and the wheelchair is steering. The same principle is used to the second scheme, only that here are used conical friction transmission (2), (4) with and intermediate element (3). The transmission ratio is changed rotating the element (8), with maximum 10° from the middle position and in that case the rubber roll (3) translate between elements (2) and (4) changing the transmission ratio.

These design solutions are difficult to implement and in our design will use two motors and two chain transmission, as presented in Fig. 2. The motion from motors (3) and (3') is transmitted with chain transmission to the back wheels (1). The front wheels (2) are self-directional. The chain transmissions ratio is 1:2. The motor used has a rated torque of 20 Nm and a nominal speed by 22 rpm.

The construction details of the motors and wheel hub with chain sprockets are shown in Fig. 3.

For straight line motion, the distance travelled by the wheelchair is calculated with Eq. (1):

$$S = 2\pi R \cdot n / i_t \tag{1}$$



**Fig. 3** Wheelchair wheel hub design and chain transmission

where:  $R$  is the back wheel rolling radius, in [m];  $n$  is the motors nominal speed, in [rpm];  $i_t$  is the transmission ration between motor and back wheel.

The wheelchair rolling radius is 0.292 m and the transmission ratio is 2. With these values it results that the wheelchair travels 12.8 m in one minute. The propulsion power for wheelchair travel on a ramp is computed with Eq. (2):

$$P_{rul} = \frac{f \cdot G \cdot \cos \alpha}{360} \cdot V; [kW] \tag{2}$$

where:  $f$  is the rolling resistance coefficient, (with value of 0.1 in case of concrete);  $G$  is the vehicle weight, in [N];  $\alpha$  is the ramp angle (6 degrees' maximum);  $V$  is the wheelchair speed, computed as 0.21 m/s.

With these values the power needed for propulsion is computed to be 0.05 kW. The total power is increased by the power needed for the transmission losses. Considering the transmission efficiency to be 0.9 results that the motors must provide a power by 55 W.

The differential wheelchair geometric configuration is shown in Fig. 4.

To the wheelchair are imposed the following constraints: rolling without slipping, zero lateral motion, and these constraints are expressed by Eq. (3).

$$\begin{aligned} \dot{y}_c \cos \theta - \dot{x}_c \sin \theta + d\dot{\theta} &= 0 \\ \dot{x}_c \cos \theta + \dot{y}_c \sin \theta + b\dot{\theta} - r\dot{\psi}_r &= 0 \\ \dot{x}_c \cos \theta + \dot{y}_c \sin \theta + b\dot{\theta} - r\dot{\psi}_l &= 0 \end{aligned} \tag{3}$$

where:  $T_a$  is the wheelchair reference system;  $T_w$  is the global reference system;  $\theta$  –is the angle of rotation.

The wheelchair kinematics is studied in MSC.ADAMS multibody software. The model designed in ADAMS with proper joints, ground contact is shown in Fig. 5.

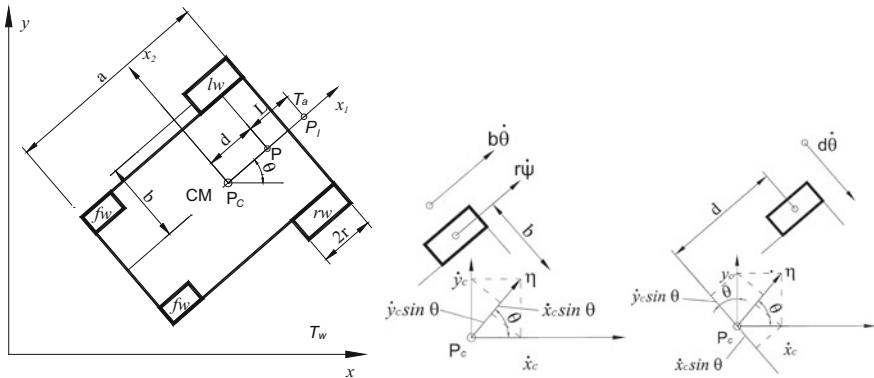
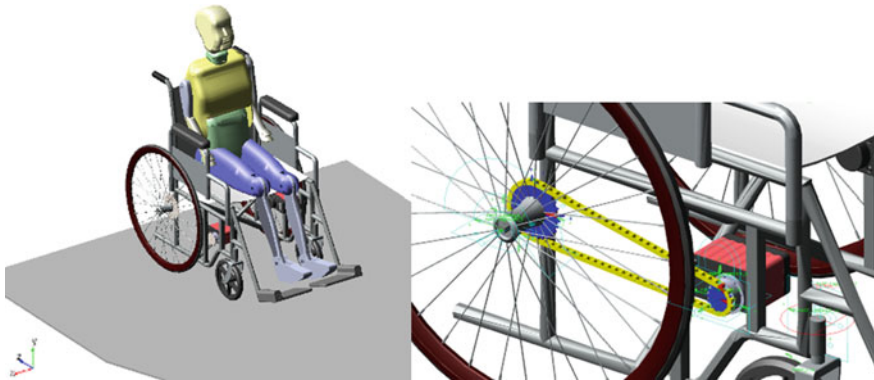
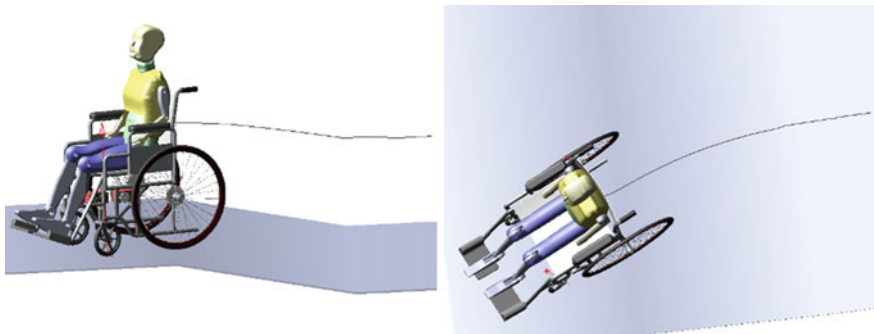


Fig. 4 Wheelchair geometric configuration and constraints



**Fig. 5** Simulation model of the wheelchair in ADAMS



**Fig. 6** ADAMS computed trajectory of the wheelchair

Using ADAMS Machinery features are designed also the chain transmissions. The simulation model is completed with a human virtual mannequin. The simulation is made for the situation when the wheelchair climbs an access ramp with 3 degrees' inclination. The total weight of the wheelchair and human mannequin is 800 N. For this simulation the motors speed is specified: 19.1 rpm for the left motor, and 22.92 rpm for the right motor, to achieve steering.

The wheelchair computed trajectory in ADAMS is presented in Fig. 6. The wheelchair computed translational displacement and velocity magnitude are shown in Fig. 7. Results show that the wheelchair moves 2 meters in 6 s with a medium velocity of 250 mm/s. Computed wheelchair wheels torque, presented in Fig. 8, reaches a maximum value of 25 Nm.

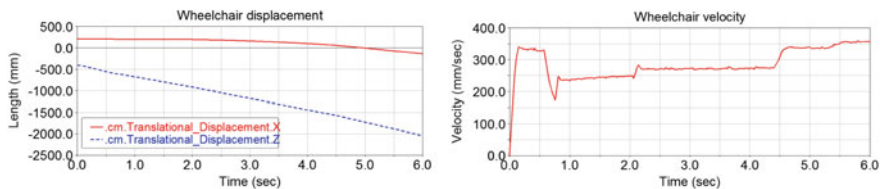


Fig. 7 ADAMS computed displacement and velocity

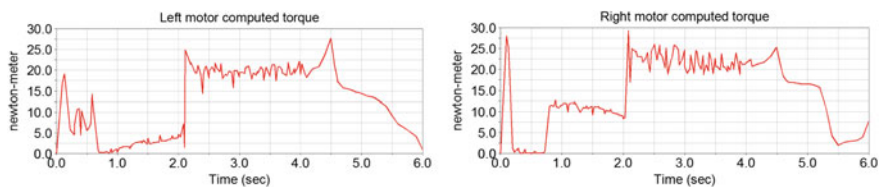


Fig. 8 ADAMS computed motors torque

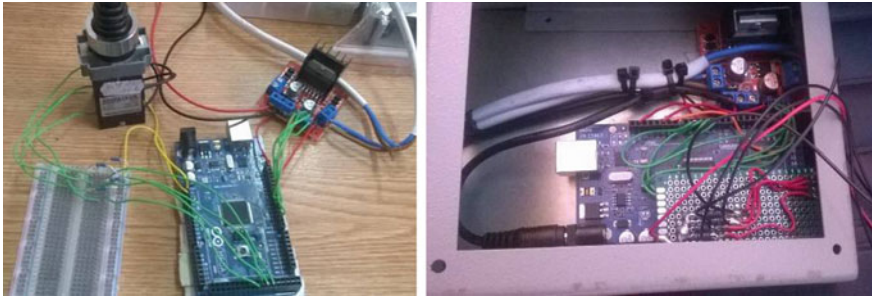
### 3 Wheelchair Prototype

A real prototype of the wheelchair is developed, as presented in Fig. 9. The motors used are DC motors with reduction gears, with a nominal torque of 20 Nm at 12 V. The motors are powered by a 12 V accumulator and draws approximately 6 A at full load.

The controller implemented is based on a L298 N Dual H Bridge Motor controller module, as shown in Fig. 10. An H Bridge represents an electronic circuit



Fig. 9 Wheelchair experimental model

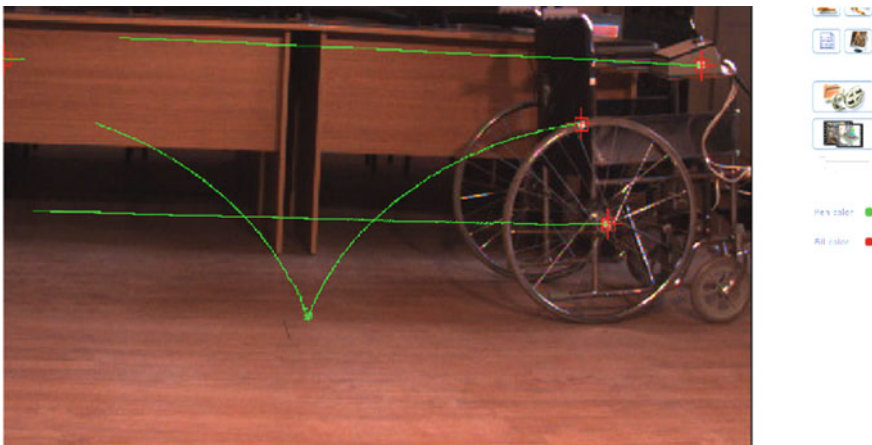


**Fig. 10** Wheelchair control unit

that contains transistors and can drive a current in either polarity. This circuit can be controlled by Pulse Width Modulation (PWM). The microcontroller used is based on Arduino Mega 2560 board, and the control program for PWM it is written in Arduino language.

Experimental investigation of the motion, in biomechanics applications is performed with ultraspeed video cameras systems [11]. Another method used for motion analysis is based on wearable sensors [12, 13].

In this study, the motion analysis of the wheelchair is achieved experimentally with Contemplas motion analysis software, which is based on ultraspeed video cameras. The analysis principle consists in attaching reflective markers on the wheelchair and tracking the markers trajectories, as presented in Fig. 11.



**Fig. 11** Wheelchair marker trajectories tracking in Contemplas

Marker tracking allows calculation in Contemplas of the wheelchair speed, but also of the angular velocity of the wheels, as can be seen in Fig. 12.

Wheelchair computed velocity for straight line displacement and angular velocity of the wheels is presented in Fig. 13.

The wheelchair computed velocity in Contemplas is 300 mm/s, as presented in Fig. 13. The wheel computed angular velocity is 57 deg/s. The obtained result for the wheel angular velocity is feasible, because the motor speed is 19.1 rpm and the chain transmission ratio is 2.



Fig. 12 Wheelchair marker tracking for computation of angular velocity of the wheels

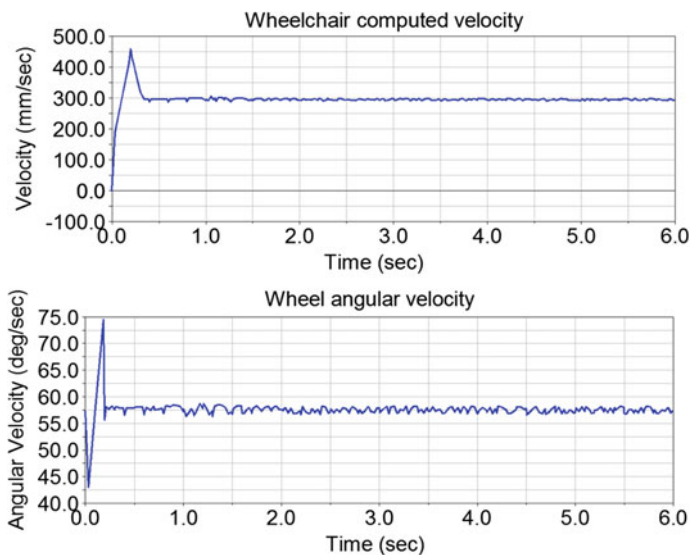


Fig. 13 Wheelchair computed parameter in Contemplas

## 4 Conclusions

In this paper is presented the design model and experimental development of a wheelchair for disabled people. A real prototype is developed and tested in room operation conditions. Developed wheelchair is equipped with two motors and chain transmission. Implemented controller is based on a dual H bridge motor controller and one Arduino board to generate Pulse Wave Modulation. A dynamic simulation is performed in MSC. Adams multibody dynamics software, when the wheelchair is running on a 3° inclined ramp and are obtained the wheels motor torque. The experimental prototype is developed and tested for room operation condition. The motion analysis of the wheelchair is performed with ultraspeed video camera equipment. The experimental prototype can be used for motion of disabled people with success.

## References

1. Braga R et al (2009) Concept and design of the intellwheels platform for developing intelligent wheelchairs. In: Informatics in control, automation and robotics, pp 191–203
2. Dumitru N, Malciu R, Geonea I (2010) Differential transmission for robotizing a powered wheelchair. In: Proceedings of the OPTIROB, pp 47–51
3. Geonea I, Dumitru N, Margine A (2015) Design and motion study of a wheelchair for disabled people. *Lect Notes Eng Comput Sci* 2218:1028–1033
4. Geonea I, Dumitru N (2016) Motion analysis of a robotic wheelchair. In: *Advances in Robot Design and Intelligent Control*. Springer International Publishing, pp 471–479
5. Kumar V (1997) Assistive devices for people with motor disabilities. In: *Wiley encyclopedia of electrical and electronics engineering assistive devices for people with motor disabilities*
6. Miller DP et al (1995) Design and testing of a low-cost robotic wheelchair prototype. *Auton Robots* 2(1):77–88
7. Morales R et al (2006) Kinematic model of a new staircase climbing wheelchair and its experimental validation. *Int J Robot Res* 25(9):825–841
8. Pires G (1997) Autonomous wheelchair for disabled people. In *Proceedings of the IEEE International Symposium on Industrial Electronics (ISIE97)*, Guimarães, pp 797–801
9. Rebsamen B et al (2007) Controlling a wheelchair indoors using thought. *IEEE Intell Syst* 22 (2)
10. Simpson R et al (2005) A prototype power assist wheelchair that provides for obstacle detection and avoidance for those with visual impairments. *J NeuroEng Rehabil* 2(1):30
11. Tarnita D, Catana M, Tarnita DN (2013) Experimental measurement of flexion-extension movement in normal and osteoarthritic human knee. *Rom J Morphol Embryol* 54(2):309–313
12. Tarnita D, Geonea I, Petcu A, Tarnita DN (2016) Experimental characterization of human walking on stairs applied to humanoid dynamics. In: *Advances in Robot Design and Intelligent Control*. Springer, pp 293–301
13. Tarnita D (2016) Wearable sensors used for human gait analysis. *Rom J Morphol Embryol* 57 (2):373–382



# Methodology for Determining the Positions of the Human Spine Vertebrae



S. Butnariu and C. Antonya

**Abstract** Assessing the posture of the human body in real time is a great challenge, given the alarming increase of diseases in the bone system, in general and of the spine, in particular, generated by the adoption of inadequate positions in the current activities. Knowing the posture of the spine can help the doctor in preventing or diagnosing a disease and designing a customized treatment. The data presented in this paper is part of the research carried out in the SPINE project [13]. The aim of this paper is to present a methodology for the reconstruction and visualization of a human spine, i.e. calculating the positions and representation of vertebrae in 3D format, using mechanical software applications.

**Keywords** Human spine kinematics • Inertial sensors • Spine posture  
MATLAB SimMechanics

## 1 Introduction

The changes that have occurred in recent years in human activities, either at work or at home, have conduct to the adoption of non-conforming posture. Therefore, the positions of the spine has been extensively studied lately, in order to establish consistency between human activity and the diseases that can be acquired. In some papers, the posture of the spine was analyzed according to the subject's activity. For example, in [2] is followed the position in the seating position and in [4] in the walk time. In others, the posture was studied in laboratory conditions, in vivo [11] or in vitro [3].

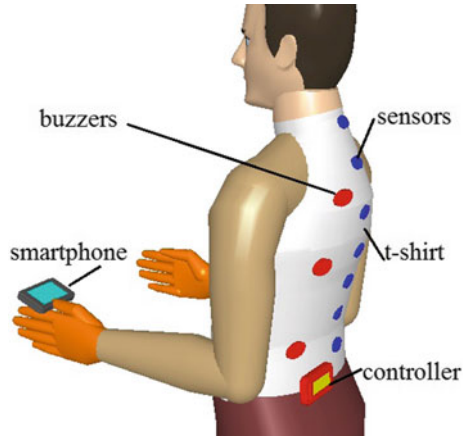
In order to achieve the proposed objective, research from the SPINE project [13] (Fig. 1) led to the design of a portable device which can track the body posture in

---

S. Butnariu (✉) · C. Antonya  
Transilvania University of Braşov, Braşov, Romania  
e-mail: butnariu@unitbv.ro

C. Antonya  
e-mail: antonya@unitbv.ro

**Fig. 1** Portable device for body posture tracking



real time. The measured data (angles), collected by IMU sensors, are filtered, analyzed and used to calculate splines that reproduce the spine posture. There are some drawbacks: sensors performance, sensors slippage on the skin, the anatomical conformation of the patient which led to the realization of mathematical models that take into account approximations, interpolations and simplifying hypotheses.

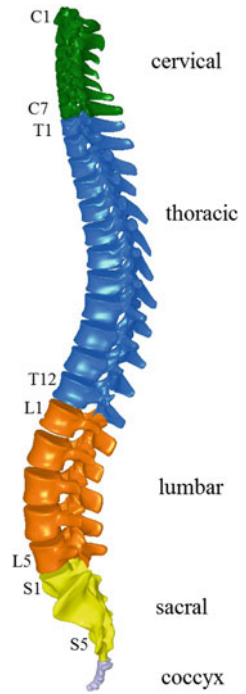
The spine represents the axial segment of the skeleton, consists of 33–34 vertebrae metamERICALLY arranged and is divided into five regions: cervical, thoracal, lumbar, sacral and coccyx (Fig. 2). Articulations—the intervertebral disc and its connection to vertebrae are considered a secondary cartilage joint, or symphysis (Fig. 3). The literature shows the functional anatomy of the spine in various ways, one of the most accepted beings that the spine can be represented as a succession of functional units called “motor units” or “motor segments”. This elemental functional unit of the spine consists of two neighboring vertebrae, the intervertebral disc between them, the entire ligaments and muscles corresponding to these vertebrae as well as the vascular-neural elements of this spinal column segment.

So it is easy to understand that each vertebra is also part of the neighboring functional unit (supra-or underlying), thus achieving an overall, unitary vision of anatomy and function of the whole spine.

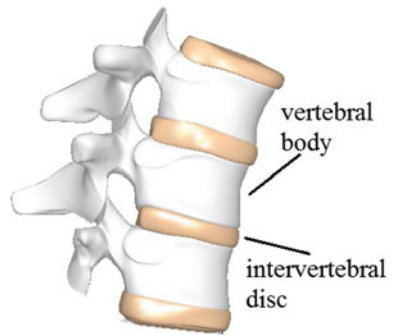
The study of the biomechanics of the spine requires two aspects: static and dynamic. The harmony of the two components provides the column with the prerequisites for fulfilling the main functions: (I) support function: giving the spine the possibility to achieve and maintain the orthostatic position; (II) protective function of the spinal cord and other medullary vascular-nerve structures, both in the resting state and in the state of mobilization of the spine; (III) dynamic function: through which the whole body is moved to the environment.

In order to maintain a static balance of the spine, the anatomic and functional integrity of all component structures is essential: rigid (bones), elastic (ligaments), mobile (joints), motor (muscle) and nerve. All the anatomical elements mentioned above have the task of ensuring: (a) first of all, joining together all the components

**Fig. 2** Human spine



**Fig. 3** Spinal anatomy



of the spine and forming a structure that is as tough as one organ; (b) secondly, they must ensure the possibility of maintaining the vertical position against gravitational force; (c) Thirdly, all the components of the column must allow it to perform space mobilizations in all directions of motion, at all its functional segments and to withstand very high dynamic loads and in many different positions. The spine must fulfill all these tasks, must support and allow the mobilization in all directions of the head, provide support for the scapular belt and the insertion of the viscera from the chest and abdominal cavity. The static spinal column is conditional of an intrinsic equilibrium and an extrinsic equilibrium. In general, the mobility of the spine is

difficult to assess as pure movement, as usually the movements of the spine are combined, more in the cervical region and less in the lumbar spine. It is sufficient for the multitude of the joints involved in the movement to produce a break in the symmetry of the dynamics of the studied vertebral segment so as to cause an alteration of the plan of motion and associated movements to occur: lateral inflexion associated with a slight rotation movement, a flexion is associated with a moderate lateral inflexion, etc.

## 2 Algorithm for 3D Reconstruction of the Human Spine

In order to obtain the intended result, respectively a 3D model of the reconstructed spine, a multistage work algorithm has been established, shown below (Fig. 4).

Step 1 The posture is calculated using the portable equipment based on the angles measured by the IMU sensors and the mathematical models (based on Bezier curves [1] or circular arcs [15]) (Fig. 4, ①). This curve represents a mold of the human body located on the patient’s skin surface. The medical doctor is interested in a model of the spine, he needs to visualize the arrangement of the vertebrae in the 3D space to identify the possible diseases.

Step 2 An existing 3D model of the spine, based on measured anthropometric parameters or images obtained using medical imaging methods, is scaled. Each vertebra is analyzed, measuring two features:  $d_i$  and  $h_i$ , based on which a graphic

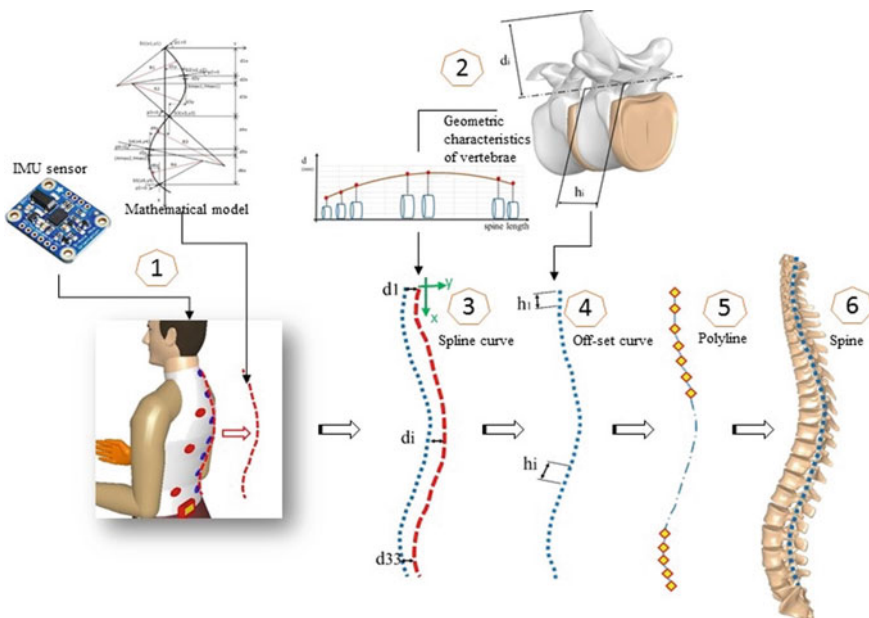
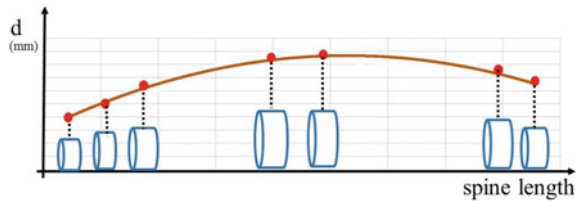


Fig. 4 Algorithm for 3D reconstruction of the spine

**Fig. 5** The measured off-set values ( $d_i$ )



will be drawn (Fig. 4, ②). The physician has a standard 3D digital model of the spine and a software application able to scale this model, depending on the patient's characteristics (age, sex, anthropometric dimensions). The 3D model obtained after scaling can be analyzed with engineering software applications (CATIA, Solid-Works, ProE). Thus, the distances from the center of the vertebral bore of each vertebra to the extremity of the thoracic apophysis ( $d_i$ ) and the width of a vertebra, including the thickness of the intervertebral disc ( $h_i$ ), are measured. With these measured data, a graph is made, as shown in Fig. 5.

**Step 3** An offset curve of the posture obtained by calculation is made using the distances from the graph at the previous point (Fig. 4, ③). The blue curve is obtained by joining the points obtained by summing the coordinates of the corresponding points on the red curve with the corresponding measured values of  $d_i$ .

**Step 4** The curve thus obtained, in which we know the coordinates of all points, will be divided into arcs having the lengths equal to the  $h_i$  values determined in Step 2 (Fig. 4, ④).

**Step 5** Thus, a polyline formed by segments with known coordinates of the end-points will be obtained. Corresponding to these segments, the 3D models of all vertebrae will be oriented and positioned (Fig. 4, ⑤).

**Step 6** The 3D model of the spine can be viewed in various positions using MATLAB applications (Fig. 4, ⑥).

For a correct representation of a human spine it should be taken into consideration limitations that come from human anatomy and from the biomechanics of the human body [6]. Scientific studies show that the angles of orientation of L1 vertebrae compared to those of the T12 vertebra may have relatively high values. The values presented in Table 1 correspond to the six studies [5, 7–10, 14]. These maximum admissible values are the basis of the developed cinematic model.

### 3 The Developed Kinematic Model Using SimMechanics

Kinematics is the study of the movement of rigid bodies without considering the forces that act upon them and their masses. The objective of the kinematic analysis is to determine the trajectories of the various points of interest of the kinematic elements (positions, speeds and linear and angular accelerations).

**Table 1** The angles of orientation of L1 compared with T12 vertebra [5, 7–10, 14]

	Van Verp, 2000	Pearcy, 1985	Pearcy, 1989	Hindle, 1999	Peach, 1998	Russel, 1993
Flexion	56,4	51	75,6	74,6	71,6	75,1
Extension	22,5	16	23	26,8	–	25,8
Bend to the left	25,8	18	27,9	29	29,7	28
Bend to the right	26,2	17	28,5	29	30,8	28
Rotate to the left	14,4	5	16	15	16,6	16,4
Rotate to the right	12,8	4	15,4	15	15,6	16,4

The program chosen to develop the kinematic model of the column is SimMechanics [12, 16]. SimMechanics is part of the Matlab program and is dedicated to multibody simulations. The kinematic model of the spine contains the following elements: (i) a global reference system in which the positions of all vertebrates will be analyzed; (ii) vertebrae, using 3D model geometry and a local reference system attached to each; (iii) because vertebrae are not connected by kinematic joints, comparative positions of the adjacent vertebrae will be introduced to analyze the relative positions of the vertebrae.

The vertebra is modeled as a non-deformable element in the kinematic model. The SimMechanics model of the vertebra is shown in Fig. 6 and comprises the following elements: (1) link to the global reference system; (2) translational transformation: coordinates of the local reference system (in the global reference system) of the vertebra; (3) rotation transformation: rotation of the local reference system into the global vertebrae system; (4) the coordinates of the vertebra in the global system; (5) translational transformation: to identify the relative position of the neighboring vertebra; (6) the link with the comparator element; (7) information on the vertebra geometry.

If the vertebra position is compared to two neighboring vertebrae, then the vertebral model has two exits (2 and 3 of Fig. 7). The vertebrae are positioned in the global reference system by the parameters read from a file in which the vertebrae coordinates are calculated and stored. Also in this file, the vertex orientation angles are calculated according to the maximum admissible values in Table 1.

The complete kinematic model of the human spine is shown in Fig. 8. This model comprises vertebrae L1 ... L5 and T1 ... T10. The components are: (1) the global reference system; (2) the model of a vertebra (as shown in Figs. 6 and 7); (3) comparison blocks for adjacent surfaces.

Comparison blocks (Fig. 9) consist of: (1) a comparison element of the relative positions of the two adjacent surfaces; (2) a block of transformation from geometric data (lengths, angles) into numerical data; (3) measured data display blocks.

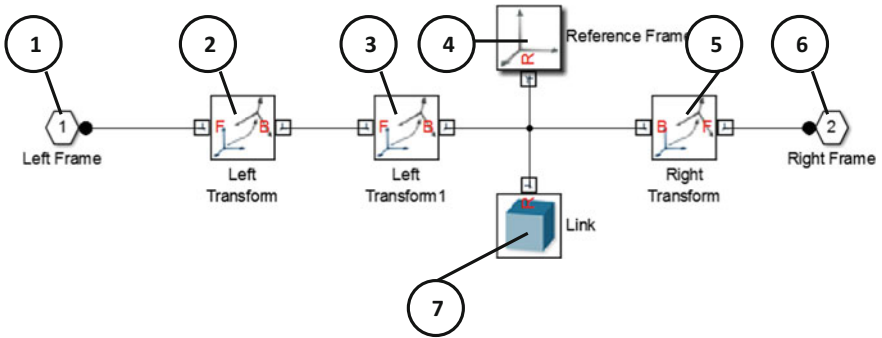


Fig. 6 The SimMechanics model of the vertebra

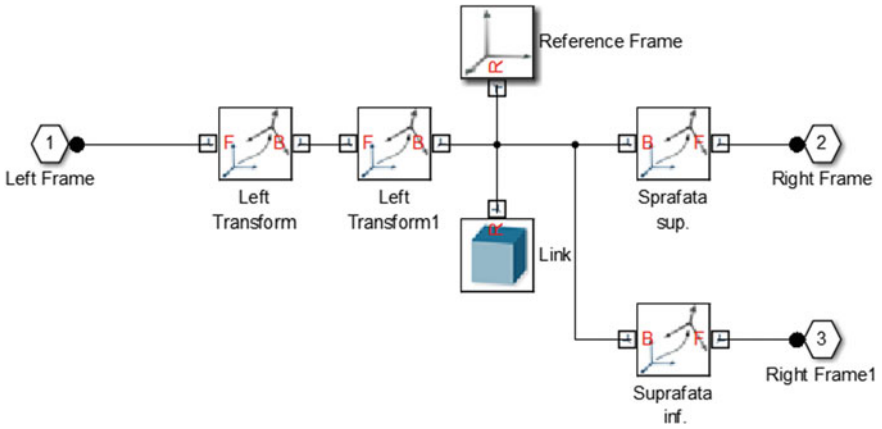


Fig. 7 A vertebra position compared to neighboring vertebrae

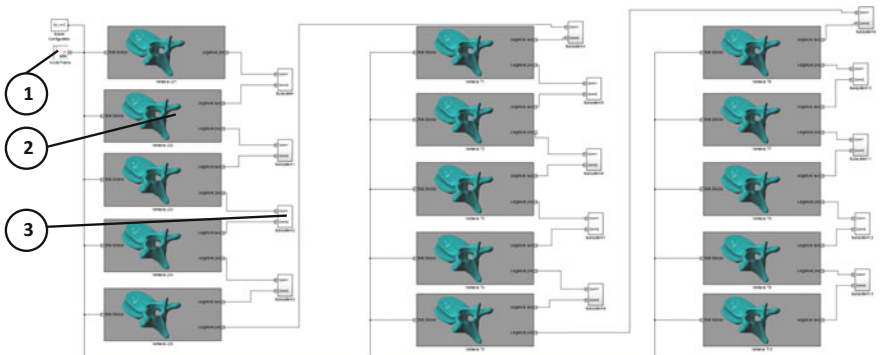


Fig. 8 Kinematic model of the human spine

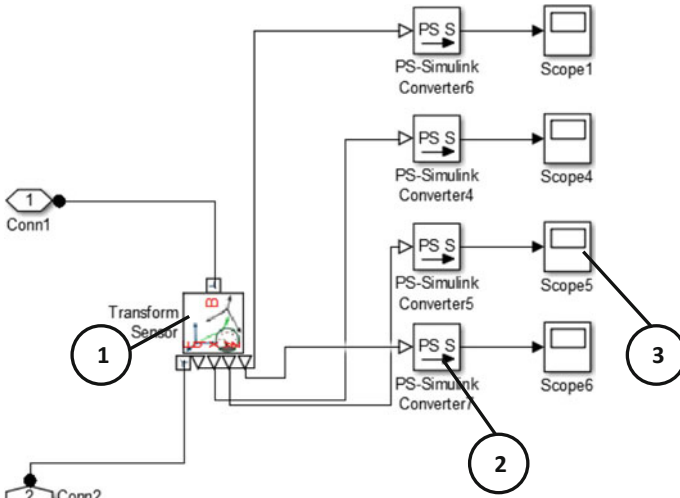


Fig. 9 Comparison blocks

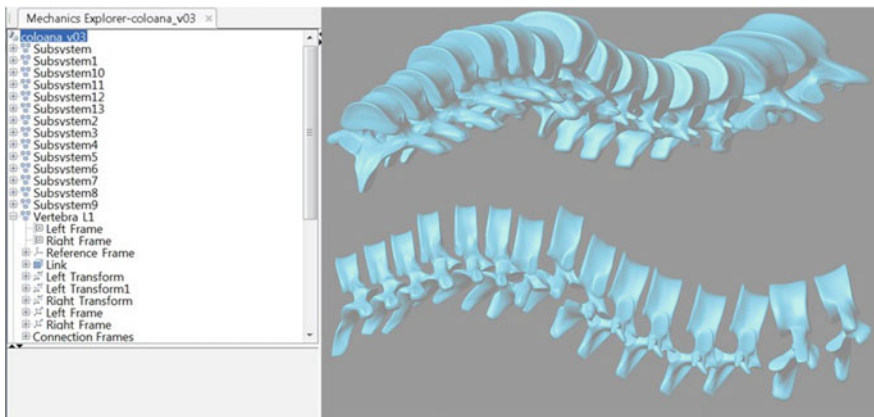


Fig. 10 Final 3D model of spine

Following the kinematic model of the human spine, the results presented in Fig. 10 were obtained.

This 3D model can be viewed from any position at any scale with various mechanical engineering programs. Body positioning deficiencies can be immediately observed by the physician.



## 4 Conclusions

This paper presents a methodology for visualizing the vertebrae of a human spine without medical imaging investigations. The working principle consists in identifying human body posture using special equipment based on IMU sensors, then generating a spline curve over which 3D vertebral models are positioned using the SimMechanics software application. Connections between the vertebrae are made on the basis of the kinematic couplings described above, having implemented operating limits obtained from the specialized literature. Each vertebra has attached a local coordinate system with the center on the axis of the vertebral bore, at the upper extremity. The positioning of the vertebra on the polyline obtained involves rotation and displacement transformations. This method of body posture analysis can be used in off-line mode, having as input data the recordings obtained by the portable equipment over a period of time (minutes, hours). On the other hand, the portable equipment can also be used for real-time tracking, using a smartphone, provided that the mathematical models and algorithms used are simplified in order to reduce processing time.

**Acknowledgements** This paper was realized within the Partnership Programme in priority domains—PN-II, which runs with the financial support of MEN-UEFISCDI, Project no. 227/2014, System for Diagnosis and Therapy of Spine Diseases.

## References

1. Antonya C, Butnariu S, Pozna C (2016) Real-time representation of the human spine with absolute orientation sensors. In: The 14th international conference on control, automation, robotics and vision (ICARCV 2016), Phuket, Thailand
2. Baumgartner D, Zemp R, List R, Stoop M, Naxera J, Elsig JP, Lorenzetti S (2012) The spinal curvature of three different sitting positions analysed in an open MRI scanner. *Sci World J*. <https://doi.org/10.1100/2012/184016>
3. Dugailly P-M, Beyer B, Sobczak S, Salvia P, Feipel V (2014) Global and regional kinematics of the cervical spine during upper cervical spine manipulation: a reliability analysis of 3D motion data. *Man Ther* 19:472–477
4. Gombatto S, Brock T, DeLork A, Jones G, Madden E, Rinere C (2015) Lumbar spine kinematics during walking in people with and people without low back pain. *Gait Posture* 42:539–544
5. Hindle RJ, Pearcy MJ, Cross AT, Miller DHT (1990) Three-dimensional kinematics of the human back. *Clin Biomech* 5:218–228
6. Monheit G, Badler N (1990) A kinematic model of the human spine and torso. Technical Reports (CIS), Paper 746
7. Peach JP, Surtane C, McGill S (1998) Three-dimensional kinematics and trunk muscle myoelectric activity in the young lumbar spine: a database. *Arch Phys Med Rehabil* 79:663–669
8. Pearcy MJ, Hindle RJ (1989) New method for the non-invasive three-dimensional measurement of human back movement. *Clin Biomech* 4:73–79
9. Pearcy MJ, Portek I, Shepherd J (1985) The effect of low back pain on lumbar spinal movements measured by three-dimensional analysis. *Spine* 10:150–153

10. Russell P, Percy MJ, Unsworth A (1993) Measurement of the range and coupled movements observed in the lumbar spine. *Br J Rheumatol* 32:490–497
11. Salem W, Klein P (2013) In vivo 3D kinematics of the cervical spine segments during pre-manipulative positioning at the C4/C5 level. *Man Ther* 18:321–326
12. Schlotter M (2003) Multibody system simulation with SimMechanics. University of Canterbury
13. SPINE Project (2017) Sistem de diagnosticare și terapie a afecțiunilor coloanei vertebrale. <http://spine.unitbv.ro/index.php>. Accessed Apr 2017
14. Van Herp G, Rowe P, Salter P, Paul JP (2000) Three-dimensional lumbar spinal kinematics: a study of range of movement in 100 healthy subjects aged 20 to 60+ years. *Rheumatology* 39:1337–1340
15. Voinea G-D, Butnariu S, Mogan G (2016) Measuring and geometric modelling of human spine posture for medical rehabilitation purposes using a wearable monitoring system based on inertial sensors. *Sensors* 16(12) (Special Issue—Body Worn Behavior Sensing)
16. Wood GD, Kennedy DC (2003) Simulating mechanical systems in simulink with SimMechanics. The Mathworks Report

# Neurorobotic Investigation into the Control of Artificial Eye Movements



A. Mussina, M. Ceccarelli and G. Balbayev

**Abstract** In this paper, a neurorobotic robot ‘eye’ for investigating the neural control of eye movements is developed and the performance of a computational model of image stabilization based on the adaptive filter model of the cerebellum is evaluated. For in-depth analysis, the cerebellum microcircuit is investigated and bioinspired control algorithm is developed. Inverse oculomotor plant model is simulated on Matlab/Simulink; first using simple Vestibulo-Ocular Reflex model; then using a second order model with Model Reference Adaptive Control. In addition, the robot ‘eye’ is built as a camera mount gimbal system and its architecture is calibrated.

**Keywords** Neurorobotic • Robot ‘eye’ • Vestibulo-Ocular reflex model  
Adaptive filter model • Bioinspired control algorithm • Cerebellum

## 1 Introduction

Recent developments in the experimental understanding of cerebellar microcircuit are based on Marr and Albus models. Dean and Porrill introduced a concept of recurrent decorrelation control, in which Marr-Albus model can learn without

---

A. Mussina · G. Balbayev (✉)

Almaty University of Power Engineering and Telecommunications, Almaty, Kazakhstan  
e-mail: gani\_b@mail.ru

A. Mussina  
e-mail: kz.a.mussina@gmail.com

M. Ceccarelli  
University of Cassino and South Latium, Cassino, Italy  
e-mail: ceccarelli@unicas.it

A. Mussina · M. Ceccarelli  
International Joint Research Laboratory of Service Robotics, Cassino, Italy

A. Mussina · G. Balbayev  
International Joint Research Laboratory of Service Robotics, Almaty, Kazakhstan

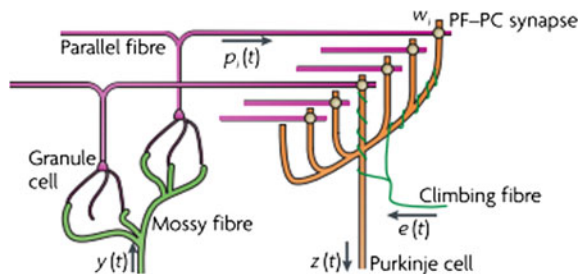
requiring motor error [8]. Dean et al. validate models by Marr and Albus and using recent knowledge and evidences from anatomy, they state that the function of the cerebellum is assumed to be related to motor commands [4].

Test cases of implementation and evaluation of bioinspired adaptive control algorithm in the control of a robot eye show promising performance. For instance actuation by pneumatic artificial muscles as a model of cerebellar function, which is analogue to the VOR, is analysed in [7]. It is important that these excellent results be extended to neurorobotics. To this end, it is necessary to further investigate the neurobotic adaptive control in order to validate and extend current research findings [1, 5, 10, 12].

### 1.1 Cerebellar Control Structure

Ito (1984) suggests that role of the cerebellum and how it works in the adaptation process of vestibulo-ocular reflex could be examined from control theory point of view. It can be seen, according to Figs. 1 and 2, which illustrate how simplified cerebellar microcircuit can be mapped as an adaptive filter structure. For illustrative purposes each component of microcircuit is specified by color. On Fig. 1 the (MF) filter inputs are analyzed into (PF) component signals, which are then weighted (PF-PC synapses) and recombined to form the filter. The main reason why the filter is adaptive is that its weights could be adjusted by techniques as teaching or error signal using covariance learning rule [11]. “Input signal in this microcircuit is MF(r), which synapse on granule cells. The axons of granule cells (GC) form parallel fibres (PFs) that synapse on Purkinje cells (PCs), which are the output cell from cerebellum and cause of simple spikes. In models of Marr-Albus type correlated firing of a PF and the single climbing fibre (CF) that wind around the PC alters the strength of the PF-PC synapse” [9]. The diagram on Fig. 2 could be identified as analysis-synthesis adaptive filter architecture. Processing of MF

**Fig. 1** Adapted from [4]. Simplified diagram of cerebellar cortical microcircuit



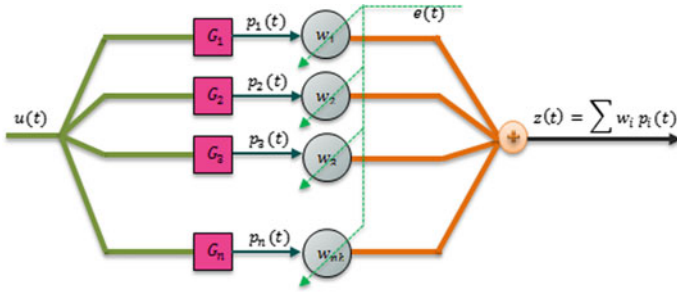


Fig. 2 Adaptive filter structure

input signal  $u(t)$  by the granule cell layer is interpreted as analyses by bank of fixed filters  $G_i(t)$ , that means the PFs carry signals

$$p_i(t) = G_i \cdot u(t) \tag{1}$$

The weighted sum of PF inputs is an output of PC

$$z(t) = \sum w_i \cdot p_i(t), \tag{2}$$

so PC implements a linear filter

$$C = \sum w_i \cdot G_i. \tag{3}$$

The CF input adapts synaptic weights by learning rule and interpreted as a training signal  $e(t)$ , which is error signal. Weights are adjusted by this learning rule

$$\delta w_i = -\beta(ep_i(t)), \tag{4}$$

where  $\beta$  is a small positive learning rate. The learning rule is called the covariance learning rule [11] or the least mean square rule, because when  $e(t)$  is the error in the output  $u(t)$ , it can be shown to minimize the mean square performance error, or the decorrelation learning rule because learning stops when errors  $e(t)$  are uncorrelated with all filter inputs  $p_i$  [4].

Due to Figs and explanation above, it can be stated that similarities are obvious. Basically, adaptive filter is especially suited to carry out two functions, which are associated with the cerebellum:

- prediction of the sensory effects of organism’s own movement;
- accurate movement control.

## 2 Experimental Layout

To find an optimal VOR control solution it should be clear that the retinal slip would be produced by movements of the head, as it happens in locomotion. The VOR operates to counter-rotate the eyes to prevent retinal slip for maintaining the stable gaze. Therefore the VOR control scheme uses measurement of the head velocity to control the eye velocity.

$$x(t) = P(t)u(t) \tag{5}$$

where,

$$u(t) = \frac{B(t)}{1 - B(t)C(t)} \tag{6}$$

where the cerebellar filter  $C(t)$  is the time-varying component.

$$P(t)^{-1} = \frac{B(t)}{1 - B(t)C(t)^*}, \tag{7}$$

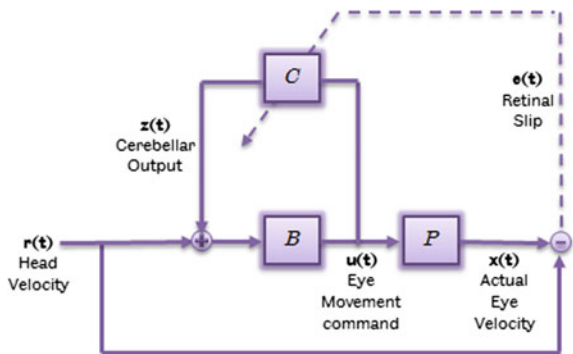
According to Eq. (7) the optimal cerebellar filter is:

$$C(t)^* = B(t) - P(t)^{-1}. \tag{8}$$

The convergence of a recursive learning algorithm to the optimal cerebellar filter  $C(t)^*$  is discussed by Porrill et.al. (2004), where stability is proved using the Lyapunov’s direct method. Characteristics of model of basic VOR system (Fig. 3), was chosen according to [6] as follows.

P—the first order dynamic model of oculomotor plant, with transfer function  $P(s)$  between eye-in-head velocity  $x(t)$  and motor command  $u(t)$  as a Laplace transform in Eq. 9.

**Fig. 3** The basic VOR system



$$P(s) = \frac{ks}{s + 1/T_p}, \quad (9)$$

where  $T_p = 0.2$  s is time constant,  $k = 1$  is a gain.

B—brainstem, which is modelled as a first-order leaky integrator (more extended in A1) plus a pure dc gain. Transfer function of brainstem model  $B(s)$  is presented as Laplace transform in Eq. 10. The output is a motor command  $u(t)$ ; input is a conjunction of the vestibular system  $r(t)$  and the cerebellar output  $z(t)$ .

$$B(s) = G_d + \frac{G_i}{s + 1/T_i}, \quad (10)$$

where  $G_d = 1$  is the direct path gain and  $G_i = 1/T_p = 5$  is the indirect path gain and  $T_i = 0.5$  s is a time constant.

Further simulations were executed with different versions of the parameters  $T_p, G_d, G_i, T_i$ . It has to be noted, that the exact values are not important at this stage, but time constants should be in the 100 ms range.

Brainstem provides a control, which the cerebellum improves by adjusting the response via the filter weights. The perfect compensation of plant could be achieved by brainstem itself, when  $T_i = \infty, G_d = 1, G_i = 1/T_p$ .

The cerebellum is implemented as an adaptive FIR (finite impulse response) filter  $C$ , with output  $z(t)$ , which is given in Eq. 11.

$$z(t) = \sum_{i=0}^L w_i p(t - i \cdot \Delta T), \quad (11)$$

where input  $u(t)$  to the adaptive filter  $C$ , which was split into number of  $L$  components  $p_1(t), \dots, p_n(t)$ , with delays between them of  $\Delta T$ .  $\Delta T = 0.02$  s (2 s in total).  $w_i$ —weight of the component  $p_i$ .

For reducing the perceived visual slip from the input, the weights of adaptive filter have to be changed. As it was mentioned before the weights are analogue to the parallel fibre Purkinje cell synapses of the cerebellar cortex. The inverse oculomotor plant is realized when the learning algorithm is successfully applied and adjustment of the weights is done in combination with the brainstem. As it could be seen in Fig. 3 the sensory error  $e(t)$  is a direct result of the performance of the adaptive filter  $C$ .

$$e(t) = (P - B^{-1} + C) \cdot x(t) \quad (12)$$

As it can be seen in Eq. 12 error is reduced to zero when  $C = B^{-1} - P$ .

Efficiently, this learning topology subsequently does not need a translation of the sensory error into a motor-command error. For that reason, the observed visual slip

is expected to build the suitable teaching signal for the adaptation of the filter. Rule to adjust the weights is shown in Eq. 13.

$$\delta w_j = -\beta \langle p_j(t) \cdot \hat{u}(t) \rangle, \tag{13}$$

where

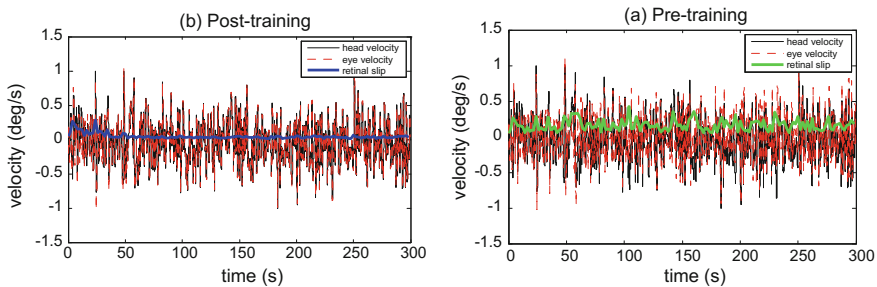
- $\delta w_j$  is the change in the  $j$ th weight  $w_j$
- $\beta$  a learning rate constant. The value of that is adjusted to give rapid learning without instability.
- $\hat{u}(t)$  the value of retinal slip at time  $t$
- $p_j(t)$  the value of the  $j$ th filter signal at time  $t$
- $\langle \rangle$  denotes the expected value of the enclosed quantity over the time period used for training.

The features of learning rule is that it is identical to the LMS rule of adaptive control theory, also learning stops when CF and PF inputs are uncorrelated, which is a property of decoration control.

Model architecture of the system was programmed by using Matlab and Simulink. Program was developed by using scripts from [2]. Experiments below were done for simple, first order plant, to prove the usefulness of the algorithm.

Performance of the system to band limited white noise input, i.e. head velocity, gave rise to retinal slip with low frequency, which is expected because of the existing brainstem controller (Fig. 4a). According to these graphs it can be stated that it is unable to maintain eccentric gaze. The time course of the plant and the brainstem is directly effected on how fast eye position returns to initial value.

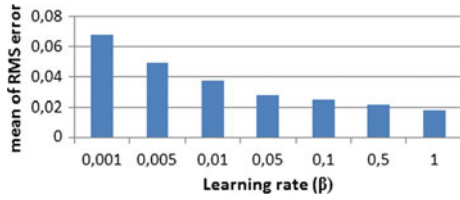
The performance of the model during and after training, with the first order plant  $P$  and brainstem controller  $B$  illustrated below. The characteristics of  $P$  and  $B$  are the same as in the previous experiment. Input for that system is a head-velocity signal modelled as a band limited white noise as before. Learning starts at 30 s. For testing how the value of learning rate effects on performance, each time the same set of signals are used as input  $r$ . The effect of training is shown in Fig. 4b.



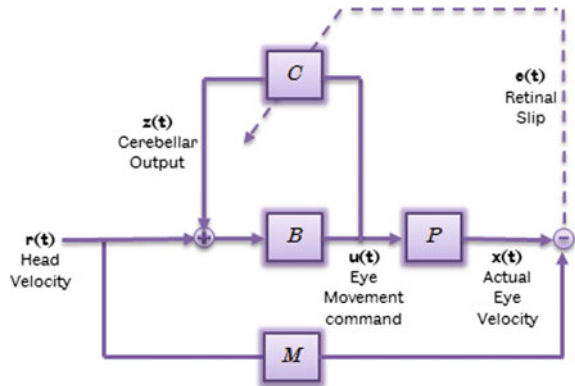
**Fig. 4** Displacement tracking and retinal slip **a** for pre-training, **b** for post-training



**Fig. 5** Mean of RMS error against learning rate



**Fig. 6** Block-scheme for system with model reference



The graph on Fig. 5 was plotted to analyze how the learning rate ( $\beta$ ) affects to error. Actually, if the learning rate is changed, simulation time also has to be changed. Reason for this is that system needs appropriate time to apply that learning. For instance, if the learning rate is small it takes time and applying to the system is slow.

For next experiments plant with equal numbers of poles and zeroes were used. However, to provide a more generally applicable solution the algorithm has to be augmented to extend a range of specific control tasks and to be suitable for a range of plants with any order. To solve that the concept of model reference adaptive control (MRAC) is used (Fig. 6). The role of MRAC is to identify a feedback control law that changes the dynamics of the plant and reference model describes the desired input/output properties of the closed-loop plant [13].

The reference model  $M$  determines the behaviour of the controlled model. Figure 7 illustrated how  $\tau$  effects on the response of the reference model. The original signal is 0–0.1 Hz band limited white noise in the range from 0.2 to 0.4. If  $\tau$  is small and frequency is high response starts to roll off.

Bode plots for a first order (Fig. 8a) and second order (Fig. 8b) reference model for a range of time constants. According to those plots it can be seen that with the greater order of model rolls-off faster and phase shift is larger. The original signal has not changed a lot by the reference model if a value of  $1/\tau$  is larger than the maximum frequency in the signal [13].

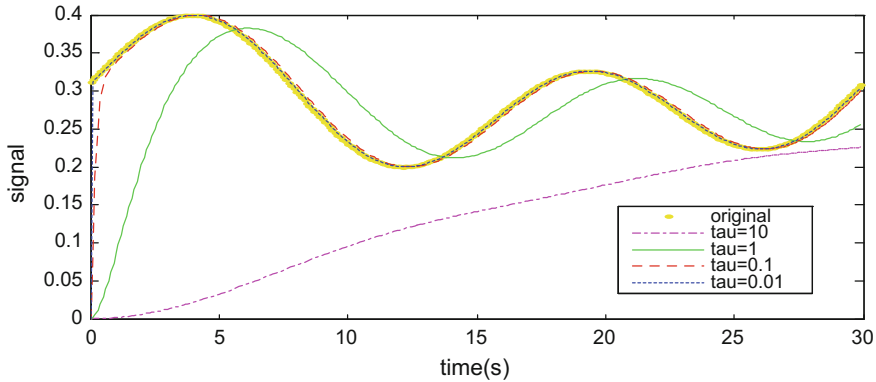


Fig. 7 Time domain plot for second order reference model M with different  $\tau$

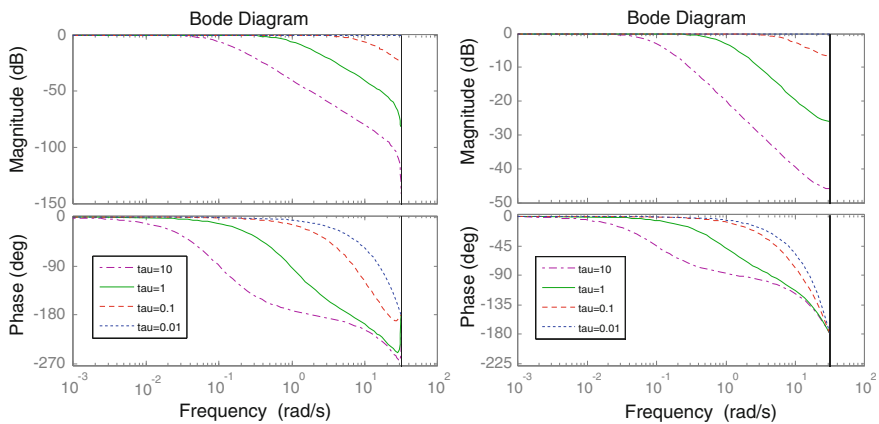


Fig. 8 Bode plot for a first and b second order M

The experiment is done with second order plant; therefore the simulated plant has two poles and no zeroes.

$$P(S) = \frac{kp}{(s + 1/T_1)(s + 1/T_2)}, \tag{14}$$

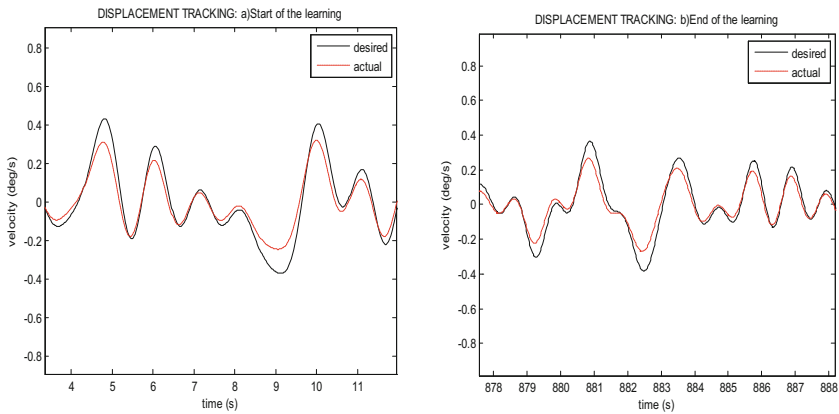
The corresponding fixed brainstem controller  $B$  (15) was chosen to be an approximate feedforward controller for the plant  $P$  (14). It is approximately equivalent to  $MP^{-1}$ , however plant time constants are slightly degraded and  $g$  represents how there are changes

$$B(s) = \frac{(s + 1/T_1 \cdot g)(s + 1/T_2 \cdot g)}{kp \cdot g \cdot (\tau s + 1)^2}, \tag{15}$$

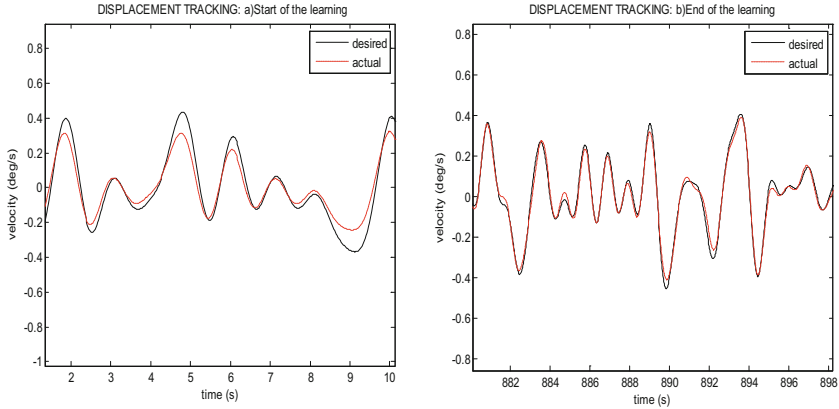
The reference model has to specify realistic response of the controlled plant; it is represented in the following equation with time constant  $\tau = 0.1$  s

$$M(s) = \frac{1}{(\tau s + 1)^2} \tag{16}$$

Left side of Figs. 9 and 10 shows tracked response at the start of learning, right side—tracked response at the end of learning. In Fig. 9 can be seen that plant cannot be achieved, because the actual response lags the desired responses an instantaneous response of the controller, while on Fig. 10, which represents the performance with reference model, it can be seen that at the end of the learning error decreased and plant achieved.



**Fig. 9** Start and end of the learning when no reference model was used



**Fig. 10** Start and end of the learning when reference model was used

The performance of the controller is critically depends on the learning rate. If the value of the learning rate is small, the adaptation will be slow, because of large tracking errors and large transients. Whereas the extremely large value of the learning rate can be a cause of highly oscillatory parameter estimations that would negatively excite the high frequency unmodelled plant dynamics [3]. Also those results are consistent with the results obtained in [12].

### 3 Conclusion

The control challenges arise because of developing of autonomous robots and their operations. An algorithm which is capable of adapting to such dynamic environments is required. This study of cerebellar inspired adaptive control, which is augmented by reference model, provides a potential general solution for robotic control. Control of oculomotor plant is significantly improved by bioinspired adaptive filter control. The performance of the adaptive filter control is dependent on the learning rate; thus it is vital that for any design, an optimal choice of learning rate be sought.

The main goal of this project was developing a neurobotic robot ‘eye’ for investigating the neural control of eye movements and evaluating the performance of a computational model of image stabilization based on the adaptive filter model of the cerebellum. Control algorithm was developed by investigating the cerebellum microcircuit and inverse plant modeling.

## References

1. Anderson SR (2010) Adaptive cancelation of self-generated sensory signals in a whisking robot. *IEEE Trans Robot* 26(6):1065–1076
2. Anderson SR, Wilson E (2011) SimulinkAdaptiveFilterCode\_TDLs. [Simulink block and Matlab scripts]
3. Bishop R (2008) *Mechatronic system control, logic, and data acquisition*. Taylor & Francis Group
4. Dean P (2010) The cerebellar microcircuit as an adaptive filter: experimental and computational evidence. *Nat Rev Neurosci* 11(1):30–43
5. Dean P (2013) An adaptive filter model of cerebellar zone C3 as a basis for safe limb control? *J Physiol* 591(Pt 22):5459–5474
6. Dean P, Porrill J, Stone JV (2002) Decorrelation control by the cerebellum achieves oculomotor plant compensation in simulated vestibulo-ocular reflex. *Proc Biol Sci/R Soc* 269 (1503):1895–1904
7. Lenz A (2009) Cerebellar-inspired adaptive control of a robot eye actuated by pneumatic artificial muscles. *IEEE Trans Syst Man Cybern. Part B. (Cybernetics : a publication of the IEEE Syst Man Cybern Soc)* 39(6):1420–1433
8. Porrill J, Dean P, Stone JV (2004) Recurrent cerebellar architecture solves the motor-error problem. *Proc Biol Sci/R Soc* 271(1541):789–796
9. Porrill J, Dean P (2007) Cerebellar motor learning: when is cortical plasticity not enough? *PLoS Comput Biol* 3(10):1935–1950
10. Shibata T, Schaal S (2001) Biomimetic gaze stabilization based on feedback-error-learning with nonparametric regression networks. *Neural Netw (the official journal of the Int Neural Netw Soc)* 14(2):201–216
11. Sejnowski TJ (1977) Storing covariance with nonlinearly interacting neurons. *Math Biol* 4:303–321
12. Wilson ED (2013) Developing the cerebellar chip as a general control module for autonomous systems, pp 1–12
13. Widrow B, Samuel S (1985) *Adaptive signal processing*. Prentice-Hall, New Jersey

# New Concepts of Ankle Rehabilitation Devices—Part I: Theoretical Aspects



C. M. Racu (Cazacu) and I. Doroftei

**Abstract** The ankle structure holds one of the most important role in the human biomechanics. Due to complexity of everyday activities this joint is the most prone to be injured part of the lower limb. For a complete recovery of the locomotor function, recovery exercises are mandatory. The existent ankle rehabilitation equipments allow only simple rehabilitation exercises, which cannot be used safely without the aid of a therapist. The introduction of robotic physical recovery systems represents a modern alternative to traditional recovery. Actuated devices are advantageous because they allow many types of exercises on same device, and also they accurate measure forces and angular motions. The purpose of this two part paper is to propose two rehabilitation devices, based on different actuating mechanisms. In this first part, structural synthesis, some kinematic and designing aspects of two new ankle rehabilitation devices are presented. The systems are based on the spatial four-bar and Scotch Yoke mechanism, respectively. As requirements for the proposed devices the following aspects have been considered: the systems must be easy to program, financially affordable and they need to offer the two movements (dorsiflexion/plantar flexion and inversion-eversion) required for a complete recovery of the injured ankle.

**Keywords** Robot · Ankle rehabilitation device · Scotch Yoke mechanism  
Spatial four-bar mechanism

---

C. M. Racu (Cazacu) · I. Doroftei (✉)  
“Gheorghe Asachi” Technical University of Iasi, Iași, Romania  
e-mail: idorofte@mail.tuiasi.ro

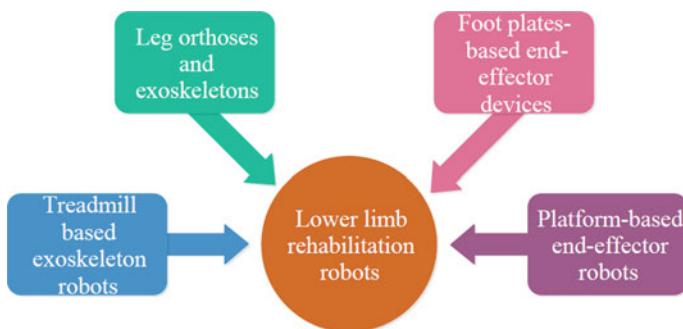
C. M. Racu (Cazacu)  
e-mail: cristina.racu@tuiasi.ro

## 1 Introduction

During the last decades, robotic research focused on assistive technologies for rehabilitation branch, aiming to improve the rehabilitation process, from currently used primitive mechanisms to superior technologies. This trend is a result of statistically growing number of aging population, which requires assistance after injuries [1]. The ankle structure has a defining role in everyday life of an individual, providing locomotion, balance and stability. This leads to multiple types of injuries: fracture, strain or sprain, with a high incidence of the last one [2]. In the first stage of ankle recovery the bleeding and swelling is treated with rest, ice, compression bandage (or prostheses) and anti-inflammatory drugs. Although the first stage reduces the discomfort felt by the patient, rehabilitation exercises are required. Injured ankle ligaments will form scar tissue while healing, thus people will experience activity limitation without proper and sufficient rehabilitation [3].

Traditional rehabilitation therapies use simple devices like elastic bands, wooden wobble board and foam rolls. It also requires the assistance of a therapist. As a result the exercises are low-term, repetitive and require patients and therapists' effort. Another disadvantage is that the evolution of the patient is not accessible. To counteract these drawbacks robot-assisted ankle rehabilitation devices have been developed [4–7]. We can divide these devices in the following generic categories: exoskeleton, orthotics and end-effectors robots. A classification of lower limb rehabilitation robots is presented in Fig. 1.

To achieve a fully recovered ankle joint one must consider ankle movements and range of motion: plantar flexion (extension), dorsiflexion (flexion), eversion and inversion. Motion amplitudes range from  $0^\circ$  to  $25^\circ$  for flexion and eversion, and  $0^\circ$  to  $50^\circ$  for extension and inversion (for a healthy subject) [8–10].



**Fig. 1** Classification of lower limb rehabilitation robots

## 2 First Concept of Rehabilitation Device

In designing the rehabilitation device one of the condition considered was that the device must provide two movements (dorsiflexion/plantar flexion and inversion/eversion). Hence the system should be spatial oriented, allowing rotations around two perpendicular axes. Also, some other conditions refer to low cost, low weight and easy to manufacture process of the device.

Considering all the above requirements a device based on the simple spatial four bar mechanism was proposed, presented in Fig. 2 [11, 12]. The plate 4 will support the sole, while links 1 and 1' will actuate the mechanism. For inversion/eversion movement, the actuated links 1 and 1' must rotate with same angle and the same direction, while for plantar flexion/dorsiflexion movement the links must move in opposite direction with the same angle.

A geometrical synthesis is required in order to determine the dimensions of the mechanism. For the inversion/eversion movement a simplified planar mechanism has been used (Fig. 3a). The known considered dimensions are:  $l_h$ ,  $l_v$  and  $l_4$ . They resulted from anatomical and space considerations. The angular strokes of the sole (link 4) have been imposed as:  $\theta_4$  ( $\theta_{41}$  for inversion, and  $\theta_{42}$  for eversion, respectively). The angular stroke of the driving link 1 is  $\theta_1$  (composed from  $\theta_{11}$  and  $\theta_{12}$ ).

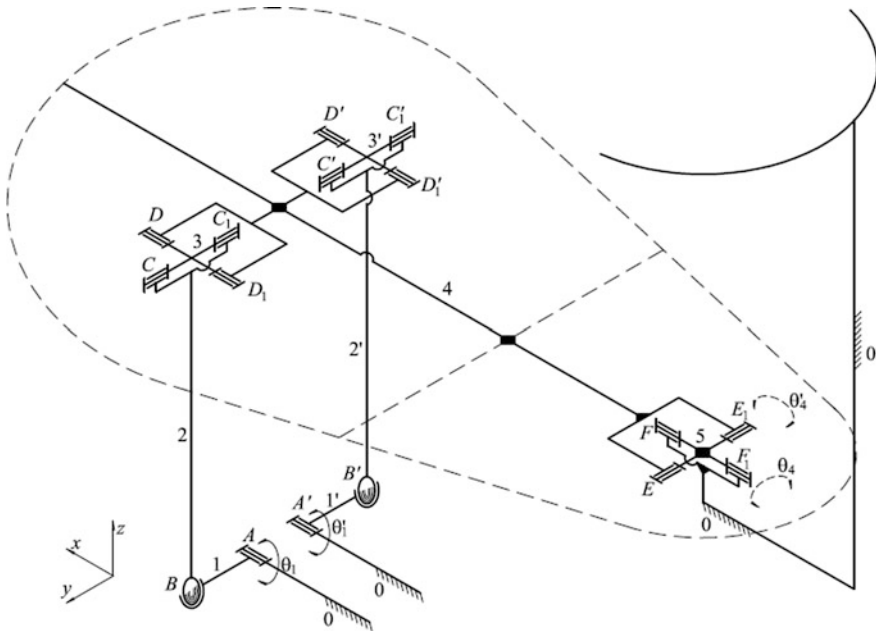
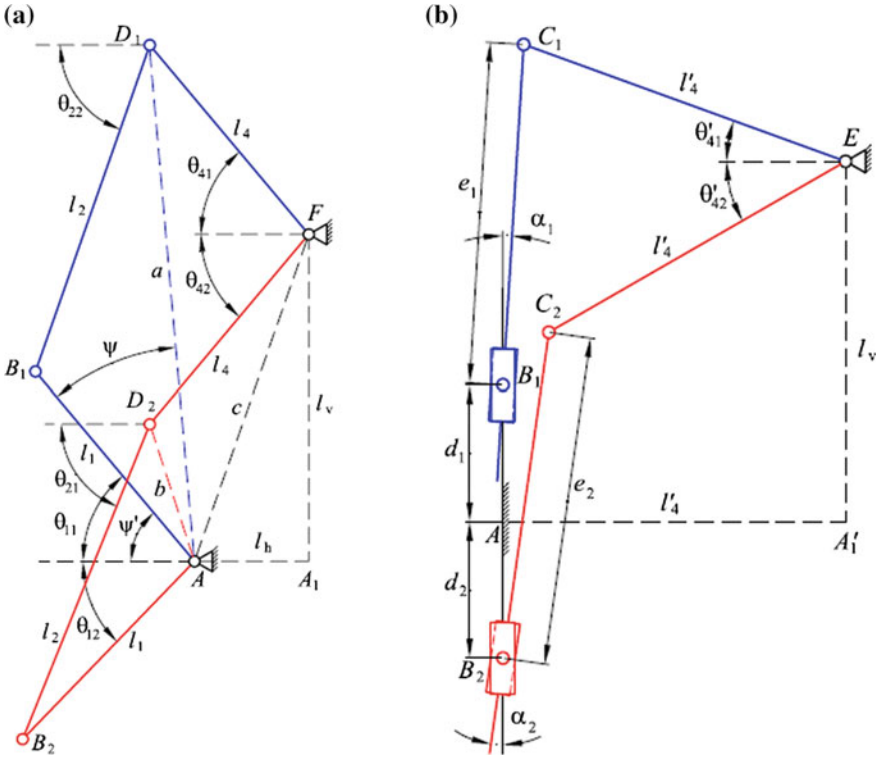


Fig. 2 Kinematics of the first concept based on the spatial four-bar mechanism





**Fig. 3** Equivalent planar mechanism for: **a** inversion/eversion movement; **b** flexion/extension movement

The unknown link lengths,  $l_1$  and  $l_2$  have been found as:

$$l_1 = \frac{a^2 - b^2}{-2b \cos(\psi' + \theta_{12}) + 2a \cos \psi}, \quad (1)$$

$$l_2 = \sqrt{l_1^2 + b^2 - 2l_1 b \cos(\psi + \theta_{12})}, \quad (2)$$

with

$$a = \sqrt{l_v^2 + l_h^2 + l_4^2 - 2(l_v^2 + l_h^2)^{1/2} l_4 \cos(\psi'' + \theta_{41} + \theta_{42})}, \quad (3)$$

$$b = \sqrt{l_v^2 + l_h^2 + l_4^2 - 2(l_v^2 + l_h^2)^{1/2} l_4 \cos \psi_1}, \quad (4)$$

$$\psi' = 90 + \arccos\left(\frac{l_v}{\sqrt{l_h^2 + l_v^2}}\right) - \arccos\left(\frac{l_h^2 + l_v^2 + b^2 - l_4^2}{2b\sqrt{l_h^2 + l_v^2}}\right), \quad (5)$$

$$\psi = 90 + \arccos\left(\frac{l_v}{\sqrt{l_h^2 + l_v^2}}\right) - \arccos\left(\frac{l_h^2 + l_v^2 + a^2 - l_4^2}{2a\sqrt{l_h^2 + l_v^2}}\right) - \theta_{11}, \quad (6)$$

$$\psi'' = 90 + \arccos\left(\frac{l_v}{\sqrt{l_h^2 + l_v^2}}\right) - \theta_{42}. \quad (7)$$

The geometrical synthesis of flexion/extension mechanism is based on the planar mechanism presented in Fig. 3b. From the geometrical synthesis of the previous mechanism some dimensions are known:  $d_1 = l_1 \sin \theta_{11}$ ,  $e_1 = l_2 \sin \theta_{21}$ ,  $d_2 = l_1 \sin \theta_{12}$ ,  $e_2 = l_2 \sin \theta_{22}$  and  $l_v$ . Also, the maximum angular strokes of the link 4 for flexion/extension movement have been considered known, as  $\theta'_{41}$  and  $\theta'_{42}$  respectively. For the two extreme positions of the mechanism, the required dimension  $l'_4$  has been found as:

$$l'_4 = \frac{(d_1 - l_v) \sin \theta'_{41} + \sqrt{(d_1 - l_v)^2 \sin^2 \theta'_{41} - 2(1 - \cos \theta'_{41}) [(d_1 - l_v)^2 - e_1^2]}}{2(1 - \cos \theta'_{41})} \quad (8)$$

or

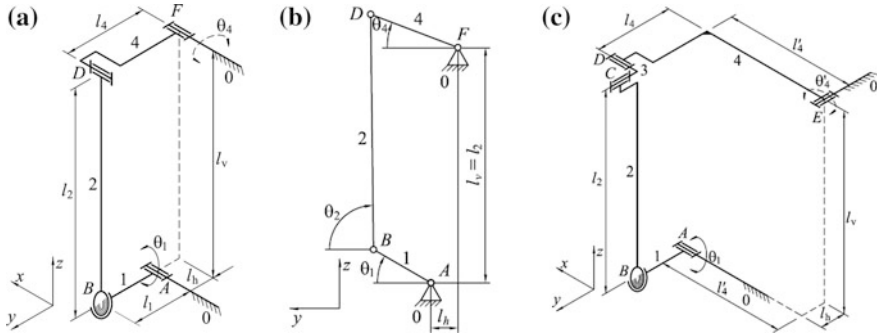
$$l'_4 = \frac{(d_2 + l_v) \sin \theta'_{42} + \sqrt{(d_2 + l_v)^2 \sin^2 \theta'_{42} - 2(1 - \cos \theta'_{42}) [(d_2 + l_v)^2 - e_2^2]}}{2(1 - \cos \theta'_{42})}. \quad (9)$$

In order to properly control the mechanism the inverse kinematics is required. Starting from the inversion/eversion movement mechanism (Fig. 4a), a simplified planar mechanism has been drawn (Fig. 4b). Based on this, the equations of the position loop closure have been written, which led to the following result:

$$\theta_1 = 2 \arctan\left(\frac{-B \pm \sqrt{A^2 + B^2 - C^2}}{C - A}\right), \quad (10)$$

where

$$\begin{cases} A = (2l_h l_1 - 2l_1 l_4 \cos \theta_4) \\ B = (-2l_2 l_1 - 2l_1 l_4 \sin \theta_4) \\ C = l_1^2 + l_4^2 + l_h^2 + 2l_4(l_2 \sin \theta_4 - l_h \cos \theta_4) \end{cases}. \quad (11)$$



**Fig. 4** Mechanism for inverse kinematics: **a** equivalent mechanism with a single motor for inversion/eversion; **b** simplified planar mechanism for inversion/eversion; **c** equivalent mechanism with a single motor for plantar flexion/dorsiflexion

As in the previous case, an equivalent mechanism is considered for plantar flexion-dorsiflexion movement (see Fig. 4c). The standard Denavit—Hartenberg convention applied to this closed-loop mechanism leads to:

$$\theta_1 = 2 \arctan \left( \frac{-B' \pm \sqrt{A'^2 + B'^2 - C'^2}}{C' - A'} \right), \tag{12}$$

where, in this case,

$$\begin{cases} A' = 2l_1(l_4 - l_h) \\ B' = -2l_1(l_2 - l'_4 \sin \theta'_4) \\ C' = l_1^2 + l_4^2 + l_h^2 + 2l_4^2 - 2l_4 \cdot (l_2 \sin \theta'_4 + l'_4 \cos \theta'_4) - 2l_h l_4 \end{cases} . \tag{13}$$

Based on mechanism synthesis and kinematic models, a simulation analysis could be performed.

### 3 Second Concept of Rehabilitation Device

Another proposed solution is based on a scotch-yoke mechanism, which converts the rotary motion into translational one, presented in Fig. 5 [13–16]. The advantages of this mechanism are: a high torque output and a smooth operation. To obtain the inversion/eversion movement the actuated links 3 and 3' are rotating with the same angle  $\theta_3 = \theta'_3$  (clockwise or counterclockwise direction), while the link 7 will achieve the desired  $\theta_7$  movement, with an angular stroke given by  $\theta'_7$  angle, around  $x$  axis.

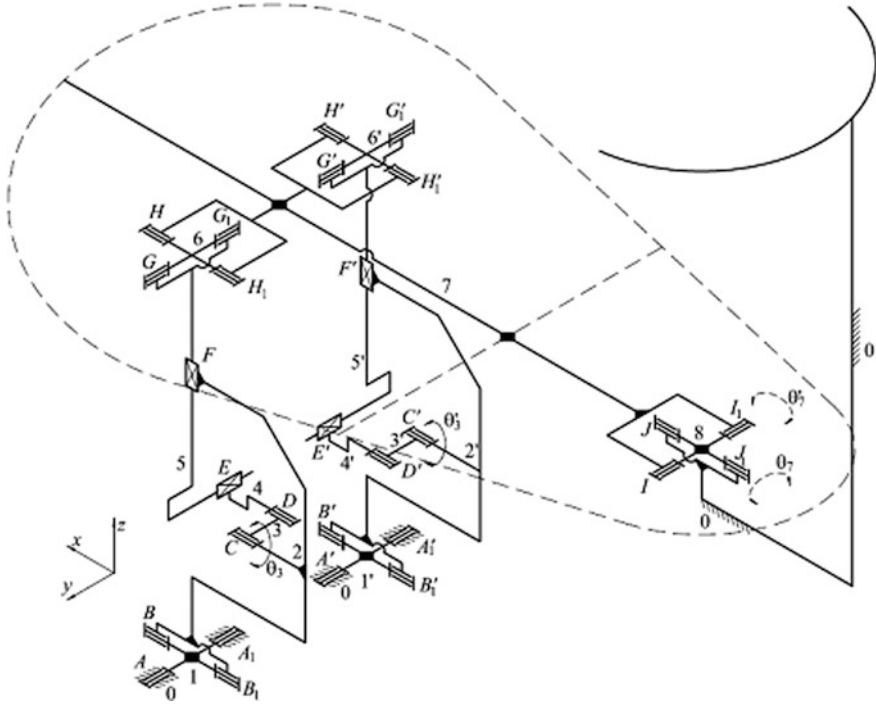


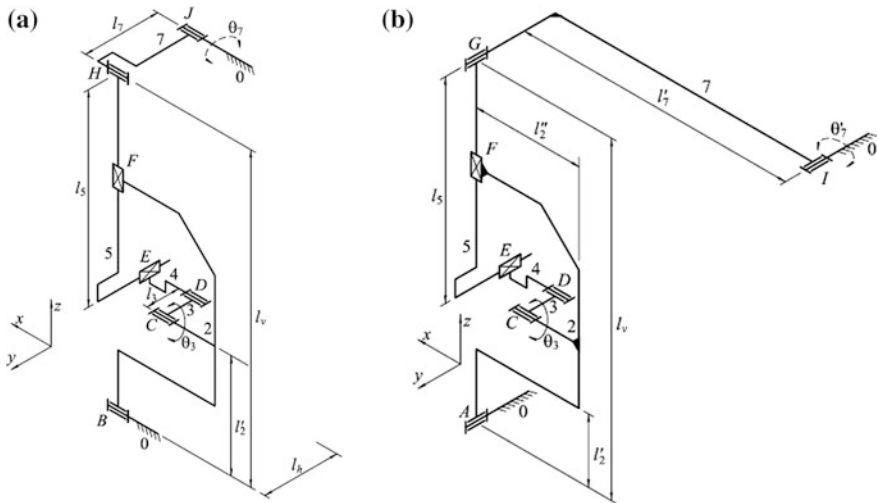
Fig. 5 Kinematics of the second concept, based on Scotch Yoke mechanism

In order to compute the inverse kinematics two equivalent mechanisms have been considered, one for each movement. Although it has two actuated links, the mechanism can be represented with only one motor (the second one being redundant). For inversion/eversion movement the equivalent mechanism with one actuated link shown in Fig. 6a has been used, resulting the  $\theta_3$  angle:

$$\theta_3 = \arcsin\left(\frac{\sqrt{l_7^2 + l_h^2 + l_v^2 + 2l_7(l_v \sin \theta_7 - l_h \cos \theta_7)} - l_2 - l_5}{l_3}\right). \quad (14)$$

The equivalent mechanism with one actuated link for flexion/extension movement is presented in Fig. 6b. The actuated links 3 and 3' are rotating with the same angle but in opposite directions  $\theta_3 = -\theta'_3$  and the result is the movement of the platform 7 with an angular stroke given by  $\theta'_7$  angle. Based on the equivalent mechanism the inverse kinematics can be written as follows:

$$\theta_3 = \arcsin\left[\frac{\sqrt{l_7^2 + l_h^2 + l_v^2 + 2 \cdot l_7 \cdot (l_v \cdot \sin \theta'_7 - l_h \cdot \cos \theta'_7)} - l_2 - l_5}{l_3}\right]. \quad (15)$$



**Fig. 6** Equivalent mechanism with one actuated link: **a** for inversion/eversion movement; **b** for plantar flexion/dorsiflexion movement

The inverse kinematic model can be used to perform a motion analysis, in order to validate the proposed solution.

## 4 Conclusions

In this first part of the paper some structural and kinematic aspects have been presented on the development of light weight, low cost and easy to manufacture ankle rehabilitation devices. Two simple solutions of ankle rehabilitation platforms have been proposed. The systems are based on Scotch Yoke mechanism and spatial four-bar mechanism respectively. Both solutions have two degrees of freedom, in order to offer the two required movements for a complete recovery of the injured ankle. The second part of the paper will present 3D models and motion simulation results of the devices. Future work will be orientated to safety measures, user-friendly interface and clinical verification of the robotic platforms.

## References

1. Krebs HI, Volpe BT (2013) Rehabilitation robotics. *Handb Clin Neurol* 110:283–294
2. Waterman B, Owens B, Davey S, Zacchilli M, Belmont PJ Jr (2010) The epidemiology of ankle sprains in the United States. *J Bone Jt Surg* 92:2279–2284
3. Braun BL (1999) Effects of ankle sprain in a general clinic population 6 to 18 months after medical evaluation. *Arch Fam Med* 8:143–148

4. Díaz I, Gil JJ, Sánchez E (2011) Lower-limb robotic rehabilitation: literature review and challenges. *J Robot* 2011
5. Racu (Cazacu) CM, Doroftei I (2014) An overview on ankle rehabilitation devices. *Adv Mater Res* 1036:781–786
6. Meng W, Liu Q, Zhou Z, Ai Q, Sheng B, Xie SS (2015) Recent development of mechanisms and control strategies for robot-assisted lower limb rehabilitation. *Mechatronics* 31:132–145
7. Sui P, Yao L, Dai JS, Wang H (2011) Development and key issues of the ankle rehabilitation robots. In: 13th world congress in mechanism and machine science, Guanajuato, pp A12-416
8. Pederson TS, Ricard MD, Merrill G, Schulthies SS, Allsen PE (1997) The effects of spating and ankle taping on inversion before and after exercise. *J Athl Train* 32:29–33
9. Ricard MD, Sherwood SM, Schulthies SS, Knight KL (2000) Effects of tape and exercise on dynamic ankle inversion. *J Athl Train* 35(1):31–37
10. Verhagen EA, van der Beek AJ, van Mechelen W (2001) The effect of tape, braces and shoes on ankle range of motion. *Sports Med* 31(9):667–677
11. Racu (Cazacu) CM, Doroftei I (2016) Motion simulation of a new ankle rehabilitation device. *Robot Manag* 21(1):30–35
12. Racu CM, Doroftei I (2016) Design, modelling and simulation aspects of an ankle rehabilitation device. In: IOP Conference Series. *Mater Sci Eng* 145(5):052008
13. Racu (Cazacu) CM, Doroftei I (2014) Structural and kinematic aspects of a new ankle rehabilitation device. *Appl Mech Mater* 658:507–512
14. Racu (Cazacu) CM, Doroftei I (2015) Design aspects of a new device for ankle rehabilitation. *Appl Mech Mater* 809–810:986–991
15. Racu (Cazacu) CM, Doroftei I (2015) Ankle rehabilitation device with two degrees of freedom and compliant joint. In: IOP Conference Series. *Mater Sci Eng* 95(1), id. 012054
16. Racu (Cazacu) CM, Doroftei I (2015) Preliminary ideas on the development of a new ankle rehabilitation device. In: Proceedings of the 14th IFToMM world congress, pp 439–447

# New Concepts of Ankle Rehabilitation Devices—Part II: Design and Simulation



C. M. Racu (Cazacu) and I. Doroftei

**Abstract** Ankle exercises are long-term and repetitive and cannot offer information about patient's evolution. Due to these aspects a need for easy-to-use mechatronic devices emerges. The purpose of this two parts paper is to propose two rehabilitation devices, based on different actuating mechanisms (spatial four-bar and Scotch Yoke mechanism respectively). In the first part the structural synthesis and some kinematic aspects of the proposed devices have been presented. For the second part, 3D models and preliminary numerical simulations of the systems are performed. The simulation results are encouraging, both mechanisms covering all the required movements for a complete recovery of the ankle joint.

**Keywords** Robot · Ankle rehabilitation device · Scotch Yoke mechanism  
Spatial four-bar mechanism

## 1 Introduction

A large number of humans experience lower limb injuries, with a high incidence of sprains [1]. For a complete recovery and a normal life without activity limitations, recovery exercises are mandatory [2]. Hence, multiple devices are used, but they cannot offer information about the evolution of the patient. This leads to the development of robot-assisted ankle rehabilitation devices to counteract these drawbacks [3–7].

To achieve a fully recovered ankle joint one must consider ankle movements and range of motion: plantar flexion (extension), dorsiflexion (flexion), eversion and inversion. Motion amplitudes range from  $0^\circ$  to  $25^\circ$  for flexion and eversion, and  $0^\circ$  to  $50^\circ$  for extension and inversion (for a healthy subject). Considering these range

---

C. M. Racu (Cazacu) · I. Doroftei (✉)  
“Gheorghe Asachi” Technical University of Iasi, Iași, Romania  
e-mail: idorofte@mail.tuiasi.ro

C. M. Racu (Cazacu)  
e-mail: cristina.racu@tuiasi.ro

of motions and requirements as light weight, low cost and easy to manufacture, two ankle rehabilitation devices have been proposed.

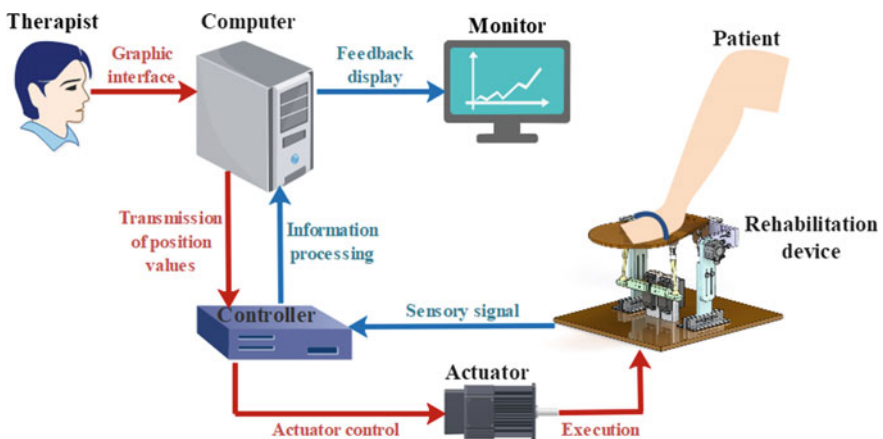
Based on the structural synthesis and some kinematic aspects presented in the first part of this paper, the 3D models and preliminary numerical simulations are presented in the following sections.

## 2 Design of the First Rehabilitation Device

The general architecture of a rehabilitation system is shown in Fig. 1. The therapist should set the values of the rehabilitation exercise amplitudes through the graphical interface generated by the computer, providing the input values for the microcontroller. This microcontroller will send the range of the necessary angular strokes executed by the actuators. The data collected from the position/force sensors will be sent back, resulting in visual feedback for both the patient and the therapist.

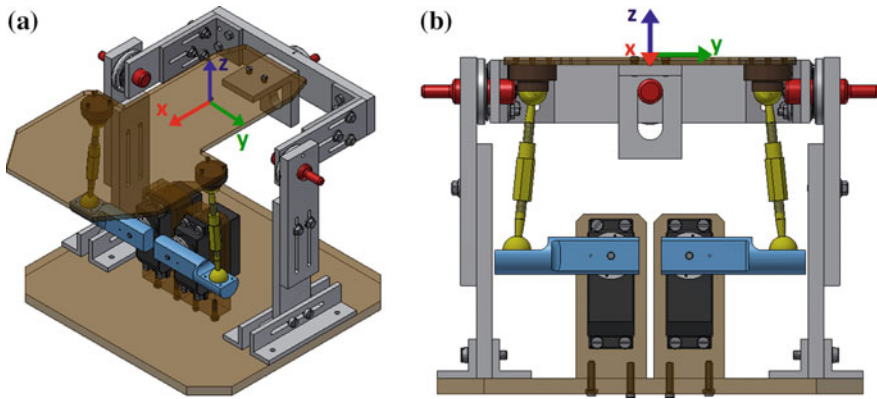
Based on this general architecture, on the mechanism synthesis and kinematics and, also, on a previous simulation [8, 9], the 3D CAD model has been designed, and it is presented in Fig. 2. In order to demonstrate that the designed platform offers the required angular strokes for a complete recovery of the ankle articulation, a simulation analysis has been performed. In our simulation we have used next dimensions:  $l_h = 25$  mm;  $l_1 = 60$  mm;  $l_2 = 103$  mm;  $l_4 = 75$  mm (see Fig. 1 in the first part).

For the dorsiflexion/plantar flexion movement the driving links will rotate with the same angle but in opposite direction,  $\theta_1 = -\theta'_1$ . The angular position,  $\theta'_4$  of the driven link, according to the angular positions of the driving links ( $\theta_1 = -\theta'_1$  and  $\theta_1 = -\theta'_1$ ) is presented in Fig. 3a. We may see that the extreme angular positions of



**Fig. 1** General architecture of a rehabilitation system



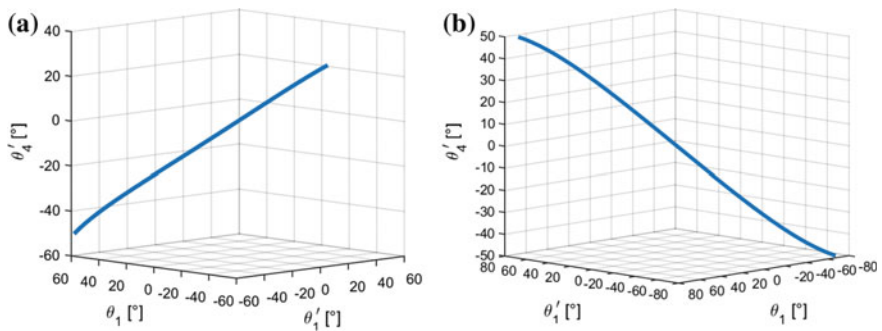


**Fig. 2** CAD design of the first ankle rehabilitation device: **a** isometric view; **b** front view

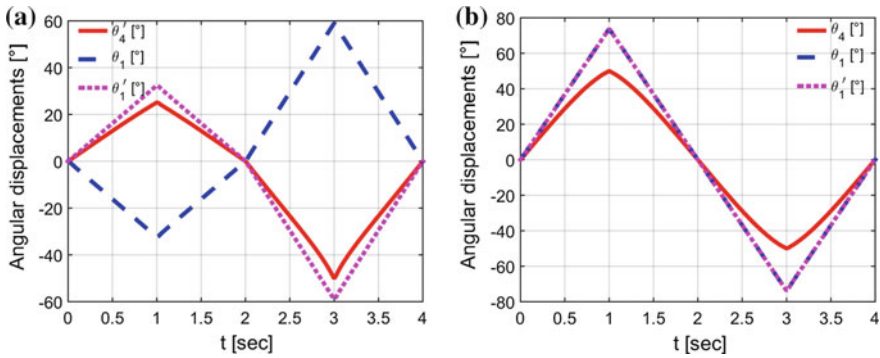
the ankle joint, considering the plantar flexion/dorsiflexion ankle movements ( $-50^\circ$  to  $0^\circ$  for plantar flexion;  $0^\circ$  to  $25^\circ$  for dorsiflexion), lead to the next range of the driving links angular positions:  $\theta_1 = -32.4 \div 59^\circ$ ,  $\theta'_1 = -59 \div 32.4^\circ$ .

For inversion/eversion movement the driving links will rotate with the same angle in the same direction,  $\theta_1 = -\theta'_1$ . The angular position  $\theta_4$  of the driven link, according to the angular positions of the driving links is shown in Fig. 3b. Because the device should be used to recover both legs,  $\theta_4$  was considered to range between  $-50^\circ$  and  $50^\circ$  (ankle angular positions of the sole, for a healthy subject, are:  $-50^\circ$  to  $0^\circ$  for inversion and  $0^\circ$  to  $25^\circ$  for eversion—for one leg—and  $-25^\circ$  to  $0^\circ$  for eversion and  $0^\circ$  to  $50^\circ$  for inversion—for the other leg). In these conditions, the required strokes for driving links have been found as:  $\theta_1 = \theta'_1 = -73.8 \div 73.8^\circ$ .

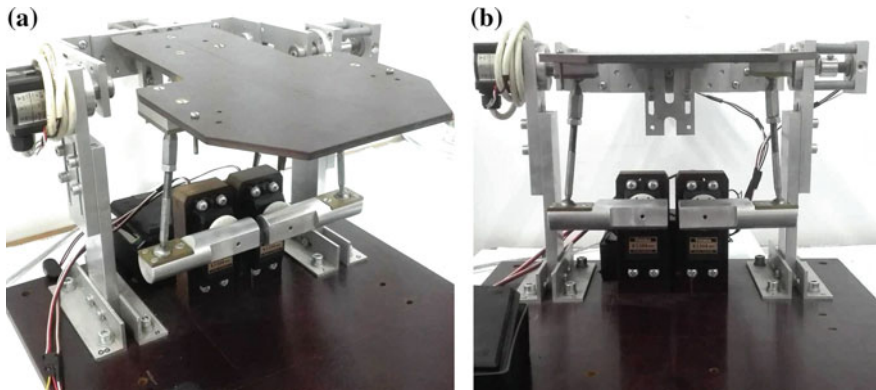
In Fig. 4, the angular positions  $\theta_1$ ,  $\theta'_1$ ,  $\theta'_4$  and  $\theta_4$  over time are presented. One should see that, using the dimensions considered above, the platform could perform the necessary movements for a complete recovering of the ankle joint.



**Fig. 3** Angular positions of the driven link according to the angular positions of the driving link, for the first mechanism: **a** dorsiflexion/plantar flexion movement; **b** inversion/eversion movement



**Fig. 4** Angular positions of the driving and driven links over time, for first mechanism: **a** dorsiflexion/plantar flexion movement; **b** inversion/eversion movement



**Fig. 5** The first experimental device based on spatial four-bar mechanism

Based on the general architecture and 3D design shown before, a first experimental device has been manufactured (Fig. 5). Two servomotors are actuating the driven links, which will result in the movement of the support link (the plate which support the sole). The actual angular positions of this plate are measured using two rotational resistive sensors. Two microcontrollers are used to control the device, one is recording the angular position values from the sensors, and the other one sends information to the motors. More work is required to be done for safety measures and friendly user interface.

For safety reasons (to avoid injuries or supplementary pain to the patient), torque sensors will be used for each ankle movements. In this way, the robotic platform should rotate the driven link to the position limited by the maximum torque imposed by the user and it should offer a gradual recovering of the ankle joint.

### 3 Design of the Second Rehabilitation Device

The other proposed solution is based on a Scotch Yoke mechanism, which converts the rotary motion into translational one. Considering the general architecture of a rehabilitation device (see Fig. 1), the mechanism synthesis and kinematics [10–13], a 3D model has been designed, and it is presented in Fig. 6.

The dimensions used in our simulations for this second platform are:  $l_1= 35$ ;  $l_3= 77.5$ ;  $l_5= 135$ ;  $l_7= 60$  and total  $l_v= 245$  mm (see Fig. 5 in the first part of the paper). Taking into account the space conditions the actuated links were placed facing each-other resulting in a more compact device.

Due to motors positions, for the dorsiflexion/plantar flexion movement the driving links will rotate with the same angle but in opposite direction,  $\theta_3 = -\theta'_3$ . The angular strokes of the driven link ( $\theta'_7$ ) have been considered using the plantar flexion/dorsiflexion ankle movement for a healthy subject, described before. In these conditions, the required angular positions of the driving links resulted as:  $\theta_3 = -19.2 \div 35.5^\circ$ ,  $\theta'_3 = -35.5 \div 19.2^\circ$ . The angular position,  $\theta'_7$  of the driven link, according to the angular positions of the driving links ( $\theta_3$  and  $-\theta'_3$ ) is presented in Fig. 7a.

For the inversion/eversion movement the angular strokes of the driven link ( $\theta_7$ ) will have the amplitude of  $-50^\circ$  and  $50^\circ$ . The required angular amplitudes for driving links were found:  $\theta_3 = \theta'_3 = -20.3 \div 20.3^\circ$ . The angular position  $\theta_7$  of the driven link, according to the angular positions of the driving links is shown in Fig. 7b.

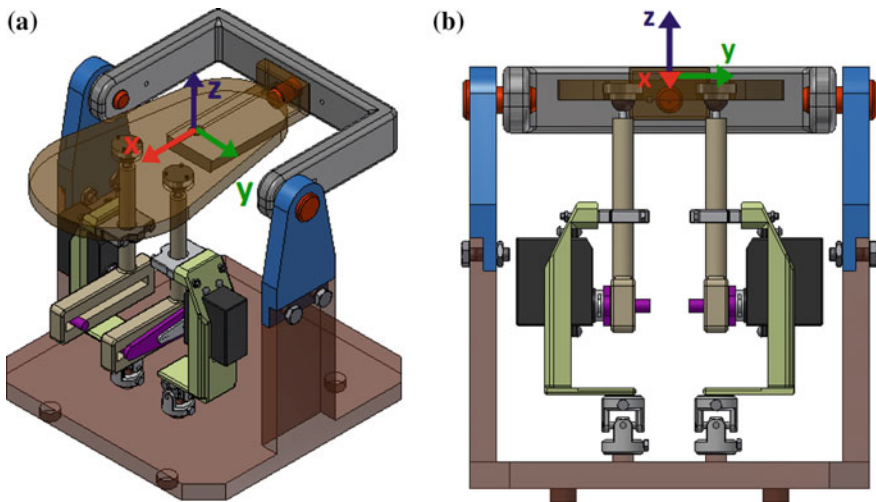
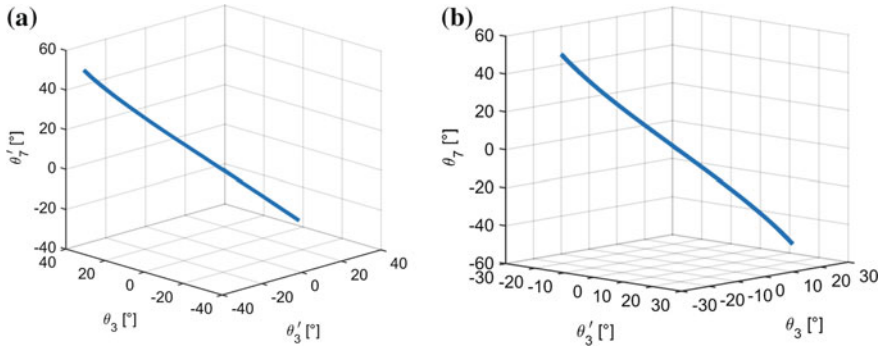
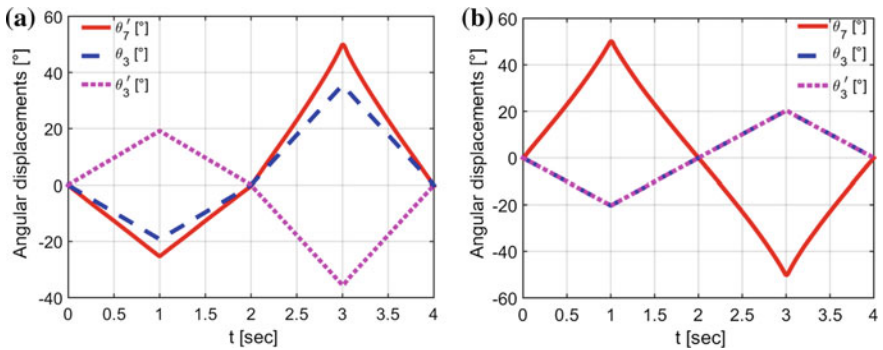


Fig. 6 CAD design of the second ankle rehabilitation device: **a** isometric view; **b** front view



**Fig. 7** Angular positions of the driven link according to the angular positions of the driving link, for the second mechanism: **a** dorsiflexion/plantar flexion movement; **b** inversion/eversion movement



**Fig. 8** Angular displacements function of time (planar representation) for scotch-yoke based mechanism: **a** dorsiflexion/plantar flexion movement; **b** inversion/eversion movement

In Fig. 8, the angular positions  $\theta_3$ ,  $\theta_3'$ ,  $\theta_7$  and  $\theta_7$  over time are presented. For both required movements it can be observed a smooth and almost linear variation, suggesting that the mechanism synthesis and inverse kinematics are validated.

### 4 Conclusions

Two simple solutions of ankle rehabilitation platforms have been proposed, one based on the spatial four-bar mechanism and the second one based on Scotch Yoke mechanism, respectively. Both solutions have two degrees of freedom, in order to offer the two required movements for a complete recovery of the injured ankle. This second part of the paper presents 3D models and preliminary numerical simulations

of the devices. The obtained results were encouraging, both mechanisms offering a smooth and almost linear motion for the driven link (the plate which supports the sole). For safety reasons (to avoid injuries or supplementary pain to the patient), torque sensors will be used for each ankle movements. In this way, the robotic platform should rotate the driven link to the position limited by the maximum torque imposed by the user and it should offer a gradual recovering of the ankle joint. Future work will be orientated to safety measures, user-friendly interface and clinical verification of the robotic platform.

## References

1. Waterman B, Owens B, Davey S, Zacchilli M, Belmont PJ Jr (2010) The epidemiology of ankle sprains in the United States. *J Bone Jt Surg* 92:2279–2284
2. Braun BL (1999) Effects of ankle sprain in a general clinic population 6 to 18 months after medical evaluation. *Arch Fam Med* 8:143–148
3. Díaz I, Gil JJ, Sánchez E (2011) Lower-limb robotic rehabilitation: literature review and challenges. *J Robot* 2011
4. Racu (Cazacu) CM, Doroftei I (2014) An overview on ankle rehabilitation devices. *Adv Mater Res* 1036:781–786
5. Krebs HI, Volpe BT (2013) Rehabilitation robotics. *Handb Clin Neurol* 110:283–294
6. Meng W, Liu Q, Zhou Z, Ai Q, Sheng B, Xie SS (2015) Recent development of mechanisms and control strategies for robot-assisted lower limb rehabilitation. *Mechatronics* 31:132–145
7. Sui P, Yao L, Dai JS, Wang H (2011) Development and key issues of the ankle rehabilitation robots. In: 13th world congress in mechanism and machine science, Guanajuato, pp A12-416
8. Racu (Cazacu) CM, Doroftei I (2016) Motion simulation of a new ankle rehabilitation device. *Robot Manag* 21(1):30–35
9. Racu CM, Doroftei I (2016) Design, modelling and simulation aspects of an ankle rehabilitation device. In: IOP Conference Series. *Mater Sci Eng* 145(5):052008
10. Racu (Cazacu) CM, Doroftei I (2014) Structural and kinematic aspects of a new ankle rehabilitation device. *Appl Mech Mater* 658:507–512
11. Racu (Cazacu) CM, Doroftei I (2015) Design aspects of a new device for ankle rehabilitation. *Appl Mech Mater* 809–810:986–991
12. Racu (Cazacu) CM, Doroftei I (2015) Ankle rehabilitation device with two degrees of freedom and compliant joint. In: IOP Conference Series. *Mater Sci Eng* 95(1), id. 012054
13. Racu (Cazacu) CM, Doroftei I (2015) Preliminary ideas on the development of a new ankle rehabilitation device. In: Proceedings of the 14th IFToMM world congress, pp 439–447

**Part III**  
**Mobile Robots**

# Service Robots for Cultural Heritage Applications



G. Carbone

**Abstract** This paper outlines the potential of service robots as applied in frames of Cultural Heritage. Several applications are discussed such as inspection, searching/surveillance operations, identification, analysis, preservation and restoration of Cultural Heritage goods. Key design requirements are outlined for robots to be applied for servicing Cultural Heritage goods or sites. Related experiences at LARM in Cassino are outlined in order to clarify aspects of engineering feasibility and implementation.

**Keywords** Service robotics • Design requirements • Cultural heritage

## 1 Introduction

Cultural Heritage can be understood as tangible culture (such as historical cities, buildings, monuments, landscapes, books, works of art and artefacts), intangible culture (such as folklore, music, traditions, language and knowledge) and natural heritage (including culturally-significant landscapes and biodiversity). Thus, Cultural Heritage (CH) attention can be given to objects and facts that are on very different levels of the scale. Small objects, such as artworks and other cultural masterpieces, are collected in museums, art galleries, exhibition sites, and archives.

Heritage recovering usually involves preliminary tasks such as inspection or searching/surveillance operations. Finding valuable objects or discovering areas of interest represent an usual objective in these activities. Service robots can play a key role in this context. Service robots are ‘robots which operate semi or fully autonomously to perform services useful to the well-being of humans and equipment, excluding manufacturing operations’, [1]. Service robotics covers a wide range of applications, which are rapidly growing and expanding. Among them some very

---

G. Carbone (✉)

University of Cassino and South Latium, Cassino, Italy

e-mail: carbone@unicas.it

interesting preliminary attempts have been made in using robots in CH frames such as inspection, servicing, restoration of CH sites, [2–12].

LARM, Laboratory of Robotics and Mechatronics is an internationally recognized research center having international collaborations and exchange programs with several countries worldwide. Since 1990 a long term research line has been established at LARM as referring with servicing Cultural Heritage goods or sites with a multidisciplinary approach. In the following, key design requirements for service robots in Cultural Heritage applications are briefly outlined as referring to related experiences at LARM in Cassino such as those reported in [13–26].

## 2 Requirements for Cultural Heritage Applications

Cultural Heritage goods are usually considered as objects to be preserved, as indicated by several national and international law prescriptions for Cultural Heritage such as the Convention Concerning the Protection of the World Cultural and Natural Heritage, which was adopted by UNESCO in 1972, [27]. Based on the above, a proper intervention on Cultural Heritage goods or sites requires a deep knowledge of it by looking at aspects such as identification, analysis, preservation and restoration with a wide interdisciplinary approach.

In general, main challenges for service robots in Cultural Heritage frames can be understood as: operating together with human users not have specific training and expertise in robotics, with suitable behaviors and careful user-friendly and safe operation in interaction with Cultural Heritage goods; operating service tasks with proper user-friendly operation, which should be considered from acceptability and cost for actions viewpoints as referring to Cultural Heritage goods.

The above result in specific expectations and requirements from engineering viewpoint. For instance, referring to the level of autonomy, a full autonomy with artificial intelligence might be desirable only for specific standardized service restoration/identification goals within a well-structured configuration of the environment. In some cases, instead, a very limited or no autonomy is required/possible due to the need of a continuous and unpredictable interaction with human users and/or environment conditions leading to mostly tele-operated applications.

A general approach for designing service robots can be outlined by considering specific aspects and challenges for identification, restoration, and preservation. In particular, the main flow is the data consideration for technical constraints/issues, analysis of service operations and goals and system programming. Then, checks are worked out by operators, restorers and robot users. Technical care in the design activity is indicated by the system design and operation planning. This is strongly influenced by aspects and activities that concerning with human beings and environment. The reported aspects are not exhaustive as they should be considered as useful guidelines for successful service robots in Cultural Heritage applications where special emphasis has to be addressed to the acceptance of the operators,

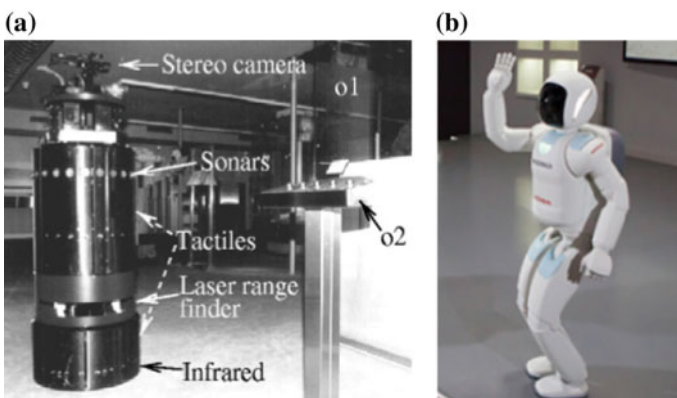


restorers and users. Just to cite few other key aspects one could refer to grasping/handling issues, as discussed for example in [28–30] as well as energy efficiency aspects, as discussed for example in [31].

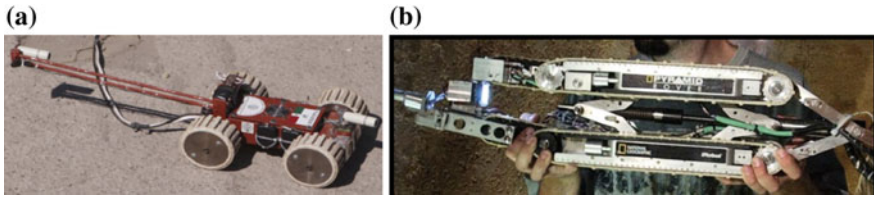
### 3 Robot Architectures for Cultural Heritage

Architectures and solutions for service robots for cultural heritage applications may significantly vary according to the specific applications. First attempts have started with systems to be used for indoor environments in applications such as museum or tour guide. For the purpose, common architectures are based on wheeled mobile robots such as shown in Fig. 1 where Fig. 1a shows a RHINO mobile platform, [2]; Fig. 1b shows a TPR-Robina Toyota human-like mobile robot, [9]; Fig. 1c shows Honda Asimo humanoid robot for museum guided applications, [4]. It is interesting to note the evolution of these robotic systems over the years where the appearance is carefully designed to increase the users' acceptance. This has led to some attempts of using humanoids such as Honda Asimo although the complexity of legged locomotion can be unnecessary when the environment is only composed of flat surfaces.

Other cultural heritage applications might be requiring completely different architectures to cope with complex environments and outdoor conditions. Significant examples can be based on using toothed wheels or crawlers such as the robot Tlaloc 1, [10], which is a 30 cm wide robot that has been used for exploring a tunnel in Teotihuacan ruins, Fig. 2a, or the iRobot Pyramid rover which has been used for exploring a narrow tunnel and finding a hidden door and chamber in the Great Pyramid of the pharaoh Khufu, Fig. 2b, [11]. Even more challenging



**Fig. 1** Examples of robots for tour guiding applications: **a** RINHO, [2]; **b** Toyota Robina, [9]; **c** Honda Asimo, [4]



**Fig. 2** Examples of robots for applications of in-tunnel exploration: **a** Tlaloque 1, [10]; **b** iRobot Pyramid rover, [11]



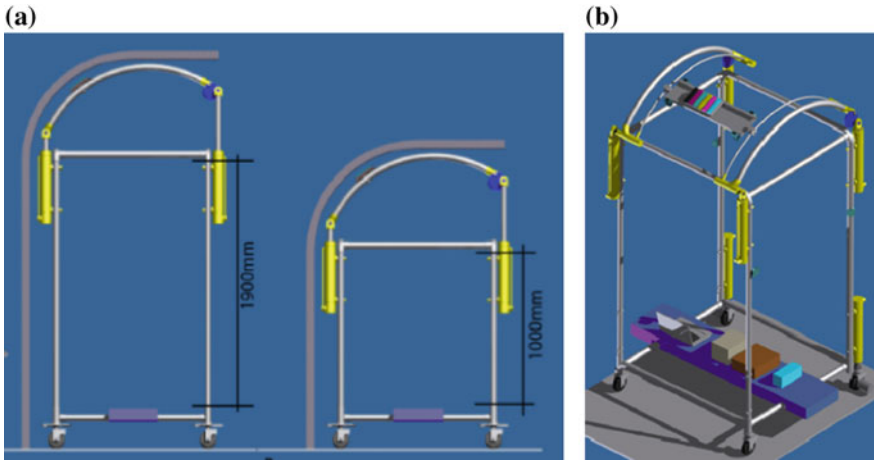
**Fig. 3** Robots for undersea exploration: **a** SeaBED AUV, [8]; **b** Ocean One, [12]

environments can be found when cultural heritage goods are hidden under seas or rivers. For example, it is the case of the SeaBED AUV for underwater exploration, Fig. 3a, [8], or the underwater humanoid robot Ocean One, Fig. 3b, [12].

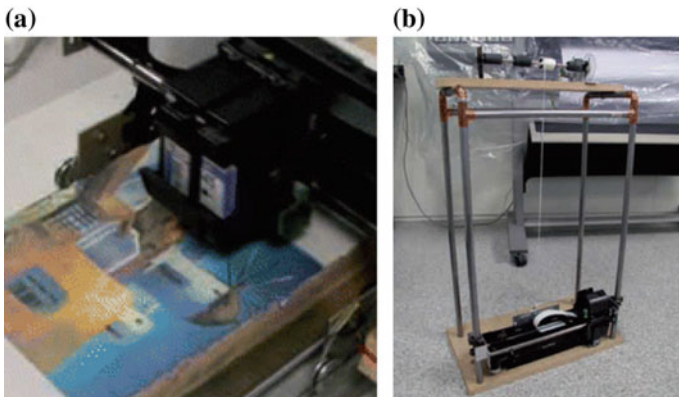
## 4 Experiences at LARM

### 4.1 *An Architecture for Frescos Painting*

Specific applications at LARM in Cassino are discussed as illustrative examples to show the feasibility for the design and implementation of service robots in applications for Cultural Heritage as coming from direct experiences of the author within LARM team. Fresco paintings are usually decorative products, which are produced on large surfaces such as walls or dome surfaces. The main problem for a proper intervention of restoration of a fresco is when there are large damaged or missing areas, which make unclear the original meaningfulness and beauty of the fresco. Preliminary studies and attempts to address this issue were successfully carried out with computer graphics means, as reported in [13]. In particular, it is possible to use inkjet printing to create sketches, which can fill the missing/damaged areas such as proposed in a collaboration among Technical University of Valencia, technicians from Hewlett-Packard, and consultants from ARSU PAER company, [13].



**Fig. 4** A modular robotized structure as proposed for the inkjet fresco painting: **a** a side view; **b** a 3D view, [13]



**Fig. 5** A laboratory test of fresco printing with the inkjet printer: **a** view of the modular robotized structure; **b** a zoom view of the inkjet fresco painting, [13]

The procedure has been set up with the following three steps: acquisition and computer-based elaborations of existing images; drawing of damaged/missing images with computer graphics means; inkjet printing for filling of large damaged or missing areas with inkjet-printed images.

A robotic system was developed to perform the last step by adapting a commercial Hewlett-Packard inkjet printer. This system was designed with different solutions for flat or curved surfaces as proposed in Figs. 4 and 5. The purpose of the robotized system is to work out direct fresco reintegration in a user-friendly and low-cost manner while keeping a reasonable image quality. It is also necessary to

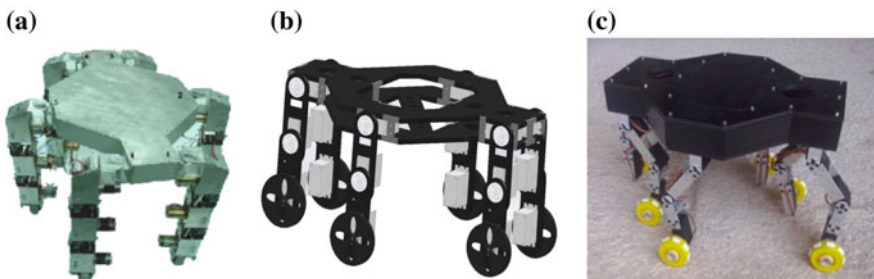
keep a clear understanding to customers of the difference between original paintings and reproductions of damaged/missing images. The main aims from restorer viewpoint can be seen as facilitating and substantially reducing the working time as well as guaranteeing printing quality uniformity, and consistency. The robot in Figs. 4 and 5 has maximum sizes as  $1,900 \times 1,000 \times 1,000$  mm, which can fit within the painting environment. The main structure works as a portable support. It has a modular mechanical design, as shown in Fig. 5.

## 4.2 *Cassino Hexapod Series*

Cassino Hexapod is a series of mobile robots, which has been designed and built at LARM in Cassino, starting from 2000, [14–20]. Solutions have been ranging from Cassino Hexapod version I, Fig. 6a, Cassino Hexapod version II, Fig. 6b, to the latest solution Cassino Hexapod version III, Fig. 6c and have resulted also in an Italian Patent, [21]. Main characteristics of the Cassino Hexapod series are the combination of legs and wheels as well as the use of low-cost control architectures with user-friendly operation interfaces. Cassino Hexapods have been applied for different inspection operations in non-accessible historical sites such as Montecassino Abbey. An evolution of Cassino Hexapod Series is R3HC robot in Fig. 7, which has been developed in collaboration with University of Huelva for servicing Cultural Heritage sites, [22].

## 4.3 *HeritageBot*

HeritageBot is a robotic architecture, which combines a legged mobile robot module with a drone module in order to achieve a system, which is capable of ground operation and small flights at same time as shown in Fig. 8. This robot can be equipped with sensors and instrumentation for specific applications in Cultural



**Fig. 6** The Cassino hexapod robots: **a** version I, **b** version II, **c** version III

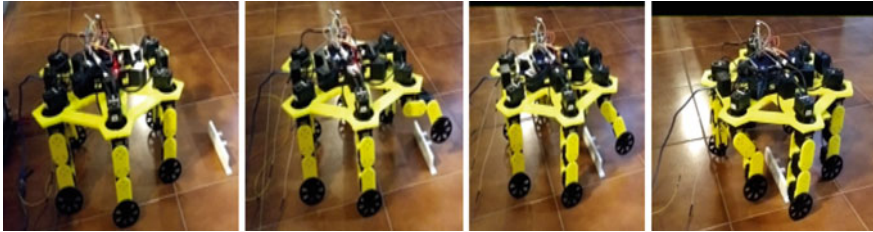


Fig. 7 Snapshots of R3HC in a lab. test for obstacle overcoming maneuver, [20]

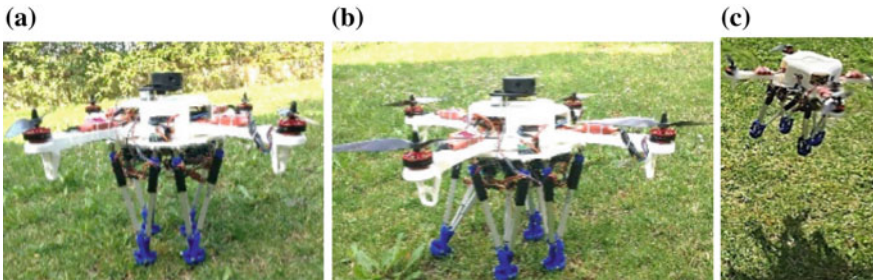


Fig. 8 An outdoor test of HB3 prototype: a starting pose; b a walking step; c flying

Heritage frames. It has been developed within the Latium regional project “Heritagebot”.

The design of HeritageBot has so far evolved in three versions HB1, HB2 and HB3 as reported in [23–26].

HeritageBot robot can have two main operation modes namely: walking mode and small-flight with altitude-hold. When altitude hold mode is selected, the throttle is automatically controlled to maintain the current altitude. The user directly controls the roll and pitch lean angles and the heading. Tests have been carried out indoor and outdoor for validation purposes. In particular, Fig. 8a shows the starting position, Fig. 8b shows a walking step. Figure 8c shows the prototype performing a stable flight in outdoor conditions for HB3 prototype.

## 5 Conclusions

This paper describes main features and requirements for service robots as applied in frames of Cultural Heritage such as inspection, searching/surveillance operations, identification, analysis, preservation and restoration of Cultural Heritage goods or sites. Three specific robotic architectures are described as successful engineering design experiences within LARM team in Cassino in Cultural Heritage related tasks.

**Acknowledgements** The author is grateful to the Latium Region government for supporting the research project Heritagebot through 2015–17 grant FILAS-RU-1044.

## References

1. IFR International Federation of Robotics (2017). <https://ifr.org/>. Accessed Oct 2017
2. Burgard W, Cremers AB, Fox D, Lakemeyer G, Hahnei D, Schulz D, Steiner W, Thrun S (1998) The interactive museum tour-guide robot. In: Fifteenth national conference on artificial intelligence, Madison, pp 11–18
3. Macaluso I, Ardizzone E, Chella A, Cossentino M, Gentile A, Gradino R, Infantino I, Liotta M, Rizzo R, Scardino G (2005) Experiences with Cicerobot, a museum guide cognitive robot. In: 9th conference on advances in artificial intelligence, Milan
4. Falconer J (2017) Honda's ASIMO get a new job at museum. IEEE Spectrum. Accessed Oct 2017
5. Tate Britain (2017) Tate after dark. <http://www.tate.org.uk/whats-on/tate-britain/special-event/after-dark>. Accessed Oct 2017
6. Thrun S, Bennewitz M, Burgard W, Cremers AB, Dellaert F, Fox D, Hähnel D, Rosenberg CR, Roy N, Schulte J, Schulz D (1999) MINERVA: a tour-guide robot that learns. In: 23rd annual german conference on artificial intelligence: advances in artificial intelligence, Bonn, pp 14–26
7. Willeke T, Kunz C, Nourbakhsh IR (2001) The history of the mobot museum robot series: an evolutionary study. In: 14th international Florida artificial intelligence research society conference, Key West, pp 514–518
8. Bingham B, Foley B, Singh H, Camilli R, Delaporta K, Hole W, Mallios A, Mindell D, Roman C, Sakellariou D (2010) Robotic tools for deep water archaeology: surveying an ancient shipwreck with an autonomous underwater vehicle. *J Field Robot* 27(6):702–717
9. Toyota newsroom webpage (2017) TPR-Robina. <http://newsroom.toyota.co.jp/en/detail/279478>. Accessed Oct 2017
10. Csmonitor webpage (2017) Tlaloque 1. <https://www.csmonitor.com/World/Latest-News-Wires/2010/1112/Teotihuacan-ruins-explored-by-a-robot>. Accessed Oct 2017
11. Bauval R (2017) Pyramid rover photo. <http://www.robertbauval.co.uk/photos/n07.html>. Accessed Oct 2017
12. Stanford Robotics Lab. Webpage (2017) Ocean One project. <http://cs.stanford.edu/group/manips/ocean-one.html>. Ocean One. Accessed Oct 2017
13. Ceccarelli M, Blanco-Moreno F, Carbone G, Roig P, Cigola M, Regidor JL (2015) A robotic solution for the restoration of fresco paintings. *Int J Adv Robot Syst* 12(11)
14. Cigola M, Pelliccio A, Salotto O, Carbone G, Ottaviano E, Ceccarelli M (2005) Application of robots for inspection and restoration of historical sites. In: 22nd international symposium on automation and robotics in construction, ISARC 2005, Ferrara, p 37
15. Carbone G, Shrot A, Ceccarelli M (2007) Operation strategy for a low-cost easy operation Cassino hexapod. *Appl Bion Biomech* 4(4):149–156
16. Carbone G, Ceccarelli M (2008) A low-cost easy-operation hexapod walking machine. *Int J Adv Robot Syst* 5(2)
17. Tedeschi F, Carbone G (2014) Design issues for hexapod walking robots. *Int J Robot* 3(2):181–206
18. Carbone G, Tedeschi F, Gallozzi A, Cigola M (2015) A robotic mobile platform for service tasks in cultural heritage. *Int J Adv Robot Syst* 12(88):1–10
19. Carbone G, Ceccarelli M (2004) A mechanical design of a low-cost easy-operation anthropomorphic wheeled leg for walking machines. *Int J Robot Manag* 9(2):3–8
20. Tedeschi F, Cafolla D, Carbone G (2014) Design and operation of Cassino hexapod II. *Int J Mech Control* 15(1):19–25

21. Carbone G, Tedeschi F (2017) Sistema robotico a gambe per telerilevamento (legged robotic system for teleoperation tasks). Italian Patent Application IS2014A000001, 3 March 2014, Isernia, Italy. Italian Patent Released no. 102014902238772, 23 Jan 2017
22. Gomez-Bravo F, Carbone G, Villadoniga P (2017) A searching robot for cultural heritage tasks. In: Ceccarelli M et al (eds) *New activities for cultural heritage*, pp 140–149
23. Ceccarelli M, Cafolla D, Russo M, Carbone G (2017) Design and construction of a demonstrative Heritagebot platform. *Advances in service and industrial robotics*. In: 26th international conference on robotics in Alpe-Adria-Danube region RAAD 2017. Springer, pp 355–363
24. Ceccarelli M, Cafolla D, Russo M, Carbone G (2017) Prototype and testing of heritagebot platform for service in cultural heritage. In: Ceccarelli M et al (eds) *New activities for cultural heritage*, pp 104–112
25. Ceccarelli M, Cafolla D, Carbone G, Russo M, Cigola M, Senatore LJ, Gallozzi A, Di Maccio R, Ferrante F, Bolici F, Supino S, Colella N, Bianchi M, Intrisano C, Recinto G, Micheli AP, Vistocco D, Nuccio MR, Porcelli M (2017) HeritageBot service robot assisting in cultural heritage. In: *IEEE first international workshop on robotic computing for cultural heritage, IRCCH 2017*, Taichung City, pp 440–445
26. Ceccarelli M, Cafolla D, Russo M, Carbone G (2016) Dispositivo di piattaforma a gambe ed eliche (Device with legs and helices), Italian Patent Application n. 102016000103321, Italy, 14 Oct 2016
27. UNESCO 2017 (2017). <http://whc.unesco.org/?cid=175>. Accessed Oct 2017
28. Carbone G, Rossi C, Savino S (2015) Performance comparison between FEDERICA hand and LARM hand. *Int J Adv Rob Syst* 12(7):90
29. Carbone G, Iannone S, Ceccarelli M (2010) Regulation and control of LARM hand III. *Robot. Comput. Integr Manuf* 26:202–211. <https://doi.org/10.1016/j.rcim.2009.05.002>. ISSN: 0736-5845
30. Carbone G, Lim HO, Takanishi A, Ceccarelli M (2006) Stiffness analysis of the humanoid robot WABIAN-RIV. *Mech Mach Theory* 41(1):17–40
31. Carbone G, Ceccarelli M, Oliveira PJ, Saramago SFP, Carvalho JCM (2008) Optimum path planning of CaPaMan (Cassino parallel manipulator) by using inverse dynamics. *Robot Int J* 26(2):229–239

# Dimensional Synthesis of a Robotic Arm for Mobile Manipulator Using an Interactive Geo-metric Software



S. Maraje, J. C. Fauroux, B. C. Bouzgarrou and L. Adouane

**Abstract** This paper aims to demonstrate a systematic procedure for the structural selection and dimensional synthesis of the arm to be integrated into a mobile manipulator. The manipulator will be utilized for Bots2ReC H2020 project which aims at developing an autonomous robotic solution for removing asbestos contamination from real world-rehabilitation sites. The synthesis procedure is initiated by identifying requirements and constraints on the mobile manipulator. The Interactive Geometric Software (**IGS**) is used to carry out the preliminary synthesis. The synthesis procedure highlights the utility of IGS in developing the conceptual and dimensional design of the arm and assesses its performance to satisfy given requirements and constraints. Redundancy is used to meet the desired requirements while satisfying the constraints.

**Keywords** Structural selection • Dimensional synthesis • Skeleton modeling  
Interactive geometric software • Redundant architecture • Mobile manipulator

---

S. Maraje · J. C. Fauroux (✉) · B. C. Bouzgarrou  
Institut Pascal, SIGMA Clermont, Université Clermont Auvergne, CNRS,  
63000 Clermont-Ferrand, France  
e-mail: Jean-Christophe.Fauroux@sigma-clermont.fr

S. Maraje  
e-mail: Siddharth.Maraje@sigma-clermont.fr

B. C. Bouzgarrou  
e-mail: Belhassen-Chedli.Bouzgarrou@sigma-clermont.fr

L. Adouane  
Institut Pascal, Université Clermont Auvergne, CNRS,  
63000 Clermont-Ferrand, France  
e-mail: Lounis.Adouane@uca.fr



# 1 Introduction

Mobile manipulators have gained an increasing popularity in automated industrial environments with applications ranging from assembly of large scale parts, surface processing, material handling, flexible manufacturing, etc [2]. Mobile base enables movement of the robotic arm in the work environment which then performs the required task. Thus, while synthesizing robotic arms for mobile manipulators; mobility of the base needs to be considered in order to determine the exact positioning of the robotic arm for performing a given task.

Synthesis methods and optimization techniques [6, 10, 13] have been proposed for dimensional synthesis of serial and parallel manipulators. The design process generally starts with conceptual design that permits fast exploration of many solutions and preliminarily assessment of their functionality. Geometry sketchers and CAD tools are well known for performing such design activity. In [11], two geometry sketchers and two CAD systems were compared. Interactive Geometric Software (IGS) were found to be particularly efficient for fast, preliminary dimensional synthesis of linkages. IGS are mostly used for educational purposes [4, 8]. In [9, 12] common IGS used into different fields regarding synthesis were compared. GeoGebra [7] was found better with regard to its interface and use for design methodology. In [1] a new method for determination and optimization of the workspace of parallel manipulators is presented. The proposed method is based on a geometrical approach, and offers the possibility to generate automatically the workspace in a CAD environment. By taking motivation from these works, this paper presents a technique for the preliminary synthesis of arm architecture for a mobile manipulator that will be used for the H2020-Bots2ReC project [3]. A broad objective of this project is “introducing, testing and validating an operational process for the automated removal of asbestos contamination at a real world rehabilitation site using a robotic system”.

The emphasis while designing the entire operational process will be to optimize the performance of the system by improving asbestos *cleaning productivity* while ensuring a safe and stable operation. Cleaning productivity can be maximized using one or several optimization functions such as—amount of asbestos cleaned per unit time, surface area cleaned per unit time or total time required to clean a standard rehabilitation site. Productivity is impacted by several factors such as: *maximum achievable displacement speed, trajectory planning of the robotic arm, motion planning of the moving platform, task allocation and planning*, etc.

In Sect. 2, requirements and constraints of the cleaning operation which serve as an input to arm synthesis are identified. Section 3 presents the dimensional synthesis of the arm using the IGS Geogebra. In Sect. 4, workspace of the synthesized architecture is characterized. Section 5 concludes the dimensional synthesis procedure presented in this paper.

## 2 Requirements and Constraints

Identifying requirements is the first necessary step while formalizing a design problem. The challenge in satisfying these requirements is overcoming constraints imposed by the interaction of the system with real world. This section identifies all such requirements and constraints that will be taken into account for the synthesis of the arm architecture and dimensions.

Performing asbestos removal while the mobile base is in motion is a critical task as the control of the grinding becomes difficult. Hence, it was decided to first fix the mobile base in a given pose with stabilizers and then to operate the arm from this pose. In such scenario, as the stabilization of the mobile platform takes some time, the robotic arm must be able to clean as much area as possible for the given pose of the mobile platform. To achieve this, the workspace of the arm should be as large as possible. Thus, productivity improvement is associated with the dimensional synthesis of the arm architecture (Table 1).

**Table 1** Requirements and constraints on the mobile manipulator expressed as design rules

Requirements and constraints	Design rule
The end-effector must reach floor, wall, ceiling ( <b>3 m high</b> ), skirting, etc and still be capable to work	<b>DR_Env</b> Types of surfaces to be cleaned; The mobile manipulator has a minimal reach of 3 m from the ground and is free of singular configurations, even on the workspace boundary
Surfaces to be cleaned can be horizontal, vertical, inclined, flat or curved, etc.	<b>DR_Surf</b> Shape of surfaces to be cleaned; Required DoFs are: 3 translations and 2 rotations (disc tool) or 3 rotations (cylindrical tool)
Safe and stable cleaning operation of the mobile manipulator is required	<b>DR_Stab</b> Static stability; Lateral and longitudinal stability margins must be satisfied throughout cleaning operation
The mobile manipulator should be transported to cleaning sites through elevators	<b>1. DR_Mass</b> Mass of the mobile manipulator; The overall mass of the mobile manipulator must be lower than 300 kg <b>2. DR_Short arm;</b> Arm should be as short as possible
The mobile manipulator must pass through doors of dimensions (80 × 200 cm) and fit in an elevator 200 cm high	<b>DR_Dim</b> Overall dimensions; The mobile manipulator must provide a pose fitting in a parallelepiped envelope of (80 × 60 × 190 cm)
The mobile manipulator should be capable to clean corridors as narrow as 70 cm	<b>DR_Narrow_Corridors</b> The projected workspace on the walls of the corridors should be as wide as possible
Collision of links of the arm with the mobile platform or environment surfaces must be avoided	<b>DR_Non_Collision</b> Collision avoidance; Link lengths must be optimized for avoiding collisions

The choice of suitable arm kinematics for the arm must be made considering DR\_Surf and DR\_Env. Two rotational *DoFs* of the *end-effector* can be assumed in the wrist for orienting the tool while the three translational *DoFs* for reaching desired position. For dimensional synthesis, wrist can be ignored which leaves us with kinematics of 3 translational *DoFs*. Such kinematics can be realized as RPR or RRR serial chain. The design team chose to focus on the first RRR solution and other kinematics will be considered if the first one does not bring a solution.

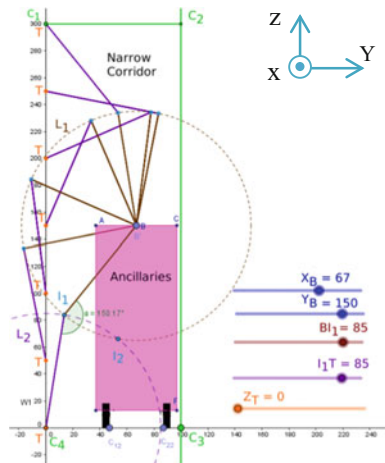
### 3 Dimensional Synthesis of the Arm

For the synthesis, a skeleton modeling approach is used through which, links are represented by lines and joints are reduced to points and/or motion axis [5, 11]. One solution to satisfy simultaneously contradictory design rules {DR\_Env}, that requires a sufficient reach of the arm and {DR\_Dim, DR\_Non\_Collision, DR\_Short\_ARM}, that tend to limit link lengths, is the following design rule: DR\_Mid\_Dist: locating the arm base at mid-distance between ground and 3 m high ceiling and provide arm reach superior to 1.5 m.

The analysis can be restricted to 2D by fixing the base revolute joint which reduces kinematics to RR. Moreover, DR\_Narrow\_Corridor is also critical and likely to affect the link lengths. Thus, considering the most critical case, dimensional synthesis is performed for cleaning inside narrow corridors. To summarize the design problem, the important design parameters are identified as: *reachability*, *singularity avoidance*, *collision avoidance* and *continuous trajectory*. For a continuous horizontal motion along X, the most critical pose is when the arm is in the plane BYZ.

In Fig. 1, a narrow corridor is represented in a Geogebra model in cross-section by the rectangle  $C_1C_2C_3C_4$ . The parametrizing capacity of Geogebra is used to explore the design space and move the end-effector vertically along the wall.

**Fig. 1** Arm-wall and arm—platform collisions

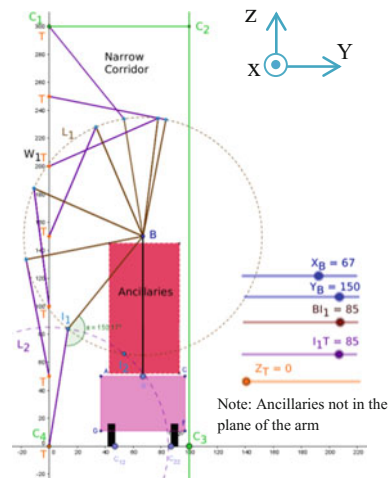


Point B represents the base of the arm and is adjusted at 150 cm height with the Y\_B slider, according to DR\_Mid\_Dist. By fixing the base B, circle ( $L_1$ ) that characterizes the first link is (parameterized by slider  $BI_1$ ). For constructing the second link, the end-effector point T is first fixed at a position on the wall represented by the Y-axis. Another circle ( $L_2$ ) that characterizes the length of second link is parameterized by slider  $I_1T$ . Two intersection points  $I_1$  and  $I_2$  are obtained that are the two possible elbow points. Point  $I_1$  (elbow-up) configuration is chosen.

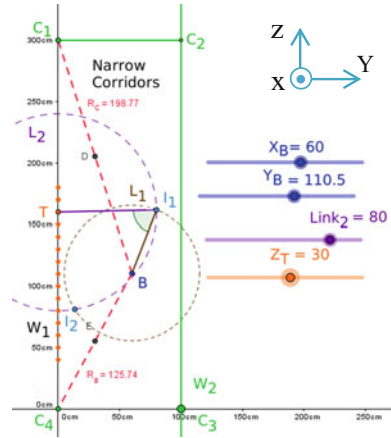
Figure 1 shows the issue of collision of the elbow joint with the wall as well as Link 1 with the mobile platform while performing vertical trajectory. Figure 2 proposes an alternate design of the mobile platform to avoid arm-platform collision. In this design, the red box indicating ancillaries is mounted behind the working plane of the arm and hence does not interfere within the workspace. However, arm-wall collisions can't be avoided. Thus, DR\_Non\_collision is not satisfied. one solution to satisfy the design rule DR\_non\_collision is to infer the new following design rule: "DR\_Link\_1: for avoiding collision, the link length of the first link must not exceed the distance between the base position, B and the front wall. Thus, the input radius for circle  $L_1$  (which controls the link length  $L_1$ ) is given as the X-coordinate of the point B. Hence any change in the position of B automatically modifies link 1. Similarly, to avoid the collision of elbow with wall  $C_2C_3$ , a design rule for second link can be obtained as: "DR\_Link2: link 2 should be less that the width of the corridor".

However, for link lengths obtained by following these two rules, it is impossible to reach both ceiling and ground points by keeping the base position fixed. Hence, need of a vertical shift in the base point B is identified. This adds another joint i.e, a prismatic joint in the base of the robot, hence making the architecture redundant. Thus, redundancy is used to avoid the issue of collision in corridors. Figures 3 and 4 show that the DR\_Env is satisfied. Maximum and minimum vertical displacement of the point B is 180 cm and 100 cm respectively (Figs. 5 and 6).

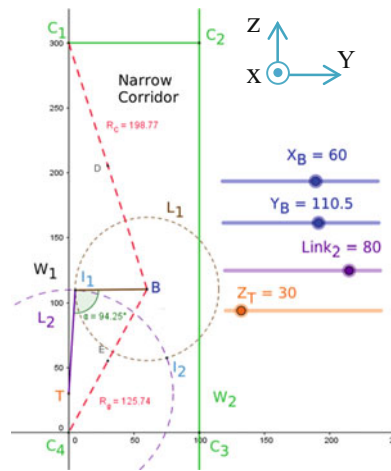
Fig. 2 Arm-wall collisions



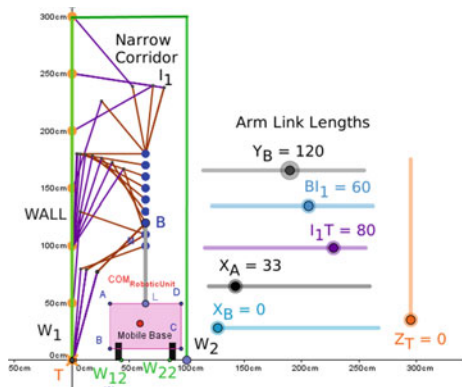
**Fig. 3** Collision avoidance with wall  $C_1C_4$



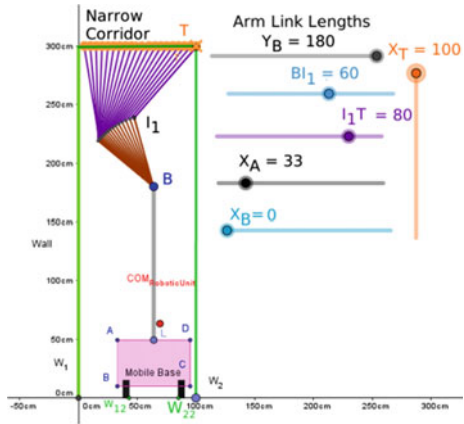
**Fig. 4** Collision avoidance with wall  $C_2C_3$



**Fig. 5** Continuous wall vertical trajectory



**Fig. 6** Continuous ceiling trajectories

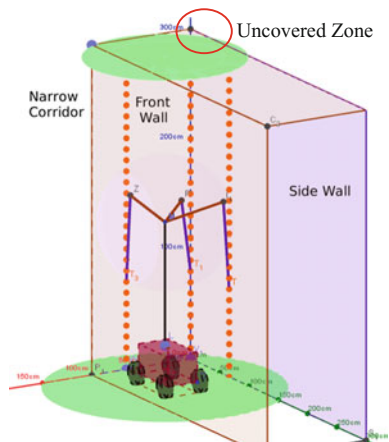


### 4 Estimation of 3-D Workspace

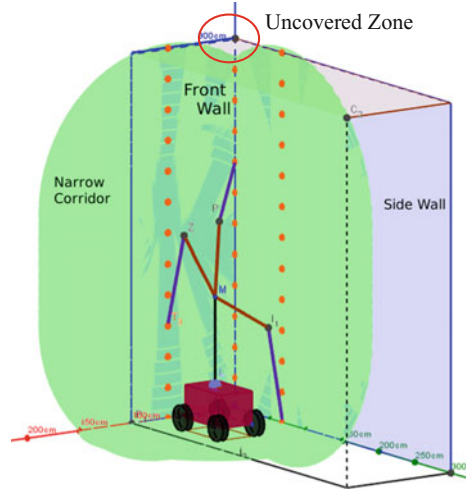
The analysis carried out in Sect. 3 was limited to 2D where only one working plane of the workspace was considered. In this section, a 3D workspace is evaluated using Geogebra 3-D module. The interest of plotting the workspace is to evaluate the area covered by it on the cleaning walls.

In Fig. 7, intersection of the 3D workspace with plane ceiling and ground is presented. The size of the ground and ceiling workspace directly depend on the slider stroke positioning; the ceiling workspace can be enlarged and the ground workspace can be reduced if the slider stroke is positioned higher. A wider ground—workspace for covering the ground all around the mobile base can be seen In Fig. 7. Similarly in Fig. 8, intersections of the workspace with the front and the side wall are presented. Zones not covered inside the workspace, mostly in the corners are highlighted with

**Fig. 7** Intersection of the workspace with ground and ceiling



**Fig. 8** Intersection of the workspace with side and front wall



red circles showing that the workspace will not be completely reached by the arm with the current configuration of the mobile platform. To access such areas, one needs to relocate the platform. However, the designed arm is seen to cover most of the cleaning area without collisions.

## 5 Conclusions

In this paper, an anthropomorphic arm structure is synthesized using inference of design rules and 2D parametrized models in an Interactive Geometric Software (IGS). The synthesis method is based on a loop of series of two stages:

1. Inference of design rules that determine geometrical properties represented in simplified models.
2. The geometric model is simulated. If the design rule is seen to be violated (e.g. collision, singularity ...), a better restrictive design rule is inferred and the loop continues.

The kinematics designed has a sufficient workspace and can perform a 3 m high continuous trajectory while avoiding singularities. The width of the workspace is constrained in the narrow corridor scenario: the most critical pose is when the arm is located on the lateral plane (BYZ) passing through the arm base point. As the RR arm architecture generates too many collisions a redundant PRR kinematics was proposed. Adding redundancy to the originally considered architecture was proved to generate a better compact design avoiding collisions and allowing singularity-free continuous vertical trajectories.

This work proved the interest of combining design rule inference and skeleton modelling using IGS in order to perform dimensional synthesis of an arm for mobile manipulator. The design rules are helpful for converting requirements into geometrical constraints. The IGS is powerful software for expressing design constraints in the Cartesian space and exploring the design space through parametrization. The IGS permitted to extract new design rules that allow local geometrical optimization of the mechanism in the design space.

**Acknowledgements** The Bots2ReC (Robots to Re-Construction, [www.bots2rec.eu](http://www.bots2rec.eu)) project has received funding from the European Union's Horizon 2020 research and innovation program under grant agreement No 687593.

## References

1. Arrouk KA, Bouzgarrou BC, Stan SD, Gogu G (2010) CAD based design optimization of planar parallel manipulators. *Solid state phenomena*, vol 166. Trans Tech Publications, pp 33–38
2. Bostelman R, Hong T, Marvel J (2016) Survey of research for performance measurement of mobile manipulators. *J Res Nat Inst Technol* 121:342–366
3. Bots2ReC The robots to re-construction project. <http://www.bots2rec.eu/>
4. Corves B (2004) Computer-aided lectures and exercises. In: *Proceedings of the 11th world congress in mechanisms and machine science*
5. Fauroux J-C, Sartor M, Paredes M (2000) Using the skeleton method to define a preliminary model for the three-dimensional speed reducers. *Eng Comput* 16:117–130 (Springer)
6. Gosselin C (1992) The optimum design of robotic manipulators using dexterity indices. *Robot Autom Syst* 9:213–226
7. Hohenwarter M (2017) Geogebra, the graphing calculator for functions, geometry, algebra, calculus, statistics and 3D math. [www.geogebra.org](http://www.geogebra.org)
8. Kurtenbach S, Mannheim T, Husing M, Corves B (2013) Content and realization of mechanism theory at RWTH Aachen University. In: *Proceedings of ISEMMS*, pp 39–46
9. Kurtenbach S, Prause I, Weigel C, Corves B (2013) Comparison of geometry software for the synthesis and analysis in mechanism theory. In: *Proceedings of ISEMMS 2013*, pp 193–202
10. Ottaviano E, Ceccarelli M (2002) Optimum design of parallel manipulators for workspace and singularity performances. In: *Proceedings of the workshop on fundamental issues and future research directions for parallel mechanisms and manipulators*, pp 98–105
11. Prause I, Fauroux J-C, Husing M, Corves B (2015) Using geometry sketchers and CAD tools for mechanism synthesis. In: *Proceedings of the 14th IFToMM World Congress, Taipei, Taiwan*
12. Prause I, Kurtenbach S, Weigel C, Husing M, Corves B (2013) Vergleich von dynamisch interaktive Geometrie software fur die massynthese von ebenen getrieben. *Kolloquium Getriebetechnik*, pp 39–56
13. Vijaykumar R, Waldron KJ, Tsai MJ (1986) Geometric optimization of serial chain manipulator structures for working volume and dexterity. *Int J Robot Res* 5:91–103



# Design and Simulation of a Snake like Robot



L. Ciurezu-Gherghe, N. Dumitru and C. Copilusi

**Abstract** This paper present a novel design and a kinematic analysis of a variable neutral-line manipulator. Variable stiffness, as well as a high flexibility are the most wanted characteristics for snake like robots. In the last few years in modern medicine, Minimally Invasive Surgery played an important role. In endoscopic surgery or single-port surgery the main goals are: reducing the operative and post-operative stresses for the patients, fast healing process, reducing the number of days of hospitalization. The paper presents the design and some considerations of a snake like robot unit, followed by preliminary simulation of the proposed model.

**Keywords** Snake like robot · Minimally surgery · Hyper redundant manipulator

## 1 Introduction

Due to their many advantages, such as: flexibility, dexterity, miniaturization, snake-like manipulators are increasingly used in medicine and especially in surgery. Two major categories of manipulators are known in the literature: flexible manipulators and hyper-redundant manipulators. Flexible manipulators are made from sot materials [8, 10, 20], like trunk and tentacle like devices and they are characterized by inherent passive compliance.

Hyper redundant manipulators are characterized by the fact that they contain many rigid elements and joints. The actuation can be done with embedded motors [1],

---

L. Ciurezu-Gherghe (✉) · N. Dumitru · C. Copilusi  
Faculty of Mechanics, University of Craiova, Craiova, Romania  
e-mail: leonard.ciurezu@yahoo.com

N. Dumitru  
e-mail: nicolae\_dtru@yahoo.com

C. Copilusi  
e-mail: cristache03@yahoo.co.uk

or with external actuators and transmission components such as flexible shafts or tendons [7, 11].

Externally actuated manipulators achieve passive compliance as well as flexible ones. These have a property that offers them the possibility of a human-robot interaction, manipulation of fragile objects or multi-arm cooperation, in safe conditions. The pose of the manipulators [10] and the material stiffness determine manipulator's compliance.

Thus, the minimization potential used by snake like manipulators received high attention, because they can be successfully use in minimally invasive surgery (MIS) and natural orifice transluminal endoscopic surgery (NOTES) [9, 14–17]. Due to their abilities, snake-like devices are well suited to enter into patient's abdominal cavity through a small entry point. Researchers wants for snake like devices to achieve high stiffness for high payload operation and exact positioning, and in the same time a low stiffness for safe movement without harming internal organs [13, 16]. The snake like devices present many advantages, like fast healing, minimal or no scarring and low trauma, therefore various stiffening mechanisms have been developed. Solutions that use wire tension and friction between rigid links [3, 7] must overcome an important problem: wire tension is very high, and the links must be strong enough to endure high tension and they occupy a substantial space. For that reason it is difficult to create a compact manipulator. The stiffening force arises solely from the friction between the links.

One possible solution to overcome that drawback can be the use of tunable-stiffness materials, thermally activated materials such as wax or solder [5, 18], particle jamming technology using granular media [2, 6] or field-activated materials like: magnetorheological or electrorheological fluids [4]. These solutions have limitations.

Some researchers [12, 19] believe that those limitations can be overcome by using variable neutral-line mechanism.

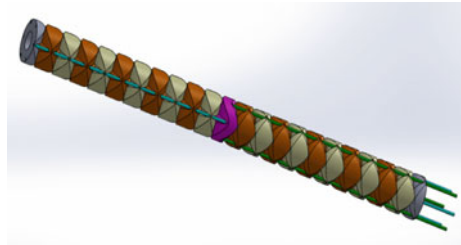
The paper consist on the following sections: first section represents some studies regarding similar snake-like robots and peculiarities of these. On the Sect. 2 a CAD model is designed.

Section 3 represents the kinematic analysis of the proposed solution. Finally, some kinematic data were obtained and these are shown on the Sect. 4. The research ends with final conclusions.

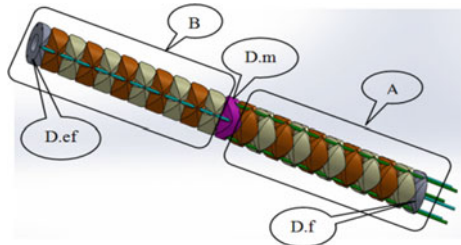
## 2 Snake-like Robot Cad Model

The CAD model was made in SOLIDWORKS 2014. Our solution proposal have a new variable neutral-line mechanism as shown in Fig. 1. One of the main characteristic of this solution consists in the fact that the stiffness can be changed continuously, even while in motion. The snake like manipulator is composed of rigid links actuated by tendons. By varying the tension of the tendons it is

**Fig. 1** Snake like unit CAD model



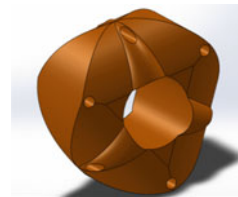
**Fig. 2** Snake like unit segment identification



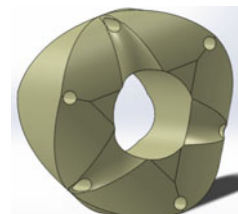
controlled the manipulator stiffness. By its dimensions and construction, the proposed solution is suitable for surgical application such as MIS or NOTES.

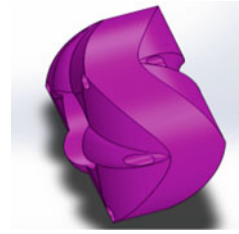
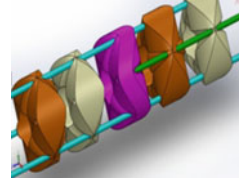
In Fig. 2 is represented the snake-like robot segments, each segment have 10 disks (D), separated by a median disk (D.m) as it can be seen in Figs. 3, 4 and 5, a fixed disk (D.f) and effector disk (D.ef). Disk's contact surfaces are arranged at 120 degrees and each disk has 15 mm in diameter and 10 mm thickness. Total length from the end effector to fixed disk is 176 mm. Each disk has a central hole through which multiple surgical tools and instruments can be inserted. For achieving stiffness and in the same time to be flexible enough the manipulator has the deformable tendons and the disks are rigid links. Each segment is actuated by 3 tendons and for that we use 6 tendons, three for each (Fig. 6).

**Fig. 3** Disk 1



**Fig. 4** Disk 2

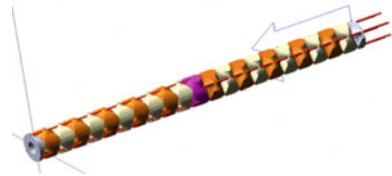


**Fig. 5** Median disk**Fig. 6** Detailed view

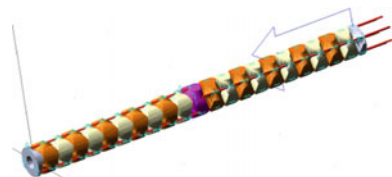
### 3 The Kinematic and Dynamic Analysis for the Proposed Solution

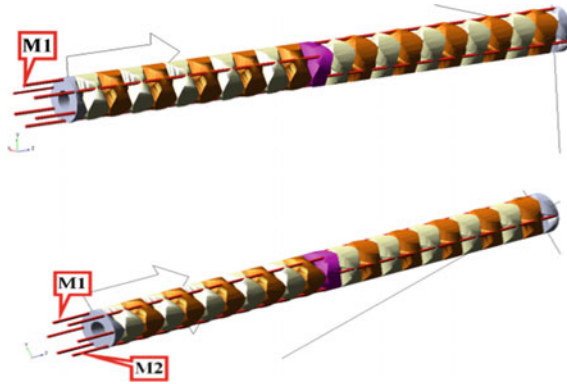
Dynamic analysis was made in ADAMS 2014 software with ADAMS-VIEW module. We imported the snake like robot virtual model from SolidWorks to ADAMS, with a help of an interface by creating a parasolid file. The imported model is shown in Fig. 7, which will be used in kinematic simulations. In order to obtain the center of mass markers, the proper materials were assigned on each component. It was used steel for the disks and tendons. Figure 8 presents the 102 translational joints defined between the disks and tendons. Contact between all the disks was defined with the following input parameters: stiffness of  $1.0E + 005 \text{ N/mm}^2$ ; penetration depth of 0.1 mm; damping factor 10; force exponent of 2.2. In Fig. 9 are presented the two modes of actuation, with one actuator (M1) and after that with two

**Fig. 7** Snake like unit imported model on MSC Adams environment

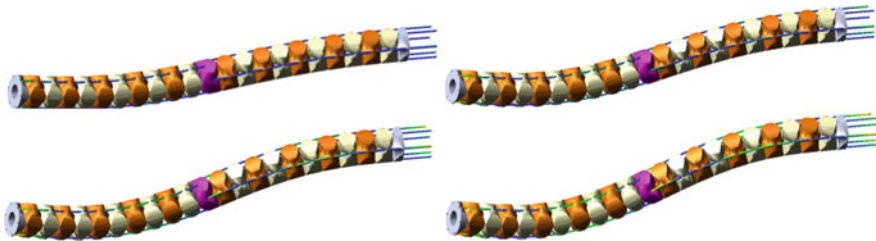


**Fig. 8** Joints definition of the analyzed model





**Fig. 9** A 3D model of the proposed snake like unit manipulator with two modes for actuation



**Fig. 10** Snake like unit snapshots during simulation

actuators (M1 and M2), which were used for kinematic analysis. The following notations were made: D.ef—end effector disk; D.m—median disk; D.f—fixed disk; T1 to T6 actuating tendons in which T1, T2, T3 are attached to the end effector disk and T4, T5, T6 were attached to the fixed disk. The tendons T2 and T6 were pulled by the actuators M1 and M2, and others were left free. Also, it is denoted by: D.ef<sup>1</sup>, D.ef<sup>2</sup>, D.ef<sup>3</sup> interest points on the end effector corresponding tendons T1, T2, T3; D.m<sup>1</sup> to D.m<sup>6</sup> interest points on the median disk corresponding tendons T1 to T6; D.f<sup>1</sup> to D.f<sup>6</sup> interest points on the fixed disk corresponding tendons T1 to T6.

For kinematic analysis all deformable tendons were considered. In order to achieve this, some markers were defined and translated in the proper position. In Fig. 10 are presented some snapshots during the video sequence. Kinematic analysis were done by depending on time which was 1 s and the step size was defined as 0.01.

### 4 Data Processing

The obtained results were represented by the displacement components of each joint and also link. For us the most important results were characterized by displacement components of the end effector and a flexible tendon, the one which was pulled out. Processing and numerical simulation were performed for two dynamic models: first dynamic model involves actuating flexible robot unit with 2 motors (M1 and M2). In this case the deformed shape is a snake like form and the robot workspace is more complex. In this case the oscillations occur in variation diagram of displacement after x-axis of the cross-section plane, mainly when the segment A is deformed. Diagrams were determined from variation depending on time for the center of mass of the end effector (Figs. 11, 12 and 13).

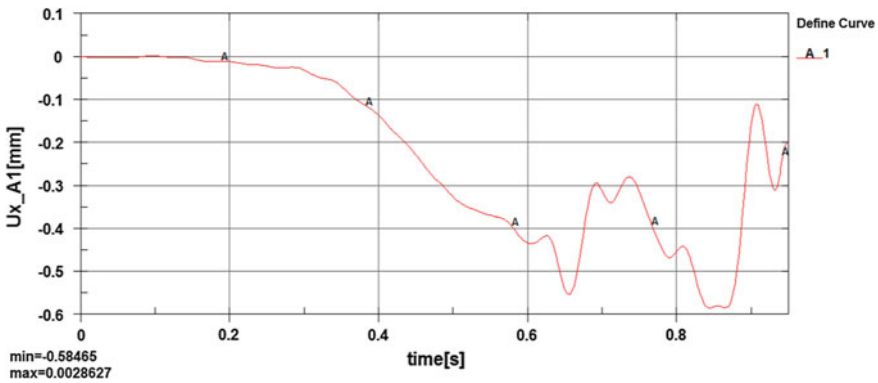


Fig. 11 Variation diagram of displacement on X-axis

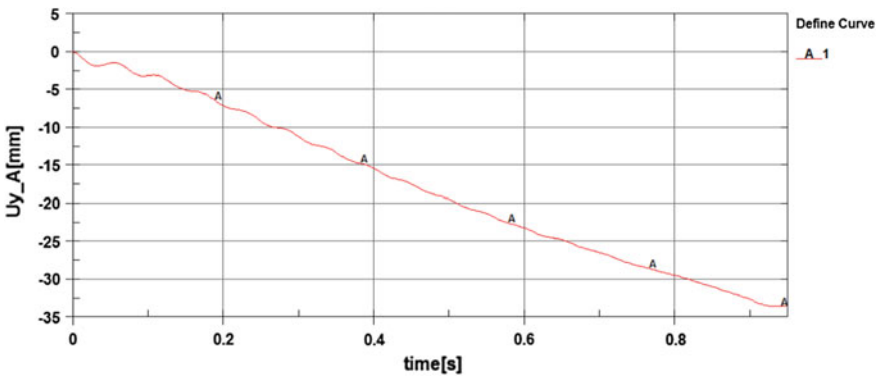


Fig. 12 Variation diagram of displacement on Y-axis

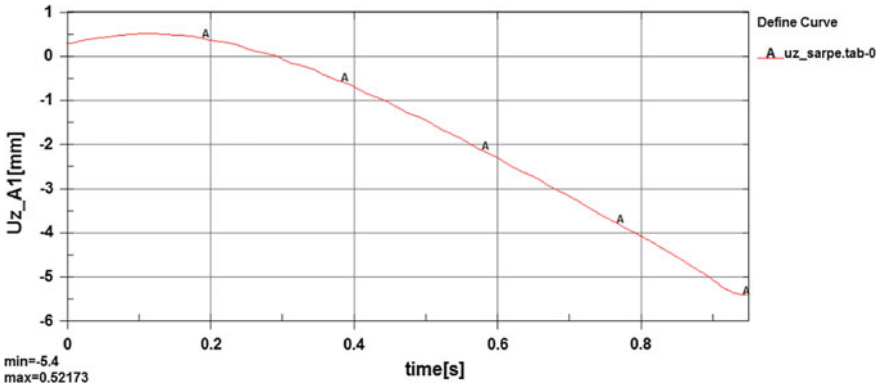


Fig. 13 Variation diagram of displacement on Z-axis

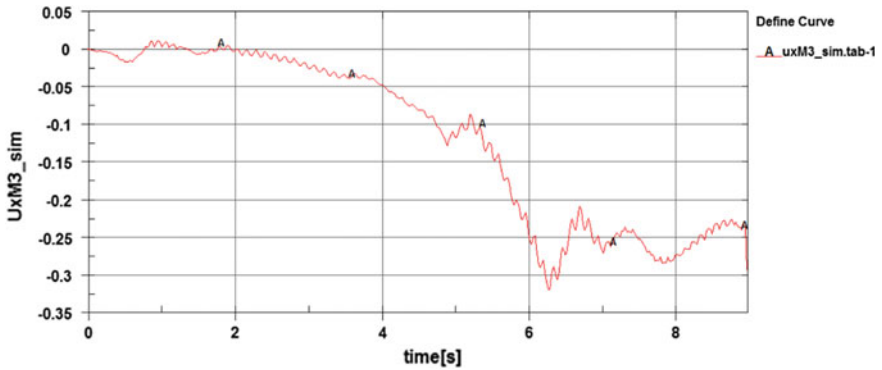


Fig. 14 Variation diagram of displacement on X-axis

Second dynamic model involves a single drive motor (M1) and the free tendons are tensioned by springs. In this case it results a deformed shape of flexible robot unit which can be independently controlled in each of the three planes. We also determined depending on time variation diagram of the end effector center of mass.

The oscillations that occur in the diagram of Fig. 14 (x-axis) were explained by the fact that the robotic system has two sections of different stiffness (Figs. 15, 16 and 17).

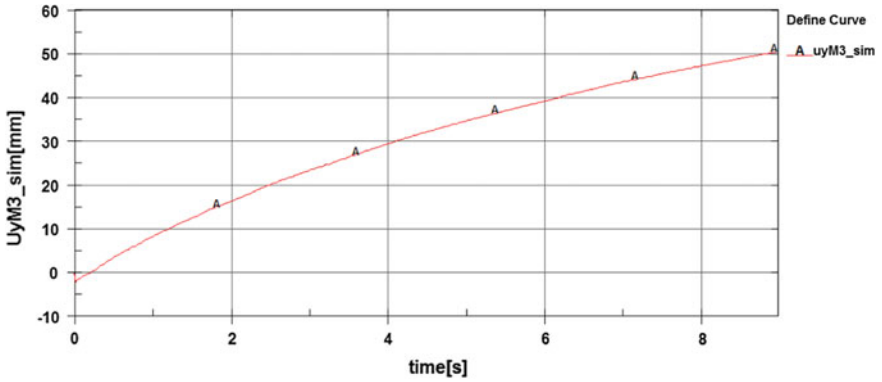


Fig. 15 Variation diagram of displacement on Y-axis

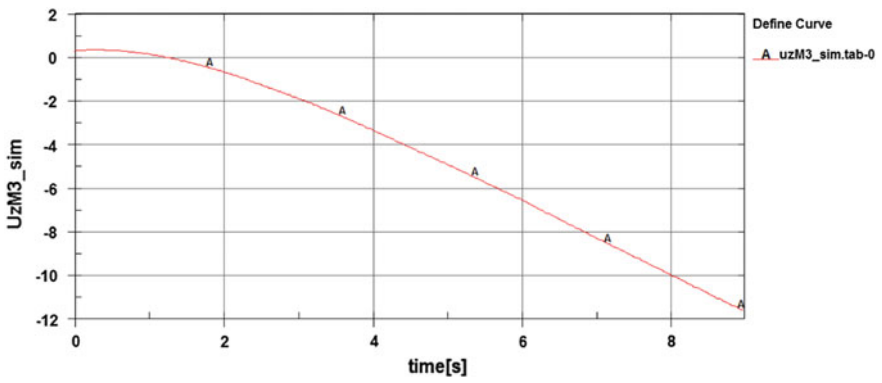


Fig. 16 Variation diagram of displacement on Z-axis

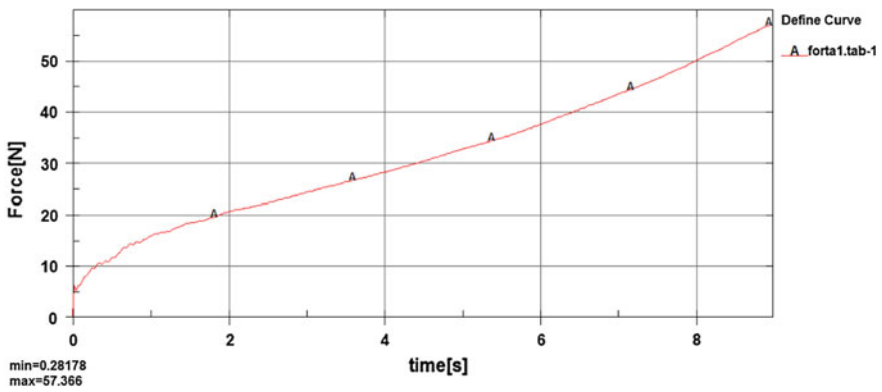


Fig. 17 Motor joint force variation diagram



## 5 Conclusions

Through this research a new model of a snake like unit manipulator is proposed and simulated. The obtained results demonstrate the feasibility study of a new prototype. It can be observed the numerical values of the current results that can certify the use of this prototype on medical domains such as laparoscopy and some surgical intervention with minim invasive characterization. Modeling and numerical simulation of the proposed model was based on overlapping movement of the rigid solid with the deformable solid. The process consists from two stages: modal analysis stage which were determined natural frequencies and vibration modes and respectively dynamic analysis stage. The built model enables laws identification over time variation of the kinematic and dynamic parameters of the rigid or deformable solid movement. CAD model parameterization enables new constructive variants which are easy to adapt to the wanted purpose. Modeling and numerical simulation in dynamic conditions enable the identification of the laws of variation over time of the motor joint forces necessary for controlling motor drive system.

The current results can serve for choosing and dimensioning the actuation system of the proposed snake like unit manipulator.

## References

1. Brown HB, Schwerin M, Shamma E, Choset H (2007) Design and control of a second-generation hyper-redundant mechanism. In: Proceedings of IEEE/RSJ international conference on intelligent robots and systems, San Diego, CA, USA
2. Brown E, Rodenberg N, Amend J, Mozeika A, Steltz E, Zakin M, Lipson H, Jaeger H (2010) Universal robotic gripper based on the jamming of granular material. In: Proceedings of the national academy of sciences USA, vol 107
3. Chen Y, Chang JH, Greenlee AS, Cheung KC, Slocum AH, Gupta R (2010) Multi-turn, tension-stiffening catheter navigation system. In: Proceedings of IEEE international conference on robotics and automation, Anchorage, AK, USA (2010)
4. Chen J, Liao W (2007) Design and control of a magnetorheological actuator for leg exoskeleton. In: Proceedings of IEEE international conference on robotics and biomimetics, Sanya, China, pp 1388–1393
5. Cheng N, Ishigami G, Hawthorne S, Hao C, Hansen M, Telleria M, Playter R, Iagnemma K (2010) Design and analysis of a soft mobile robot composed of multiple thermally activated joints driven by a single actuator. In: Proceedings of IEEE international conference on robotics and automation, Anchorage, AK, USA, pp 5207–5212
6. Cheng N, Lobovsky M, Keating S, Setapen A, Gero K, Hosoi A, Iagnemma K (2012) Design and analysis of a robust, low-cost, highly articulated manipulator enabled by jamming of granular media. In: Proceedings of IEEE international conference on intelligent robots and systems (2012)
7. Degani A, Choset H, Zubiate B, Ota T, Zenati M (2008) Highly articulated robotic probe for minimally invasive surgery. In: Proceedings of IEEE international conference on EMBS, Vancouver, BC, Canada, pp 3273–3276

8. Ding J, Xu K, Goldman R, Allen P, Fowler D, Simaan N (2010) Design, simulation and evaluation of kinematic alternatives for insertable robotic effectors platforms in single port access surgery. In: Proceedings of IEEE international conference on robotics and automation, pp 1053–1058
9. Dogangil G, Davies BL, Baena FR (2010) A review of medical robotics for minimally invasive soft tissue surgery. In: Proceedings of the Institution of Mechanical Engineers. Part H J Eng Med 224(653):653–679
10. Grissom M, Chitrakaran V, Dienno D, Csencsits M, Pritts M, Jones B, McMahan W, Dawson DM, Rahn C, Walker ID (2006) Design and experimental testing of the octarm soft robot manipulator. In: Proceedings of SPIE, Orlando, FL
11. Hannan MW, Walker ID (2000) A novel ‘elephant’s trunk’ robot. In: Proceedings of 2000 IEEE/RSF international conference on intelligent robots and systems, Takamatsu, Japan
12. Lee J, Kim J, Lee KK, Hyung S, Kim YJ, Kwon W, Roh K, Choi JY (2014) Modeling and control of robotic surgical platform for single-port access surgery. In: IEEE/RSJ International Conference on Intelligent Robots and Systems (IROS 2014), Chicago, IL, USA, 14–18 Sept 2014
13. Loeve A, Breedveld P, Dankelman J (2010) Scopes too flexible...and too stiff. IEEE Pulse 1 (3):26–41
14. Navarra G, Pozza E, Occhionorelli S, Carcoforo P, Donini I (1997) One-wound laparoscopic cholecystectomy. Br J Surg 84(5)
15. Pettersson A, Davis S, Grayb JO, Doddc T, Ohlsson T (2010) Design of a magnetorheological robot gripper for handling of delicate food products with varying shapes. J Food Eng 98(3):332–338
16. Shaikh S, Thompson C (2010) Natural orifice transluminal surgery: flexible platform review. World J Gastrointest Surg 2(6):210–216
17. Thompson C, Ryou M, Soper N, Hungess E, Rothstein R, Swanstrom (2009) Evaluation of a manually driven, multitasking platform for complex endoluminal and natural orifice transluminal endoscopic surgery applications. Gastrointest Endos 70(1):121–125
18. Telleria M, Hansen M, Campbell D, Servi A, Culpepper M (2010) Modeling and implementation of solder-activated joints for single-actuator, centimeter-scale robotic mechanisms. In: Proceedings of IEEE international conference on robotics and automation, Anchorage, AK, USA, pp 1681–1686
19. Kim YJ, Cheng S, Kim S, Iagnemma K (2014) A stiffness-adjustable hyperredundant manipulator using a variable neutral-line mechanism for minimally invasive surgery. IEEE Trans Robot 30(2)
20. Webster RJ (2009) Mechanics of precurved-tube continuum robots. Trans Robot 25(1):263–273

# Single DOF Leg Mechanisms Analysis Using GIM Software



F. Pop, C. Pop, E.-C. Lovasz, S. M. Grigorescu and I. Cărăbaș

**Abstract** For developing better walking machines researchers are studying different types of leg configuration. Among the variety of leg configurations designed and tested around the world there are few simple and single DOF leg mechanisms that offer a good and economical solution for artificial locomotion. These configurations were already successfully implemented in the structure of various walking prototypes. Choosing the best leg configuration for building a walking robot to ensure stability and certain step characteristics during motion, it can be done by analysing the kinematic characteristics and the path curve shape described by the end point. For this reason, three single DOF leg mechanisms configurations are chosen for being analysed and compared in terms of kinematic properties. Specialized mechanism simulation software was used.

**Keywords** Leg mechanism · Kinematic analysis · Path curve Simulation

---

F. Pop · C. Pop (✉) · E.-C. Lovasz · S. M. Grigorescu · I. Cărăbaș  
Politehnica University of Timisoara, Timișoara, Romania  
e-mail: cristian.pop@upt.ro

F. Pop  
e-mail: florina.pop@upt.ro

E.-C. Lovasz  
e-mail: erwin.lovasz@upt.ro

S. M. Grigorescu  
e-mail: sanda.grigorescu@upt.ro

I. Cărăbaș  
e-mail: iosif.carabas@upt.ro

## 1 Introduction

Legged locomotion represents a large subject of research in the last period. Many leg mechanisms configurations are analyzed and implemented in the structure of different walking machines. Implementing this type of legged locomotion on robots in order to achieve a better displacement on uneven terrains and hostile environments represents the main advantage when compared to wheel locomotion. The efficiency of these machines is measured and analyzed within different software computer environments and laboratory experiments [9, 11].

Various studies, of several biological leg configurations, regarding locomotion type and walking gaits are used to design and analyze bio-inspired leg mechanisms [3, 4]. It has been observed that some mechanisms can be used for plantigrade type of locomotion and others for digitigrade locomotion [2]. There are also a series of single DOFs leg mechanism configurations that reproduce path curves similar to an animal, an insect or a human. Due to this fact it can be utilized for designing walking machines. There are a series of crank based leg mechanisms such as the pantograph, Chebyshev, Klann and Jansen mechanism. These configurations were implemented in the structure of a variety of walking prototypes and tested in different environments.

A complete and relevant MBD analysis for Chebyshev, Klann and Jansen leg mechanism configurations is presented in [8]. By comparing these relatively simple leg configurations with more complex one that possess more DOF, the advantage of the first category consist in the simple design, reduced DOFs that conducts to simple control and low power consumption.

The aim of this paper consists in the analysis and comparison of three types of crank-based leg mechanisms for developing economical walking machines with better gait locomotion. The mechanisms chosen are Chebyshev lambda-mechanism, Klann and Jansen mechanism. The main criteria for comparison are related to the kinematic properties such as velocity, acceleration and curvature of the end point of leg mechanisms. GIM computer simulation software was used for extracting the results based on the 2D models of the leg mechanisms investigated. This is an open source program that permits to quickly design and perform kinematic analysis for various forms of planar and spatial mechanisms.

## 2 Curvature Analysis. General Approach

For studying the gait pattern of a walking robot, researchers came with different methods regarding path tracking [15]. From tracking the path curve described by robotic legs, conclusions related to the stability and velocity changes during walking are pointed out.

Another specific method for analyzing a path curve described by a leg mechanism consist in determining of few kinematic parameters with help of a specialized

mechanism simulation software. The investigated parameters in this situation are velocity, acceleration and curvature for the end point of leg mechanism. This approach is useful for choosing the best leg mechanism solution before designing a walking robot structure.

Path curvature interpretation can offer information about the rate of speed direction change of the end point during a complete locomotion cycle. In this way, the stance and swing phases of the leg gait can be studied on specific portions of the path. In addition, the initial and final point, that define the stride length during the support phase can be determined.

General properties of the curvature and radius of curvature for planar curves can be found in [10]. A short theoretical approach of the curvature along a path curve  $y = f(x)$  described by a point expressed in Cartesian coordinates  $x$  and  $y$  is presented in Fig. 1.

The curvature  $K$  can be expressed as the rate of change in the direction of the tangent line at that point with respect to arc length  $ds$  [6]. The radius  $r$  of the curvature is defined as the radius of the osculating circle:

$$r = \frac{(1 + (\frac{dy}{dx})^2)^{3/2}}{|\frac{d^2y}{dx^2}|} \tag{1}$$

where:

$$ds = r \cdot d\theta, \quad n = \frac{dy}{dx}, \quad r = \frac{1}{|K|} \tag{2}$$

For an easier interpretation, the path curve can be normalized, and the  $x$  and  $y$  coordinates can be given parametrically by  $x = x(t)$  and  $y = y(t)$ .

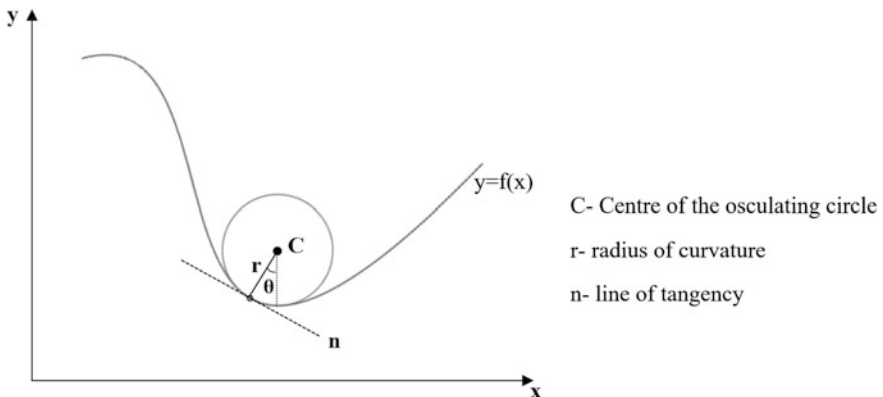


Fig. 1 The characteristics of the curvature along a path described by a point

### 3 Single DOF Leg Mechanisms GIM Analysis

The 2D models and path curves described by single DOF crank-based leg mechanisms are analyzed in this paragraph with help of GIM software [14].

Using this software, the results of the mathematical model computation for the kinematics, dynamics and synthesis of the mechanism can be easily verified. Another advantage that this software consists is the friendly user interface with possibility to simulate the path curve of the elements, to obtain numerical values and graphical results for any point or element analyzed.

#### 3.1 Chebyshev Lambda-Mechanism

Chebyshev type of mechanism was studied and implemented for developing walking machines that reproduce a plantigrade locomotion style [1, 13]. A 2D model realized in GIM of Chebyshev lambda-mechanism is presented in Fig. 2.

In case of Chebyshev lambda-mechanism the input motion is a full crank rotation, while the output is an approximately straight-line motion. The mechanism consists of a four-bar mechanism  $A_0ABB_0$  with an extended coupler  $AM$ .

For designing a walking machine based on this type of mechanism it is important to analyze the path curve described by the end point  $M$  during a complete motion. The simple linkage structure with a single DOF can generate a path curve similar to the one presented in left side of Fig. 2. The curvature of the path is shown in the right.

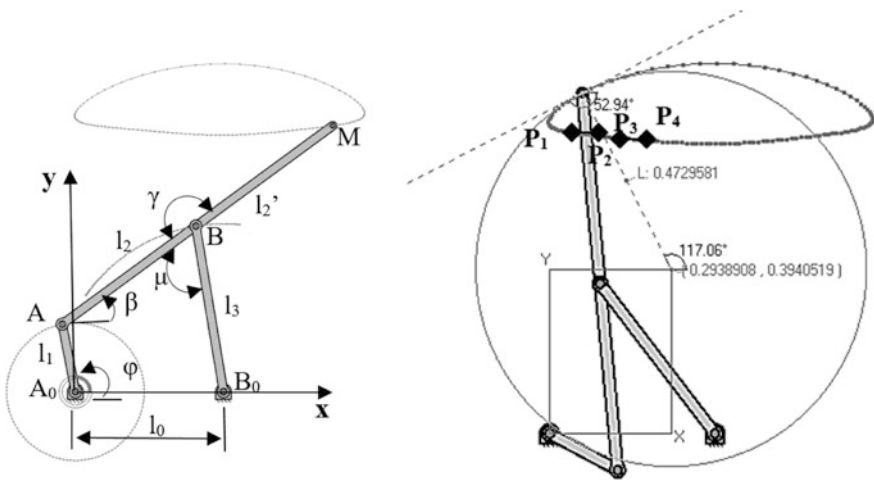


Fig. 2 A 2D model of Chebyshev lambda-mechanism and point M path curvature

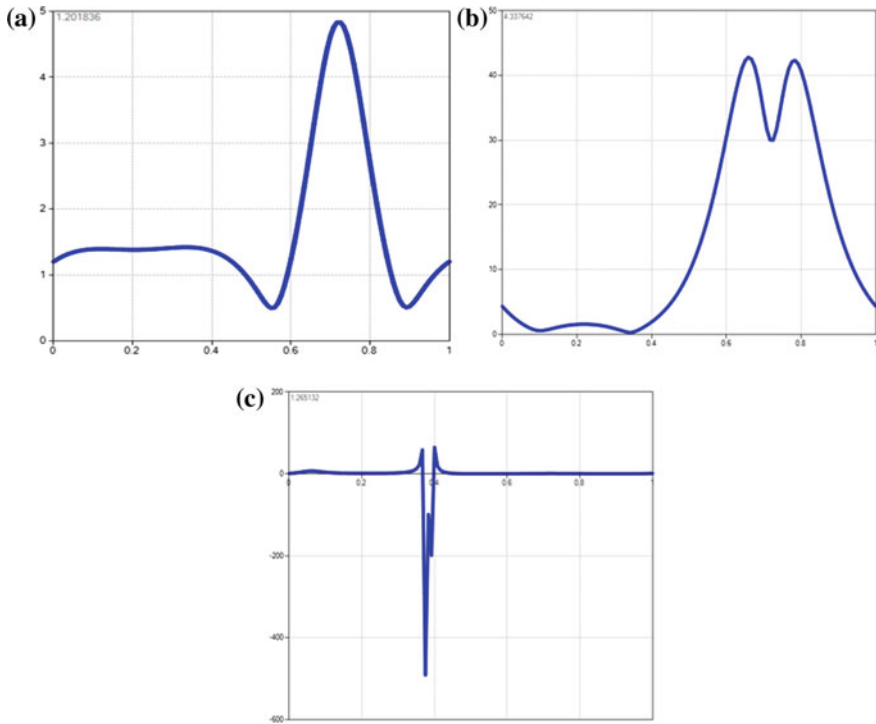


Fig. 3 Graphical results for point M kinematic parameters (a velocity, b acceleration module, c curvature center)

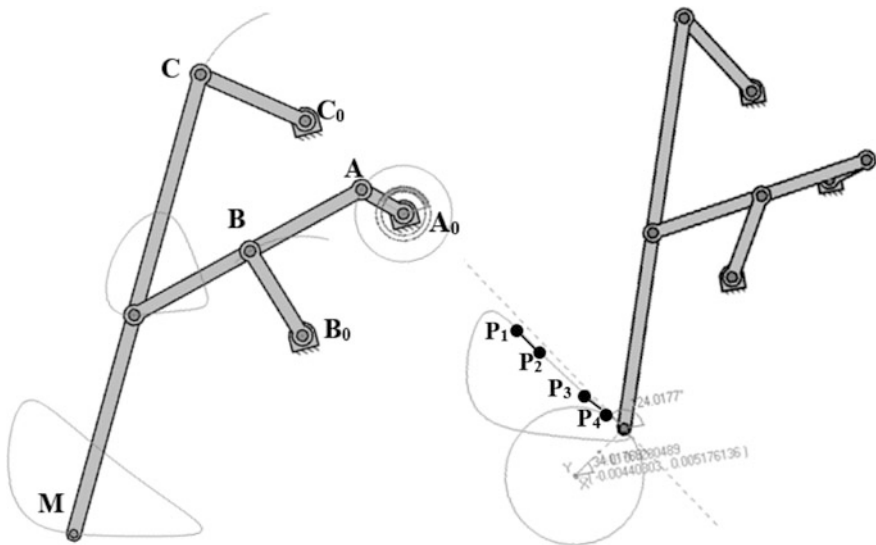


Fig. 4 A 2D variant of Klann leg mechanism and point M path curvature

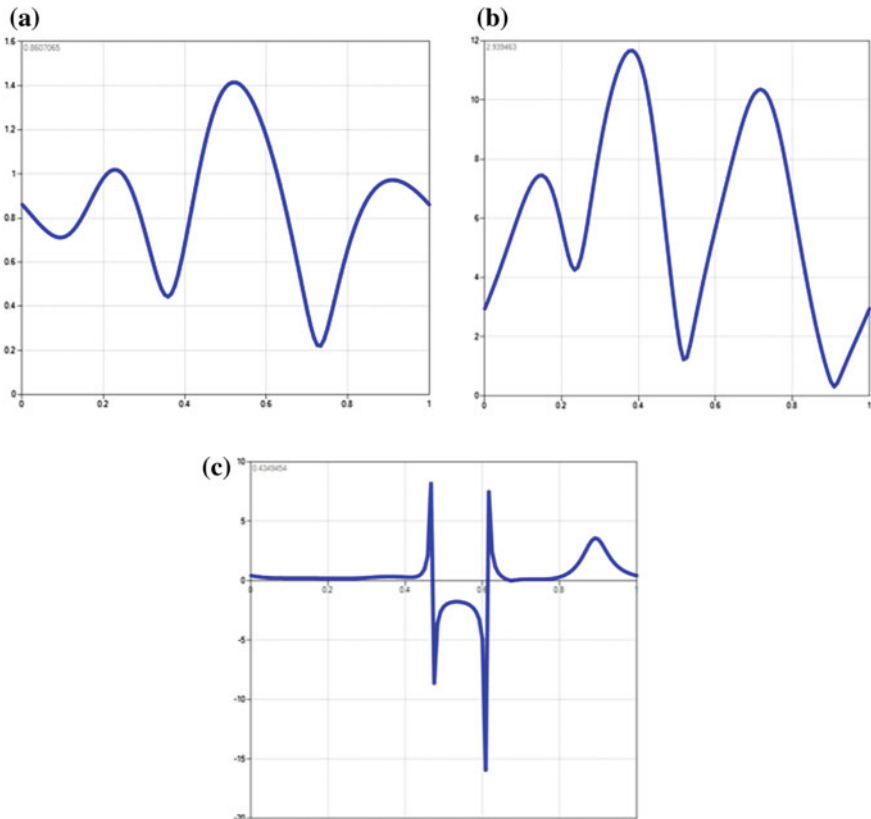
The end point M Cartesian coordinates can be expressed as in Eq. (3):

$$\begin{aligned} x_M &= l_1 \cos \varphi + (l_2 + l'_2) \cos(\beta) \\ y_M &= l_1 \sin \varphi + (l_2 + l'_2) \sin(\beta) \end{aligned} \tag{3}$$

By taking the derivatives of the position Eq. (3), velocity and acceleration of M point can be computed.

The dimensions used for modeling the Chebyshev lambda-mechanism are presented in [13].

The kinematic analysis run through GIM software permitted to obtain the kinematic parameters presented in Fig. 3 recorded versus time during a complete motion cycle.



**Fig. 5** Kinematic analysis results of end point M (a velocity, b acceleration module, c curvature center)



### 3.2 Klann Mechanism

Another crank-based leg mechanism developed by Klann [7], for mimic spider locomotion is analyzed in an analogue manner as the previous one. The 2D model of the leg mechanism along with the path curve and its curvature are presented in Fig. 4. The results for kinematic analysis from GIM environment, regarding the velocity, acceleration and center point curvature modules of the end point M versus time are shown in Fig. 5.

### 3.3 Jansen Mechanism

The twelve-bar crank-based leg mechanism developed by Theo Jansen [5] is also analyzed. It has been observed that this type of leg mechanism mimics an animal locomotion. The 2D model of the leg mechanism and the path curvature are presented in Fig. 6. All link lengths used for this model can be found in [5]. A mathematical model for the kinematic analysis of Jansen leg mechanism including the position equation of M point can be found in [12].

Results from kinematic analysis of this leg configuration performed in GIM are presented in Fig. 7.

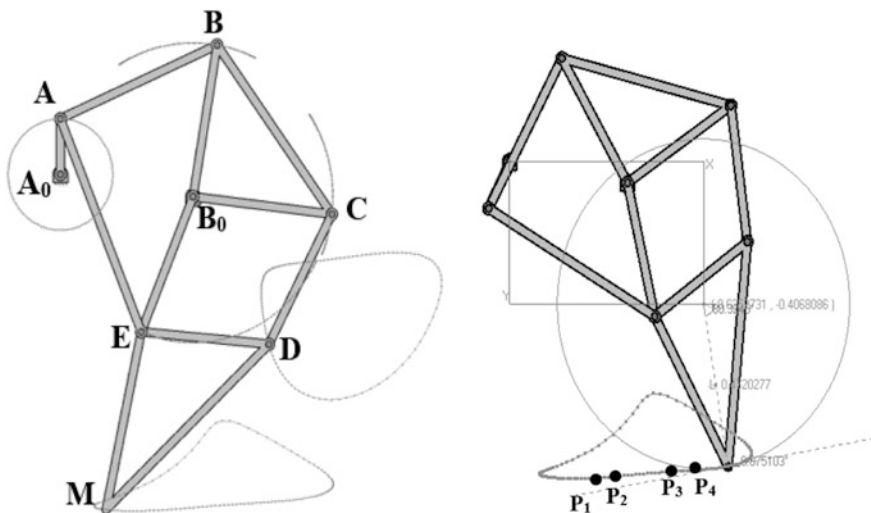
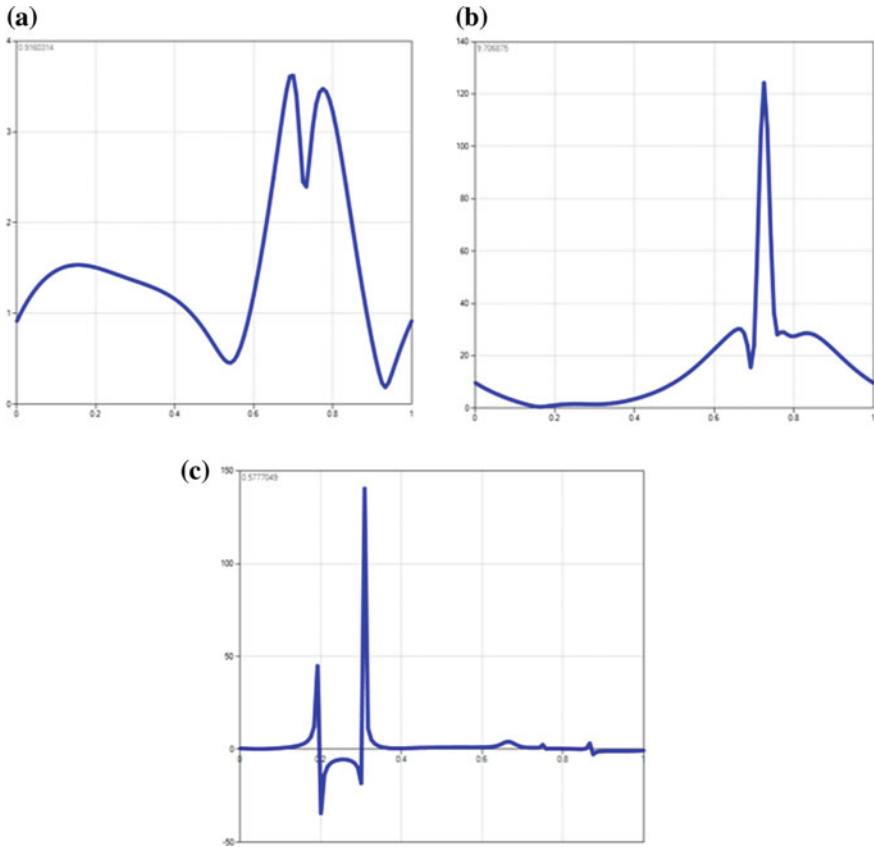


Fig. 6 A 2D model of Jansen leg mechanism and point M path curvature



**Fig. 7** Kinematic analysis results of end point M (**a** velocity, **b** acceleration module, **c** curvature center)

## 4 Conclusions

From the comparative analysis for the kinematic parameters of the three leg mechanism configurations it can be observed the way velocity, acceleration and curvature center varies along with the path. The software permits to visualize the exact values of the curvature radius in all the set of points that correspond to the termination of the leg. All the three leg mechanism configurations were simulated as being actuated by the same revolute motor with a certain speed ratio.

The walking behavior of the leg can be interpreted by identifying the portions of the path that correspond to the stride length and to verify the rate of speed change when the leg changes phases between stance and swing. The results can be used further for path synthesis and optimization.

By examining the point of curvature center module variation during time it can be observed, for example, in case of Chebyshev lambda-mechanism sudden variations of curvature radius appear along the support phase in the portions of the path curve between marked points on Fig. 2.

Analogue, in case of Klann mechanism sudden changes of curvature radius appear during the descending portion between  $P_1$ - $P_2$  points and  $P_3$ - $P_4$  placed along the path curve marked on Fig. 4

In case of Jansen linkage, the peak values of center of curvature variation appear during the support phase. This means the path curve isn't exactly linear at the bottom in the portion of  $P_1$ - $P_2$  and  $P_3$ - $P_4$  segments marked on Fig. 6. This will conduct probably to a stability issue during walking on flat terrain.

As final remarks regarding the support phase of the path curve during walking, Klann mechanism appear to have no curvature variations, while Jansen and Chebyshev have. The largest support path during walking is offered by Chebyshev linkage followed by Jansen. As for step height Klann linkage is more suitable.

For a better understanding of the behavior of the three leg mechanisms, related to the stability and support during walking, a comparison between three walking robots based upon these configurations need to be further analyzed.

Chebyshev type of leg mechanism represents the simplest solution for designing a walking robot while the most complex is Jansen mechanism.

**Acknowledgements** The authors wish to acknowledge Alfonso Hernández, CompMech, Department of Mechanical Engineering, UPVEHU for the permission to use the GIM<sup>®</sup> software. ([www.ehu.es/compmech](http://www.ehu.es/compmech)).

## References

1. Artobolevsky II, Levitsky NI (1948) Models of mechanisms of P. L. Tchebyshev. The complete works of P. L. Tchebyshev, Theory of mechanisms, vol 4, Moscow, Leningrad, AS USSR, pp 227–228 (Russian)
2. Bertram A (2016) Understanding mammalian locomotion: concepts and applications, Wiley Blackwell, p 27. ISBN 9780470454640
3. Gasparetto A, Vidoni R, Zanotto V, Brusa E (2008) Attaching mechanisms and strategies inspired by the spiders' leg, final ESA report contract number: 20272/07/NL/HE. <https://www.esa.int/gsp/ACT/doc/ARI/ARI%20Study%20Report/ACT-RPT-BIO-ARI-066201-Spider%20Attachment-Udine.pdf>
4. Jakimovski B (2011) Biologically inspired approaches for locomotion, anomaly detection and reconfiguration for walking robots, biologically inspired approaches, COSMOS, vol 14, pp 1–3. Springer, Berlin Heidelberg
5. Jansen T (2007) The great pretender. Nai010 Publishers, Rotterdam
6. Jia YB (2016) Curvature, Com. S 477/577, Notes. <http://web.cs.iastate.edu/~cs577/handouts/curvature.pdf>
7. Klann J (2002) Walking device, US Patent 6478314, 12 Nov 2002
8. Komoda K, Wagatsuma H (2016) Energy-efficacy comparisons and multibody dynamics analyses of legged robots with different closed-loop mechanisms. Multibody Syst Dyn, 1–31, Springer. <https://doi.org/10.1007/s11044-016-9532-9>. ISSN: 1384-5640

9. Larsen JC, Stoy K (2011) Energy efficiency of robot locomotion increases proportional to weight. *Procedia Comput Sci* 7:228–230
10. Lawrence JD (1972) *A catalog of special plane curves*. Dover, New York
11. Liang C, Ceccarelli M, Carbone G (2011) Design and simulation of legged walking robots in Matlab environment. *Matlab for engineers—applications in control, electrical engineering, IT and robotics*. InTech, pp 459–492. ISBN 978-953-307-914-1
12. Lovasz EC, Pop C, Pop F, Dolga V (2014) Novel solution for leg motion with 5-link belt mechanism. *Int J Appl Mech Eng* 19(4):699–708
13. Manickavelan K, Balkeshwar S, Sellappan N (2014) Design, fabrication and analysis of four bar walking machine based on Chebyshev's parallel motion mechanism. *Eur Int J Sci Technol* 3(8)
14. Petuya V, Macho E, Altuzarra O, Pinto C, Hernández A (2011) Educational software tools for the kinematic analysis of mechanisms. *Comp Appl Eng Educ*. <https://doi.org/10.1002/cae.20532>. ISSN: 1061-3773. Accessed 24 Feb 2011
15. Zhang F (2007) Curve tracking control for legged locomotion. In: *Proceedings of American control conference, 2007. ACC '07*. IEEE Xplore

# Design and Simulation of a Novel Hybrid Leg Mechanism for Walking Machines



M. Demirel, G. Carbone, M. Ceccarelli and G. Kiper

**Abstract** This paper introduces a novel hybrid structure design that is composed of rigid links and cables for a robotic leg with static walking. The proposed mechanism is characterized by actuated hip joints, passive knee joints and an actuated prismatic foot joint. The foot is the moving platform of the proposed mechanism which possesses pure translational motion due to the passive parallelograms with cables. Kinematic analysis has been worked out for evaluating a typical human-like gait trajectory. A 3-D model has been developed and simulation are made in SolidWorks® environment. Simulation results show that the proposed mechanism is able to perform an ovoid walking cycle of a foot point and the computed actuator torques and forces are in a feasible range for a low-cost and easy-operation design. The simulation results will be used for a prototype construction in a future work.

**Keywords** Walking machines · Hybrid mechanisms · Leg mechanisms  
Static walking simulation

---

M. Demirel (✉) · G. Kiper  
RAML: Rasim Alizade Mechatronics Laboratory,  
Izmir Institute of Technology, Izmir, Turkey  
e-mail: muratdemirel@iyte.edu.tr

G. Kiper  
e-mail: gokhankiper@iyte.edu.tr

G. Carbone · M. Ceccarelli  
LARM: Laboratory of Robotics and Mechatronics,  
DiMSAT – University of Cassino, Cassino, Italy  
e-mail: carbone@unicas.it

M. Ceccarelli  
e-mail: ceccarelli@unicas.it

## 1 Introduction

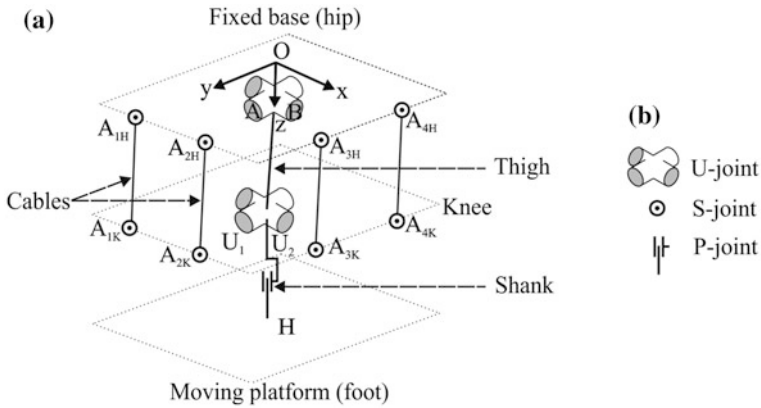
Walking machines are of special interest to researchers since the beginning of the technology of transportation machinery due to their better obstacle avoidance capability than wheeled systems [1, 2]. Most of the existing biped robots are based on serial kinematic architectures with 6-degrees of freedom (dof) legs, such as [3–5, 8, 11]. There are some other walking machines with linkage mechanisms [1, 2]. If human anatomy is considered, human leg movement can be described as parallel manipulator because of the muscular system of a leg [6]. Parallel manipulators have good performance in terms of accuracy, rigidity and payload to weight ratio [7]. However, their workspaces are more limited than serial manipulators. Walking machines with parallel manipulators have successful examples, such as [9, 10].

New leg architectures with less than 6-dof are suggested in [6] which are composed of rigid links and cables (hybrid structures). It is shown that a human leg 6-dof is required for rough terrain adaptability. Less than 6-dof parallel manipulators can be used as leg design for flat surface applications, since orientation dofs are not required for these applications. Even turning requirement of leg can be solved by waist rotation [1]. Walking machines with reduced numbers of dof leg architectures still need to be investigated with new solutions.

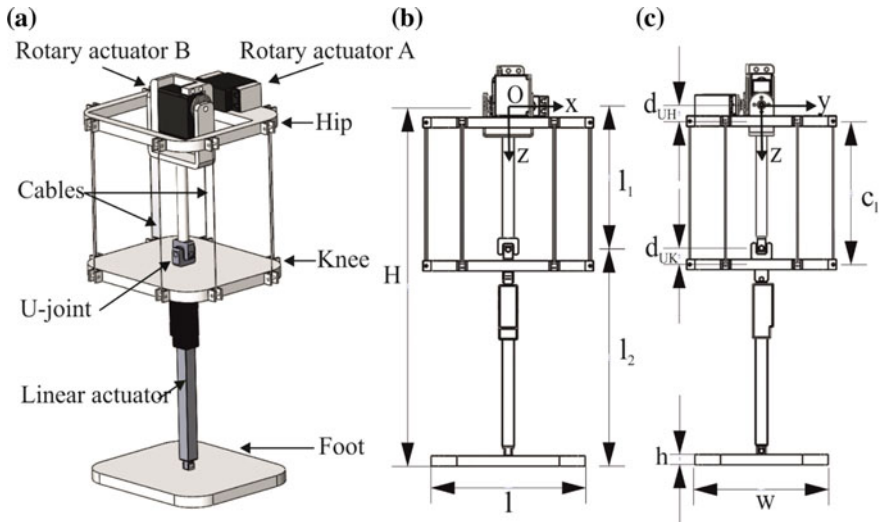
In this paper, a novel hybrid structure leg design with 3 translational dofs is proposed. Kinematic analysis of the proposed architecture has been worked out for evaluating a typical human-like gait trajectory. Kinematic simulation of a three-dimensional (3-D) model has been computed in Solidworks® environment with the aim to evaluate the operation performances of proposed hybrid leg mechanism for walking machines.

## 2 Configuration and a CAD Model

Kinematic architecture of the proposed leg mechanism is (UU-(4-SS))-P as shown in Fig. 1 where underlined joints U and S represent fixed joints. This mechanism consists of a fixed base (hip), a middle platform (knee), a moving platform (foot), two rigid links (thigh and shank) and four passive cables. The thigh connects the hip to the knee by two universal joints (U-Joint) at each end. The shank connects the knee to the foot by a prismatic joint (P-joint). Each passive cable is equivalent to a rigid link and it has spherical joints (S-joint) at each end. UU link provides a rotational and a translational constraint to the knee. Two cables make a parallelogram loop which also provide one rotational constraint to the knee. Hence, combination of UU link and two parallelogram loops ensures to constrained the orientation of the foot. That is, the foot has pure translational motion. U joint on the hip (rotary actuators A and B, see Fig. 2a) and prismatic joint (linear actuator) between the knee and the foot are actuated.



**Fig. 1** Kinematic architecture of the proposed mechanism; **a** a scheme, **b** schemes of the used constraints



**Fig. 2** Proposed leg mechanism; **a** CAD model, **b** dimension parameters of the CAD model from sagittal view ( $xz$  plane) **c** front view ( $yz$  plane)

A 3-D model of the proposed leg mechanism is designed in SolidWorks® environment as shown in Fig. 2a. The main specifications of the proposed mechanism are listed in Table 1. Dimension parameters are indicated and listed in Fig. 2b, Fig. 2c and Table 2, respectively. The distance between the actuated U-joint centers and anchor points of cables ( $A_{1H}$ ,  $A_{2K}$ , etc.) are called as  $d_{UH}$ ,  $d_{UK}$  and they should be equal to each other so that the cable lengths are kept constant and the platform possesses pure translational motion. Eight cables are used in the

**Table 1** Main specifications of the proposed mechanism in Fig. 2

DOF	Weight (kg)	Dimension (mm)	Step size (mm)	Step cycle (s)
3	0.75	150 × 130 × 351	200 × 50	1

**Table 2** Dimension parameters (in mm) and mass values (in grams) of the model in Fig. 2

$l$	$w$	$h$	$l_1$	$l_2$	$d_u$	$c_l$	$H$
150	130	10	140	211	11	140	351

**Table 3** Mass values (in grams) of the CAD model

$m_H$	$m_K$	$m_F$	$m_U$	$m_{L1}$	$m_A$
95	195	195	12	74	80

CAD model instead of four due to the kinematic constraint requirements of the CAD program. Mass values of cables are almost negligible, and therefore addition of four cables does not contribute as additional mass in the simulation. Since cables are passive, they can be installed to the platforms without pulleys. Cables are modeled as cylindrical links by assuming they are always in tension. Angular displacements of the rotary actuators A and B are denoted as  $\theta_1$  and  $\theta_2$ , where displacement of linear actuator is  $L_2$ .  $L_2$  can be expressed in Eq. (1) as the sum of initial length ( $l_2$ ) and stroke ( $s$ ),

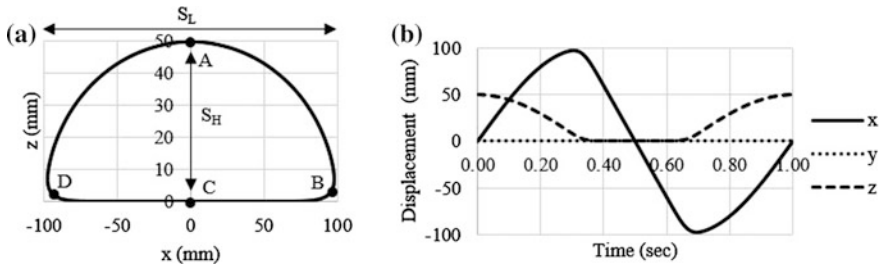
$$L_2 = l_2 + s \quad (1)$$

Mass centers of each platform are set in geometric center of the platforms. Mass values of each component are listed in Table 3, as hip platform ( $m_H$ ), knee platform ( $m_K$ ), foot ( $m_F$ ), universal joint ( $m_U$ ), thigh ( $m_{L1}$ ), rotary actuators ( $m_A$ ), linear actuator ( $m_L$ ). The torques of rotary actuator are denoted as  $\tau_1$  and  $\tau_2$ , where the force of linear actuator is  $F_L$ . Feasibility of the proposed design is ensured by selecting light-weight materials for the platforms (like ABS) and commercial products (U-joint, linear actuator and rotary actuators). These components are modelled properly in a 3-D model for static walking simulation.

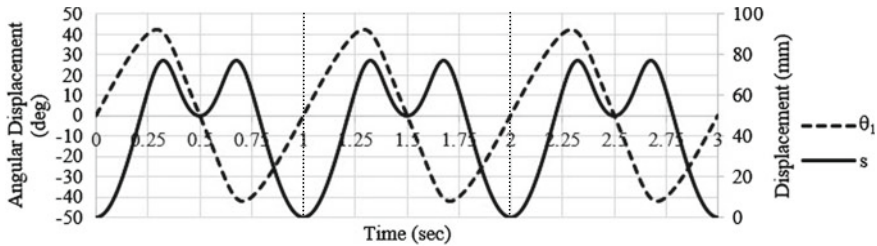
### 3 Simulation Model and Results

The aim of this paper is to confirm feasibility of the proposed hybrid leg architecture for walking machine. Therefore, a kinematic analysis of a human-like walking trajectory is carried out through for the simulation. This trajectory is an ovoid curve as shown in Fig. 3a and it is composed of two phases called as swinging and supporting phases. The straight-line segment represents the supporting phase where the curved segment represents the swinging phase. Two length parameters are enough to describe step cycle as step length ( $S_L$ ) and step height ( $S_H$ ). Walking gait





**Fig. 3** Walking cycle; **a** ovoid curve cycle for  $S_H = 50$ ,  $S_L = 200$  mm, **b** displacement of foot point H



**Fig. 4** Input angular displacement of rotary actuator A ( $\theta_1$  vs. time) and input displacement of the linear actuator ( $s$  vs. time)

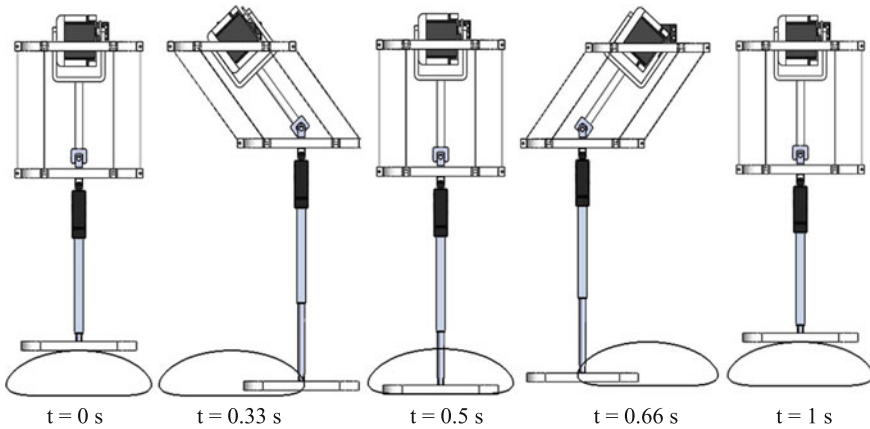
of foot point H is defined as A-B-C-D-A for 1 s step cycle. Displacement of foot point is shown in Fig. 3b a for walking cycle  $S_L = 200$  mm and  $S_H = 50$  mm. Static walking simulation requires only motions of the rotary actuator A ( $\theta_1$ ) and the linear actuator ( $s$ ). Rotary actuator B has no motion ( $\theta_2 = 0$ ) in the planned trajectory.  $\theta_1$  and  $s$  values are calculated by using inverse kinematics equations through Eqs. (2) and (3) according to the position of the foot point H in reference frame (O, x, y, z).

$$\theta_1 = \arcsin\left(\frac{x_P}{l_1}\right) \tag{2}$$

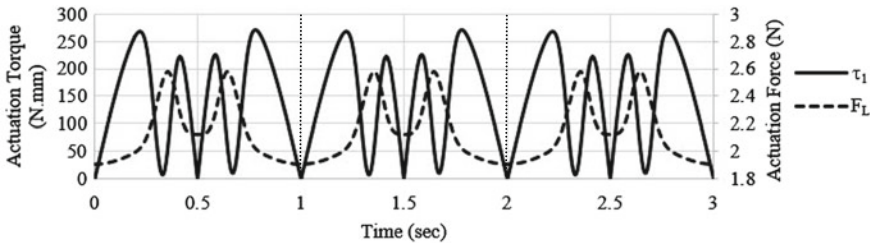
$$s = z_P - l_1 \cdot \cos(\theta_1) - l_2 \tag{3}$$

For a walking cycle of three steps in 3 s, input position data of rotary actuator A and linear actuator are shown in Fig. 4. In particular, it is found,  $\Delta\theta_1 = \pm 42^\circ$  and  $\Delta s = 0-72$  mm. Simulation of three steps is performed in SolidWorks® environment by using “Motion Analysis” toolbox. This toolbox uses MSC Adams® solver. Snapshots of the first step cycle for points A ( $t = 0$  s)—B ( $t = 0.33$  s)—C ( $t = 0.5$  s)—D ( $t = 0.66$  s)—A ( $t = 1$  s) are shown in Fig. 5 from sagittal view.

Computed  $\tau_1$  and  $F_L$  values of the simulation are shown in Fig. 6. Maximum torque and force values of actuators are required at the step phase changes, point B



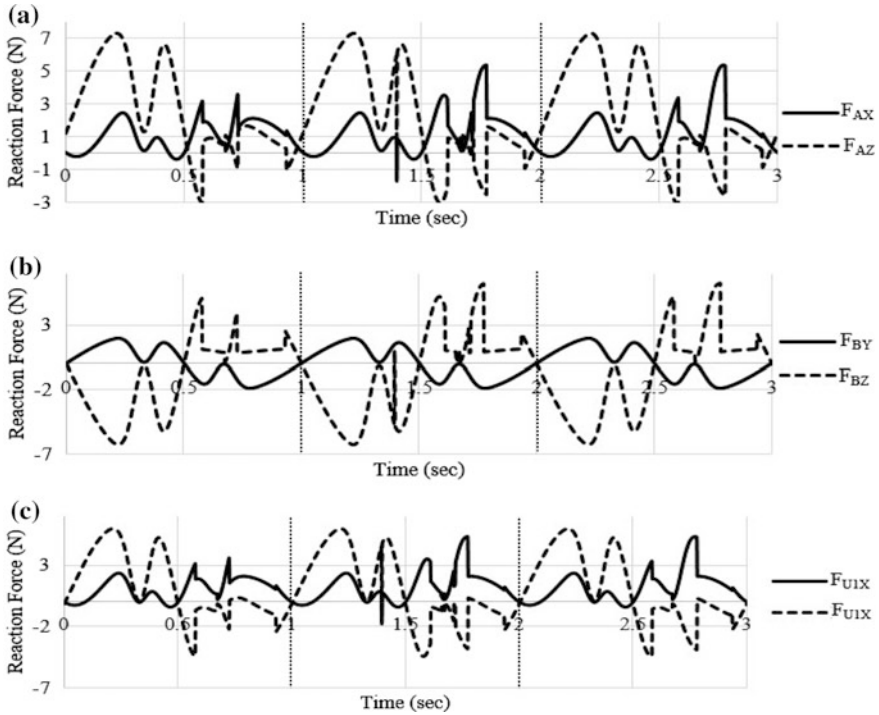
**Fig. 5** Snapshots of the simulated motion in  $xz$ -plane



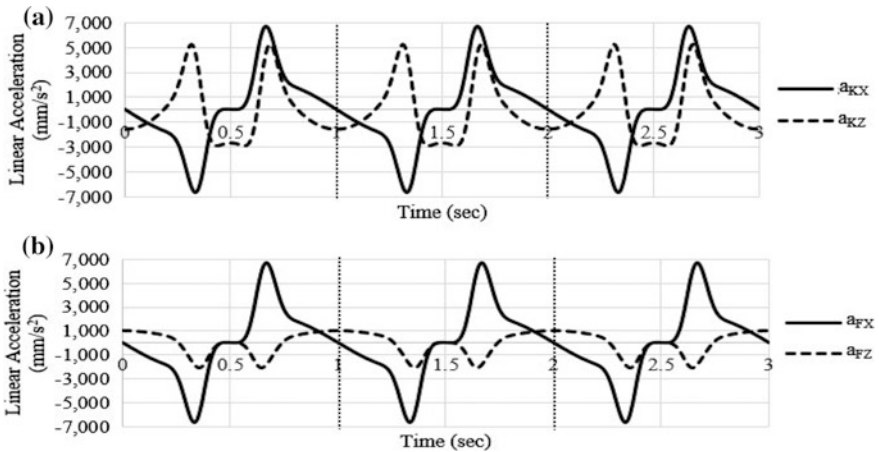
**Fig. 6** Computed actuation torque of rotary actuator A ( $\tau_1$ ) and force of linear actuator ( $F_L$ )

and D:  $\tau_{1\max} = 0.271$  N mm and  $F_{L\max} = 2.6$  N. Computed joint reaction forces of hip joints A, B and knee joint  $U_1$  in  $x$ -,  $y$ - and  $z$ -directions are shown in Fig. 7. Some numerical errors can be seen in Fig. 7a for  $F_{AZ}$  and  $F_{BZ}$ . Maximum joint reaction forces are about 6 N in all revolute joints. Since total weight of the mechanism is about 7.5 N, the computed reaction forces are reasonable. Note that reaction forces are computed without friction.

As mentioned before, mass centers of the platforms are chosen as the geometric centers of the platforms. Acceleration values of these points in  $x$ - and  $z$ -directions are shown in Fig. 8. Maximum speed and acceleration values of center of masses of the knee and the foot are computed as  $V_{KX} = 611$  mm/s,  $V_{KZ} = 305$  mm/s,  $a_{KX} = 6669$  mm/s<sup>2</sup>,  $a_{KZ} = 0.2$  mm/s<sup>2</sup> and  $V_{FX} = 611$  mm/s,  $V_{FZ} = 204$  mm/s,  $a_{FX} = 6669$  mm/s<sup>2</sup>,  $a_{FZ} = 2044$  mm/s<sup>2</sup>. Since there is only translational motion in  $z$ -direction between the knee and the foot platforms,  $a_{KX}$  and  $a_{FX}$  values are equal during the simulation. Maximum values are occurring in step phase changes (point B and D) again. These sudden changes are due to inertial effects of the mechanism.



**Fig. 7** Computed reaction forces of the joints; **a** hip joint A  $F_{AX}$ ,  $F_{AZ}$  **b** hip joint B  $F_{BY}$ ,  $F_{BZ}$  **c** knee joint  $U_1$   $F_{U1X}$ ,  $F_{U1Z}$



**Fig. 8** Computed center of mass accelerations in  $O_x$  and  $O_z$  direction; **a** the knee point, **b** the foot point

## 4 Conclusions

In this paper, a novel hybrid leg mechanism is presented for walking machines. Kinematic analysis of the proposed leg mechanism has been worked out to characterize the operation performance. Static walking simulation is computed in Solidworks® environment and simulation results show that the proposed leg mechanism is able to accomplish a human-like foot step trajectory. Computed torque and force values of the actuators and reaction forces ensure feasibility of the proposed design for a low-cost design. The simulation results will be used for a prototype construction in future work.

**Acknowledgements** Part of this work was developed during an Erasmus visit of the first author at LARM: Laboratory of Robotics and Mechatronics, Cassino University, Italy in 2017.

## References

1. Carbone G, Ceccarelli M (2005) Legged robotic systems. Cutting Edge Robotics, Wien-New York, pp 553–577
2. Ceccarelli M, Kececi F (2015) Designs and prototypes of mobile robots. Momentum Press
3. Kaneko K, Kanehiro F, Morisawa M, Miura K, Nakaoka SI, Kajita S (2009) Cybernetic human HRP-4C, Humanoid robots. In: Proceedings of 9th IEEE-RAS international conference, pp 7–14
4. Kondo H, Morishima A, Ogura Y, Momoki S, Shimizu J, Lim HO, Takahashi A (2008) Algorithm of pattern generation for mimicking disabled person's gait. In: Proceedings of 2nd IEEE RAS and EMBS international conference on biomedical robotics and biomechanics, pp 724–729
5. Lohmeier S, Buschmann T, Ulbrich H (2009) Humanoid robot LOLA. In: Proceedings of IEEE international conference on robotics and automation ICRA'09, pp 775–780
6. Marco C, Giuseppe C (2009) A new leg design with parallel mechanism architecture. In: Proceedings of IEEE/ASME international conference on advanced intelligent mechatronics, pp 1447–1452
7. Merlet JP (2006) Parallel robots (series: solid mechanics and its applications). Springer
8. Rocchi A, Hoffman EM, Fanioli E, Tsagarakis NG (2015) A whole-body stack-of-tasks compliant control for the humanoid robot COMAN
9. Sugahara Y, Endo T, Lim HO, Takahashi A (2002) Design of a battery-powered multi-purpose bipedal locomotor with parallel mechanism. In: Proceedings of IEEE/RSJ international conference on intelligent robots and systems, vol 3, pp 2658–2663
10. Wang M, Ceccarelli M, Carbone G (2016) A feasibility study on the design and walking operation of a biped locomotor via dynamic simulation. *Front Mech Eng* 11(2):144–158
11. Yu Z, Huang Q, Ma G, Chen X, Zhang W, Li J, Gao J (2014) Design and development of the humanoid robot BHR-5. *Adv Mech Eng* 6

# Modular Reconfigurable Robots



M. O. Tătar and C. I. Cirebea

**Abstract** In this paper, the authors present hexagonal and parallelepipedic modules used for reconfigurable mobile robots. These modules are equipped with types of wheels like the classic and omnidirectional type. By combining these modules the authors achieve multiple types of constructive solutions of wheeled mobile robots. By equipping the hexagonal modules with legs the authors propose new development direction in this domain.

**Keywords** Robots • Reconfigurable • Modular • Hexagonal  
Parallelepipedic

## 1 Introduction

The modular robots are composed of modules that can be disconnected and reconnected in different types of arrangements to form new robot which allows new functionalities [7].

Modular robots can be consisting of:

- the same kind of modules, homogeneous modules (unimodular robots);
- two different modules, the modules being heterogeneous (bimodular robots);
- several different modules (multimodular robots).

In the case of heterogeneous modules, they can be active (actuated) or passive (without actuation). Modular robots can be manually reconfigured or auto-reconfigured if the modules are able to connect and disconnect without human intervention.

---

M. O. Tătar (✉)

Technical University of Cluj-Napoca, Cluj-Napoca, Romania

e-mail: Olimpiu.Tatar@mdm.utcluj.ro

C. I. Cirebea

Cluj-Napoca, Romania

e-mail: cclaudyu@gmail.com

These modular robots are of interest because they allow the construction of a wide range of specialized robots, from a set of standard components.

The feature of these modular robots is versatility, robustness and low cost.

Through the achievements presented in this paper, the authors make contributions in the field of these modular reconfigurable robots.

Compared with the robots presented in the literature [3, 4, 8, 9, 12] the ones proposed by the authors have a simple structure, and they are easy to manufacture. The use of these robots may be in education and research.

Further, the work is structured as follows: the second section presents the hexagonal prism modules and the parallelepiped modules, and in the third section the robots made with these modules are presented. Details on the proposed robot control, conclusions and directions of development are presented in sections four and five of the paper.

## 2 The Developed Modules

### 2.1 Prism Hexagonal Modules

The developed module used for making the mobile robots proposed by the authors and presented below are prism hexagonal modules with a 49 mm side and a 45.5 mm height. These modules are made of PMMA and are equipped with wheels.

The synthetic presentation of these modules is made in Fig. 1, thus [1, 2]:

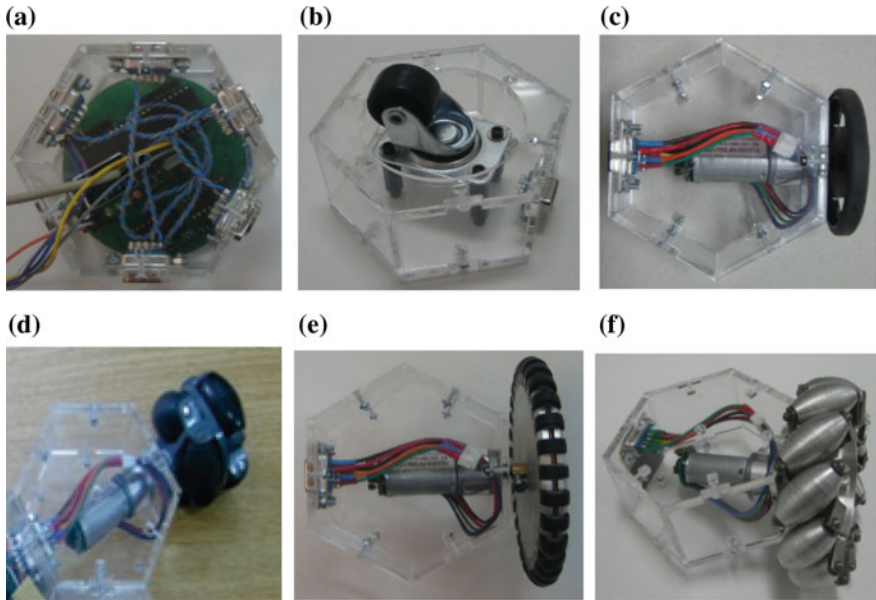
- the passive module for the command,
- passive module with castor wheel,
- active module (motor) with a classic wheel,
- active module (motor) with Swedish wheel, with the rolls at 0 and 45°.

By interconnecting the active and passive modules, a series of modular, re-configurable modular robots with wheels can be obtained. Reconfiguration, in this case, is done manually. Figure 1 shows the types of modules proposed by the authors.

The module structure is as follows:

*The central module* (Fig. 1a): is the module used for commanding robots, it has an electronic circuit component and on the side faces a connection system. The connection system consists of a permanent magnet [13] and a DB9 connector for transmitting data to the modules with which it is to be connected.

*The passive module with unpowered castor wheel* (Fig. 1b): it also has a prismatic shape with a hexagonal base having a side connection system. It has been designed to be used with differential drive robots.



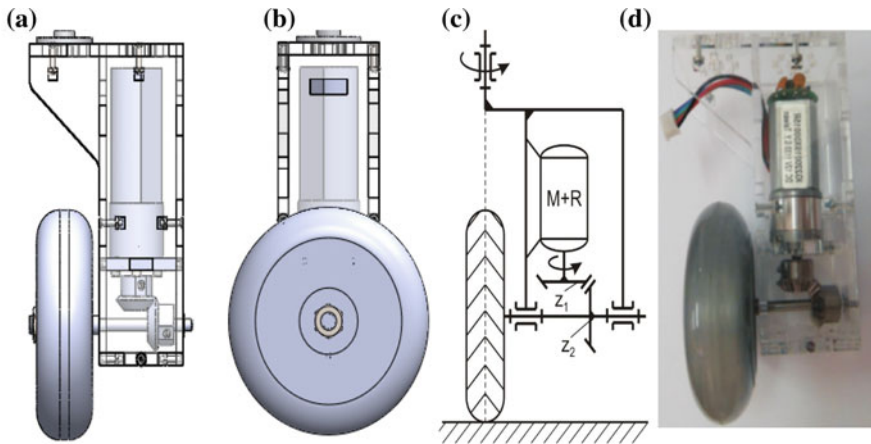
**Fig. 1** Proposed types of modules **a** central module **b** module with unpowered castor wheel **c** module with motorized standard wheel **d, e** module with motorized Swedish wheel  $\gamma = 0^\circ$  **f** module with motorized Swedish wheel  $\gamma = 45^\circ$  (where  $\gamma$ : the angle between the roller axle and the main axis of the wheel)

*The active module with a standard wheel* (Fig. 1c) is composed of a DC motor with reducer (reduction ratio 19: 1) and the encoder. The wheel attached to the module has a 65 mm radius. The module is provided on a side face with a connection system.

*Active modules with omnidirectional wheels* (Fig. 1d–f) also have a DC motor with reducer (19: 1 reduction ratio), encoder and a connection system.

The wheels used in these modules are:

- Universal wheel 1 ( $\gamma = 0^\circ$ ) with a radius of 60 mm having six rollers on each side (Fig. 1d).
- Universal wheel 2 ( $\gamma = 0^\circ$ ) with 55 mm radius consisting of 30 rollers and an aluminum hub. The rolls are perpendicular to the wheel rotation axis and are made of rubber having a diameter of 12 mm and a width of 5 mm (Fig. 1e).
- The Mecanum wheel ( $\gamma = 45^\circ$ ) consists of a circular aluminum hub surrounded by 12 rolls. The rolls each have a diameter of 18 mm in the center and 14 mm at each end and are made of aluminum. The roll radius is 320 mm. The designed wheel has a radius  $R_w = 100$  mm and a width of 35 mm (Fig. 1f) [5].



**Fig. 2** The parallelepiped module with the classic wheel **a, b** 3D model **c** structural diagram **d** functional module

## 2.2 The Parallelepipedic Module

The parallelepiped module has a height of 15 mm and the lower base a square with 38 mm side. The module is attached to a rotary actuated joint that has the rotation axis intersecting the point of contact between the wheel and the ground.

Inside the module is a DC motor with gearbox and conical gears with straight teeth (teeth). The module is fitted with a standard 76 mm diameter wheel. The 3D model, the structural diagram of the module and a photograph are presented in Fig. 2 [6].

## 3 Modular Robots

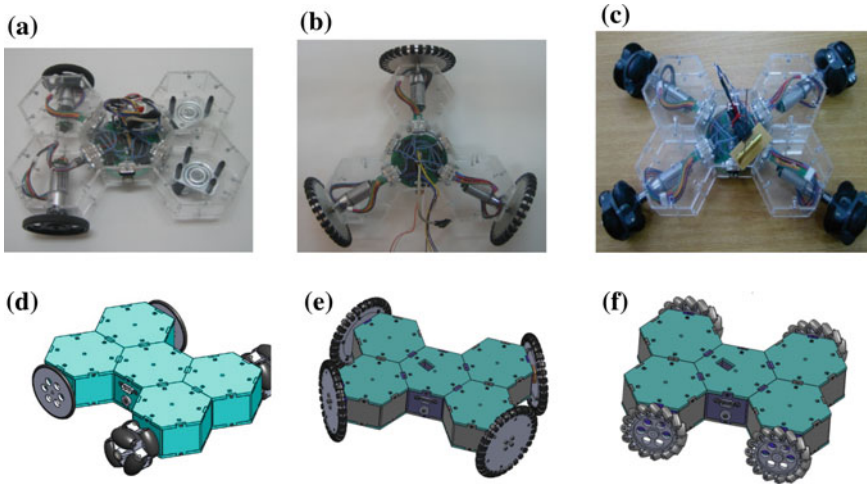
### 3.1 Modular Robots with Hexagonal Modules

By interconnecting the active and passive modules, a series of modular wheel robots can be obtained as presented in Fig. 3.

Among these robots we mention [1, 2]:

- a mobile robot with differential drive,
- a mobile robot with classic wheels,
- a mobile robot with four Swedish wheels,
- a mobile robot with three Swedish wheels,
- a mobile robot with four Mecanum wheels,
- a mobile robot with combined locomotion system (classic wheels and omnidirectional wheels).





**Fig. 3** a–c Manufactured prototypes and d–f other 3D models obtained with the hexagonal modules

Figure 3 shows the prototypes (Fig. 3a–c) and the 3D models obtained using these hexagonal modules (Fig. 3d–f).

The robot presented in Fig. 3a, is a differential driven robot that has a central control module and two modules with castor wheels and two active modules with classic wheels. Similarly, using the central module and corresponding wheel modules as the basis for construction, the other robots shown in Fig. 3e, f are obtained.

### 3.2 Synchronous Modular Robot

By using four modules as shown in Fig. 2, the synchronous robot presented in Fig. 4 was obtained [6].

As can be seen in Fig. 4, four servomotors have to be synchronized for the orientation of the wheels, and four other motors must be synchronized with the movement of the robot.

The four servomotors are arranged on a hexagonal platform located at the top of a robot. This platform is made of PMMA with hexagonal side of 12.5 mm.

The electronic boards required for robot control are also disposed on this platform.

The robot’s wheels have a diameter of 76 mm, the robot height is 22 mm, and the mass of the robot is 1698 g.

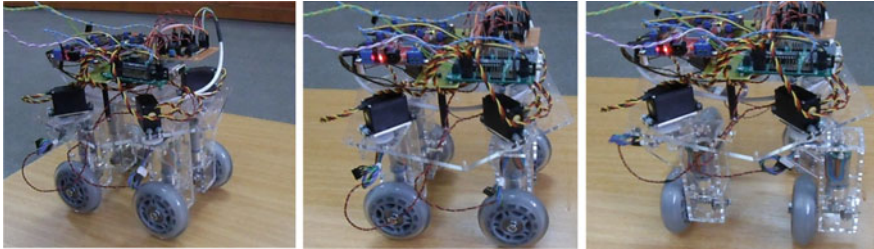


Fig. 4 Synchronous four-wheeled robot

### 3.3 Robots with Combined Modules

By combining the two modules described above, the modular unit shown in Fig. 5 can be obtained.

Robots that can be achieved by combining these two modules are presented below. Thus, Fig. 6a shows a three wheeled modular robot and Fig. 6b a four wheeled modular robot. In both situations, a hexagonal passive hexagonal command module is used in the center.

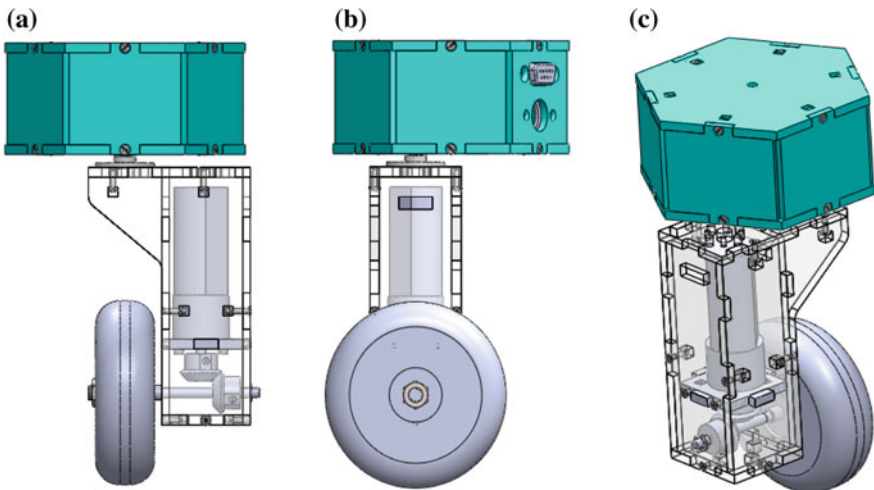
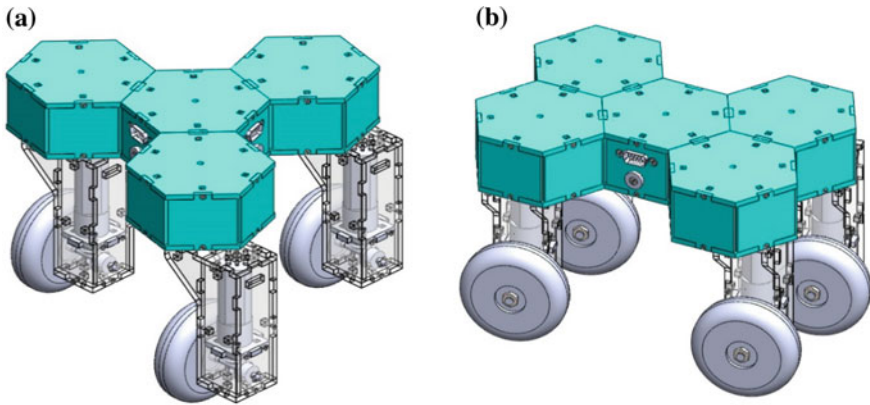


Fig. 5 Modular unit obtained by combining hexagonal and parallelepiped modules



**Fig. 6** Modular robots obtained by combining hexagonal and parallelepipedic modules

## 4 Robots Control

The robots with hexagon modules are controlled using a custom designed electronic boards consisting of an ATMEL microcontroller and auxiliary components.

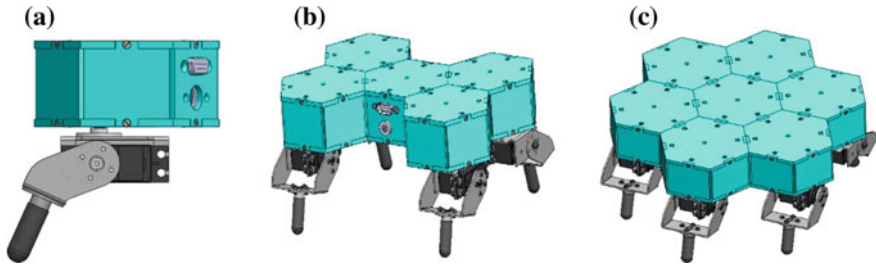
The electronic circuit of the passive central module as well as of the active and passive modules was designed to allow the implementation of an SPI or I2C communication protocol. By doing this, the user is not restricted, having the possibility of choosing the protocol of communication.

The microcontroller inside the passive module is master and deals with the identification of the attached modules and their command as well as the input data received from the user. The microcontroller inside the active module handles data processing from the central module, reads and decodes the quadrature encoder, and generates a PWM signal to control the DC motor [1].

For testing of the prototype synchro-drive, the robot (Fig. 4) was equipped with two microcontroller boards like Cerebot II [10] and SSC-32 [11], where the Cerebot is the master and commands the angle of the four servo motors through serial communication with the slave board SSC-32 (used for servomotors control). Cerebot board is also used to generate PWM signals to command the H-bridge modules, PmodHB5 [10], for the four DC motors and read the encoders for the control loop [6, 10].

## 5 Conclusions

Integrating suitable modular components can easily achieve various particular solutions of reconfigurable robots. In this area of omnidirectional robots, the authors consider that an important direction of research is the development of



**Fig. 7** a Hexagonal module with leg b, c Modular robots with three and four legs

reconfigurable modular robots. The proposed modular robots include the following modules: a passive command module, a passive module with castor wheel, classic wheel active module, a Swedish wheel active modules—with the arrangement of the rollers at  $0^\circ$  and  $45^\circ$ . By interconnecting said modules, a series of modular reconfigurable mobile robots can be obtained.

### 5.1 Directions for Future Development

Development of modules with legs is a line of research that is envisaged by the authors. In this respect, the authors propose CAD models of reconfigurable modular robots with hexagonal modules as shown in Fig. 7. The leg attached to the hexagonal module (Fig. 7a) has 2 DOF, and the robots obtained are with 4 and 6 ft.

There will also be developed modules in which the leg will have 3 DOF or a hybrid type. Another research objective is the development of hybrid robots that combine legs and wheels, and it is also a necessity to equip the robots with sensors.

## References

1. Cirebea CI (2012) Research concerning of the mobile robots for inspection and exploration, Ph.D. thesis, Technical University of Cluj-Napoca, Romania (in Romanian)
2. Cirebea CI, Tătar MO (2014) Development of a modular robotic platform. *Robot Manag* 19 (2):17–22
3. Jorgensen MW, Ostergaard EH, Lund HH (2004) Modular ATRON: Modules for a self-reconfigurable robot. In: *Proceedings of the 2004 IEEE/RSJ international conference on intelligent robots and systems, (IROS 2004)*, vol 2, pp 2068–2073
4. Qiao G, Song G, Wang W, Zhang Y, Wang Y (2014) Design and implementation of a modular self-reconfigurable robot. *Int. J. Adv Robot Syst* 11(3):47. <http://cdn.intechopen.com/pdfs/46412.pdf>
5. Tătar MO, Popovici C, Măndru D, Ardelean I, Pleșa A (2014) Design and development of an autonomous omni-directional mobile robot with mecanum wheels. In: *The 2014 IEEE*

- international conference on automation, quality and testing, robotics, AQTR 2014—THETA 19, May 22–24, Cluj-Napoca, Romania, pp 1–6
6. Tătar MO, Haiduc F, Szalontai A, Pop A (2016) Design and development of the synchronous mobile robots. In: The 2016 IEEE international conference on automation, quality and testing, robotics, AQTR 2016—THETA 20, May 19–21, Cluj-Napoca, Romania; pp 197–202
  7. Yim MH, Duff DG, Homans SB, Roufas KD, Suh JW (2003) Robotic toy modular system. US Patent No 6,605,914. Washington, DC: US Patent and Trademark Office
  8. Yim M, Shen WM, Salemi B, Rus D, Moll M, Lipson H, Chirikjian GS (2007) Modular self-reconfigurable robot systems [Grand challenges of robotics]. *IEEE Robot Autom Mag* 14 (1):43–52
  9. Zykov V, William P, Lassabe N, Lipson H (2008) Molecubes extended: diversifying capabilities of open-source modular robotics. In: IROS-2008 self-reconfigurable robotics workshop, pp 22–26
  10. <http://store.digilentinc.com/>
  11. <http://www.lynxmotion.com>
  12. <http://www.robotpark.com/academy/all-types-of-robots/modular-robots/12>
  13. <http://www.supermagnete.de/eng/pot-magnets-with-countersunk-borehole>

# Velocity Variation Analysis of an Autonomous Vehicle in Narrow Environment



T. M. Girbacia and G. L. Mogan

**Abstract** In this paper is presented an analysis on velocity variation for an autonomous vehicle that is navigating in narrow environment and following a predefined path. The autonomous vehicle is based on an Ackermann steering model that can be simplified to a bicycle dynamic model. For safety navigation along the path the vehicle must taking into account the cinematic and dynamic considerations to avoid lateral slipping and rolling off. In a virtual environment, created with the use of the Virtual Robot Experimentation Platform, was simulated the way in which the Ackermann steering vehicle followed two predefined paths for which the turns have been smoothed by using clothoids as additional curves. The first path consisted in a linear segment, a turn and another linear segment, while the second path consisted in a turn and linear segment. The variation of the velocity was analysed for both scenarios taking into account that in the first one the vehicle accelerates on a straight line, while in the second one it accelerates while steering.

**Keywords** Autonomous vehicles · Ackermann steering · Path planning  
Narrow environment

## 1 Introduction

Determining optimal trajectories for autonomous vehicles is a recent and of high-interest research area and requires both the establishment of an optimal path and the speed with which it has to be followed by the vehicle. Narrow spaces are most often encountered in industrial environments where navigation can become difficult and require a large number of turning maneuvers.

---

T. M. Girbacia · G. L. Mogan (✉)  
“Transilvania” University of Brasov, Eroilor 29, Brasov, Romania  
e-mail: mogan@unitbv.ro

T. M. Girbacia  
e-mail: teodora.girbacia@unitbv.ro

In order to obtain an autonomous vehicle, the main problems that need to be solved regard the path planning, its localization and trajectory following. The path planning solution must take into account the type of environment in which the vehicle navigates and the obstacle placed in it and also constraints imposed by the vehicle [13]. In order to ensure the safety while avoiding obstacles at a low speed a barrier function controller can be implemented [4].

The speed with which the autonomous vehicle is navigating can be determined with a system based on stereo vision concepts using images provided even by a single camera [8]. To control a vehicle with a bicycle dynamic model the longitudinal, lateral and orientation errors are rectified by adjusting the steering angle and the velocity using different methods such as a non-linear approach or a sliding mode approach [1]. A non-linear approach is the model predictive controller which controls the vehicle velocity and steering simultaneously, based on genetic algorithms [5].

Many steering systems for autonomous vehicles have been analyzed to solve the trajectory tracking problem, but the Ackermann steering vehicle presents many advantages such as avoiding front tire slippage and achieving pure rolling [2, 7]. Compared to the differential platform, the Ackermann vehicle cannot turn without forward or backward motion and it has a limited radius of curvature [12].

The article is structured as follows: in Sect. 2 are presented the characteristics of an Ackermann steering vehicle, especially the restrictions regarding the steering speed, in Sect. 3 is presented the virtual environment in which the Ackermann steering vehicle is following a planned trajectory and in Sect. 4 is presented an analysis of velocity variation for two case scenarios in which the vehicle accelerates on a straight line or while steering.

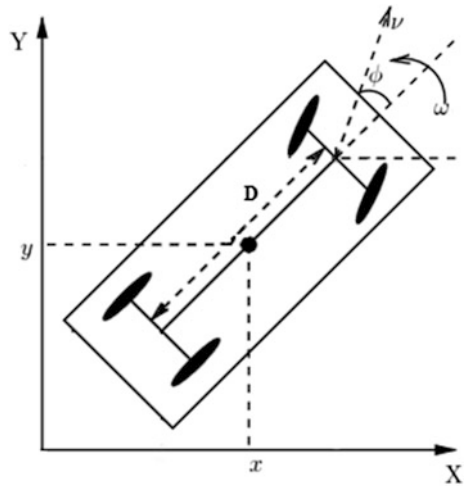
## 2 Ackermann Steering Constrains

The Ackermann vehicle is frequently composed of four wheels and two axels, but its kinematic model can be simplified to a bicycle model. The variables on which this model depends are the longitudinal velocity,  $v(t)$ , and,  $\phi(t) \in (-\frac{\pi}{2}, \frac{\pi}{2})$  which represents the steering angle of the vehicle [9]. These variables determine the way in which the vehicle follows an imposed trajectory, as shown in Fig. 1. The vehicle system is nonholonomic by the restrictions related to the axial movements of the wheels that model this kinematic constraint for the rear axle wheels with the following form:

$$\dot{x} \cos \phi - \dot{y} \sin \phi = 0 \quad (1)$$

From the dynamic point of view, the pattern of vehicle movement on the imposed path must meet engine capacity restrictions, like the maximum speed and acceleration, the friction constrains at the wheel level and the vehicle stability when turning. Also, the safety measures must be taken into account when the vehicle is

**Fig. 1** Kinematic model of an Ackermann steering vehicle



used for person transportation. Maintaining reduced transverse forces to avoid transverse sliding or overturning involves limiting the centripetal acceleration which in turn is dependent on the travelling speed and the radius of curvature of the path.

When an Ackermann steering vehicle is navigating on a curvilinear trajectory with a constant speed  $v(t)$  in the transverse plane, the following forces act on it:

- Centrifugal force:

$$F_{cf} = \frac{m v_t^2}{r} \tag{2}$$

- Gravitational force:

$$G = mg \tag{3}$$

- Frictional force:

$$F_f = \mu m g \tag{4}$$

In these relationships,  $m$  is the mass of the vehicle,  $g$  the gravitational acceleration and  $\mu$  the coefficient of friction between the wheel and the road. For the safe movement of the Ackermann vehicle on the road it is necessary to maintain the balance by simultaneously obeying the lateral no slipping restriction:

$$F_f > F_{cf} \tag{5}$$



and the no rolling off restriction:

$$\mathbf{G} \frac{D}{2} > \mathbf{F}_{cf} H \quad (6)$$

where  $D$  is the distance between the wheels, and  $H$  is the distance from the center of the Ackermann steering vehicle to the tread.

These restrictions, taking into account the equations presented above, are synthesized in the general no slipping and no rolling off on-spill restriction in the following form:

$$\mathbf{v}_t < \min(\sqrt{\mu r \mathbf{g}}, \sqrt{\frac{D}{2H} r \mathbf{g}}) \quad (7)$$

In addition to the above mentioned restrictions, the movement of the Ackermann vehicles must also comply to the restrictions resulting from cinematic and dynamic considerations derived from the driving engine capabilities and the platform stability and comfort conditions:

$$\mathbf{v} \leq \mathbf{v}_{\max}; \mathbf{a} \leq \mathbf{a}_{\max} \quad (8)$$

### 3 Trajectory Planning for an Ackermann Vehicle in a Virtual Environment

In order to achieve continuous movement along the path of a vehicle, especially when necessary to avoid obstacles, the transition between a straight segment and a circle arc is accomplished by using an additional curve. Among these additional curves, the most important are: the clothoids, Bezier or G3 curves. The most important feature of the clothoid is the property that the curve varies linearly with its arc length and this allows the vehicle to move along the route at a constant high velocity even when performing [11]. The main disadvantage of the clothoid is that it requires high computational complexity, however it is more and more often used in planning the paths of autonomous robots and vehicles. [3].

To obtain uniform trajectory, the turns required to bypass the obstacles are composed of: a steering entrance clothoid arc, a circular arc needed to avoid the obstacle and a steering exiting clothoid arc. Therefore the path is composed of elementary trajectories such as: linear segments, clothoid arcs, circular arcs. Taking into account that the vehicle navigates into a narrow environment, the clothoid arc is the maximum permitted by the vehicle [6].

The velocity variation while an Ackerman vehicle makes a turning maneuver in a narrow virtual environment, that requires for the trajectory to be composed of the maximum clothoids provided by the vehicle, is simulated using the Virtual Robot

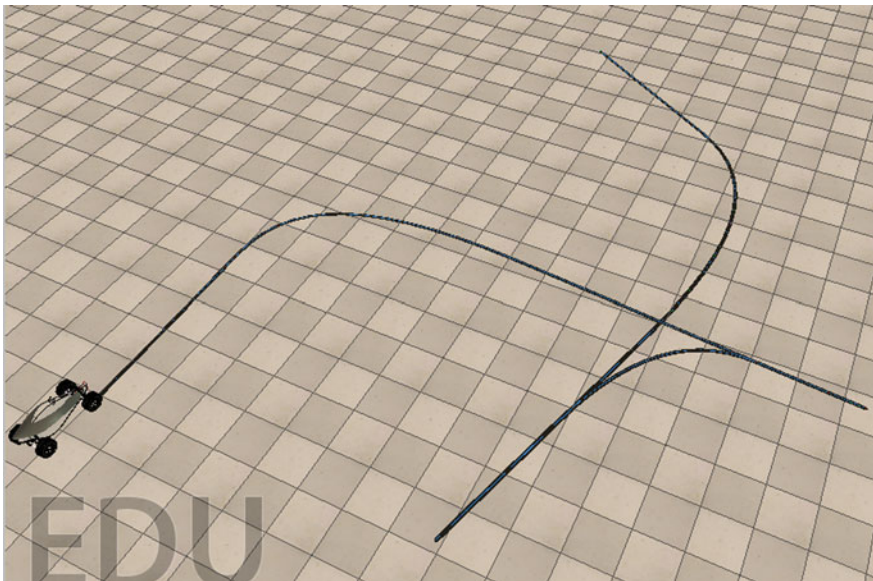
Experimentation Platform (V-REP). V-REP provides the user with numerous facilities for simulating complex scenarios in virtual environments [10].

The virtual environment consists of a resizable floor on which the path is loaded by specifying its component points. The characteristics of the path can be modified to meet the user's requirements.

The starting point of the trajectory is placed in the origin of the virtual environment. Defining the trajectory is accomplished by using path nodes in the virtual environment and is composed of the pumps that delimit the path components. The starting point is located in the origin of the coordinate system of the virtual environment. Furthermore, in the environment can be placed a collection of obstacles that have cuboid shapes with the dimensions established by the user (Fig. 2).

In the virtual environment is loaded a vehicle model with the Ackermann steering system which will follow the trajectory defined by its intermediate points. The virtual vehicle will be located in the origin of the virtual environment coordinate system. The vehicle is controlled by calculating the necessary time of navigating each segment or arch that composes the path by taking into consideration the travelling speed.

For every type of trajectory segment a function was created in Matlab that uses as input parameters the necessary time for reaching the intermediate target point and the maximum velocity, whether the vehicle is driving with constant speed or it varies by accelerating.



**Fig. 2** The experimental virtual environment created with V-REP

### 4 The Experimental Analysis of the Velocity Variation

The experiment consists in analyzing the velocity variation for two case studies. The first one simulates the navigation of the vehicle on a path consisting in a linear segment on which the vehicle accelerates, a turn on which the velocity decreases and another linear segment along which the velocity increases again, as shown in Fig. 3.

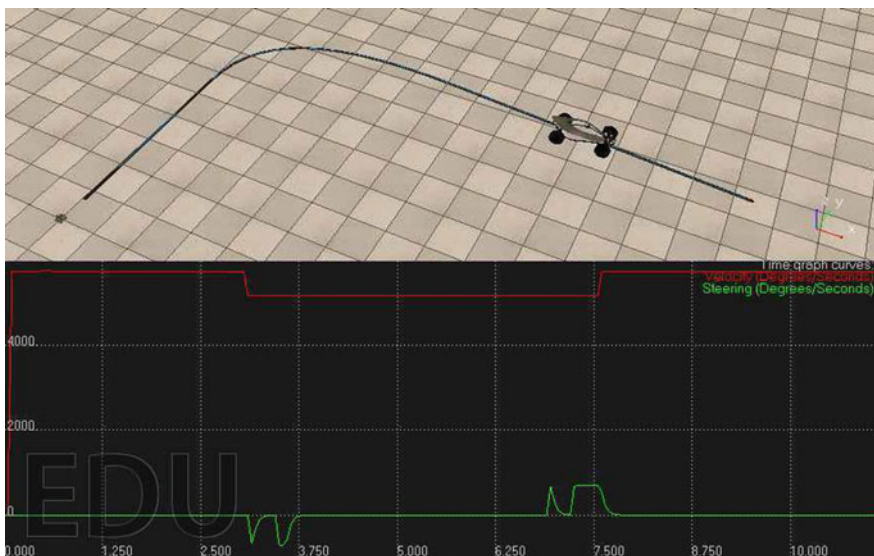
Taking into consideration that the navigation takes place into narrow environment, the turn is made with maximum clothoid arcs. With the red line is represented the variation of the speed of the propulsion motors and with the green line is represented the speed of the motor for steering.

Due to the uniform variation of the curvature, the consequence of the uniform winding on specific trajectories, the centrifugal force has progressive action at curve entry and regression at the exit of the curve.

The second scenario is when the narrow environment does not offer the possibility for the vehicle to accelerate on a linear segment and the driver must accelerate while performing a steering.

In this case the speed reached when the vehicle accelerates is slower than in the first case and is maintain while the steering is completed and afterwards the velocity increases, as shown in Fig. 4.

After analyzing the simulations of the two scenarios presented above, it can be observed that if an obstacle is placed next to the starting position of the vehicle and in order to avoid it the car must accelerate while performing a turn, the velocity



**Fig. 3** Velocity variation analysis when the vehicle accelerates on a linear segment in a industrial narrow environment



**Fig. 4** Velocity variation analysis when the vehicle accelerates while steering in a industrial narrow environment

reached while steering in this case is smaller than the one reached while steering after accelerating on a linear segment.

Also the necessary time to reach the target in the second scenario is greater than the time needed for the first scenario, although the first path is longer than the second one.

## 5 Conclusions

In this paper is presented the analysis of velocity variation for an autonomous vehicle that is navigating in narrow virtual environment. The autonomous vehicle is based on an Ackermann steering model and must taking into account the cinematic and dynamic considerations to avoid lateral slipping and rolling off. The experimental analysis of the velocity variation consists in simulating the way in which an Ackermann steering vehicle follows two predefined paths for which the turns have been smoothed by using clothoids as additional curves. Because the navigation takes place in narrow environments the clothoid arc is the maximum permitted by the vehicle. The difference between the two scenarios is that in the first one the vehicle accelerates on a straight line, while in the second one it accelerates while

steering. The velocity reached while steering in the first case is smaller than the one reached while steering after accelerating on a linear segment, while the time needed for the first scenario is shorter than for the second, although the first path is longer than the second one.

**Acknowledgements** This paper is supported by the Romanian Government, specifically MEN—UEFISCDI authority under the program PNII “Partnerships in priority areas”, under the project number 240/2014—NAVIEYES, supporting the collaboration between the company Route 66 and University Transilvania of Braşov.

## References

1. Alcalá E, Sellart L, Puig V, Quevedo J, Saludes J, Vázquez D, López A (2016) Comparison of two non-linear model-based control strategies for autonomous vehicles. In: 24th mediterranean conference on control and automation, pp 846–851
2. Bascetta L, Cucci DA, Matteucci M (2016) Kinematic trajectory tracking controller for an all-terrain Ackermann steering vehicle, vol 49(15). IFAC-PapersOnLine, pp 13–18
3. Brezak M, Petrovic I (2014) Real-time approximation of clothoids with bounded error for path planning applications. *IEEE Trans Robot* 30(2):507–515
4. Chen Y, Peng H, Grizzle J (2017) Obstacle avoidance for low-speed autonomous vehicles with barrier function. *IEEE Trans Control Syst Technol* 1–13
5. Du X, Htet KKK, Tan KK (2016) Development of a genetic-algorithm-based nonlinear model predictive control scheme on velocity and steering of autonomous vehicles. *IEEE Trans Ind Electron* 63(11):6970–6977
6. Giurgiu E, Girbacia T, Mogan GL (2016) Programming an autonomous mini-vehicle in narrow environments. In: International congress of automotive and transport engineering, pp 729–736
7. Lakkad S (2017) Modeling and simulation of steering systems for autonomous vehicles
8. Lins RG, Givigi SN, Kurka PRG (2016) Velocity estimation for autonomous vehicles based on image analysis. *IEEE Trans Instrum Meas* 65(1):96–103
9. Miah M, Farkas P, Gueaieb W, Chaoui H, Hossain MA (2017) Linear time-varying feedback law for vehicles with Ackermann steering
10. Rohmer E, Singh SP, Freese M (2013) V-REP: a versatile and scalable robot simulation framework. In: IEEE/RSJ international conference on intelligent robots and systems, pp 1321–1326
11. Shan Y, Yang W, Chen C, Zhou J, Zheng L, Li B (2015) CF-pursuit: a pursuit method with a clothoid fitting and a fuzzy controller for autonomous vehicles. *Int J Adv Rob Syst* 12(9):134
12. Shoemaker AK (2016) Nonholonomic control utilizing kinematic constraints of differential and Ackermann steering based platforms (Doctoral dissertation, Virginia Polytechnic Institute and State University)
13. Souissi O, Benatitallah R, Duvivier D, Artiba A, Belanger N, Feyzeau P (2013) Path planning: a 2013 survey. In: Proceedings of 2013 international conference on industrial engineering and systems management, pp 1–8

**Part IV**  
**Mechanism Theory**

# Charts of Relative and Absolute Velocities of Chosen Parts of Plane Biplanetary Gear



J. Drewniak, J. Kopeć, J. Marszałek, K. Stańco and S. Zawisłak

**Abstract** The aim of the present paper consists in presentation of new method of kinematical analysis of biplanetary gear. In particular, the method lies in preparation of charts of relative and absolute tangent velocities of particular gear parts. The algorithm is based on less complicated approach of determination of distribution of relative tangent velocities of wheels and arms of the considered gear. The obtained value of kinematical ratio was additionally achieved via other known analytical method, for comparison.

**Keywords** Cylindrical · Plane biplanetary gear · Chart of relative tangent velocities

## 1 Introduction

The biplanetary gear (Fig. 1) consists of two planetary gears—external (basic, main) and internal [1]. The main gear has the following parts: sun wheel 1 engaged with the satellites (satellite wheels) 2, carrier h and pair of wheels, i.e. satellites 6

---

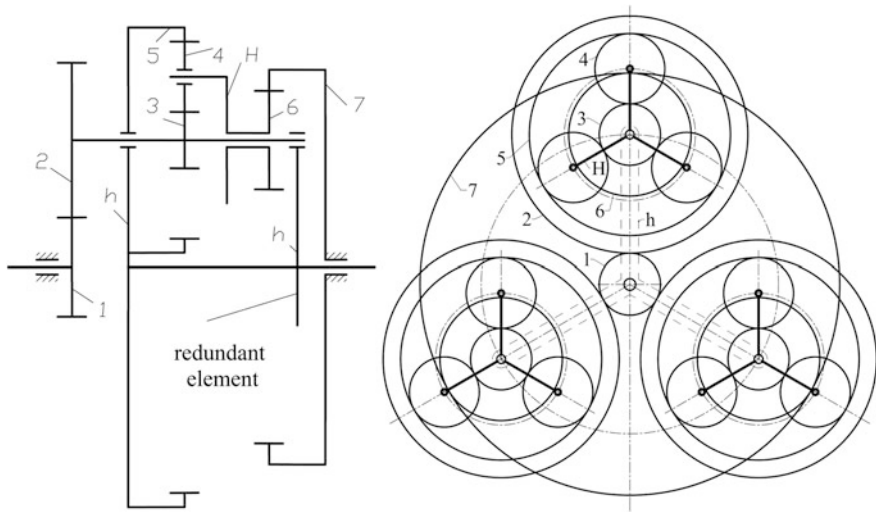
J. Drewniak · J. Kopeć · J. Marszałek · K. Stańco · S. Zawisłak (✉)  
University of Bielsko-Biała, Bielsko-Biała, Poland  
e-mail: szawislak@ath.bielsko.pl

J. Drewniak  
e-mail: jdrewniak@ath.bielsko.pl

J. Kopeć  
e-mail: jkopec@ath.bielsko.pl

J. Marszałek  
e-mail: jmarszalek@ath.bielsko.pl

K. Stańco  
e-mail: kstanco@ath.bielsko.pl



**Fig. 1** Kinematic scheme of biplanetary gear

engaged with the fixed central wheel 7 (ring type, internal toothing). The internal gear is called as satellite epicyclic mechanism [1], consists of sun wheel 3, satellites 4, internal wheel 5 and carrier H. The carrier H drives the satellite wheels 6 belonging to the main gear. The central wheel 5—belonging to the satellite epicyclic mechanism—is simultaneously the carrier *h* of main planetary gear.

The characteristic property of the considered gear (in papers [2, 3], as well) is that the satellites of the epicyclic satellite mechanism perform a complex motion rotating around three axes—own, central of planetary mechanism and central of main epicyclic gear. We can calculate the DoF (degree of freedom or mobility) for the gear as a whole based on the so called Kutzbach formula:

$$W = 3 \cdot n + 2 \cdot p_5 - p_4 = 15 - 10 - 4 = 1, \tag{1}$$

where:  $n = 5$ —number of movable elements/links,  $p_5 = 5$ —number of 5-th class joints (carrier *h* is redundant in the right-hand subsystem—i.e. unnecessary),  $p_4 = 4$ —number of pairs of 4-th class (engagements, gears in mesh).

The DoF value  $W = 1$ , therefore the velocity of a particular gear elements can be determined based on one unknown i.e. the value of input rotational velocity  $n_1$  or input rotational velocity  $n_h$ . The theoretical considerations are general, but the following data has been assumed for the considered biplanetary gear, to give a reader some sense of relationships: teeth numbers  $z_1 = 21$ ,  $z_2 = 81$ ,  $z_3 = 21$ ,  $z_4 = 24$ ,  $z_5 = -69$ ,  $z_6 = 21$ ,  $z_7 = -72$ . Moreover the moduli were considered in the following manner: modulus of geared wheels 1 and 2— $m_{1,2} = 2$  mm, modulus of geared wheels 3, 4 and 5— $m_{3,4,5} = 2$ , modulus of geared wheels 6 and 7— $m_{6,7} = 4$ ,



respectively. The input rotational velocity is equal  $n_1 = 1470 \text{ rev/min}$ , whereas angular velocity  $\omega_1$  can be recalculated:

$$\omega_1 = \pi \cdot n_1 / 30 = \pi \cdot 1470 / 30 = 153,938 \text{ rad/s.} \quad (2)$$

## 2 Kinematic Ratio—Chart of Velocities

Charts of velocities can be recognized as an additional approach to the classical kinematical calculations for particular elements of planetary gears performed by means of the Willis formula. They can give an additional insight into the operation behavior of a particular mechanism. In case of kinematic analysis of the biplanetary gears, the graphic-analytical method, more precisely the vector method, consisting in determination of charts of velocities has not been considered in known references, at all. The cause of neglecting is a necessity of an analysis of kinematics of a gear taking into account the relative motions, because the gear poses two carriers—external  $h$  and internal  $H$ , respectively. Distribution of velocities can be presented in more clear and simple way i.e. on front view of geared wheels belonging to two considered gears. Additionally, the algorithm of preparation of the charts of velocities is based on the adequate approach, therefore at the beginning the method of distribution of velocities in the front view of the geared wheels will be discussed.

We are looking for the output rotational velocity  $n_h$  of the biplanetary gear (i.e. rotational velocity of the external carrier  $h$ ), and simultaneously the kinematical ratio of the gear  $i_{1,h}^7$ :

$$i_{1,h}^7 = (n_1/n_h)_{n_7=0} = (\omega_1/\omega_h)_{\omega_7=0} \quad (3)$$

Unfortunately, the set (given) angular velocity  $\omega_1$  cannot be directly used for determination of kinematical ratio of the biplanetary gear neither the method of determination of distribution of velocities nor the method of velocities' charts. In case when we are looking for the output angular velocity  $\omega_h$  of the carrier  $h$ , we do assume that its value is  $\omega_h = 1 \text{ rad/s}$  and oriented e.g. right. Next, we consider the relative motion of all gear elements in regard to the external carrier  $h$ . Thereby, we enter the relative velocities for the gear elements  $\omega_j^h$  (in regard to the external carrier  $h$ ):

$$\omega_j^h = \omega_j - \omega_h \quad \text{dla } j = 1, 2, 3, \dots, 6, 7, h, H. \quad (4)$$

For example, the relative angular velocity of the carrier  $h$  in relation to the carrier  $h$  is obviously equal to:

$$\omega_h^h = \omega_h - \omega_h = 0, \quad (5)$$

Having the established relative angular velocity  $\omega_7^h = \omega_7 - \omega_h = \omega_7 - 1 = -1$  rad/s of wheel 7 (i.e. directed left), it is possible to calculate the relative tangential velocity  $v_{7,6}^h$  of wheel 7, in the contact point with wheel 6 (Fig. 2):

$$v_{7,6}^h = \omega_7^h \cdot |r_7| = 0,5 \cdot \omega_7^h \cdot m_{6,7} \cdot |z_7|, \tag{6}$$

where radius of pitch circle  $|r_7|$  of wheel 7 is equal  $|r_7| = 0,5 \cdot m_{6,7} \cdot |z_7|$ .

Obviously, the relative tangential velocities  $v_{7,6}^h$  of wheel 7 and velocity  $v_{6,7}^h$  of wheel 6, in its common contact point are equal (taking into account the values):

$$v_{7,6}^h = v_{6,7}^h. \tag{7}$$

Current center of rotation of the carrier  $H$ —in its relative rotational movement—is the immovable axis of wheels 2 and 3 (in accordance with the condition (4)). Distributions of relative tangential velocities  $v_{H,4}^h$  and  $v_{6,7}^h$  of end points on carrier  $H$ , for the considered case, are shown in Fig. 2. Furthermore, based on the Tales formula, we can established the relationship between these velocities:

$$v_{H,4}^h / r_H = v_{6,7}^h / r_6, \tag{8}$$

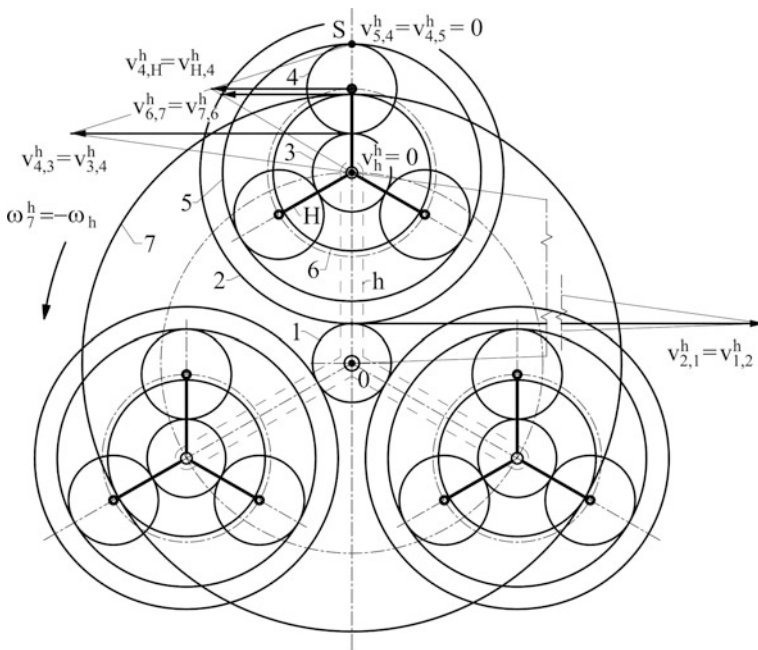


Fig. 2 Relative tangential velocities of wheels of biplanetary gear

therefore relative velocity  $v_{H,4}^h$  of the endpoint of carrier  $H$ , in consequence  $v_{4,H}^h$  velocity of the center of satellite 4 (based on  $v_{H,4}^h = v_{4,H}^h$ ) is equal to:

$$v_{H,4}^h = v_{4,H}^h = v_{6,7}^h \cdot r_H / r_6 = \omega_7^h \cdot |r_7| \cdot r_H / r_6 = 0,5 \cdot \omega_7^h \cdot m_{3,4,5} \cdot |z_7| \cdot (z_3 + z_4) / z_6, \quad (9)$$

where:  $r_H = (d_3 + d_4) / 2 = 0,5 \cdot m_{3,4,5} \cdot (z_3 + z_4)$  and  $r_6 = 0,5 \cdot m_{6,7} \cdot z_6$ .

Current center of rotation of the internal satellite 4 is its contact point with wheel 5 (in fact, being a part of the external carrier  $h$ ), therefore it is possible to determine the tangential velocity of satellite 4 being in mesh with sun wheel 3 (Fig. 2)—based on the following equation:

$$v_{4,H}^h / r_4 = v_{4,3}^h / (2 \cdot r_4), \quad (10)$$

therefore we can write:

$$v_{4,3}^h = 2 \cdot v_{4,H}^h = \omega_7^h \cdot |r_7| \cdot r_H / r_6 = \omega_7^h \cdot m_{3,4,5} \cdot |z_7| \cdot (z_3 + z_4) / z_6. \quad (11)$$

Due to the equivalence  $v_{4,3}^h = v_{3,4}^h$ , according to Fig. 2, relative angular velocity  $\omega_3^h$  of sun wheel 3 is equal to:

$$\omega_3^h = v_{3,4}^h / r_3 = 2 \cdot \omega_7^h \cdot m_{6,7} \cdot |z_7| \cdot (z_3 + z_4) / (m_{6,7} \cdot z_6 \cdot z_3). \quad (12)$$

where pitch radius of wheel 3 is equal to  $r_3 = 0,5 \cdot m_{3,4,5} \cdot z_3$ .

Relative angular velocity  $\omega_3^h$  of internal sun wheel 3 is equal to relative angular velocity  $\omega_2^h$  of external satellite 2:

$$\omega_3^h = \omega_2^h. \quad (13)$$

For known relative angular velocity  $\omega_2^h$  of satellite 2, we can calculate relative tangential velocity of contact point of wheel 2 with sun wheel 1 (Fig. 2):

$$v_{2,1}^h = \omega_2^h \cdot r_2 = \omega_7^h \cdot m_{1,2} \cdot z_2 \cdot |z_7| \cdot (z_3 + z_4) / (z_6 \cdot z_3), \quad (14)$$

where: pitch radius of the wheel 2 is equal to  $r_2 = 0,5 \cdot m_{1,2} \cdot z_2$ .

Utilizing the condition of equilibrium of relative tangential velocity  $v_{2,1}^h$  of wheel 2 and  $v_{1,2}^h$  of wheel 1 for their common contact point, we can calculate relative angular velocity of wheel 1:

$$\omega_1^h = v_{1,2}^h / r_1 = \omega_7 [2 \cdot z_2 \cdot |z_7| \cdot (z_3 + z_4) / (z_1 \cdot z_3 \cdot z_6)]. \quad (15)$$

In consequence, the formula for absolute angular velocity  $\omega_1 = \omega_1^h + \omega_h$  of wheel 1, assuming the value of angular velocity  $\omega_h = 1 \text{ rad/s}$ , taking into account the relationship  $z_4 = 0,5 \cdot (|z_5| - z_3)$ —is equal to:

$$(\omega_1)_{\omega_7=0} = \omega_h \cdot [1 + z_2 \cdot |z_7| \cdot (|z_5| + z_3) / (z_1 \cdot z_3 \cdot z_6)]. \tag{16}$$

In accordance with Eq. 3, kinematical ratio is equal to:

$$i_{1,h}^7 = (\omega_1 / \omega_h)_{\omega_7=0} = \omega_h \cdot (1 + z_2 \cdot |z_7| \cdot (|z_5| + z_3) / (z_1 \cdot z_3 \cdot z_6)) / \omega_h. \tag{17}$$

and finally we can write:

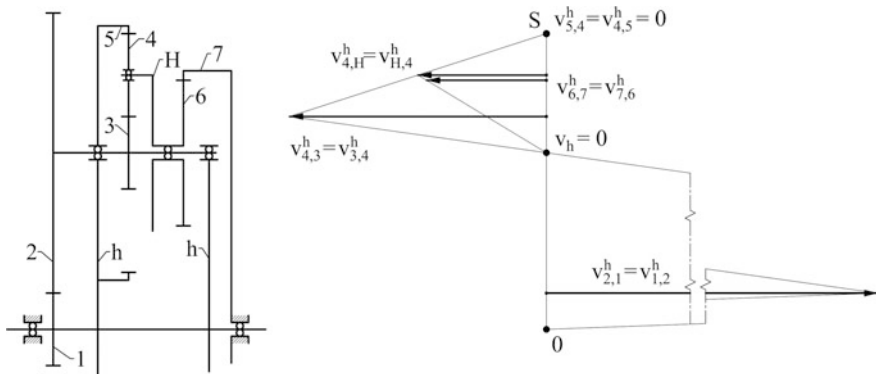
$$i_{1,h}^7 = 1 + 81 \cdot 72 \cdot (69 + 21) / (21 \cdot 21 \cdot 21) = 57,676. \tag{18}$$

Having kinematical ratio  $i_{1,h}^7$  (Eq. 18) and current angular velocity  $\omega_1$  (Eq. 2), we can calculate current angular velocity  $\omega_h$  of output carrier:

$$\omega_h = (\omega_1 / i_{1,h}^7) = 153,938 / 57,676 = 2,669 \text{ rad/s}. \tag{19}$$

In practice, we use the chart of velocities drawn for an adequate intersection and not for a front view of geared wheels. Chart of relative tangential velocities of the analyzed biplanetary gear is shown in Fig. 3. A drawing algorithm for this chart is analogical like for distribution of relative velocities of particular wheels and carriers of the gear (Fig. 2). It is more clear in comparison to previous chart of velocities, but rather for experienced engineers in the field of biplanetary gears.

In fact, an aim of kinematical analysis of biplanetary gear is determination of current (i.e. absolute) velocities. Namely, after obtaining relative angular velocity  $\omega_1^h$  (Eq. 15), we determine kinematical ratio  $i_{1,h}^7$  (Eq. 17) and current (absolute)



**Fig. 3** Chart of relative rotational velocities of biplanetary gear (S—an origin of relative current velocities  $v_{5,4}^h = v_{4,5}^h = 0$ )

output velocity  $\omega_h$  (Eq. 19). For the assumed numerical data, we can calculate absolute tangential velocities of particular wheels and carrier  $H$  according to the discussed algorithm and Fig. 4 in the following way:

$$v_{1,2} = \omega_1 \cdot r_1 = 0,5 \cdot \omega_1 \cdot m_{1,2} \cdot z_1 = 0,5 \cdot 153,938 \cdot 2 \times 10^{-3} \cdot 21 = 3,233 \text{ m/s}, \tag{20}$$

$$v_h = \omega_h \cdot r_h = 0,5 \cdot \omega_h \cdot m_{1,2} \cdot (z_1 + z_2) = 0,5 \cdot 2,669 \cdot 2 \times 10^{-3} \cdot 102 = 0,272 \text{ m/s}, \tag{21}$$

$$(v_{2,1} - v_h)/r_2 = (v_{3,4} + v_h)/r_3, \tag{22}$$

$$\begin{aligned} v_{3,4} &= (v_{2,1} - v_h) \cdot r_3/r_2 - v_h = (v_{2,1} - v_h) \cdot m_{3,4,5} \cdot z_3/(m_{1,2} \cdot z_2) - v_h \\ &= (3,233 - 0,272) \cdot 21/81 - 0,272 = 0,496 \text{ m/s}, \end{aligned} \tag{23}$$

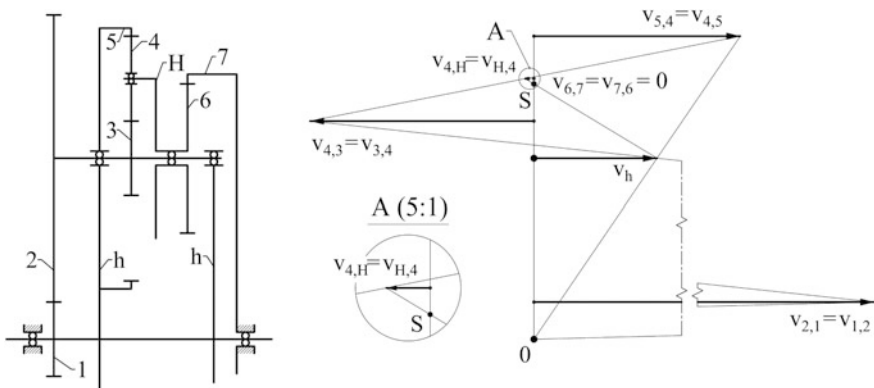
$$\begin{aligned} v_{4,5} &= \omega_h \cdot (r_h + r_H + r_4) = 0,5 \cdot \omega_h \cdot [m_{1,2} \cdot (z_1 + z_2) + m_{3,4,5} \cdot (z_3 + z_4) + m_{3,4,5} \cdot z_4] \\ &= 0,5 \cdot 2,669 \times 10^{-3} \cdot 2 \cdot [(21 + 81) + (21 + 24) + 24] = 0,456 \text{ m/s}. \end{aligned} \tag{24}$$

$$v_{4,H}/(r_H - r_6) = v_h/r_6, \tag{25}$$

$$\begin{aligned} v_{4,H} &= v_h \cdot (r_H - r_6)/r_6 = v_h \cdot [m_{3,4,5} \cdot (z_3 + z_4) - m_{6,7} \cdot z_6]/(m_{6,7} \cdot z_6) \\ &= 0,272 \cdot [2 \cdot (21 + 24) - 4 \cdot 21]/(4 \cdot 21) = 0,0194 \text{ m/s}. \end{aligned} \tag{26}$$

Checking the correctness of calculations (based on velocity chart in Fig. 4):

$$(v_{4,5} + v_{4,H})/r_4 = (v_{4,3} - v_{4,H})/r_4, \tag{27}$$



**Fig. 4** Chart of absolute tangential velocities for the biplanetary gear (S—centre of absolute current velocities  $v_{6,7} = v_{7,6} = 0$ )

in consequence, we can calculate the value of velocity ( $v_{4,3} = v_{3,4}$ ):

$$v_{4,3} = (v_{4,5} + v_{4,H}) + v_{4,H} = 0,456 + 2 \cdot 0,0194 = 0,495 \text{ m/s} = v_{3,4}. \quad (28)$$

### 3 Kinematical Ratio—Verification

In the present chapter, we would like to confirm the correctness of calculations of gear kinematical ratio for the considered biplanetary gear. Above calculations were done utilizing the methods: graphical-analytical and chart of velocities, underneath—the analytical method will be used (according to [1]). It should be underlined that for some biplanetary gears considered by authors in book chapters [2, 3], ratios of biplanetary gears were obtained based on the Willis formula. The method adapted from [1] is more simple and easier for understanding. Similarly, like in other kinematical analysis approaches, one have to consider relative motions of gear elements in relation to the external carrier  $h$ . Thereby, in accordance with formula (4), relative velocity of carrier  $h$  is equal to:  $\omega_h^h = 0$ , whereas relative velocity of immobile wheel 7 is as follows:  $\omega_7^h = -\omega_h$ .

The initial relationship for total relative kinematical ratio of the analyzed gear (in relation to external carrier  $h$ ) is:

$$i_{1,7}^h = i_{1,2}^h \cdot i_{3,H}^h \cdot i_{6,7}^h, \quad (29)$$

where component ratios  $i_{1,2}^h$  and  $i_{6,7}^h$  can be expressed as follows:

$$i_{1,2}^h = -z_2/z_1, \quad i_{6,7}^h = -z_7/z_6. \quad (30)$$

Internal gear relative ratio  $i_{3,H}^h$  is defined via known relationship:

$$i_{3,H}^h = 1 - i_{3,h}^H = 1 - i_{3,h}^5 = 1 - (-z_4/z_3) \cdot (-z_5/z_4) = 1 - z_5/z_3, \quad (31)$$

because wheel 5 is placed in carrier  $h$ , therefore  $5 \equiv h$  (Fig. 1).

Analogical relationship can be derived for the ratio  $i_{1,7}^h$ :

$$i_{1,7}^h = 1 - i_{1,h}^7, \quad (32)$$

where:  $i_{1,h}^7$  is the searched kinematical ratio of biplanetary gear. Therefore:

$$i_{1,h}^7 = 1 - i_{1,7}^h = 1 - (1 - z_5/z_3) \cdot z_2 \cdot z_7 / (z_1 \cdot z_6). \quad (33)$$

Inserting the teeth numbers, the value of the gear is:

$$i_{1,h}^7 = 1 + (1 + 69/21) \cdot 81 \cdot 72 / (21 \cdot 21) = 57,676. \quad (34)$$

Based on the second approach, the same value of ratio was obtained which confirms the correctness of considerations and calculations.

## 4 Conclusions

The Willis-formula-based method of kinematical analysis of planetary gears is an universal and most frequently applied method in engineering practice. In the present paper, it has been shown that chart of velocities can be recognized as equally important and effective method of kinematical analysis of biplanetary gears, and in consequence of complex planetary gears. In practice, it is a graphically-analytical (vector) method, which is slightly more difficult in case of analysis of biplanetary gears. As, there are two carriers i.e.—internal  $H$  and external  $h$  therefore the considerations have to be performed for the relative velocities of elements of both gears. Just after determination of the value of kinematic ratio and remaining output or input velocity, one can draw a classic chart of the current absolute velocities for the characteristic points of the gear. Such charts of velocities are frequently used for optimization of the structure of planetary gear, and therefore biplanetary ones, as well, aiming for establishing of kinematical ratio. Additionally, less complicated method was utilized for determination of tangent velocities of particular gear elements.

## References

1. Cyplakov JC (1966) Bi-Planetary mechanisms. Mas'instroenie, Moskwa (in Russian)
2. Drewniak J, Deptuła A, Kądziołka T, Zawisłak S (2017) Kinematics of biplanetary epicyclic gear. Computational kinematics, poitiers. (in printing)
3. Drewniak J, Kądziołka T, Zawisłak S (2017) Kinematics of bevel biplanetary gear. In: Goldfarb V (ed) Advanced gear engineering. Springer, Cham. (in printing)

# Modelling of the Static Response of a Wind/Hydro Turbine with Two Rotors and a 1DOF Speed Increaser



R. Saulescu, M. Neagoe and C. Jaliu

**Abstract** The wind/hydro energy conversion systems that integrate speed increasers are known on the market for more than half a century, the classical solutions with one rotor being currently widely implemented worldwide. The issue of increasing their energy performance is still of great interest, many innovative solutions being presented in the literature. A relatively new variant with high performances uses counter-rotating rotors and a speed increaser, being able to supply additional energy due to the use of a secondary rotor and a planetary transmission summing the input motions or torques and, consequently, obtaining higher power compared to a classical system with one input and one output. The solution of speed increaser with two independent inputs requires a complex control to correlate the power generated at the inputs to the generator requirements. A possible solution to avoid this impediment may be the use of a 1DOF planetary speed increaser with two inputs and one output, which sums the input torques and, thus, allows an additional supply of power compared to the classical turbines by using a secondary rotor that is kinematically dependent of the main one. Therefore, the paper is focused on determining the operating point (the parameters of the steady-state regime) for the counter-rotating turbine containing a 1DOF planetary speed increaser with two inputs and one output, considering the mechanical characteristics of the rotors and generator, and the transmission functions of the speed increaser established by taking into account the friction losses. Finally, the obtained analytical model is numerically simulated on a case study.

**Keywords** Counter-rotating turbine • Planetary speed increaser  
Steady-state • Operating point

---

R. Saulescu · M. Neagoe (✉) · C. Jaliu  
Transilvania University of Brasov, Braşov, Romania  
e-mail: mneagoe@unitbv.ro

R. Saulescu  
e-mail: rsaulescu@unitbv.ro

C. Jaliu  
e-mail: cjaliu@unitbv.ro



## 1 Introduction

Electricity production from renewable energy sources is an essential requirement in the sustainable development of today's society. Therefore, the improvement of the performances of renewable energy conversion systems is an ongoing concern of scientists and developers towards optimizing the systems in use or seeking new solutions with higher performances.

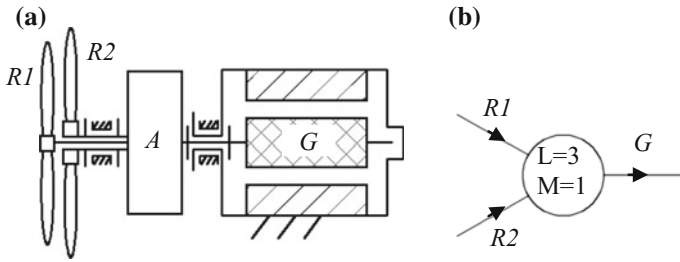
The design and development of wind/hydro energy conversion systems fit into this general effort to increase renewable energy production capacity and efficiency. Many innovative ideas have been promoted in the literature and in practice, many of which being in the concept or prototype stage. Thus, the systems that have more rotors [13], systems with two counter-rotating rotors [3], classical systems (single rotor) that integrate speed increasers of planetary type and that have a servomotor [14] or a variable speed drive [2, 8] at the second input can be noted among these concepts.

One solution to increase the energy capacity of a wind/hydro turbine refers to the improvement of the speed increaser performance, with the purpose of ensuring a good correlation between the rotors (which have high efficiency at low speeds) and the electric generator (which operates efficiently at higher speeds). An important step in exemplifying the functioning of the planetary transmissions consisted in unifying the terminology [1]. An example of a kinematic analysis of complex planetary transmissions by using graph theory is presented in [5], being further developed with a general algorithm for analysing the transmission ratios and efficiencies [9] and continued with the dynamic analysis and establishment of the system operation point [6]. Several general methods for the analytical modelling of the planetary transmissions efficiency are presented in [4].

A new solution of 1DOF planetary speed increaser with three inputs and outputs is considered in the paper. The transmission was proposed by the authors for connecting two wind/hydro counter-rotating rotors to a classic generator with fixed stator. The analytical modelling of the operating point for the considered wind/hydro system is presented in the first part of the paper, followed by a case study that includes numerical simulations for different adjustments of the secondary rotor. Finally, the properties and functional performances of the counter-rotating system that integrates a 1DOF planetary speed increaser with two inputs and one output are highlighted based on the simulation results.

## 2 Problem Formulation

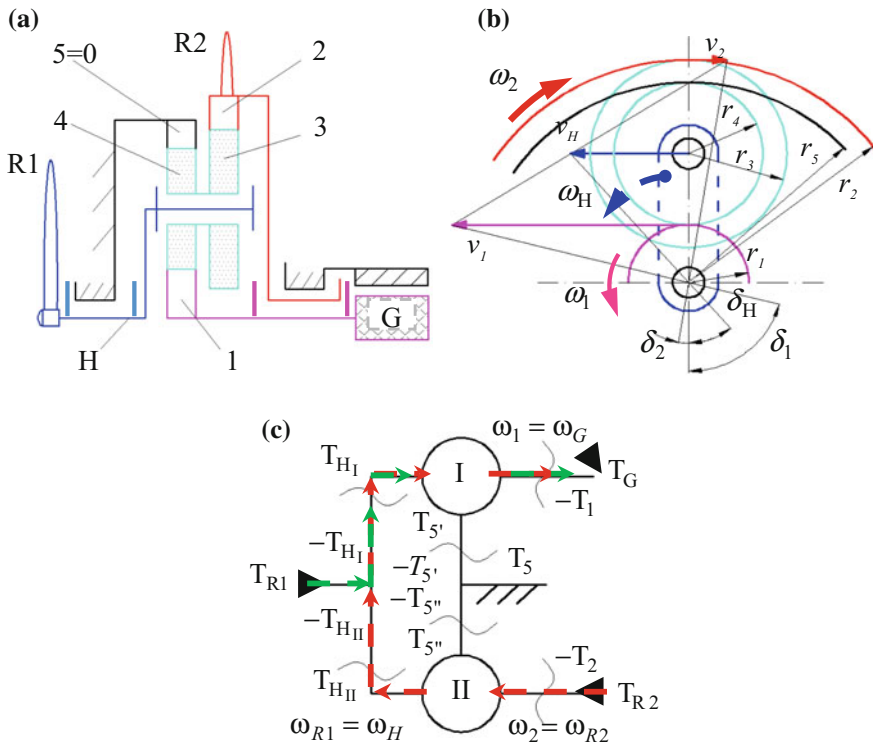
In practice, the speed increasers with three inputs and outputs ( $L = 3$ ) can function in two cases: (a) by summing the two input motions (2DOF transmission,  $M = 2$ ) [10–12] and (b) by summing the two input torques (1DOF transmission,  $M = 1$ ), Fig. 1, topic discussed in [7]. Compared to conventional systems with one rotor,



**Fig. 1** Wind/hydro system with counter-rotating rotors and conventional electric generator: **a** conceptual scheme, and **b** block diagram

the counter-rotating turbines generate a higher amount of energy due to the additional energy given by the secondary rotor, characterized either by independent speed (case a) or independent torque (case b).

The 1DOF speed increaser with three inputs and outputs (case b) from Fig. 2 is further considered. The transmission consists of two planetary units



**Fig. 2** Planetary speed increaser ( $M = 1, L = 3$ ), with two inputs (R1 and R2) and one output (G), consisting of two PU (I:H-1-4-5 = 0 and II:H-2-3 = 4-5 = 0): **a** structural scheme, **b** speed diagram, and **c** block diagram indicating the power flow

( $PU_I: H-1-4-5 = 0$  and  $PU_{II}: H-2-3 = 4-5 = 0$ ) with joint carrier (H) that is connected to the main rotor R1. The planetary speed increaser (Fig. 2a) has two ring gears, gear 5 being blocked and gear 2 mobile, a double satellite gear 3–4 and a sun gear 1 as the output body, to be connected to the electric generator G with fixed stator.

The 1DOF speed increaser (Fig. 2b) ensures the rotation of the secondary input (R2) in the opposite direction versus the main one (R1) and, consequently, sums up the input torques.

According to Fig. 2b, the speed of the secondary rotor ( $v_2$ ) depends on the speed of the main rotor ( $v_H$ ), being in the opposite direction. The case in which the torque generated by the secondary rotor,  $T_{R2}$ , is smaller than the one of the main rotor,  $T_{R1}$ , is further considered.

The objective of this paper consists in modelling and establishing the operating point in the steady-state regime of a system containing two counter-rotating rotors—a 1DOF speed increaser—a conventional generator, based on the kinematic and static analysis of the planetary transmission, Fig. 2, described in [7].

### 3 The Operating Point of the 1DOF System with Two Inputs and One Output

The operating point of a system can be determined in the steady-state regime based on the mechanical characteristics of the motors and end-effectors, and of the transmission functions for motions and forces/torques of the transmission.

In order to describe the functional ranges of the wind/hydro rotors and of the dc generator for the system from Fig. 2, the following mechanical characteristics of linear functions are considered:

- the main rotor R1:

$$T_{R1} = -a_{R1}\omega_{R1} + b_{R1} = -a_{R1}\omega_H + b_{R1}, \quad (1)$$

- the secondary rotor R2:

$$T_{R2} = -a_{R2}\omega_{R2} + b_{R2} = -a_{R2}\omega_2 + b_{R2}, \quad (2)$$

- the electric generator G:

$$-T_g = a_g\omega_g - b_g = a_g\omega_1 - b_g. \quad (3)$$

The kinematic and static equations of the 1DOF speed increaser with two inputs and one output (Fig. 2) can be obtained on the basis of the modelling algorithm presented in [7]:

- the planetary unit  $PU_I$  ( $1-4-5' = 0-H_I$ )

$$\omega_{15} = \omega_{H5}(1 - i_{0I}), \quad (4)$$

$$\omega_g = \omega_{R1} \cdot (1 - i_{0I}), \quad (5)$$

$$\omega_{H5} T_{H_I} \eta_{H1}^5 + \omega_{15} T_1 = 0, \quad (6)$$

$$T_{H_I} = T_1 \left( \frac{i_{0I}}{\eta_{0I}} - 1 \right), \quad (7)$$

- the planetary unit  $PU_{II}$  ( $2-3-4-5'' = 0-H_{II}$ )

$$\omega_{25} = \omega_{H5}(1 - i_{0II}), \quad (8)$$

$$\omega_{R2} = \omega_{R1}(1 - i_{0II}), \quad (9)$$

$$\omega_{H5} T_{H_{II}} \eta_{H2}^5 + \omega_{25} T_2 = 0, \quad (10)$$

$$T_{H_{II}} = T_2 \left( \frac{i_{0II}}{\eta_{0II}} - 1 \right), \quad (11)$$

where:  $i_{0I} = -\frac{Z_5}{Z_1}$ ,  $i_{0II} = \frac{Z_3 Z_5}{Z_2 Z_4}$ ,  $\eta_{0I} = \eta_{14}^H \eta_{45}^H$ ,  $\eta_{H1}^5 = \frac{1-i_{0I}}{1-i_{0I}/\eta_{0I}} = \frac{1-i_{0I}}{1-i_{0I}}$ ,  $\eta_{0II} = \eta_{23}^H \eta_{45}^H$ ,  $\eta_{H2}^5 = \frac{1-i_{0II}}{1-i_{0II}\eta_{0II}} = \frac{1-i_{0II}}{1-i_{0II}}$ ,  $H_I \equiv H_{II} \equiv H \equiv R_1$ ,  $2 \equiv R2$ ,  $1 \equiv G$ ,  $5 \equiv 5' \equiv 5''$ , Fig. 2c.

The relation for the torque on the output shaft, rel. (12), can be written based on the energy balance Eqs. (6) and (10), and the correlations between the interior connections (see Fig. 2 and [7]:  $T_{R1} - T_{H_I} - T_{H_{II}} = 0$ ,  $T_{R2} - T_2 = 0$ ,  $T_g - T_1 = 0$ ):

$$T_1 = -\frac{T_{R1}}{1 - i_{0I}/\eta_{0I}} - \frac{T_{R2}(1 - i_{0II}\eta_{0II})}{1 - i_{0I}/\eta_{0I}}. \quad (12)$$

Considering the Eqs. (1), (2), (5), (9) and the equality  $\omega_g = \omega_1$ , the mechanical characteristics of the two rotors R1 and R2 are reduced on the output shaft as follows:

$$T_1 = -a_1 \omega_1 + b_1, \quad (13)$$

$$a_1 = \frac{a_{R1} + a_{R2}(1 - i_{0II})(1 - \overline{i_{0II}})}{(1 - i_{0I})(1 - i_{0I})} \text{ and } b_1 = -\frac{b_{R1} + b_{R2}(1 - \overline{i_{0II}})}{1 - i_{0I}}. \quad (14)$$

A case study for establishing the system operating point (Fig. 2a) is further presented based on the previous relationships.

## 4 Case Study

The case study presents the establishment of the operating point for a wind turbine, which has the mechanical characteristics of the two rotors and the electric generator with the coefficients from Table 1.

The constants  $a_1$  and  $b_1$  have different values depending on the turbines operating cases; therefore, the system can function: (I) only with the main rotor R1, case in which  $a_{R2}$  and  $b_{R2}$  are zero; (II) only with the secondary rotor R2, case in which  $a_{R1}$  and  $b_{R1}$  are null, or (III) with both rotors, case in which  $a_{R1}$ ,  $b_{R1}$ ,  $a_{R2}$  and  $b_{R2}$  have the values from Table 1. The values of the coefficients  $a_1$  and  $b_1$  for the three cases are systematized in Table 2, depending on the coefficient values of the two rotors mechanical characteristics.

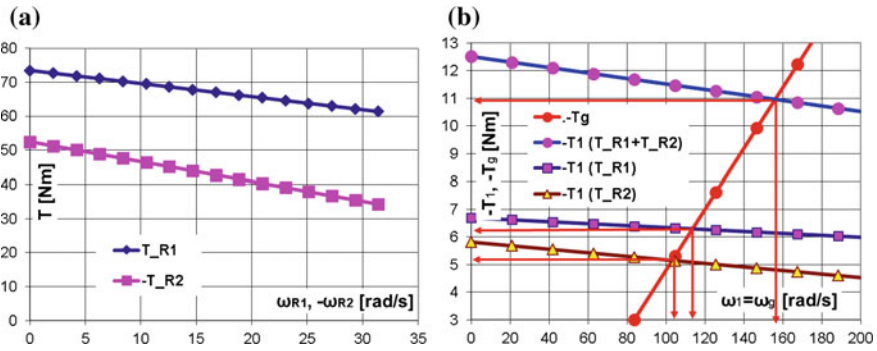
The operating point in the steady-state regime represents the intersection between the mechanical characteristic of the generator, rel. (3) and the rotors mechanical characteristic reduced on the output shaft 1, Table 2 ( $i_{0I} = -9$ ,  $i_{0II} = 2$ ,  $\eta_{0I} = \eta_{0II} = 0.9025$  were considered as input data). Based on these data, the system operating point for the three functioning cases is illustrated in Fig. 3.

**Table 1** The constant coefficients of the rotors and generator mechanical characteristics

$a_{R1}$	$b_{R1}$	$a_{R2}$	$b_{R2}$	$a_g$	$b_g$
0.3857	73.5	0.58	-52.5	0.11	6

**Table 2** The values of the mechanical characteristics coefficients for three functioning cases

Functioning case	$a_{R1}$	$b_{R1}$	$a_{R2}$	$b_{R2}$	$a_1$	$b_1$
I.	0.3857	73.5	0	0	-0.00352	-6.69869
II.	0	0	0.58	-52.5	-0.00643	-5.81861
III.	0.3857	73.5	0.58	-52.5	-0.00994	-12.5173



**Fig. 3** Operating point of the system consisting of two counter-rotating wind rotors—1DOF speed increaser with 2 inputs and one output—electric generator: **a** the mechanical characteristics of the rotors, **b** the rotors mechanical characteristics reduced on the output shaft of the speed increaser and the operating point for the three analysed cases

### 5 Results and Discussions

The diagram from Fig. 3b allows determining the mechanical power on the output shaft of the speed increaser, which is connected to the generator shaft, for each of the three functioning cases that were previously analysed within the case study:

- I. As the driving torque is provided only by the main rotor (i.e.  $T_{R2} = 0$ ), the following values are obtained  $n_{g(T_{R1})} = 1088.62$  rpm and  $P_{g(T_{R1})} = 718.2$  W, case in which the main rotor speed is  $n_{R1} = 108.86$  rpm;
- II.  $n_{g(T_{R2})} = 993.13$  rpm,  $P_{g(T_{R2})} = 540.8$  W,  $n_{R1} = 99.3$  rpm are obtained when the mechanical input power is generated only by the secondary rotor (i.e.  $T_{R1} = 0$ );
- III.  $n_{g(T_{R1} + T_{R2})} = 1489.69$  rpm and  $P_{g(T_{R1} + T_{R2})} = 1716$  W result when both rotors operate simultaneously; in this case, the main rotor speed will be  $n_{R1} = 148.9$  rpm

Therefore, the considered example for establishing the operating point of the system in steady-state regime highlights the fact that the system with two counter-rotating rotors under load (case III) produces a significantly higher amount of energy than the system operating with one rotor: the mechanical power on the generator shaft is 2.39 times bigger than in the case I and 3.17 than in case II. The wind turbine with two counter-rotating rotors also allows obtaining additional energy compared to two different wind turbines with rotors R1 and R2, respectively (and a generator G):  $P_{g(T_{R1} + T_{R2})} = 1.36(P_{g(T_{R1})} + P_{g(T_{R2})})$ .

## 6 Conclusions

The paper presents an algorithm for modelling the response (operating point) in static regime of a wind/hydro turbine with two counter-rotating rotors, a conventional electric generator with fixed stator, and a 1DOF planetary speed increaser that sums the input torques, while is kinematically connecting the two rotors. The planetary speed increasers allow obtaining higher efficiencies at reduced overall dimensions, compared to the transmissions with fixed axis.

This type of system can operate with one or both rotors under load. While operating with one rotor, the torque generated by the other rotor is disannulled by an appropriate adjustment of blade orientation, the rotor rotating idle.

Due to the properties of 1DOF planetary transmission with two inputs and one output of summing the input torques simultaneously with the amplification of speed, the numerical results obtained for the operating point highlight that the counter-rotating systems increase the output power compared to a classical system with an input and an output, as they make use of a secondary input that is kinematically dependent on the first one.

## References

1. Arnaudov K et al (2005) For an unified and correct IFToMM terminology in the area of gearing. *Mech Mach Theory* 40:993–1001
2. Bottiglione F et al (2014) Infinitely variable transmissions in neutral gear: torque ratio and power re-circulation. *Mech Mach Theory* 74:285–298
3. Climescu O et al (2011) Specific features of a counter-rotating transmission for renewable energy systems. *Environ Eng Manag J* 10:1105–1113
4. del Castillo JM (2002) The analytical expression of the efficiency of planetary gear trains. *Mech Mach Theory* 37:197–214
5. Gomà Ayats JR et al (2012) Hypergraphs for the analysis of complex mechanisms comprising planetary gear trains and other variable or fixed transmissions. *Mech Mach Theory* 51:217–229
6. Munteanu O (2016) Dynamic modelling and simulation of a planetary speed increaser. *Bul Transilv Univ Braşov* 9(1):27–34
7. Neagoe M et al (2017) Novel Speed increaser used in counter-rotating wind turbines. *New Adv Mech Mech Transm Robot Mech Machine Sci* 46:143–151
8. Pennestri E et al (2012) Efficiency evaluation of gearboxes for parallel hybrid vehicles: theory and applications. *Mech Mach Theory* 49:157–176
9. Salgado DR et al (2014) Analysis of the transmission ratio and efficiency ranges of the four-, five-, and six-link planetary gear trains. *Mech Mach Theory* 73:218–243
10. Saulescu R et al (2014) Planetary gear for counter-rotating wind turbines. *Appl Mech Mater* 658:135–140

11. Saulescu R et al (2011) On the use of 2 DOF planetary gears as “speed increaser” in small hydros and wind turbines. In: Proceedings of the ASME 2011 international design engineering technical conferences & computers and information in engineering conference, IDETC/CIE 2011
12. Saulescu R et al (2016) Comparative analysis of two wind turbines with planetary speed increaser in steady-state. *Appl Mech Mater* 823:355–360
13. Shin C (1999) Multi-unit rotor blade system integrated wind turbine, US Patent Nr 5876181
14. Zhao X et al (2003) A novel power splitting drive train for variable speed wind power generators. *Renew Energy* 28:2001–2011



# Higher-Order Cayley Transforms for SE(3)



D. Condurache and I.-A. Ciureanu

**Abstract** This paper presents a new pose parametrization technique based on  $n$ -th order Cayley transforms. Our study is built on the properties of maps that link the dual vectors with the special Euclidean displacement Lie group SE(3) and the Lie group of the orthogonal dual tensors. The resulted parametrization framework is complete and embeds multiple of the reported attitude parameterization Cayley maps, while extending them towards pose parameterization.

**Keywords** Cayley maps • Lie group SE(3) • Dual vectors • Orthogonal dual tensors • Modified rodrigues parameters

## 1 Introduction

Rigid body motion representation can be displayed through different techniques if dual numbers, dual vectors or dual matrices are used in the context of screw theory. Consequently, a complete parameterization framework of the rigid body motion provides the best premises for new developments in robotics, machine vision, biomechanics, relative orbital motion or neuroscience.

The tensors represent the newest approach for parameterization of rotation and motion. Tensor analysis expresses the invariance of the laws of physics with respect to the change of basis and change of frame operations. It was showed that any rigid body motion can be globally parametrized using a curve from the Lie group of the orthogonal dual tensors [3–5]. This result can be used to improve research in multiple connected areas. Cayley maps represent a useful tool when a Lie group needs to be linearized near its identity. This is also true of the exponential map but

---

D. Condurache (✉)

“Gheorghe Asachi” Technical University of Iasi, Iași, Romania  
e-mail: daniel.condurache@tuiasi.ro

I.-A. Ciureanu

“Grigore T. Popa” University of Medicine and Pharmacy Iasi, Iași, Romania  
e-mail: adrian.ciureanu@umfiasi.ro

the Cayley maps are rational, that is it doesn't involve transcendental functions. This is useful in numerical applications since evaluating transcendental functions can be time-consuming. In this paper we introduce a new approach for pose parameterization by using higher-order Cayley transforms. This approach completely embeds multiple of the reported attitude parameterization Cayley maps and extends them towards pose parameterization. The structure of the paper is the following: the first section presents mathematical preliminaries followed by the parametrization of the rigid body motion using orthogonal dual tensors. In the end, we reveal the n-th order modified Cayley transform for pose representation.

## 2 Preliminaries on Dual Vectors and Dual Tensors

In this section we present properties of: dual numbers, dual vectors and dual tensors. More details can be found in [1–6]

- **Dual numbers**

Let the set of real dual numbers be denoted by

$$\underline{\mathbb{R}} = \{a + \varepsilon a_0 \mid a, a_0 \in \mathbb{R}, \varepsilon^2 = 0, \varepsilon \neq 0\} \tag{1}$$

where  $a = Re(\underline{a})$  is the real part and  $a_0 = Du(\underline{a})$  the dual part. The sum and product between dual numbers generate a ring with zero divisors structure for  $\underline{\mathbb{R}}$  [3].

Any differentiable function  $f: \mathbb{C}\underline{\mathbb{R}} \rightarrow \mathbb{R}, f = f(a)$  is completely defined on  $\mathbb{C}\underline{\mathbb{R}}$  such that:

$$f: \mathbb{C}\underline{\mathbb{R}} \rightarrow \underline{\mathbb{R}}, f = f(\underline{a}) = f = f(a) + \varepsilon a_0 f'(a) \tag{2}$$

- **Dual vectors**

In the Euclidean space, the linear space of free vectors with dimension 3 will be denoted by  $V_3$ . The ensemble of dual vectors is defined as  $\underline{V}_3 = \{\underline{\mathbf{a}} = \mathbf{a} + \varepsilon \mathbf{a}_0; \mathbf{a}, \mathbf{a}_0 \in V_3, \varepsilon^2 = 0\}$ , where  $a = Re(\underline{\mathbf{a}})$  is the real part and  $\mathbf{a}_0 = Du(\underline{\mathbf{a}})$  the dual part. For any three dual vectors  $\underline{\mathbf{a}}, \underline{\mathbf{b}}, \underline{\mathbf{c}}$  the following notations will be used for the basic products:

$\underline{\mathbf{a}} \cdot \underline{\mathbf{b}}$ —scalar product,  $\underline{\mathbf{a}} \times \underline{\mathbf{b}}$ —cross product,  $\langle \underline{\mathbf{a}}, \underline{\mathbf{b}}, \underline{\mathbf{c}} \rangle$ —scalar triple product. Regarding algebraic structure,  $(\underline{V}_3, +, \cdot, \underline{\mathbb{R}})$  is a free  $\underline{\mathbb{R}}$ -module [3].

The magnitude of  $\underline{\mathbf{a}}$ , denoted by  $|\underline{\mathbf{a}}|$ , is the dual number computed from

$$|\underline{\mathbf{a}}| = \begin{cases} \|\mathbf{a}\| + \varepsilon \frac{\mathbf{a}_0 \cdot \mathbf{a}}{\|\mathbf{a}\|}, Re(\underline{\mathbf{a}}) \neq 0 \\ \varepsilon \|\mathbf{a}\|_0, Re(\underline{\mathbf{a}}) = 0 \end{cases} \tag{3}$$

where  $\|\cdot\|$  is the Euclidean norm. If  $|\underline{\mathbf{a}}| = 1$  then  $\underline{\mathbf{a}}$  is called unit dual vector.

For any  $\underline{\mathbf{a}} \in \underline{V}_3$  a dual number  $\underline{\lambda} \in \underline{\mathbb{R}}$  and a unit dual vector  $\underline{\mathbf{u}} \in \underline{V}_3$  exist in order to have  $\underline{\mathbf{a}} = \underline{\lambda}\underline{\mathbf{u}}$ , with  $\lambda = |\underline{\mathbf{a}}|$ .

• **Dual tensors**

An  $\underline{\mathbb{R}}$ —linear application of  $\underline{V}_3$  into  $\underline{V}_3$  is called an Euclidean dual tensor:

$$T(\underline{\lambda}_1\underline{\mathbf{v}}_1 + \underline{\lambda}_2\underline{\mathbf{v}}_2) = \underline{\lambda}_1T(\underline{\mathbf{v}}_1) + \underline{\lambda}_2T(\underline{\mathbf{v}}_2), \underline{\lambda}_1, \underline{\lambda}_2 \in \underline{\mathbb{R}}, \forall \underline{\mathbf{v}}_1, \underline{\mathbf{v}}_2 \in \underline{V}_3 \tag{4}$$

Let  $\mathbf{L}(\underline{V}_3, \underline{V}_3)$  be the set of dual tensors, then any  $T \in \mathbf{L}(\underline{V}_3, \underline{V}_3)$  can be decomposed as  $T = T + \epsilon T_0$ , with  $T, T_0 \in \mathbf{L}(V_3, V_3)$ . Also, the dual transposed tensor denoted by  $T^T$  is defined by

$$\underline{\mathbf{v}}_1 \cdot (T\underline{\mathbf{v}}_2) = \underline{\mathbf{v}}_2 \cdot (T^T\underline{\mathbf{v}}_1), \forall \underline{\mathbf{v}}_1, \underline{\mathbf{v}}_2 \in \underline{V}_3 \tag{5}$$

While  $\forall \underline{\mathbf{v}}_1, \underline{\mathbf{v}}_2, \underline{\mathbf{v}}_3 \in \underline{V}_3, Re(\langle \underline{\mathbf{v}}_1, \underline{\mathbf{v}}_2, \underline{\mathbf{v}}_3 \rangle) \neq 0$ , the determinant is:

$$\langle T\underline{\mathbf{v}}_1, T\underline{\mathbf{v}}_2, T\underline{\mathbf{v}}_3 \rangle = \det T \langle \underline{\mathbf{v}}_1, \underline{\mathbf{v}}_2, \underline{\mathbf{v}}_3 \rangle. \tag{6}$$

For any dual vector  $\underline{\mathbf{a}} \in \underline{V}_3$ , the associated skew-symmetric dual tensor will be denoted by  $\underline{\hat{\mathbf{a}}}$  and will be defined

$$\underline{\hat{\mathbf{a}}}\underline{\mathbf{b}} = \underline{\mathbf{a}} \times \underline{\mathbf{b}}, \forall \underline{\mathbf{b}} \in \underline{V}_3. \tag{7}$$

The previous definition can be directly transposed into the following result: for any skew-symmetric dual tensor  $\underline{\hat{\mathbf{A}}} \in \mathbf{L}(\underline{V}_3, \underline{V}_3)$ ,  $\underline{\hat{\mathbf{A}}} = -\underline{\hat{\mathbf{A}}}^T$ , a uniquely defined dual vector  $\underline{\mathbf{a}} = vect(\underline{\hat{\mathbf{A}}})$ ,  $\underline{\mathbf{a}} \in \underline{V}_3$  exists in order to have  $\underline{\hat{\mathbf{A}}}\underline{\mathbf{b}} = \underline{\mathbf{a}} \times \underline{\mathbf{b}}, \forall \underline{\mathbf{b}} \in \underline{V}_3$ . The set of skew-symmetric dual tensors is structured as a free  $\underline{\mathbb{R}}$ —module of rank 3 and is isomorph with  $\underline{V}_3$  [3].

### 3 Isomorphism by Special Euclidean Group SE(3) and Dual Orthogonal Tensors SO(3)

Orthogonal dual tensorial maps are a powerful instrument in the study of the motion. More on dual numbers and dual vectors, can be found in [1, 3–5].

Let the orthogonal dual tensor set be denoted by.

$$\underline{SO}_3 = \{ \underline{R} \in \mathbf{L}(\underline{V}_3, \underline{V}_3) \mid \underline{R}\underline{R}^T = \underline{I}, \det \underline{R} = 1 \} \tag{8}$$

where  $\underline{SO}_3$  is the set of special orthogonal dual tensors and  $\underline{I}$  is the unit orthogonal dual tensor.

The internal structure of any orthogonal dual tensor  $\underline{R} \in \underline{SO}_3$  is illustrated in a series of results which were detailed in our previous work [3, 4].

**Theorem 1** (Structure Theorem) *For any  $\underline{R} \in \underline{SO}_3$  an unique decomposition is viable*

$$\underline{R} = (I + \varepsilon \tilde{\rho})Q \tag{9}$$

where  $Q \in \underline{SO}_3$  (real special orthogonal tensor set) and  $\rho \in V_3$  are called **structural invariants**.

Taking into account the Lie group structure of  $\underline{SO}_3$  and the result presented in previous theorem, it can be concluded that any orthogonal dual tensor  $\underline{R} \in \underline{SO}_3$  can be used globally parametrize displacements of rigid bodies.

**Theorem 2** (Representation Theorem) *For any orthogonal dual tensor  $\underline{R}$  defined as in Eq. (9), a dual number  $\underline{\alpha} = \alpha + \varepsilon d$  and a dual unit vector  $\underline{\mathbf{u}} = \mathbf{u} + \varepsilon \mathbf{u}_0$  can be computed to have [3]:*

$$\underline{R}(\underline{\alpha}, \underline{\mathbf{u}}) = \underline{I} + \sin \underline{\alpha} \underline{\tilde{\mathbf{u}}} + (1 - \cos \underline{\alpha}) \underline{\tilde{\mathbf{u}}}^2 = \exp(\underline{\alpha} \underline{\tilde{\mathbf{u}}}) \tag{10}$$

The parameters  $\underline{\alpha}$  and  $\underline{\mathbf{u}}$  are called the **natural invariants** of  $\underline{R}$ . The unit dual vector  $\underline{\mathbf{u}}$  gives the Plucker representation of the Mozzi-Chalses axis, while the dual angle  $\underline{\alpha} = \alpha + \varepsilon d$  contains the rotation angle  $\alpha$  and the translated distance  $d$ . The recovery of  $\underline{\alpha}$ ,  $\underline{\mathbf{u}}$  can also be done if we use the linear and structural invariants [3, 4].

The Lie algebra of the Lie group  $\underline{SO}_3$  is the skew-symmetric dual tensor set denoted by  $\underline{so}_3 = \{ \tilde{\underline{\alpha}} \in \mathbf{L}(\underline{\mathbf{V}}_3, \underline{\mathbf{V}}_3) \mid \tilde{\underline{\alpha}} = -\tilde{\underline{\alpha}}^T \}$ , where the internal mapping is  $\langle \tilde{\underline{\alpha}}_1, \tilde{\underline{\alpha}}_2 \rangle = \tilde{\underline{\alpha}}_1 \tilde{\underline{\alpha}}_2$ . The link between the Lie algebra  $\underline{so}_3$ , the Lie group  $\underline{SO}_3$ , and the exponential map is given by the following.

**Theorem 3** *The mapping*

$$\exp: \underline{so}_3 \rightarrow \underline{SO}_3, \exp(\tilde{\underline{\alpha}}) = e^{\tilde{\underline{\alpha}}} = \sum_{k=0}^{\infty} \frac{\tilde{\underline{\alpha}}^k}{k!} \tag{11}$$

*is well defined and surjective.*

Any screw axis that embeds a rigid displacement can be parameterized by a unit dual vector, whereas the screw parameters (angle of rotation about the screw and the translation along the screw axis) can be structured as a dual angle. The computation of the screw axis is linked with the problem of finding the logarithm of an orthogonal dual tensor  $\underline{R}$ , which is a multifunction defined by

$$\log: \underline{SO}_3 \rightarrow \underline{so}_3, \log \underline{R} = \left\{ \tilde{\underline{\psi}} \in \underline{so}_3 \mid \exp(\tilde{\underline{\psi}}) = \underline{R} \right\} \tag{12}$$

and is the inverse of Eq. (11).

Based on Theorems 2 and 3, for any orthogonal dual tensor  $\underline{R}$ , a dual vector  $\underline{\Psi} = \underline{\alpha} \underline{\mathbf{u}} = \Psi + \varepsilon \Psi_0$  can be computed and represents the screw dual vector,

which embeds the screw axis and screw parameters. The form of  $\underline{\Psi}$  implies that  $\tilde{\underline{\Psi}} \in \log \underline{R}$ , with  $\underline{\Psi}$  being named **Euler dual vector**.

Also,  $|\underline{\Psi}| < \pi$ , Theorems 2 and 3 can be used to uniquely recover the screw dual vector  $\underline{\Psi}$ , which is equivalent with computing  $\log \underline{R}$ .

**Theorem 4** *The natural invariants  $\underline{\alpha} = \alpha + \varepsilon d$ ,  $\underline{\mathbf{u}} = \mathbf{u} + \varepsilon \mathbf{u}_0$  can be used to directly recover the structural invariants  $Q$  and  $\rho$  from Eq. (9):*

$$\begin{aligned} Q &= I + \sin \alpha \underline{\mathbf{u}} + (1 - \cos \alpha) \underline{\mathbf{u}}^2 \\ \rho &= d\underline{\mathbf{u}} + \sin \alpha \mathbf{u}_0 + (1 - \cos \alpha) \mathbf{u} \times \mathbf{u}_0 \end{aligned} \quad (13)$$

To prove Eq. (13), we need to use Eqs. (9) and (10). If these equations are equal, then the structure of their dual parts leads to the result presented in Eq. (13)

**Theorem 5** (Isomorphism theorem) *The special Euclidean group and  $(SE_3, \cdot)$  and  $(S\mathbb{O}_3, \cdot)$  are connected via the isomorphism of the Lie groups*

$$\begin{aligned} \Phi: SE_3 &\rightarrow S\mathbb{O}_3 \\ \Phi(g) &= (I + \varepsilon \tilde{\rho})Q \end{aligned} \quad (14)$$

where  $g = \begin{bmatrix} Q & \rho \\ 0 & 1 \end{bmatrix}$ ,  $Q \in S\mathbb{O}_3$ ,  $\rho \in V_3$

*Proof* For any  $g_1, g_2 \in SE_3$ , the map defined in Eq. (14) yields

$$\Phi(g_1 \cdot g_2) = \Phi(g_1) \cdot \Phi(g_2) \quad (15)$$

Let  $\underline{R} \in S\mathbb{O}_3$ . Based on Theorem 1, which ensures a unique decomposition, we can conclude that the only choice for  $g$ , such that  $\Phi(g) = \underline{R}$  is  $g = \begin{bmatrix} Q & \rho \\ 0 & 1 \end{bmatrix}$ . This underlines that  $\Phi$  is a bijection and keeps all the internal operations.

*Remark 1* The inverse of  $\Phi$  is

$$\Phi^{-1}: S\mathbb{O}_3 \leftrightarrow SE_3; \Phi^{-1}(\underline{R}) = \begin{bmatrix} Q & \rho \\ 0 & 1 \end{bmatrix} \quad (16)$$

where  $Q = Re(\underline{R})$ ,  $\rho = vect(Du(\underline{R}) \cdot Q^T)$ .

## 4 Dual Tensor-Based Parameterizations of Rigid Body Motion

The Lie group  $S\mathbb{O}_3$ , isomorphic with  $SE_3$  admits multiple parametrizations and few of them will be discussed in this section [1–9].

### A. The exponential parametrization

If  $\underline{R} = \underline{R}(\underline{\alpha}, \underline{\mathbf{u}})$  then we can construct the dual vector  $\underline{\Psi} = \underline{\alpha}\underline{\mathbf{u}}, \underline{\Psi} \in V_3$  which combined with Theorems 2 and 3 lead to

$$\underline{R} = \exp(\tilde{\underline{\Psi}}) = I + \text{sinc}(|\underline{\Psi}|)\tilde{\underline{\Psi}} + \frac{1}{2}\text{sinc}^2\left(\frac{|\underline{\Psi}|}{2}\right)\tilde{\underline{\Psi}}^2 \quad (17)$$

where

$$\text{sinc}(|\underline{x}|) = \begin{cases} \frac{\sin|\underline{x}|}{|\underline{x}|}, & |\underline{x}| \notin \varepsilon \mathbb{R} \\ 1, & |\underline{x}| \in \varepsilon \mathbb{R} \end{cases} \quad (18)$$

### B. The first order Cayley Transforms for dual vectors (The Rodrigues Dual Vector Parametrization)

The first order Cayley transform is a map defined as:

$$\text{cay}(\underline{\mathbf{v}}): \underline{V}_3 \rightarrow \underline{S}\underline{O}_3, \text{cay}(\tilde{\underline{\mathbf{v}}}) = (\underline{I} + \tilde{\underline{\mathbf{v}}})(\underline{I} - \tilde{\underline{\mathbf{v}}})^{-1} \quad (19)$$

**Theorem 6** *The map  $\text{cay}(\underline{\mathbf{v}})$  is well defined and surjective.*

*Proof* For any  $\underline{\mathbf{v}} \in \underline{V}_3$ , the value of  $\det(\text{cay}(\underline{\mathbf{v}}))$  is:

$$\det(\text{cay}(\underline{\mathbf{v}})) = \det\left[(\underline{I} + \tilde{\underline{\mathbf{v}}})(\underline{I} - \tilde{\underline{\mathbf{v}}})^{-1}\right] = \frac{1 + |\underline{\mathbf{v}}|^2}{1 + |\underline{\mathbf{v}}|^2} = 1 \quad (20)$$

while

$$\text{cay}(\underline{\mathbf{v}})[\text{cay}(\underline{\mathbf{v}})]^T = (\underline{I} + \tilde{\underline{\mathbf{v}}})(\underline{I} - \tilde{\underline{\mathbf{v}}})^{-1}(\underline{I} - \tilde{\underline{\mathbf{v}}})(\underline{I} + \tilde{\underline{\mathbf{v}}})^{-1} = \underline{I} \quad (21)$$

Equations (20) and (21) prove that the first order Cayley transform is well defined.

The computational solution for  $(\underline{I} - \tilde{\underline{\mathbf{v}}})^{-1}$  is

$$(\underline{I} - \tilde{\underline{\mathbf{v}}})^{-1} = \frac{1}{1 + |\underline{\mathbf{v}}|^2}(\tilde{\underline{\mathbf{v}}}^2 + \tilde{\underline{\mathbf{v}}}) + \underline{I} \quad (22)$$

Combining the results from Eqs. (19) and (22), leads to:

$$\text{cay}(\underline{\mathbf{v}}) = \underline{I} + 2\frac{|\underline{\mathbf{v}}|}{1 + |\underline{\mathbf{v}}|^2}\frac{\tilde{\underline{\mathbf{v}}}}{|\underline{\mathbf{v}}|} + \left(1 - \frac{1 - |\underline{\mathbf{v}}|^2}{1 + |\underline{\mathbf{v}}|^2}\right)\frac{\tilde{\underline{\mathbf{v}}}^2}{|\underline{\mathbf{v}}|^2} \quad (23)$$

Taking into account

$$\sin \underline{\alpha} = \frac{2 \tan \frac{\alpha}{2}}{1 + \tan^2 \frac{\alpha}{2}}; \cos \underline{\alpha} = \frac{1 - \tan^2 \frac{\alpha}{2}}{1 + \tan^2 \frac{\alpha}{2}} \quad (24)$$

we can conclude that

$$\text{cay}(\underline{\mathbf{v}}) = \underline{I} + \sin \underline{\alpha} \underline{\tilde{\mathbf{u}}} + (1 - \cos \underline{\alpha}) \underline{\tilde{\mathbf{u}}}^2 \quad (25)$$

where  $\underline{\alpha} = 2 \arctan |\underline{\mathbf{v}}|$  and  $\underline{\mathbf{u}} = \underline{\mathbf{u}}_{\underline{\mathbf{v}}}$ . This proves that the first order Cayley transform is surjective.

This result shows that  $\forall \underline{R} \in \underline{SO}_3, \underline{R} = \underline{R}(\underline{\alpha}, \underline{\mathbf{u}})$  and  $Re(\underline{\alpha}) \neq k\pi, k \in \mathbb{Z}$  a dual vector  $\underline{\mathbf{b}} = (\tan \frac{\alpha}{2}) \underline{\mathbf{u}}$  (a.k.a. dual Rodrigues vector) exists in order to have  $\text{cay}(\underline{\mathbf{b}}) = \underline{R}$ .

### C. The n-th order Cayley transforms

The n-th order Cayley transform is a map defined by:

$$\text{cay}_n(\underline{\mathbf{v}}): \underline{V}_3 \rightarrow \underline{SO}_3, \text{cay}_n(\underline{\mathbf{v}}) = (\underline{I} + \underline{\tilde{\mathbf{v}}})^n (\underline{I} - \underline{\tilde{\mathbf{v}}})^{-n}, \forall n \in \mathbb{N}^* \quad (26)$$

**Theorem 7** The n-th order Cayley transform (26) is well defined and can also be parameterized by:

$$\text{cay}_n(\underline{\mathbf{v}}) = \exp \left[ (2n \arctan |\underline{\mathbf{v}}|) \underline{\tilde{\mathbf{u}}}_{\underline{\mathbf{v}}} \right] \quad (27)$$

*Proof* In order to demonstrate this theorem we will use induction knowing that  $\text{cay}_{n+1}(\underline{\mathbf{v}}) = \text{cay}_n(\underline{\mathbf{v}}) \text{cay}(\underline{\mathbf{v}})$  and Theorem 6.

The representation (27) is equivalent to

$$\text{cay}_n(\underline{\mathbf{v}}) = \underline{I} + \frac{1}{(1 + |\underline{\mathbf{v}}|^2)^n} [P_n(|\underline{\mathbf{v}}|) \underline{\tilde{\mathbf{v}}} + Q_n(|\underline{\mathbf{v}}|) \underline{\tilde{\mathbf{v}}}^2] \quad (28)$$

where the terms  $P_n$  and  $Q_n$  are polynomials defined by:

$$P_n(|\underline{\mathbf{v}}|) = \sum_{k=0}^{n-1} a_k |\underline{\mathbf{v}}|^{2k}; a_k = (-1)^k \binom{2k+1}{2n} \quad (29)$$

and

$$Q_n(|\underline{\mathbf{v}}|) = \sum_{k=1}^n b_k |\underline{\mathbf{v}}|^{2(k-1)}; b_k = \binom{k}{n} + (-1)^{k+1} \binom{2k}{2n} \quad (30)$$

where  $\binom{k}{n}$  denotes the binomial coefficients.

These result shows that  $\forall R \in \underline{SO}_3, R = R(\underline{\alpha}, \underline{\mathbf{u}})$  and  $\frac{Re(\underline{\alpha})}{2n} \neq k\pi, k \in \mathbb{Z}$ , a dual vectors  $\underline{\sigma}_n = \left(\tan \frac{\alpha + 2p\pi}{2n}\right) \underline{\mathbf{u}}, p \in \{0, 1, \dots, n-1\}$  exists in order to have  $cay_n(\underline{\sigma}_n) = R$ . If  $p=0$   $\underline{\sigma}_n = \left(\tan \frac{\alpha}{2n}\right) \underline{\mathbf{u}}$  is the **n-th order Modified Rodrigues Parameter dual vector** and if  $p=1, \dots, n-1$ , we recover the **shadow representation** that can be used to describe the same pose. If  $Re\left(\tan \frac{\alpha}{2n}\right) \rightarrow +\infty$ , than  $Re\left(\tan \frac{\alpha + 2p\pi}{2n}\right) \rightarrow -\cot \frac{p\pi}{n}$  which allows the avoidance of any singularity of type  $Re\left(\frac{\alpha}{2n}\right) = \frac{\pi}{2} (mod \pi)$ . In fact, we've demonstrated the following theorem:

**Theorem 8** *The inverse of the n-th order Cayley transform (26) is the multifunction with n branches given by:*

$$cay_n^{-1}(\mathbf{v}): \underline{SO}_3 \rightarrow \underline{V}_3, cay_n^{-1}[R(\underline{\alpha}, \underline{\mathbf{u}})] = \left(\tan \frac{\alpha + 2p\pi}{2n}\right) \underline{\mathbf{u}}, p = \overline{0, n-1} \quad (31)$$

The dual vector parametrization from Theorems 7 and 8 is minimal.

## 5 Conclusions

In this paper we have presented the results of our investigations over vectorial parameterization of rigid motions using the n-th order Cayley transform. These investigations revealed some results specific to the minimal parametrization of the orthogonal dual tensors. Using the isomorphism theorem between Lie group  $\underline{SE}_3$  and the Lie group of the orthogonal dual tensors is obtained a minimal parametrization for the special Euclidean displacement group  $\underline{SE}_3$ . The obtained results are in closed form and they are coordinate-free. Further research will evaluate their performance in different applications.

## References

1. Angeles J (1998) The application of dual algebra to kinematic analysis. *Comput Methods Mech Syst* 161:3–32
2. Bauchau O, Li L (2011) Tensorial parameterization of rotation and motion, *J Comput Nonlinear Dyn* 6:031007.1–031007.8
3. Condurache D, Burlacu A (2014) Dual tensors based solutions for rigid body motion parameterization. *Mech Mach Theory* 74:390–412
4. Condurache D, Burlacu A (2016) Orthogonal dual tensor method for solving the  $AX = XB$  sensor calibration problem. *Mech Mach Theory* 104:382–404
5. Condurache D, Burlacu A (2016) Fractional order Cayley Transforms for dual quaternions based pose representation. *Adv Astronaut Sci Ser* 156:1317–1339
6. Pennestri E, Valentini P (2009) Linear dual algebra algorithms and their application to kinematics. *Multibody Dyn Comput Methods Appl* 12:207–229



7. Selig JM (2007) Cayley maps for  $SE(3)$ . In: Proceedings of the international federation of theory of machines and mechanisms, 12-th world congress, Besançon, France
8. Tanygin S (2012) Attitude parameterizations as higher-dimensional map projections. *J Guid Control Dyn* 35(1):13–24
9. Tsiotras P, Junkins J, Schaub H (1997) Higher-order Cayley transforms with applications to attitude representations. *J Guid Control Dyn* 20(3):528–534

# Kinetostatic of Knife Edge Translating Follower Under Dry Friction Conditions



S. Alaci, F.-C. Ciornei, E.-V. Alexandru and C. Filote

**Abstract** The paper presents the effect of dry friction upon the follower from a mechanism with rotating cam and translating knife edge follower. The contact between the ground and follower is regarded by equivalence as two non-conforming contacts positioned symmetrically about the symmetry plane of the prismatic pair, normal to the direction of velocity of the follower. There are discussed all possible contact solutions. An algorithm is proposed and verified concerning the identification of the actual contact case and the time when this position is reached. For an actual mechanism with imposed uniform rotational motion of the cam, there are found all reactions working upon the follower, for both assumptions: with and without dry friction.

**Keywords** Translating follower · Dry friction · Kinetostatic

## 1 Introduction and Theoretical Remarks

The cam mechanisms are both classical widely used solution and also applied for modern cutting edge engineering appliances, [1–4]. A mechanism with rotating cam and translating knife edge follower is considered. The assumption that the cam rotates with constant angular speed  $\omega$  is extensively accepted, [5–9]. The contact between the cam and the follower is made in  $B$  point. The contact between the follower and the ground is made in the lower pair  $C$  where the contact has made on a cylindrical surface of radius  $a$  and length  $b$ . The basic geometrical parameters of the mechanism are: the eccentricity of the mechanism,  $e$  representing the distance between the rotation centre of the cam and the direction of translation of the follower; the minimum distance  $s_0$  between the tip of the follower and the centre of the cam, obtained only when the follower is positioned on the circle of minimum radius. Under the hypothesis of regular rotation of the cam with angular speed

---

S. Alaci (✉) · F.-C. Ciornei · E.-V. Alexandru · C. Filote  
“Stefan cel Mare” University of Suceava, Suceava, Romania  
e-mail: alaci@fim.usv.ro

$\omega = const.$ , the motion of the follower is described by the laws illustrating the variation of space, velocity and acceleration:

$$s = s(\varphi), \quad v(\varphi) = \omega ds/d\varphi, \quad a(\varphi) = \omega^2 d^2s/d\varphi^2 \quad (1)$$

With the assumption of dry friction in the contacts between the elements of the mechanism, the reaction forces acting upon the follower are wished-for. The distance between the centre of the cam and the plane of symmetry of the contact region is denoted by  $d$ . Upon the follower there are acting the following forces:

- The technological force  $F_t$ , parallel to the direction of the follower:

$$\mathbf{F}_t = -F_t(\varphi, \dot{\varphi}, t)\mathbf{j} \quad (2)$$

- The elastic force  $F_e$  composed by the pre-stressing  $F_{e0}$  and work force  $k\Delta x$ :

$$F_e = F_{e0} = k_e\Delta x_0 \quad (3)$$

where the static deformation of the spring  $\Delta x_{0z}$  is given by the relation:

$$\Delta x_0 = L_0 - (D - s_0 - c/2) \quad (4)$$

where  $L_0$  is the length of unloaded spring and  $k$  is the elastic constant.

- The inertial force  $F_i$ :

$$\mathbf{F}_i = -m\mathbf{a}(\varphi) = -m\frac{d^2s}{d^2\varphi}\omega^2\mathbf{j} \quad (5)$$

The reaction forces from the cam-follower higher pair are reduced to the normal reaction  $\mathbf{R}_{21}$  with the directed along the normal to the profile of the cam and making the  $\alpha$  angle with the direction of the follower, found using the relation:

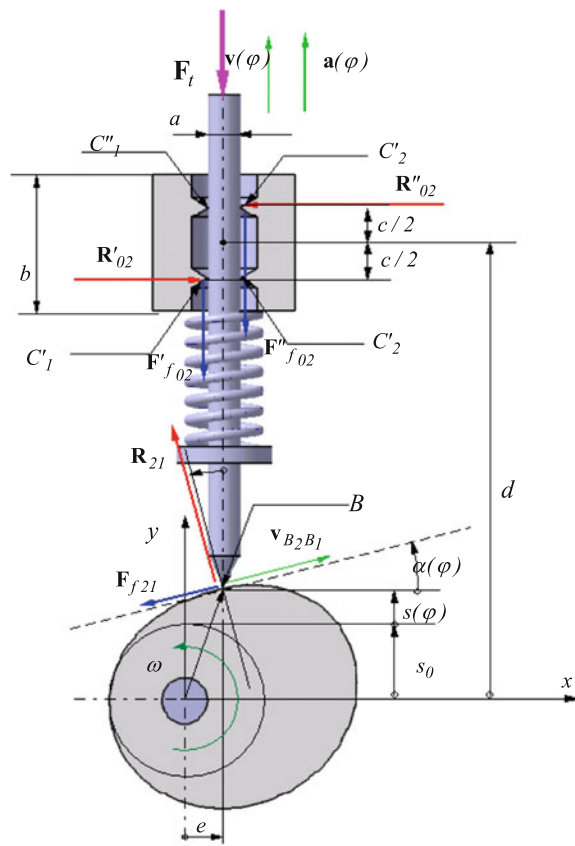
$$\tan \alpha(\varphi) = [(v(\varphi)/\omega) - e]/[s(\varphi) + s_0] \quad (6)$$

The friction force from the higher pair  $\mathbf{F}_{f_{21}}$  is tangent to the profile of the cam and has the expression:

$$\mathbf{F}_{f21} = -\mu_{12}R_{21}\mathbf{v}_{B_2B_1}/v_{B_2B_1} \tag{7}$$

where  $\mathbf{v}_{B_2B_1}$  is the speed at which the tip of the follower moves on the profile of the cam. Under the adopted hypothesis of constant angular velocity of the cam, the angle between the velocity  $\mathbf{v}_{B_2B_1}$  and the  $Ox$  axis is within the range  $(-\pi/2, \pi/2)$ . In a general case, the reaction from the prismatic pair has a component normal to the translation direction, and a tangent friction force, parallel to the translation direction and a reaction torque. In the prismatic pair the distribution of contact pressure is quite complex and for finding it there are required contact mechanics theory knowledge. In order to simplify the kinetostatic study, Duca [5] replaces the normal reaction and the reaction torque by two forces directed along two directions perpendicular to the direction of motion, symmetrical with respect to the centre of the pair and situated at  $c$  distance between them, the value of this distance  $c$  depending on the gap from the pair. To offset this aspect, it is considered that the prismatic pair is constructed as shown in Fig. 1, a case when the contact between the follower and the bushing is theoretically made in two cross-sections, denoted by (') and (") symmetrical with respect to the centre of the bushing and having the

**Fig. 1** Mechanism with rotating cam and translating knife edge follower



$c$  distance between them. As consequence, the assembly constituted by the normal reaction and reaction torque is replaced by a couple of forces  $\mathbf{R}'_{02}$ ,  $\mathbf{R}''_{02}$  placed in the plane of the sketch and action in the two cross-sections. The reactions  $\mathbf{R}_{02}$  and  $\mathbf{R}'_{02}$  are considered sliding vectors due to the hypothesis of rigid follower and ground. These two reactions have the same effect no matter the point of action,  $C'_1$  or  $C'_2$ , and  $C''_1$  or  $C''_2$  respectively. The coefficient of friction from prismatic pair is denoted  $\mu_{02}$  and the friction forces are parallel to the vertical direction and defined by the relations:

$$\mathbf{F}'_{f02} = -\mu_{02}\mathbf{R}'_{02}\text{sgn}(v)\mathbf{v}/v, \mathbf{F}''_{f02} = -\mu_{02}\mathbf{R}''_{02}\text{sgn}(v)\mathbf{v}/v \tag{8}$$

The absolute values of the reactions  $R_{12}$ ,  $R'_{02}$ ,  $R''_{02}$  are the unknowns to be found. To this end, the equations of kinetostatic equilibrium are applied:

$$\sum \mathbf{F} = 0; \quad \sum \mathbf{M}_B = 0 \tag{9}$$

With reference to Eq. 9, for the first two of them, the points where the reactions forces  $R'_{02}$ ,  $R''_{02}$  act are not important but for the equation of moments, the points where these operate are essential since they give the sign of friction torque. It is obvious that depending on the position of the follower, it is possible that any pair of points ( $C'_1, C'_1$ ), ( $C'_2, C'_1$ ), ( $C'_1, C'_2$ ), ( $C'_2, C'_2$ ) becomes the actual pair of contact points.

For the four potential situations illustrated in Fig. 2 the equations of moments are given below, written with respect to tip of the follower (B point form Fig. 1):

$$R'_{02}[\mu_{02}\text{sgn}(v)a/2 - (d - c/2)] + R''_{02}[\mu_{02}\text{sgn}(v)a/2 - (d + c/2)] = 0 \tag{10.a}$$

$$R'_{02}[\mu_{02}\text{sgn}(v)a/2 - (d - c/2)] - R''_{02}[\mu_{02}\text{sgn}(v)a/2 - (d + c/2)] = 0 \tag{10.b}$$

$$-R'_{02}[\mu_{02}\text{sgn}(v)a/2 - (d - c/2)] + R''_{02}[\mu_{02}\text{sgn}(v)a/2 - (d + c/2)] = 0 \tag{10.c}$$

$$-R'_{02}[\mu_{02}\text{sgn}(v)a/2 - (d - c/2)] - R''_{02}[\mu_{02}\text{sgn}(v)a/2 - (d + c/2)] = 0 \tag{10.d}$$

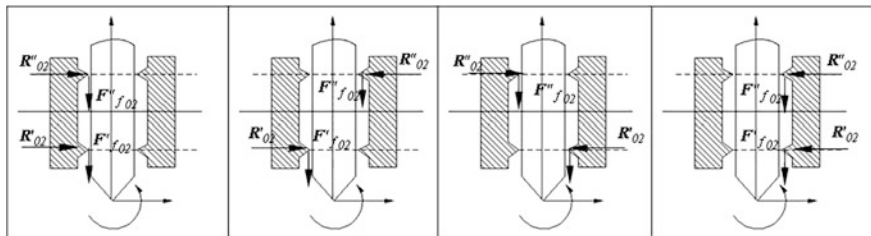


Fig. 2 Possible situations

The explicit form of force Eq. 9 is:

$$\mathbf{F}_t + \mathbf{R}_{12} + \mathbf{F}_{f_{12}} + \mathbf{R}'_{02} + \mathbf{R}''_{02} + \mathbf{F}'_{f_{12}} + \mathbf{F}''_{f_{12}} = 0 \tag{11}$$

where  $\mathbf{F}_t$  is the sum between inertial force  $\mathbf{F}_i$ , technological force  $\mathbf{F}_T$  and elastic force  $\mathbf{F}_e$ , this resultant being permanently oriented on the vertical direction. The vector Eq. 11 has two scalar projection equations and together to each of the equation of moments 10 gives a linear system of three equations, with reactions  $R_{12}, R'_{02}, R''_{02}$  as unknowns. One can show that all the four systems can be written in the following compact form:

$$\begin{bmatrix} -\sin \alpha - \mu_{12} \cos \alpha & s' & s'' \\ \cos \alpha - \mu_{12} \sin \alpha & -\mu_{02} \operatorname{sgn} v & -\mu_{02} \operatorname{sgn} v \\ 0 & s' [\mu_{02} \operatorname{sgn} v \frac{g}{2} - (d - \frac{\xi}{2})] & [\mu_{02} \operatorname{sgn} v \frac{g}{2} - (d + \frac{\xi}{2})] s'' \end{bmatrix} \begin{bmatrix} R_{12} \\ R'_{02} \\ R''_{02} \end{bmatrix} = \begin{bmatrix} 0 \\ -F_T \\ 0 \end{bmatrix} \tag{12}$$

The reactions  $R_{12}(s', s'')$ ,  $R'_{02}(s', s'')$  and  $R''_{02}(s', s'')$  can be found from the system 12 for all the cases presented in Fig. 2. The issue arising is how to choose the appropriate solution from the four cases. With this aim, it is used the Heaviside step function  $\Phi(x)$  and an additional function defined as:

$$g(x) = \begin{cases} 1, & x=2 \\ 0, & \text{otherwise} \end{cases} \tag{13}$$

To all possible contact situations from the prismatic pair, form Fig. 2, correspond pairs of  $(s', s'')$  parameters, with values  $\pm 1$ . A considered contact can be actual contact if the reactions  $R'_{02}$  and  $R''_{02}$  are simultaneously directed towards the material of the follower, that is, they should be simultaneously positive. The expression allowing for the selection of the aimed  $R'_{02}$  and  $R''_{02}$  is written as:

$$\tilde{\mathbf{X}}(\varphi) = \begin{bmatrix} X(\varphi, 1, 1) \\ X(\varphi, -1, 1) \\ X(\varphi, 1, -1) \\ X(\varphi, -1, -1) \end{bmatrix}^T \begin{bmatrix} g[\Phi(R'_{02}(\varphi, 1, 1) + \Phi(R''_{02}(\varphi, 1, 1)))] \\ g[\Phi(R'_{02}(\varphi, -1, 1) + \Phi(R''_{02}(\varphi, -1, 1)))] \\ g[\Phi(R'_{02}(\varphi, 1, -1) + \Phi(R''_{02}(\varphi, 1, -1)))] \\ g[\Phi(R'_{02}(\varphi, -1, -1) + \Phi(R''_{02}(\varphi, -1, -1)))] \end{bmatrix} \tag{14}$$

where  $X(\varphi, s', s'')$  is any of the reactions  $R_{12}(s', s'')$ ,  $R'_{02}(s', s'')$  or  $R''_{02}(s', s'')$  found with the hypothesis of presence of friction in the pair. The relation (14) ensures that the found reactions are directed towards the follower and the contact between the ground and the follower is certainly maintained. The notation  $\tilde{X}0(\varphi, s', s'')$  was used for any of the above reactions calculated with the assumption of lack of friction in all the kinematical pairs of the mechanism. In fact, the expression (14) is a sum of

four terms having the form  $X(\varphi, s', s'')g[\Phi(R'_{02}(\varphi, s', s'') + \Phi(R''_{02}(\varphi, s', s''))]$ , and according to the definition of  $g(x)$  function, this term is zero when at least one of the reactions  $R'_{02}(\varphi, s', s'')$ ,  $R''_{02}(\varphi, s', s'')$  cancels for the actual values of  $s'$  and  $s''$  parameters. Another problem to be solved refers to the identification of the actual contact situation from the four possibilities occurring when the rotation angle of the cam has a certain value. With this purpose, for the four possible contact situations from Fig. 2, the indices 1, 2, 3 and 4 are used. A function  $G$  is created, having the expression:

$$G(\varphi) = \begin{bmatrix} 1 \\ 2 \\ 3 \\ 4 \end{bmatrix}^T \begin{bmatrix} g[\Phi(R'_{02}(\varphi, 1, 1) + \Phi(R''_{02}(\varphi, 1, 1)))] \\ g[\Phi(R'_{02}(\varphi, -1, 1) + \Phi(R''_{02}(\varphi, -1, 1)))] \\ g[\Phi(R'_{02}(\varphi, 1, -1) + \Phi(R''_{02}(\varphi, 1, -1)))] \\ g[\Phi(R'_{02}(\varphi, -1, -1) + \Phi(R''_{02}(\varphi, -1, -1)))] \end{bmatrix} \quad (15)$$

Similar to relation (14), the  $G(\varphi)$  returns the index of the contact case, which for a indicated value of the  $\varphi$  angle ensures for both reactions  $R'_{02}$  and  $R''_{02}$  positive values simultaneously; thus, the contact is validated as actual contact.

## 2 Exemplifying Method. Discussions

A cam mechanism is considered for exemplifying the methodology and the following dimensions and parameters were used:  $s_0 = 40$  mm,  $e = 30$  mm,  $h = 40$  mm,  $t_1 = 0.2$  s,  $t_2 = 0.04$  s,  $t_3 = 0.2$  s,  $t = 0.08$  s,  $c = 30$  mm,  $a = 20$  mm,  $d = 60$  mm,  $\mu_{02} = 0.3$ ,  $\mu_{12} = 0.3$ ,  $M = 0.4$  kg,  $k_e = 50$  N/m,  $F_{e0} = k_e h/3$ .

The forces acting upon the follower are presented in Fig. 3: the technological force, the elastic force and the inertial force. Using the above data, the reactions

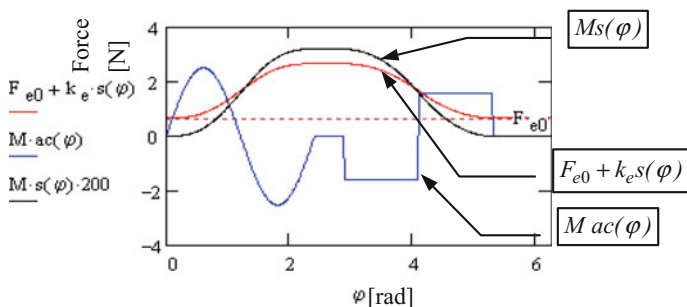


Fig. 3 Forces acting upon the follower

$R_{fn12}, R_{f02}, R''_{f02}$  found when friction is present, are shown in Fig. 4 together to the reactions  $R_{n12}, R_{n02}, R''_{n02}$  found in the absence of friction, and the sum  $T(\varphi)$  of all known forces from Fig. 3. From Fig. 4 it can be observed that as concerning the reaction  $R_{12}$  the presence of friction does not change the plot essentially but the referring to the reactions from the prismatic pair the friction plays a major effect in the pairs and it can increase (even two times) the value of reaction forces. During a complete running cycle, as presented in Fig. 5, all the four situations of possible contact form Fig. 2 can be met and these can even repeat. From Fig. 5 it is noticed that, for the data considered in exemplifying, there are six changes in the configuration of reactions from the prismatic pair for a complete cam rotation.

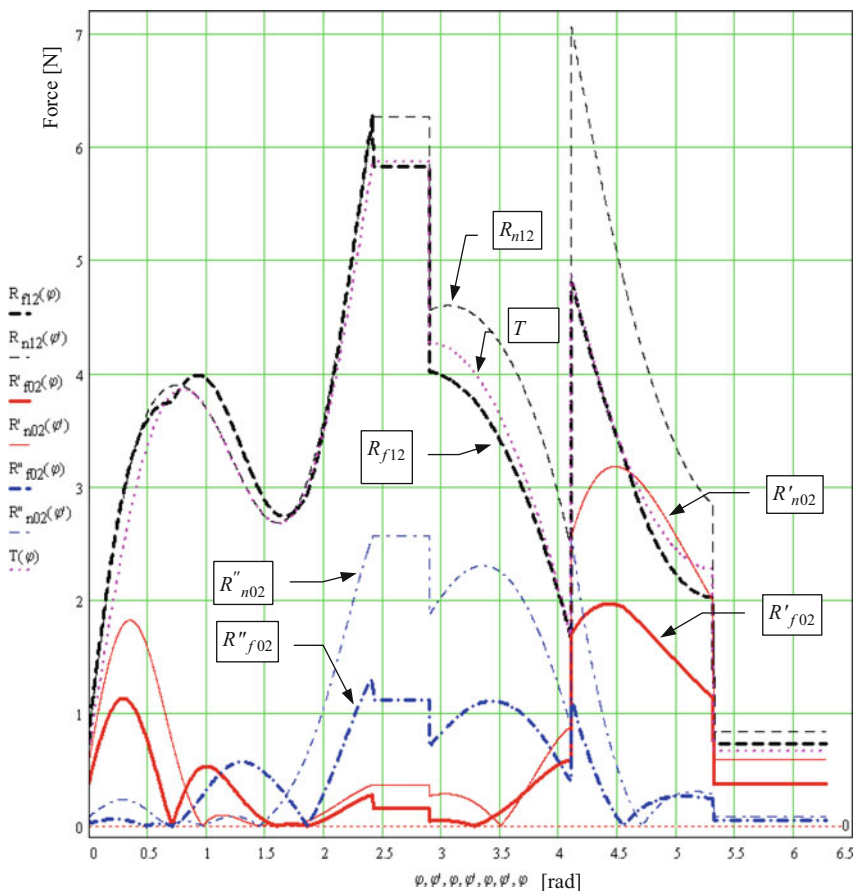


Fig. 4 The reactions from the contacts of the follower, with and without friction



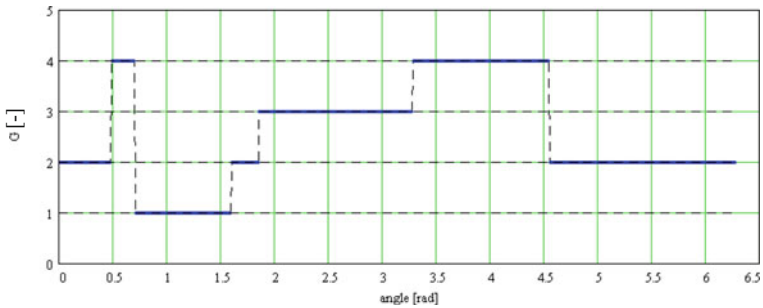


Fig. 5 The identification of the actual contact case

### 3 Conclusions

The paper presents the result of kinetostatic analysis for a rotating cam mechanism with translating knife edge follower, assuming the hypotheses of dry friction existence in the pairs of the mechanism and of known motion of the cam. It is proved that four configurations of reaction forces can occur in the prismatic pair of the mechanism and the analytical expressions of the reactions acting upon the follower are found for all four cases. Then the criteria for the selection of the actual contact from the four possible cases are presented. It is also presented a criterion for identifying the actual configuration of reaction forces for a specified position of the cam. To facilitate the estimation of the effect dry friction from the pairs of the follower, the same reactions were found and represented in the absence of friction, too. It is noticed that the most powerful effect of friction occurs in the prismatic pair. For suitable values of the geometrical parameters and operating parameters, it is possible that, during a complete running cycle, all the four possible configurations are met and they also could repeat in the course of period.

### References

1. Alaci S et al (2007) A new type of cam mechanism, Oradea. F Man Tech Eng XVI 587
2. Alaci S et al (2011) Some aspects regarding computer aided design of cam mechanisms with flat face oscillating follower, Fiabil Durab 1(7):65
3. Alaci S, Ciomei F-C, Filote C (2015) Rotating cam and knife edge follower mechanism optimisation from cam curvature constraints. AMM 809–810:598
4. Angeles J, Lopez-Cajun CS (1991) Optimization of cam mechanisms. Publ, Kluwer Acad
5. Duca C (1983) Mecanisme. I.P, Iasi
6. Norton RL (2002) Cam design and manufacturing handbook. Industrial Press, New York
7. Pandrea N, Popa D, Stanescu ND (2017) Classical and modern approaches in the theory of mechanisms. Wiley
8. Rider MJ (2015) Design and analysis of mechanisms: a planar approach. Wiley
9. Uicker Jr JJ, Pennock GG (2016) Theory of machines and mechanisms. Oxford, UP

# Tetrapod Coupling



S. Alaci, F. Buium, F.-C. Ciornei and D.-I. Dobincă

**Abstract** The paper presents a solution for coupling two shafts with non-coplanar axes using an intermediary element. The intermediary part is connected with the ground via a spherical pair while, to the shafts, two point-surface contacts are used. For the proposed model, the positional analysis, a CAD model and numerical validation of the solution are presented. The advantage of the *tetrapod coupling* consists in constructive simplicity and controlled reliability by the possibility of replacing the higher pairs of the intermediary element with linkages with lower pairs.

**Keywords** Kinematics · Shaft coupling · Linkage · Transmission ratio

## 1 Introduction

A problem frequently met in technical applications is the coupling of two shafts. Several criteria must be satisfied in designing an actual coupling solution. From these principle factors, constructive plainness, low cost price and acceptable quality of transmitted motion can be encountered. In some cases, the condition on transmission ratio is strictly imposed, such as constant (in homo-kinetic couplings) or varying between preset limits. Gears represent a general feasible solution for direct coupling of two shafts, no matter the relative position of the axes, the motion being transmitted via a higher pair composed by the flanks of teeth. The gear transmissions present the advantage of constant ratio but the drawback consists in the high price, disadvantage that diminishes in the mass production case. Sometimes the constraints concerning the transmission ratio are not very severe and a variation of

---

S. Alaci (✉) · F.-C. Ciornei · D.-I. Dobincă  
“Stefan cel Mare” University of Suceava, Suceava, Romania  
e-mail: alaci@fim.usv.ro

F. Buium  
“Gheorghe Asachi” Technical University of Iasi, Iași, Romania  
e-mail: fbuium@mail.tuiasi.ro

the ratio is accepted for the benefit of constructively simple models or lower price or transmission reliability. There are various works regarding the coupling of two shafts solutions [6, 8, 9]. The relative position of the axes between which the motion must be transmitted is the essential factor in solving the coupling problem. There are classical solutions for the particular cases when the axes are coplanar. Thus, for concurrent axes the universal joint or Cardan coupling solution exists while for parallel shafts, Oldham coupling and Schmidt couplings are several of the most used. For crossed axes, there are multiple solutions, like Rzeppa coupling, tripod coupling with curve-curve contact [1] or point-surface contact [2, 3].

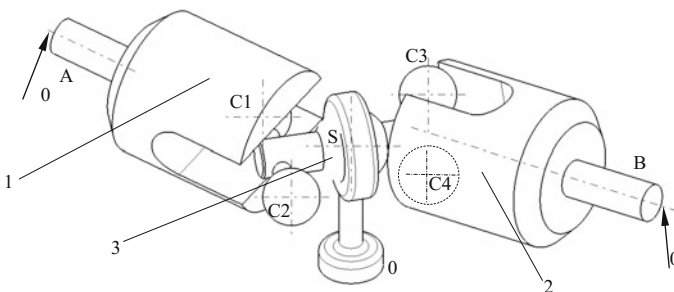
## 2 Structural Synthesis Approach

The mobility  $M_f$  of a spatial mechanism belonging to  $f$  family is given by [7]:

$$M_f = 6(n-1) - \sum_{k=f+1}^5 (k-f)c_k \quad (1)$$

It is observed straight away that in the case of zero family mechanisms, when direct coupling between the shafts exists,  $n=3$  elements (shafts and the ground); the revolute joints already exist in the structure—being the joints  $c_k$  between the shafts and the ground and the only possible structural solution is  $c_1=1$ ,  $c_k=0, k > 1$ .

When an intermediary coupling element is accepted,  $n=4$  from the  $6 \cdot 3 = 18$  degrees of freedom  $2 \cdot 5 = 10$  are cancelled by the joints of the shafts and additionally another degree of freedom corresponds to the driving element. So, it remains a number of 7 degrees of freedom that must be ensured by the linkage occurring between the intermediary coupling element and the rest of the elements. Obviously, there are multiple structural solutions. The present work considers the solution from Fig. 1, where the coupling element 3 makes two point contacts with



**Fig. 1** Tetrapod coupling

each of the two shafts and a spherical pair with the ground. The existence of the four contacts between spherical surfaces and plane surfaces directed to the implementation of *tetrapod coupling* name.

### 3 Positional Analysis of the Coupling

For the spatial mechanisms with lower pairs a very valuable tool is the method proposed by Hartenberg–Denavit [5] or the method of homogenous operators. In order to apply the method for the actual case, the replacement of the four contacts with kinematical chains with lower pairs is required. It results an equivalent mechanism with a large number of elements that necessitates complex calculus.

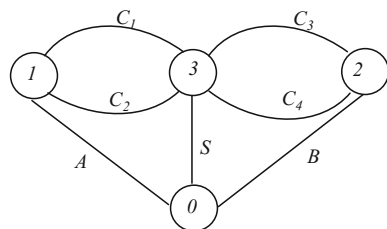
From the graph attached to the mechanism, Fig. 2, it also results the fact that the mechanism is very complex. The graph shows that all four independent cycles must be simultaneously considered for the analysis of the mechanism.

In order to solve the problem, the same procedure as in work [2] is applied. Basically, the position of the coupling elements is obtained by imposing the condition that the centres of the balls are permanently on the planes of symmetry of the grooves from the two shafts. With the aim of applying the proposed methodology, it is required that the equations of the planes of symmetry and the coordinates of the centres of the balls are expressed in the same coordinate system. To this end, the following frames of reference are defined:

1. the coordinate system attached to the ground  $Ox_0y_0z_0$ , having the features: the origin  $O$  of the fixed system coincides with the centre of the spherical joint of intermediary element; the  $Ox_0$  axis is chosen parallel to the common normal of the driving axis and driven axis; the positive sense is chosen from the leg of  $O_{out}$  normal towards the leg of  $O_{in}$  normal; each of the driving and driven axis define a plane, respectively; the bisector plane of the dihedral angle made by the two planes has the normal parallel to  $Oy_0$  axis; the  $Oz_0$  axis completes a right tri-orthogonal system.

Choosing the coordinate system of the ground as described above presents the advantage that the axes of the driven element and driving element have the same inclination with respect to horizontal plane,  $Ox_0y_0$  (Figs. 3 and 4).

Fig. 2 Graph of the mechanism



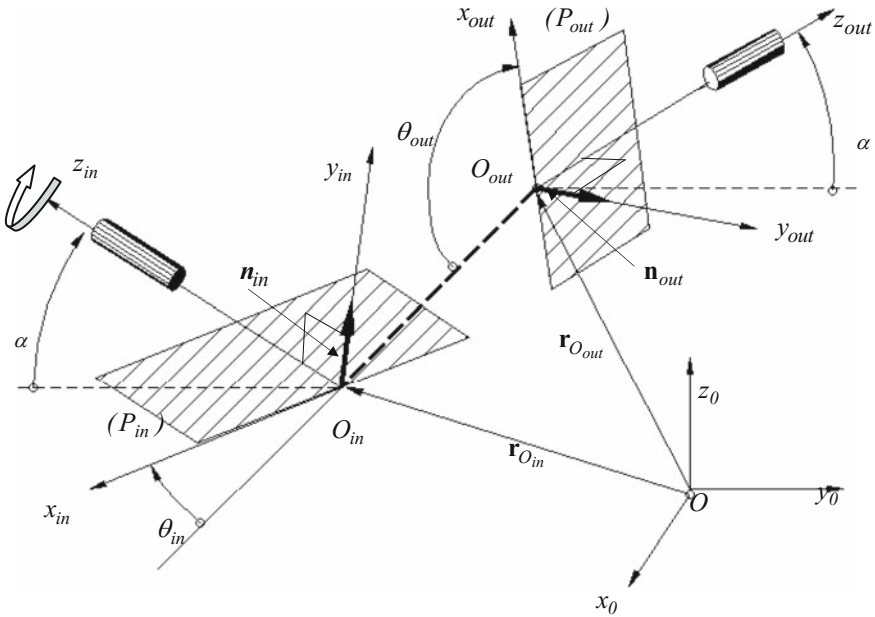
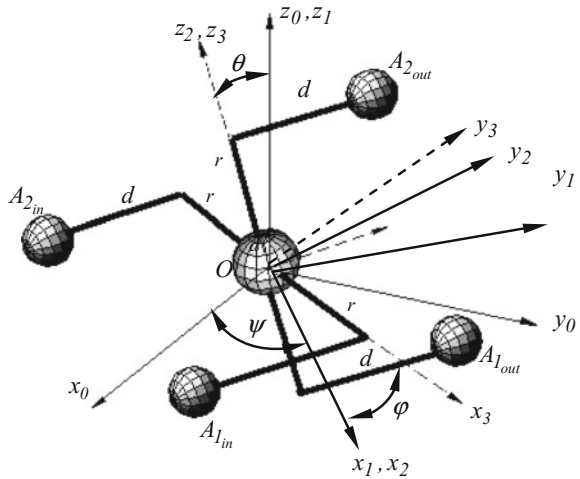


Fig. 3 Coordinate systems attached to the ground and to the two shafts, respectively

Fig. 4 Coordinate systems attached to the intermediary coupling element



- frames of reference defined for the driving shaft and driven shaft respectively, with the axes  $z_{in}$  and  $z_{out}$  in coincidence with the rotation axis of the shafts, and the axes  $Ox_{in}$  and  $Ox_{out}$ , respectively, in coincidence with the common normal: the  $y_{in}$  and  $y_{out}$  axes are each one completing a corresponding right coordinate

system. The unit vectors of these axes are the unit vectors of the normals to the planes of symmetry  $P_{in}$  and  $P_{out}$  of the grooves from the two shafts ( $\mathbf{n}_{in}$  and  $\mathbf{n}_{out}$  are the normals to the two planes); the manner the system  $x_0y_0z_0$  was chosen makes that in this system, the points  $O_{in}$  and  $O_{out}$  have identical coordinates, except for the abscissas:  $O_{in}(x_{O_{in}}, y_O, z_O), O_{out}(x_{O_{out}}, y_O, z_O)$ ; the rotation angles of the two shafts are denoted by  $\theta_{in}$  and  $\theta_{out}$ , respectively. The motion from the spherical joint completed by the ground and the intermediary coupling element is viewed as a sequence of three rotations of (313) type about the  $Oz_0, Ox_1$  and  $Oz_2$  axes. Using this series of rotations, the fixed frame overlies the system fixed to the intermediary element,  $Ox_3y_3z_3$ .

The centres of the balls are placed in the points  $A_{1_{in}}(r, -d, 0), A_{2_{in}}(-r, -d, 0)$  and  $A_{1_{out}}(0, d, -r), A_{2_{out}}(0, d, r)$ , respectively (defined in  $Ox_3y_3z_3$  frame). The following simple displacements [4] are defined in Table 1 in order to be able to describe the necessary coordinate transformations.

The displacement indicating the superposition of the coordinate system  $x_0y_0z_0$  is:

$$\mathbf{R}(\psi, \theta, \varphi) = \mathbf{Z}(\psi)\mathbf{X}(\theta)\mathbf{Z}(\varphi). \tag{5}$$

The coordinates of the centres of the balls in  $x_0y_0z_0$  system are obtained using the relations:

$$\begin{bmatrix} \mathbf{r}0_{A1,2_{in,out}} \\ 1 \end{bmatrix} = \mathbf{R}(\psi, \theta, \varphi) \begin{bmatrix} \mathbf{r}3_{A1,2_{in,out}} \\ 1 \end{bmatrix} \tag{6}$$

where  $\mathbf{r}0_{A1,2_{in,out}}, \mathbf{r}3_{A1,2_{in,out}}$  are column vectors that include the coordinates of the centres of the balls expressed in  $x_0y_0z_0$  and  $x_3y_3z_3$  frames, respectively. For the displacement of “0” frame over the reference system fixed to the driving/driven shaft, the following transformation is applied:

$$\mathbf{D}_{0,in} = \mathbf{T} \left( \begin{bmatrix} x_{0in} \\ y_0 \\ z_0 \end{bmatrix} \right) \mathbf{X} \left( \frac{\pi}{2} - \alpha \right) \mathbf{Z}(\theta_{in}) \tag{7}$$

The unit vector  $\mathbf{n}_{in}$  of the normal to the  $P_{in}$  plane expressed in “0” frame of reference is:

**Table 1** Matrices of homogenous operators of simple displacements

The translation of the vector $\mathbf{v}(v_x, v_y, v_z)$	The rotation with $\theta$ angle about $Oz$ axis	And the rotation with $\alpha$ angle about $Ox$ axis
$\mathbf{T}(\mathbf{v}) = \begin{bmatrix} 1 & 0 & 0 & v_x \\ 0 & 1 & 0 & v_y \\ 0 & 0 & 1 & v_z \\ 0 & 0 & 0 & 1 \end{bmatrix}$ <p>(2)</p>	$\mathbf{Z}(\theta) = \begin{bmatrix} \cos \theta & -\sin \theta & 0 & 0 \\ \sin \theta & \cos \theta & 0 & 0 \\ 0 & 0 & 1 & 0 \\ 0 & 0 & 0 & 1 \end{bmatrix}$ <p>(3)</p>	$\mathbf{X}(\theta) = \begin{bmatrix} 1 & 0 & 0 & 0 \\ 0 & \cos \alpha & -\sin \alpha & 0 \\ 0 & \sin \alpha & \cos \alpha & 0 \\ 0 & 0 & 0 & 1 \end{bmatrix}$ <p>(4)</p>

$$\mathbf{n}\mathbf{0}_{in} = \mathbf{D}\mathbf{0}_{,in} \left( \begin{bmatrix} 0 \\ 1 \\ 0 \\ 1 \end{bmatrix} - \begin{bmatrix} 0 \\ 0 \\ 0 \\ 1 \end{bmatrix} \right) \quad (8)$$

In a similar manner the unit vector  $\mathbf{D}\mathbf{0}_{,out}$  of the normal to the  $P_{out}$  plane is found:

$$\mathbf{D}\mathbf{0}_{,out} = \mathbf{T} \left( \begin{bmatrix} x_{0out} \\ y_0 \\ z_0 \end{bmatrix} \right) \mathbf{X} \left( \frac{\pi}{2} + \alpha \right) \mathbf{Z}(\theta_{out}) \quad (9)$$

The equations of the planes  $P_{in}$  and  $P_{out}$  in the “0” coordinate system are:

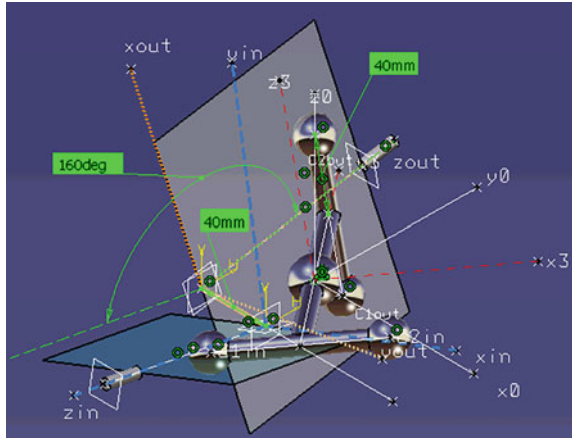
$$\mathbf{n}_{in,out} \left( \begin{bmatrix} x \\ y \\ z \\ 1 \end{bmatrix} - \begin{bmatrix} x_{in,out} \\ y_0 \\ z_0 \\ 1 \end{bmatrix} \right) = 0 \quad (10)$$

The condition that the coordinates of the  $\mathbf{r}\mathbf{0}_{A1,2in,out}$  points representing the centres of the balls expressed with respect to “0” coordinate system verify the equations of the planes 10 conduct to a system of four nonlinear trigonometric equations. With the assumption that the position of the driving element is specified by the parameter  $\theta_1$ , the parameters  $\psi, \theta, \varphi$  and  $\theta_{out}$  are found by solving the system:

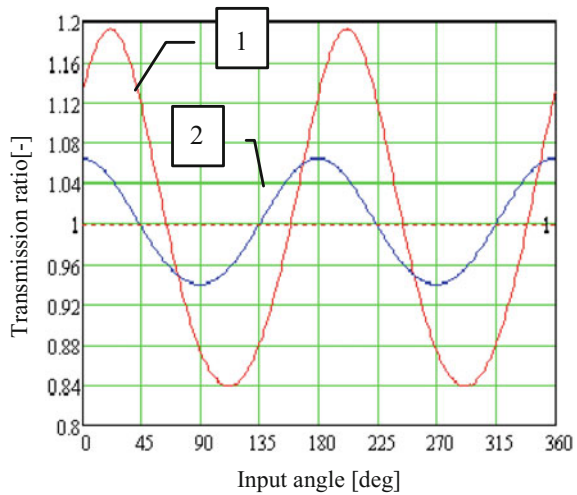
$$\begin{cases} [(-\sin \psi \cos \theta \sin \varphi + \cos \psi \cos \varphi) \sin \theta_m + .. \\ (-\sin \alpha \cos \psi \cos \theta \sin \varphi - \cos \alpha \sin \theta \sin \varphi) \cos \theta_m = 0 \\ (-\sin \alpha \cos \psi \cos \theta \cos \varphi - \cos \alpha \sin \theta \cos \varphi + \sin \alpha \sin \psi \sin \varphi) \cos \theta_m + \\ -\sin \theta_m (\sin \psi \cos \theta \cos \varphi + \cos \psi \sin \varphi) d - \sin \alpha \cos \theta_{in} y_0 - \cos \alpha \cos \theta_{in} z_0 + \sin \theta_{in} x_{0in} = 0 \\ (\sin \alpha \cos \psi \sin \theta + \cos \alpha \cos \theta) \cos \theta_{out} + \sin \psi \sin \theta \sin \theta_{out} = 0 \\ [(\cos \psi \sin \varphi + \sin \psi \cos \theta \cos \varphi) \sin \theta_{out} + (\sin \alpha \cos \psi \cos \theta \cos \varphi - \cos \alpha \sin \theta \cos \varphi \\ - \sin \alpha \sin \psi \sin \varphi) \cos \theta_{out}] d + \sin \theta_{out} x_{0out} \sin \alpha \cos \theta_{out} y + \cos \alpha \cos \theta_{out} z_0 = 0 \end{cases} \quad (11)$$

The form of the equations requires applying a Newton-Raphson [4] numerical procedure for solving the system. The most difficult part of the numerical algorithm consists in identifying the guess value for a convergent procedure. To overcome this issue, the transmission was modeled using CAD software with the purpose to obtain a series of suitable parameters for the system, Fig. 5. The equations can be verified and additionally an estimation of the transmission ratio of the coupling can be made and compared to the cardanic joint, the same angle, Fig. 6. As input data there were considered:  $\alpha = 10^\circ$ ;  $\theta_{in} = 20^\circ$ ;  $x_{0in} = -40$  mm;  $y_{0in} = -30$  mm;  $z_{0in} = -10$  mm;  $x_{0out} = 0$ ;  $y_{0out} = -30$  mm;  $z_{0out} = -10$  mm;  $d = 60$  mm;  $r = 40$  mm and the solutions of system 11 obtained using CAD software are:  $\theta_{out} = -101.588^\circ$ ;  $\psi = -84.802^\circ$ ;  $\theta = 11.499^\circ$ ;  $\varphi = 124.866^\circ$ .

**Fig. 5** CAD modelled tetrapodic coupling



**Fig. 6** Tetrapodic (1) and cardanic (2) transmission ratios



## 4 Conclusions

The paper presents a solution for the coupling of two shafts with crossed axes, using an intermediary rigid element.

In the first part of the paper there are identified the types of pairs where the intermediary element is involved employing structural analysis elements. The proposed structural solution consists in a link that together with the ground makes a spherical pair and in two point-surface contacts, formed with each of the two shafts (like the pier tetrapods) thus the chosen name of tetrapod coupling is justified.

The last part of the work is dedicated to positional analysis of the designed coupling. To apply the Hartenberg–Denavit homogenous operators methodology,



the equivalent linkages of the point-surface contacts are required. The obtained replacing mechanism is complex as structure and from here, complicated calculus is expected. To avoid this aspect, the geometrical constraint is exploited in the work and a system of four transcendental trigonometric equations is obtained. Since the analytical solution cannot be found, coupling was modelled in CAD software and a particular solution was obtained for testing the system of equations.

The designed *tetrapod coupling* presents a constructive simplicity and assumes controlled reliability since there is the option (for future work) of replacing the higher pairs of the intermediary element with linkages with lower pairs.

## References

1. Akbil E, Lee TW (1984) On the motion characteristics of tripode joints. Part 1: general case, Part 2: applications. ASME J Mech Transm Autom Des 106:228–241
2. Alaci S, Ciornei F-C, Filote C (2013) Considerations upon a new tripod joint solution. Mechanika 19(5):567–574
3. Alaci S., Ciornei M-C, Filote C, Ciornei F-C, Gradinariu MC (2016) Considerations upon applying tripodic coupling in artificial hip joint. In: IOP Conference series: materials science and engineering, vol 147. <https://doi.org/10.1088/1757-899x/147/1/012074>
4. Hamming RW (1987) Numerical methods for scientists and engineers, 2nd edn. Dover books on mathematics
5. Hartenberg RS, Denavit J (1965) Kinematic synthesis of linkages, McGraw-Hill series in mechanical engineering. McGraw-Hill, New York
6. Mariot JP, K'nevez J-Y (1999) Kinematics of tripode transmissions. A new approach. Multibody Syst Dyn 3:85–105
7. McCarthy JM (1990) Introduction to theoretical kinematics. MIT Press
8. Miloiu G, Dudiță F, Diaconescu DV (1980) Transmisii mecanice moderne, 2nd edn. Tehnică, București
9. Wang XF, Chang DG, Wang JZ (2009) Kinematic investigation of tripod sliding universal joints based on coordinate transformation. Multibody Syst Dyn 22:97–113

# Some Mechanisms Using Internal Gears with Small Difference in Numbers of Teeth



O. Crivoi and I. Doroftei

**Abstract** Despite of some drawbacks (interference, small contact ratio) internal gears with small difference in numbers of teeth have some advantages, especially when they are used in hypocycloid mechanisms (high transmission ratio and high torque at small size). This paper is focusing on using these kinds of gears in mechanisms that are using the benefits of them. Some mechanisms converting rotary motion into translation and hypocycloid mechanisms will be discussed.

**Keywords** Internal gear · Motion converting · Hypocycloid mechanism

## 1 Introduction

Internal gears with small difference in the teeth numbers have some advantages, especially when they are used in planetary or differential mechanisms [2]. Due to internal meshing and also to the small difference in numbers of teeth, there is the possibility of multiple teeth meshing simultaneously in the planetary gear drive with small teeth difference. The load could be shared among more than one pair of mating teeth, which will lead to a stronger load capability at the same size of gearbox, if we compare with countershaft one [6]. This problem has been also investigated by other researchers, their works dealing with clearance estimation, backlash calculation on gearing teeth and related experiments. Some others are keeping on doing research in recent years [3, 8].

But, beside this, they also have some drawbacks as interference (involute, trochoid and trimming interference) and small contact ration (the contact ratio decreasing when the difference of the teeth numbers is decreasing) [2]. In planetary gear drive with small difference in teeth numbers, addenda modification on tooth

---

O. Crivoi · I. Doroftei (✉)

“Gheorghe Asachi” Technical University of Iasi, Iași, Romania  
e-mail: idorofte@mail.tuiasi.ro

O. Crivoi  
e-mail: crivoi2003@yahoo.com

form is necessary to avoid potential teeth interference. This leads to complicity in design and cutting process [8]. This is why research on optimizing the geometry of the gear is required.

This paper is not focused on the internal gears with small difference in teeth numbers optimization but on presenting some examples on how to use the benefits of these gears in building some mechanisms.

## 2 Some Specific Aspects of Internal Gears

Internal gears are commonly used in planetary gear systems and compact gear boxes. The primary advantage of an internal gear set is the compactness of the drive. Also, both the pinion and gear rotate in the same direction. Other advantages are the lower contact stresses because the surfaces conform better than external gear sets. There are also lower relative sliding between teeth and a greater length of contact possible between mating teeth since there is no limit to the involute profile of the flank of the internal gear.

But, beside this, they also have some drawbacks as: interference and small contact ration when the difference of the teeth numbers is small. If the contact ratio is less than 1, contact will be lost part of the time, and the gear pair cannot function properly. If the contact ratio is close to 1, variations caused by errors in mounting or wear may cause loss of contact. This is why, in practice, contact ratio smaller than 1.2 should be avoided.

There are three different types of interference encountered in the case of internal gears: involute interference, trochoid interference and trimming interference.

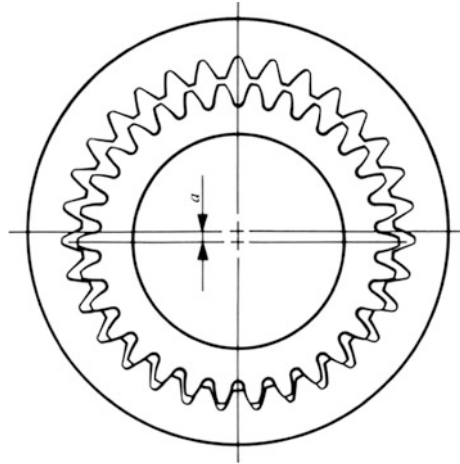
The first type of interference occurs between the dedendum of the external gear and the addendum of the internal gear. It is possible to happen when the external gear teeth number is small. Assuming that an internal gear pair becomes interesting when the numbers of teeth is big, in order to get a high transmission ratio, the involute interference could be avoided [5].

The second type of interference (trochoid interference) may occur during recess tooth action at the addendum of the external gear and the dedendum of the internal gear. This interference tends to appear when the teeth numbers difference is small, which is the case of a hypocycloid mechanism with high transmission ratio, for example. Trochoid interference could be avoided if the teeth numbers difference,  $z_2 - z_1$ , is bigger than 9 [5].

Trimming interference tends to happen when the teeth numbers difference of the two gears is very small (see Fig. 1) [5]. In this case, the assembling of the gear pair could be done using axial sliding of the gears.

When the difference between the teeth numbers is very small, a profile shifted gear could prevent the interference. In Table 1 is presented an example of preventing the interference, when  $z_2 = 50$  and the teeth numbers difference of the two gears ranges from 1 to 8 [5].

**Fig. 1** Internal gear with the difference  $z_2 - z_1 = 1$  [5]



**Table 1** The Meshing of internal and external gears of small difference of numbers of teeth ( $m = 1, \alpha = 20^\circ$ ) [5]

$z_1$	$z_2$	$x_1$	$x_2$	$\alpha_w$ ( $^\circ$ )	$a$ (mm)	$\epsilon$
79	50	0	1.00	61.0605	0.971	1.105
48			0.60	46.0324	1.354	1.512
47			0.40	37.4155	1.775	1.726
46			0.30	32.4521	2.227	1.835
45			0.20	28.2019	2.666	1.933
44			0.11	24.5356	3.099	2.014
43			0.06	22.3755	3.557	2.053
42			0.01	20.3854	4.010	2.088

All the combinations presented in Table 1 may avoid involute interference or trochoid interference, but not the trimming interference. As it was mentioned before, for a successful assembling, the external gear should be mounted by inserting it in the axial direction [5]. A profile shifted internal gear pair with a small teeth numbers difference may be used in building mechanisms with some benefits.

### 3 Mechanisms for Converting Rotary Motion into Linear Motion

The use of internal gears with a small difference in teeth number and fixed axes is of little interest since the transmission ratio of them is very close to the unit. At the limit, when this difference is zero, the transmission ratio is equal to the unit and that transmission can be used as a coupling between two parallel axes with a small distance between their axes.

There are different mechanisms for converting rotary motion into linear motion, the screw nut mechanism being one of them. A precision machine or those concerned with high efficiency often uses a ball screw nut mechanism. If the efficiency should be accompanied by very fine linear positioning and high load, the problem could not be solved using a simple ball screw nut transmission.

However, combining internal gears with a small difference  $z_2 - z_1$  with the screw nut mechanism, for example, we can get mechanisms that provide a large transmission ratio to a small size, which can convert rotary motion of the driving screw in a translational motion of the driven link. Some such mechanisms will be presented below.

We will consider the mechanism shown in Fig. 2, where: 0—base; 1—internal gear; 2—external gear; 3—coupling that allows the movement between two parallel shafts with a small distance between their axes (Oldham, internal gear with a zero difference between the teeth numbers); 4—mobile beam; 5—driving screw; 6—nut.

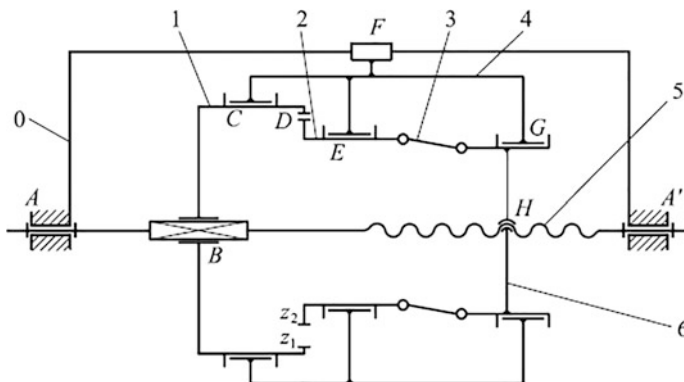
Considering  $\omega_1$  and  $\omega_2$  the angular speeds (in [radian/s]) of the internal 1 and external 2 gears, the speed of the mobile beam 4 will be:

$$v = \frac{\omega_1 p}{2\pi} \left( \frac{z_2 - z_1}{z_2} \right) \text{ (mm/s).} \tag{1}$$

where:  $p$ —the thread pitch of the driving screw, in (mm);  $z_1$ —the teeth number of the internal gear 1;  $z_2$ —the teeth number of the external gear 2.

For the same teeth number  $z_1$ , the speed  $v$  will be minim when the difference  $z_2 - z_1 = -1$  and it will be:

$$v = - \frac{\omega_1 p}{2\pi z_2} \text{ (mm/s).} \tag{2}$$



**Fig. 2** Kinematics of a mechanism that converts the rotational movement of the driving link into a translational one, using an internal gear

When the speed  $v$  and the thread pitch  $p$  are imposed, the minimum size of the mechanism will be also when the difference  $z_2 - z_1 = -1$ .

If 1 is an external gear and 2 is an internal gear, and  $z_2 - z_1 = 1$ , respectively, then:

$$v = \frac{\omega_1 p}{2\pi z_2} \text{ (mm/s)}. \tag{3}$$

The displacement  $d$  of the mobile beam 4, for a complete rotation of the driving screw 5, will be:

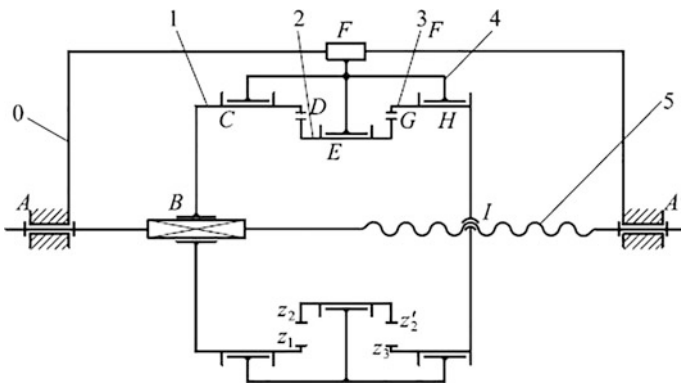
$$d = p \left( \frac{z_2 - z_1}{z_2} \right) \text{ (mm)}. \tag{4}$$

For  $z_2 - z_1 = \pm 1$ ,

$$d = \pm \frac{p}{z_2} \text{ (mm)}. \tag{5}$$

One may see that, for the same value of the screw step  $s$ , the displacement  $d$  is smaller when the teeth number  $z_2$  is bigger. Thanks to the internal gear with small difference in teeth numbers, the screw step could be bigger. It means we may use a ball screw-nut transmission, resulting a bigger precision and higher efficiency of the entire mechanism.

If we want to get smaller speed  $v$  and, consequently, a smaller displacement  $d$ , for the same overall size of the mechanism, or to reduce the size for the same values of the speed  $v$  and displacement  $d$ , two internal gear pairs may be used (see Fig. 3).



**Fig. 3** Kinematics of a mechanism that converts the rotational movement of the driving link into a translational one, using two internal gear pairs

In that case, the speed of the driven mobile beam will be:

$$v = \frac{\omega_1 p}{2\pi} \left( \frac{z_2 z_3 - z_1 z_2'}{z_2 z_3} \right) \text{ (mm/s)}. \tag{6}$$

The displacement  $d$  will be:

$$d = p \left( \frac{z_2 z_3 - z_1 z_2'}{z_2 z_3} \right) \text{ (mm)}. \tag{7}$$

The speed  $v$  and the displacement  $d$  will get minimum values (for the same value of  $z_2$ ) when  $z_2 z_3 - z_1 z_2' = -1$ , it means when  $z_2 = z_3 = z$ ,  $z_1 = z + 1$  and  $z_2' = z - 1$ , respectively,

$$v = \frac{\omega_1 p}{2\pi z_2 z_3} = \frac{\omega_1 p}{2\pi z^2} \text{ (mm/s)}, \tag{8}$$

$$d = \frac{p}{z_2 z_3} = \frac{p}{z^2} \text{ (mm)}. \tag{9}$$

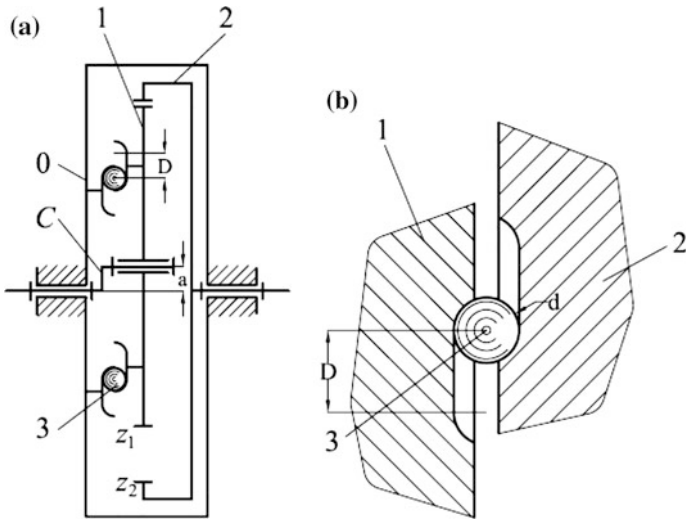
### 4 Hypocycloid Mechanisms

Thanks to the small difference of the internal gears teeth numbers, planetary mechanisms with a single solar gear may be designed. These mechanisms are compact and, also, they offer a high transmission ratio and high torque at a small size [1, 4, 7].

Due to the small difference in the number of teeth, the distance between the gear pair axes is very small, which makes it possible to collect the rotary motion from the planet gear (when the sun gear is fixed) or to avoid the rotation of the planet gear around its axis (when the sun wheel is mobile). For this purpose various types of couplings can be used, which allow a small distance between two parallel axes. Generally, Oldham coupling, universal joint or some flexible couplings may be used. If, at the limit, the difference  $z_2 - z_1 = 0$ , the second gear pair may be used as coupling.

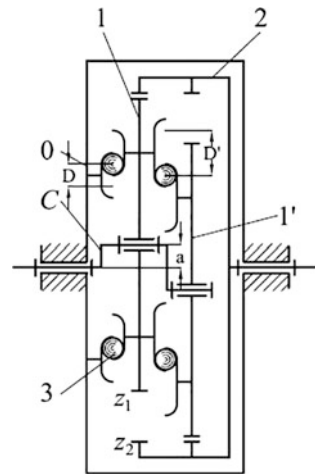
We will now consider a mechanism using some balls that may eliminate the rotation of the planet gear around its axis (see Fig. 4). In these conditions, the planet gear  $1$  will have a circular translation, given by the planet carrier  $C$ . The internal ring gear  $2$  is fixed. If we consider  $d$ —the diameter of the balls  $3$ , and  $a$ —the center distance of the gear (equal to the eccentricity of the planet carrier), the diameter  $D$  of the circular trajectory of the balls will be  $D = a$ .

If, for dynamic balancing reasons, we are using two planet gears (Fig. 5), trajectory of the balls between the two planet gears will be  $D' = 2a$



**Fig. 4** Kinematics of a first planetary mechanism with a single planet gear: **a** kinematics; **b** detail of the solution used to avoid the rotation of the planet gear around its axis

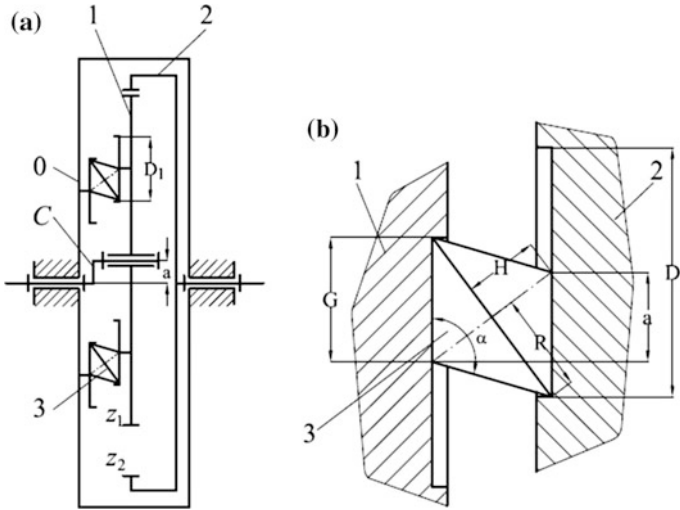
**Fig. 5** Kinematics of a first planetary mechanism with two planet gears



If double conical rollers are used instead of balls (see Fig. 6), we may find next relations between the center distance and the geometry of the roller,

$$e = 2H \cos \frac{\alpha}{2} = 2R \frac{\cos \frac{\alpha}{2}}{\tan \frac{\alpha}{2}} \tag{10}$$





**Fig. 6** Kinematics of the second planetary mechanism with a single planet gear: **(a)** kinematics; **(b)** detail of the solution used to avoid the rotation of the planet gear around its axis

or

$$H = \frac{e}{2 \cos \frac{\alpha}{2}} \tag{11}$$

or

$$R = e \frac{\tan \frac{\alpha}{2}}{2 \cos \frac{\alpha}{2}} \tag{12}$$

and

$$\alpha = 2 \arccos \left( \frac{e}{2H} \right), \tag{13}$$

respectively.

The diameter of the hollow is

$$D_1 = 2G = \frac{2H}{\cos \frac{\alpha}{2}} = \frac{e}{\cos^2 \frac{\alpha}{2}}. \tag{14}$$

For the same value of the center distance and the same distance between the gears faces, this diameter will be the lower when  $\alpha$  or  $R$  will be lower (Fig. 6b).

If, for dynamic balancing reasons, two planet gears are used, the value of the hollows at the separation plan of the planet gears will have a double value (see

**Fig. 7** Kinematics of the second planetary mechanism with two planet gears

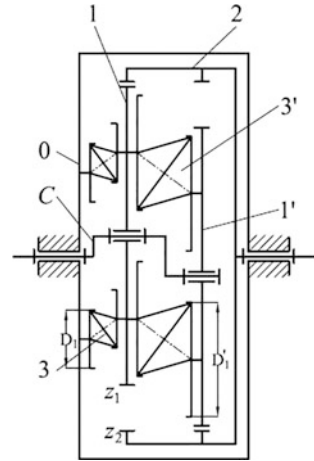


Fig. 7), for the same distance between the gears. The rollers will also have a bigger size.

The transmission ratio of these mechanisms may be computed as following:

- If the planet carrier *C* is driving link (the mechanism is a reducer)

$$i_{H2}^1 = \frac{z_2}{z_2 - z_1}; \tag{15}$$

- If the planet carrier *C* is driven link (the mechanism is a multiplier)

$$i_{2H}^1 = \frac{z_2 - z_1}{z_2}. \tag{16}$$

If the difference of the teeth numbers is  $z_2 - z_1 = 1$ , then  $i_{H2}^1 = z_2$  and  $i_{2H}^1 = \frac{1}{z_2}$ .

## 5 Conclusions

Thanks to the small difference of the internal gears teeth numbers, planetary mechanisms with a single solar gear may be designed. These mechanisms are compact and, also, they offer a high transmission ratio and high torque at a small size. In this paper some original mechanisms that are taking the advantage of using internal gears with small difference in the numbers of teeth have been discussed.

First, two mechanisms for converting the rotary motion into linear motion have been proposed. Then, two solutions of hypocycloid mechanisms offering a high ratio at a small size have been presented.

## References

1. Borislavov B, Borisov I, Panchev V (2012) Design of a planetary-cyclo-drive speed reducer: cycloid stage, geometry, element analyses. Linnaeus University, Sweden
2. Doroftei I (1995) The influence of the geometrical parameters on the continuity and on the interference of the internal gears with  $z_2 - z_1 = 1$ . In: Proceedings of ninth world congress on the theory of machines and mechanisms, Milano, Italy, vol 1, pp 450–453
3. Feng XN (2013) Study on numbers of multi-tooth meshing teeth pairs for involute internal gear pairs with small tooth number difference. *Adv Mater Res* 655–657:578–585
4. Hsu MH, Yan HS, Liu JY, Hsieh LC (2008) Epicycloid (Hypocycloid) mechanisms design. In: Proceedings of the international multiconference of engineers and computer scientists, vol 2, pp 1565–1570
5. [http://www.khkgears.co.jp/de/gear\\_technology/pdf/gear\\_guide2.pdf](http://www.khkgears.co.jp/de/gear_technology/pdf/gear_guide2.pdf)
6. Sunaga T, Nishida N, Gotou Y, Matsuo R, Sogame H, Yano S (1974) Differential Reducers Using Internal Gears with Small Tooth Number Difference: The First Report. *Fundam Des Bull JSME* 17(108):828–834
7. Suohuai Z, Jiangfeng Z, Lei L (2007) A review on the inner planetary gear transmission with small tooth number difference. *Mech Sci Technol* 26(12):1560
8. Zhou YQ, Zeng G, Sun C (2011) X-Zero gear drive with minor teeth difference. *Appl Mech Mater* 86:112–115

# Mechanical System for Determining the Shot Force at Football



E. Merticaru, R. M. Iacob and E. Budescu

**Abstract** The aim of this paper is to determine the components of shot force at football. With this aim in view, there is proposed a simply device which can be used to determine the components of shot force. This device, having a simple construction, can be used personalized, determining both the force of the shot and the angle of the force vector. Using the relationships presented in the paper, the angular velocity of the leg can be also calculated during the shot of the ball.

**Keywords** Biomechanics • Mechanisms • Force • Football Device

## 1 Introduction

Some studies deal with the problem of the impact foot-ball [1–3], offering mathematical models of the impact. The impact between the foot and the ball was analyzed as an impact between a body and a sphere [4, 5].

The paper is proposing a device to assess the force of hitting the ball, about two horizontal directions. The device is useful for football.

---

E. Merticaru (✉) · E. Budescu  
“Gheorghe Asachi” Technical University of Iasi, Iași, Romania  
e-mail: eugenmerti@yahoo.com

E. Budescu  
e-mail: budescu@gmail.com

R. M. Iacob  
“Alexandru Ioan Cuza” University of Iasi, Iași, Romania  
e-mail: ginditorul@hotmail.com

## 2 Schematics and Modeling of the System

The device is schematically presented in Fig. 1 and it is composed by a bar 1 which is connected to the frame through a rotation joint O, with the axis parallel to x axis.

The bar 2 is connected to bar 1 through a rotation joint A, with the axis parallel to y axis. At the end of bar 2 there is fixed a ball M.

Initially, the bars 1 and 2 are oriented downward about z axis (the angles  $\varphi_1$  and  $\varphi_2$  are equal to zero).

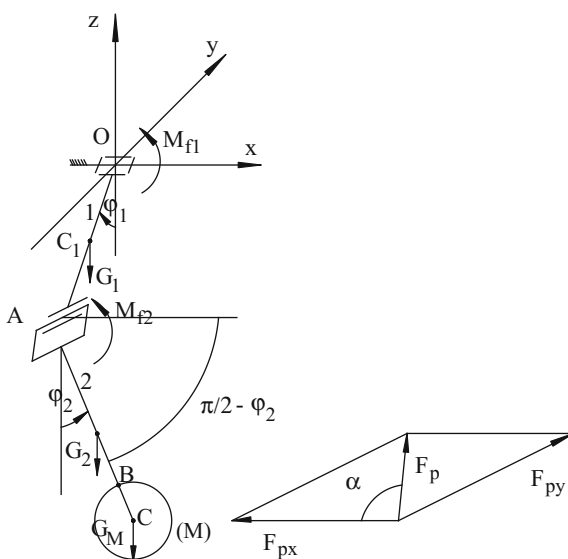
When the ball M is hit with a force  $F_p$  which has components about the tow directions x and y ( $F_{px}$  and  $F_{py}$ ), the bar 2 is rotating around y axis and the bar 1 is rotating around x axis, and are remaining positioned at certain angles  $\varphi_2$  and  $\varphi_1$  which can be measured.

The bars are maintained in rotated position because the joints O and A are conceived as joints with friction, as presented in Fig. 2.

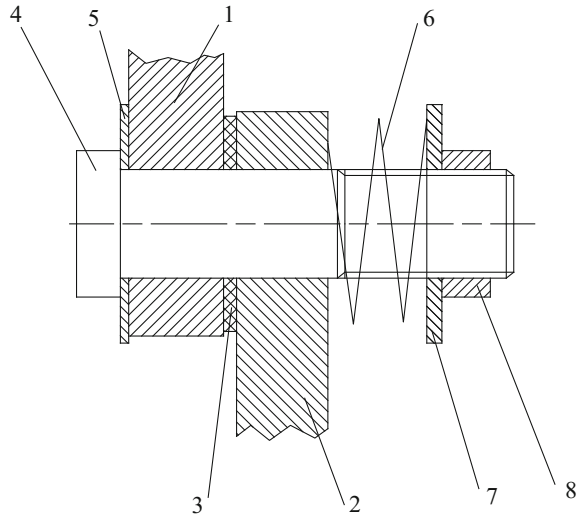
In Fig. 2, the notations represent: 1 and 2 are the elements connected by the rotation joint; 3 is a friction disc; 4 is a screw; 5 and 7 are washers; 8 is a screw-nut; 6 is a spring.

The screw 4 and the screw-nut 8 are tightened so the spring 6 is pressing the elements 1 and 2 on the friction disc 3. In this way there is created a friction torque in the rotation joint. The friction torque  $M_{f2}$  in the rotation joint A is balancing the the maximum values of the torques of the weight forces  $G_2$  and  $G_M$  of the bar 2 and the ball M.

**Fig. 1** Kinematics of the device



**Fig. 2** The construction of the rotation joint with friction



The maximum value of the friction torque  $M_{f2}$  can be written as:

$$M_{f2} = \left[ \frac{m_2 \cdot l_2}{2} + M \cdot (l_2 + r) \right] \cdot g \tag{1}$$

The friction torque  $M_{f1}$  in the rotation joint O is balancing the maximum values of the torques of the weight forces  $G_1$ ,  $G_2$  and  $G_M$  of the bar 1, bar 2 and the ball M. The maximum value of the friction torque  $M_{f1}$  can be written as:

$$M_{f1} = \left[ \frac{m_1 \cdot l_1}{2} + m_2 \cdot l_1 + M \cdot l_1 \right] \cdot g \tag{2}$$

In relations (1) and (2), the notations are representing:  $l_1 = OA$ ,  $l_2 = AB$ ,  $r = BC$  is the radius of the ball M,  $m_1$  is the mass of bar 1,  $m_2$  is the mass of bar 2, M is the mass of the ball, g is the gravity acceleration.

When the ball is hit, it receives a kinetic energy that can be written as:

$$E_c = E_{c1} + E_{c2} + E_{cM} \tag{3}$$

where:

$E_{c1}$  is the kinetic energy of bar 1,

$$E_{c1} = \frac{1}{6} \cdot m_1 \cdot l_1^2 \cdot \omega_1^2 \tag{4}$$

$E_{c2}$  is the kinetic energy of bar 2,

$$E_{c2} = \frac{1}{2} \cdot \left[ \frac{m_2 \cdot l_2^2}{3} \cdot \cos^2(\varphi_2) + m_2 \cdot l_1^2 \right] \cdot \omega_1^2 + \frac{1}{6} \cdot m_2 \cdot l_2^2 \cdot \omega_2^2 \quad (5)$$

$E_{cM}$  is the kinetic energy of the ball,

$$E_{cM} = \frac{1}{2} \cdot M \cdot OC^2 \cdot \omega_1^2 + \frac{1}{2} \cdot M \cdot (l_2 + r)^2 \cdot \omega_2^2 \quad (6)$$

where

$$OC^2 = [(l_2 + r) \cdot \sin(\varphi_2)]^2 + [l_1 \cdot \sin(\varphi_1)]^2 + [l_1 + (l_2 + r) \cdot \cos(\varphi_2)]^2 \cdot \cos^2(\varphi_1) \quad (7)$$

After the ball is hit, the bar 1 and the bar 2 are rotating with the angles  $\varphi_1$  respectively  $\varphi_2$ , and the kinetic energy is transformed in potential energy and friction energy, as in relation below:

$$E_c = E_{fA} + E_{fO} + E_p \quad (8)$$

where  $E_{fA}$  is the friction energy in joint A,

$$E_{fA} = M_{f2} \cdot \varphi_2 \quad (9)$$

$E_{fO}$  is the friction energy in joint O,

$$E_{fO} = M_{f1} \cdot \varphi_1 \quad (10)$$

$E_p$  is the potential energy,

$$E_p = E_{p1} + E_{p2} + E_{pM} \quad (11)$$

In relation (11), the notations are representing:

$E_{p1}$  is the potential energy of bar 1,

$$E_{p1} = m_1 \cdot g \cdot \frac{l_1}{2} \cdot (1 - \cos(\varphi_1)) \quad (12)$$

$E_{p2}$  is the potential energy of bar 2,

$$E_{p2} = m_2 \cdot g \cdot \left[ l_1 \cdot (1 - \cos(\varphi_1)) + \frac{l_2}{2} \cdot (1 - \cos(\varphi_2) \cdot \cos(\varphi_1)) \right] \quad (13)$$

$E_{pM}$  is the potential energy of the ball,

$$E_{pM} = M \cdot g \cdot [l_1 \cdot (1 - \cos(\varphi_1)) + (l_2 + r) \cdot (1 - \cos(\varphi_2) \cdot \cos(\varphi_1))] \quad (14)$$

In relation (8),  $E_c$  may be written as:

$$E_c = E_{cx} + E_{cy} \quad (15)$$

where  $E_{cx}$  is the kinetic energy imprinted by  $F_{py}$  and  $E_{cy}$  is the kinetic energy imprinted by  $F_{px}$ :

$$E_{cx} = \frac{1}{6} \cdot m_1 \cdot l_1^2 \cdot \omega_1^2 + \frac{1}{2} \cdot \left[ \frac{m_2 \cdot l_2^2}{3} \cdot \cos^2(\varphi_2) + m_2 \cdot l_1^2 \right] \cdot \omega_1^2 + \frac{1}{2} \cdot M \cdot OC^2 \cdot \omega_1^2 \quad (16)$$

$$E_{cy} = \frac{1}{6} \cdot m_2 \cdot l_2^2 \cdot \omega_2^2 + \frac{1}{2} \cdot M \cdot (l_2 + r)^2 \cdot \omega_2^2 \quad (17)$$

Also, in relation (8),  $E_p$  may be written as:

$$E_p = E_{px} + E_{py} \quad (18)$$

where  $E_{px}$  is the potential energy by the rotation around x axis and  $E_{py}$  is the potential energy by the rotation around y axis:

$$E_{px} = m_1 \cdot g \cdot \frac{l_1}{2} \cdot (1 - \cos(\varphi_1)) + m_2 \cdot g \cdot l_1 \cdot (1 - \cos(\varphi_1)) + M \cdot g \cdot l_1 \cdot (1 - \cos(\varphi_1)) \quad (19)$$

$$E_{py} = m_2 \cdot g \cdot \frac{l_2}{2} \cdot (1 - \cos(\varphi_2) \cdot \cos(\varphi_1)) + M \cdot g \cdot (l_2 + r) \cdot (1 - \cos(\varphi_2) \cdot \cos(\varphi_1)) \quad (20)$$

Thus, the relation (8) becomes:

$$E_{cx} = E_{fO} + E_{px} \quad (21)$$

and

$$E_{cy} = E_{fA} + E_{py} \quad (22)$$

In order to assess the impact force  $F_p$ , we can use the second Lagrange equations for impulsive motion [6]:



$$J_{red}^1 \cdot \omega_1 = \overline{M_{Ox}}(P_y) \cdot \frac{\overline{\omega_1}}{\omega_1} \quad (23)$$

and

$$J_{red}^2 \cdot \omega_2 = \overline{M_{Ay}}(P_x) \cdot \frac{\overline{\omega_2}}{\omega_2} \quad (24)$$

where:

$P_x$  is the percussion about x axis,  $P_y$  is the percussion about y axis,

$$P_x = \int_{t_0}^t F_{px} dt = \int_{t_0}^t F_p \cdot \cos(\alpha) dt \quad (25)$$

$$P_y = \int_{t_0}^t F_{py} dt = \int_{t_0}^t F_p \cdot \sin(\alpha) dt \quad (26)$$

$$J_{red}^1 = \frac{m_1 \cdot l_1^2}{3} + \frac{m_2 \cdot l_2^2}{12} + m_2 \cdot \left( l_1 + \frac{l_2}{2} \right)^2 + M \cdot (l_1 + l_2 + r)^2 \quad (27)$$

$$J_{red}^2 = \frac{m_2 \cdot l_2^2}{3} + M \cdot (l_2 + r)^2 \quad (28)$$

$$\overline{M_{Ox}}(P_y) = P_y \cdot (l_1 + l_2 + r) \quad (29)$$

$$\overline{M_{Ay}}(P_x) = P_x \cdot (l_2 + r) \quad (30)$$

Hence, it results:

$$P_x = \frac{J_{red}^2 \cdot \omega_2}{(l_2 + r)} \quad (31)$$

$$P_y = \frac{J_{red}^1 \cdot \omega_1}{(l_1 + l_2 + r)} \quad (32)$$

Assuming that the force of impact  $F_p$  is constant during the duration of impact  $\Delta t = t - t_0$ , then:

$$P_x = \Delta t \cdot F_p \cdot \cos(\alpha) \quad (33)$$

and

$$P_y = \Delta t \cdot F_p \cdot \sin(\alpha) \quad (34)$$

and

$$F_p = \frac{P_y}{\Delta t \cdot \sin(\alpha)} = \frac{P_x}{\Delta t \cdot \cos(\alpha)} \quad (35)$$

where

$$\alpha = \arctg\left(\frac{P_y}{P_x}\right) \quad (36)$$

Case 1:

When the ball is hit about the direction y, the bar 1 will rotate, together with the bar 2 and the ball, around the x axis and will stop at a certain angle  $\varphi_{1f}$  that can be measured. The bar 2 is not rotating around y axis.

The initial conditions are:  $\varphi_{1i} = 0$ ,  $\varphi_2 = 0$ ,  $\omega_2 = 0$ ,  $\omega_{1f} = 0$ .

The relation (8) becomes:

$$\omega_{1i}^2 \cdot A_1 = B_1 \cdot \varphi_{1f} + g \cdot (1 - \cos(\varphi_{1f})) \cdot C_1 \quad (37)$$

where

$$A_1 = \frac{m_1 \cdot l_1^2}{6} + \frac{m_2 \cdot l_2^2}{6} + \frac{m_2 \cdot l_1^2}{2} + \frac{M}{2} \cdot [l_1^2 + (l_2 + r) \cdot (2 \cdot l_1 + l_2 + r)] \quad (38)$$

$$B_1 = \left(\frac{m_1}{2} + m_2 + M\right) \cdot l_1 \cdot g \quad (39)$$

$$C_1 = \left(\frac{m_1 \cdot l_1}{2} + m_2 \cdot \left(l_1 + \frac{l_2}{2}\right) + M \cdot (l_1 + l_2 + r)\right) \quad (40)$$

If the angle  $\varphi_{1f}$  can be measured, then the angular velocity  $\omega_{1i}$  can be calculated:

$$\omega_{1i} = \sqrt{\frac{B_1 \cdot \varphi_{1f} + g \cdot (1 - \cos(\varphi_{1f})) \cdot C_1}{A_1}} \quad (41)$$

$$P_y = \frac{J_{red}^1 \cdot \omega_{1i}}{(l_1 + l_2 + r)} \quad (42)$$

$$F_p = F_{py} = \frac{P_y}{\Delta t \cdot \sin(\alpha)} \text{ where } \alpha = 90^\circ \quad (43)$$

Case 2:

When the ball is hit about the direction  $x$ , the bar 2 will rotate, together with the ball, around the  $y$  axis and will stop at a certain angle  $\varphi_{2f}$  that can be measured. The bar 1 is not rotating around  $x$  axis.

The initial conditions are:  $\varphi_{2i} = 0$ ,  $\varphi_1 = 0$ ,  $\omega_1 = 0$ ,  $\omega_{2f} = 0$ .

The relation (8) becomes:

$$\omega_{2i}^2 \cdot A_2 = B_2 \cdot \varphi_{2f} + g \cdot (1 - \cos(\varphi_{2f})) \cdot C_2 \quad (44)$$

where

$$A_2 = \frac{m_2 \cdot l_2^2}{6} + \frac{M}{2} \cdot (l_2 + r)^2 \quad (45)$$

$$B_2 = \left( \frac{m_2 \cdot l_2}{2} + M \cdot (l_2 + r) \right) \cdot g \quad (46)$$

$$C_2 = \frac{m_2 \cdot l_2}{2} + M \cdot (l_2 + r) \quad (47)$$

If  $\varphi_{2f}$  can be measured, then the angular velocity  $\omega_{2i}$  can be calculated:

$$\omega_{2i} = \sqrt{\frac{B_2 \cdot \varphi_{2f} + g \cdot (1 - \cos(\varphi_{2f})) \cdot C_2}{A_2}} \quad (48)$$

$$P_x = \frac{J_{red}^2 \cdot \omega_{2i}}{(l_2 + r)} \quad (49)$$

$$F_p = F_{px} = \frac{P_x}{\Delta t \cdot \cos(\alpha)} \text{ where } \alpha = 0^\circ \quad (50)$$

Case 3:

When the ball is hit with a force which has components about the axes  $x$  and  $y$ , the bar 2 will rotate, together with the ball, around the  $y$  axis and will stop at a certain angle  $\varphi_{2f}$  that can be measured. The bar 1 will rotate, together with the bar 2 and the ball, around the  $x$  axis and will stop at a certain angle  $\varphi_{1f}$  that can be measured.

The initial conditions are:  $\varphi_{1i} = 0$ ,  $\omega_{1f} = 0$  and  $\varphi_{2i} = 0$ ,  $\omega_{2f} = 0$ .

Thus, from the relations (21) and (22) we obtain:

$$\omega_{1i} = \sqrt{\frac{M_{f1} \cdot \varphi_{1f} + (1 - \cos(\varphi_{1f})) \cdot B_3}{A_3}} \quad (51)$$

where

$$A_3 = \frac{1}{6} \cdot m_1 \cdot l_1^2 + \frac{1}{2} \cdot \left[ \frac{m_2 \cdot l_2^2}{3} \cdot \cos^2(\varphi_2) + m_2 \cdot l_1^2 \right] + \frac{1}{2} \cdot M \cdot OC^2 \quad (52)$$

$$B_3 = m_1 \cdot g \cdot \frac{l_1}{2} + m_2 \cdot g \cdot l_1 + M \cdot g \cdot l_1 \quad (53)$$

and

$$\omega_{2i} = \sqrt{\frac{M_{f2} \cdot \varphi_{2f} + (1 - \cos(\varphi_{2f}) \cdot \cos(\varphi_{1f})) \cdot B_4}{A_4}} \quad (54)$$

where

$$A_4 = \frac{1}{6} \cdot m_2 \cdot l_2^2 + \frac{1}{2} \cdot M \cdot (l_2 + r)^2 \quad (55)$$

$$B_4 = m_2 \cdot g \cdot \frac{l_2}{2} + M \cdot g \cdot (l_2 + r) \quad (56)$$

and

$$P_x = \frac{J_{red}^2 \cdot \omega_{2i}}{(l_2 + r)} \quad (57)$$

$$P_y = \frac{J_{red}^1 \cdot \omega_{1i}}{(l_1 + l_2 + r)} \quad (58)$$

$$F_p = \frac{P_y}{\Delta t \cdot \sin(\alpha)} \text{ where } \alpha = \arctg\left(\frac{P_y}{P_x}\right) \quad (59)$$

It can be observed that there can rather be assessed the percussions  $P_x$  and  $P_y$ , instead of the impact force  $F_p$ . The impact force  $F_p$  can be assessed only if there is known the duration of impact  $\Delta t = t - t_0$  when the ball is hit.

### 3 Conclusions

Using the proposed experimental device, as well as the analysed possible cases of kicking the ball, any trainer can test and determine the kicking force of a football player, so that it can make the best choice. The initial force of propulsion of the ball, as well as the angle of motion starting of the ball, determine its trajectory and the success of the hit.

The paper combines the theoretical analysis and experimental determination in sport, proposing a device which is simply to be done.

## References

1. Daish CB (1972) *The physics of ball games*. English Universities Press, London
2. Townend MS (1984) *Mathematics in sport (Mathematics and its applications)*. Ellis Horwood, Chichester, UK
3. De Mestre N (1990) *The mathematics of projectiles in sport*. Cambridge University Press, Cambridge, UK
4. Asai T, Carte MJ, Akatsuka T, Haake SJ (2002) The curve kick of a football I: impact with the foot. *Sports Eng* 5(4):183–192
5. Neilson P (2003) *The dynamic testing of soccer balls*. Thesis of PhD, Loughborough University, UK
6. Mangeron D, Irimiciuc N (1980) *Mecanica rigidelor cu aplicatii in inginerie, vol II. Mecanica sistemelor de rigide*, Editura Tehnica, Bucuresti
7. Chadwick SG, Haake SJ (2000) The drag coefficient of tennis balls. In: Subic AJ, Haake S (eds) *The engineering of sport: proceedings of the 3rd international conference on the engineering of sport*, pp 169–176. Oxford, UK: Blackwell Science
8. Cooke AJ (2000) An overview of tennis ball aerodynamics. *Sports Eng* 3(1):123–129

**Part V**  
**Manipulators**

# Design and Simulation of a Parallel-Serial LARMbot Arm



Matteo Russo and Marco Ceccarelli

**Abstract** In this paper, a novel robotic arm for LARMbot humanoid is designed as based on parallel-serial structure is described. The upper arm is a tripod parallel structure with 3-Degrees-of-Freedom that are actuated by linear motors, while the forearm is a serial link controlled by a single servomotor. The structure is characterized with its kinematics and a CAD design is proposed in order to test its functioning.

**Keywords** Humanoid robots · Robot design · Arm mechanisms  
Parallel robots · Manipulators

## 1 Introduction

Robotic manipulators can be classified as serial manipulators, parallel manipulators and hybrid manipulators. Serial manipulators are based on a single serial chain, while parallel manipulators are composed of several chains in parallel connecting a fixed platform to a moving one. A hybrid manipulator is characterized by the combination of both kinds of structure. While serial manipulators usually have a large workspace volume, most parallel manipulators show high payload, stiffness and accuracy [3, 6]. A hybrid structure is able to combine the advantages of both serial and parallel ones [5].

An example of a parallel-serial structure developed in LARM laboratory is shown in [2]. Other examples of manipulators with a parallel-serial structure are analysed in [10, 11].

---

M. Russo · M. Ceccarelli (✉)  
LARM – Laboratory of Robotics and Mechatronics, University of Cassino  
and South Latium, Cassino, Italy  
e-mail: ceccarelli@unicas.it

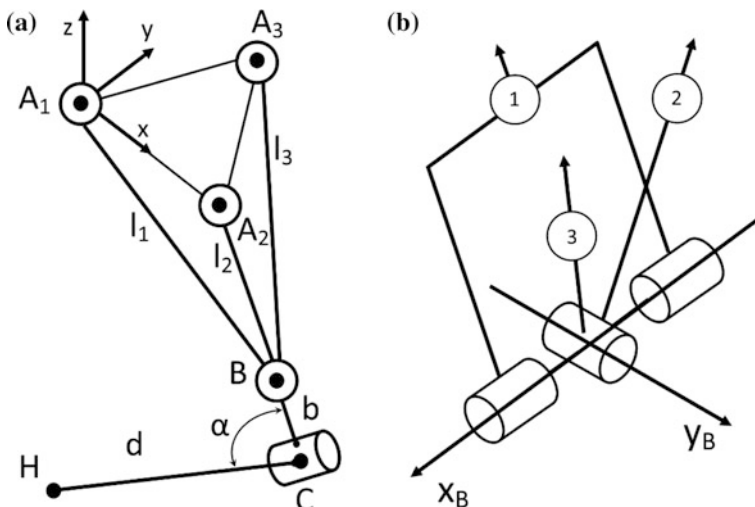
M. Russo  
e-mail: matteo.russo@unicas.it

The proposed arm is composed of a serial chain with a combination of a parallel mechanism as upper arm and a single link as forearm. The upper arm mechanism is the tripod structure that is described in [9] and patented in [8], because of its particular end-effector joint [4]. In the proposed arm design, the extremity of the tripod is shaped to install the elbow servomotor. The kinematics of the structure is solved in Sect. 2, while Sect. 3 presents a CAD model for the manufacturing of a prototype of the structure and its characteristics.

## 2 Kinematic Design

The proposed arm mechanism is a 4 Degrees-of-Freedom structure with three linear actuators in the upper arm and a servomotor in the elbow. The kinematic diagram of the manipulator is shown in Fig. 1a. The upper arm mechanism is composed of three parallel chains  $A_iB$ , which are characterized by a  $\underline{UPR}$  structure. The prismatic joint of each chain is a linear actuator with length  $l_i$  and stroke  $s$  that is connected to the fixed frame by a universal joint in  $A_i$  and to the elbow point B by a revolute joint. The three revolute joints in B are connected with the elbow mechanism shown in Fig. 1b and described in [9], where link 1 rotates around the x-axis of the mechanism, while link 2 and link 3 can only rotate around its Y-axis.

The position of point B can be found as the intersection of three spheres centred in  $A_i$  with radius equal to  $l_i$ , for  $i = \{1, 2, 3\}$ . When the  $A_1A_2A_3$  shoulder frame is an equilateral triangle with side length  $a$  with



**Fig. 1** Kinematic diagrams of the proposed arm mechanism: **a** arm structure; **b** end-effector mechanism at upper arm extremity



$${}^0\mathbf{A}_1 = \begin{pmatrix} 0 \\ 0 \\ 0 \end{pmatrix}; {}^0\mathbf{A}_2 = \begin{pmatrix} a \\ 0 \\ 0 \end{pmatrix}; {}^0\mathbf{A}_3 = \begin{pmatrix} a/2 \\ \sqrt{3a/2} \\ 0 \end{pmatrix}, \quad (1)$$

the Direct Kinematics of the upper arm structure can be solved as

$$\begin{aligned} x_B &= \frac{1}{2a} (l_1^2 - l_2^2 + a^2) \\ y_B &= \frac{1}{2\sqrt{3}a} (l_1^2 + l_2^2 - 2l_3^2 + a^2) \\ z_B &= -\sqrt{\frac{-l_1^4 - l_2^4 - l_3^4 - a^4 + l_1^2 l_2^2 + l_1^2 l_3^2 + l_2^2 l_3^2 + a^2 (l_1^2 + l_2^2 + l_3^2)}{3a^2}}. \end{aligned} \quad (2)$$

where  $x$ ,  $y$ ,  $z$  are the coordinates of the upper arm extremity point B. The positive root for the  $z$ -coordinate is not physically possible for the assembly configuration. In order to find the position of the arm end-point point H, the orientation of the reference frame of the elbow platform, which is shown in Fig. 1b, with respect to the fixed frame XYZ, in Fig. 1a, is solved with Euler angles as Eq. (3),

$$\begin{aligned} \alpha_B &= \tan^{-1} \frac{(l_1^2 + l_2^2 - 2l_3^2 + a^2)}{2\sqrt{-l_1^4 - l_2^4 - l_3^4 - a^4 + l_1^2 l_2^2 + l_1^2 l_3^2 + l_2^2 l_3^2 + a^2 (l_1^2 + l_2^2 + l_3^2)}} \\ \beta_B &= \arctan \frac{l_1^2 - l_2^2}{\sqrt{4a^2 l_3^2 - l_2^4 - l_1^4 + 2l_1^2 l_2^2}} \\ \gamma_B &= 0 \end{aligned} \quad (3)$$

where  $\alpha_B$  is the rotation angle of the platform around the X-axis,  $\beta_B$  is the intrinsic rotation around the Y-axis and  $\gamma_B$  is the one around the Z-axis. The servomotor is placed on the elbow platform and the elbow is described by link **BC**. The motor allows for a further rotation of forearm body **CH** around its axis, characterized by the servomotor actuation angle  $\alpha$ . Therefore, the position of the arm-end point in the fixed reference frame in Fig. 1a can be written as Eq. (4),

$${}^0\mathbf{H} = {}^0\mathbf{B} + \mathbf{R}_X(\alpha_B)\mathbf{R}_Y(\beta_B)\mathbf{R}_Z(\gamma_B) \left[ \begin{pmatrix} 0 \\ 0 \\ -b \end{pmatrix} + \mathbf{R}_Y(\alpha) \begin{pmatrix} d \\ 0 \\ 0 \end{pmatrix} \right] \quad (4)$$

Equation (4) can be also used to evaluate the workspace of the proposed mechanism as a point cloud by discretising the step of the actuators [3]. In order to compute it, a particular size, which is based on existing commercial actuators, has been assumed for the arm design as in Table 1. Figure 2 shows the computed workspace of the LARMBot arm with sizes in Table 1.

**Table 1** Size of the design parameters of the arm mechanism in Fig. 1

Variable	$a$	$l_{i,min}$	$l_{i,max}$	$s$	$b$	$d$
Length (mm)	60	185	235	50	53	230

Figure 2 shows the workspace of the LARMbot arm computed as a cloud of reachable points with mechanism size in Table 1. The workspace is characterized by an apple void [3] in the region that surrounds the elbow of the mechanism, due to the length of link CH. This void can be seen in the XZ section of the workspace in Fig. 2b.

### 3 CAD Model and Simulation

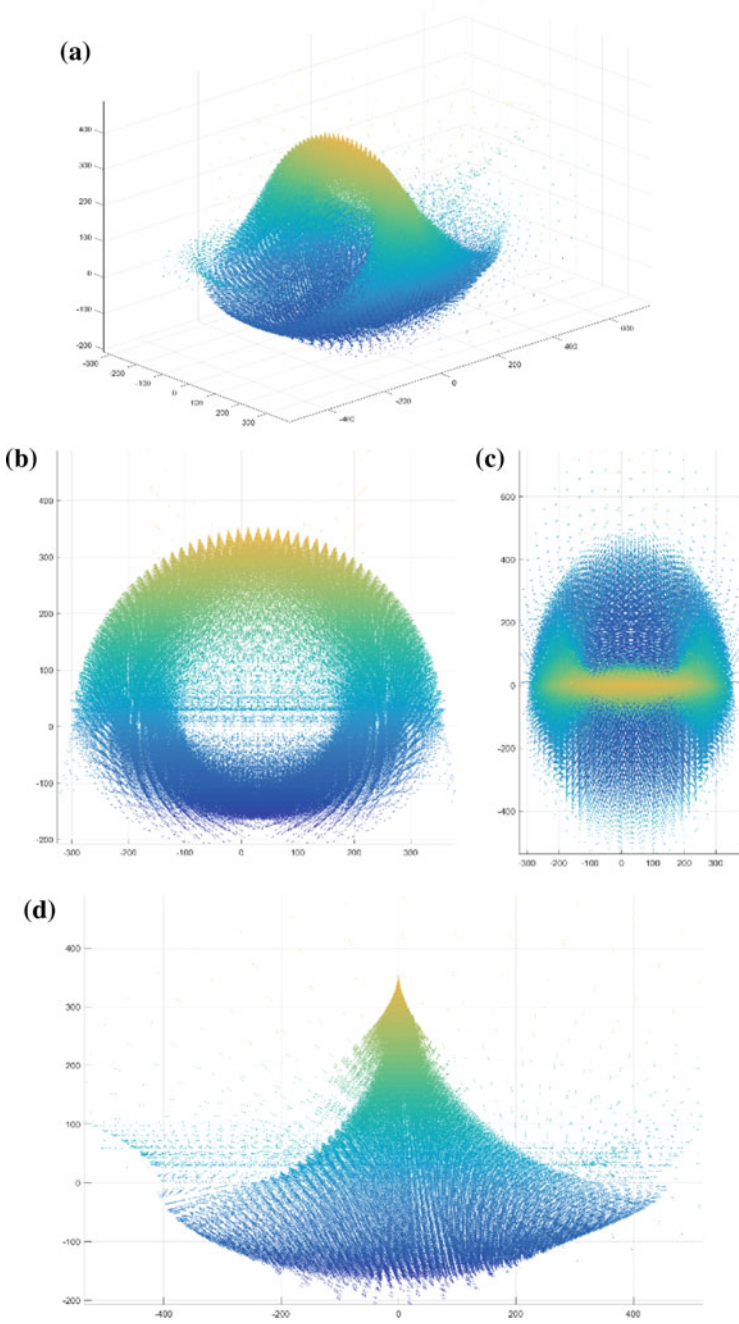
In order to check for the functioning of the proposed mechanism, a CAD model of the arm was designed. The model is sized on the dimensions in Table 1 and it is based on two commercial actuators: the Actuonix L16R [1] linear motor with a stroke of 50 mm for the upper arm and the Robotix Dynamixel AX12-A servomotor for the elbow joint [7]. The universal joints in the base are modelled on commercial ones, while all the other components are designed for easy manufacturing through 3D printing in PLA plastic. The CAD model of the entire arm is shown in Fig. 3.

A swing of the arm has been simulated in order to compute the actuation forces of the actuators. The path is shown in Fig. 4, while the swing is characterized by its motion law as

$$\begin{aligned}
 l_1 &= 200 + 30 \cos 0.2\pi t \\
 l_2 &= 205 + 40 \cos 0.4\pi t \\
 l_3 &= 200 + 30 \cos 0.2\pi t \\
 \alpha &= \frac{5}{12}\pi + \frac{1}{4}\pi \cos 0.2\pi t
 \end{aligned} \tag{5}$$

The acceleration of the arm-end point computed during the dynamic simulation is shown in Fig. 5.

The results of the dynamic simulation are compared with the maximum payloads of the actuators, which are respectively 50.0 N for the Actuonix L16R [1] and 1.50 Nm for the Dynamixel AX12-A [7]. The computed actuation forces are shown in Fig. 6, while the torque in the servomotor is shown in Fig. 7 and the reaction force in point B is shown in Fig. 8. All the values are within the limits of the actuators with a large safety coefficient, which is larger than 20 for the linear motors and larger than 2 for the servomotor. This values clearly show the better dynamic performance of the parallel part of the structure when compared to the serial chain. Therefore, in order to improve the efficiency and the payload of the structure it is necessary to improve the load capacity of the elbow motor.



**Fig. 2** Reachable workspace of the mechanism; **a** isometric view; **b** section on plane XZ; **c** upper view; **d** section on plane YZ

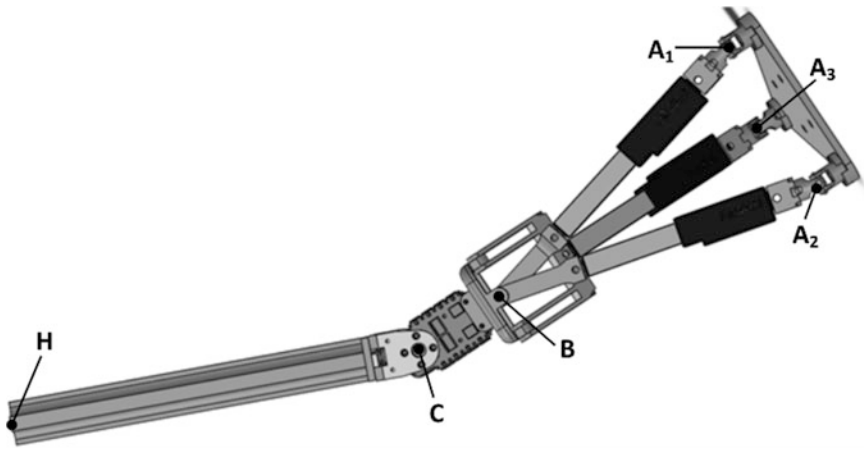


Fig. 3 A CAD model of the proposed arm mechanism in Fig. 1

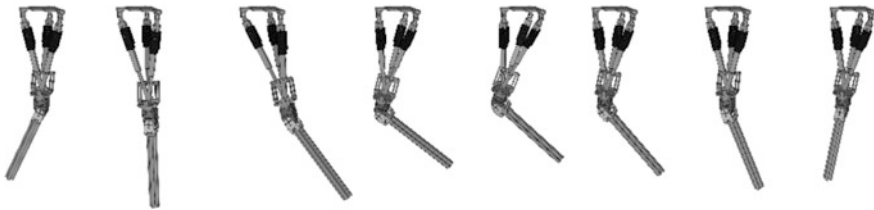


Fig. 4 Simulated swing motion of the CAD design in Fig. 3

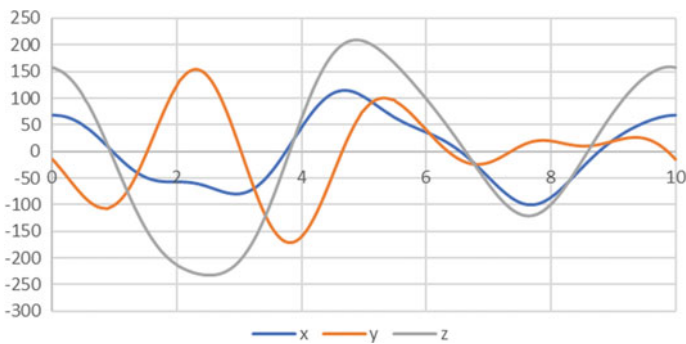


Fig. 5 Results of simulated motion in terms of acceleration of point H during the motion illustrated in Fig. 4

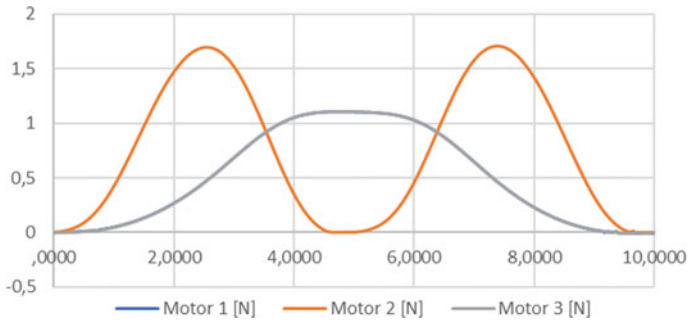


Fig. 6 Simulated actuation forces (N) in the linear motors. Force 1 and 3 overlap in the graph

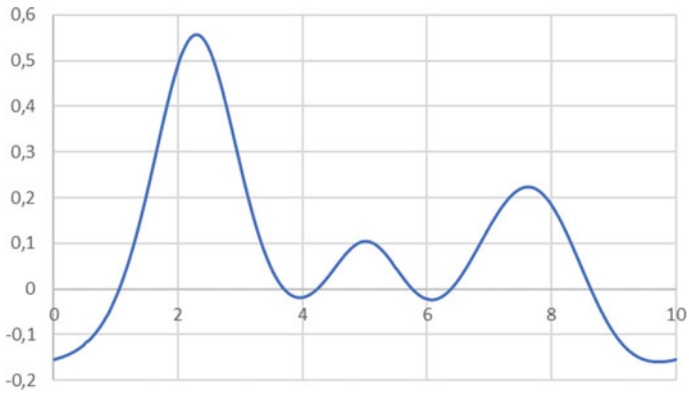


Fig. 7 Simulated actuation torque (Nm) in the servomotor

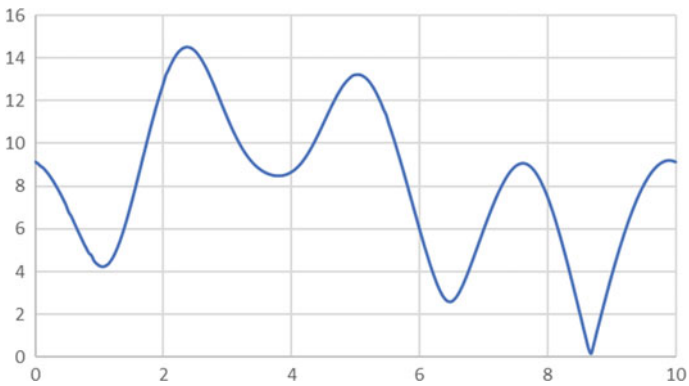


Fig. 8 Simulated reaction force (N) in point B of Fig. 3

## 4 Conclusions

This paper presents a novel parallel-serial arm mechanism for the LARMbot humanoid. First of all, the mechanism design is introduced with its functioning diagrams and its kinematics are evaluated. Then, a CAD model of the arm is used for dynamic simulation in order to prove the feasibility of the novel design. The results of the simulation are reported and discussed to show the feasibility of the design and to characterize its operation in terms of human-like performance. Future development for this work will include the manufacturing of a prototype in order to check for the feasibility and the performance of the mechanism with experimental tests.

## References

1. Actuonix (2016) Firgelli L16 datasheet. [http://www.actuonix.com/category\\_s/1823.htm](http://www.actuonix.com/category_s/1823.htm). Accessed 2 Jan 2017
2. Carbone Giuseppe, Ceccarelli Marco (2004) A stiffness analysis for a hybrid parallel-serial manipulator. *Robotica* 22(05):567–576
3. Ceccarelli M (2004) Fundamentals of mechanics of robotic manipulation, vol. 27. Springer, Dordrecht
4. Ceccarelli M, Russo M (2016) Device for the spherical connection of three bodies. Italian Patent Application no 10201600009369 (in Italian)
5. Gallardo-Alvarado J (2005) Kinematics of a hybrid manipulator by means of screw theory. *Multibody Sys Dyn* 14(3–4):345–366
6. Merlet JP (2012) Parallel robots, vol 74. Springer, Dordrecht
7. Robotis (2016) Dynamixel AX12-A datasheet. [http://en.robotis.com/index/product.php?cate\\_code=101010](http://en.robotis.com/index/product.php?cate_code=101010). Accessed 16 Jan 2017
8. Russo M, Cafolla D, Ceccarelli M (2016) Device for tripod leg. Italian Patent Application no 102016000097258 (in Italian)
9. Russo M, Ceccarelli M (2017) Kinematic design of a tripod parallel mechanism for robotic legs. In: Mechanisms, transmissions and applications, mechanism and machine science, vol 52. Springer, Cham, pp 121–130
10. Tanev TK (2000) Kinematics of a hybrid (parallel–serial) robot manipulator. *Mech Mach Theory* 35(9):1183–1196
11. Yang G, Chen W, Ho EHL (2002) Design and kinematic analysis of a modular hybrid parallel-serial manipulator. In: 7th IEEE international conference on control, automation, robotics and vision, 2002. ICARCV 2002, vol 1, pp 45–50

# Kinematically Redundant Octahedral Motion Platform for Virtual Reality Simulations



G. Nawratil and A. Rasoulzadeh

**Abstract** We propose a novel design of a parallel manipulator of Stewart Gough type for virtual reality application of single individuals; i.e. an omni-directional treadmill is mounted on the motion platform in order to improve VR immersion by giving feedback to the human body. For this purpose we modify the well-known octahedral manipulator in a way that it has one degree of kinematical redundancy; namely an equiform reconfigurability of the base. The instantaneous kinematics and singularities of this mechanism are studied, where especially “unavoidable singularities” are characterized. These are poses of the motion platform, which can only be realized by singular configurations of the mechanism despite its kinematic redundancy.

**Keywords** Stewart-Gough platform · Kinematic redundancy · Singularities  
Motion simulator

## 1 Introduction

The geometry of a Stewart-Gough (SG) platform is given by the six base anchor points  $M_i$  with coordinates  $\mathbf{M}_i := (A_i, B_i, C_i)^T$  with respect to the fixed frame and by the six platform anchor points  $m_i$  with coordinates  $\mathbf{m}_i := (a_i, b_i, c_i)^T$  with respect to the moving frame (for  $i = 1, \dots, 6$ ). Each pair  $(M_i, m_i)$  of corresponding anchor points of the fixed body (base) and the moving body (platform) is connected by an SPS-leg, where only the prismatic joint ( $P$ ) is active and the spherical joints ( $S$ ) are passive. The distance between the centers of the two  $S$ -joints of the  $i$ th leg is denoted by  $r_i$ . Note that for a SG platform,  $(M_i, m_i) \neq (M_j, m_j)$  holds for pairwise distinct

---

G. Nawratil (✉) · A. Rasoulzadeh  
Center for Geometry and Computational Design, Vienna University of Technology,  
Vienna, Austria  
e-mail: nawratil@geometrie.tuwien.ac.at

A. Rasoulzadeh  
e-mail: rasoulzadeh@geometrie.tuwien.ac.at

$i, j \in \{1, \dots, 6\}$ . Moreover if two base points  $M_i$  and  $M_j$  (resp. platform points  $m_i$  and  $m_j$ ) coincide, then we just write  $M_{i,j}$  (resp.  $m_{i,j}$ ).

A certain drawback of such 6-degree of freedom (dof) robotic platforms is the limitation of their singularity-free workspace. A promising approach for overcoming this problem is redundancy, where basically two types can be distinguished:

- (a) **Actuation redundancy:** One possibility is to add a 7th SPS-leg to the manipulator (e.g. [2, 3, 20]), but it should be noted that there exist dangerous locations for the attachments  $m_7$  and  $M_7$  (cf. [9]), which do not result in a reduction of singularities. Clearly more than one SPS-leg can be attached, but we have to keep in mind that every extra leg may yield a restriction of the workspace due to leg constraints and leg interference [3]. Moreover [17] pointed out that this so-called branch redundancy<sup>1</sup> causes internal loads, whose control increases considerably the complexity and costs.
- (b) **Kinematic redundancy:** This can be achieved by attaching active joints in a way that the geometry of the platform or base (or both) can be modified. Therefore they are also known as *reconfigurable manipulators*<sup>2</sup> of SG type. In [1] a design is suggested, which has six redundant dofs (3 in the platform and 3 in the base). The weak points of this so-called *dodekapod* are that on the one hand additional mass/inertia (motor of active joints) is added to the platform and that on the other hand passive prismatic joints are used, which are difficult to implement in practice (cf. [17]). Not faced with these points of criticism are the designs suggested in [11, 19], where one base point is traced on a circle (realized by an extra R-joint [19]) or a straight line (realized by an extra P-joint [11]). We complete this review by noting a different approach to kinematic redundancy; namely the usage of *parallel redundant legs* introduced in [17].

Another advantage of approach (b) over (a) beside the already mentioned ones above is that (a) increases the workspace only by removing singularities, but (b) additionally enlarges the workspace itself due to the reconfigurability of the anchor points. Further differences between both concepts are pointed out at the end of Sect. 2.1.

## 1.1 Aim and Basic Concept

Within the Doctoral College “Computational Design” of the Vienna University of Technology, we are interested amongst other things in the optimization of motion platforms of SG type for virtual reality (VR) application of single individuals. In detail, we want to mount an omni-directional treadmill onto the motion platform (cf.

<sup>1</sup>A further possibility to imply actuation redundancy in a SG platform is to replace passive joints by active ones. No attempts to this so-called in-branch redundancy are known to the authors.

<sup>2</sup>The modules in a variable geometry truss (VGT) can also be seen as reconfigurable manipulators (cf. [14, Fig. 9]). In this context see also [18], where a VGT is combined with a SG structure.



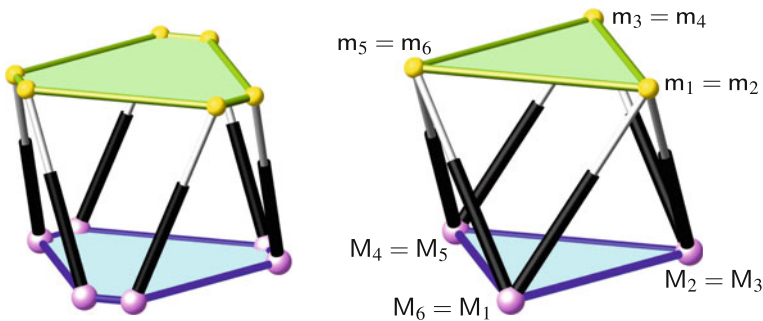
Fig. 2) in order to improve VR immersion by giving feedback to the human body (e.g. simulating slopes, earthquakes, ...). There are different locomotion systems commercially available; e.g. Cyberith Virtualizer ([www.cyberith.com](http://www.cyberith.com)), Omni Virtuix ([www.virtuix.com](http://www.virtuix.com)), SpaceWalkerVR ([www.spacewalkervr.com](http://www.spacewalkervr.com)), Kat Walk ([www.katvr.com](http://www.katvr.com)) and Wzdish ROVR ([www.wzdish.com](http://www.wzdish.com)).

Due to safety reasons we prefer a system where the individuals are fixed inside a hip-ring by belts and straps. Thus we are only left with the Omni Virtuix and the Cyberith Virtualizer. We favor the latter system as it has one more dof, which allows to kneel/crouch/sit down or even to jump up, and a flat base plate with a suitable friction coefficient for simulating slopes. Contrary, the Omni Virtuix's base has a very low friction (too slippery for slope simulations) and a concave shape.

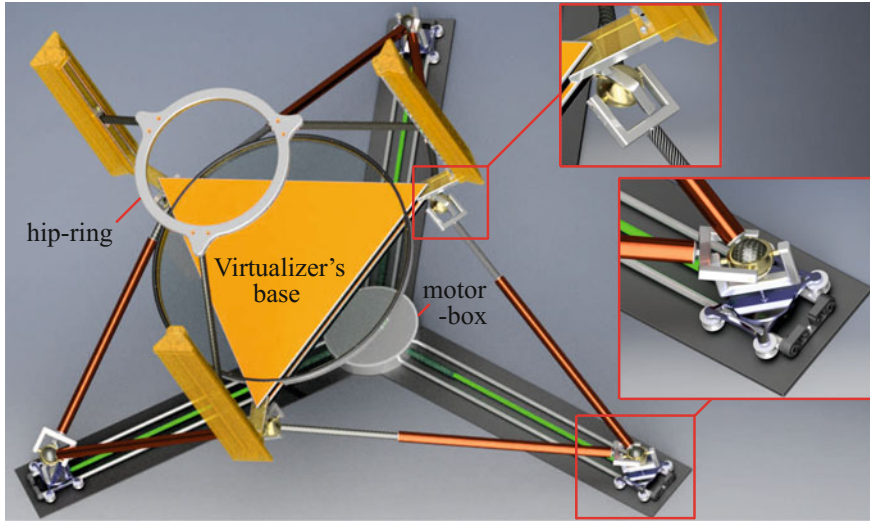
All currently offered 6-dof motion simulators of SG type have a planar semi-hexagonal base and platform (see Fig. 1 (left)). This design is preferred over the so-called octahedral SG manipulator (see Fig. 1 (right)) as it avoids double S-joints, which have a lot of disadvantages regarding costs, stiffness and joint-range. Nevertheless we focus within this *concept study* on the octahedral design (as many other academic studies e.g. [18], [19, Sect. 4], [4–6, 8, 10, 12, 13], ... done in the past), due to its kinematic simplicity. But this application-alien abstraction can also be brought back to real-world solutions as pointed out in Sect. 3.

Due to the arguments given above we want to use concept (b) of kinematic redundancy in order to increase the singularity-free workspace of the octahedral manipulator. Having our practical application in mind, the resulting reconfigurable manipulator should still be of kinematic simplicity (the symmetry of the manipulator should not be destroyed) and cheap; i.e. we want to get by with standard components (less or even no expensive custom products).

Taking all these requests under consideration, we came up with the design illustrated in Fig. 2. We use three additional active P-joints (green), which are driven simultaneously by only one motor mounted at the center of the base. Therefore the



**Fig. 1** (Left) SG manipulator with planar semi-hexagonal base and platform. (Right) Octahedral SG manipulator, which is also known as MSSM (Minimal Simplified Symmetric Manipulator) in the literature (e.g. [13]). This parallel robot is characterized by:  $m_1 = m_2$ ,  $m_3 = m_4$ ,  $m_5 = m_6$ ,  $M_1 = M_2$ ,  $M_3 = M_4$ ,  $M_5 = M_6$ . Therefore all attachments are double spherical joints, which form a triangle in the platform and the base. Moreover we assume that both triangles are equilateral



**Fig. 2** Octahedral SG manipulator with a 1-dof kinematic redundancy (equiform reconfigurability of the base) and a Virtualizer mounted on top. In practice one S-joint of an SPS-leg is replaced by an universal joint (U), thus all double S-joints can be replaced by concentric SU-joints (blow-ups)

base triangle remains equilateral during the reconfiguration process. The proposed manipulator can be seen as a combination of a SG hexapod and a so-called hexaglide (e.g. [7]). As the linear sliding of the points  $M_{i,i+1}$  along the lines  $g_{i,i+1}$  can be realized by parallel guiding rails, the whole structure can still be built very stiff with a high load-carrying capacity. Moreover the complete additional equipment for the performance of the reconfiguration (motor, rails, ...) is placed on the resting base such that the legs and platform are not stressed by additional mass/inertia.

*Remark 1* Let us assume that the three additional prismatic joints are passive instead of active (but still coupled). Moreover we lock the six  $\underline{P}$ -joints of the legs. Then the base has in each pose of the manipulator at least a 1-dimensional self-motion with respect to the platform, due to the equiform reconfigurability of the base. These relative motions (of the base with respect to the platform) are studied in [6].  $\diamond$

## 2 Instantaneous Kinematics and Singularities

The  $i$ th leg of the 7-dof reconfigurable manipulator fulfills the basic relation  $r_i(\tau)^2 = \|\mathbf{n}_i(\tau) - \mathbf{M}_i(\tau)\|^2$ , where  $\mathbf{n}_i$  is the coordinate vector of  $m_i$  with respect to the fixed system. Differentiation with respect to the time  $\tau$  yields:

$$r_i \dot{r}_i = (\mathbf{n}_i - \mathbf{M}_i)(\dot{\mathbf{n}}_i - \dot{\mathbf{M}}_i) \Rightarrow \dot{r}_i = \mathbf{l}_i(\dot{\mathbf{n}}_i - \dot{\mathbf{M}}_i), \tag{1}$$

where  $\mathbf{l}_i$  is the unit-vector along the  $i$ th leg (pointing from the base point to the platform point). As the velocity of  $\mathbf{n}_i$  can be expressed in terms of the instantaneous screw  $(\mathbf{q}, \hat{\mathbf{q}})$  of the platform with respect to the fixed system by  $\dot{\mathbf{n}} = \hat{\mathbf{q}} + \mathbf{q} \times \mathbf{n}_i$  we get:

$$\dot{r}_i + \mathbf{l}_i \dot{\mathbf{M}}_i = \mathbf{l}_i \hat{\mathbf{q}} + \mathbf{l}_i (\mathbf{q} \times \mathbf{n}_i) \quad \Rightarrow \quad \dot{r}_i + \dot{g} \mathbf{g}_i \mathbf{l}_i = \mathbf{l}_i \hat{\mathbf{q}} + \hat{\mathbf{l}}_i \mathbf{q}, \quad (2)$$

where  $\mathbf{g}_i$  is the unit-vector along  $\mathbf{g}_i$ ,  $\dot{g}$  the velocity along  $\mathbf{g}_i$  and  $\hat{\mathbf{l}}_i$  the moment vector of the  $i$ th leg. Note that  $(\mathbf{l}_i, \hat{\mathbf{l}}_i)$  are the spear coordinates of the  $i$ th leg. Thus we end up with:

$$\begin{pmatrix} \dot{r}_1 \\ \vdots \\ \dot{r}_6 \end{pmatrix} + \dot{g} \begin{pmatrix} \mathbf{g}_1 \mathbf{l}_1 \\ \vdots \\ \mathbf{g}_6 \mathbf{l}_6 \end{pmatrix} = \mathbf{J} \begin{pmatrix} \mathbf{q} \\ \hat{\mathbf{q}} \end{pmatrix} \quad \text{with} \quad \mathbf{J} := \begin{pmatrix} \hat{\mathbf{l}}_1^T & \mathbf{l}_1^T \\ \vdots & \vdots \\ \hat{\mathbf{l}}_6^T & \mathbf{l}_6^T \end{pmatrix}. \quad (3)$$

This equation relates the velocities  $\dot{r}_1, \dots, \dot{r}_6, \dot{g}$  of the active  $\underline{\mathbf{P}}$ -joints with the instantaneous screw  $(\mathbf{q}, \hat{\mathbf{q}})$  of the platform. If we fix all prismatic joints the left side of Eq. (3) equals the zero vector. Then an infinitesimal motion of the platform is only possible if the Jacobian matrix  $\mathbf{J}$  of the octahedral manipulator is singular; which is well studied problem (e.g. [4, 8] or [13, pp. 202–204]).

## 2.1 Unavoidable Singularities

**Definition 1** If for a given pose of the platform the corresponding configuration of the mechanism is singular for all kinematically redundant dofs, we call this singular pose of the platform an “unavoidable singularity”.

To the best knowledge of the authors there are no studies on “unavoidable singularities” in the literature, with the following two exceptions:

- In [17, Sect. 5(D)] it is stated that for the octahedral manipulator with three redundant legs “any Cartesian pose of the moving platform can be reached with a non-singular configuration of the mechanism”. Moreover, it is “conjectured that this result can be extended to mechanisms whose spherical joints on the platform do not coincide by pairs”, but this is disproved in Appendix 1.
- For the kinematically redundant SG manipulator of [19], there exist up to 40 positions of the platform causing an unavoidable singularity for a given orientation (cf. [19, Sect. 4.4.2]). Some special orientations causing a higher-dimensional set of unavoidable singularities were studied in [19, Sect. 4.4.3].

For the proposed mechanism of the paper at hand, we can chose an appropriate scaling factor and coordinate systems in the fixed and moving space in a way that:

$$\mathbf{m}_{1,2} = (1, 0, 0)^T, \quad \mathbf{m}_{3,4} = \left( -\frac{1}{2}, \frac{\sqrt{3}}{2}, 0 \right)^T, \quad \mathbf{m}_{5,6} = \left( -\frac{1}{2}, -\frac{\sqrt{3}}{2}, 0 \right)^T, \quad (4)$$

$$\mathbf{M}_{4,5} = g(-1, 0, 0)^T, \quad \mathbf{M}_{6,1} = g\left(\frac{1}{2}, -\frac{\sqrt{3}}{2}, 0\right)^T, \quad \mathbf{M}_{2,3} = g\left(\frac{1}{2}, \frac{\sqrt{3}}{2}, 0\right)^T, \quad (5)$$

hold, where  $g > 0$  is the reconfiguration variable (= radius of the circumcircle of the equilateral base triangle). Based on this coordinatization we can compute the entries of  $\mathbf{J}$  by  $(\mathbf{l}_i : \hat{\mathbf{l}}_i) := (\mathbf{R}\mathbf{m}_i + \mathbf{s} - N\mathbf{M}_i : \mathbf{M}_i \times \mathbf{l}_i)$  with the rotation matrix

$$\mathbf{R} = \begin{pmatrix} e_0^2 + e_1^2 - e_2^2 - e_3^2 & 2(e_1e_2 - e_0e_3) & 2(e_1e_3 + e_0e_2) \\ 2(e_1e_2 + e_0e_3) & e_0^2 - e_1^2 + e_2^2 - e_3^2 & 2(e_2e_3 - e_0e_1) \\ 2(e_1e_3 - e_0e_2) & 2(e_2e_3 + e_0e_1) & e_0^2 - e_1^2 - e_2^2 + e_3^2 \end{pmatrix},$$

$N = e_0^2 + e_1^2 + e_2^2 + e_3^2$  and the translation vector  $\mathbf{s} = (x, y, z)^T$ . Note that  $(e_0 : e_1 : e_2 : e_3) \neq (0 : \dots : 0)$  are the so-called Euler parameters.

Then the singularity condition  $\Sigma: \det \mathbf{J} = 0$  has the following structure:

$$\Sigma : \quad 83\sqrt{3}Ng^3(Q[12]N^2g^2 + L[56]Ng + A_1[29]A_2[8]) = 0, \quad (6)$$

where the number in the brackets gives the number of terms. Note that  $Q$  and  $A_2$  depend linearly on  $x, y, z$  and that  $L$  and  $A_1$  are polynomials in  $z^2, xz, yz, x, y, z$ .

**Theorem 1** *The unavoidable singularities of the 1-dof kinematic redundant octahedral manipulator of SG type studied in the paper at hand are listed in the following table containing the positions of the unavoidable singularities in the 3rd column for the orientations given in the 2nd column and the 4th column gives the dimension of the singularity set. The following expressions are referred in the mentioned table:*

$$z = \frac{(e_0^2 + e_3^2)(e_1^3e_3 - 3e_1e_2^2e_3 - 3e_1^2e_2e_0 + e_2^3e_0)}{(e_3^2 - e_0^2)(e_2^2 + e_1^2)}, \quad (7)$$

$$x = \frac{(e_0^2 + e_3^2)(e_3^2e_1^2 - e_3^2e_2^2 - 4e_1e_2e_0e_3 - e_1^4 + 6e_2^2e_1^2 - e_2^4 - e_0^2e_1^2 + e_0^2e_2^2)}{2(e_2^2 + e_1^2)(e_0^2 - e_3^2)}, \quad (8)$$

$$y = \frac{(e_3^2 + e_0^2)(e_1e_2e_3^2 + e_1^2e_3e_0 - e_2^2e_3e_0 + 2e_1^3e_2 - 2e_1e_3^2 - e_1e_2e_0^2)}{(e_2^2 + e_1^2)(e_3^2 - e_0^2)}, \quad (9)$$

$$x = \frac{e_3^4e_1^2 - e_3^4e_2^2 + 3e_3^2e_1^2e_2^2 - e_3^2e_2^4 + 2e_3e_0e_1^3e_2 + 2e_3e_0e_1e_2^3 - e_1^4e_0^2 + 3e_1^2e_2^2e_0^2 - e_0^4e_1^2 + e_0^4e_2^2}{(e_2^2 + e_1^2)(e_0^2 - e_3^2)}, \quad (10)$$

$$y = \frac{2e_3^4e_1e_2 + 3e_3^2e_1^3e_2 + e_3e_2^4e_0 - e_2^3e_1e_3^2 - e_3e_0e_1^4 - 2e_0^4e_1e_2 + e_0^2e_1^3e_2 - 3e_0^2e_1e_2^3}{(e_2^2 + e_1^2)(e_3^2 - e_0^2)}. \quad (11)$$

*Proof* For an unavoidable singularity the conditions  $Q = L = A_1A_2 = 0$  have to hold. This system of equations can be solved explicitly<sup>3</sup> for  $x, y, z$ . The detailed case study

<sup>3</sup>In contrast to [19], where the unavoidable singularities are obtained as the numeric solution of an univariate polynomial of degree 40.

Row	Orientation	Position	Dim
1	$e_1 = e_2 = 0$	$z = 0$	3
2	$e_1 = e_2 = 0, e_0 = \pm e_3$	arbitrary	3
3	$e_0 = e_3 = 0$	arbitrary	4
4	$e_0 = \pm e_3, e_2 = \mp e_1$	$z = 2e_1e_3$	3
5	$e_0 = \pm e_3, e_2 = \mp e_1$	$z = -\frac{e_3(2e_3^2+2e_1^2\pm y)}{e_1}, x = 0$	2
6	$e_0 = \pm e_3, e_2 = \mp e_1$	$z = -4e_1e_3, y = \pm 2(e_1^2 - e_3^2)$	2
7	$e_0 = e_3, e_1 = (2 \pm \sqrt{3})e_2$	$z = \frac{4e_2e_3}{1\mp\sqrt{3}}$	3
8	$e_0 = e_3, e_1 = (2 \pm \sqrt{3})e_2$	$x = \frac{16e_3^2\pm 8e_3^2\sqrt{3}+y-4e_3^2}{\pm\sqrt{3}}, z = \frac{8e_2e_3}{\pm\sqrt{3}-1}$	2
9	$e_0 = e_3, e_1 = (2 \pm \sqrt{3})e_2$	$x = \mp y\sqrt{3}, z = \frac{2e_3(e_3^2+4e_2^2\pm 2e_2^2\sqrt{3}-y)}{e_2(1\pm\sqrt{3})}$	2
10	$e_0 = -e_3, e_1 = (-2 \pm \sqrt{3})e_2$	$z = \frac{4e_2e_3}{\mp\sqrt{3}-1}$	3
11	$e_0 = -e_3, e_1 = (-2 \pm \sqrt{3})e_2$	$x = \frac{16e_3^2\mp 8e_3^2\sqrt{3}-y-4e_3^2}{\mp\sqrt{3}}, z = \frac{8e_2e_3}{1\pm\sqrt{3}}$	2
12	$e_0 = -e_3, e_1 = (-2 \pm \sqrt{3})e_2$	$x = \mp y\sqrt{3}, z = \frac{2e_3(e_3^2+4e_2^2\mp 2e_2^2\sqrt{3}+y)}{e_2(\pm\sqrt{3}-1)}$	2
13	$e_0 = e_2 = 0$	$z = e_1e_3$	3
14	$e_1 = e_3 = 0$	$z = -e_0e_2$	3
15	$e_0 = e_1 = 0$	$y = z = 0$	2
16	$e_2 = e_3 = 0$	$y = z = 0$	2
17	$e_0e_1 + e_2e_3 = 0$	$z$ of Eq. (7)	4
18	$e_3^2e_2^2 - 3e_2^2e_0^2 + 8e_2e_1e_0e_3 - 3e_1^2e_3^2 + e_1^2e_0^2 = 0$	$z$ of Eq. (7)	4
19	$e_0 = \frac{e_2e_3}{e_1}$	$y = 2e_2\frac{e_1^2+e_3^2}{e_1}, z = \frac{e_3(e_1^4-6e_1^2e_3^2+e_3^4)}{e_1(e_1^2-e_3^2)}$	3
20	$e_0 = -\frac{e_1e_3}{e_2}$	$y = 2e_1\frac{e_3^2-e_2^2}{e_2}, z = -4e_1e_3$	3
21	arbitrary	$z$ of Eq. (7), $x$ of Eq. (8), $y$ of Eq. (9)	3
22	arbitrary	$z$ of Eq. (7), $x$ of Eq. (10), $y$ of Eq. (11)	3

yielding the above table is presented in Appendix 2. Note that for a given orientation the positions are (unions of) affine subspaces of  $\mathbb{R}^3$ . □

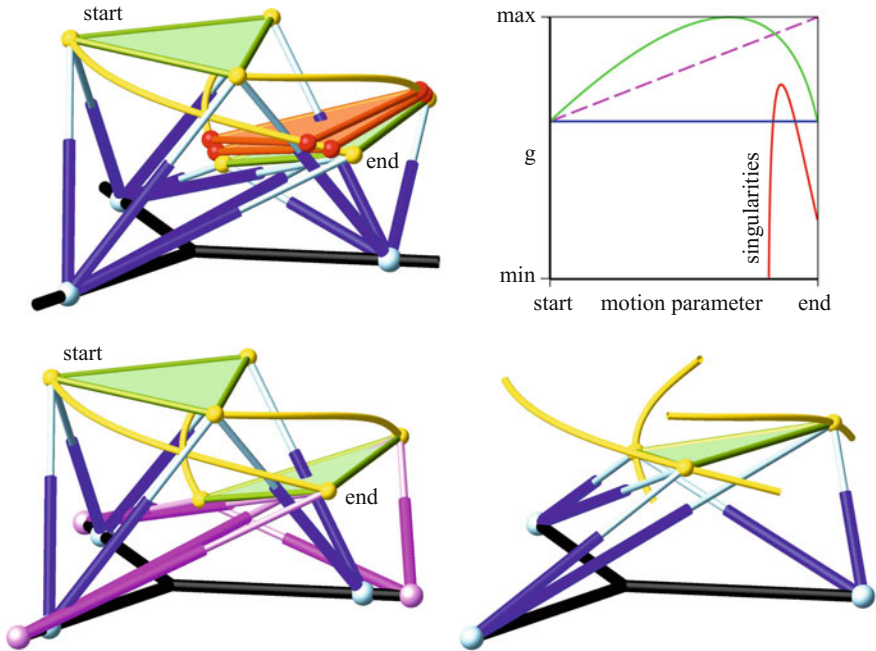
As the unavoidable singularities are low-dimensional varieties (cf. Theorem 1) in the 6-dimensional workspace, they can always be bypassed during path-planning. But this does not imply the existence of a singularity-free path as the singularity variety is a hypersurface in the mechanism’s configuration space.<sup>4</sup> Due to topological reasons two points of the configuration space can be separated by this hypersurface.

In contrast, actuation redundancy reduces the dimension of the singularity variety by the number of redundant dofs (cf. [3, Sect. 3]) and therefore a singularity can always be avoided during path-planning.

But in the case of a given path of the platform, kinematic redundancy is superior to actuation redundancy, as kinematically redundant dofs can be used to avoid singularities (if possible) and to increase the performance of the manipulator during the

---

<sup>4</sup>For our mechanism this is a 7-dimensional space, as a mechanism configuration is given by the pose of the platform (6 dofs) and by the size of the base triangle (1 dof).



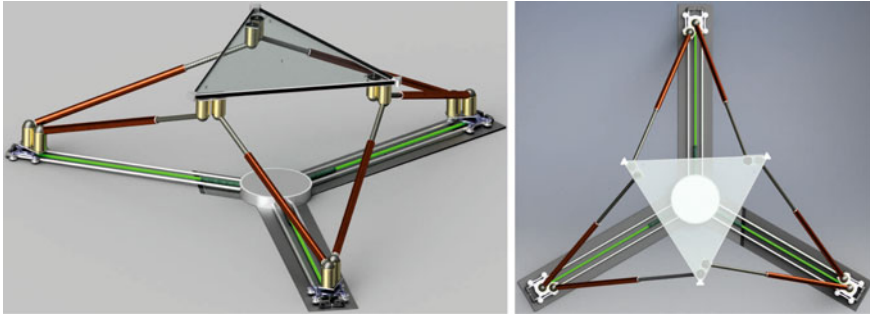
**Fig. 3** Singularity avoidance by kinematical redundancy: In the upper left picture the given motion of the platform between the start- and end-pose is displayed. Without reconfiguration of the base the manipulator will pass two singular configurations, which are highlighted in red. They correspond to the two intersection points of the blue horizontal line and the red *singularity curve* in the diagram in the upper right corner. One can avoid these singularities by performing a reconfiguration of the base indicated by the dashed line in the diagram, but then there is a collision of legs in the end-pose, which is illustrated in the lower left picture. The green parabola in the diagram corresponds to a solution, which is free of leg-interference and singularities. The robot-configuration of this solution with  $g = \max$  is displayed in the lower right picture. An animation can be downloaded from: <http://www.geometrie.tuwien.ac.at/nawratil/reconfiguration.gif>

prescribed motion (cf. Fig. 3). The study of the optimal reconfiguration of the base of the proposed mechanism during a given motion is dedicated to future research.

*Remark 2* Note that a so-called modular parallel robot [15] also changes its geometry with respect to a given end-effector motion, but there is no reconfiguration of the robot's base/platform *during* the motion of the end-effector.  $\diamond$

### 3 Conclusion

This paper contains a *concept study* of an octahedral SG manipulator with one degree of kinematic redundancy (equiform reconfigurability of the base) for VR simulations of single individuals (see Fig. 2). In a side-note we also proposed SU-joints



**Fig. 4** Axonometric view (left) and top view (right) of a kinematic equivalent mechanism to Fig. 2. On this design further studies (e.g. construction of a small scale prototype, optimal reconfiguration of the base for a given motion, ...) are based

(see Fig. 2) as an alternative to the problematic double S-joints within the octahedral structure. Clearly a deeper study of these SU-joints (regarding stiffness, joint-range, dynamic behavior, ...) has to be done in order to judge their applicability. Another possibility is the substitution of all double S-joints by double U-joints (e.g. see [5, Fig. 16] and [12, Sect. 4]) and to replace the  $\underline{P}$ -joints by cylindrical joints, with a passive rotation and an active translation component.

But we pursue another strategy for the technical realization; namely the usage of a design which is totally free of double joints but kinematically equivalent to the octahedral manipulator (cf. [16]). Therefore the resulting design illustrated in Fig. 4 can be built with standard components; i.e. without expensive custom products.

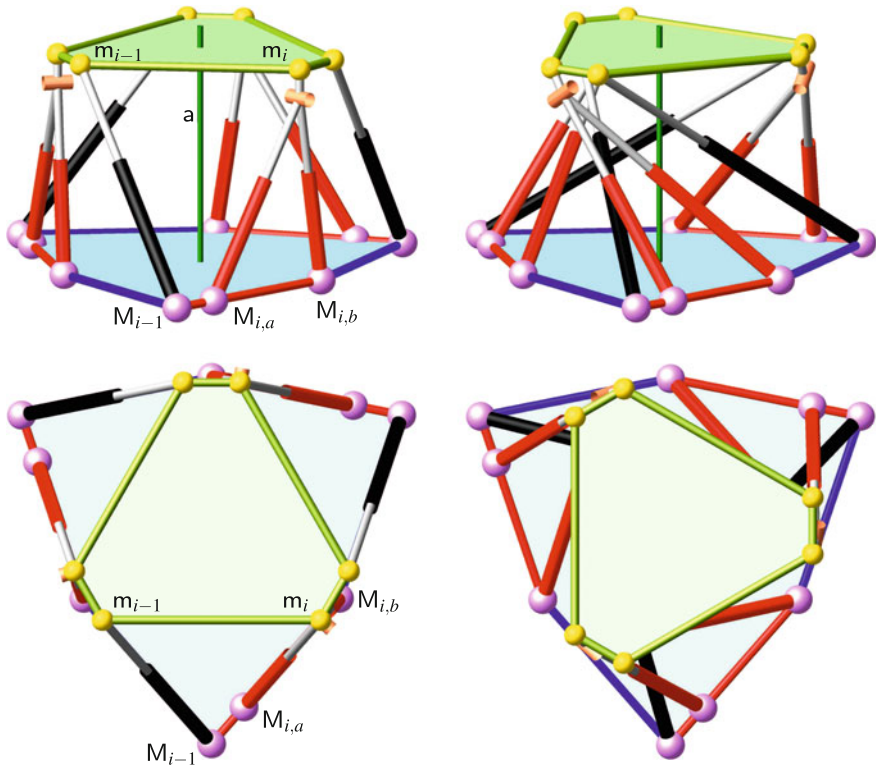
**Acknowledgements** The first author is supported by Grant No. P 24927-N25 of the Austrian Science Fund FWF. The second author is funded by the Doctoral College “Computational Design” of TU Vienna. Moreover the authors want to thank Hannes Kaufmann of the “Center for Geometry and Computational Design” at TU Vienna for fruitful discussions on VR motion simulations.

## Appendix 1

As already mentioned in the first bullet of Sect. 2.1, the authors of [17] stated in Sect. 5(D) that for the octahedral manipulator with three redundant legs “any Cartesian pose of the moving platform can be reached with a non-singular configuration of the mechanism”.<sup>5</sup> Moreover, it is “conjectured that this result can be extended to mechanisms whose spherical joints on the platform do not coincide by pairs”. In this section we construct a counter example to the conjecture.

According to Assumption 1 of [17, Sect. 5(D)] the base anchor points have to fulfill the following property:

<sup>5</sup>This is only true under Assumption 2 of [17, Sect. 5(D)]. Without this assumption all poses where the platform and the base are coplanar are “unavoidable singularities”.



**Fig. 5** Non-redundant legs are displayed in black and redundant ones are illustrated in red. In the upper row the axonometric views and in the lower row the top views of a non-singular configuration (left) and an unavoidable singularity (right), respectively, are given

$$M_{i,a}, M_{i,b}, M_{i-1} \text{ are collinear for } i = 1, 3, 5 \pmod{6}, \tag{12}$$

where  $M_{i-1}$  is the base point of a non-redundant leg and  $M_{i,a}, M_{i,b}$  denote the two base anchor points of a redundant leg. The geometric structure of the redundant leg can be seen in Fig. 5 (upper left). It should only be noted that the orange cylinders represent passive rotational joints and that the 3 gray bars linked by this joint are coplanar.

We start with a semi-hexagonal platform parallel to the base plane  $\delta$ . Then we determine the corresponding base point(s) of  $m_j$  as follows: We construct a plane  $\epsilon_j$  orthogonal to  $\delta$ , which touches the circumcircle of the semi-hexagonal platform in  $m_j$ . The intersection line of  $\epsilon_j$  and  $\delta$  is illustrated in Fig. 5 (left) in red (for  $j = 1, 3, 5$ ) and blue (for  $j = 2, 4, 6$ ), respectively. Under consideration of (12) we select the base point(s) on these intersection lines.



Then we rotate the platform by  $-90$  degrees about the center axis  $a$  and end up with a singular configuration (so-called Fichter singularity [5]) illustrated in Fig. 5 (right). It can easily be checked that this is an unavoidable singularity.

## Appendix 2

We split the proof of Theorem 1 into two subsections. In the first one very special cases are discussed and in the second one we attack the general case.

### Special Cases

1. Within this first item we study all cases where at least two of the four Euler parameters are zero.

- a.  $e_1 = e_2 = 0$ : Then  $Q$  and  $L$  are fulfilled identically and we remain with  $A_1A_2 = 0$ , which factors into

$$z^3(e_0^2 + e_3^2)(e_0 - e_3)(e_0 + e_3) = 0. \tag{13}$$

For  $z = 0$  the legs are in a field of lines, whose carrier plane is the base ( $\Rightarrow$  row 1 of the table given in Theorem 1). For  $e_0 = \pm e_3$  we get the Fichter singularity (cf. [5]); i.e. rotation of the platform by  $\pm 90^\circ$  about the  $z$ -axis ( $\Rightarrow$  row 2).

- b.  $e_0 = e_3 = 0$ : This is already a singular configuration ( $\Rightarrow$  row 3), which is not of practical relevance as the platform is upside down.
- c.  $e_0 = e_2 = 0$  and  $e_1e_3 \neq 0$ : It can easily be seen that  $Q = L = A_1A_2 = 0$  can only hold for  $z = e_1e_3$  ( $\Rightarrow$  row 13). The lines are in a singular linear line complex.
- d.  $e_1 = e_3 = 0$  and  $e_0e_2 \neq 0$ : Analogous considerations as in item (1c) yield  $z = -e_0e_2$  ( $\Rightarrow$  row 14). The lines are in a singular linear line complex.
- e.  $e_0 = e_1 = 0$  and  $e_2e_3 \neq 0$ : It is not difficult to verify that the unavoidable singularities are given by  $y = z = 0$  ( $\Rightarrow$  row 15).
- f.  $e_2 = e_3 = 0$  and  $e_0e_1 \neq 0$ : Analogous considerations as in item (1e) yield  $y = z = 0$  ( $\Rightarrow$  row 16).

2.  $e_0 = e_3 \neq 0$ : In this case  $Q$  factors into

$$2e_3^3(e_1 + e_2)(e_1 - 2e_2 - \sqrt{3}e_2)(e_1 - 2e_2 + \sqrt{3}e_2). \tag{14}$$

We remain with the following three cases:

- a.  $e_2 = -e_1$  and  $e_3 \neq 0$ : Now we get

$$\begin{aligned} L &= 4e_1^2e_3(z - 2e_1e_3)(e_1z + 2e_1^2e_3 + 2e_3^3 + ye_3), \\ A_1A_2 &= 4xe_1e_3(z - 2e_1e_3)(2e_1e_3y - e_3^2z + e_1^2z), \end{aligned} \tag{15}$$

thus the following cases can occur:

- i.  $e_1 = 0$ : We get again the Fichter singularity.
  - ii.  $z = 2e_1e_3$  and  $e_1 \neq 0$ : In this case all legs intersect a line and therefore they belong to a singular linear line complex ( $\Rightarrow$  row 4, upper sign).
  - iii.  $e_1z + 2e_1^2e_3 + 2e_3^3 + ye_3 = 0$  and  $(z - 2e_1e_3)e_1 \neq 0$ : We can solve this equation for  $z$  and then  $A_1A_2$  can only vanish without contradiction for  $x = 0$  ( $\Rightarrow$  row 5, upper sign) or  $y = 2e_1^2 - 2e_3^2$  ( $\Rightarrow$  row 6, upper sign). Therefore we get two lines in the position space.
- b.  $e_1 = (2 + \sqrt{3})e_2$  and  $(e_1 + e_2)e_3 \neq 0$ : By inspecting  $L$  and  $A_1A_2$  in a similar way as done in very detail in item (a) we get the following solutions:
- i.  $z = -\frac{4e_2e_3}{\sqrt{3}-1}$ : In this case all legs intersect again a line and therefore they belong to a singular linear line complex ( $\Rightarrow$  row 7, upper sign).
  - ii.  $x = \frac{16e_2^2+8e_2^2\sqrt{3+y-4e_3^2}}{\sqrt{3}}$  and  $z = \frac{8e_2e_3}{\sqrt{3}-1}$ : For a given orientation we get a line in the position space ( $\Rightarrow$  row 8, upper sign).
  - iii.  $x = -y\sqrt{3}$  and  $z = \frac{2e_3(e_3^2+4e_2^2+2e_2^2\sqrt{3-y})}{e_2(\sqrt{3}+1)}$ : For a given orientation we get again a line in the position space ( $\Rightarrow$  row 9, upper sign).
- c.  $e_1 = (2 - \sqrt{3})e_2$  and  $(e_1 + e_2)e_3 \neq 0$ : Exactly the same computations as in item (b) yield the solutions given in the rows 7, 8, and 9, but now for the lower signs.
3.  $e_0 = -e_3 \neq 0$ : This is the same discussion as in item (2). The resulting solutions are given in the rows 4, 5 and 6, but now for the lower signs, and in the rows 10, 11 and 12 (upper and lower signs).

**General Case**

We start by solving  $Q = 0$  for  $z$  which yields Eq. (7). The denominator vanishes only for the special cases (1a), (1b), (2) and (3), respectively. We insert this expression for  $z$  into  $L = 0$  and  $A_1A_2 = 0$  and consider the greatest common divisor of the resulting numerators, which reads as follows:

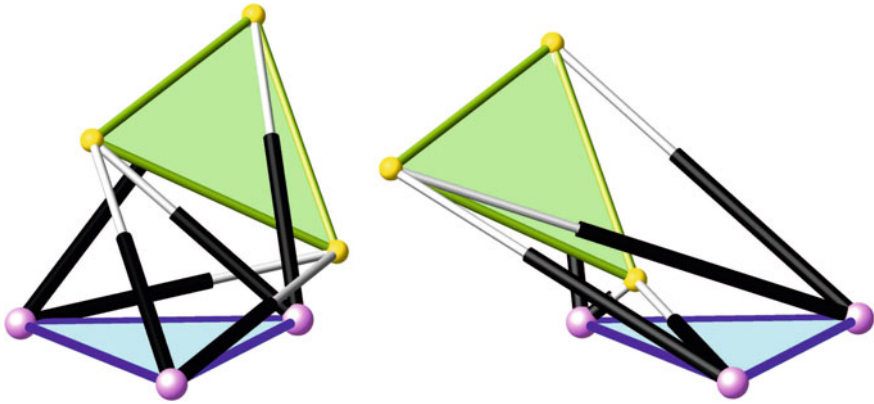
$$(e_0e_1 + e_2e_3)(e_2^2e_3^2 - 3e_2^2e_0^2 + 8e_2e_1e_0e_3 - 3e_1^2e_3^2 + e_1^2e_0^2). \tag{16}$$

If one of these two factors vanish we get the solutions given in the rows 17 and 18, respectively. The remaining factor of  $L$  has 40 terms and is linear in  $x$ . As the coefficient of  $x$  equals

$$2(e_2^2 + e_1^2)(e_0 - e_3)(e_0 + e_3)(e_0e_1 - e_2e_3)(e_0e_2 + e_1e_3) \tag{17}$$

we have to distinguish the following three cases:

- 1.  $e_0e_1 - e_2e_3 = 0$ : If one of the  $e_i$ 's is equal to zero, this equation implies that also a second one has to vanish. Therefore we get one of the already discussed special cases (1a, b, c, d). As a consequence we can set  $e_0 = \frac{e_2e_3}{e_1}$ . Then the numerator of  $L$  simplifies to



**Fig. 6** For the orientation given by the Euler parameters  $e_0 = \frac{4\sqrt{105}}{175}$ ,  $e_1 = \frac{\sqrt{105}}{21}$ ,  $e_2 = \frac{8\sqrt{105}}{105}$ ,  $e_3 = -\frac{16\sqrt{105}}{525}$  the unavoidable singularities of row 21 and row 22 are illustrated in the left and right figure, respectively. The position of row 21 equals  $x = -\frac{148327}{130830}$ ,  $y = -\frac{66032}{65415}$ ,  $z = \frac{12304}{13083}$  and the one of row 22 is given by  $x = \frac{40969}{65415}$ ,  $y = -\frac{85772}{65415}$ ,  $z = \frac{12304}{13083}$

$$e_3^4(e_1 - e_2)(e_1 + e_2)(e_2^2 + e_1^2)^3(2e_2e_1^2 - ye_1 + 2e_2e_3^2). \tag{18}$$

As  $e_1 = \pm e_2$  implies  $e_0 = \pm e_3$  we can only end up with a case studied in the special case (2) and (3), respectively. Therefore we only remain with  $2e_2e_1^2 - ye_1 + 2e_2e_3^2 = 0$  which implies row 19.

2.  $e_0e_2 + e_1e_3 = 0$ : For the same reasons as in item (1) of the general case we can set  $e_0 = -\frac{e_1e_3}{e_2}$ . Analogous considerations imply the condition  $2e_1e_2^2 - 2e_1e_3^2 + ye_2 = 0$  resulting in row 20.
3.  $(e_0e_1 - e_2e_3)(e_0e_2 + e_1e_3) \neq 0$ : In this case we can solve  $L = 0$  for  $x$ . Plugging the resulting expression into  $A_1A_2$  yields two factors, which are linear in  $y$ . They imply the solutions given in row 21 and 22, which are illustrated in Fig. 6.

End of all cases. □

## References

1. Bande P, Seibt M, Uhlmann E, Saha SK, Rao PVM (2004) Kinematics analyses of Dodekapod. Mech Mach Theory 40(6):740–756
2. Cao Y, Zhou H, Li B, Long S, Liu M (2011) Singularity elimination of Stewart parallel manipulator based on redundant actuation. Adv Mater Res 143–144:308–312
3. Dasgupta B, Mruthyunjaya TS (1998) Force redundancy in parallel manipulators: theoretical and practical issues. Mech Mach Theory 33(6):727–742
4. Downing DM, Samuel AE, Hunt KH (2002) Identification of the special configurations of the octahedral manipulator using the pure condition. Int J Robot Res 21(2):147–159

5. Fichter EF (1982) A Stewart platform-based manipulator: general theory and practical construction. *Int J Robot Res* 5(2):157–182
6. Hamdoon FM, Abdel-All NH (2004) An investigation of an octahedral platform using equiform motions. *J Geom Graph* 8(1):33–39
7. Hebsacker, M.: Entwurf und Bewertung Paralleler Werkzeugmaschinen – das Hexaglide. Dissertation, ETH Zürich (2000)
8. Hunt KH, McAreë PR (1998) The octahedral manipulator: geometry and mobility. *Int J Robot Res* 17(8):868–885
9. Husty M, Mielczarek S, Hiller M (2002) Redundant spatial Stewart-Gough platform with a maximal forward kinematics solution set. In: Lenarcic J, Thomas F (eds) *Advances in Robot Kinematics: Theory and Applications*. Kluwer, pp 147–154
10. Jiang Q, Gosselin CM (2009) Geometric optimization of the MSSM Gough-Stewart platform. *J Mech Robot* 1:031006
11. Kotlarski J, Heimann B, Ortmaier T (2012) Influence of kinematic redundancy on the singularity-free workspace of parallel kinematic machines. *Front Mech Eng* 7(2):120–134
12. Lee J, Duffy J, Hunt KH (1998) A practical quality index based on the octahedral manipulator. *Int J Robot Res* 17(10):1081–1090
13. Merlet J-P (2006) *Parallel robots*, 2nd edn. Springer, Berlin
14. Merlet J-P (1996) Redundant parallel manipulators. *Lab Robot Autom* 8(1):17–24
15. Merlet J-P (2003) Determination of the optimal geometry of modular parallel robots. *Proc IEEE Int Conf Robot Autom* 1:1197–1202
16. Rojas N, Borrás J, Thomas F (2012) The octahedral manipulator revisited. In: *Proceedings of the IEEE international conference on robotics and automation*. Saint Paul, USA, pp 14–18
17. Schreiber LT, Gosselin C (2016) Kinematically redundant spatial parallel mechanisms for singularity avoidance and large orientational workspace. *Trans Robot* 32(2):286–300
18. Stoughton RS, Salerno R, Canfield S, Reinholtz C (1994) A redundant, 6-dof parallel manipulator structure with improved workspace and dexterity. In: *Proceedings of the 5th international symposium on robotics and manufacturing*. Maui, USA, pp 14–18
19. Wang J, Gosselin CM (2004) Kinematic analysis and design of kinematically redundant parallel mechanisms. *J Mech Design* 126:109–118
20. Zhang Y, Gong J, Gao F (2007) Singularity elimination of parallel mechanisms by means of redundant actuation. In: *12th IFToMM world congress*. Besancon, France, pp 18–21

# Kinematic Analysis of a 3-RRPS Manipulator



S. M. Grigorescu, E.-C. Lovasz and C. Pop

**Abstract** The paper propose an iterative method for computing the direct kinematic of a 3-RRPS manipulator by considering for each leg a rotary and a linear actuator. It was calculated the error due to difference between the computed mobile triangle vertices and its sides length. To identify the possible angles solutions, it was developed a special function that determine a threshold value applied to the calculated sides of mobile triangle, depending on iteration phases and manipulator dimensional values. The iterations steps lead to refine the range values of  $\psi$  angles and its inappropriate values removal. The method can be successfully used for the kinematic analysis of several structure types of legs, by preserving the distance between the connection joints with the fixed and mobile frames.

**Keywords** 3-RRPS parallel manipulator • Forward kinematics  
Inverse kinematics

## 1 Introduction

Many researchers [1–13] investigated several 6-DOF parallel manipulator's configurations, with different kinematic chains, regarding the geometry, direct kinematic analysis resolving methods, singularity loci efficiency, workspace, manipulators dexterity, dynamics and design.

---

S. M. Grigorescu · E.-C. Lovasz · C. Pop (✉)  
Politehnica University of Timișoara, Timișoara, Romania  
e-mail: cristian.pop@upt.ro

S. M. Grigorescu  
e-mail: sanda.grigorescu@upt.ro

E.-C. Lovasz  
e-mail: erwin.lovasz@upt.ro

Angeles, in his book [1], developed the direct kinematic analysis the Stewart-Gough manipulator, using the Denavit-Hartenberg parameters of the leg and reaching a 12-th degree characteristic polynomial. The conclusion: “while the inverse kinematics of the leg is quite straightforward, its direct kinematics is not” is the same that Merlet presented in his book [2]. This researcher reduced the direct kinematic analysis to the solution of one variable polynomial equation and reached to the conclusion that direct kinematic equation may have up to  $16^{\circ}$  so, up to 16 solutions.

Villalibre [3] takes into account the two ways of solving the direct kinematics, analytically and numerically. While the analytically method can't always solve the problem, the numerically iterative Newton-Raphson method is time consuming and has local convergences.

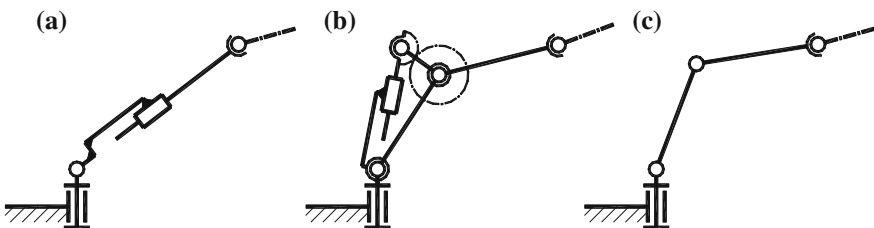
Laribi [4] considers that the solution of equations system is equivalent to intersection points of given spheres, which guides to two possible configurations of moving platform with respect to the base.

Staicu, in [5], analyses a 3-DOF parallel mechanism with revolute actuators and one passive leg in the center of fixed platform, for increasing robots stiffness.

## 2 Kinematic Analysis Method

The spatial parallel robots present 3–6 kinematic chains, connecting the mobile to the fixed platform. The robot's legs might have different kinematic structures, depending on mobile platform's degrees of freedom (DOF) and on specific applications goals. Figure 1 represents some possible leg's kinematic schemes of RRPS generic base structure and 6 DOF of the mobile manipulators platform.

Referring to the 3-RRPS structure, presented in Fig. 2, the two reference systems are: mobile platforms system (1) and fixed reference system (0), attached to the base platform. The mobile platform's pose is defined by the M point Cartesian coordinates and system (1) orientation angles with respect to the fixed coordinates system (0). The points  $C_i$  coordinates transformation, from mobile system to the fixed one, is expressed in Eq. (1).



**Fig. 1** Leg's kinematic schemes

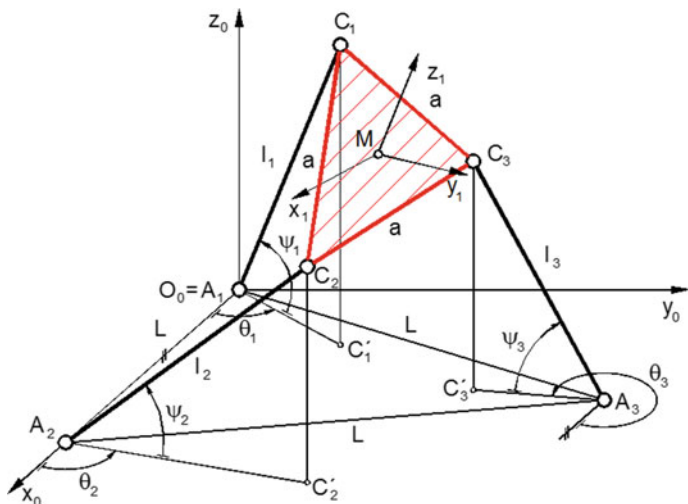


Fig. 2 3-RRPS parallel manipulators notations for kinematics model

$$\begin{bmatrix} {}^0X_{Ci} \\ {}^0Y_{Ci} \\ {}^0Z_{Ci} \\ 1 \end{bmatrix} = {}^0T_1 \cdot \begin{bmatrix} {}^1x_{Ci} \\ {}^1y_{Ci} \\ {}^1z_{Ci} \\ 1 \end{bmatrix}; i = \overline{1,3} \tag{1}$$

where the  ${}^0T_1$  is:

$${}^0T_1 = \begin{bmatrix} & & {}^0X_M \\ {}^0R_1 & & {}^0Y_M \\ & & {}^0Z_M \\ 0 & 0 & 0 & 1 \end{bmatrix} \tag{2}$$

The rotation matrix R [8] expresses the mobile platform orientation relative to the base platform (Eq. (3)).

$${}^0R_1 = \begin{bmatrix} \cos \alpha \cdot \cos \beta & \cos \alpha \cdot \sin \gamma \cdot \sin \beta - \cos \gamma \cdot \sin \alpha & \sin \gamma \cdot \sin \alpha + \cos \gamma \cdot \sin \alpha \\ \cos \beta \cdot \sin \alpha & \cos \gamma \cdot \cos \alpha + \sin \gamma \cdot \sin \beta \cdot \sin \alpha & \cos \gamma \cdot \sin \alpha \cdot \sin \beta - \cos \alpha \cdot \sin \gamma \\ -\sin \beta & \cos \beta \cdot \sin \gamma & \cos \gamma \cdot \cos \beta \end{bmatrix} \tag{3}$$

with rotation angles, noted with:  $\alpha$  around the OZ axis,  $\beta$  around the OY axis and  $\gamma$  around the OX axis.

Referring to the Fig. 2 and knowing the M coordinates ( ${}^0X_M, {}^0Y_M, {}^0Z_M$ ), the  $\alpha, \beta, \gamma$  angles values, the fixed (L) and mobile triangle (a) side lengths, it might be

calculated the  $\theta_i$ ,  $l_i$  and  $\psi_i$  values in Eqs. (5) and (5'), deduced from Eq. (4) of mobile platform's  $C_i$  points.

$$\begin{aligned} {}^0X_{C_1} &= l_1 \cdot \cos \psi_1 \cdot \cos \theta_1 & {}^0X_{C_2} &= L + l_2 \cdot \cos \psi_2 \cdot \cos \theta_2 & {}^0X_{C_3} &= \frac{L}{2} + l_3 \cdot \cos \psi_3 \cdot \cos \theta_3 \\ {}^0Y_{C_1} &= l_1 \cdot \cos \psi_1 \cdot \sin \theta_1 & {}^0Y_{C_2} &= l_2 \cdot \cos \psi_2 \cdot \sin \theta_2 & {}^0Y_{C_3} &= \frac{L \cdot \sqrt{3}}{2} + l_3 \cdot \cos \psi_3 \cdot \sin \theta_3 \\ {}^0Z_{C_1} &= l_1 \cdot \sin \psi_1 & {}^0Z_{C_2} &= l_2 \cdot \sin \psi_2 & {}^0Z_{C_3} &= l_3 \cdot \sin \psi_3 \end{aligned} \quad (4)$$

$$\begin{aligned} \theta_1 &= \arctan\left(\frac{{}^0Y_{C_1}}{{}^0X_{C_1}}\right) & l_1 &= \sqrt{{}^0X_{C_1}^2 + {}^0Y_{C_1}^2 + {}^0Z_{C_1}^2} \\ \theta_2 &= \arctan\left(\frac{{}^0Y_{C_2}}{{}^0X_{C_2} - L}\right) & l_2 &= \sqrt{({}^0X_{C_2} - L)^2 + {}^0Y_{C_2}^2 + {}^0Z_{C_2}^2} \\ \theta_3 &= \arctan\left(\frac{{}^0Y_{C_3} - L \cdot \sqrt{3}/2}{{}^0X_{C_3} - L/2}\right) & l_3 &= \sqrt{({}^0X_{C_3} - L/2)^2 + ({}^0Y_{C_3} - L \cdot \sqrt{3}/2)^2 + {}^0Z_{C_3}^2} \end{aligned} \quad (5)$$

$$\begin{aligned} \psi_1 &= \arctan\left(\frac{\sqrt{{}^0X_{C_1}^2 + {}^0Y_{C_1}^2}}{{}^0Z_{C_1}}\right), & \psi_2 &= \arctan\left(\frac{\sqrt{({}^0X_{C_2} - L)^2 + {}^0Y_{C_2}^2}}{{}^0Z_{C_2}}\right) \\ \psi_3 &= \arctan\left(\frac{\sqrt{({}^0X_{C_3} - L/2)^2 + ({}^0Y_{C_3} - L \cdot \sqrt{3}/2)^2}}{{}^0Z_{C_3}}\right) \end{aligned} \quad (5')$$

For each kinematic chain RRPS, it is considered that the angles  $\theta_i$  and the length  $l_i$ ,  $i = 1 \div 3$  have given values by the rotary and linear actuators and the  $\psi_i$  is the determined parameter in Eq. (5'), assuming that mobile platform moves always in one side of the fixed base.

Direct kinematic analysis starts with Eq. (4), where it is considered known the actuated parameters:  $\theta_i$ ,  $l_i$ ,  $i = 1 \div 3$  and are unknown the  ${}^oC_i$  points Cartesian coordinates and the angles  $\psi_i$ . Accordingly, to the 9 equations (Eq. (6)), there are added 3 equations that express the distances between mobile platform triangle vertices,  $C_1C_2$ ,  $C_1C_3$  and  $C_2C_3$  (noted with Eq. (7)).

$$\begin{aligned} {}^0X_{C_1} &= a_1 \cdot \cos \psi_1 & {}^0X_{C_2} &= L + a_2 \cdot \cos \psi_2 & {}^0X_{C_3} &= \frac{L}{2} + a_3 \cdot \cos \psi_3 \\ {}^0Y_{C_1} &= b_1 \cdot \cos \psi_1 & {}^0Y_{C_2} &= b_2 \cdot \cos \psi_2 & {}^0Y_{C_3} &= \frac{L \cdot \sqrt{3}}{2} + b_3 \cdot \cos \psi_3 \\ {}^0Z_{C_1} &= c_1 \cdot \sin \psi_1 & {}^0Z_{C_2} &= c_2 \cdot \sin \psi_2 & {}^0Z_{C_3} &= c_3 \cdot \sin \psi_3 \end{aligned} \quad (6)$$

$$\begin{aligned} |\overline{C_1C_2}| &= \sqrt{({}^0X_{C_1} - {}^0X_{C_2})^2 + ({}^0Y_{C_1} - {}^0Y_{C_2})^2 + ({}^0Z_{C_1} - {}^0Z_{C_2})^2} = a; \\ |\overline{C_1C_3}| &= \sqrt{({}^0X_{C_1} - {}^0X_{C_3})^2 + ({}^0Y_{C_1} - {}^0Y_{C_3})^2 + ({}^0Z_{C_1} - {}^0Z_{C_3})^2} = a; \\ |\overline{C_2C_3}| &= \sqrt{({}^0X_{C_2} - {}^0X_{C_3})^2 + ({}^0Y_{C_2} - {}^0Y_{C_3})^2 + ({}^0Z_{C_2} - {}^0Z_{C_3})^2} = a. \end{aligned} \quad (7)$$



The proposed method for resolving the forward kinematic analysis comprises several steps, presented above. The goal is finding the appropriate values of angles  $\psi_i$  for which the calculated values of  ${}^0X_{C_i}$ ,  ${}^0Y_{C_i}$ ,  ${}^0Z_{C_i}$  in Eq. (6), respect the equalities in Eq. (7) as close as possible to value of  $a$ , namely the mobile platform triangle side length. The process of seeking the values of  $\psi_i$ ,  $i = 1 \div 3$  has 5 iterations, in each iteration the range of search decreases 10 times. The calculated error, noted with  $e_{ij}$  (Eq. 8) and also the allowable errors value or threshold, noted with  $q_i$  decrease accordingly. The main parameters of each iteration step are presented in Table 1.

Firstly, for the incremented values of  $\psi_i$ , there are calculated the errors for the sides of mobile triangle  $C_1C_2$  and  $C_1C_3$ , namely  $e_{12k}$  and  $e_{13k}$  in Eq. (9).

$$e_{ij} = d_{ij} - a = \sqrt{({}^0X_{C_i} - {}^0X_{C_j})^2 + ({}^0Y_{C_i} - {}^0Y_{C_j})^2 + ({}^0Z_{C_i} - {}^0Z_{C_j})^2} - a; i = \overline{1,3}; j = \overline{1,3} \tag{8}$$

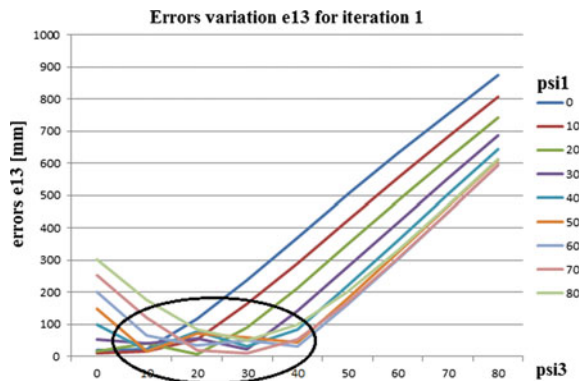
These matrices  $e_{12k}$  and  $e_{13k}$  are used in the determination process of threshold value  $q$ , in each iteration loop. Finding a proper value for  $q$  is the clue of refining and getting correct solution of the problem.

In Fig. 3 is presented an example of errors variation in a specific dimensional case, for the first iteration. It can be observed that the errors variation is in large range and some  $\psi_3$  variations curves, for a specific  $\psi_1$  value present local minima.

**Table 1** Iteration main parameters

Iteration	Increment's values for angle $\psi_{i,j,k}$ (°)	Allowable error (mm)
1	10	$q_1$
2	1	$q_2$
3	0.1	$q_3$
4	0.01	$q_4$
5	0.001	$q_5$

**Fig. 3** Caption of errors variation in a specific numerical case



After the threshold  $q_{iteration}$  determination, next step includes numerical processing on  $e_{12k}$  and  $e_{13k}$  matrices (elimination of inappropriate values of  $\psi_1, \psi_2, \psi_3$ ) for those matrix elements that don't fulfill the condition expresses in Eq. (9). Only the appropriate values continue the checking process, that is the calculus of errors  $e_{12}, e_{13}, e_{23}$ , corresponding to the mobile triangle sides in different poses.

$$((e_{12k} < q)_{iteration} \wedge (e_{13k} < q)_{iteration}) \wedge (e_{23k} < q)_{iteration}; iteration = \overline{1, 5}; k = \overline{1; 10} \tag{9}$$

Passing from an iteration step to another, the range values of  $\psi_i$  angles is refined and is done only for those sets of  $(\psi_1, \psi_2, \psi_3)$  determined with conditions Eq. (9). Finally, eliminating the sets of  $(\psi_1, \psi_2, \psi_3)$  values by imposing the condition above and proper  $q$  values, solution is obtained.

### 3 Numerical Example

There was developed a set of programs and functions for the forward and inverse kinematic analysis, in several numerical cases and geometric dimensions of 3-RRPS parallel manipulator. An example of inverse kinematic analysis outcome figures is given in Figs. 4, 5 and 6. For a given position of  $M$  point, the mobile platform orientation, defined by  $\alpha, \beta, \gamma$ , are respectively altered. The mobile triangle is represented in 3-D and in 2-D perspective.

Figure 7 is the captured screen of a specific Graphical User Interface (GUI), dedicated to the 3-RRPS parallel manipulator. The left side of GUI's panel is dedicated to inverse kinematic and the right side to forward analysis. By inserting numerical values in input sets of parameters, there are displayed the program outcome values. This way of GUI's data display allows the user to visualize the

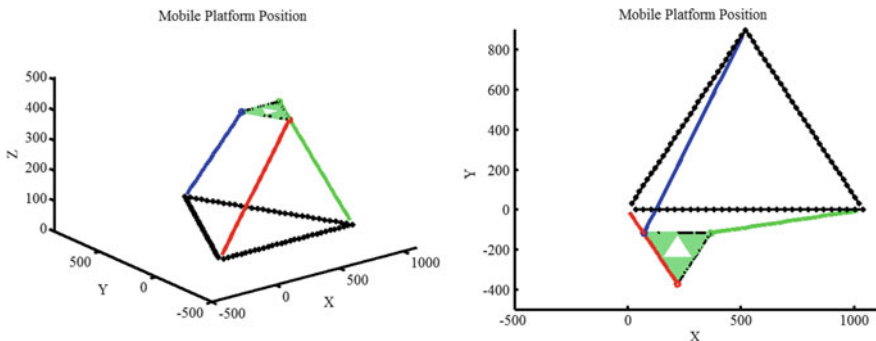


Fig. 4 3-D and 2-D perspective for mobile triangle orientation  $\alpha = 60^\circ, \beta = 0^\circ, \gamma = 0^\circ$

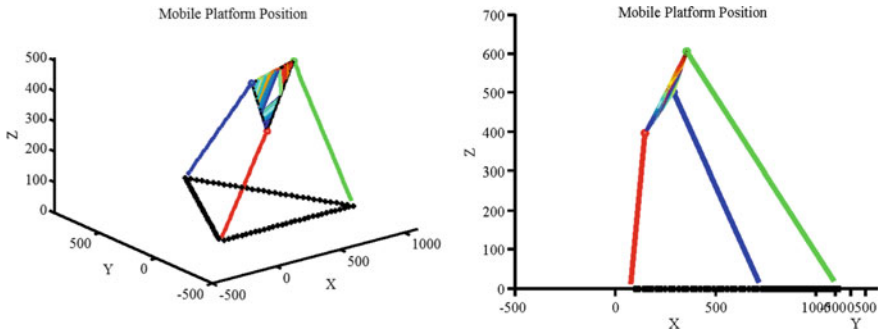


Fig. 5 3-D and 2-D perspective for mobile triangle orientation  $\alpha = 0^\circ, \beta = -45^\circ, \gamma = 0^\circ$

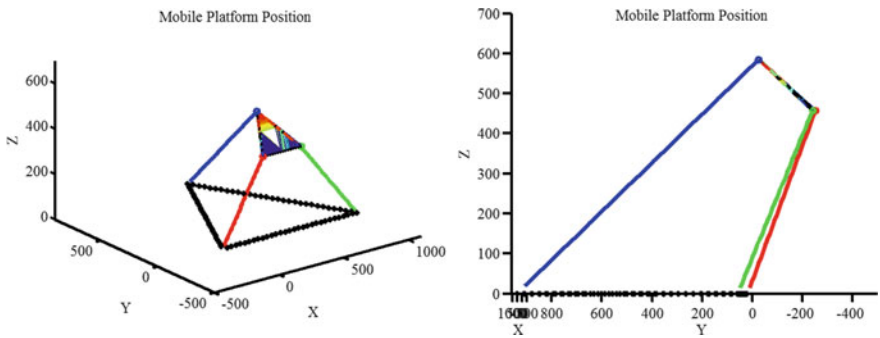


Fig. 6 3-D and 2-D perspective for mobile triangle orientation  $\alpha = 0^\circ, \beta = 0^\circ, \gamma = -30^\circ$

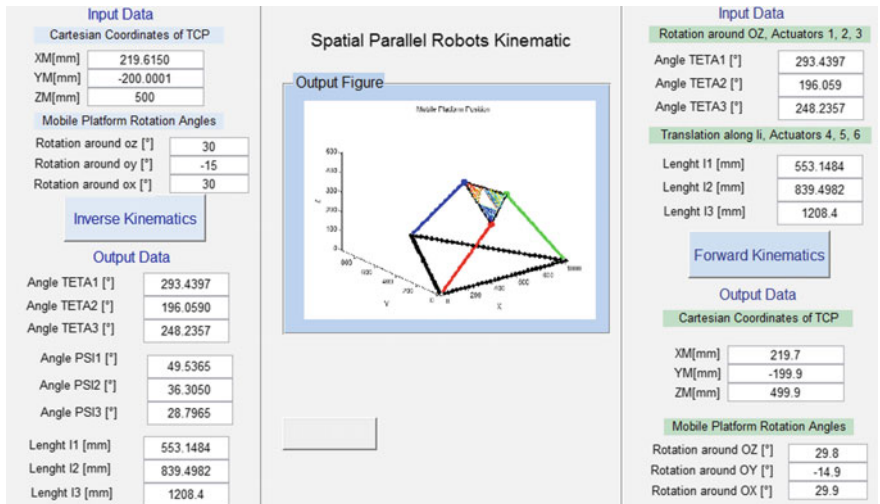
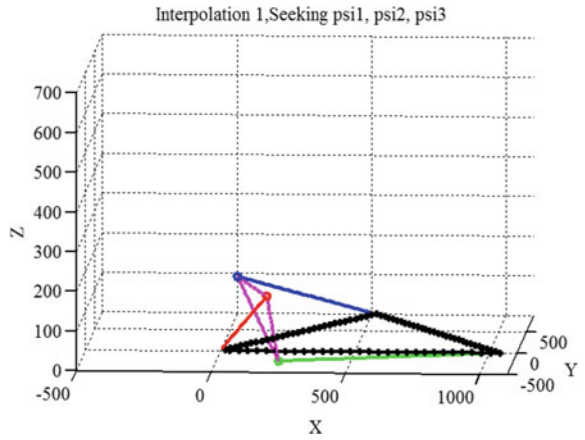
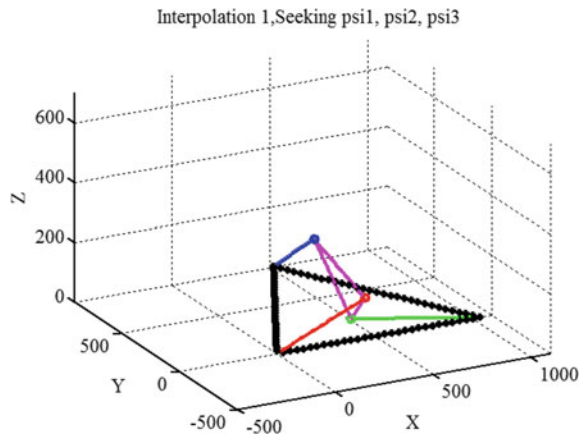


Fig. 7 GUI for kinematic analysis

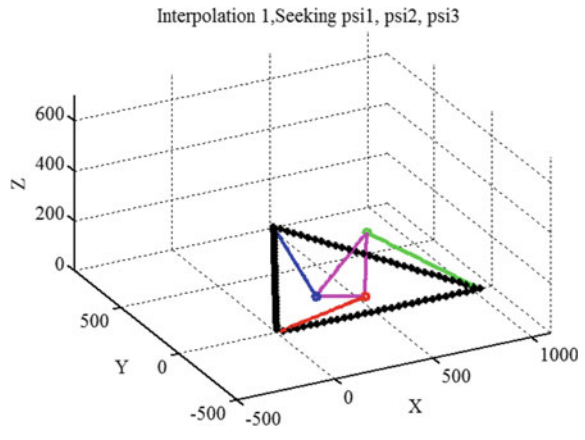
**Fig. 8**  $\psi_1 = 20^\circ$ ,  $\psi_2 = 0^\circ$ ,  
 $\psi_3 = 10^\circ$



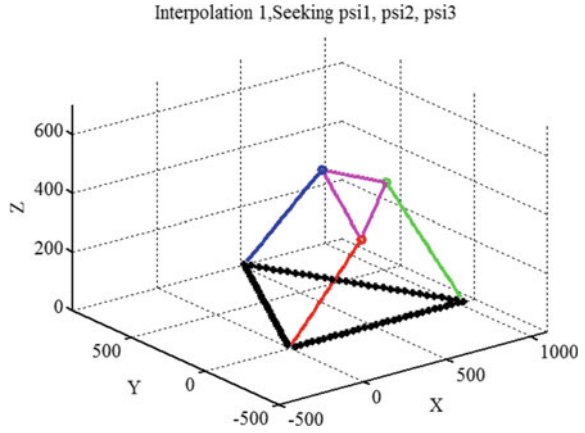
**Fig. 9**  $\psi_1 = 30^\circ$ ,  $\psi_2 = 10^\circ$ ,  
 $\psi_3 = 20^\circ$



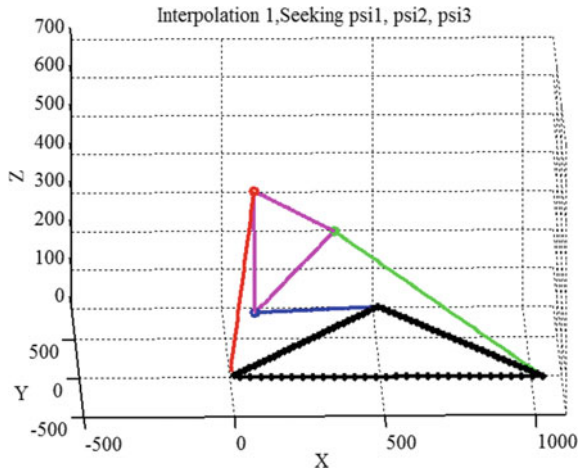
**Fig. 10**  $\psi_1 = 30^\circ$ ,  
 $\psi_2 = 30^\circ$ ,  $\psi_3 = 10^\circ$



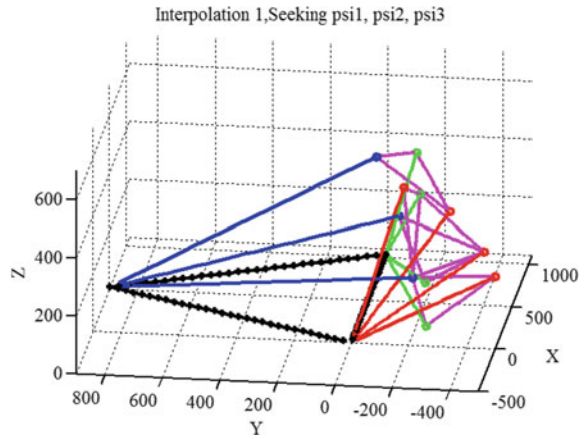
**Fig. 11**  $\psi_1 = 50^\circ$ ,  
 $\psi_2 = 40^\circ$ ,  $\psi_3 = 30^\circ$



**Fig. 12**  $\psi_1 = 70^\circ$ ,  
 $\psi_2 = 30^\circ$ ,  $\psi_3 = 10^\circ$



**Fig. 13** 3D view for all 5  
 found solutions



obtained values of both kinematic analysis and to check its validity. The direct kinematic program, for the input data presented in Fig. 7, in the first iteration, gives 5 possible sets of  $\psi_1, \psi_2, \psi_3$ . Figures 8, 9, 10, 11 and 12 represent the 3D view of these solutions and Fig. 13 a 3D view of all solutions.

## 4 Conclusions

The paper proposes an iterative method for computing the direct kinematic of a 3-RRPS manipulator with 6 DOF. The method can be successfully used for the kinematic analysis of several structure types of legs, by preserving the  $l_i$  given values. For the forward kinematic, the solving method is iterative and refines the  $\psi_i$  values of possible solutions. There is developed a special function to calculate the threshold value for errors between lengths of  $C_iC_j$  and side's length of mobile triangle. The paper doesn't take into consideration geometric dimensions constraints regarding the actuator's strokes, the kinematic joints (especially spherical ones) and also the singularity loci of the structure. The computational program running times are low, not exceeding 10 s and the  $\psi_i$  angles errors are limited to  $0.001^\circ$ .

## References

1. Angeles J (2007) Fundamentals of robotic mechanical systems. In: Theory, methods, and algorithms, 3rd edn. Springer Science and Business Media
2. Merlet J-P (2006) Parallel robots. Solid mechanics and its applications. Springer
3. Villalibre SH (2016) Design methodology for MAST-type parallel manipulators based on kinematics, dynamic and stiffness criteria: theoretical and experimental application to the 2PRU-1PRS. PhD thesis, University of the Basque Country, Bilbao
4. Laribi MA, Romdhane L, Zedhloul S (2007) Analysis and dimensional synthesis of the DELTA robot for a prescribed workspace. *Mech Mach Theory* 42:859–870
5. Staicu S, Zhang D (2008) A novel dynamic modeling approach for parallel mechanisms analysis. *Robot Comput-Integr Manuf* 24:167–172
6. Tsai M-S, Yuan W-H (2010) Inverse dynamics analysis for a 3-PRS parallel mechanism based on a special decomposition of the reaction forces. In: Mechanism and machine theory
7. Dash AK, Chen I-M, Yeo SH, Yang G (2005) Workspace generation and planning singularity-free path for parallel manipulators. *Mech Mach Theory* 40:776–805
8. Kim D, Chung W (1999) Analytic singularity equation and analysis of six-DOF parallel manipulators using local structurization method. *IEEE Trans Robot Autom* 15(4)
9. Monsarrat B, Gosselin CM (2003) Workspace analysis and optimal design of a 3-leg 6-DOF parallel platform mechanism. *IEEE Trans Robot Autom* 19(6)
10. Jiang Z, Li Y, Xu L (2014) Kinematic analysis of a novel 4-DOF parallel mechanism. In: Proceedings of 2014 workshop on fundamental issues and future research directions for parallel mechanisms and manipulators, Tianjin

11. El-Khasawneh B, AlAli A, AlAzzam A, Gan D, Tayeh MA (2014) A novel 5 degrees-of-freedom hybrid serial-parallel kinematics manipulator (two-3PRR): inverse and forward kinematics. In: Proceedings of 2014 workshop on fundamental issues and future research directions for parallel mechanisms and manipulators, Tianjin
12. Neagoe M, Diaconescu D (2009) General method and algorithms used for accuracy modeling of parallel robots. *Int J Biomechatron Biomed Robot* 1(1):22–30
13. Ceccarelli M, Carbone G, Ottaviano E (2005) An optimization problem approach for designing both serial and parallel manipulators. In: Proceedings of MUSME 2005, the international symposium on multibody systems and mechatronics, Uberlandia, Brazil

# Dynamic Modeling and Simulation of Sliding Mode Control for a Cable Driven Parallel Robot



F. Inel, Z. Mansouri, M. Ceccarelli and G. Carbone

**Abstract** In this paper we propose a dynamic sliding mode control strategy for a cable-driven parallel robot. The proposed control algorithm provides stability of the end-effector for improving the robot performance in terms of tracking a desired path. A non-linear control technique is proposed for a robust management of uncertainty and error conditions. Numerical simulations have been carried out by developing a specific code which includes a graphical user interface for a user-friendly real time visualization of end-effector position as well as modification of the system parameters. Results of simulation for a dynamic model with sliding mode control are discussed for different trajectories applied for this robot, in order to confirm the validity of accurate tracking of a desired path. The effectiveness of the proposed robust control scheme is demonstrated through different simulation results.

**Keywords** Cable parallel robot · Sliding mode control · Modeling Simulation

---

F. Inel (✉)

Mechanical Engineering Department, University of Skikda, Skikda, Algeria  
e-mail: inelfouad@yahoo.fr

Z. Mansouri

Technology Department, University of Skikda, Skikda, Algeria  
e-mail: manzedinf@yahoo.fr

M. Ceccarelli · G. Carbone

LARM: Laboratory of Robotics and Mechatronics, DICeM: University of Cassino and South Latium, Cassino, Italy  
e-mail: ceccarelli@unicas.it

G. Carbone

e-mail: carbone@unicas.it



## 1 Introduction

Cable driven parallel manipulators are a special class of parallel mechanisms, whose trusts consist of cables having adjustable length to control the end-effector's position and orientation [1, 2]. This last is a fully parallel mechanism in closed chains with  $N$  degrees of freedom for the end effector. Cable robots are relatively simple in form, with multiple cables attached to a mobile platform or end-effector. The end-effector is manipulated by motors that can extend or retract the cables [3]. The cables arrangement results in closed chains that can be seen as a parallel mechanism. Considering that cables can only pull, usually a cable driven robot has  $n - 1$  degrees of freedom for the end effector with  $n$  being the number of cables, since one cable is usually needed to keep the others in tension.

Cable-driven robots are a type of parallel manipulators where the end-effector is supported in-parallel by  $n$  cables with  $n$  tensioning actuators. Indeed, the end-effector is operated by actuators that can extend or retract cables [4].

Cable driven robots have few moving parts with reduced mass and inertia. Accordingly, they are most suitable for tasks requiring high performance such as speed and accuracy, and large workspace, [5, 6]. A well-known application of a cable driven system is the Skycam, which can operate a camera in a whole stadium area, [7]. Among other applications of cable-driven robots it is worth to mention haptic interfaces [8], and systems for lifting loads [9]. Some other examples at LARM in Cassino are also reported for rehabilitation applications such as in [10] and as a passive tracking systems such as reported in [11]. One of the key aspects for cable driven robots is the need of a proper control strategy to achieve proper motions without breaking the cables. The sliding mode method has been designed to improve the robustness of robotic system control, as reported for example in [12]. In particular, an adaptive sliding mode controller can adjust the control torque based on real-time position tracking error in the set-point control of the end-effector. In this paper, a robust sliding mode controller is developed in order to tracking control of the end effector into a closed loop around the cable-parallel robot for ensuring point to point transfer operations as well as trajectory tracking and present graphical user interface, which composed two parts: view 3D of the homemade prototype of 4 cable-parallel robot and the parameter's position for real time visualization of end-effector.

## 2 System Structure and Modeling

This section proposes a model of a low-cost wire driven robot that has been designed and built at LARM in Cassino. In particular [13], Fig. 1 shows the structure of robot with 4 cables and Fig. 2 shows the proposed graphical user interface which is composed of two parts a 3D schematic view of the proposed robot and the input interface for the position parameters of the end effector.

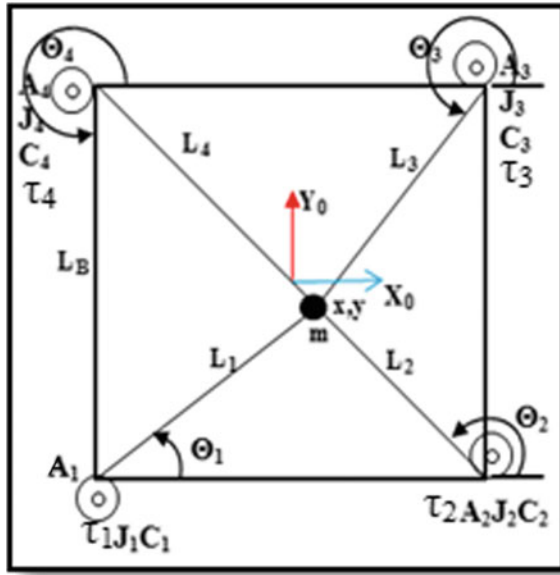
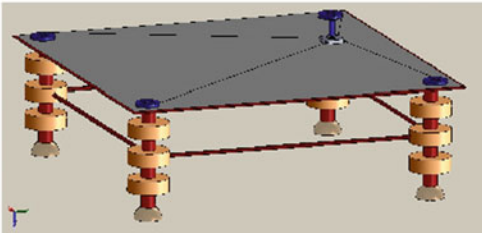


Fig. 1 Scheme of a parallel robot with four cables

Determination the Parameter's Position of the end Effectors for a Parallel Robot With 4 Cables



View of the homemade prototype of cable-based robot

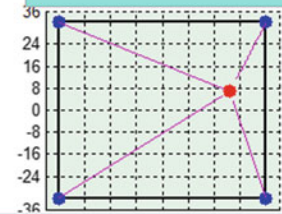
Clear All

L1=	65.6398	Theta1	38.4533
L2=	40.407	Theta2	140.644
L3=	27.4849	Theta3	219.249
L4=	58.5771	Theta4	322.042

Y= 6.853

X= 20.91

The End Effector Paramtrs



The End Effector Position

Fig. 2 The proposed graphical user interface

The elements involved in the scheme of Fig. 1 are:  $A_i$ : the attachment points of the cables to the motors.;  $L_i$ : the lengths of the cables that connect the base to the mobile platform.;  $\Theta_i$ : the rotational angles of the cables with respect to the X axis;  $m$ : The mass of the end-effector;  $C_i$ : The viscous damping coefficients of each motor shaft;  $J_i$ : The inertia of the rotor and the pulley of each motor;  $L_B$ : The lengths of the side of the workspace;  $\tau$ : The torque exerted by the motor on the cable.

In order to analyze the input-output behavior of the cable-based robot under consideration, we exploit the study developed and presented in [14] and [15] the inverse geometric model, the direct geometric model, the inverse kinematic model, the direct kinematic model are derived as well as the study of static forces and dynamic model. Hereafter, we present the dynamical model which describes the motion of the end-effector. It combines the end-effector and the motor characteristics. It can be represented by a system of two coupled nonlinear differential equations:

$$M(X)\ddot{X} + N(X, \dot{X}) = S(X)\tau \quad (1)$$

where

$$\tau = \begin{pmatrix} \tau_1 \\ \tau_2 \\ \vdots \\ \tau_i \end{pmatrix} \quad (2)$$

$$M = \begin{pmatrix} M_{11} & M_{12} \\ M_{21} & M_{22} \end{pmatrix}, \text{ et } N(X, X^*) = \begin{pmatrix} N_1(X, X^*) \\ N_2(X, X^*) \end{pmatrix} \quad (3)$$

$$X = \begin{pmatrix} x \\ y \end{pmatrix} \quad (4)$$

$$F = S * t \quad (5)$$

Moreover,

$$F = m * \ddot{X} \quad (6)$$

where

$$F = \begin{pmatrix} f_x \\ f_y \end{pmatrix} \quad (7)$$

Is The relationship between the applied forces acting on the end-effector and the cable tensions.

S is the jacobian matrix, in the form

$$S = \begin{pmatrix} -\cos \Theta_1 & -\cos \Theta_2 & -\cos \Theta_3 & -\cos \Theta_4 \\ -\sin \Theta_1 & -\sin \Theta_2 & -\sin \Theta_3 & -\sin \Theta_4 \end{pmatrix} \tag{8}$$

To present the dynamical model in the state space representation, we introduce the state variables:

Therefore, by introducing the state variables, Eq. (1) can be expressed as

$$\begin{aligned} \dot{x}_{12d}(t) &= x_{22d}(t) \\ M_{11}\dot{x}_{22d}(t) + M_{12}\dot{x}_{42d}(t) &= u_1(t) - N_{11}x_{22d}(t) - N_{12}x_{42d}(t) \\ \dot{x}_{33}(t) &= x_{42}(t) \\ M_{21}\dot{x}_{22d}(t) + M_{22}\dot{x}_{42d}(t) &= u_2(t) - N_{21}x_{22d}(t) - N_{22}x_{42d}(t) \end{aligned}$$

with

$$\begin{aligned} x_{12d}(t) &= x(t) \\ x_{22d}(t) &= \dot{x}_{12d}(t) \\ x_{32d}(t) &= y(t) \\ x_{42d}(t) &= \dot{x}_{32d}(t) \end{aligned} \tag{9}$$

We also take into consideration the dynamic behavior of the lumped motor shaft/ cable pulley is shown in Fig. 3. The combined motor shaft/cable pulley dynamics equations are expressed by the relationship [14]

$$J\ddot{\beta} + C\dot{\beta} = \tau - rt. \tag{10}$$

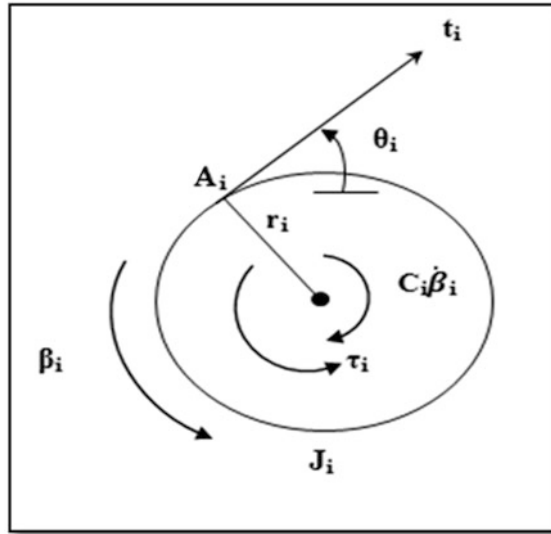
$\beta$ : is the angle of rotation of the pulley.

Where

$$J = \begin{pmatrix} J_1 & 0 & 0 & 0 \\ 0 & J_2 & 0 & 0 \\ 0 & 0 & J_3 & 0 \\ 0 & 0 & 0 & J_4 \end{pmatrix}, \text{ and } C = \begin{pmatrix} C_1 & 0 & 0 & 0 \\ 0 & C_2 & 0 & 0 \\ 0 & 0 & C_3 & 0 \\ 0 & 0 & 0 & C_4 \end{pmatrix} \tag{11}$$

We consider that all the rays (ri) of the pulley are  $r_i = r(i = 1.2...4)$ .

**Fig. 3** The structure diagram the pulley/shaft



So

$$t = \frac{1}{r} (\tau - J \ddot{\beta} - C \dot{\beta}) \tag{12}$$

$$\beta = \begin{pmatrix} \beta_1(X) \\ \beta_2(X) \\ \vdots \\ \beta_i(X) \end{pmatrix} = \frac{1}{r} \begin{pmatrix} L_{10} - L_1 \\ L_{20} - L_2 \\ \vdots \\ L_{i0} - L_i \end{pmatrix} \tag{13}$$

Substituting (12) we obtain

$$t = \frac{1}{r} \left( \tau - J \left( \frac{d}{dt} \left( \frac{\delta \beta}{\delta X} \right) \dot{X} + \frac{\delta \beta}{\delta X} \ddot{X} \right) - C \frac{\delta \beta}{\delta X} \dot{X} \right) \tag{14}$$

And by manipulating equations: (5), (6) and (14), we can express *M* and *N*:

$$M = r^* m + S(X) J \frac{\delta \beta}{\delta X}; \tag{15}$$

$$N(X, \dot{X}) = S(X) \left( J \frac{d}{dt} \frac{\delta \beta}{\delta X} + C \frac{\delta \beta}{\delta X} \dot{X} \right) \tag{16}$$

The state space representation can be derived in the general form

$$X(t) = F(X, t) + g(X, t) * U(t) \tag{17}$$

where:

$$U(t) = \begin{bmatrix} 0 \\ u_1(t) \\ 0 \\ u_2(t) \end{bmatrix} \tag{18}$$

$X(t)$  represents the state space vector  $F(X, t)$ ,  $g(X, t)$  are nonlinear functions  $U(t)$  represents the command vector. The resulting tension at the end effector leads it to move towards a corresponding position on its workspace. However, to working properly, there is an additional constraint that should be fulfilled concerning the dynamical equilibrium of the end-effector. This means that, at any instant, all the cables should be maintained under minimal and positive tensions to avoid the collapsing of any cable [16].

### 3 Control Law and Architecture

The robust sliding mode control (SMC) is to bring the state trajectory to the sliding surface and to switch by means of a switching logic appropriate around it to the balance point. Nevertheless, the SMC requires a switching law of control which has the drawback to generate scattering over the controlled system, [17]. The main advantage of sliding mode control is that the system is insensitive to extraneous disturbance and internal parameter variations while the trajectories are on the switching surface, [18].

To define a sliding mode controller we need to determine an appropriate sliding surface along x and y. The sliding surface of a common sliding mode controller for a system is generally defined as:

$$s_{2dx} = C_{12dx} * (x_{12d}(t) - x_{1ref}) + C_{22dx} * x_{22d}(t) \tag{19}$$

$$s_{2dy} = C_{12dy} * (x_{32d}(t) - x_{2ref}) + C_{22dy} * x_{42d}(t) \tag{20}$$

$C_{12dx}$ ,  $C_{22dx}$ ,  $C_{12dy}$ ,  $C_{22dy}$ : are parameters to be determined to meet some required performances.

$x_{1ref}$ ,  $x_{2ref}$ : are the set point along X and Y.

By eliminations of  $\dot{x}_4$  from the two Eqs. (3) and (4), we can express  $\dot{x}_{22}$  as follows:

$$\dot{x}_{22d}(t) = \frac{\alpha_1 * x_{22d}(t) + \alpha_2 * x(t) + M_{22} * u_1(t) - M_{12} * u_2(t)}{\beta i} \tag{21}$$

And also by manipulating Eqs. (3) and (4), we can express  $\dot{x}_{24}(t)$  as follows:

$$\dot{x}_{42d}(t) = - \frac{\rho_1 * x_{22d}(t) + \rho_2 * x_{42d}(t) + M_{21} * u_1(t) - M_{11} * u_2(t)}{\beta i} \tag{22}$$

To determine the order of law we worked with a new synthesis method that is the approach to the finish law [18].

$$\dot{s}_{2dx} = -K_{2dx}s_{2dx} - Q_{2dx}sign(s_{2dx}) \tag{23}$$

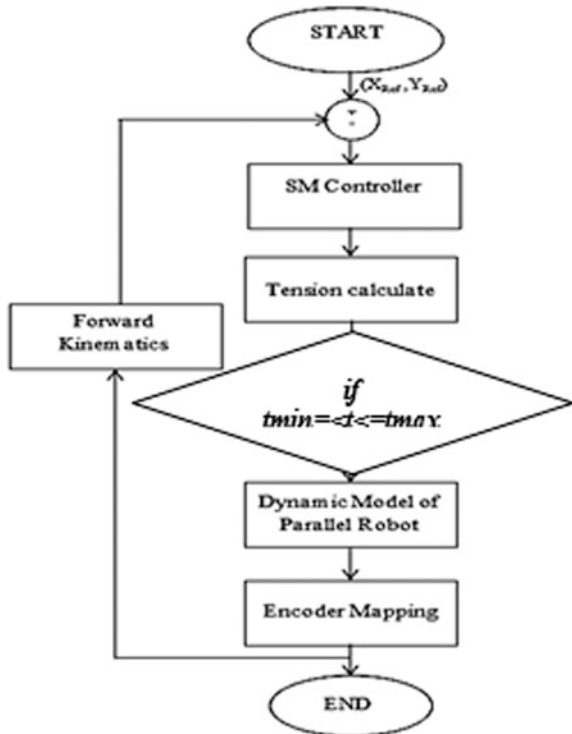
$$\dot{s}_{2dy} = -K_{2dy}s_{2dy} - Q_{2dy}sign(s_{2dy}) \tag{24}$$

where

$K_{2dx}, Q_{2dx}, K_{2dy}, Q_{2dy}$ : are parameters determined by simulation.

$Sign(s_{2dx})$ : is The sign of surface (+1 or -1).

**Fig. 4** A flow-chart of the sliding mode control algorithm



By comparing (21), (23) and (22), (24) we obtain the following relationship:

$$u_{2dx}(t) = u_1(t) = -K_{12dx} * x_{22d}(t) - \sigma_x x_{42d}(t) - K_{22dx} * (x_{12d}(t) - x_{1ref}) - Q_x sign(s_{2dx}) \tag{25}$$

$$u_{2dy}(t) = u_2(t) = -K_{12dy} * x_{42d}(t) - \sigma_y x_{22d}(t) - K_{22dy} * (x_{32d}(t) - x_{2ref}) - Q_y sign(s_{2dy}) \tag{26}$$

This equation  $U(t)$  along  $X$  and  $Y$  represent the command vector of the cable-based robot.

The algorithm of sliding mode in closed-loop case is shown in Fig. 4.

### 4 Simulation Results

In this part we present the simulation of the response of four cables-based robot which has a non-linear equation system. For this purpose, we use a Runge Kutta method because it's methods as a means of solving non-linear partial differential equations and we then implement a Cartesian of the sliding mode controller method.

In our system, we do not have direct access to Cartesian position of the end-effector. Instead, we get the direct measurements of the rotation angles  $\beta_i$  of the pulleys. Then these values are converted into the cable lengths  $L_i$ , these lengths are then used as inputs to the forward kinematics to obtain the Cartesian position  $X$  and  $Y$  [19].

The following parameters values that provides an acceptable compromise on performances have been selected by manual trial error compared  $X$  and  $Y$  for our SMC:  $C_{12dx} = 55000$ ;  $C_{22dx} = 150$ ;  $K_{2dx} = 150$ ;  $Q_{2dx} = 100$ ;  $C_{12dy} = 55000$ ;  $C_{22dy} = 150$ ;  $K_{2dy} = 150$ ;  $Q_{2dy} = 100$ .

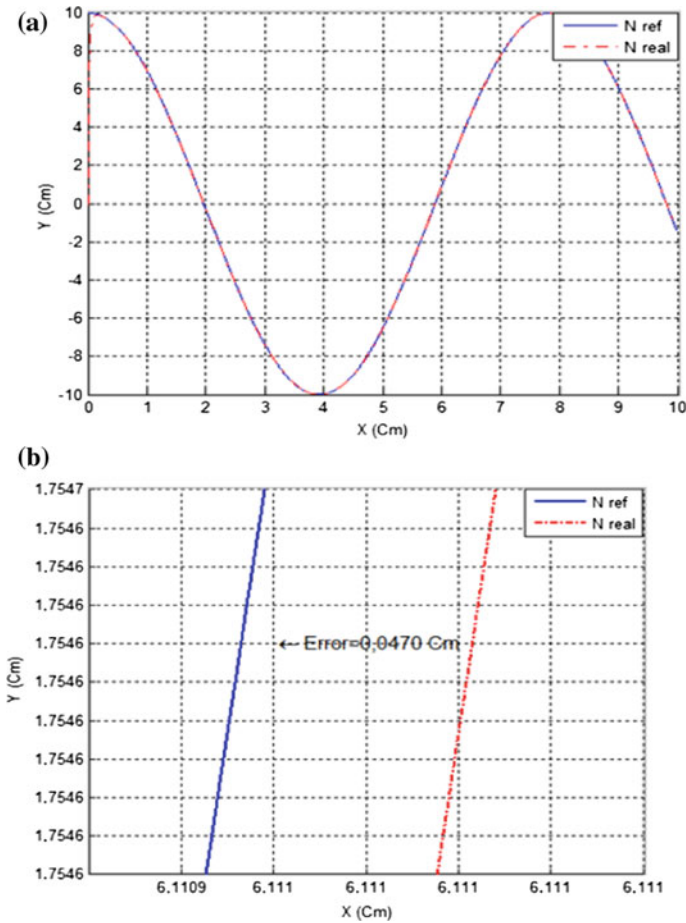
And the parameters for the dynamic Eq. (1) for our robot with 4 cables are mention in the Table 1.

To illustrate the SMC, we present the results concerning the tracking of a sinusoidal trajectory. Figure 5 shows the tracking of a sinusoidal trajectory in the  $(x, y)$  plane and error ( $E = 0.047$  with mean squared error) between the real and the

**Table 1** Initial values for the robot parameters

Variables	Initial Value	Unit
M	0.01	kg
Lb	65.80	cm
C	0.01	Nms
J	0.0008	kgm <sup>2</sup>
Ri	1.5	cm
L(1, 2, 3, 4)	45.25	cm



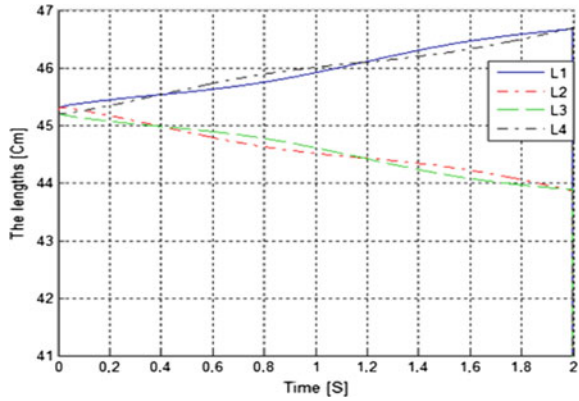


**Fig. 5** The tracking of a sinusoidal trajectory( $w = 4$  rad/s): **a** plot of the end-effector position in X-Y plane; **b** a zoom view of plot **a**

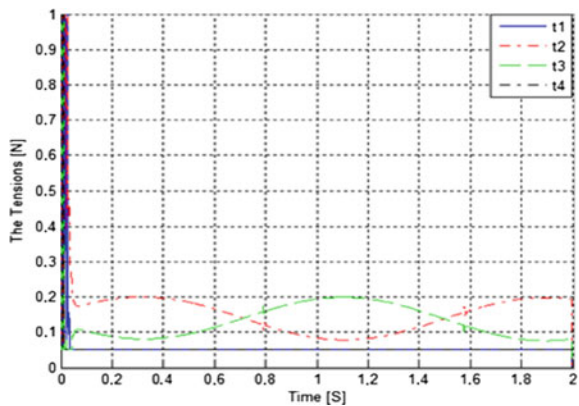
reference paths. Figure 6 shows the temporal evolution of the cable lengths, and Fig. 7 the evolution of the tensions on cables. In this particular case, we can also observe the symmetry on cable lengths and concerning the tensions, it is noted that when the length of the cables (L1 and L4) have increased the tensions have decreased ( $t_1$  and  $t_4$ ), i.e. the motors in the release position (ensure that always the cables taut with  $t_{min}$  positive), and when the cables have decreased (L2 and L3) at the opposite, the necessary tensions have increased ( $t_2$  and  $t_3$ ), that is to say the motors in tightening position.

Cable's flexibility in such robots is another source of error which has not been considered in our study.

**Fig. 6** Evolution of cable lengths



**Fig. 7** Evolution of tensions applied on the cables

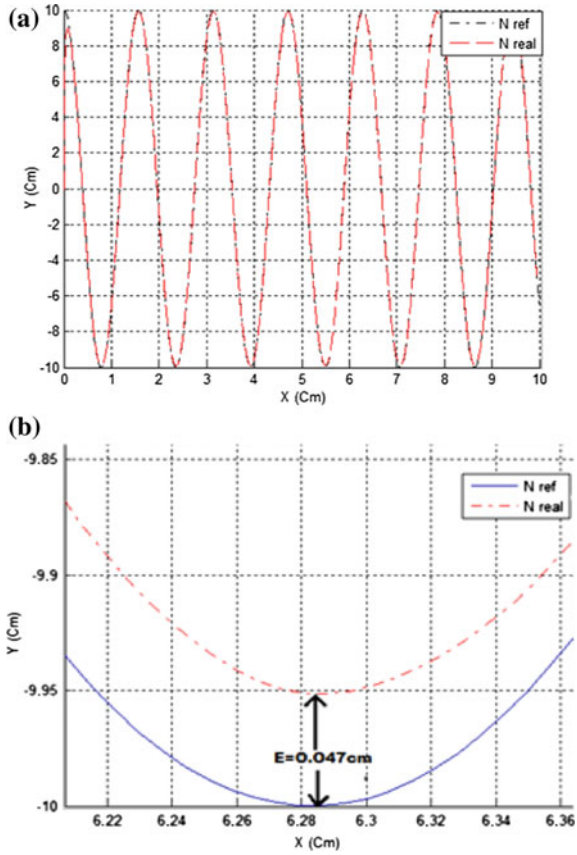


The analysis of previous presented simulation results confirms the possibility to use successfully this controller for tracking in case of curves in low and high speed. In fact, the sliding mode control applied for this robot always checks the constraints to achieve adequate electrical voltages to the motors in order to generate tensions on the cables.

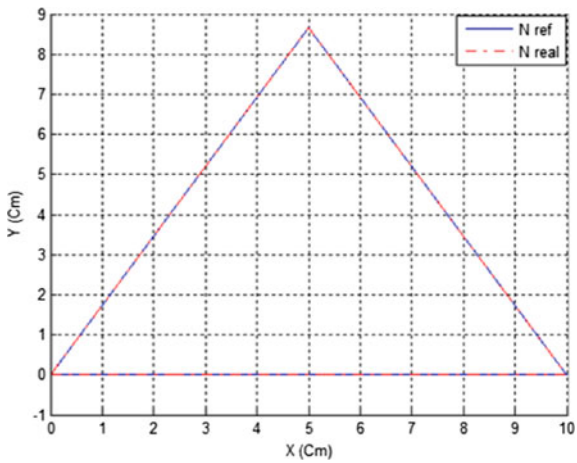
To illustrate this last situation, we compare the tracking of two sinusoidal paths (Figs. 5 and 8). We notice that the tracking process of Fig. 5 was successfully performed because of the low frequency of the tracked signal ( $w = 4$  rad/s). In contrary, the tacking process of the sinusoidal path in Fig. 8 ( $w = 20$  rad/s) was also successfully performed, we can say that this controller is suitable and more effective than PID [20].

Also, to illustrate more the role of our controller, we present the example of tracking some typical trajectories such as a triangular path with a low speed ( $w = 4$  rad/s) and high speed ( $w = 20$  rad/s) (Figs. 9 and 10).

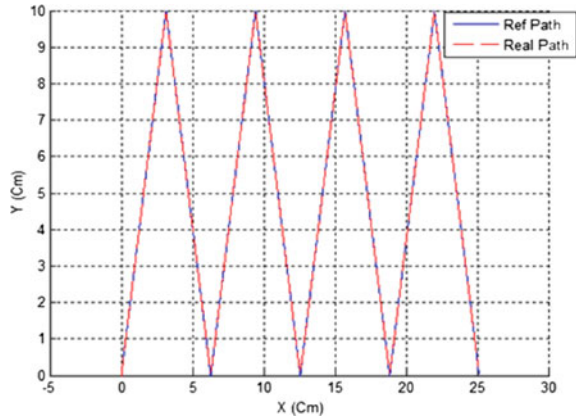
**Fig. 8** The tracking of a sinusoidal trajectory ( $\omega = 20$  rad/s): **a** plot of the end-effector position in X-Y plane; **b** a zoom view of plot **a**



**Fig. 9** The tracking of a triangular trajectory ( $\omega = 4$  rad/s)



**Fig. 10** The tracking of a triangular trajectory ( $w = 20$  rad/s)



**Table 2** The Error performance between sliding mode and PID controllers

Error (Ex)	Sliding mode control (cm)	PID control (cm)
Sinusoidal trajectory	0.047	0.26
Triangular trajectory	0.047	0.36

The analysis of previous presented simulation results confirm that, whatever complicates the trajectories, sliding mode control give high performance to tracking the desired path specially the detection process resulted from the sinusoidal input and also we have proved that sliding mode controller is very fast to tracking the desired path and can maintain the values of error between the real and desired paths despite the high speed (Figs. 9 and 10).

The following table mention the error performance between sliding mode and the classical controller (PID) [20] (Table 2).

## 5 Conclusion

This paper describes the dynamical modeling and simulation of a cable-driven parallel robot in particular, this paper proposes a sliding mode controller for low-cost wire driven robot. Specific simulations have been carried out in Matlab environment. Simulations included the design of a specific user interface for verifying the influence of specific parameters in the path following of cassino low-cost wire driven robot. Simulation results demonstrated that the sliding mode controller has positive stretching influences on the stability of the system in spite of the chattering phenomenon. The proposed control also shows a better performance as comparing with a PID controller in most operation conditions.

## References

1. Ceccarelli M (2004) Fundamentals of mechanics of robotic manipulation. Springer, Dordrecht
2. Ceccarelli M, Romdhane L. (2010) Design issues for human-machine platform interface in cable-based parallel manipulators for physiotherapy applications. *J Zhejiang Univ Sci A* 11 (4):231–239. ISSN 1673-565X. <https://doi.org/10.1631/jzus.a1000027>
3. Alikhani A, Vali M (2012) Sliding mode control of a cable-driven robot via double-integrator sliding surface. In: ICCRC, vol 43, Singapore, pp 1–7
4. Ceccarelli M, Ottaviano E, Tavolieri C (2007) Experimental activity on cable-based parallel manipulators: issues and results at LARM in Cassino. In: 2nd international congress design and modelling of mechanical systems, Monastir, CD proceedings, Paper n.ID-27
5. Surdilovic D, Zhang J, Bernhard R (2007) STRING-MAN: wire-robot technology for safe, flexible and human-friendly gait rehabilitation. In: Proceedings of the ICORR international conference, pp 446–453
6. Alp AB, Agrawal SK (2002) Cable suspended robots: design, planning and control. In: Proceeding of international conference of robotics and automation, Washington, pp 4275–4280
7. Cone L (1985) Skycam, an aerial robotic camera system. *Byte* 10:122–132
8. Gosselin C, Poulin R, Laurendeau D (2008) A planar parallel 3-DOF cable-driven haptic interface. In: Proceedings of the 12th world multi-conference on systemics, cybernetics and informatics (WMSCI), Orlando, USA, pp 266–271
9. Williams RL (2005) Novel cable-suspended RoboCrane support. *Ind Robot: Int J* 32(4): 326–333
10. Ceccarelli M (2013) Problems and experiences on cable-based service robots for physiotherapy applications. In: New trends in medical and service robots. Springer, Dordrecht, pp 27–42
11. Hernández-Martínez EE, Ceccarelli M, Carbone G, López-Cajún CS, Jáuregui-Correa JC (2010) A characterization of milli-CaTraSys system with a parallel manipulator architecture. *Int J Mech Based Des Struct Mach* 38(1):25–49. <https://doi.org/10.1080/15397730903386101>
12. Zi B, Duan BY, Du JL, Bao H (2008) Dynamic modeling and active control of a cable-suspended parallel robot. *Mechatronics* 18(1):1–12
13. Carbone G, Aróstegui Cavero C, Ceccarelli M, Altuzarra O (2017) A study of feasibility for a limb exercising device. In: Mechanisms and machine science, vol 47. Springer, pp 11–21
14. Gallina P, Williams II RL (2001) Part II: planar cable-direct-driven robots dynamics and control. In: Proceedings of the 2001 ASME design technical conferences, 27th design automation conference, Pittsburgh, PA, 9–12 Sept 2001, pp 1–8
15. Williams II RL, Vadia J (2003) Planar translational cable-direct-driven robots: hardware implementation. In: CD proceedings of ASME design technical conferences, 29th design automation conference, Chicago, IL, 2–6 Sept 2003
16. Zaatri A, Bouchemal B (2014) Sliding mode versus PD control for cable-based robots. *World J Eng* 11:287–296
17. Shiler Z, Filter S, Dubowski S (1987) Time optimal paths and acceleration lines of robotic manipulators. In: Proceedings of the 26th conference on decision and control, Korea, pp 98–99
18. Young KD (1999) A control engineer's guide to sliding mode control. *IEEE Trans Control Syst Technol* 7(3):328–342
19. Gallina P, Williams II RL (2001) Planar cable-direct-driven robots, part I: kinematics and statics. In: 2001 ASME design technical conferences 27th design automation conference, Pittsburgh, 9–12 Sept 2001, pp 1–9
20. Inel F, Khochemane L (2014) Comparison performance between PID and PD controllers for cable based robots. *World J Eng* 2:543–556

# Optimization of a Spatial 2 DOF Parallel Mechanism Used for Orientation



C. Boanta, S. Besoiu and C. Brisan

**Abstract** The aim of the paper is to develop an optimization method of a spatial 2 degrees of freedom (DOF) parallel mechanism (PM) used for orientation of a solar panel. The purpose of the optimization is to define the right set of geometrical parameters of the PM that assure a correlation between the angular workspace of the PM with the relative angles of the sun (azimuth, elevation) between the winter and summer solstices. The spatial PM is actuated using three FESTO fluidic muscles and the corresponding kinematics of the PM have been included in the fitness function of the optimization. The numerical model of the angles of the sun between the winter and summer solstices has been developed as a scattered grid of angles considered for the city Cluj-Napoca.

**Keywords** Parallel · Optimization · Kinematic analysis · Workspace  
Solar panel

## 1 Introduction

Parallel structures have become more and more common in the past few years, mainly due to their advantages in comparison to the serial ones as accuracy, operational velocities, high accelerations and stiffness. Although these advantages assure high kinematic performance [6, 10] one of the disadvantages of the PM is the low ratio between the size of the workspace and the dimensions of the robot. Therefore, this paper focuses on overcoming this specific disadvantage of the PM. The aim of the paper is to develop an optimization method of a spatial 2 degrees of

---

C. Boanta · S. Besoiu · C. Brisan (✉)  
Technical University of Cluj-Napoca, Cluj-Napoca, Romania  
e-mail: Cornel.Brisan@mdm.utcluj.ro

C. Boanta  
e-mail: Catalin.Boanta@rezi.utcluj.ro

S. Besoiu  
e-mail: Sorin.Besoiu@mdm.utcluj.ro

freedom (DOF) PM used for orientation of a solar panel taking into account both the size of the workspace and the dimensions of the robot. The paper is organized as it follows. The Sect. 2 reviews some of the latest articles related to this specific subject by illustrating already developed methods in this research area. In the Sect. 3, the topology of the PM and the kinematic analysis are presented. The Sect. 4 presents the numerical model of desired workspace of the robot, identified with the angles of the sun relative to the Earth between the winter solstice (WiS) and the summer solstices (SuS). The Sect. 5 presents the optimization and the numerical results and some conclusions and future research directions are presented in the Sect. 6.

## 2 State of the Art

Optimization methods are specific algorithms that overcome the large amount of experience demanded in order to design a specific product. Mathematically, optimization finds the extreme point of a function subject to a set of constraints [3]. As presented in the following, there are two algorithms mainly used to optimize problems similar to the one presented in this paper.

Genetic Algorithms (GA) are evolutionary algorithms inspired by human genetics that have proven to be very efficient and effective in finding a global solution in both single and multi-objective optimization methods. Many scholars propose the use of this algorithm when it comes to optimize PMs or robots subject to the size of the workspace (WS) or the kinematic performance [1, 4, 13, 14].

Another evolutionary algorithm inspired by the behavior of bird flocks or schools of fishes is the Particle Swarm Optimization (PSO). PSO is proposed for optimizing several problems related to robot design as presented in [7, 9, 12]. Both GA and PSO have been considered as appropriate for finding the solution of the problem addressed in this paper, considering also the fact that their efficiency and computational time are similar [5]. However, the GA have been chosen because the implementation was realized using the Global Optimization Toolbox of Matlab 2015b [2] which does not allow constraints in the case of the PSO.

The main shortcomings of typical electric drive systems of photovoltaic panels are the danger of a fire and low resistance to rain, wind or storm. The paper presents a new type of actuation of photovoltaic panels based on pneumatic muscles, powered by compressed air, the parallel PM optimized in this paper being actuated by Festo Fluidic muscles. This type of actuator is not sensitive to water and mud, reducing the risk of fire to zero, at least for the actuation system, and because of the elastic nature of these types of actuations, the forces and loads generated by wind are greatly reduced.

### 3 Architecture and Kinematics of the PM

The PM is composed by a fixed platform (FP) and a mobile platform (MP) and four kinematic open loops i.e. three identical variable length legs and one passive constraining leg. The kinematic open loops that are associated with the three variable length legs are composed (from bottom to the top) by a universal (U) joint, a Festo fluidic muscle (similar to a prismatic joint—P) and a spherical (S) joint, creating a UPS open loop. The passive constraining leg is composed by a fixed link attached to the FP, a universal joint and a moving link attached to the MP. The MP has only two degrees of freedom (DOF), two rotations allowed by the U joint of the passive constraining leg, fact that allows the orientation of a solar panel in order to match the relative sun angles i.e. azimuth and elevation. The number of degrees of freedom (DOF)  $M$  has to be lower than the number of actuators  $N$  with a constant factor of 1 due to the fact that the actuators (the Festo Fluidic muscles) are able to exert force only on contraction. Therefore, the PM is similar to the cable robots. The architecture is presented in the Fig. 1a. The topology of the PM is presented in the Fig. 1b (with only one UPS open loop).

In order to optimize the geometrical lengths of the linkages of the PM with regard to the WS, the kinematics has to be well defined. Since the purpose of the PM is to orientate a solar panel, the desired WS of the PM is given as a set of angles  $(\gamma_1, \gamma_2)$  of the U joint A (Fig. 1b). These angles are the input in the inverse kinematic; the matching lengths of the fluidic muscles are computed. The Fig. 1b illustrates the topology of the PM. The other notations from the Fig. 1b represent:

- $O_0x_0y_0z_0$  and  $Pxyz$  are the coordinate systems attached to the FP and MP;
- $O_0$  and  $P$  have been chosen as the centers of the circles containing the U and S joints attached to the FP and MP due to the fact that the complexity of the mathematical model is reduced by the symmetry;

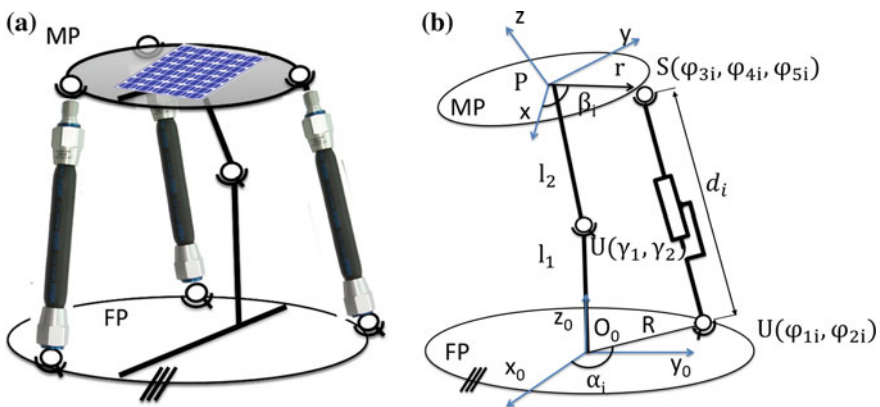


Fig. 1 Architecture of the PM



- $l_1$  and  $l_2$  are the lengths of the elements of the constraining leg;
- $\alpha_i$  and  $\beta_i$  are the angles of positioning the U and S joints on the FP and MP. Each two consecutive U or S joints are positioned  $2\pi/3$  radians apart (due to symmetry reasons). If the first angles  $\alpha_1$  or  $\beta_1$  are known the others are computed by adding  $2\pi/3$  radians for  $\alpha_2$  or  $\beta_2$  and  $2\pi/3$  radians for  $\alpha_3$  or  $\beta_3$ ;
- $R$  and  $r$  are the radii of the FP and MP;
- The angles  $\varphi_{ji}$  are the passive angles of U and S joints,  $j = 1 \dots 5$ ;  $i = 1 \dots 3$ ;
- $d_i$  represents the active length of the Festo Fluidic muscles.

The inverse kinematic problem has been developed using the same approach as presented in [11]. The value of the active lengths of the actuators are evaluated as a function of the orientation of the MP, as presented in the Eq. (1). Also, the active and passive angles have limitations in their value, as presented in the Eq. (2), where  $i = 1 \dots 3$ ,  $j = 1 \dots 5$ .

$$d_i = d_i(\gamma_1, \gamma_2) \quad (1)$$

$$\begin{aligned} \gamma_{1,2\min} \leq \gamma_{1,2} \leq \gamma_{1,2\max} \\ \varphi_{j\min} \leq \varphi_{ji} \leq \varphi_{j\max} \end{aligned} \quad (2)$$

In order to include the kinematics in the optimization problem, desired orientations of the MP have to be computed as a set of angles that define the orientation of the sun, aspects presented in the next section.

## 4 Orientation of the Sun

The solar panel has to be aligned with the sun in order to maximize the efficiency of the solar irradiance. As presented in [8], the position of the sun relative to the Earth can be defined by two angles, the elevation  $\alpha_s$  and the azimuth  $\gamma_s$ , which have to define also the orientation of the solar panel from the MP. A complete set of angles  $\gamma_s$  and  $\alpha_s$  has been computed using the approach from [8]. for the city Cluj-Napoca, Romania between 6 a.m. and 17 p.m. for several days between WiS and SuS. This hour interval assures positive elevation (i.e. above the horizon, therefore visible sun) even in the winter solstice. This set of angles illustrated in Fig. 2 is the input into the optimization problem. In ideal case, the PM presented in the Fig. 1 is able to cover each combination of azimuth—elevation angles ( $\gamma_s$ ,  $\alpha_s$ ).

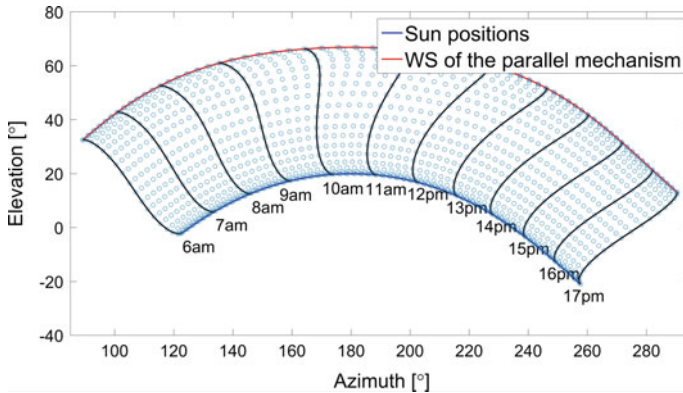


Fig. 2 The angles of the sun between the WiS and SuS

## 5 Optimization of the PM

### 5.1 Design Vector

An optimization problem computes the optimal values of a design vector. For the case of the problem from this paper, the design vector  $x$  from the Eq. (3) is represented by the geometrical characteristics of the robot. Therefore, the design vector contains the lengths of the passive constraining leg ( $l_1$  and  $l_2$  measured in m), the radii of the FP and MP ( $R$  and  $r$  measured in m) and the angles of positioning of the first U and S joints ( $\alpha_1$  and  $\beta_1$  measured in radians) from the FP and MP, the other angles being evaluated from the first ones, as presented in the Sect. 3.

$$x = [l_1, l_2, R, r, \alpha_1, \beta_1] \tag{3}$$

### 5.2 Constraints

The constraints imposed for this optimization refer to lower and upper bounds of the parameters and some other relations given with the Eq. (4).

$$\begin{aligned} 0.05 < l_1, l_2 < L_M \\ 0.07 < r, R < L_M \\ \pi/18 < \alpha_1, \beta_1 < 2\pi/3 \\ l_1 + l_2 < 1.2 \cdot L_M \\ r < R \\ R + r < l_1 + l_2 \end{aligned} \tag{4}$$

The parameter  $L_M$  represents the length of the Fluidic muscle (0.5 m) contracted with 12.5% of its length presuming a maximal contraction up to 25% [1]. For a feasible architecture of the mechanism, the values  $l_1$  and  $l_2$  have to be lower than  $L_M$  and the angles  $\alpha_1$  and  $\beta_1$  to respect the sizes of the U and S joints. Also, it has been considered that the sum of radii  $r$  and  $R$  to be lower than the sum of  $l_1$  and  $l_2$  in order to keep the lateral dimensions of the mechanism as low as possible.

### 5.3 Objective Function

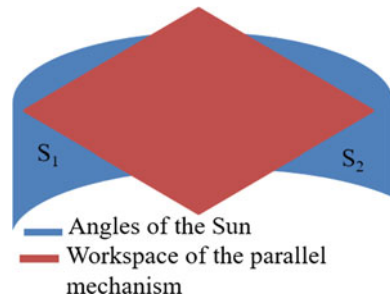
The objective function evaluates two components. The first is represented by the area of the 2-dimension illustration of the angles of the sun presented in the Fig. 2 that are not covered by the workspace of the mechanism. Referring to the Fig. 3 the uncovered areas  $S_1$  and  $S_2$  from the angles of the sun represent one part of fitness value, the sum of  $S_1$  and  $S_2$  being a surface (a scalar value). The second component of the fitness value is the total area of the FP and MP (a scalar value). By subtracting the second term from the first one it is assured that the PM covers as many sun angles as possible, but keeping its geometrical dimensions to minimum as seen in the Eq. (5).

$$fit = S_1 + S_2 - \pi(R^2 + r^2) \quad (5)$$

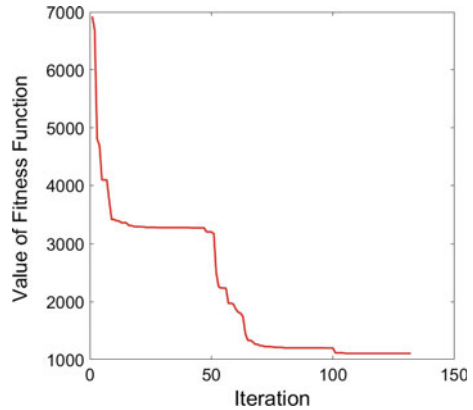
### 5.4 Optimization and Numerical Results

The GA has been implemented in the Global Optimization Toolbox from Matlab [2]. The algorithm used different sizes of the population, from 100 up to 200 members, using steps of 10 and tuned using basic parameters from Matlab. The best value returned by the fitness function is presented in the Eq. (6). This value may or not be the global solution, due to the stochastic modelling of GA.

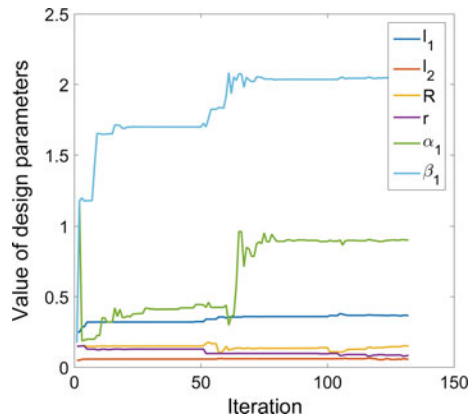
**Fig. 3** Evaluation of fitness value



**Fig. 4** Convergence of the fitness value



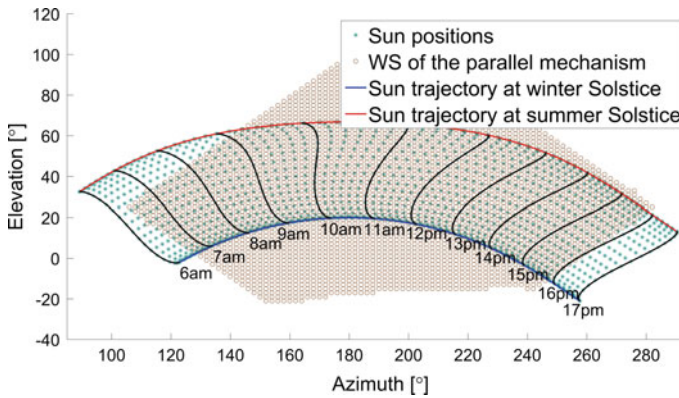
**Fig. 5** Variation of the design vector



$$fit = 1106.01 \tag{6}$$

The GA passed through 132 generations until the fitness value was achieved, using a population of 160 members. The computational time of the optimization has been 1078.5 s. The convergence of the fitness value of the function is presented in the Fig. 4. The fitness value suffers a quick descent in the first 10 generations and the stationary value being obtained around the generation 110. The variation of the design vector is presented in the Fig. 5. The parameters that have the most important variation are  $\alpha_1$  and  $\beta_1$ , which are being given in radians. The other parameters suffer a small changed between the imposed constraints. The Eq. (7) presents the optimal values of the design vector.

The parameters that have been obtained by the genetic algorithm correspond to a PM configuration that assures very high coverage of the sun angles but keeping the geometrical lengths as low as possible. The Fig. 6 illustrates the WS of the optimized PM in comparison to the sun angles between the winter and summer



**Fig. 6** WS of the PM compared to the angles of the sun between the summer and winter solstices

solstices. Almost all the daylight hours between 6 a.m. and 17 p.m. are covered most of the time of the year, the peak being during the winter solstice.

$$x_{Best} = [0.37, 0.058, 0.15, 0.085, 0.90, 2.05] \quad (7)$$

## 6 Conclusions

This paper has presented an optimization method of a two degrees of freedom PM used for orientation of a solar panel. The novelty of the papers relies on the fact that the actuation is realized using Festo fluidic muscles, fact that influences the optimization process i.e. the behavior of the PM is similar to the cable robots. The algorithm used for optimization is the GA, which have computed reliable results in an adequate computational time of 1078.5 s. The future outlook of the presented work includes the development of the real prototype of the PM and the development of the control using real-time control hardware (dSpace).

**Acknowledgements** The work presented in this paper has been founded by the Technical University of Cluj-Napoca, grant “Competitie Interna”, no. 10/1.2/2015.

## References

1. Fluidic Muscle DMSP/MAS (2017) [https://www.festo.com/rep/en\\_corp/assets/pdf/info\\_501\\_en.pdf](https://www.festo.com/rep/en_corp/assets/pdf/info_501_en.pdf). Accessed 20 Feb 2017
2. Global Optimization Toolbox, Matlab (2015) Mathworks. Product information. <http://uk.mathworks.com/products/global-optimization/features.html>

3. Iqbal K (2013) *Fundamental engineering optimization methods*, 1st edn. ISBN: 978-87-403-0489
4. Nianfeng W, Shuai W, Xianmin Z (2012) Optimization design for linkage mechanism based on reliability of kinematic accuracy. In: 2012 IEEE international conference on robotics and biomimetics (ROBIO). IEEE, pp 944–949
5. Rania H et al (2005) A comparison of particle swarm optimization and the genetic algorithm. In: Proceedings of the 1st AIAA multidisciplinary design optimization specialist conference, pp 18–21
6. Tian H et al (2004) Optimal kinematic design of 2-DOF parallel manipulators with well-shaped workspace bounded by a specified conditioning index. *IEEE Trans Robot Autom* 20(3):538–543
7. Xu Q, Li Y (2006) Stiffness optimization of a 3-DOF parallel kinematic machine using particle swarm optimization. In: IEEE International conference on robotics and biomimetics, 2006. ROBIO'06. IEEE, pp 1169–1174
8. Yilmaz S et al (2015) Design of two axes sun tracking controller with analytically solar radiation calculations. *Renew Sustain Energy Rev* 43:997–1005
9. Zhang D, Wei B (2015) Kinematic analysis and optimization for 4PUS-RPU mechanism. In: 2015 IEEE international conference on advanced intelligent mechatronics (AIM). IEEE, pp 330–335
10. Zhang D, Gao Z (2012) Forward kinematics, performance analysis, and multi-objective optimization of a bio-inspired parallel manipulator. *Robot Comput-Integr Manuf* 28(4): 484–492
11. Zhang D (2000) Kinetostatic analysis and optimization of parallel and hybrid architectures for machine tools. PhD Thesis, Laval University, Quebec, Apr 2000
12. Zhang Z et al (2015) Design and kinematic analysis of a parallel robot with remote center of motion for minimally invasive surgery. In: 2015 IEEE international conference on mechatronics and automation (ICMA). IEEE, pp 698–703
13. Zhen G et al (2015) Performance analysis, mapping, and multiobjective optimization of a hybrid robotic machine tool. *IEEE Trans Ind Electron* 62(1):423–433
14. Zhibin L et al (2013) Type synthesis, kinematic analysis, and optimal design of a novel class of Schönflies-motion parallel manipulators. *IEEE Trans Autom Sci Eng* 10(3):674–686

# Tensioned Carbon Fiber Winding on a Collaborative Robots Cell. Part 1 (System)



M. P. Sbanca and G. L. Mogan

**Abstract** In this paper are presented aspects concerning winding process of complex shapes products. The focus is related to the carbon fiber tensioning systems. The goal of the study is to obtain composite complex structures made of impregnated carbon fiber. In order to obtain a product with a good behaviour it is necessary to establish nominal values of the parameters and more important to keep them constant to different steps of the processes. A new system structure for the tensioning device regarding the hardware components and the software system will be presented.

**Keywords** Industrial robot · Robots cooperation · Winding system  
Fiber tension control

## 1 Introduction

Nowadays, the majority of the products, from industry, are made of plastic or, for better performance, made of aluminum or steel. These type of material has a big disadvantage in the weight of the final product. Therefore, another type of material is necessary, with similar behavior to steel but similar weight to plastics. The solution is the composite materials, processed in several methods [5, 8]. One of the most popular methods, to produce the composite products, is the fiber winding method.

Several cases of the winding process are using a simple mandrel for the fiber in order to be rolled, or mechanical and electrical components to keep the fiber in a constant position [4, 9]. The tensioning can be realized directly by the friction of the winding head with the mandrel [22]. Actuators are used also for applications where

---

M. P. Sbanca · G. L. Mogan (✉)  
Transilvania University of Brasov, Braşov, Romania  
e-mail: mogan@unitbv.ro

M. P. Sbanca  
e-mail: madalinsbanca@gmail.com

the tensioning is made before the winding head, in order to create a pneumatic spring, using two fixed rolls and other one connected to the actuator [11].

Some motors can be implemented in order to assure a constant rolling for the mandrel [20, 22] but also for the source fiber roll tensioning system [11].

This components must be controlled by specialize processor or software platform. In a platform can be implemented different types of algorithm. In simple rolling it is enough a P or PI controller [6, 15]. When the application is more complex, then more complex solutions are chosen, like fuzzy methods [5, 7, 10, 22]. Fuzzy control is used in other studies only for the angle and a differential controller is used for position [22]. In the tensioning area there are 3 types of implementation, mechanical tension control, electrical tension control and computerized tension control. A mixed system was chosen in previous research [15], using electrical components like AC motors but also a PLC (Programmable Logic Controller) to control the tension. The motor is driving the mandrel and another small roller, which are producing friction. Researches can also involve complex trajectory. There can appear 2 main problems: insufficient fiber compactness and tension losses of the roving during winding. In these cases the winding speed must be also taken into consideration especially on the trajectory curves together with the control of the winding tension. Nominal value for the tensioning can be proposed, related to the application and the quantity of the resin necessary [13].

This study presents another tensioning system approach for the carbon fiber. Comparing with the other tensioning methods, this case present a different method using industrial robots and tensioning devices, all connected to a master platform that controls all the equipment.

## **2 Flexible Collaborative Robots Cell**

The study presents a solution with no pretension necessary before the robot. It is proposed to integrate the tensioning system in a robot tool. The first step consists of a mechanical system approach, in order to observe the influence of the movement direction around to the matrix but also in relation with the fiber source roll. The goal is to compensate the influence of the trajectory, in order to define the position of the matrix and the fiber source space independent, comparing with the equipment in the system.

### ***2.1 Industrial Robots Flexible Cell***

Robotized filament winding technology involves a robot that winds a roving, impregnated by resin on a die, along the stress directions given by the robot trajectory. The robot moves a deposition head along a winding trajectory in order to deposit roving. This study considers the possibility to use multiple robot system in



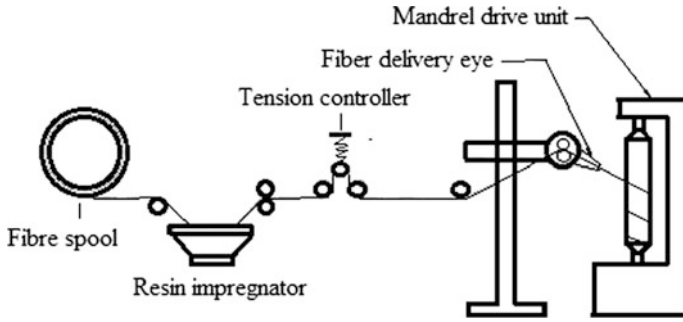


Fig. 1 Components of a filament winding machine [17]

cooperation [19] in order to execute complex 3D parts and to have bigger space flexibility.

In the majority of the studies two kinds of systems are presented. The first one is placing the fiber roll on the robot. The second one is made using a pre-impregnation system and pre-tensioning system using mechanical or electrical actions, Fig. 1. The scope of this system is to have tension between the fiber roll and the winding head by making a longer or shorter path between this two [1–3, 12].

There is no system which makes the tensioning between the matrix and the peg for a complex matrix, where there is no contact between the matrix and the disposing head. In order to provide the fabric tension required to suppress compression force, in [21] the tension is placed directly on the supply rolls.

This study analyze 2 ABB IRB robots (2400 and 1600), with IRC 5 controllers. For the force measuring it is used a JR3force cell and PCI controller, Fig. 2. The

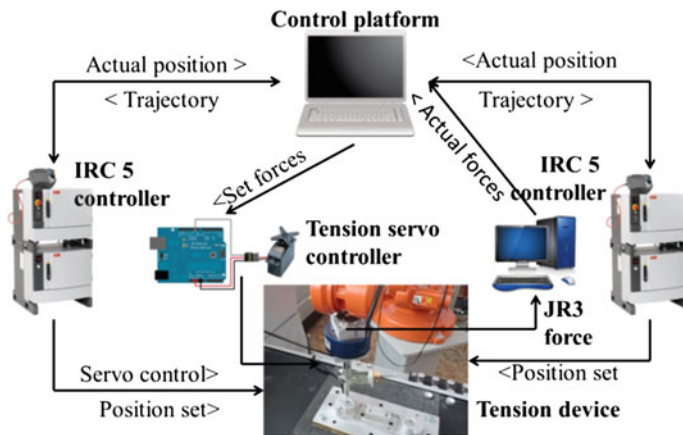


Fig. 2 Hardware system structure

tensioning device will be manual adjusted, considering that the system is able to integrate a tension control based on a controller and servo motor. The system components are controlled of a master platform developed in C#, which needs only a PC with Ethernet connection. The trajectory and the enable signals are transferred from the master platform to the robots according to the matrix which has to be wound around. One robot is programmed to hold the deposition head and the second one is programmed to hold the matrix to have bigger space flexibility and control.

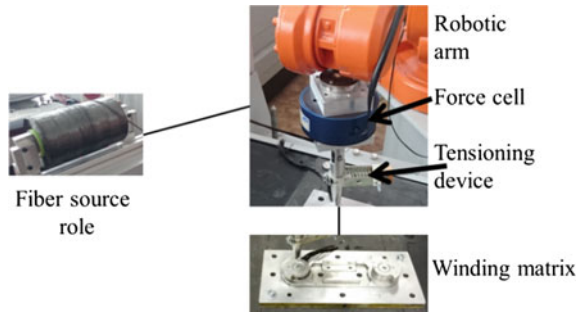
## 2.2 Tensioning Subsystem

Fiber tension is controlled by passing the roving over a deposition head, a peg or a tensioning device. This study presents a hybrid model is presented, having a tensioning device included in the peg, as in the Fig. 3.

The fiber is passed directly from the source roll to the deposition head which made the tensioning. Then the fiber is passed directly to the matrix which is wound. In this way the tensioning before the robot is not important, therefore the trajectory of the robot can be very complex. Although, it is important to control the tensioning between the deposition head and the matrix.

Taking into consideration the electrical part there are two main types of feedback systems. In regulator type feedback systems, the reference signal is constant and the main objective of the control is to keep the output at a constant value. For the servo systems the reference signal is variable. The aim of the control system is to ensure that control variable follows the variations of the input reference as accurately and as quickly as necessary, while being relatively unaffected by any disturbance inputs.

**Fig. 3** Hybrid tension system



### 3 Control System and Software Structure

Typically, a filament winding tension control system consists of three parts, the convolution section, the measurement section, the control section and auxiliary transmission apparatus. The tension control system uses a closed loop control mode in order to get real-time detection tension feedback signal [10].

#### 3.1 Hybrid Control System

A master-slave control is referring to multiple robots or motion devices where one of them gets the information and is executing and the other one are following it. This study present a different model of control, where a hybrid control system is developed in 2 directions. One of them is referring to the robots, where one of the robot is making the winding and is sending to the second robot information about when it should move [16]. The second control system is about the master platform which is sending the entire path to a robot and then is collecting all the information necessary to control the movement of the second robot [19] and also of the tensioning system directly or using another intermediary control unit for the tensioning motor as presented in Fig. 4.

Comparing with [9], where is proposed a system which calculates the amount of the fibers taking into consideration the density or the width of the fiber, in this case

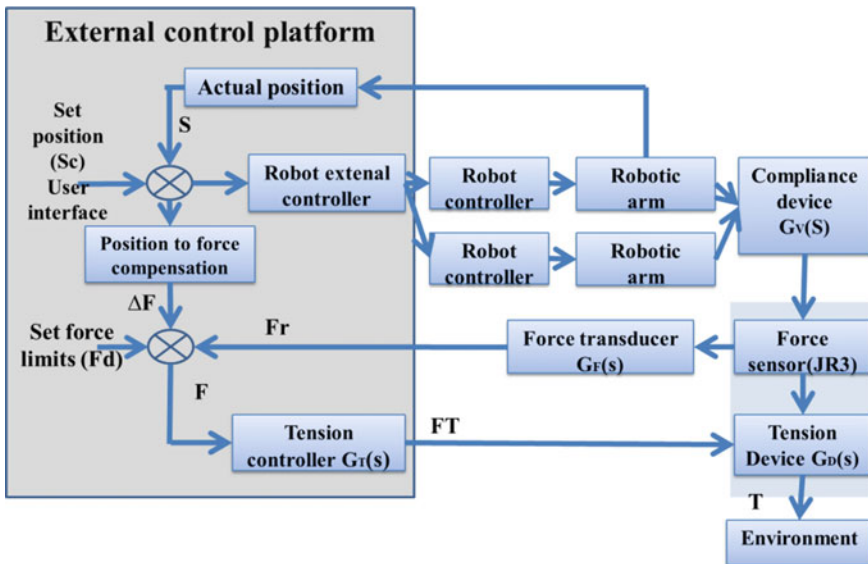


Fig. 4 System control diagram

the software platform calculates and influences the process after process start, in order to assure that the calculated nominal parameters are accordingly. There is the option to implement a strain gauge pressure sensor [10], to have a fast response. This sensor measure only the value for the tension forces, without the force directions. The position of the force sensor is also different, this one being implemented before the robot peg, in the 3 rolls base tensioning system. An implementation with multi forces has the advantage of showing the direction of the force and together with the position and trajectory direction the force and tensioning compensation can be calculated with bigger accuracy.

Currently the tension controller uses a traditional PID algorithm. It is easy to implement, but the parameter setup requires experience and practice. In this study, the tension control system with fuzzy neural network control algorithm can achieve higher control precision. Difference between simulation and experiment results made with a conventional PID controller proved that the proposed fuzzy neural network controller has the advantages of fast convergence, good dynamic response, robustness, small overshoot, control high accuracy and good stability [10].

## 4 Models and System Software Structure

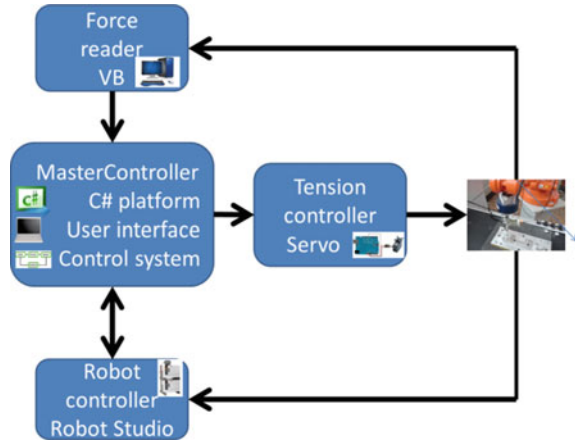
Previous studies propose a single robot system with the fiber roll mounted directly on the robot [14]. The winding device has been designed and built on the basis of compactness, structural lightness, stiffness, and functionality principles, in order to guarantee both the maximum dexterity of the robot, to minimize the probability of crashes between the winding die and the components of the cell, and to improve the control of the process parameters for accuracy and repeatability. This kind of system can be used only when the fiber is already pre-impregnated with resin. In this study it is proposed to use a robot cooperative system through a master platform in order to be able to execute complex winding processes around 3D matrix.

To have a constant tension on the fiber, besides the mechanical components it is necessary also a study on the software and algorithm side. The master controller, Fig. 5, is sending to the robot the right path to follow. The robots are sending back the actual position to the Master Controller. The force component of the system is implemented using an Visual Basic application in order to record the data and transformation.

Considering the present equipment for this study multiple algorithms can be selected to control the fiber tension. One option, was to select the tri-positional and bi-positional controlling models [16–18]. These are applied in this case for the tensioning device like in the Eq. (1)

$$u(t) = \begin{cases} -u_m \text{ for } \varepsilon < -\varepsilon_p \\ 0 \text{ for } -\varepsilon_p < \varepsilon < +\varepsilon_p \\ +u_m \text{ for } \varepsilon > +\varepsilon_p \end{cases} \quad (1)$$

**Fig. 5** System software structure



where  $u(t)$  is the value for the units to move the tensioning device in order to press on the fiber to create tension,  $-um$  and  $+um$  value to add, calculated in the controller base on force feedback,  $\epsilon$  the actual value of the units in the tensioning device and  $\pm\epsilon_p$  are the limits adjusted by user in the interface. Because it is planned to use the actual position of the robots and the force feedback in all directions in the same time, in this study is suitable to use Fuzzy method approach. In order to be able to realize parts with requested characteristic, there was necessary to establish nominal expected values for the fiber tension.

## 5 Conclusions

This study presents a new model of tensioning system more robust and easy to use. Main advantages that the components before the deposition head are not important in the process. In order to create a new tensioning device and to test it was necessary to design also a new Hardware and Software structure to measure and analyze the values. The structure from this study gives the information that with a new design of the tensioning system can be set a constant tensioning between the winding head and the matrix. To define the nominal values for a good winding process having the master platform developed to control all the processes, this study will continue in order to establish nominal parameters value and forward to a complete automatic tensioning system, with an automated tensioning system using 2 industrial robots in cooperation.

**Acknowledgements** This paper is supported by the Romanian Government, specifically MEN—UEFISCDI authority under the program PNII “Partnerships in priority areas”, under the project number 240/2014—NAVIEYES.

## References

1. Abdallah MG (2010) Highly flexible carbon fiber semi-production line
2. Akkus N, Genc G, Girgin C (2008) Control of the pretension in filament winding process. *Actamechanica et automatic 2*
3. Brayton C, Santos T, Shijo G, Sandy A, Weimann D (2009) Composite filament winding machine. In: Multi-disciplinary senior design conference, Kate Gleason College of Engineering, Rochester Institute of Technology, Rochester
4. Harry NE, Gale S (2012) Clean filament winding: process optimization. The University of Birmingham for the degree of doctor of philosophy
5. Hazra T (2011) Low cost 2-axis PLC controlled filament winding machine with simplified fiber winding angle and tension control system. Dalhousie University Halifax, Nova Scotia, Master degree
6. Imamura T, Akamine K, Honda S, Terashima K, Takemoto H (2002) Modeling and tension control of filament winding process. *IFAC Proc Vol 35:13–18*
7. Koussios S (2004) Filament winding: a unified approach. Aerospace Engineering Faculty
8. Krishnamurthy TN, Muralidhar I (2014) Fabrication of low cost filament winding machine. *Int J Recent Trends Electr Electron Eng 4:30–39*
9. Kuppusamy V (2008) Development of virtual control panel for single spindle configuration 2-axis filament winding machine (SSFWM). Faculty of Electrical and Electronics Engineering, University Malaysia Pahang
10. Li Z (2015) Tension control system design of a filament winding structure based on fuzzy neural network. *Eng Rev 35:9–17*
11. Molina J (2015) Adaptation and study of a filament winding machine for in-situ consolidation of thermoplastic composites. Institute of design materials and fabrication, Laboratory of composite materials and adaptive structure
12. Parsons ID, White S, Therriault D, Bignell J (2002) Manufacture and testing of a filament wound composite bridge superstructure. In: Innovations deserving exploratory analysis programs
13. Polini W, Sorrentino L (2005) Influence of winding speed and winding trajectory on tension in robotized filament winding of full section parts 65:1574–1581
14. Polini W, Sorrentino L (2005) Winding trajectory and winding time in robotized filament winding of asymmetric shape parts. *J Compos Mater 39:1391–1411*
15. Ren S, Lu H, Wang Y, Fu H (2007) Development of PLC-based tension control system. *Chin J Aeronaut 20:266–271*
16. Sbanca MP, Mogan GL (2015) Cooperative assembly using two industrial robots. *Advances in intelligent systems and computing*. Springer
17. Sbanca MP, Mogan GL (2015) Winding of carbon wire composite structures using two cooperative industrial robots. *Appl Mech Mater 762:291–298*
18. Sbanca MP (2014) Trajectory planning for winding carbon wire of composite structures using cooperative robots. *Appl Mech Mater 656:280–287*
19. Sbanca MP, Mogan GL (2014) Cooperation of two industrial robots for manipulation rigid objects using SCADA system. *Appl Mech Mater 555:312–319*
20. Sorrentino L, Polini W, Carrino L, Anamateros E, Paris G (2007) Robotized filament winding of full section parts: comparison between two winding trajectory planning rules. *Adv Compos Mater 17:1–23*
21. Wollner BA (2011) Development of a fabric winding system for the automated manufacture of prefabricated wind turbine blade roots. Iowa State University, Graduate Theses and Dissertations
22. Xiaodong H, Yaoyao S, Chao K (2016) Research on fuzzy control based flexible composite winding system. *Adv Fuzzy Syst*

# Tensioned Carbon Fiber Winding on a Collaborative Robots Cell. Part 2 (Tests)



M. P. Sbanca and G. L. Mogan

**Abstract** In this paper are presented aspects concerning winding process of complex shapes products. The focus is related to the carbon fiber tensioning methods. The goal of the study is to obtain composite complex structures made of impregnated carbon fiber. In order to obtain an material with similar or better characteristics comparing with steel or aluminium alloy, the material properties must be constant. The carbon fiber density must be same in all points. Density is characterized by parameters like winding trajectory, resin quantity, fiber layers and especially carbon fiber tension during the winding process.

**Keywords** Composite materials • Carbon fiber winding methods  
Fiber tension control

## 1 Introduction

In some areas, actual materials are not satisfying the necessity to have high stress resistance and low weight. Usual materials like steel or aluminum are used less. In some of the cases the replacement is plastic. Plastic alloys have the stress resistance much smaller and due to the fact that in industry is the request to reduce the energy consumption a new range of materials appear, represented by composite materials [2, 5, 6]. One of the most popular methods to produce the composite products is the fiber winding method. Using this method carbon fiber, glass fiber or Kevlar can be processed. The most common applications are air tank, fuel tank, pressure and storage vessel, air craft and military parts [8]. The winding process components are a fiber roll, a resin bath, a tensioning device, a deposition head and the mandrel (matrix).

---

M. P. Sbanca · G. L. Mogan (✉)  
Transilvania University of Brasov, Braşov, Romania  
e-mail: mogan@unitbv.ro

M. P. Sbanca  
e-mail: madalinsbanca@gmail.com

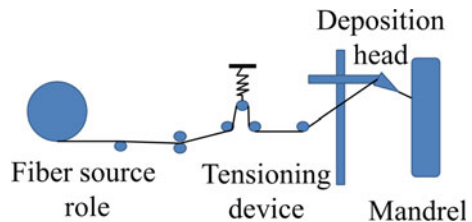
The main goal of this study is to present another tensioning method for the carbon fiber. Comparing with the other tensioning methods this is tensioning the fiber between the matrix and the deposition head. This tensioning method has the big advantage, that it can be used for very complex shapes to be wound. In order to apply this method in this study a very complex matrix is presented, which needs two robots [11] to realize the winding process. Together with the robots the proposal is to use the hardware system and software platform developed in the previous research in this field [12]. This has the advantage of complete and autonomous fiber winding and tensioning possibility with the right winding method.

## 2 Tensioned Carbon Fiber Winding Process

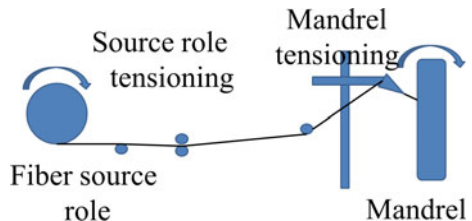
In the majority of the production cases the carbon fiber is use in the winding process to obtain simple construction of cylindrical products. This products are used in aeronautics domain [6, 14]. The system construction can be implemented in different forms [6], taking into consideration the size or the part [15] or the type of the final product [1]. Some studies analyze the influence of the distributor speed or trajectory for the fiber density [7]. According to the previous tests the most influencing parameter is the fiber tension during the winding process [10, 11]. This parameter can be checked and controlled with several types of fiber tensioning like presented in Figs. 1, 2 and 3.

In this study is proposed a real time control system, using a force measuring device to measure the tension, in the first step, then to check which actions can be taken to solve the constant tensioning during the winding process.

**Fig. 1** Spring tensioning system

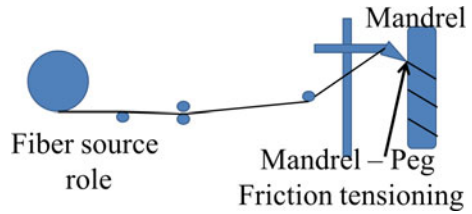


**Fig. 2** Roll tensioning system





**Fig. 3** Contact tensioning system



In some studies methods to control speed in a curved trajectory of the robot are presented [9]. It is proposed to divide the trajectory in more points, which help to modify the speed, but in the same time can appear brakes in the trajectory which are influencing the constant tensioning of the fiber. In the direction of speed controlling, is proposed a system which is controlling the speed of the source roller and the mandrel roll with the same constant speed in order to have a constant speed of the winding process [4].

In many studies a 2 steps solution is proposed. First one is to establish an advanced filament winding system, to identify the right technique [15]. The second one is proposing the final complex control solution, like PID controllers or fuzzy controllers [5]. In our case the trajectory is defined [10] but it is still necessary to adjust other parameters in order to have a constant density of the fibers.

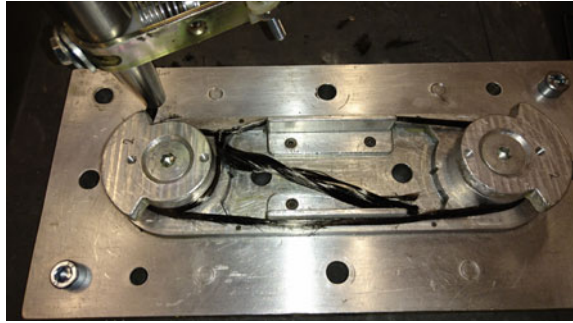
Fiber tension has a significant effect on the composite properties. Fiber density in the composite, increases in the same time with the fiber tension. Absorption capacity of the fiber decreases with tension increasing. The tension was limited in order to avoid the tow failure [3].

In a preferred method of fiber tension control, the fiber tension is sensed by an in-line tension sensor and on the basis of measured force the tension is adjusted [12]. This method provides a constant fiber tension throughout the winding process [9, 13]. The choice of the value for winding tension and the need to keep constant the winding tension to the chosen value are two aspects strongly connected with the geometry of the part to wind. In previous studies is showing that the offset rule makes it possible both to keep the tension on roving near to the nominal value.

### 3 Winding Tests

In previous research, several results regarding the winding process are presented [10, 11], but the majority of them are related to simple form of composite structure which doesn't need a special control for the robot trajectory, this being constant.

In this case study a 2D winding trajectory is presented, in which the winding head is moving around the matrix in order to realize the complex composite product. The carbon fiber roll is placed aside and having in consideration the trajectory in one of the direction, the carbon fiber wire will be loose. This means it is necessary a pre tensioning device. One solution is to use a pretension between the

**Fig. 4** Winding trajectory

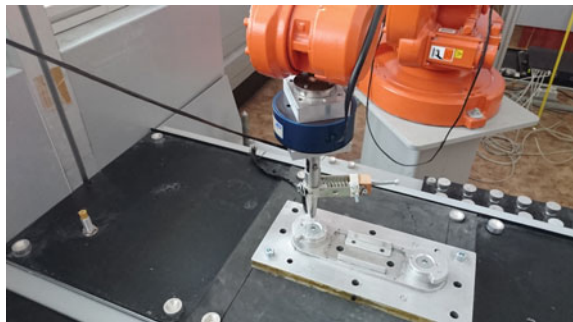
roll and the winding head. The option chosen in this case is different, making the tensioning directly at the winding head, meaning that the tension is between the matrix and the winding head presented in Fig. 4.

The goal of these tests is to analyze the influence of the fiber source roll on the winding tensioning if the roll is not tensioned before, and how can this influence be eliminated, using the system and the platform proposed by us in the previous study [12].

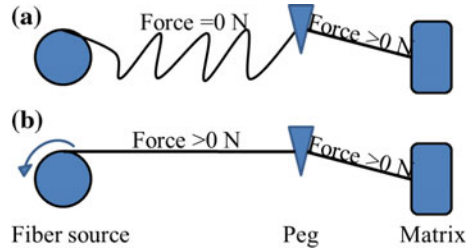
We propose to use a peg with a tensioning system integrated in the peg, as presented in Fig. 5. This tensioning system can be adjusted manually to observe the differences in the density of the fibers.

Between the peg and the robot head is used a 6 axis force cell in order to establish the direction of the force from the peg [12]. The fiber source roll will be fixed in a position located on the minimum X axis. The matrix will be placed under the peg meaning that there should be forces in both directions also for X axis but also on Y axis. We use this kind of force cell to determine if the force is coming from the matrix-peg connection or from the fiber roll-peg connection.

For the beginning it is used a fix matrix with trajectory in 2 directions, X and Y to see the influences forces. The matrix shape is made by 2 circular trajectory and another 2 straight paths, one of them will be in positive direction and the other one will be in negative direction. The X negative direction is the most problematic when is no tensioning system because the fiber will be loose, like in Fig. 6a. When the

**Fig. 5** In Peg tension system

**Fig. 6** Fiber disposal between the source and the peg



fiber is loose can appear waves in the deposition direction, called marcols. On the other direction when the winding is too tight the fiber can be damaged and cause irregular compressions in the part, like in Fig. 6b.

#### 4 Carbon Fiber Winding with Tension Measure

Was performed 7 tests of winding process around the matrix using different types of setup to observe the difference and also to establish the nominal configuration for the automated winding process. For this product after mechanical tests a nominal density of the fiber was established, resulting a nominal range of the tension force between 15 and 35 N in the matrix fiber. This tension was established for straight line trajectory with constant speed and no noise effects. Results are presented in the next Figs. 7, 8 and 9.

In Fig. 7a can be seen that even if there is no influence from the source roll there are values on the negative range, meaning the tension is now between the peg and the matrix. When there is an influence from the fiber source roll, Fig. 7b the tension forces are just amplified, the direction is not changing, meaning that the tension is still forces between the matrix and the peg. In Fig. 7 was applied 18 N in the fiber tension between the peg and the matrix, with manual adjustment of the pre-tensioning device, for both cases, with another 10 N from the source roll in Fig. 7b. In Fig. 8a, b the force was increased to 23 N and the differences can already be seen: the maximum forces increase in both sides. There can also be seen some fluctuations when the roll tension is present, making the tensioning inconsistent and difficult to control.

In Fig. 9, the tension force was increased to 35 N and the sensing force by the force cell also increase to a maximum of all measurements in both X and Y and both directions positive and negative with a faster transition without any influence from the fiber source roll. The most important result of the composite structures is the density of the fibers. Considering the same trajectory every time the parameter which is defining the density can be consider to be the total length for each complete path.

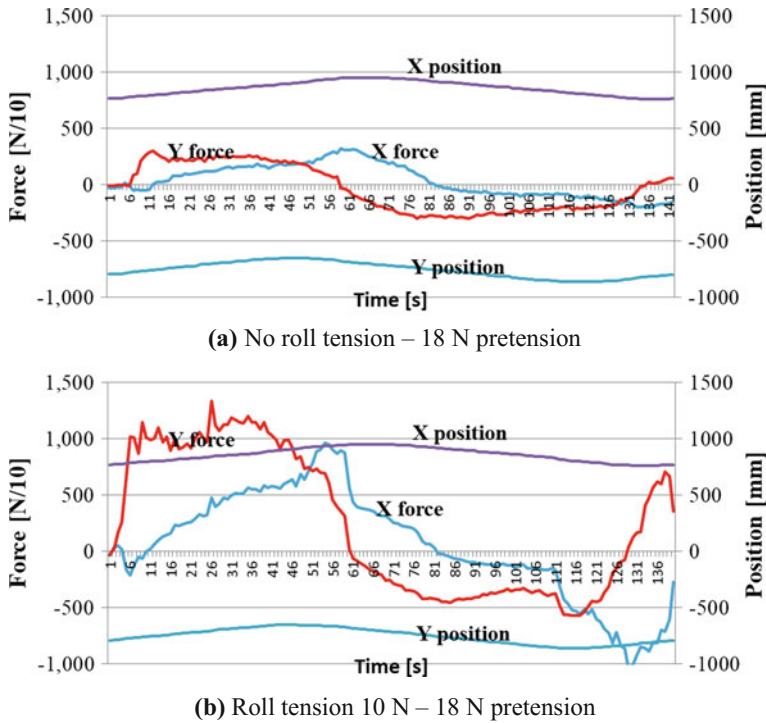


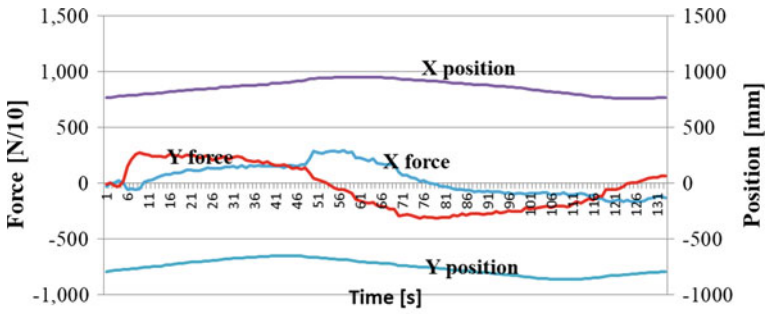
Fig. 7 a No roll tension—18 N pretension. b Roll tension 10–18 N pretension

### 5 Results Comments

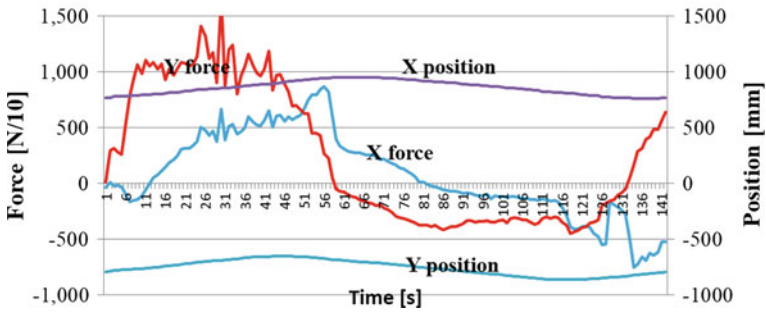
In Table 1 the same tests are presented, including the total fiber length for one complete path around the matrix. Comparing the results, the fiber tension increases, the total length decreases. When there is also a force influence from the fiber source, the quantity of the fiber is even less, but having the right setup of the tensioning in the peg setup, this influence can be compensated.

The tests from this study show that with a new design, of the tensioning system, can be set a constant tensioning between the winding head and the matrix. All the components placed before the winding head, like resin bath or fiber roll are not changing the tensioning of the final part. In this way we can control the tension, the length of the total fiber and the density of the result product. Also the tests results reveal that when the fiber tension is increase the density of the final product is bigger; therefore the total length of the used fiber is less.

Once the fiber tension value has been set, it is necessary to assure that the tension acting on the roving during winding is as near as possible to the set nominal value for best mechanical characteristics of the final product.



(a) No roll tension – 23 N pretension



(b) Roll tension 10 N – 23 N pretension

Fig. 8 a No roll tension—23 N pretension. b Roll tension 10–23 N pretension

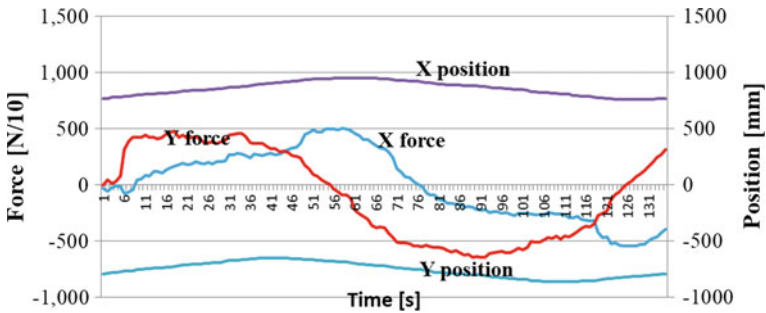


Fig. 9 No roll tension—35 N pretension

**Table 1** Tension and length measurements

Case		Setup	Tension from roll (N)	Pretension (N)	Length (mm)
Case 1	a	No roll tension—18 N pretension	No	18	413
	b	With roll tension 10–18 N pretension	10	18	410
Case 2	a	No roll tension—23 N pretension	No	23	412
	b	With roll tension 10–23 N pretension	10	23	409
Case 3	a	No roll tension 29 N pretension	No	29	411
	b	With roll tension 10–29 N pretension	10	29	403
Case 4	a	No roll tension 35 N pretension	No	35	406

## 6 Conclusions

This study is presenting a new model of tensioning system more robust and easy to use. This is bringing a big advantage because components before the peg are not important in the process. Also, the advantage of this type of peg is that it can be used for any kind of winding process, especially for complex products where the trajectory is 3D. In order to have the possibility to control the tension from the peg there were made tests to establish the nominal values for the expected output parameters.

Taking into consideration the results of this study, presented in Fig. 10, it will be continued in order to analyze how can other internal parameters like speed, acceleration or even cooperative robotics trajectory can be synchronized with carbon fiber tensioning during the process. Having defined the nominal values for a good winding process and a master platform developed to control all the processes, this study will continue in order to realize a complete automatic winding, including the fiber tensioning system, with an automated tensioning using the actual two robots in collaboration.

**Fig. 10** Carbon fiber composite structure

**Acknowledgements** This paper is supported by the Romanian Government, specifically MEN – UEFISCDI authority under the program PNII “Partnerships in priority areas”, under the project number 240/2014—NAVIEYES.

## References

1. Abdallah MG (2010) Highly flexible carbon fiber semi-production line
2. Burgoyne CJ (1998) Advanced composites—the challenge to bridge designers. In: *Developments in short and medium span bridge engineering*
3. Cohen D (1997) Influence of filament winding parameters on composite vessel quality and strength. *Compos Part A: Appl Sci Manuf* 28:1035–1047
4. Harry NE, Gale S (2012) Clean filament winding: process optimization. The University of Birmingham for the degree of doctor of philosophy
5. Hazra T (2011) Low cost 2-axis plc controlled filament winding machine with simplified fiber winding angle and tension control system. Dalhousie University Halifax, Nova Scotia, Master degree
6. Krishnamurthy TN, Muralidhar I (2014) Fabrication of low cost filament winding machine. *Int J Recent Trends Electr Electron Eng* 4:30–39
7. Li Z (2015) Tension control system design of a filament winding structure based on fuzzy neural network. *Eng Rev* 35:9–17
8. Littlefield A, Hyland E, Andalora A, Klein N, Langone R, Becker R (2005) Carbon fiber/thermoplastic overwrapped gun tube. *Mater Manuf Process* 21:573–578
9. Molina J (2015) Adaptation and study of a filament winding machine for in-situ consolidation of thermoplastic composites. Institute of design materials and fabrication, Laboratory of composite materials and adaptive structure
10. Sbanca MP (2014) Trajectory planning for winding carbon wire of composite structures using cooperative robots. *Appl Mech Mater* 656:280–287
11. Sbanca MP, Mogan GL (2015) Winding of carbon wire composite structures using two cooperative industrial robots. *Appl Mech Mater* 762:291–298
12. Sbanca MP, Mogan GL (2017) Tensioned carbon fiber winding on a collaborative robots cell. Part 1 (system). In: *Proceeding of the 12th IFToMM international symposium on science of mechanisms and machines—SYROM*
13. Shaiq H (1994) Filament winding machine control using b-spline interpolation. The University of Nottingham
14. Smith R (2012) Guidelines for rolls used in web handling. In: *AIMCAL Europe 2012 web handling conference, Prague, Czech Republic*
15. Xiaodong H, Yaoyao S, Chao K (2016) Research on fuzzy control based flexible composite winding system. *Adv Fuzzy Syst*

# An IKP-DKP Approach Emphasizing Singularities of 9R (3-RRR) Mechanisms



Fl. Buium, D. Leohchi and C. D. Duca

**Abstract** This paper intends to present an integrated program in order to put in connection ones of fundamental problems regarding 6R(RRR) parallel mechanisms: inverse kinematics (IKP), direct kinematics (DKP), mechanism workspace and singularities avoidance. Of course, this type of mechanism represents a subject of large interest in scientific literature, all of specific enumerated problems being exhaustively treated. In this context, ours paper character is only practical one. Being a versatile instrument, this approach allows the students (e.g.), without great amount of time consumption, to determine the mechanism workspace, to solve IKP for different imposed trajectories, to verify driving movements using DKP and to verify also the presence/absence of singularities inside mechanism workspace.

**Keywords** Parallel 9R (3RRR) mechanism · IKP · DKP · Workspace Singularity

## 1 Introduction

In technical literature [1–4], the 9R(3RRR) parallel mechanism was studied regarding structure, kinematics, dynamics, workspace, singularities, actuation and other aspects from long time ago, because its practical advantages (work speed, accuracy, stiffness, load/weight report). The principal disadvantage of this mechanism is related to its relative small workspace compared with serial ones and it may contain many interior singularities. However these not represent great limitations,

---

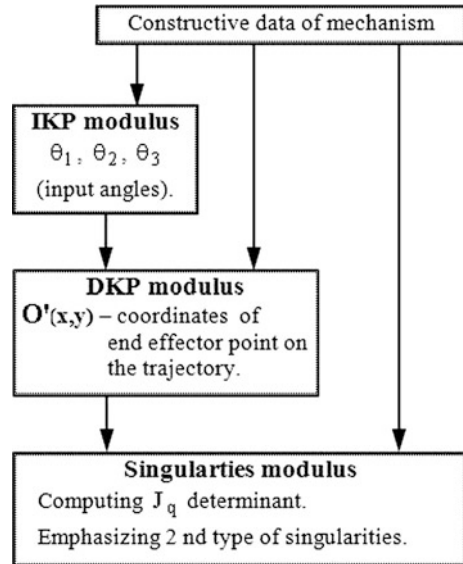
Fl. Buium (✉) · D. Leohchi · C. D. Duca  
“Gheorghe Asachi” Technical University of Iasi, Iași, Romania  
e-mail: fbuium@gmail.com

D. Leohchi  
e-mail: dleohchi@yahoo.com

C. D. Duca  
e-mail: cdduca@hotmail.com



**Fig. 1.** The program general structure



because its can be eliminated by constructive lengths scaling or by singularities avoidance of the workspace.

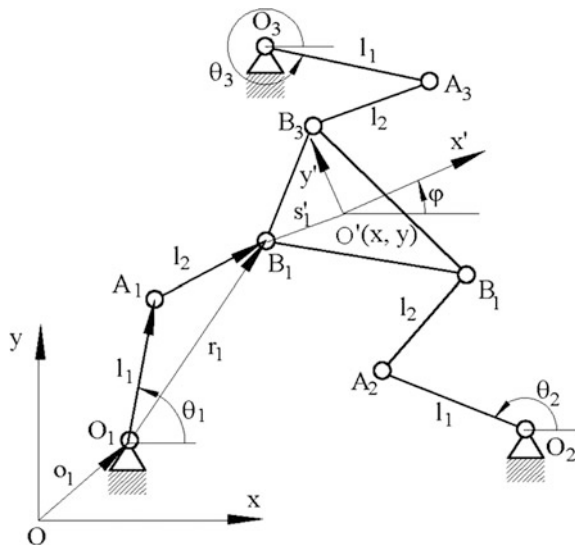
The 3 RRR parallel mechanism contains three actuated chains, each of them containing three revolute joints: first—between fixed platform and proximal links, second—between proximal and distal links and third—between the distal links and mobile platform. Depending on the driving links of the 3 RRR mechanism there are three actuating mods (3-RRR, 3-R $\bar{R}$ R, 3-R $\bar{R}$ \bar{R}) [2–4], among which the first is the most favorable by dynamic and constructive reasons. But the 3-DoF 3 RRR planar parallel mechanism has two important disadvantages which limit their application sphere: the workspace is very limited as dimensions and shapes on one hand and inside the workspace a high density of singularities may occurs.

The proposed approach represents a three modules program (Fig. 1), each being specialized to solve one of mentioned problems (IKP i.e. inverse kinematic problem, DKP i.e. direct kinematic problem and singularities problem). In this package input data are introduced separately in each of the three module and the output data circulate as shown by arrows.

## 2 Workspace and IKP Module

In order to study workspace and IKP for an above mentioned structure, a general 3-DOF planar parallel mechanism with revolute joints, was considered as shown in Fig. 2. This mechanism is characterized by following elements:

**Fig. 2.** The 9R (3RRR) parallel mechanism [2]



- a triangular end-effector,  $B_1B_2B_3$ ,
- a fixed base  $O_1O_2O_3$ , joined by three serial kinematic chains,
- three proximal link,  $O_iA_i$  of  $l_1$  length,
- three distal link,  $A_iB_i$  of  $l_2$  length,
- three revolute joints  $O_i$ ,  $A_i$ , and  $B_i$ ,
- $OO_i$ ,  $O_iA_i$ ,  $A_iB_i$ , and  $O_iB_i$  segments depicted by  $\mathbf{o}_i$ ,  $\mathbf{u}_i$ ,  $\mathbf{r}_i$ , and  $\mathbf{s}_i$  vectors [2].
- a coordinate system fixed to the mechanism base  $Oxy$ ,
- a mobile coordinate system fixed to the mobile platform  $O'x'y'$ ,
- input parameters matrix  $\Theta = [\theta_1, \theta_2, \theta_3]^T$ , defined as in figure,
- output parameters matrix  $q = [x, y, \varphi]^T$ , defined as in figure,
- the orientation  $\varphi$  angle defining the mobile platform pose,
- $R = \begin{pmatrix} \cos \varphi & -\sin \varphi \\ \sin \varphi & \cos \varphi \end{pmatrix}$  is the revolute matrix of  $\varphi$  angle and  $O'$  center,

Based on [2], and according to Fig. 2, the extreme mechanism positions occur when the proximal and distal links are in extension or superposed so, that, the following relations can be written:

$$\bar{r}_i = \bar{v} + R\bar{s}'_i - \bar{o}_i \tag{1}$$

$$\|\bar{r}_i\| = \left\{ \begin{array}{l} \left[ \begin{pmatrix} x \\ y \end{pmatrix} + \begin{pmatrix} \cos \varphi & -\sin \varphi \\ \sin \varphi & \cos \varphi \end{pmatrix} \begin{pmatrix} x'_{Bi} \\ y'_{Bi} \end{pmatrix} - \begin{pmatrix} x_{Oi} \\ y_{Oi} \end{pmatrix} \right]^T \\ \cdot \left[ \begin{pmatrix} x \\ y \end{pmatrix} + \begin{pmatrix} \cos \varphi & -\sin \varphi \\ \sin \varphi & \cos \varphi \end{pmatrix} \begin{pmatrix} x'_{Bi} \\ y'_{Bi} \end{pmatrix} - \begin{pmatrix} x_{Oi} \\ y_{Oi} \end{pmatrix} \right] \end{array} \right\}^{1/2} \tag{2}$$

$$(l_1 \pm l_2)^2 = (x + x'_{Bi} \cos \varphi - y'_{Bi} \sin \varphi - x_{Oi})^2 + (y + y'_{Bi} \sin \varphi - y'_{Bi} \cos \varphi - y_{Oi})^2. \quad (3)$$

For a  $\varphi = \text{const.}$  end-effector orientation, Eq. (3) represents two concentric circles:

$$\begin{aligned} a_i &= -x'_{Bi} \cos \varphi + y'_{Bi} \sin \varphi + x_{Oi} \\ b_i &= -x'_{Bi} \sin \varphi - y'_{Bi} \cos \varphi + y_{Oi} \end{aligned} \quad (4)$$

The mechanism workspace is mathematically depicted by  $\|\overline{O_i B_i}\|_{\min}^{\max} = |l_1 \pm l_2|$ .

In order to solve the inverse kinematics, it write the relation resulting from Fig. 2 [2]:

$$\bar{l}_2 = \bar{v} + R\bar{s}'_i - \bar{u}_i - \bar{o}_i \quad (5)$$

Using this relation, the input rotation angles  $\Theta = [\theta_1, \theta_2, \theta_3]^T$  can be expressed as follows:

$$\theta_i = 2 \arctg \frac{y - b_i + d_i \sqrt{D_i}}{x + C_i - a_i}. \quad (6)$$

where:  $A_i = x - a_i$ ,

$$B_i = y - b_i,$$

$$C_i = \left[ (x - a_i)^2 + (y - b_i)^2 + l_1^2 - l_2^2 \right] / (2l_1),$$

$$d_i = \pm 1,$$

$$D_i = (x - a_i)^2 + (y - b_i)^2 - C_i.$$

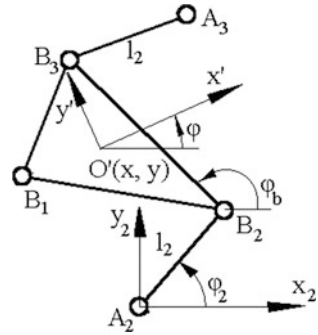
It results  $2^3 = 8$  possible solutions for IKP problem, corresponding to the 8 assembling modes of this mechanism.

### 3 DKP Module

In order to solve direct kinematic problem (DKP), supposing as known all angular positions  $\Theta = [\theta_1, \theta_2, \theta_3]^T$  of actuated links, it determines output parameters  $q = [x, y, \varphi]^T$ , representing the pose of the mobile platform.

This problem represent in fact a verification of the IKP and in the case of this mechanism can be performed two ways. One of these consist in solving by numeric

**Fig. 3.** The vector contour  $A_2 \rightarrow B_2 \rightarrow B_3 \rightarrow A_3$



methods a system of 6 equations with 6 unknowns, coming from the conditions that proximal links and sides of triangular mobile platform to have constant lengths.

The other procedure (that is used in the paper), represents an intersection problem between a planar curve, described by point \$B\_I\$ from the planar four bar mechanism \$A\_2B\_2B\_3A\_3\$ (Fig. 3), and the circle with center in \$A\_I\$ and radius \$A\_I B\_I\$. Equation of this circle is just first equation in the system Eq. (7). In order to determine coordinates of point \$B\_I\$ it was used a classical procedure from the mechanism theory, taking into consideration the vector contour \$A\_2 \rightarrow B\_2 \rightarrow B\_3 \rightarrow A\_3\$.

Firstly, the above mentioned contour equation, is written as follows:

$$\overline{A_2 B_2} + \overline{B_2 B_3} + \overline{B_3 A_3} + \overline{A_3 A_2} = 0 \tag{7}$$

Projecting Eq. (8) on the axes of fixed referential system \$A\_2x\_2y\_2\$ and suitable arranging of terms, it obtains a system with two equations and unknowns \$\phi\_b\$ and \$\phi\_3\$:

$$\begin{cases} b \cos \phi_2 + l_2 \cos \phi_3 = x_{A_3} - x_{A_2} - l_2 \cos \phi_2 \\ b \sin \phi_2 + l_2 \sin \phi_3 = y_{A_3} - y_{A_2} - l_2 \sin \phi_2. \end{cases} \tag{8}$$

Where \$\phi\_b\$ is angle between horizontal positive axis and \$\overline{B\_2 B\_3}\$, \$\phi\_3\$—angle between horizontal positive axis and \$\overline{A\_3 B\_3}\$, \$\phi\_2\$ is here input parameter defined as in Fig. 2.

Writing down \$a = x\_{A\_3} - x\_{A\_2} - l\_2 \cos \phi\_2\$, \$c = y\_{A\_3} - y\_{A\_2} - l\_2 \sin \phi\_2\$, squaring both equations of the system and added its term to term, the following equation is obtained:

$$a \cos \phi_b + c \sin \phi_b = d. \tag{9}$$

where \$d = \frac{a^2 + b^2 + c^2 - l\_2^2}{2b}\$. Substituting now \$\tan \frac{\phi\_b}{2} = t\$, the two solutions of Eq. (10) can be expressed:

$$t_{1,2} = \frac{c \pm \sqrt{c^2 + a^2 - d^2}}{a + d}, \text{ from where } \varphi_b = 2 \cdot \arctg t_{1,2} \text{ and:}$$

$$x_{B1} = l_2 \cos \varphi_2 + b \cos(\varphi_b + \pi/3), \quad y_{B1} = l_2 \sin \varphi_2 + b \sin(\varphi_b + \pi/3). \quad (10)$$

In fact, all this calculus (at Eqs. (8)–(10)) represent the kinematics solving of the four bar planar linkage  $A_2B_2B_3A_3$  with  $A_2B_2$  driving link and  $B_2B_3, A_3B_3$ —driven links. Because of the paper space limitations, it was very concise presented.

### 4 Singularities Module

Putting length  $l_2^2 = (x_{Bi} - x_{Ai})^2 + (y_{Bi} - y_{Ai})^2$  of distal links under detailed form,

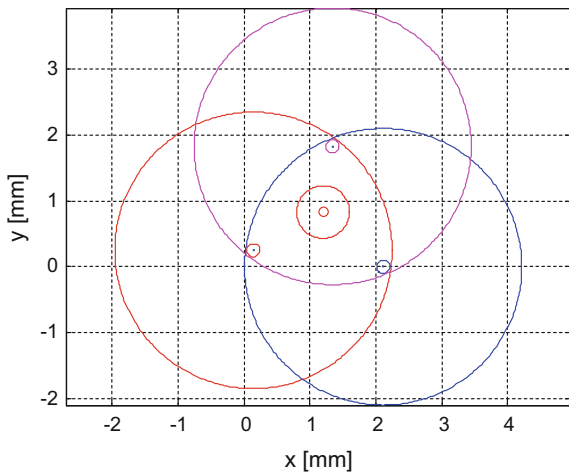
$$l_2^2 = (x + x'_{Bi} \cos \phi - y'_{Bi} \sin \phi - x_{Oi} - l_i \cos \theta_i)^2 + (y + x'_{Bi} \sin \phi + y'_{Bi} \cos \phi - y_{Oi} - l_i \sin \theta_i)^2. \quad (11)$$

and considering the function

$$F_i(x, y) = (x + x'_{Bi} \cos \phi - y'_{Bi} \sin \phi - x_{Oi} - l_i \cos \theta_i)^2 + (y + x'_{Bi} \sin \phi + y'_{Bi} \cos \phi - y_{Oi} - l_i \sin \theta_i)^2 - l_2^2. \quad (12)$$

as an implicit three dimensional function of a three dimensional variable  $q = [x, y, \phi]$ , like that,  $\mathbf{F}(\boldsymbol{\theta}, \mathbf{q}) = \mathbf{0}$ . Differentiating this relation with respect to time leads to a formula between input and output velocities [2]:  $\mathbf{J}_q \cdot \dot{\mathbf{q}} + \mathbf{J}_\theta \cdot \dot{\boldsymbol{\theta}} = \mathbf{0}$ .

Fig. 4. Mechanism workspace



Accomplishing the calculations in this matrix, it may be written  $\Delta \mathbf{J}_q$ , the Jacobian matrix determinant. Taking  $\Delta \mathbf{J}_q = \mathbf{0}$  we will be able to discuss about the situations when singularities of the 2-nd type occur.

### 5 Numerical Results

Below, after running the performed programs, a set of results is presented, based on the following constructive data  $L = 2.4$ ;  $l_1 = 1$ ;  $l_2 = 1.1$ ;  $b = 0.5$ ;  $\varphi = \pi/6$ ;  $r_1 = 0.4$ ;  $r_2 = 0.4$ ; Lengths have relative units.

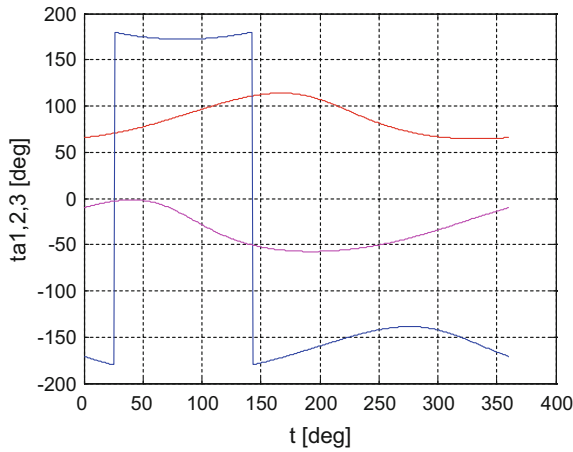


Fig. 5. Proximal links movements (IKP)

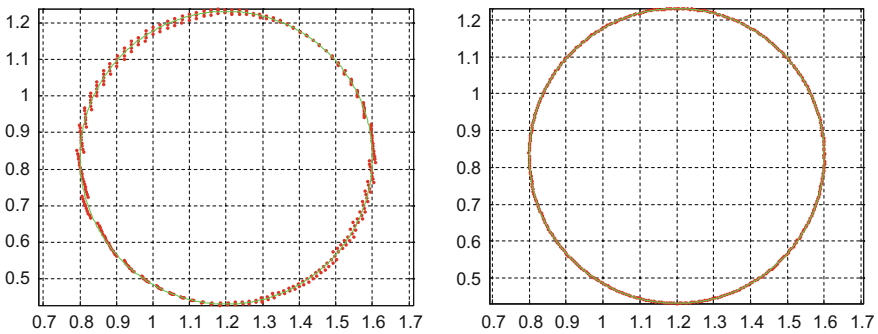


Fig. 6. DKP: End-effector follows a circle, computing step is  $1^\circ$  (left) and  $0.1^\circ$  (right). Values on the axes represent relative units of lengths

In Fig. 4, in the center of workspace, an end-effector circular trajectory was drawn. The discontinuity in Fig. 5, comes from the inverse of tangent function ( $\text{atan2}$ ), because this function returns angular values included between  $-\pi$  and  $\pi$  only. So that angles contented in III and IV quadrants are regarded as negatives.

In Fig. 6, the result of a circular end-effector trajectory following is shown.

In Fig. 7 and Fig. 8, the  $J_q$  determinant was represented, in spatial form (Fig. 7), and by level curves (Fig. 8). In this last case, only nearest to zero curves were traced, representing in fact singularity curves.

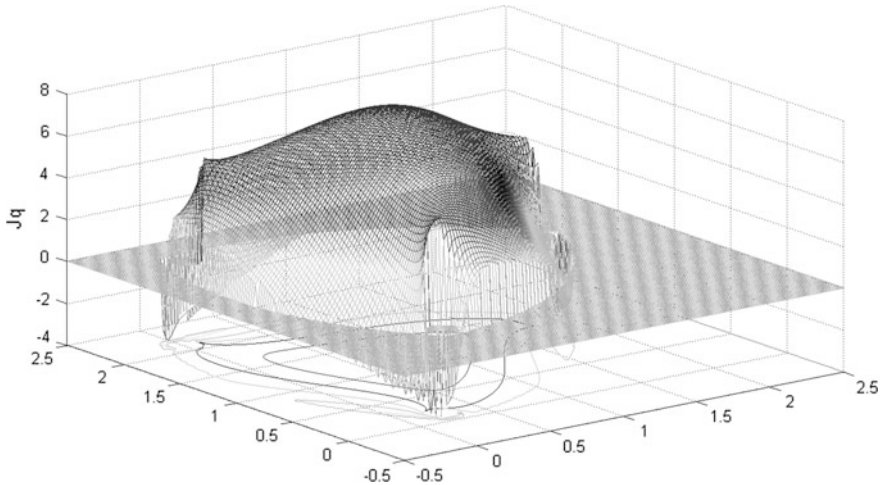


Fig. 7. 3D representation of  $J_q$  determinant. Values on the axes represent relative units of lengths

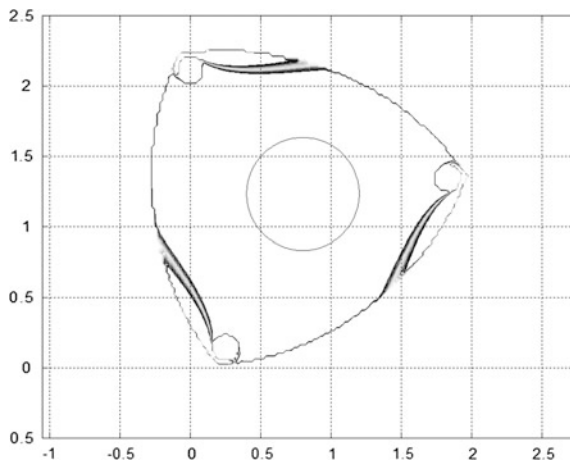


Fig. 8. Singularity curves and end-effector circular trajectory. Values on the axes represent relative units of lengths

Figure 6 shows the dependence between DKP accuracy and the computing step. Referring to Fig. 8, here a simple case was shown, when end-effector trajectory is enough distanced from the singularity curves. It represent the actual research stage. It follows to take into consideration more complex situations.

## 6 Conclusions

In the paper, an IKP-DKP instrument was presented, that may also be used in order to emphasize the singularities, especially of the 2-nd degree, of the 3 $\overline{RRR}$  parallel mechanism. This is suitable also for student learning use [5–8]. Running this set of programs it can put in relief mechanism workspace, input movements of driving (proximal links), verified by DKP modulus, and singularity curves.

## References

1. Alaci S, Ciornei F-C, Patrascu-Ciceu S (2008) Aspects concerning RCCC spatial mechanism kinematics. *Bul. Inst. Pol. Iasi, Tom. LIV(LVIII), Fasc.1, 2008, Sect. Constructii de Masini*, pp 411–422
2. Arsenault M, Boudreau R (2004) The synthesis of three-degree-of-freedom planar mechanism with revolute joints (3-RRR) for an optimal singularity-free workspace. *J Robot Syst* 21 (5):259–274
3. Buium FI, Leohchi D, Doroftei I (2014) A workspace characterization of the 3 RRR planar mechanism. *Appl Mech Mater* 658. Trans Tech Publications, Switzerland, pp 563–568. <https://doi.org/10.4028/www.scientific.net/AMM.658.563>
4. Doroftei I (2008) Singularity analysis of a 3RRR planar parallel robot I—theoretical aspects. *Buletinul Institutului Politehnic din Iasi, Tom LIV(LVIII), Fas. 1, 2008, Sectia Constructii de Masini, Iasi*, pp 465–472
5. Doroftei I (2008) Singularity analysis of a 3RRR planar parallel robot II—physical significance. *Buletinul Institutului Politehnic din Iasi, Tom LIV(LVIII), Fas. 1, 2008, Sectia Constructii de Masini, Iasi*, pp 473–480
6. Lovasz EC, Grigorescu SM, Mărgineanu DT, Pop C, Gruescu CM, Maniu I (2015) Kinematics of the planar parallel manipulator using geared linkages with linear actuation as kinematic chains 3-R (RPRGR) RR. In: *The 14th IFToMM world congress, Taipei, Taiwan, 25–30 Oct 2015*. <https://doi.org/10.6567/IFTToMM.14TH.WC.OS8.026>
7. Lovasz EC, Grigorescu SM, Mărgineanu DT, Pop C, Gruescu CM, Maniu I (2015) Geared linkages with linear actuation used as kinematic chains of a planar parallel manipulator. In: *Mechanism, Transmissions and Applications*. Springer International Publishing, Switzerland 2015. *Mechanism and Machine Science* 31. <https://doi.org/10.1007/978-3-319-17067-1-3>
8. Merlet J-P (1997) *Le robots paralleles*, 2e edition revue et augmentee. Editions Hermes, Paris



**Part VI**  
**Experimental Mechanics**

# Use of Hypocycloidal Motion in the Study of Rolling Friction



S. T. Siretean, I. Muscă, S. Alaci and F.-C. Ciornei

**Abstract** The paper proposes a device for finding the coefficient of rolling friction using a sphere in contact with the inner surface of a ring that rotates about a horizontal axis. The motion of the ball is characterized by the fact that for a stipulated rotation speed of the ring the centre of the ball executes a damped oscillatory motion and at equilibrium the centre of the ball is situated on different vertical than the one the centre of the ring is positioned. It is assumed that this feature is produced by the rolling friction torque that is proportional with the normal pressing force and the nonlinear differential equation of motion is obtained for the intended dynamic model. By the integration of the equation of motion there are confirmed the oscillatory motion of the ball and the eccentric equilibrium position and it is found a dependency of equilibrium position on the coefficient of rolling friction.

**Keywords** Rolling friction · System dynamics · Experimental rig

## 1 Introduction

Two major categories of contacts are identified when studying the interaction between bodies: conforming and non-conforming or Hertzian contacts. Conforming contacts assume the interface between bodies bounded by identical surfaces thus

---

S. T. Siretean (✉) · I. Muscă · S. Alaci · F.-C. Ciornei  
“Stefan cel Mare” University of Suceava, Suceava, Romania  
e-mail: sorin.t.siretean@gmail.com

I. Muscă  
e-mail: iliem@fim.usv.ro

S. Alaci  
e-mail: alaci@fim.usv.ro

F.-C. Ciornei  
e-mail: florina@fim.usv.ro

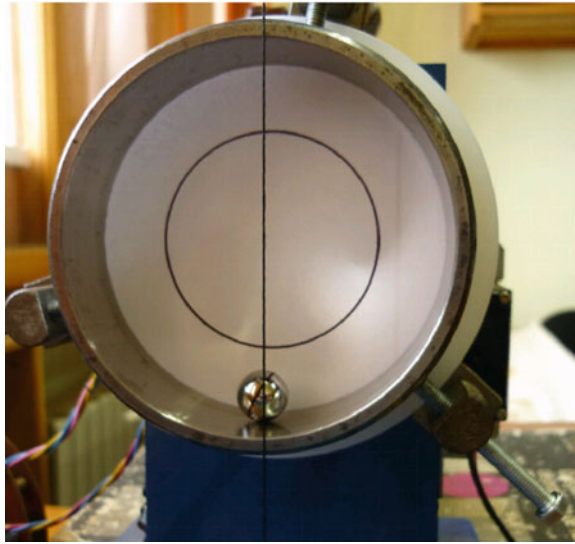
ensuring that surfaces fit exactly on a relatively large area. For these contacts, in any point of the contact zone, the only possible motion between the points from the two bodies is sliding in the common tangent plane. For the case of Hertzian contacts, the contact between boundary surfaces is made theoretically in a point line where there are defined the normal and the common tangent plane. The relative motion between two bodies in Hertzian contact is more complex than the one corresponding to a conforming contact [6]. For non-conforming contact case, besides the sliding in the common tangent plane there is possible a spatial rotation that can be considered as composed by a spin about the normal and a rolling about an axis contained in the tangent plane. A form of friction will oppose to each of these relative motions between bodies, materialized by the sliding friction force, spinning torque and rolling torque.

## 2 Experimental Evidences

The paper is based on a series of experimental researches concerning the rolling friction phenomenon. Specifically, a parallel between sliding and rolling friction was sought for in experimental tests. An attribute of rolling friction accepted in unanimity is the existence of two types of friction, static and dynamic and therefore the necessity of defining two coefficients of friction, corresponding to absence of relative motion between the two boundary surfaces and to sliding motion, respectively. One of the methods used to determine the coefficient of sliding kinetic friction uses the inclined plane and finds the angle of inclination of the flat surface on top of which the body is placed when the body starts sliding due to the own weight. The motion is more complex when the body on the inclined plane is a solid of revolution and in the general case is a combination between rotation and translation motions [2]. A significant case for industrial applications is the situation when pure rolling exists between the two bodies, characterized by the fact that in the support point there is no relative motion between the contacting points.

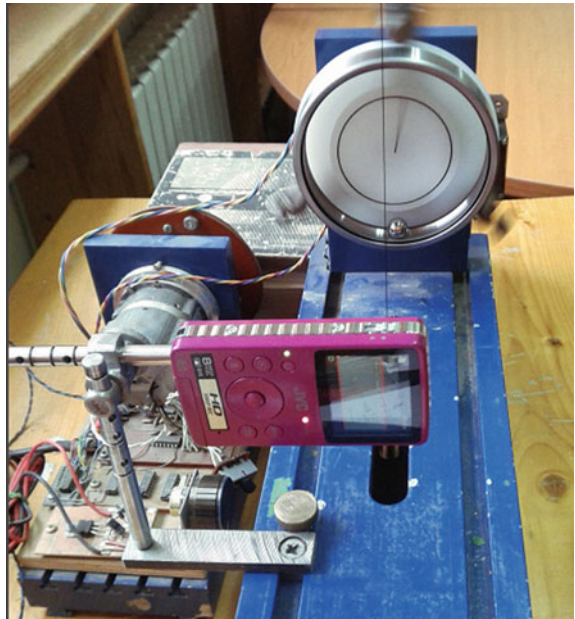
It is noticed that, similar to the sliding friction case, there is a boundary angle of the inclined plane corresponding to the delimitation between the rest at equilibrium on the plane and start of rolling motion. Applying the relations from statics for the limit equilibrium position allows determining the static coefficient of rolling friction [7]. The procedure is difficult due to small values of the rolling friction coefficient and correspondingly is not easy to indicate accurately the inclination angle of the plane for which the equilibrium is broken down (the accuracy of angle measurement is comparable to the angle to be measured). A device was planned to overcome this aspect, Fig. 1, constructed from a bearing ring 1, set into rotation motion about a horizontal axis by a d.c. electrical motor. A bearing ball is positioned on the race at rest in the lowest point of the ring. Setting a constant voltage, it is remarked that the ball performs oscillatory damped motion and there is an equilibrium

**Fig. 1** Experimental device



position when the motion becomes steady, but this position about which the ball oscillates differs from the vertical of the centre of the ring, Fig. 2. It is reached the idea that the deviation from vertical of the angle of position of equilibrium of the ball is a measure of rolling friction.

**Fig. 2** Eccentric steady ball position



### 3 Theoretical Considerations

A metallic ring of interior radius  $R$  that rotates around a horizontal axis with constant angular speed  $\omega_0$  is considered. A bearing ball having the  $r$  radius  $r$  and mass  $M$  is placed in contact with the ring in the lowest point of the ring, having, in the case of pure rolling, a hypocycloidal motion [4]. The same problem was solved in recent works using cyclic motions, evolvent [1] and cycloid motions [3]. The values of coefficient of rolling friction  $s$  and coefficient of sliding friction  $\mu$  are considered known. Two coordinate systems are used for indicating the position of the ball: a fixed one  $Oxyz$  with the origin in the centre of the ring and a mobile one  $Cx'y'z'$  attached to the ball, with the origin in the centre of it. The angles  $\theta$  characteristic to the centre of the ball and  $\varphi$  showing the rotation of the ball with respect to the fix system must be known for indicating the position of the ball. The unique exterior force acting upon the ball is  $M\mathbf{g}$ , its weight, on the vertical direction. In  $B$ , the point of contact between the ball and the ring, act the forces:

- Normal reaction  $\mathbf{N}$ , directed along the normal to the ring;
- Friction force  $\mathbf{T}$ , tangent to the ring, with opposite sense to the relative motion between the contacting points;
- Rolling friction moment  $M_r$  directed along the normal to the plane of motion and having the opposite sign of relative angular velocity  $(\dot{\varphi} - \omega)$ . The over-dot is used in short-hand notation for time derivative.

The theorem concerning the motion of the centre of mass, applied for the ball [2]:

$$M\mathbf{a} = \mathbf{G} + \mathbf{N} + \mathbf{T} \quad (1)$$

The moment of momentum theorem applied with respect to the centre of mass has projection only on the normal to the plane of motion [2]:

$$J_z \ddot{\varphi} = Tr - M_r \quad (2)$$

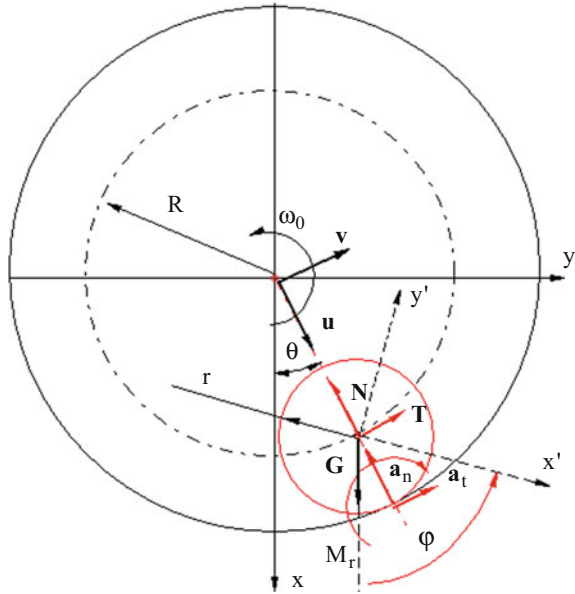
The vector Eq. 1 must be projected on the axis of a coordinate system in order to obtain the equations of motion. It is convenient to use the axes of the mobile system, with origin in the centre of the ring and unit vectors  $\mathbf{u}$  and  $\mathbf{v}$ . The acceleration of the centre of mass of the ball is written (Fig. 3):

$$\mathbf{a}_C = \mathbf{a}_C^n + \mathbf{a}_C^t = -\dot{\theta}^2 R \mathbf{u} + \ddot{\theta} R \mathbf{v} \quad (3)$$

The Eq. 1 is written using the projections on the axes of the ground system:

$$M(-\dot{\theta}^2 R \mathbf{u} + \ddot{\theta} R \mathbf{v}) = Mg \cos \theta \mathbf{u} - Mg \sin \theta \mathbf{v} - N \mathbf{u} + T \mathbf{v} \quad (4)$$

**Fig. 3** Bearing ball inside a circle (ring)



The system of equations corresponding to the motion of the ball is:

$$\begin{cases} -M\dot{\theta}^2 R = Mg \cos \theta - N \\ M\dot{\theta}R = -Mg \sin \theta + T \\ J_z \dot{\varphi} = Tr - M_r \end{cases} \quad (5)$$

and the unknowns from the system are  $\theta, \varphi, N, T, M_r$ . Two additional equations are necessary for solving the system. The first equation characterizes the rolling friction:

$$M_r = -sN \operatorname{sgn}(\dot{\varphi} - \omega_0) \quad (6)$$

According to Eq. 6, it is assumed that the moment of rolling friction is proportional to normal pressing force and the sign of x variable is given by the  $\operatorname{sgn}(x)$  function. The second equation depends on the friction type met in the ball-ring contact: for a pure rolling contact,  $N$  and  $T$  are known and the pure rolling condition is expressed as a relation between the parameters  $\theta$  and  $\varphi$ ; for a contact with sliding friction, the parameters  $\theta$  and  $\varphi$  are independent and the friction force is found using the relation:

$$T = \mu N \quad (7)$$

The device was designed starting from the study of pure rolling and thus the pure rolling condition must be deduced. The definition for pure rolling condition requires that in the contact point the velocities of the two points should be equal:

$$\mathbf{v}_{B_{ring}} = \mathbf{v}_{B_{ball}} \quad (8)$$

The explicit relation (8) becomes:

$$\omega_0 \mathbf{k} \times (R+r) \mathbf{u} = \dot{\theta} \mathbf{k} \times (R \mathbf{u}) + \dot{\varphi} \mathbf{k} \times (r \mathbf{u}), \quad (9)$$

where  $\mathbf{k}$  is the unit vector for the axis normal to the plane of motion. In relation (9), all terms are collinear to  $\mathbf{k} \times \mathbf{u}$  and as a result, the pure rolling condition results:

$$\omega_0(R+r) = \dot{\theta}R + \dot{\varphi}r. \quad (10)$$

The relations (5), (9), and (10) allow finding the reactions from the contact point and the equation of motion:

$$\ddot{\theta} = - \left( (R\dot{\theta} + g \cos \theta) \frac{S}{r} \operatorname{sgn}(\theta - \omega_0) + g \sin \theta \right) / R \left( 1 + \frac{J_z}{Mr^2} \right) \quad (11)$$

The Eq. 10 is a second-order nonlinear differential equation and the numerical method Runge-Kutta [5] was applied for integrating it. After integration, the variations of  $\theta$  angle and its derivative versus time were found. Substituting them in relation (10) permit finding the angular acceleration  $\ddot{\theta}$  and finally the dependencies of normal force  $N$  and friction force  $T$  versus time. The last two are necessary for validating the existence of pure rolling condition:

$$T < \mu N \quad (12)$$

## 4 Theoretical and Experimental Results

The method described above was applied for the device from the laboratory, having the following parameters: radius of the bearing ball  $r = 0.006$  m, inner ring radius  $R = 0.06$  m and ball mass  $M = 0.007$  kg. The angular elongation of the centre of the ball versus time is presented in Fig. 4, obtained by integrating the Eq. 10.

A comparison between the experimental and theoretical (obtained using Eq. 10) amplitudes of the first oscillations is presented in Fig. 5. It is noticed from both Figs. 4 that the position of dynamic equilibrium of the ball, eccentrically with respect to the vertical through the centre of the ring, is validated both experimentally and theoretically. After the motion becomes steady, the angle made by the position vector of the centre of the ball with vertical,  $\theta_0$  takes the value  $0.76^\circ$ . The asymmetrical position of the centre of the ball about the vertical is confirmed experimentally too. To be mentioned, there is concordance between the theoretical and experimental periods of oscillation. The time variations of normal reaction  $N$  and friction force  $T$  are presented in Figs. 6 and 7, and afterwards, using relation (11), the presence of pure rolling is tested with these values, the results being

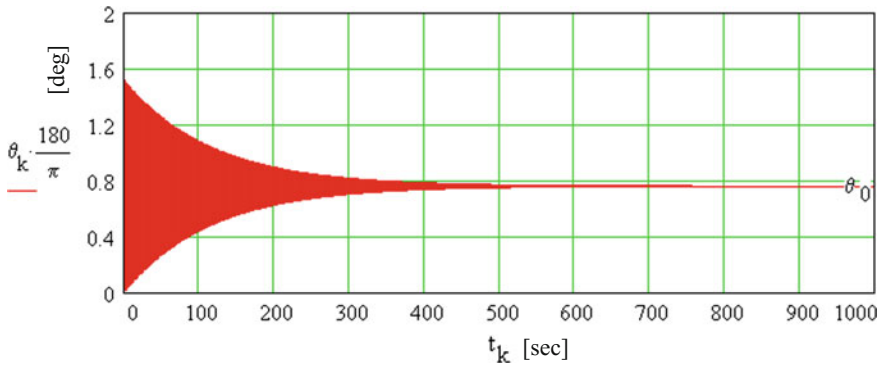


Fig. 4 Angular amplitude of ball mass center of versus time

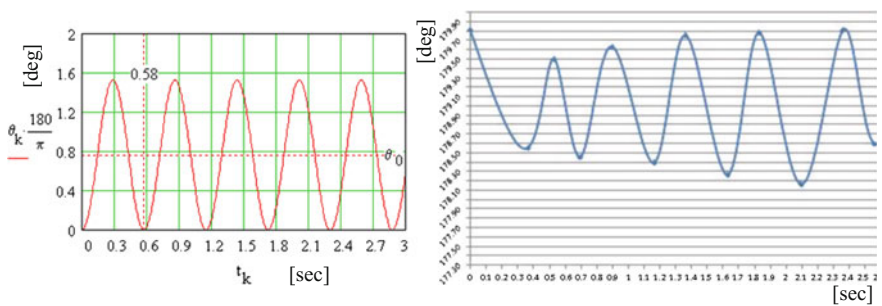
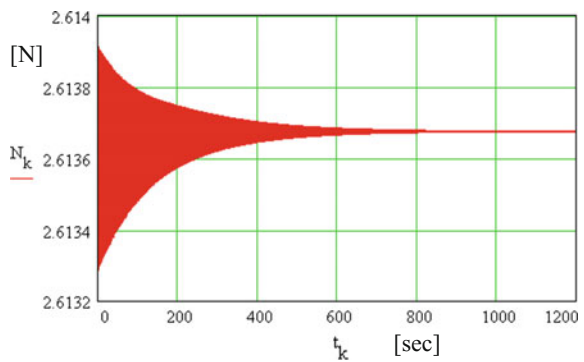


Fig. 5 Theoretical and experimental angle of centre of mass versus time

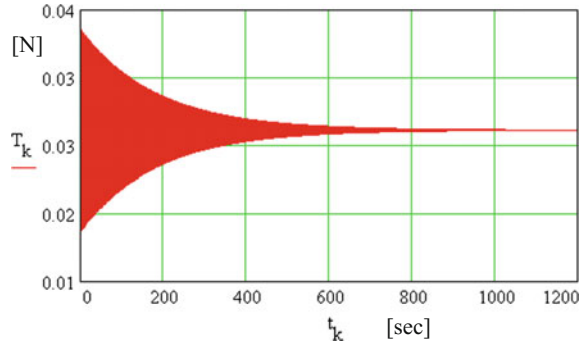
presented in Fig. 8. For a constant value of rolling friction coefficient ( $s = 80 \mu\text{m}$ ) the angular velocity of the ring was varied and the obtained variation of position parameter for steady motion is represented in Fig. 9. There are noticed two domains of behaviour of the ball.

Fig. 6 Normal reaction versus time

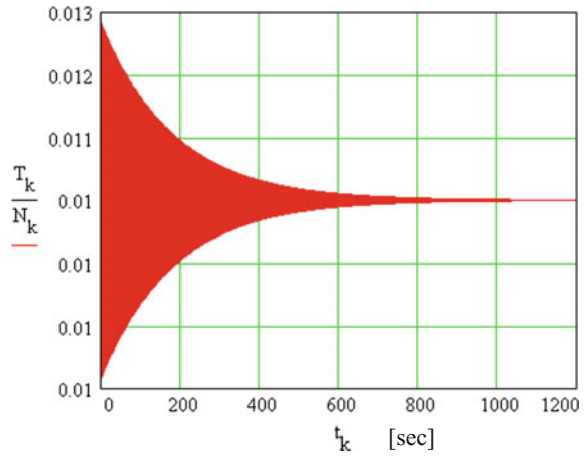




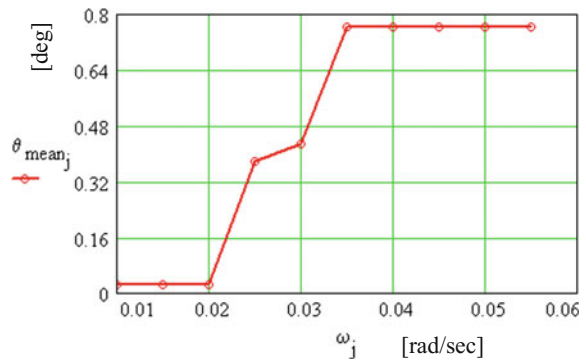
**Fig. 7** Friction force versus time



**Fig. 8** Testing the pure rolling condition



**Fig. 9** Equilibrium position versus angular speed of the ring



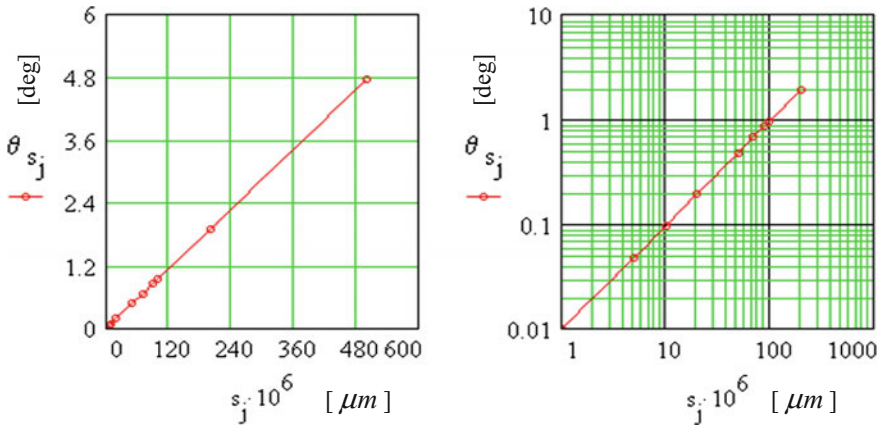


Fig. 10 Equilibrium position versus coefficient of rolling friction

Keeping constant the angular velocity of the ring, ( $\omega = 1$  rad/sec) the dependence of angle of position for steady motion on different values of rolling friction coefficient is presented in Fig. 10 in Cartesian and double logarithmic coordinates. Both plots confirm the linear dependence between the two parameters.

## 5 Conclusions

The hypocycloidal motion of a bearing ball inside the bearing ring that rotates steadily about a horizontal axis is analyzed and it is found that the ball presents a damped periodic motion that stabilizes in an eccentric point with respect to the vertical through the centre of the ring. A dynamic model for the system ball-race is proposed, assuming that the eccentric equilibrium position is caused by the occurrence of rolling friction between the ball and race. With the hypothesis that pure rolling exists between the two bodies, the differential equation of motion is found for the dynamic model. The differential equation is numerically integrated and after testing the pure rolling condition, there are confirmed the damped oscillatory motion and the eccentricity of equilibrium position. Further more, the model shows a quasi-linear dependency of the parameter of position of the ball centre on the coefficient of rolling friction. Additionally, it was noticed that for a given value of the coefficient of rolling friction, when the rotation speed of the ring varies within a certain range, two domains where the equilibrium position is independent on the rotation speed, can be distinguished. The two zones are separated by a very narrow region (where the equilibrium position is affected by the angular speed) that ensures transition between the other two neighboring regions.

## References

1. Alaci S. et al (2017) Estimation of coefficient of rolling friction by the evolvent pendulum method. IOP MSE 200
2. Ardema DM (2005) Newton-Euler dynamics. Springer
3. Ciornei MC et al (2017) A method for the determination of the coefficient of rolling friction using cycloidal pendulum. IOP MSE 227
4. Dooner DB (2012) Kinematic Geometry of gearing, Wiley
5. Gear CW (1971) Numerical initial value problems in ODE. NJ Prentice-Hall
6. Johnson KL (1985) Contact mechanics. Cambridge University Press
7. Stolarski TA, Tobe S (2000) Rolling contacts, 2nd edn. Professional Engineering Publishing Ltd, London Bury

# Experimental Bench for Spur Gears Efficiency Measurement



N. Dumitru, E. Dragut, N. Craciunoiu and I. Geonea

**Abstract** In this paper, a test bench for study the efficiency of spur gear is presented. Based on the proposed design scheme a virtual model of the test bench is developed in SolidWorks, both for manufacture and for simulation purpose. The main principle of the test bench it is that the load is performed internally on a closed circuit composed from two sets of spur gears, for that reason it is not necessary to use a brake system. Using a HBM acquisition system and strain gauge transducers it is established the experimental variation of the torque on the shafts of the gears. In this way is established the experimental efficiency of the spur gear set. The bench is designed into a modular design, for test can be used a set of different gear pairs with same axle distance.

**Keywords** Spur gears design · Efficiency · Experimental measurement  
Strain gauge transducers · Data acquisition

## 1 Introduction

The gears design, experimental efficiency study and diagnosis based on vibration are presented in numerous researches published in the literature. The experimental efficiency of gear train is studied in [16].

---

N. Dumitru · N. Craciunoiu · I. Geonea  
Faculty of Mechanics, University of Craiova, Craiova, Romania  
e-mail: nicolae\_dtru@yahoo.com

N. Craciunoiu  
e-mail: ncraciunoiu@yahoo.com

I. Geonea  
e-mail: igeonea@yahoo.com

E. Dragut (✉)  
Faculty of Engineering, University C-tin Brâncusi from Târgu-Jiu, Târgu Jiu, Romania  
e-mail: emil.dragut@yahoo.com

Complex equation systems are used to predict the coefficient of sliding friction between the gear teeth, when the lubrication regime is elastohydrodynamic [14]. The aspect of computerized design and stress analysis is subject of numerous studies [2]. In [2] is presented a computerized approach for synthesis, analysis and stress calculation for spiral bevel gears. The subject of gear diagnosis based on vibration is present in many studies [4, 17]. The authors of [17] demonstrates that the vibrations that appear in gearbox mechanical systems can be used as information to detect faults, by performing a study of vibrations in a wide range of load and speed conditions. In [10] the Adams software it is used to model gears contact. Also the gear contact is analyzed in [11] in order to predict wear.

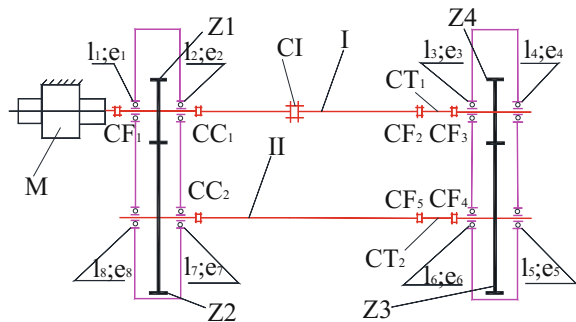
The design of spur gears for improving efficiency is presented in [1]. It is presented a method for gears power loss calculation for improved efficiency. Experimental investigations concerning the gears efficiency are presented in [3, 9, 15] for spur gear, helical gear systems and hypoid gear pairs. Dynamic analysis of involute spur gears and dynamic optimization is presented in researches presented by [5, 8]. Also are presented measurements of automotive transmission efficiency, using a chassis dynamometer, in [7, 17]. The test benches proposed for gears efficiency estimation are the object of a large number of patents [18]. Studies concerning experimental test bench for gears efficiency are presented in [6, 12, 13].

In this research it is proposed the efficiency study of a spur gears train. The designed and developed test bench uses a closed power circuit and it is not necessary to use a brake. The internal load in the closed circuit is created by torsion of the shaft assembly. The efficiency measured is including the losses in gear friction, gear lubrication and bearing friction.

## 2 Test Bench Design

The bench test for spur gears efficiency is based on the kinematic scheme presented in Fig. 1.

**Fig. 1** Kinematic scheme of the bench test for spur gears efficiency



The tested gears pairs (1, 2) and (3, 4) are mounted in the boxes fixed on a base support. The motor M it is used to transmit the motion to the tested gears. The internal torque load is created using the CI coupling with front teeth on the shaft I.

Notations used in Figs. 1 and 2 represent:  $CF_i, i = 1 \dots 4$ —flange mechanical couplings; CI—load coupling;  $l_i, i = 1 \dots 8$ —bearings;  $e_i, i = 1 \dots 8$ —sealing; 1 ... 4—spur gears;  $CT_i, i = 1 \dots 2$ —strain gauge torque transducer;

Design of gears is performed with a program elaborated by the main author, in three stages, dimensioning, geometric calculus and verification to bending and contact fatigue. The gears design parameters are visible in Table 1.

By the fact that the both gearboxes from the bench structure are identical, and the loads achieved with the load coupling CI are equal, it means that loss of bearings

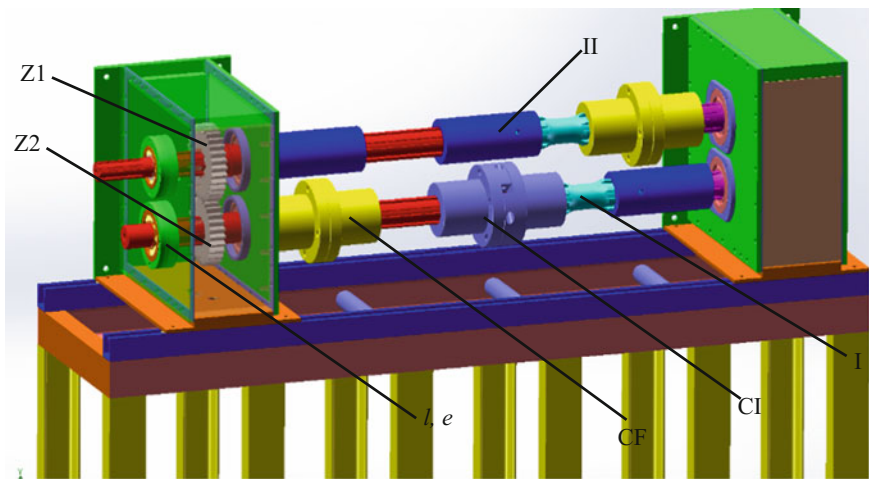


Fig. 2 Design model of the test bench for spur gears efficiency

Table 1 Gear design parameters

Teeth number	Pitch diameter [mm]	Dedendum diameter [mm]	Whole depth [mm]
$Z_1 = 27$	$d_1 = 135$	$df_1 = 123.6$	11
$Z_2 = 31$	$d_2 = 155$	$df_2 = 143.217$	Add. mod. coefficient
Center distances	Addendum diameter [mm]	Working pitch diameter [mm]	$x_{n1} = 0.11$
$a_w = 150$	$da_1 = 146.10$	$dw_1 = 139,656$	$x_{n2} = 0.071$
$a_0 = 145$	$da_2 = 165.71$	$dw_2 = 160,344$	Gear ratio: 1.148
Addendum (gear1)	Dedendum (gear 1)	Addendum (gear2)	Dedendum (gear 2)
5.55	5.70	5.355	5.895

gears and seals are comparatively equal. Marking with  $\eta$  the efficiency of each gearbox, then the power (energy) and efficiency is computed with Eq. (1):

$$P_3 = -\eta^2 \cdot P_1; \eta^2 = \frac{T_2}{i \cdot T_1} \Rightarrow \eta = \sqrt{\frac{T_2}{i \cdot T_1}} \quad (1)$$

where:  $P_3$  and  $P_1$  are the power at gear 3 and 1, in [kW],  $i$  is the gears ratio and  $T_1$  and  $T_2$  the shafts torque.

The bench is able to measure the torque on shafts 1 and 2, so the efficiency of a gear set is computed with Eq. (1).

### 3 Experimental Setup

Based on the proposed design a real model test bench it is developed. The experimental model and HBM acquisition system is presented in Fig. 3.

To measure the load torque are used strain gauge transducers, placed on shafts I and II. It is used HBM strain gauges, XY2x type, designed for torque measurement. The strain gauges are connected to a complete Wheatstone bridge electric circuit. To transmit the measurement signal from shafts to the bench frame are used brush-bearing systems SK-6 type, manufactured by HBM. A transducer calibration is performed, using a special designed lever P. The calibration diagrams of the strain gauge transducers placed on shafts 1 and 2 are presented in Fig. 4.



**Fig. 3** Experimental model of the spur gears efficiency test bench

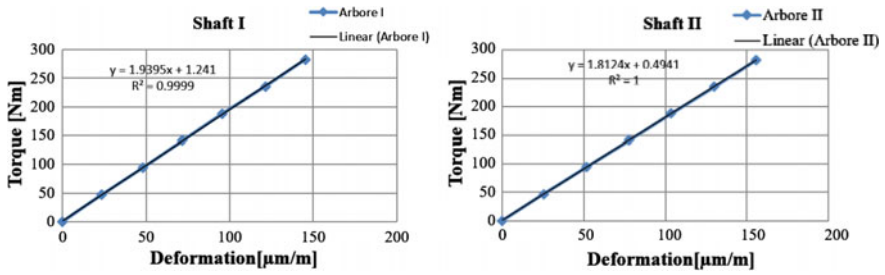


Fig. 4 Experimental calibration diagrams of the bench shafts

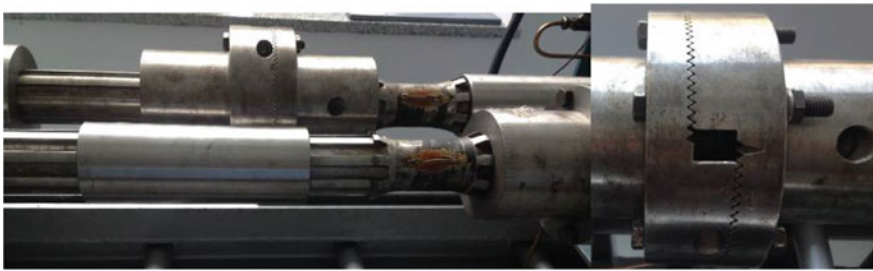


Fig. 5 Shaft II internal torsion with help of frontal teeth coupling

Having the correlation between the measured deformation and the torque load on can represent the experimental variation of the torque. To measure the torque, it is used the MGCPlus acquisition system and Catman AP software. In order to perform the torque measurement and the gears efficiency it is created an internal load, by rotating with one teeth the frontal coupling, as shown in Fig. 5.

Rotating with one teeth the frontal coupling CI (load coupling), as can be seen in Fig. 5, it is created an internal load torque of 200 Nm.

## 4 Obtained Results

Obtained results are the graphics of variation for the torque dynamic load on shafts I and II, as can be observed in Fig. 6.

As can be observed from Fig. 6, the torque measured has a medium value of 205 Nm and for the shaft II the medium value is 230 Nm. It appears a greater value of the torque on the shaft II because of the reducer gear ratio. Considering the Eq. (1) the value of the spur gear pair efficiency is 0.98. Obtained value for the gear efficiency is comparable with values presented in the literature.



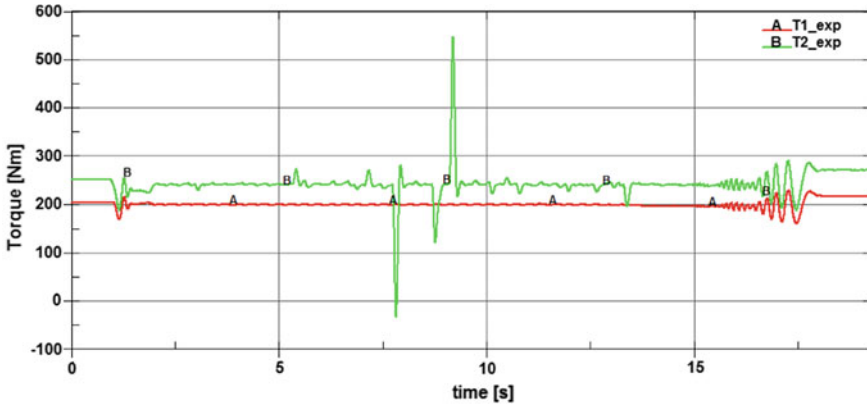


Fig. 6 Measured torque on the bench shafts

### 5 Numerical Simulation

The virtual design is performed with Adams and Ansys Workbench programs. Presents interest the shafts dynamic compartment, experimentally and by numerical simulation with Adams. The system motion is monitored in 19 s. It is established the time variation of kinematic and dynamic parameters, superposing the motion of the rigid body with that of elastic body. The virtual prototype, from Fig. 7, is analyzed in two stages: a modal dynamic analysis to establish the natural frequencies and eigen modes of vibration and the second one is dynamic analysis.

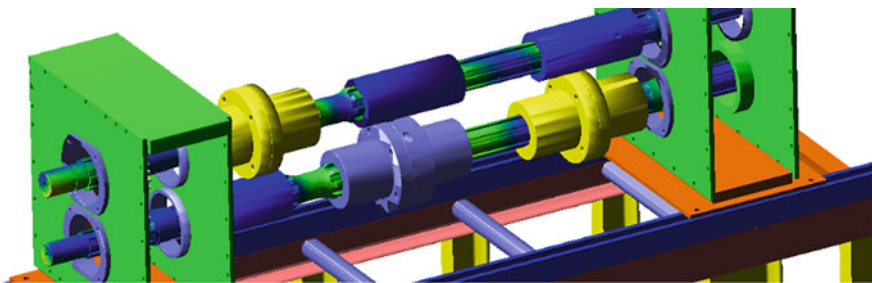


Fig. 7 Test bench virtual model in Adams

## 6 Conclusions

This paper presents the research developed in the direction of design, manufacture and testing of a test bench for spur gear efficiency. The novelty of the proposed design consists in the principle of creating the internal load by rotating the two parts of the shaft II. To establish gears efficiency, it is necessary to measure the torques on the shafts. This is made by using a data acquisition system and strain gauge transducers. A calibration of the torque transducer is performed and the obtained dependency torque-deformation for the shafts is linear. Experimental measurements performed, for the shafts torques is used to calculate the efficiency of the gear set. The jump from the torque diagrams, obtained experimentally are explained by the fact that the bench shafts with afferent gears and couplings are elastic system from

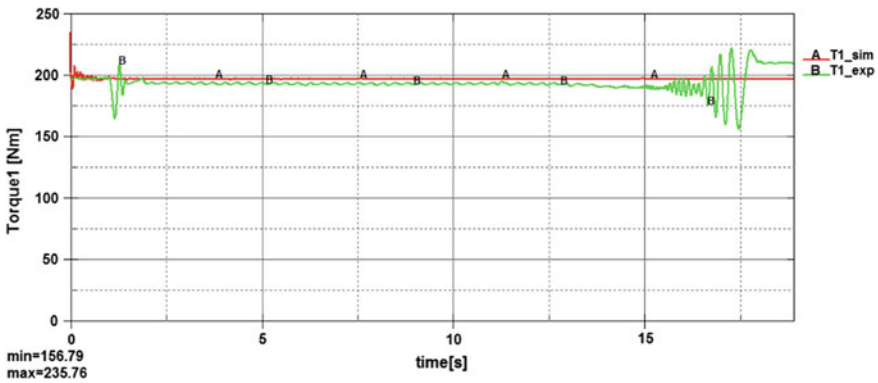


Fig. 8 Experimental and simulation torque on shaft 1

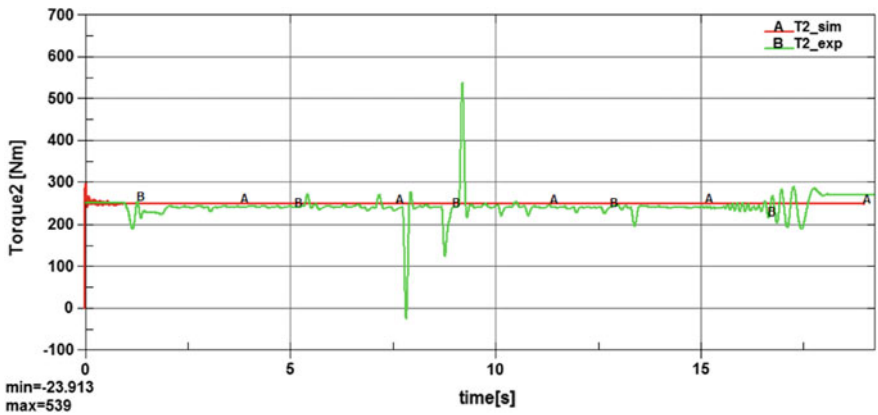


Fig. 9 Experimental and simulation torque on shaft 2

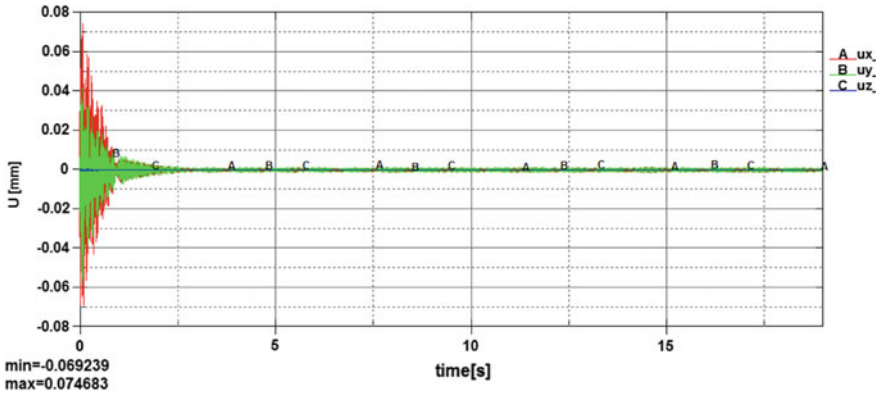


Fig. 10 Computed elastic resultant displacement

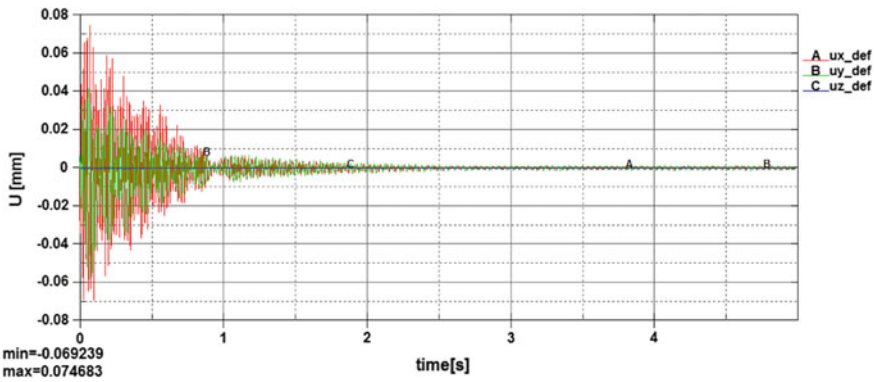


Fig. 11 Elastic resultant displacement on 5 s interval

flexional and torsional compartment. It is computed the dynamic response of the shafts, as deformable bodies, obtained results are presented in Figs. 8 and 9. It is observed that the elastic transversal displacement and longitudinal, has small values. Also the values for the longitudinal displacement from Figs. 10 and 11 are small.

## References

1. Anderson NE, Loewenthal SH (1982) Design of spur gears for improved efficiency. J Mech Des 104(4):767–774. <https://doi.org/10.1115/1.3256434>. Accessed 01 Oct 1982, (8 pages)
2. Argyris John, Fuentes Alfonso, Litvin Faydor L (2002) Computerized integrated approach for design and stress analysis of spiral bevel gears. Comput Methods Appl Mech Eng 191 (11):1057–1095

3. Baud S, Velex P (2002) Static and dynamic tooth loading in spur and helical geared systems-experiments and model validation. *J Mech Des* 124(2):334–346. (13 pages)
4. de Klerk D, Rixen DJ, Valentin C (2007) An experimental gear noise propagation method for a gearbox on a test bench. In: International modal analysis conference (IMAC)
5. Faggionia M, Samania FS, Bertacchia G, Pellicano F (2011) Dynamic optimization of spur gears. *Mech Mach Theory* 46(4):544–557, Apr
6. Fernández del Rincón A (2014) Test bench for the analysis of dynamic behavior of planetary gear transmissions. In: Advances in condition monitoring of machinery in non-stationary operations. Lecture notes in mechanical engineering. Springer, Berlin, Heidelberg
7. Irimescu A, Mihon L, Padure G (2011) Automotive transmission efficiency measurement using a chassis dynamometer. *Int J Autom Technol* 12(4):555–559
8. Karpata F, Ekwaro-Osireb S, Cavdara K, Babalika FC (2008) Dynamic analysis of involute spur gears with asymmetric teeth. *Int J Mech Sci* 50(12):1598–1610
9. Kolivand M, Li S, Kahraman A (2010) Prediction of mechanical gear mesh efficiency of hypoid gear pairs. *Mech Mach Theory* 45(11):1568–1582
10. Kong D et al (2008) Nonlinear contact analysis of gear teeth for malfunction diagnostics, <http://citeseerx.ist.psu.edu/viewdoc/download?doi=10.1.1.1024.4514&rep=rep1&type=pdf>
11. Mao K (2007) Gear tooth contact analysis and its application in the reduction of fatigue wear. *Wear* 262(11–12):1281–1288 (10)
12. Margine A, Dumitru N, Geonea I, Dragut E (2013) Electromechanical system for quality assesment of spur gear. In: ICOME 2013, Craiova, Romania. ISBN 987-606-14-0692-0
13. Marques PMT, Fernandes CMCG, Martins RC, Seabra JHO (2014) Efficiency of a gearbox lubricated with wind turbine gear oils. *Tribol Int* 71:7–16
14. Martin KF (1981) The efficiency of involute spur gears. *ASME J Mech Des* 103(4):160–169
15. Petry-Johnson TT, Kahraman A, Anderson NE, Chase DR (2008) An experimental investigation of spur gear efficiency. *J Mech Des* 130(6):062601. <https://doi.org/10.1115/1.2898876>. Accessed 14 Apr 2008, 10 pages)
16. Talbot DC, Kahraman A, Singh A (2012) An experimental investigation of the efficiency of planetary gear sets. *J Mech Des* 134(2):021003
17. Villaa LF, Reñonesa A, Perána JR, de Miguel LJ (2012) Statistical fault diagnosis based on vibration analysis for gear test-bench under non-stationary conditions of speed and load. *Mech Syst Signal Process* 29:436–446
18. Von Thun HJ (1990) US Patent No 4,939,985. Washington, DC: US Patent and Trademark Office

# Design, Development and Testing of a Dynamometer for Drill Force Measurement



I. Geonea, A. Rosca and P. Rinderu

**Abstract** In this study, a drill dynamometer for measure dynamic forces and torques, using strain gauge transducers has been designed, manufactured and tested. The dynamometer is connected to a HMB data acquisition system. Drill forces signal are captured processed and transformed into numerical data with the help of hardware and software of the MGC. Plus acquisition system. The principle of the dynamometer measurement is based on strain gauge transducers which measures elastic deformations produced by the loads. The elastic element used in the construction consists in a spoked wheel which measures simultaneously the force and torque. The elastic deformations produced by the force and torque, bends the double embedded spokes. It is presented the dynamometer design and principle of measuring. In order to verify the elastic element deformations, it is performed a FEA analysis in ANSYS. The experimental model is calibrated and in the final stage is made experimental measurements of drill force and torque.

**Keywords** Drill · Experimental measurement · Strain gauge transducers  
Data acquisition

## 1 Introduction

The measurement of forces and torque in drill operations is important in order to optimize the drill geometry and parameters of the process (cutting speed, advance). Also in some researches is pointed that the cutting force is related with the tool wear [7].

---

I. Geonea (✉) · A. Rosca · P. Rinderu  
Faculty of Mechanics, University of Craiova, Craiova, Romania  
e-mail: igeonea@yahoo.com

A. Rosca  
e-mail: adrian\_sorin\_rosca@yahoo.com

P. Rinderu  
e-mail: rinderu\_paul@yahoo.fr

A considerable volume of research it is directed to measure of the cutting forces, especially to turning process [8]. This type of measurement is important because the cutting forces which appear in the processing of pieces are correlated with the generated heat, and also with the tools wear, with the roughness of machined surface and not at least with the accuracy of generated piece. Due to the complex configuration of the machine, cutting tool and piece system, the theoretical fundamentals for estimation of force and torques which appear to metal cutting process, are not enough accurate to obtain good results [1, 3]. So, it is necessary to measure with experimental methods the cutting forces. Recently are developed many dynamometers, especially for turning process. The principle of force measurement is most time based on elastic deformation of transducer elements. The deformations are captured with strain gauge sensors.

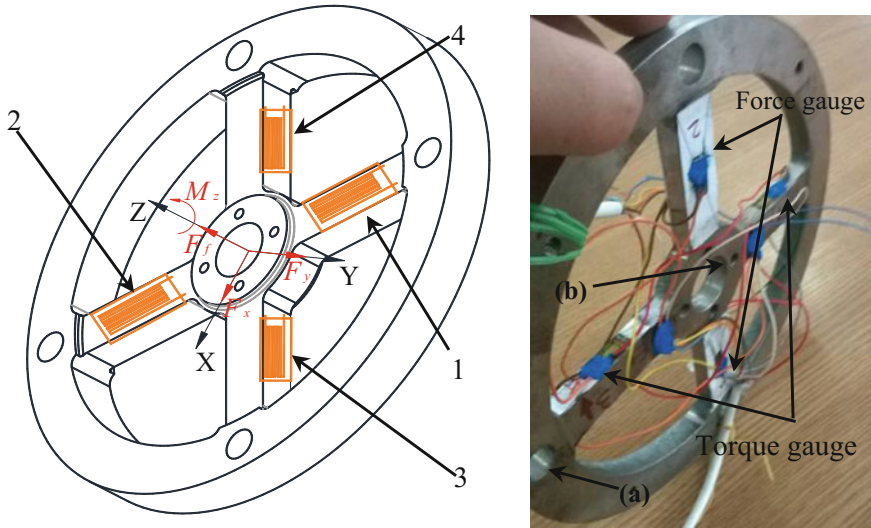
The elastic elements used for dynamometers construction is described in references [2, 4–6]. Most used elastic elements are octagonal ring, used to measure three force components for turning process.

## 2 Experimental Setup

Drilling is a manufacturing process used to cut a hole into a metal piece. Similar processes to drilling are counterboring and tapping that is based on the same kinematics, but instead uses other tools. The forces and moments which appear during drilling are presented in Fig. 1, correlated to the fixed reference system attached to the spoked wheel elastic element. As can be seen at holes machining it appears a drilling moment  $M_z$ , two deflective forces  $F_x$ ,  $F_y$  and a feed force  $F_f$ . It is two possibilities of forces and torque measurement for the drill process, either using stationary or rotating dynamometers. To existing stationary dynamometers, the forces are acquired in three directions but the torque will not be measured directly, instead will be computed from force sensors measurements signal [2]. Proposed solution of dynamometer can measure only two parameters, the drill torque  $M_z$  and feed force  $F_f$ .

Proposed and designed solution is a stationary type dynamometer, mounted on the CNC machine table. The principle of measuring of the dynamometer is based on the deformation measurement of an elastic element.

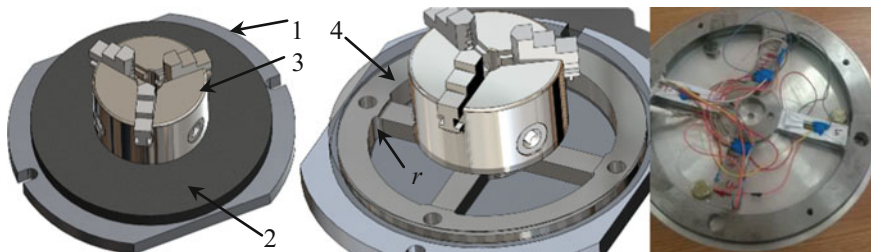
The elastic element used is a four spokes wheel designed and manufactured as in Fig. 1. The strain gauges 1 and 2 are used to measure the feed force  $F_f$ . Strain gauges 3 and 4 measure the deformations produced by the drilling torque  $M_z$ . For a proper measurement the elastic element of the dynamometer must be designed with enough rigidity and manufactured with accuracy, because it is used for dynamic loads. Used strain gauges are type HBM LY, with one measuring grid for strain measurement in one direction and nominal resistance of 120  $\Omega$ . The measuring grid is made of constantan and the material of measuring grid support is polyimide. The strain gauge is bonded with cyanoacrylate elastic adhesive (Loctite 480 type) on the wheel beams. To measure force and torque, on the opposite side of the beams



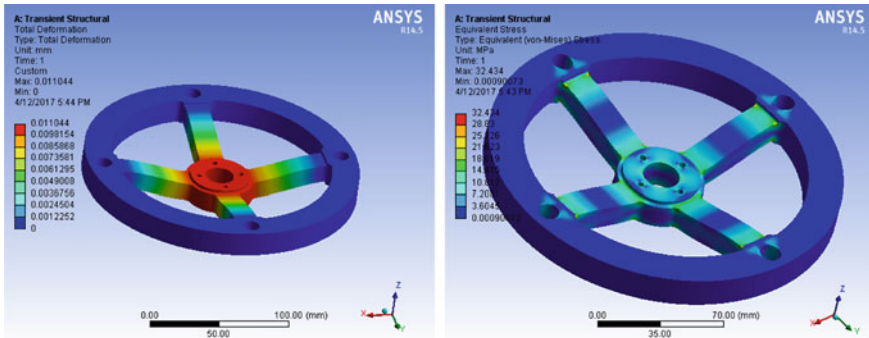
**Fig. 1** Spoked wheel elastic element (design and real model)

(Fig. 1) are bonded another two stain gauges, in order to connect the transducers in a complete Wheatstone electric bridge.

To complete the dynamometer design are manufactured two plates: one inferior plate (1) mounted on the machine plate with bolts, and one superior plate (2) with a device (3) to mount the drilled pieces, as in Fig. 2. The elastic element is mounted with bolts to plate (1) placed on the holes (a), and with bolts placed to holes (b) to the superior plate. In that case the drilling loads are transferred from the upper device (3) to the spoked wheel (3) center with bolts (b). The elastic element (4) is fixed on the exterior diameter to the lower plate (1) with bolts mounted on holes (a). Between plates (1) and (2) it is a 1 mm gap, to allow the elastic element (4) deformations. The gap is isolated with silicone rubber to prevent cooling fluid to reaches the strain gauge electric circuits.



**Fig. 2** Spoked wheel elastic element (design and real model)

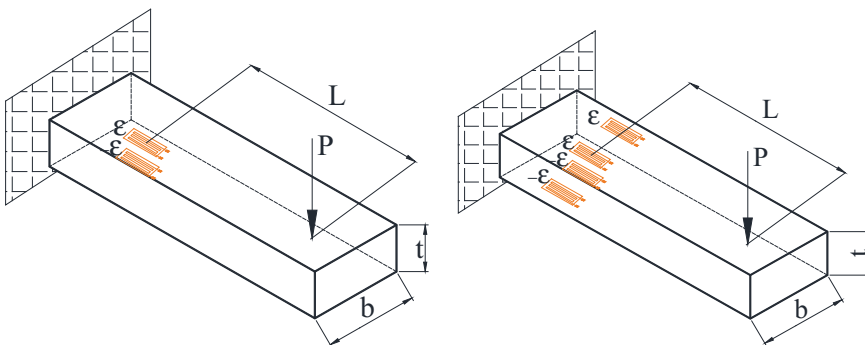


**Fig. 3** Spoked wheel FEA analysis (computed elastic deformation and equivalent stress maps)

To verify the elastic element deformations, it is performed a finite elements analysis in ANSYS, considering the torque of 800 Nmm and the feeding force of 1000 N. The maximum value of elastic deformation is 0.011044 mm, and at middle of the beam the elastic deformation is 0.0061356 mm, as shown in Fig. 3. The equivalent von Mises Stress at the middle of the beam element is 7.2 MPa, and maximum value of stress at the connection area ( $r$  indication, in Fig. 2) is of 32 MPa. So the element (4) has enough stiffness to measure deformations in a dynamic regime.

### 2.1 Setting the Wheatstone Bridges

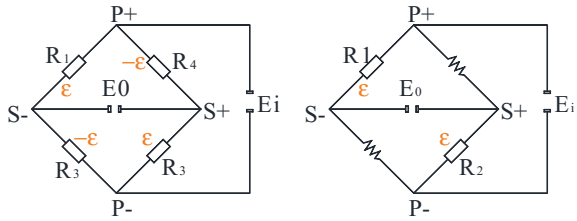
The physical arrangement of the strain gauges and electric connections are described in Fig. 4. For the half bridge configuration, in Fig. 5, are used two axial



**Fig. 4** Bending beam in half bridge and full bridge configuration



**Fig. 5** Full bridge and half bridge Wheatstone montage



gauges. The lower surface gauge is located under the gage on the top, and they measure bending stains with equal magnitude and opposite signs. Any resistance changes of the active gage produced by axial load will be canceled as a result of that configuration, because two active strain gauge are positioned in adjacent arms of the electric connection type Wheatstone bridge. In full bridge connection of the stain gauges, because the strains produced by bending are equal as magnitude but opposite as sign, the bridge voltage output is double by that produced by a single strain gauge, to the same load.

The elastic deformation of the beams from Fig. 4, are computed with Eq. (1).

$$\epsilon = \frac{6PL}{Ebt^2} \tag{1}$$

The strain which occurs in the strain gauges can be calculated with Eq. (2).

$$\frac{\Delta R}{R} = k \frac{\Delta L}{L_0} \tag{2}$$

where:  $\Delta R$ —differential resistance;  $R$ —resistance of the strain gauge before application of the voltage ( $\Omega$ );  $k$ —gauge factor, equal with 2;  $\Delta L$ —elongation due to the stress (mm);  $L_0$ —initial length;  $\Delta L/L_0 = \epsilon$ .

The output voltage of the Wheatstone bridge (Fig. 5), can be expressed as Eq. (3):

$$\frac{E_0}{E_i} = \frac{R_1}{R_1 + R_2} - \frac{R_4}{R_3 + R_4} \tag{3}$$

where,  $E_0$  is the bridge output voltage;  $E_i$  represent the bridge excitation voltage;  $R_1, R_2, R_3$  and  $R_4$  are the resistances of the strain gauges. Because the gauges have the same resistance, the full bridge output can be expressed as Eq. (4):

$$\frac{E_0}{E_i} = \left( \frac{R_1 + \Delta R_1}{2R_1 + \Delta R_1} - \frac{1}{2} \right) = \frac{\Delta R_1/R_1}{4 + 2(\Delta R_1/R_1)} \tag{4}$$

For the beams represented in Fig. 4, the output in full bridge configuration is computed with relation:  $E_0/E_i = F \cdot \epsilon$ , and for the half bridge with relation:  $E_0/E_i = F \cdot \epsilon/2 + F \cdot \epsilon$ .

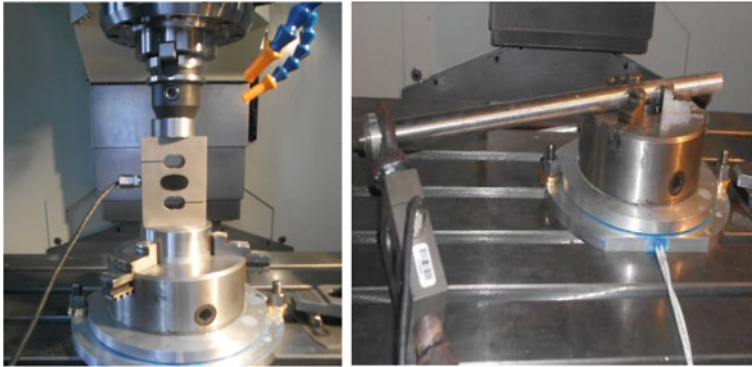


Fig. 6 Dynamometer calibration for measure of drill feed force and torque

### 2.2 Dynamometer Calibration

To establish the linear correlation from the elastic deflection of the deformable element (4) and loads, the dynamometer was calibrated. The calibration was made for the drill torque and feed force, which are able to be measured. The calibration montage is shown in Fig. 6. The principle consists in applying a known force and torque and registering the deformations of the strain gauge transducer mounted on the wheel (4). Obtained dependencies are shown in Fig. 7.

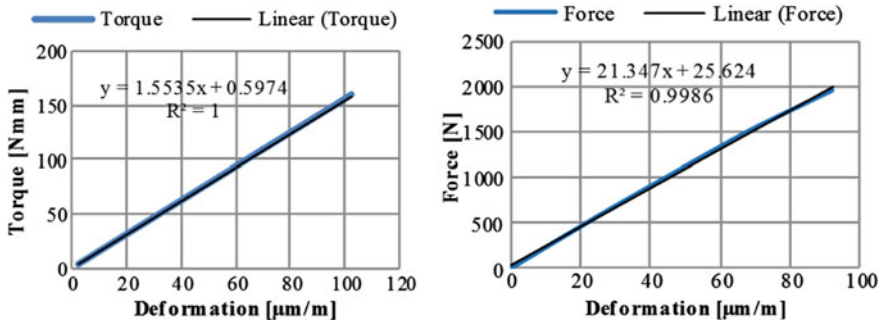


Fig. 7 Calibration results for torque and feed force measurement



**Fig. 8** Used equipment for the experimental measurement

### 3 Obtained Results

A set of drilling test was performed on fifteen circular pieces made from X17CrNi16 alloy steel, presented in Fig. 8. The used drill is type HSS-G, 8 mm diameter, manufactured by Bosch. The drill is mounted on a BT elastic cone, as shown in Fig. 8. In order to establish the drilling parameters values are considered the recommendations of the tools producer Walter. So, considering that the material of the piece is alloy steel, with ferrite structure, annealed and with a hardness of 200 HB, it is recommended a cutting speed of 11 m/min and the value of 0,094 mm/rotation for the advance. The dynamometer is mounted on a CNC machine, type YMC-1050, to perform drill operations, as is presented in Fig. 8. The technologic process it is designed in TOP SOLID software, used for CNC machining. For data acquisition and storage, it is used the HBM MGCPlus acquisition system and Catman AP operating software, installed on a Windows XP operating system.

Experimental obtained results consist in the graphics of feed force and drilling torque variation, as presented in Fig. 9. The preliminary data obtained are strain gauge transducers deformations, in  $\mu\text{m/m}$ . The data are transferred into Excel program, and considering the calibration coefficients for each transducer, presented in Fig. 7, are computed and represented the drilling parameters. The first graphic corresponds to a slow advance motion (0.08 mm/rot), the hole is machined in 8.5 s. The feed force is around 400 N and drill torque is from 800 to 1200 daN mm. The next representations correspond to a hole machined with an increased advance motion (0.16 mm/rot), this is the reason for an increased value for the measured parameters. For this cutting regime, the measured parameters are increase, the feed force reaches 700 N and the drilling torque 1900–2000 daN mm.

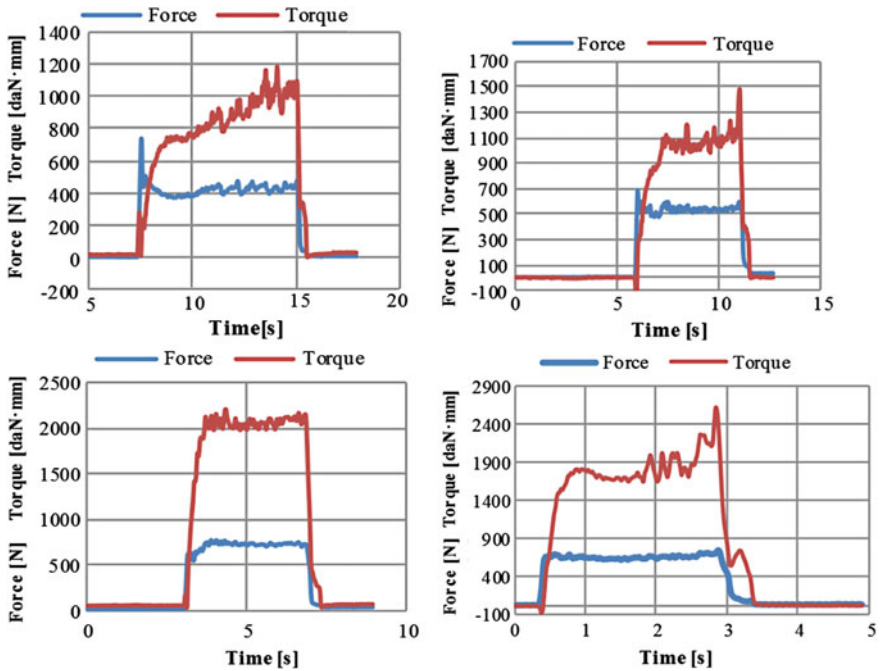


Fig. 9 Obtained experimental results

## 4 Conclusions

In this study a strain gauge based dynamometer for drilling operation is developed and tested. The dynamometer is designed to measure the axial feed force  $F_f$  and drilling torque  $M_z$ . The dynamometer was designed to measure a maximum force of 3000 N and a maximum torque of 30 Nm, and the sensibility of the system is  $\pm 0.2$  N. For establish the accuracy the dynamometer was calibrated statically and subjected to eccentricity test. For accurate results the machined axis hole must be placed into a 20 mm radius from the spoked wheel center. The obtained results for machining tests performed at different drilling parameters, shows the reliability and accuracy of designed dynamometer. Although the dynamometer was conceived primary for drilling, it can be used also for milling, counterboring.

## References

1. Ahmadi K, Savilov A (2015) Modeling the mechanics and dynamics of arbitrary edge drills. *Int J Mach Tools Manuf* 89:208–220
2. Ciurezu L, Dumitru N, Geonea I (2015) Experimental research regarding the influence of cutting regime on the wear of drills at steel processing. *Fiability Durab Suppl* 1:118–122

3. Godfrey CO, Kumar S (2006) Response surface methodology-based approach to CNC drilling operations. *J Mater Process Technol* 171(1):41–47
4. Korkut I (2003) A dynamometer design and its construction for milling operation. *Mater Des* 24:631–637
5. Sedat K (2007) Analysis of drill dynamometer with octagonal ring type transducers for monitoring of cutting forces in drilling and allied process. *Mater Des* 28:673–685
6. Sedat K (2007) Performance testing of a constructed drilling dynamometer by deriving empirical equations for drill torque and thrust on SAE 1020 steel. *Mater Des* 28:1780–1793
7. Stanimir A, Pascu I-C, Buzatu Ș, Geonea I (2008) Chip formation and cutting force in the machining of hardened RUL IV steel. In: *Annals of the ORADEA university, fascicle of management and technological engineering, vol VII (XVII)*, pp 1812–1817 (2008)
8. Suleyman Y, Faruk U (2006) A dynamometer design for measurement the cutting forces on turning. *Measurement* 39:80–89

# Frictional Contact Study of the Chain Link/Polyamide Contact



M.-T. Lateş, C. C. Gavrilă and R. Papuc

**Abstract** This paper has as subject, in a first stage, the experimental study of dynamic friction coefficients between the links of a toothed chain (steel) and two chain guides, made from PAX and PA66, in lubricated conditions. Then there are highlighted the characteristics of the contact area between the toothed links and the guide fragments by using the finite element method. At the end of the paper there are presented the conclusions regarding the tests and the finite element modelling of the frictional contact between the chain link and the PAX.

**Keywords** Tribometer · Friction coefficient · Guide · Finite elements

## 1 Introduction

The experimental research made so far had allowed different conclusions on the friction force. This depends on a variety of factors, like: normal force, sliding speed, contact type, quality and surface rugosity, material nature in contact, rigid or elastic character of surfaces, temperature and the presence of some films on the sliding surface (lubricants, impurities). Implicitly, the dynamic friction coefficient depends in the surfaces state [9–11].

---

M.-T. Lateş (✉) · C. C. Gavrilă · R. Papuc  
Transilvania University of Brasov, Braşov, Romania  
e-mail: latesmt@unitbv.ro

C. C. Gavrilă  
e-mail: cgavrilă@unitbv.ro

R. Papuc  
e-mail: radu.papuc@unitbv.ro

## 2 Describing the UMT Tribometer and Testing Elements

In the experimental determinations of the dynamic friction coefficient between the toothed link and guides is used the UMT tribometer and the reciprocating module, presented in Fig. 1. The tribometer gives informations regarding experimental determinations through a software.

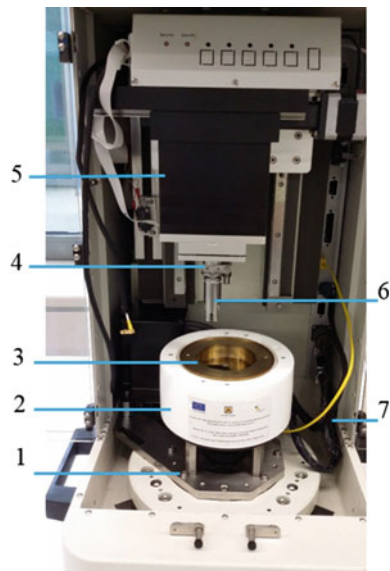
The tribometer components for determining the dynamic friction coefficients are: 1—fixing screws; 2—rotary module; 3—lid; 4—fixation device; 5—positioning device; 6—gripping element—fixing one link; 7—connecting cables.

For the beginning the lid is removed, which has the role to prevent oil expulsion during testing onto the rotary module 2. The rotary module is positioned and fixed on the tribometer UMT with interior hexagonal head screws 1; then the gripping-fixation device of a single link is mounted 7 with screws 6.

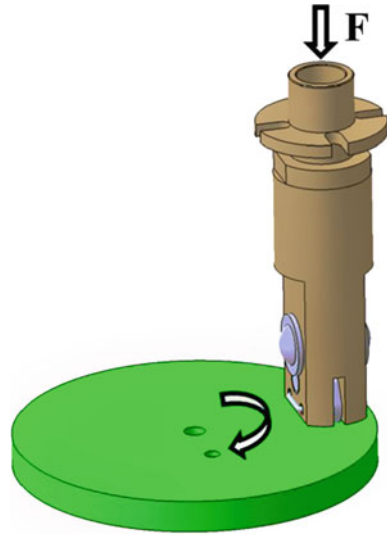
The next stage is mounting the disks made from the guide material (PA66 and Pax) inside the module rotary. The working principle of the tribometer is presented in Fig. 2: the normal force  $F$  is acting on the holder where the chain link is mounted and the polyamide disk is rotating.

The positioning is made through an interior hexagonal head screw 8, an eccentric stud, which enters in the corresponding hole of the disk. In the end, it is mounted on the fixation device 4 of the tribometer, the gripping element of a single link 7. The lubrication was made with a 15 W-40 engine oil.

**Fig. 1** UMT tribometer



**Fig. 2** The working principle of the UMT



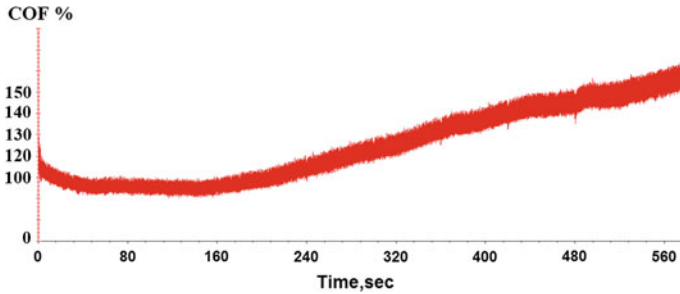
### 3 Experimental Determination of the Dynamic Friction Coefficient

Next, there are presented the experimental tests for the contact between the toothed link and the two disks from the same material as the active surface of the guide—PAx and PA66). For a rigorous determination of the dynamic friction coefficient there were made three series of tests. Thus, the imposed conditions on the first series of tests were normal force  $F_n = 9 \text{ N}$ , to which it corresponds a medium pressure  $p_{med} = 0.451 \text{ MPa}$ ; rotary module speed  $n = 1250 \text{ rot/min}$ , to which it corresponds  $v = 3.27 \text{ m/s}$ ; temperature  $T = 20\text{--}90 \text{ }^\circ\text{C}$ ; test duration  $t = 2 \text{ h}$ ; lubricant: 15 W–40 engine oil. According to the testing conditions and to the amount of the lubricant in the contact area, there are full-filled semi-fluid and boundary lubrication regime conditions.

It must be highlighted that the results regarding the obtained values friction coefficients are presented, as relative values or percentage, representing the parameters dependence for which absolute values are used. This fact was imposed by privacy clauses from including this research in the contract Chain Drive System Dynamic Friction.

After the experimental determinations, it was obtained the variation of the relative dynamic friction coefficient (the values of the friction coefficients were reported to the lowest value) according to the module speed in an imposed time interval. The first series of the experimental determinations was made for the contact between the toothed link and PA46 guide. From Fig. 3 it can be observed that for the contact between the toothed link and PA46 guide, the dynamic friction coefficient, after a quasi-constant stage, the plot increases.



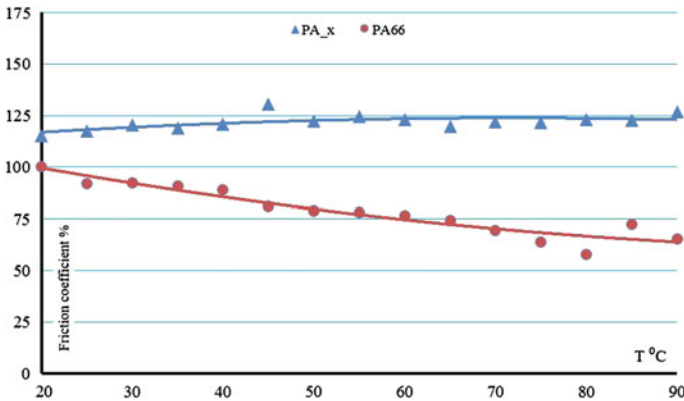


**Fig. 3** The relative dynamic friction coefficient variation between the toothed link and PA46 guide according with time

In Fig. 4 it is presented in comparison the relative dynamic friction coefficient variation according with temperature, based on the results obtained in the experimental determinations for the contact between the toothed link and two types of guide (PAx and PA66); the reference value of the friction coefficient was considered in the case of a 20 °C temperature for the PA66 polyamide.

This diagram highlights the fact that the temperature influences the dynamic friction coefficient variation for the contact between the toothed link and two types of guide. For the contact between the toothed link and PA66 guide, the relative friction coefficient drops as the temperature increases. For the contact between the toothed link and PAx guide it can be observed the relative constant value of the dynamic friction coefficient at the temperature increase.

Next, there are shown the imposed conditions for a second series of tests, thus: the normal force  $F_n = 9\text{ N}$ , to which it corresponds a medium pressure  $p_{med} = 0.775\text{ MPa}$ ; “rotary” module speed  $n = 0\text{--}3000\text{ rot/min}$ , to which it corresponds  $v = 0\text{--}8\text{ m/s}$ ; test duration:  $t = 1\text{ h}$ ; temperature  $T = 20\text{ °C}$ ; lubricant: 15 W-40 engine oil.



**Fig. 4** The dynamic friction coefficient variation according with temperature

Based on the results obtained in the experimental determinations of the friction coefficient in contact between the toothed link and the two types of guide material—PAX and PA66, it was made a comparative diagram of the relative friction coefficient according to speed, presented in Fig. 5; the reference value of the friction coefficient was considered in the case of the PA66 polyamide, for a speed of 0.4 m/s.

For the contact between the link and PA66 guide, the diagram from Fig. 5 shows a slight rise of the dynamic friction coefficient in the speed domain of 0.4–6 m/s, after which it remains constant until the end of the test cycle.

In the conditions of a limited friction regime, the friction coefficient increases with speed indicates the behavior of the toothed link—guide, for the PA66 guide as well as for PAX guide, which does not respect the Stribeck curve.

The relative friction coefficient variation for different forces and constant speeds is presented in the last series of tests. So, the test conditions are: normal force  $F_n = 3, 5, 7$ , respectively 9 N, to which corresponds a medium pressure domain of  $p_{med} = 0.150; 0.250; 0.350; 0.451$  MPa; rotary module torque  $n = 1000$  rot/min, to which corresponds a speed of  $v = 3$  m/s; test time:  $t = 1$  h; temperature  $T = 20$  °C; lubricant: 15 W–40 engine oil.

Based on the average values obtained for the relative friction coefficients there were drawn the diagrams from Fig. 6—for PAX guide, and Fig. 7—for PA66 guide.

From the comparative analysis of the diagrams from Figs. 6, and 7 it is observed that at constant torque and different forces, the relative friction coefficient drops significantly for PA66.

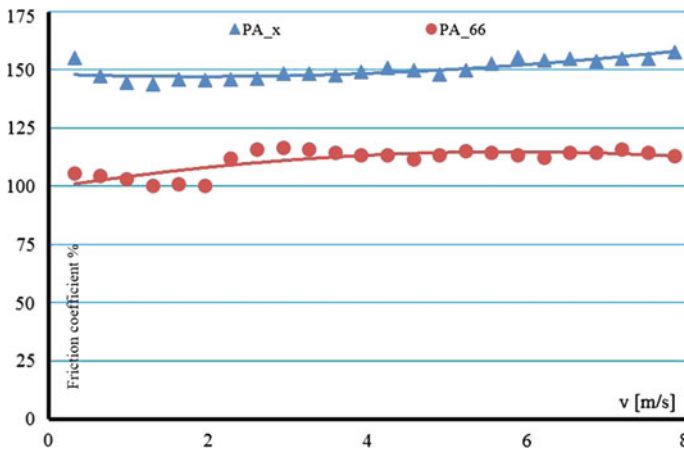


Fig. 5 The dynamic friction coefficient variation according to speed

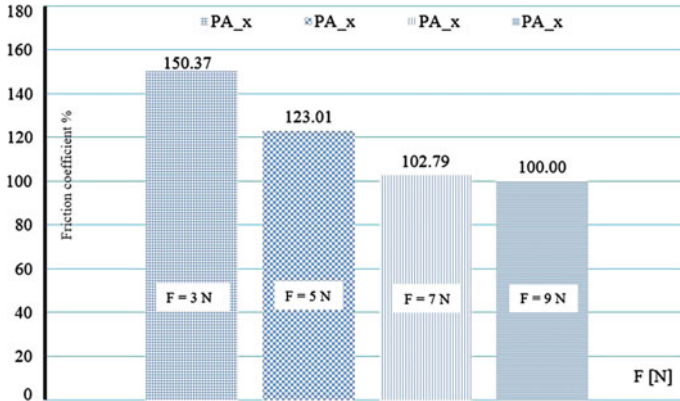


Fig. 6 The relative dynamic friction coefficients variation corresponding to force for PAx guide

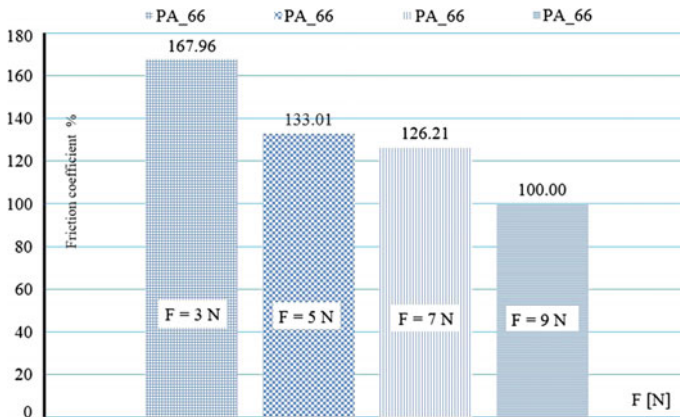


Fig. 7 The relative dynamic friction coefficients variation corresponding to force for PA66 guide

### 4 The Study of Contact Pressure

In order to determine the contact pressures variation between the toothed link and the disk made from the guide material, it will be used the finite element method.

The finite element method (MEF) is a numerical method used to solve partial derivative equations which models the physical systems with an infinite number of freedom degrees. After applying MEF, these partial derivative equations are reduced to systems of algebraic equations, namely to a discrete system with a finite number of freedom degrees [1, 3].

For the numerical evaluation of the studied model it was used the ANSYS.

The model, shown in Fig. 8, was meshed with second order tetrahedron deformable finite elements, with intermediary node, and for the components defined as rigide, the software used for meshing rigide type of elements (Fig. 9).

The materials used in this distributed analysis were PAX polyamide for the guide and steel for the other components. The model was loaded with a normal force of  $F_n = 9\text{ N}$ , resulted in the lubricating condition and for defining the contact between the link and guide was used a value for the friction coefficient of 0.2, determined from the experimental tests in lubricated conditions [6].

After applying the 9 N force, it was obtained the displacements and contact pressure distribution (Fig. 10). The maximum displacement value is 0.00131 mm and is placed in the normal force applying zone; the 0.847 MPa maximum contact pressure is positioned on the contact area between the chain link and the disk and is also presented in Fig. 10.

Fig. 8 Finite element models

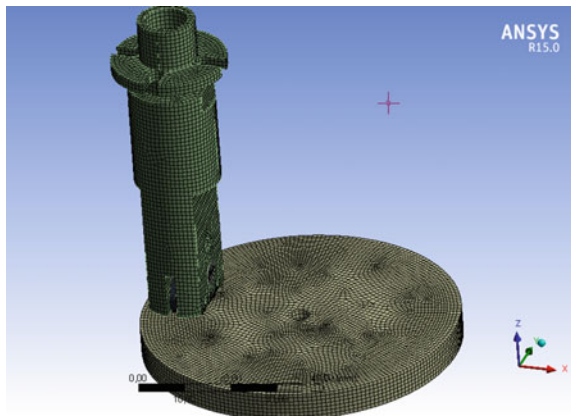
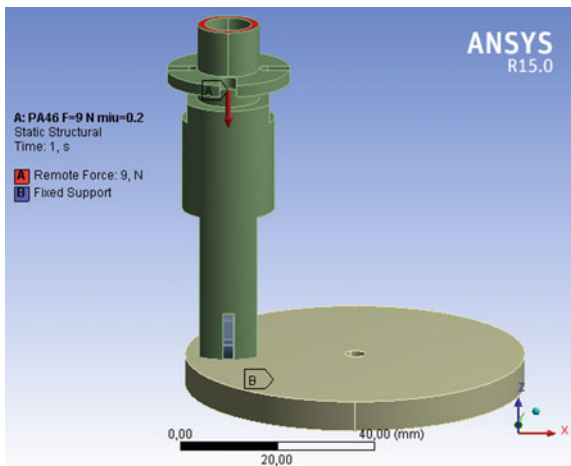


Fig. 9 The loading of the model



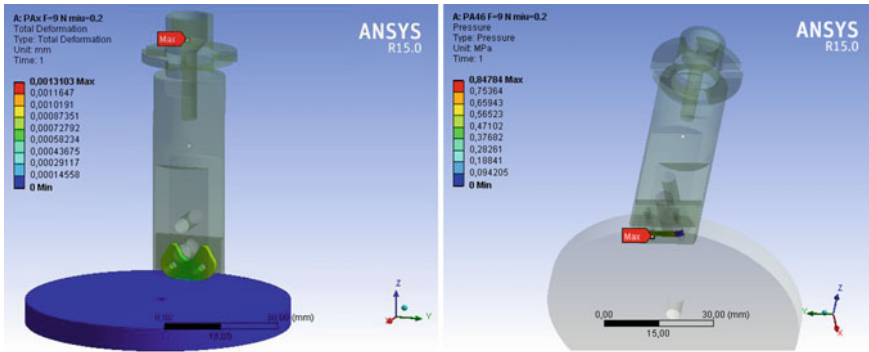


Fig. 10 Displacements and contact pressure distribution

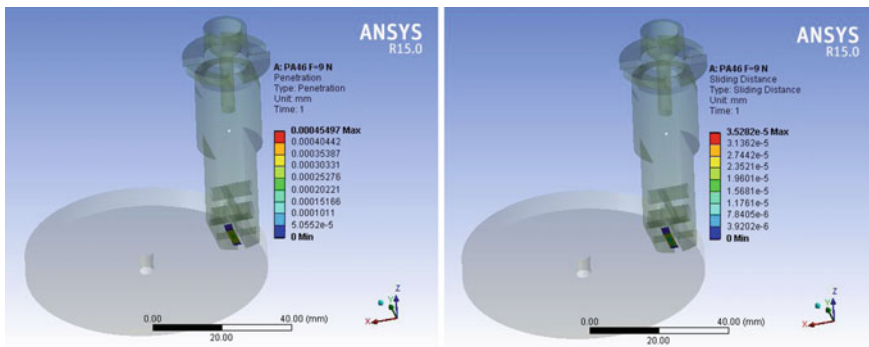


Fig. 11 The penetration and sliding distances values

The values of the penetration and of the sliding distance are presented in Fig. 11; due to the high stiffness values of the materials being in contact, there are obtained small values for the two parameters.

## 5 Conclusions

The paper offers an original and complete frictional contact study of the steel chain link/polyamide contact by achieving tests and finite element modelling. First, by performing test, it is identified the variation of the friction coefficient under different testing conditions (temperature and speed variation); in the second step, the finite element modeling of the chain link/polyamide contact, is achieved by using the value of the friction coefficient determined by tests.

The friction coefficient of link/PA66 guide determined in dynamic and limit friction conditions indicate a better efficiency at high temperatures, and a slight increase by speed and decrease by pressure. By comparison, to PAX, material taken from an existent stretching system, PA66 has better characteristics from friction reducing point of view. These results show that tribologically, the materials analyzed have a specific behavior different by the generally known and characterized by the Stribeck curve.

In concordance with the literature [4, 8], the results related to the friction coefficient, obtained in this paper, are showing that the PAX polyamide has a more stable and better behavior than the PA66 polyamide; the dynamic friction coefficient has a bigger relative decrease with the temperature increasing in the case of the PAX polyamide and a more stable relative variation with the speed. Due to confidentiality reasons (the research is achieved in the frame of a research project with a company, which produces automotive spare parts), the results obtained for the friction coefficient are presented as relative values.

The finite element analyses made for the chain link/PAX contact, shows that there are obtained small values for the contact pressures due to the high mechanical characteristics of the studied polyamide; these results are in concordance with the specific literature [2, 5, 7].

Using the finite element method it could be highlighted the equivalent tensions variation and the contact pressures for the two models. Because the force is transmitted from the applying point to the fixing point is done only through the contacts between components, there were no significantly equivalent tensions.

## References

1. Akin JE (1996) Finite element analysis for undergraduates. Academic Press, Orlando, FL, USA
2. Chiu F-C, Kao G-F (2012) Polyamide 46/multi-walled carbon nanotube nanocomposites with enhanced thermal, electrical and mechanical properties in composites, Part A, nr 43, pp 208–218
3. Goenka PK (1984) Dyn Loaded J Bear Finite Elem Method Anal Trans ASME Ser F J Tribol 106:429–439
4. De Monte M, Moosbrugger E, Quaresimin M (2010) Influence of temperature and thickness on the off-axis behavior of short glass fiber reinforced polyamide 6.6—Quasi-static loading. J Compos, part A, nr 41:859–871
5. Mouhmid B, Imad A, Benseddig N, Lecompte D (2009) An experimental analysis of fracture mechanics of short glass fibre reinforced polyamide 6.6 (SGFR-PA66). J Compos Sci Technol nr 69:2521–2526
6. Papuc R, Bobancu S, Velicu R., Eftimie L (2016) Static friction coefficient between metal-plastic couple of materials. J Balk Tribol Assoc 22(1A-I):556–565
7. Papuc R, Velicu R (2013) Tribological study of guide-chain contact. In: Annals of the Oradea university fascicle of management and technological engineering, vol XII (XXII), nr 1, pp 257–260

8. Van Ruiten J, Proost R, Meuwissen M (2012) How the choice of the polyamide type in timing chains tensioning systems affects the CO<sub>2</sub> emission and fuel economy of internal combustion engines in Presentation at VDI Veertrieb un Zylinderkopf, Nov 28th
9. Stachowiak GW, Batchelor AW (2005) Engineering tribology, 3rd edn. Elsevier, Burlington
10. Shizhu W, Ping H (2012) Principles of tribology. Wiley Publishing House, Singapore
11. Williams J (2011) Engineering tribology. Cambridge University Press, USA

# Influence of Number of Teeth and Centrifugal Force on Forces Distribution on Silent Chain Transmissions



L. Jurj and R. Velicu

**Abstract** The aim of this paper is to define and to analyse the theoretical contact forces that appear in a sprocket—silent chain joint. The contact force between the links and the teeth flanks of the sprocket can be considered as a reaction to the axial force (tensioning force) transmitted throughout the pins. The centrifugal force is considered to be constant and the friction between the elements is not considered. This paper is presenting an analysis of forces in the joints of links and between links and sprocket in order to establish a distribution along links and the influence of number of teeth of sprockets and centrifugal force on number of links transmitting the load.

**Keywords** Silent chain joint · Contact of gearing · Centrifugal force  
Force distribution

## 1 Introduction

Dynamics of the chain drive systems became of great interest in the automotive industry with the increase in importance of friction, noise and vibration.

Chain drives are used because of the high power, non-slip, relatively light weight and compact power transmission compared to belt or gear transmissions, but usually with increased noise and vibration. Timing chain transmissions are used more and more in combustion engines. In comparison with synchronized belt drives, they ensure the transmission of higher torque for a longer aggregate maintenance-free period [1].

Silent chains as timing chains have a great interest considering performance improvements of automobile engine systems, which can generate significant

---

L. Jurj (✉) · R. Velicu  
Transylvania University of Brasov, Braşov, Romania  
e-mail: jurjlenard@gmail.com

R. Velicu  
e-mail: rvelicu@unitbv.ro



improvements in reducing fuel and oil consumption, increase of engine power and torque, reducing harmful exhaust emissions; improved reliability and engine life and longer service intervals [3, 4].

References of theoretical studies on silent chain transmissions come from early 20th century [2]. A geometrical study of chain transmissions with two sprockets and a guide is presented in [9].

An FEM study of forces distribution on links of a silent chain, at the contact with a circular guide, is presented in [6] and pressure distribution between a silent chain and a guide, resulted from a tribological study, is presented in [8].

A comprehensive approach on general chain transmissions, including aspect of silent chains is [10] and experimental results on load distribution between bush chains and sprockets is presented in [7].

## 2 Theoretical Model

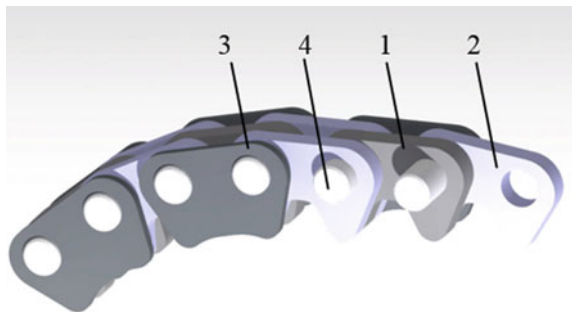
This paper intends to study the theoretical contact which appears between the silent chain's elements and the sprockets. Silent chains, Fig. 1, are usually composed of 1—inner plates, 2—middle plates, 3—outer plates and 4—pin. This type of chains are not standardized, there are different shapes and sizes of the plates; different number of inner and middle plates.

The theoretical force distribution takes in account the forces that appear between the sprocket—chain link contact— $F_{z1}$ , the tensioning force component between the silent chain links, that is transmitted by the plate—pin joint— $F_1$ , and the centrifugal force that appear during the rotational speed of the chain transmission— $F_c$ . Figure 2 presents the theoretical model of the silent chain transmission.

In this case the force distribution is varying within an angle  $\varphi$  from  $-\alpha$  to  $\alpha$ , where  $\alpha$  represents the half of the pitch angle on the sprocket. This is depending on the number of teeth that are machined on the sprocket.

The profile angle  $\gamma$  is the angle between the axis of a tooth and its flank line (plate's exterior flank). Three values of the profile angle are considered in the following study.

**Fig. 1** Silent chain assembly



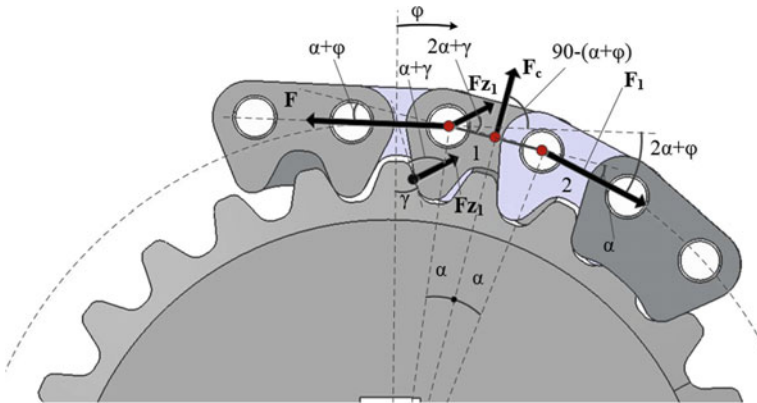


Fig. 2 Force distribution on silent chain transmission

The calculus relations for the components  $F_1$  and  $F_{z1}$  have been established from the equilibrium of link 1 [5] depending on initial tensioning of the chain  $F$ :

$$F_1 = \frac{F \sin(\alpha + \gamma - \varphi) + F_c \cos(2\alpha + \gamma)}{\sin(3\alpha + \gamma)} \quad (1)$$

$$F_{z1} = \frac{F_1 \sin(\varphi + 2\alpha) - F_c \cos(\varphi + \alpha)}{\sin(\alpha + \gamma - \varphi)} \quad (2)$$

The following equations define the other parameters:

$$\alpha = \frac{360}{2z} \quad (3)$$

$$v_t = \frac{\pi \cdot D_p \cdot n}{1000 \cdot 60} \quad (4)$$

$$F_c = \frac{m_{\text{chain}} \cdot v_t^2}{\frac{D_p}{2} \cdot 1000} \quad (5)$$

where  $z$  is the number of teeth on the sprocket,  $D_p$  is the pitch diameter of the sprocket,  $n$  is the rotational speed of the chain transmission,  $v_t$  is the tangential speed at the pitch diameter and  $m_{\text{chain}}$  is the mass of the silent chain.

For the next link  $F_1$  will take the role of the input tensioning ( $F$ ). The relative angle between the links will be constant, thus  $\varphi$  will have the value of the pitch angle  $\alpha$ . The force  $F_1$  for the second link will be  $F_2$ , while  $F_{z1}$  will become  $F_{z2}$ . The forces will still be depending on  $\varphi$  angle of rotation since all the previous components depend on  $F$  and  $\varphi$ . For the next links the forces can be computed with the following generalized formulas [5]:

$$F_m = \frac{F_{m-1} \sin(\gamma) + F_c \cos(2\alpha + \gamma)}{\sin(3\alpha + \gamma)} \tag{6}$$

$$F_{zm} = \frac{F_{m-1} \sin(3\alpha) - F_c \cos(2\alpha)}{\sin(2\gamma)} \tag{7}$$

where  $m$  represents the number of the corresponding link of the silent chain.

### 3 Results—Forces Distribution

The model for the force equilibrium presented above has been applied for  $z$  (27, 60, 90) and three values of profile angle  $\gamma$  (20°, 25°, 30°). Table 1 presents the input parameters calculated according to [11], while Figs. 3 and 4 presents the theoretical tensioning and contact force distribution for  $z = 27$ . For these the centrifugal force was not considered, to see clearly the effect of the number of teeth and the contact angle over the force distribution.

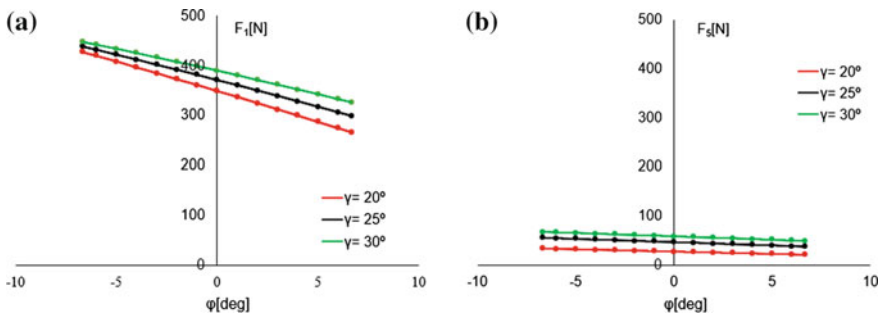
Figures 5 and 6, 7 and 8 present the tensioning and contact force distribution for  $z = 60$  and  $z = 90$  without taking into account the centrifugal force.

The centrifugal force’s effect can be seen on Fig. 9 and 10 for  $z = 90$ ,  $\gamma$  (20°, 25°, 30°),  $n = 3000$  (rpm), where  $F_c = 19.2304$  (N/plate).

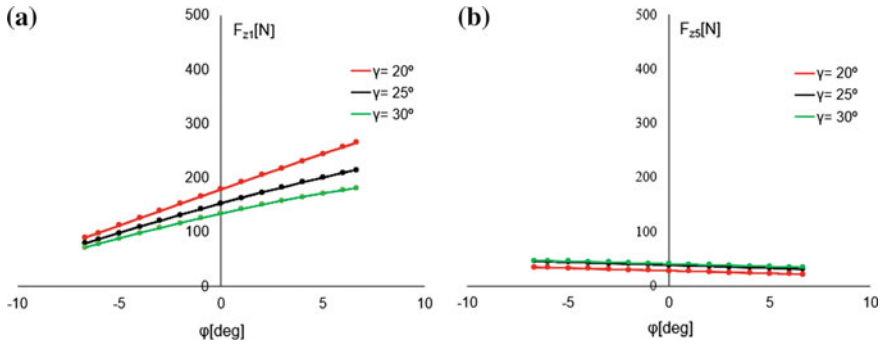
For comparison Fig. 11 shows the contact force distribution for  $z = 90$ ,  $\gamma$  (20°, 25°, 30°),  $n = 1500$  (rpm), where  $F_c = 4.8076$  (N/plate).

**Table 1** Input gear parameters

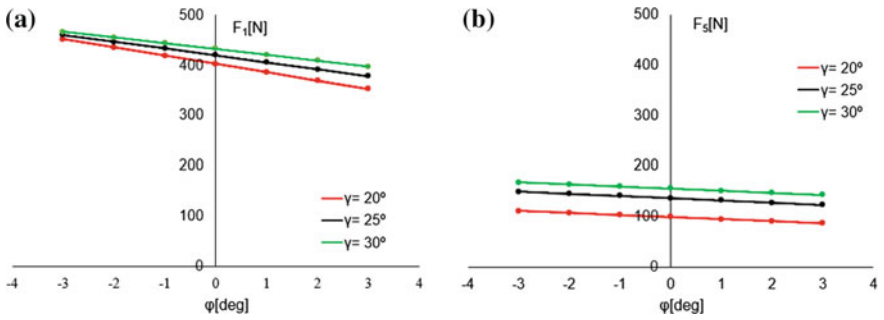
$z$ (-)	$F$ (N)	$\alpha$ (°)	$P$ (mm)	$D_p$ (mm)
27	500	6.66	8	68.9103
60	500	3	8	152.8585
90	500	2	8	229.2296



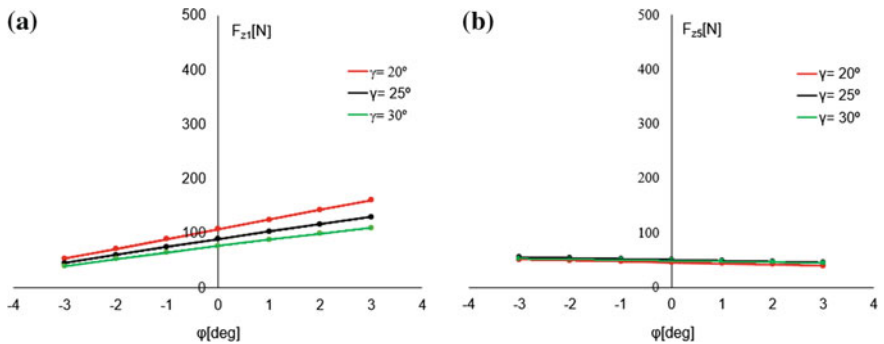
**Fig. 3** Tensioning force distribution on the first (a) and the fifth (b) link for three values of the profile angle  $\gamma$  (20°, 25°, 30°),  $z = 27$ , centrifugal force not considered



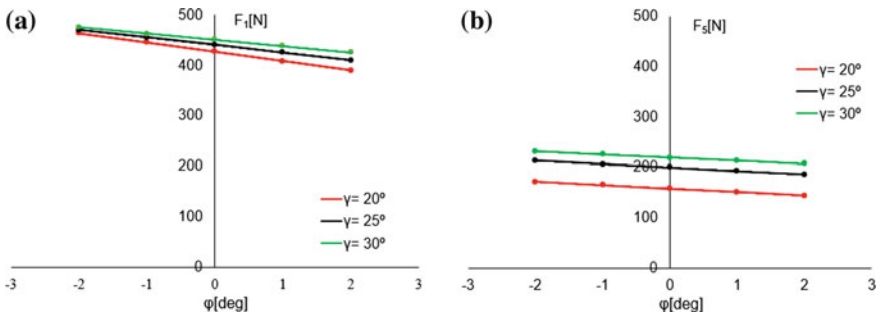
**Fig. 4** The contact force distribution on the first (a) link and the fifth (b) for three values of the profile angle  $\gamma$  ( $20^\circ$ ,  $25^\circ$ ,  $30^\circ$ ),  $z = 27$ , centrifugal force not considered



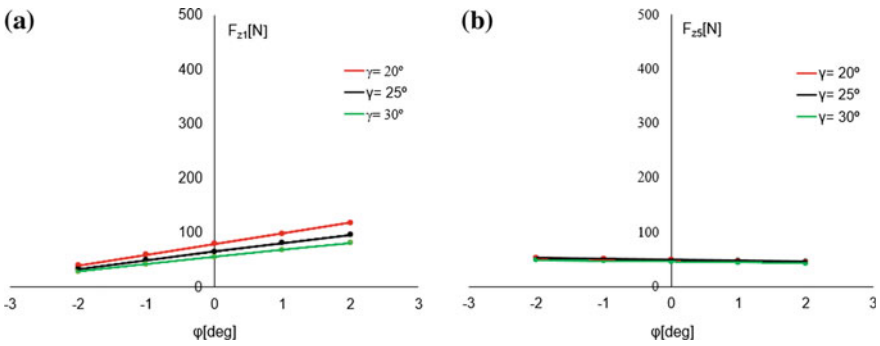
**Fig. 5** Tensioning force distribution on the first (a) and the fifth (b) link for three values of the profile angle  $\gamma$  ( $20^\circ$ ,  $25^\circ$ ,  $30^\circ$ ),  $z = 60$ , centrifugal force not considered



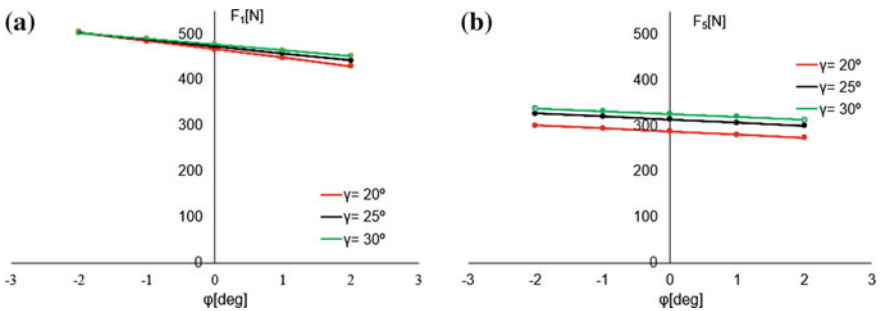
**Fig. 6** The contact force distribution on the first (a) link and the fifth (b) for three values of the profile angle  $\gamma$  ( $20^\circ$ ,  $25^\circ$ ,  $30^\circ$ ),  $z = 60$ , centrifugal force not considered



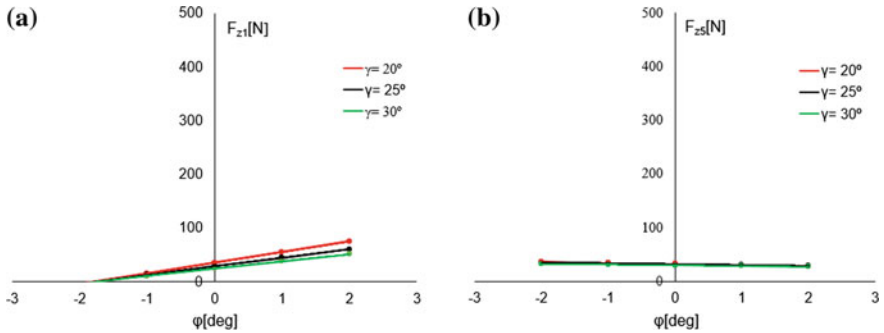
**Fig. 7** Tensioning force distribution on the first (a) and the fifth (b) link for three values of the profile angle  $\gamma$  ( $20^\circ$ ,  $25^\circ$ ,  $30^\circ$ ),  $z = 90$ , centrifugal force not considered



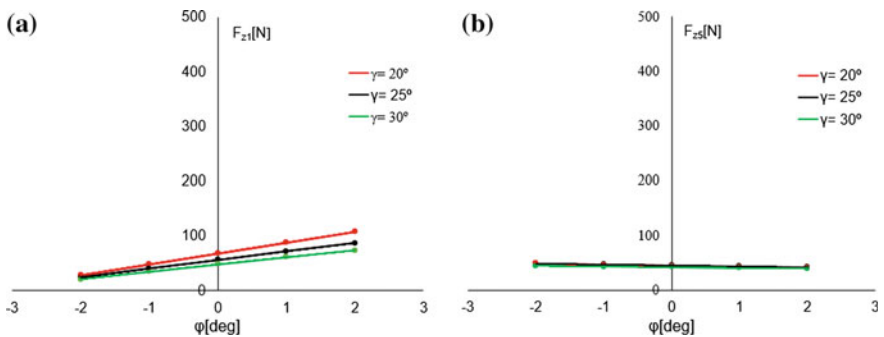
**Fig. 8** The contact force distribution on the first (a) link and the fifth (b) for three values of the profile angle  $\gamma$  ( $20^\circ$ ,  $25^\circ$ ,  $30^\circ$ ),  $z = 90$ , centrifugal force not considered



**Fig. 9** Tensioning force distribution on the first (a) and the fifth (b) link for three values of the profile angle  $\gamma$  ( $20^\circ$ ,  $25^\circ$ ,  $30^\circ$ ),  $z = 90$ ,  $n = 3000$  (rpm), centrifugal force considered



**Fig. 10** The contact force distribution on the first (a) link and the fifth (b) for three values of the profile angle  $\gamma$  ( $20^\circ$ ,  $25^\circ$ ,  $30^\circ$ ),  $z = 90$ ,  $n = 3000$  (rpm), centrifugal force considered



**Fig. 11** The contact force distribution on the first (a) link and the fifth (b) for three values of the profile angle  $\gamma$  ( $20^\circ$ ,  $25^\circ$ ,  $30^\circ$ ),  $z = 90$ ,  $n = 1500$  (rpm), centrifugal force considered

The analysis of the theoretical force distribution shows that the tensioning force in the silent chain transmission is distributed on several links and the forces are decreasing with the distance from the first link.

The increase of number of teeth of the sprocket (decrease of pitch angle  $\alpha$ ) determines a slower decrease of forces with the distance from the first link, so higher number of links transmitting the load.

The profile angle has more influence on the tensioning between links  $F_m$  at bigger number of teeth and almost no influence on sprocket—chain link contact force  $F_{zm}$  with increasing  $m$ .

The centrifugal force effect creates an increase of tensioning between links  $F_m$  and decrease of sprocket—chain link contact force  $F_{zm}$ , so smaller number of links are in contact with the sprocket.

Negative computed values for sprocket—chain link contact force  $F_{zm}$  are actually zero values and means no contact force between link and sprocket exists.

## 4 Conclusions

The main conclusion from theoretical analyze of the silent chain contact forces is that the number of chain links in contact is influenced by number of teeth of the sprocket, value of centrifugal force and the profile angle of the tooth flank.

However, this model must be improved by considering the friction between pins and plates and between plates and sprocket. The dynamics of the chain must also be considered.

## References

1. Belmer S, Fink T, Lorenz I, Neukirchner H (2005) Steuertriebe für Verbrennungsmotoren. Konzeption, Auslegung und Basiskonstruktion, *MTZ Motortechnische Zeitschrift* 66, no 6, pp 466–475
2. Cautley JR (2012) Roller and silent chains. SAE Technical Paper 140021, (1914). In: Holmberg K, Andersson P, Erdemir A (eds) *Global energy consumption due to friction in passenger cars*. *Tribology Int* 47(14)
3. Hyakutake T, Inagaki M, Matsuda M, Hakamada N, Teramachi Y (2001) Measurement of friction in timing chain. *JSAE Rev* 22:5
4. Jurj L, Velicu R, Saulescu R (2017) Influence of profile angle on forces distribution on silent chain transmissions. *Annals of the Oradea University, Fascicle of Management and Technological Engineering*, vol XXVI, (XVI) Oradea
5. Lates MT, Papuc R, Gavrilă CC (2016) Tribological modelling of the normal forces distribution on the toothed chain links. *Annals of the Oradea University, Fascicle of Management and Technological Engineering*, vol XV (XXV)/1, pp 97–102
6. Najj MR, Marshek K (1983) Experimental determination of the roller chain load distribution. *J Mech Transm Autom Des* 105:331–338
7. Papuc R, Gavrilă CC, Lates M (2016) Modeling the pressure distribution in the contact between guide and chain. *Bulletin of the Transilvania University of Brasov*, vol 9(58), no 2, Series I. In: *Proceedings of the IXth international conference on product design, robotics, advanced mechanical & mechatronic systems and innovation—Prasic*, pp 197–202
8. Papuc R, Velicu R, Gavrilă CC (2014) Geometrical study of guide-chain contact, for general chain transmission. *Annals of the Oradea University, Fascicle of Management and Technological Engineering*, vol XXIII (XIII), 2014/1, pp 123–126
9. Pfalzgraf JH (2011) *Experimentelle Reibleistungsuntersuchungen an Kettentrieben im Verbrennungsmotor*. PhD thesis, Technical University Munchen
10. Schaeffler Group Automotive (2009) *Schaeffler Chain Drive Systems*. SCDS Catalogue, pp 8–10
11. Schwaderlapp M, Koch F, Dohmen J (2000) Friction reduction—the engine’s mechanical contribution to saving fuel. In: *Seoul 2000 FISITA world automotive congress*, Seoul, Korea

# Influence of Chain Pitch Increase on Bush-Sprocket Contact for Bush Chain Drives



R. Velicu, R. Saulescu and L. Jurj

**Abstract** One of the chain types used in machine construction is the bush chain. These types of chains can be with long or short links. In this paper it is proposed a case study, in which there is considered a standardized bush chain with short links, with known geometry of chain and sprocket. This is the starting point in the establishment of the contact between the sprocket and the chain during functioning. This will enable the precise determination of the static contact forces (value and direction). According to the literature, the pitch of a new chain should be bigger than its nominal value with up to 0.1%. In functioning, the pitch of the chain increases due to the wear of pin-bush joints and due to elastic deformation. This work proposes a comparative study of the most representative parameter, the contact angle ( $\alpha$ ) between the sprocket and the chain bush, for different sprocket sizes and different deviations of the chain pitch to the standard, which influence the contact forces and transmission behaviour. The evolution of the contact angle during gearing, in function of the sprocket's number of teeth and the pitch difference ( $x$ ), is highlighted with the help of the numerical simulations which permit drawing of some recommendations regarding the functionality of the transmission, minimization of vibrations or taking out the chain from functioning.

**Keywords** Chain drive · Kinematic · Contact point · Bush-sprocket Contact angle

---

R. Velicu (✉) · R. Saulescu · L. Jurj  
Transilvania University of Brasov, Braşov, Romania  
e-mail: rvelicu@unitbv.ro

R. Saulescu  
e-mail: rsaulescu@unitbv.ro

L. Jurj  
e-mail: jurjlenard@gmail.com



## 1 Introduction

Chain transmissions used in automotive industry, regularly work at high loads and rotational speeds, fact that involve knowhow about their dynamics in order to optimize or decrease vibrations. These vibrations may be caused by the geometry of the transmission, incorrect functioning or excessive wear of the transmission.

A study regarding the geometry optimization of such transmission is presented in [10], optimization with the hypothesis that the chain elongation is done with a constant pitch; the influence of the number of teeth over the maximum pitch is presented in [2], within is stated that this decreases with the number of teeth. Different studies regarding the contact stress between the pin and the bush [3, 4], the geometry [6] or the stress between the chain guide and the chain [7], the wear phenomenon that appear between the bush and the sprocket, and also the behaviour of the bush elements, are analysed in [5], within there is stated the need to understand of such phenomenon, the contact surfaces and the contact angle between the bush and the chain. There are also discussions about the contact angle between the bush and the sprocket in [8], where two laborious modeling methods are proposed for the contact. Results from these methods are comparable with experimental ones, and based on these there is stated that the vibrations that appear during functioning of the chain transmission are due to the impact between the chain bush and the sprocket. This impact is directly influenced by the pitch change compared to the nominal dimension, therefor the contact angle analysis between the bush and the sprocket is legitimate.

## 2 Problem Statement

In a bush chain transmission, due to the speeds and the forces that are involved in the contact between the bush and the sprocket, longitudinal and transversal forces appear, that influence the dynamic behaviour of the transmission. Improving these properties presume the increase of the reliability of the transmission and simultaneously keeping for a longer period of time the geometry of the chain and the sprocket.

The change of pitch is one of the main factors that can lead to the failure of the chain transmission [13]. This change comes due to initial pitch deviations of the chain links, which is permitted up to 0.1% from the nominal pitch dimension, and the wear during functioning that can determine a supplementary increase of up to 0.2% of the nominal pitch. If the first two factors are due to internal causes, an external factor that changes the pitch of the chain is the elastic elongation caused by the tensioning forces from the transmission (determines up to 0.3% of the pitch). These deviations directly influence the functioning of the transmission by changing the contact point between the sprocket and the bush; during functioning, because of the above mentioned factors, the bush has an angular movement related to the base

of the socket, describing in this way an angle between the theoretic and real contact point, named in this work as contact angle ( $\alpha_i$ ), that is not permitted to be bigger than the half of the the roller gap angle, limited to  $120^\circ$  [9]. Consequently a case study is proposed that presents the dependency of the contact angle in function of the pitch change (noted as  $x$ ), that can get in the worst case up to 6% of the nominal pitch dimension, for the first 4 contacts ( $i$ ) between the bush and the sprocket. In this study there is proposed to consider a minimal and maximal number of teeth ( $z = 25$  and  $90$ ), recommended in automotive industry.

### 3 Geometric and Kinematic Modeling of the Transmission

In a chain transmission, knowing the real and not the nominal geometry of the sprocket [1] and the bush chain is essential because the contact between these determine the functionality and dynamics of the transmission. For this modeling there is considered a bush chain transmission with short standardized links [14], with the following known parameters: radius of the bush ( $r_B$ ), number of teeth of the sprocket ( $z$ ) and the chain pitch ( $p$ ). Noting  $B_0B_{01} = p$ , chain pitch and  $x\%$  of  $p$  than  $B_kB_{k+1} = B_0B_1 = p + x$  (Fig. 1), respectively  $A_0B_0 = A_1B_1 = A_2B_2 = \dots = A_kB_k$  in which  $A_0B_0 = r_A - r_B$  (Fig. 1a).

For the kinematic modeling and the definition of the geometric parameters, the initial position 0 is considered as the one where the points  $A_0B_0O$  are collinear, for which the first bush in contact with the sprocket ( $i$ ), the contact angle between the bush and the chain ( $\alpha_0$ ) and the deviation angle caused by the elongation of the chain pitch ( $\lambda_0$ ) are zero:  $i = 0, \alpha_0 = 0, \lambda_0 = 0$ .

Applying the general algorithm presented in [9, 12] the contact angle ( $\alpha_i$ ) and the deviation angle ( $\lambda_i$ ) can be determined:

$$B_{i-1}A_i = \sqrt{OB_{i-1}^2 + OA_i^2 - 2OB_{i-1}OA_i \cos(\tau - \lambda_{i-1})} \tag{1}$$

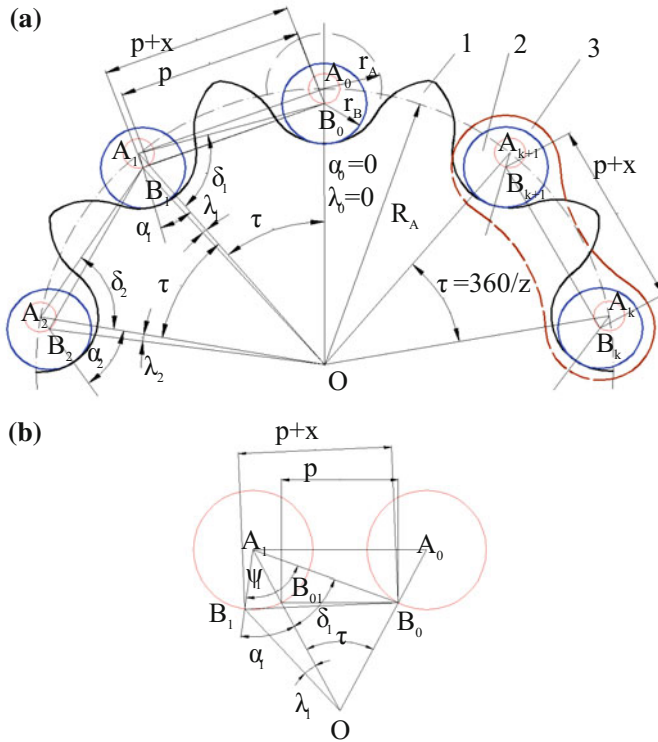
$$\delta_i = \arccos \frac{B_{i-1}A_i^2 + OA_i^2 - OB_{i-1}^2}{2B_{i-1}A_i \cdot OA_i} \tag{2}$$

$$\psi_i = \arccos \frac{B_{i-1}A_i^2 + A_iB_i^2 - B_{i-1}B_i^2}{2B_{i-1}A_i \cdot A_iB_i} \tag{3}$$

$$\alpha_i = \psi_i - \delta_i \tag{4}$$

$$OB_i = \sqrt{OA_i^2 + A_iB_i^2 - 2OA_i \cdot A_iB_i \cos \alpha_i} \tag{5}$$

$$\lambda_i = \arcsin \frac{A_iB_i \sin \alpha_i}{OB_i} \tag{6}$$



**Fig. 1** Contact geometry between the sprocket and the chain bushes: **a** representative geometric parameters (where: 1-sprocket, 2-bush, 3-link between 2 successive bushes) and **b** explanation of the geometric contact parameters  $i = 1$  in relation with the reference  $i = 0$

Finding these parameters is possible with the help of Fig. 1b [11], considering the assembled position, where  $OB_0 = R_A - r_A + r_B$  and  $OA_i = R_A$  (Fig. 1a).

Using the generalized Pythagorean and the sine theorem from  $\Delta OB_0A_1$  there is determined:

$$\delta_1 = \arcsin \frac{OB_0 \sin \tau}{B_0A_1} \tag{7}$$

where:  $B_0A_1 = \sqrt{[(R_A - r_B + r_A)^2 + R_A^2 - 2R_A(R_A - r_B + r_A) \cos \tau]}$ .

From  $\Delta B_0B_1A_1$

$$\psi_1 = \arcsin \frac{B_0A_1^2 + A_1B_1^2 - B_0B_1^2}{2B_0A_1A_1B_1} \tag{8}$$

where:  $B_0B_1^2 = B_0A_1^2 + A_1B_1^2 - 2B_0A_1A_1B_1 \cos \delta_1$ .

With the two before determined geometric angles the contact angle is obtained ( $\alpha_1$ ), for the first contact between the chain (chain bush) and the sprocket, next to the initial 0 position.

$$\alpha_1 = \psi_1 - \delta_1 \tag{9}$$

With the help of  $\Delta OA_1B_1$  the deviation angle can be computed ( $\lambda_1$ ):

$$\lambda_1 = \arcsin \frac{A_1B_1 \sin \alpha_1}{OB_1} \tag{10}$$

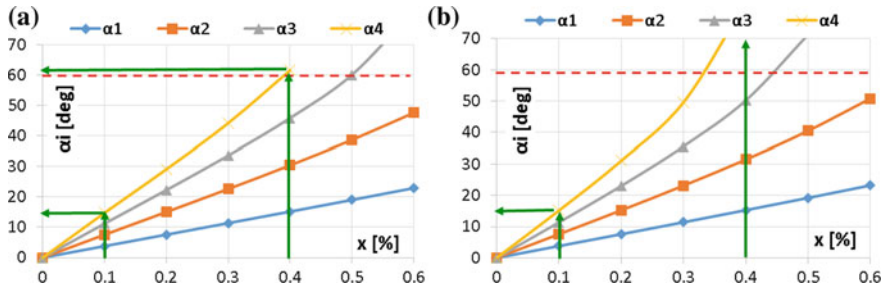
where:  $OB_1 = \sqrt{OA_1^2 + A_1B_1^2 - 2OA_1A_1B_1 \cos \alpha_1}$ .

### 4 Case Study

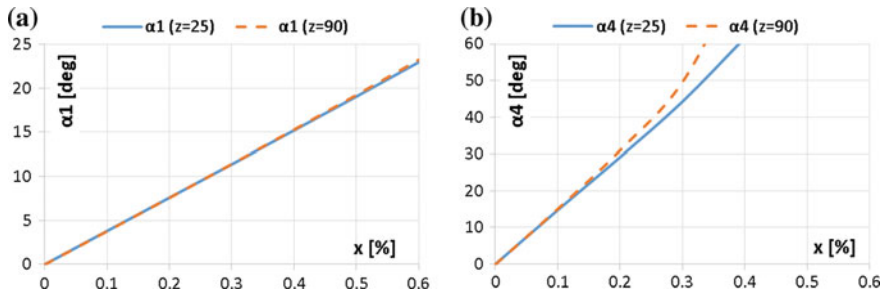
The main objective of this work is to observe the influence of the pitch increase from its nominal dimension over the contact angle between the chain bush and the sprocket. This change can influence representatively the functionality of the transmission, as well as its dynamics. Therefor a case study is proposed, starting with known and computed [12] the principal geometric and kinematic parameters, presented in Table 1. Once these parameters are determined the two angles  $\alpha_i$  and  $\lambda_i$  can be computed and presented for different specific modifications of the chain (x); taking in account that regularly the first 4 bushes in contact with the sprocket are the

**Table 1** Geometric and kinematic parameters of the sprocket—bush chain gearing

Constant parameters	z	p (mm)	$r_B$ (mm)		$r_A$ (mm)	$R_A$ (mm)
		25	9.525	2.54		2.684
Variable parameters	x (%) of p	i	$\delta_i$ (deg)	$\psi_i$ (deg)	$\alpha_i$ (deg)	$\lambda_i$ (deg)
	0	1	81.942	81.942	0	0
		4	81.942	81.942	0	0
	0.1	1	81.942	85.748	3.806	0.014
		4	81.977	96.743	14.765	0.055
	0.2	1	81.942	89.54	7.597	0.028
		4	82.043	111.215	29.171	0.105
	0.3	1	81.942	93.333	11.391	0.042
		4	82.14	126.353	44.212	0.151
	0.6	1	81.942	104.895	22.953	0.084
		4	82.78	–	–	–
	Obs.	i = number of considered contacts between sprocket and bush				



**Fig. 2** Influence of the pitch change coefficient ( $x$ ) over: **a** contact angle ( $\alpha_i$ ) for  $z = 25$  and **b** contact angle ( $\alpha_i$ ) for  $z = 90$



**Fig. 3** Influence of the pitch change coefficient ( $x$ ) over: **a** contact angle ( $\alpha_i$ ) for the first contact ( $\alpha_1$ ) and **b** contact angle ( $\alpha_i$ ) corresponding to the maximum contact point ( $\alpha_4$ ), considering  $\alpha_0 = 0$

most loaded. These simulation is limited for the first four contacts  $i = 1, \dots, 4$  (Table 1).

After the numeric simulation, based on the presented algorithm, the diagrams from Figs. 2 and 3 are illustrated for the variation of the contact angle ( $\alpha_i$ ) caused by the length difference of the pitch to the nominal value.

### 5 Results and Discussions

The correct functioning or replacement of a bush chain, used in machine construction is given to the pitch increase to the nominal dimension, change imposed by wear and elastic elongation caused by the radial and tangential forces, appearing during functioning. This difference is highlighted by the appearance of the contact angle between the sprocket and the chain bush; once with the increase of the angle described by the contact angle between the bush and the sprocket, increases also the friction surface between the bush and the sprocket, fact that has an effect over the transmission.

This work presents analyses of the influence of the pitch increase ( $x$ ) and of the number of teeth ( $z$ ) of the sprocket over the contact angle ( $\alpha_i$ ) between the bush and the sprocket. The constant parameters are: the nominal pitch of the chain is  $p = 9.525$  (mm), diameter of the bush  $d_B = 5.08$  (mm), number of teeth  $z = 25$  and 90 (minimal and maximal number of teeth considered for automotive engines) and the variation of  $x = 0 \dots 0.6\%$  of  $p$ .

From Fig. 3 can be seen that the increase of the pitch elongation ( $x$ ) leads to the contact angle increase  $\alpha$ , which determines: decrease of number of teeth in contact (i), increase in load on teeth and implicitly increase of friction surfaces between the bush and the sprocket; for ex. For  $x = 0.001p$  results  $\alpha_{i=4} = 15^\circ$ , and for  $x = 0.004p$  it is obtained  $\alpha_{i=4} > 60^\circ$ , what means that *IV*th contact moves on the top of the tooth.

From Fig. 3 it can be observed that the contact angle is influenced insignificantly by the increase of the number of teeth (its influence referring more to overall dimensions and wear in time).

Hence it can be stated that pitch differences to nominal dimensions can have a role in friction losses, thus the friction model of the transmission has to take in account the specific dimensional deviations and the elongation caused by wear and elastic deformations. According to what was presented, functioning correctly over longer time period of the chain transmission is directly influenced by the dimensional increase of the pitch over the nominal one.

Once determined the kinematic geometry of the contact between the sprocket and the chain bush, statics and dynamics of the transmission can be approached to optimize in this way the transmission.

## 6 Conclusions

Dynamic studies over bush chain transmissions used in machine construction industry represents still a domain with great interest since these have a longer lifetime because of the rolling contact which takes place between bush and sprocket.

Because the radius of the bush is smaller than the radius of the socket ( $r_B < r_A$ ), occurs a pitch difference between the chain pitch and the sprocket pitch. In reality this difference is admissible up to 0.1% form the nominal pitch of the chain. This difference, noted with  $x$ , increases due to chain wear with up to 0.2%, respectively up to 0.3% due to elastic elongation caused by the tensioning that appear during functioning. These differences have a direct effect over the contact between the bush and the sprocket, an angle that influences the dynamics, vibrations and wear of the transmission.

Looking on the comparative analysis of the obtained results it can be concluded that once the pitch difference increases, the contact angle also increases, which implies the move of the contact point to the top of the tooth of the chain after a smaller number of contacts. This will determine increased friction surfaces between

the bushes and the sprocket, modification of the contact angle of the forces during functioning and as a result the appearance of vibrations and wearing acceleration.

Using of such algorithm ensures determination of parameters that could help to optimize bush chain transmissions by placing the transversal and normal forces in the chain, minimizing the friction surfaces between the bush and the chain and minimizing transversal vibrations.

## References

1. Gotovtsev AA, Kotenok IP (1982) Proektirovanie tsepykh peredach: Spravochnik (Design of chain transmission: a handbook). Mashinostroenie, Moscow
2. Lates MT (2012) Bush chains design process. *Ann Oradea Univ Fascicle Manag Technol Eng XI(XXI) Nr 2:2.51–2.55*
3. Lateş MT et al (2012) Stresses distributions in bush chains. In: *Proceedings of modern technologies, quality and innovation ModTech international conference, Sinaia*, pp 505–508
4. Lates MT (2012) Finite element modeling of the bush chains bolt-bush contacts. *Ann Oradea Univ Fascicle Manag Technol Eng XI(XXI), Nr. 1:2.72–2.76* (2012)
5. Metil'kov SA et al (2008) Wear of hinges in roller drive chain. *Russ Eng Res* 28:839–844
6. Papuc R et al (2014) Geometrical study of guide-chain contact for general chain transmission. *Ann Univ Oradea Fascicle Manag Technol Eng XXIII(XIII):123–126*
7. Papuc R et al (2015) Guide-chain contact pressure tribological analysis. *Ann Univ Oradea Fascicle Manag Technol Eng XXIV(XIV):169–174*
8. Pedersen SL (2005) Model of contact between rollers and sprockets in chain-drive systems. *Arch Appl Mech* 74:489–508
9. Saulescu R et al (2017) Geometric modelling of the contact point between the bushing and sprocket in chain drives. In: *Rotrib'16. Galaţi, Romania, materials science and engineering—IOP conference series: materials science and engineering*, vol 174, pp 012049. <https://doi.org/10.1088/1757-899x/174/1/012049>
10. Sergeev SA et al (2009) Parametric optimization of chain-transmission sprockets. *Russ Eng Res* 29:452–455
11. Todi-Eftimie A et al (2013) Geometric modeling of power joints from bush chain drives. In: *The 11th IFToMM international symposium on science of mechanisms and machines—SYROM 2013, mechanisms and machine science*, vol 18, pp 471–479
12. Velicu R et al (2016) Contact point of bush—sprocket tooth depending on pitch differences of bush chain transmissions. In: *Iasi, Romania, materials science and engineering—IOP conference series: materials science and engineering*, vol 147(1), pp 012039. <https://doi.org/10.1088/1757-899x/147/1/012039>
13. Diamond Chain Co (2016) Technical guides. diamond chain maintenance guide. <http://www.diamondchain.co.uk/tech-guides.php>. Accessed 10 Mar 2017
14. ISO 606:2004 Short pitch transmission precision bush chains and chain wheels

# Increasing the Resistance of Scuffing for HCR External Helical Gearing



M. Rackov, M. Čavić, M. Penčić and M. Vereš

**Abstract** The paper analyses the way to increase the resistance of HCR external involute gearing from a scuffing point of view. The scuffing is the most important damage of teeth flanks of HCR involute gears. In the case of warm scuffing; it is the combined action of high pressure between surfaces, high sliding speeds, and excessive contact temperature, resulting from pressure and sliding speed values, which cause oil film rupture between the teeth flanks. Adopting suitable geometry of the tooth curve profile, it will be defined certain values addendum heights for meshing wheel according to criteria of specific slips and corrected head shape of the teeth of both wheels. The paper deals with assessment and theoretical analysis of the impact of the HCR tooth profile resistance to scuffing on the basis of integral temperature criterion according to Winter-Michaelis criterion, researching especially two factors: factor of load distribution ( $X_e$ ) and factor of gear geometry ( $X_G$ ).

**Keywords** HCR involute gears · Scuffing · Factor of load distribution  
Factor of gear geometry

---

The original version of this chapter was revised: Greek letter has been removed. The erratum to this chapter is available at [https://doi.org/10.1007/978-3-319-79111-1\\_53](https://doi.org/10.1007/978-3-319-79111-1_53)

---

M. Rackov (✉) · M. Čavić · M. Penčić (✉)

Faculty of Technical Sciences, University of Novi Sad, Novi Sad, Serbia  
e-mail: racmil@uns.ac.rs

M. Penčić

e-mail: mpencic@uns.ac.rs

M. Čavić

e-mail: scomaja@uns.ac.rs

M. Vereš

Faculty of Mechanical Engineering, Slovak University of Technology,  
Bratislava, Slovakia  
e-mail: miroslav.veres@stuba.sk



## 1 Introduction

Progressive scuffing means serious damage to the tooth profile curve, which means removing the teeth from the service [14]. Increased noise transmission over the standard border may refer in some cases also to the reason for exclusion from the transfer operation [6, 11]. Teeth scuffing can be eventually avoided by additional oil cooling and reducing load transfer, but these methods are disadvantageous from an economic perspective [3, 7]. Although, quality lubricating oils with additives (EP oils) should be used and appropriate choice of teeth geometry could be adopted. Suitable geometry of the tooth curve profile in the design of involute gearing is possible by defining certain values of addendum heights for teeth of both meshing wheels. It should be used criteria of specific slips and corrected head shape of the teeth. This paper deals with the problematic of high contact ratio gears (HCR), i.e. the gears with extended duration of contact period. The scuffing occurs more frequently in HCR gear teeth, since the path of action is larger and peripheral speed is higher [8]. This paper is trying to analyze and discuss the possibilities to reduce occurring of scuffing, or at least to postpone this damage of teeth on external HCR gears. Fracture in the tooth root due to bending stress and the formation of pitting represent fatigue damage, but the occurring of scuffing can happen after short time of transfer overload within a few hours. Beside the gear load and the peripheral speed, there are different effects which can influence the occurring of scuffing, such as material of gears, geometry of the teeth, quality of teeth flanks and the properties of the lubricating oil [2, 4, 5, 12]. When introducing higher demands on the capacity of the teeth and developing new materials having high resistance to pitting and making high flexural strength, it is shown that the limit factor at design of spur gears in many cases may be just scuffing [9].

## 2 Defining Integral Temperature Criterion for HCR Involute Gearing

According to Blok hypothesis [1], it is possible to express the flash temperature (local instantaneous flash temperature) at any point of meshing along the contact path by the formula [15, 16]. Integral temperature criterion is based on the middle temperatures of surface calculated on the basis of Blok theory [1]. Comparative medium temperature of surfaces  $\vartheta_i$  (the integral temperature) consists of two temperatures: the medium value of local instantaneous flash temperature along the action line  $\vartheta_{Blm}$  and tooth bulk temperature  $\vartheta_0$  [1]. Therefore integral temperature is calculated from the relationship:

$$\vartheta_i = \vartheta_0 + B\vartheta_{Blm} \quad (1)$$

where B is a weighting factor which takes into consideration qualitatively different temperatures influence of the actual tooth bulk temperature  $\vartheta_0$  and temperature  $\vartheta_{Blm}$ , which is defined only as a comparative temperature, and it does not reflect the actual size of the temperature in the contact points [13, 15, 16].

For determining the integral temperature  $\vartheta_i$  from the Eq. (1), it is necessary to determine the tooth bulk temperature  $\vartheta_0$ . It can be assumed that the tooth bulk temperature principally consists of two parts. The first is tooth surface temperature when it is not in contact (it is approximately equal to the temperature of the oil). Another part depends on the size of the difference between integral temperature and oil temperature and from the values of the coefficients of thermal convection in the gear material and thermal transfer from the gear to the oil. If the coefficient of thermal convection and thermal transfer are included in the dimensionless coefficient, it can be written:

$$\vartheta_0 = \vartheta_{oil} + A(\vartheta_i - \vartheta_{oil}) \tag{2}$$

The coefficients A and B in Eq. (2), resp. (1) is determined experimentally by measuring the temperature at the surface of the teeth. If  $C = B/(1 - A)$ , then:

$$\vartheta_i = \vartheta_{oil} + C\vartheta_{Blm} \tag{3}$$

where  $\vartheta_{oil}$ —oil temperature. The size of integral temperature is determined from the general relation (1), or using the Eq. (3), where  $l$  is the length of contact line ( $l = AE$ ):

$$\vartheta_i = \vartheta_{oil} + C \frac{\int_0^l \vartheta_{Bl} dx}{l} \tag{4}$$

Integral in Eq. (4) can be expressed in the form:

$$\frac{1}{l} \int_0^l \vartheta_{Bl} dx = \vartheta_{Bl(E)} X_\epsilon \tag{5}$$

where  $\vartheta_{Bl(E)}$  is local flash temperature at reference point of meshing E for contact between teeth with contact ratio  $\epsilon_\alpha = 1$ . Factor  $X_\epsilon$  is a dimensionless factor which takes into account the distribution of the load between two mating teeth, contact ratio of the head of the pinion and gear wheel and geometric characteristics of the curve of tooth profile. Therefore, Eq. (4) for integral temperature becomes:

$$\vartheta_i = \vartheta_{oil} + C\vartheta_{Bl(E)}X_\epsilon \tag{6}$$

which is analysed in [15, 16]. The factor of load distribution ( $X_\epsilon$ ) for HCR involute gearing is described in Fig. 1 within the hatched area [10].

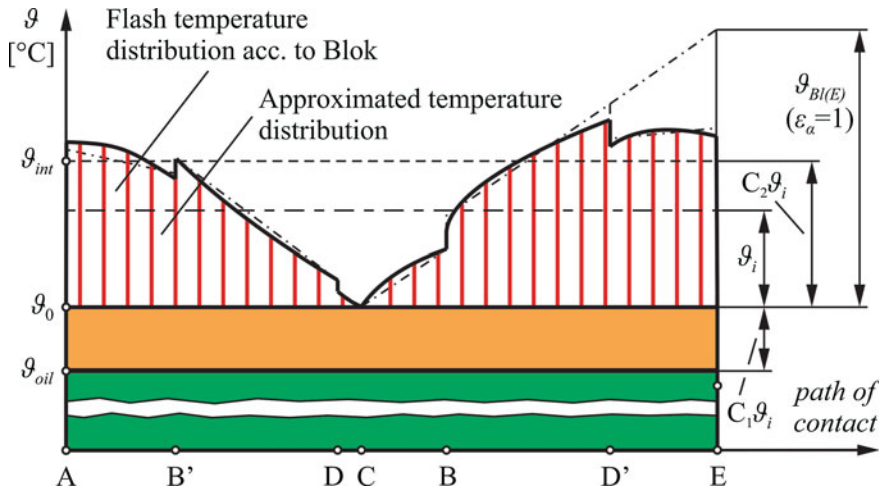


Fig. 1 Temperature distribution along the path of contact for HCR involute gearing

There are no many published relevant results of the valuation of the HCR gearing resistance against the warm scuffing damage. Nowadays, normalized calculation of load capacity of the involute gearing is used to derive the thermal scuffing calculation according to the integral temperature criterion. However, this is valid only for standard profiles. For HCR gearing it is necessary to extrapolate particular factors, which have substantial influence on the designation of the integral temperature value and in this way it is possible to extend the validity of this criterion, even on the gearing with  $\epsilon_\alpha \geq 2$ .

### 3 Calculation of Local Flash Temperature $\vartheta_{BI(E)}$ for HCR Involute Gearing

To compare the resistance of particular types of gearing against the scuffing it is necessary to identify local flash temperatures  $\vartheta_{BI(E)}$  in the reference point. Reference point is defined by the integral temperature for HCR involute gearing as endpoint of contact line on head of pinion, i.e. point E on the contact line. The temperature at reference point E can be expressed using Blok theory [1, 10, 15, 16]:

$$\vartheta_{BI(E)} = 0.62 \mu_m \left( \frac{F_{nE}}{b} \right)^{0.75} \left( \frac{E_r}{\rho_r} \right)_E^{0.25} \frac{|v_{\rho 1E} - v_{\rho 2E}|}{\sqrt{B_{M1} v_{\rho 1E}} + \sqrt{B_{M2} v_{\rho 2E}}} \quad (7)$$

If normal force  $F_{nE}$  is expressed, which acting in point E of straight tooth (spur gear), tangential force  $F_0$  on rolling circle can be obtain from  $F_{nE} = F_0 / \cos \alpha_E$  and if

it is considered that the gearing of both gear wheels is made of standard steel (i.e.  $B_{M1} = B_{M2} = B_M$ ), Eq. (7) can be expressed in the form:

$$g_{Bl(E)} = 0.62 \mu_m \left( \frac{w}{\cos \alpha_E} \right)^{0.75} \left( \frac{E_r}{\rho_r} \right)_E^{0.25} \frac{|\sqrt{v_{\rho 1E}} - \sqrt{v_{\rho 2E}}|}{\sqrt{B_M}} \tag{8}$$

where  $w = F_0 / b$ .

The values  $E_r$  and  $B_M$  depend only of material of meshing gear wheels.

If the Eq. (8) is substituted and  $\rho_{rE}$ ,  $v_{\rho 1E}$ ,  $v_{\rho 2E}$  are substituted with their relations, after modification and arranging, it follows [17]:

$$g_{Bl(E)} = \mu_m w^{0.75} v_0^{0.5} a^{-0.25} X_M X_G \tag{9}$$

where  $X_G$  is dimensionless coefficient of gear geometry which can be modified in the shape:

$$X_G = 1.24 \sqrt[4]{\frac{\tan \alpha_{wt}}{\cos^2 \alpha_{wt}}} \cdot \frac{\sqrt{u+1}}{2} \cdot \frac{\sqrt{\rho_{1E}} - \sqrt{\rho_{2E}}}{\sqrt[4]{\rho_{1E} \rho_{2E}}} \tag{10}$$

#### 4 Calculation of the Factor $X_g$ for HCR Involute Gearing

High contact ratio gears are different from the standard gear profiles since the load distribution along the contact line is different and, of course, there are also higher tangential velocities at the beginning and at the end of the teeth meshing. If Eq. (1) is considered more seriously, it is evident that two geometric parameters values have the main influence on the scuffing resistance. These values are tangential velocities and the reduced radius of curvature.

For calculation of load distribution factor ( $X_e$ ), it is necessary to know the load distribution, size of radii of curvature and tangential speed at any contact point. This is the main difference between the calculation of the integral temperature intensity for LCR and HCR gearing, since the is determination of factor of load distribution  $X_e$  is different. Equation for determination  $X_e$  is obtain as total amount of the areas under the curves of the local flash temperatures along the meshing (Fig. 1) and local flash temperatures at the point  $E_{e\alpha} = 1$  multiplied by the length of the meshing line for equivalent areas. The load distribution along the contact line for HCR gearing is shown in Fig. 2 [10].

However, Winter and Michaelis, in their criteria foresaw a simplified waveform of temperatures along the contact line. Theoretical values of these temperatures apply strictly only at points C and E and between these points the change in temperature is linear (Fig. 3) [10]. In fact, this meshing could not be with different radii of curvature of involute of both wheels, since tangent in any individual point is

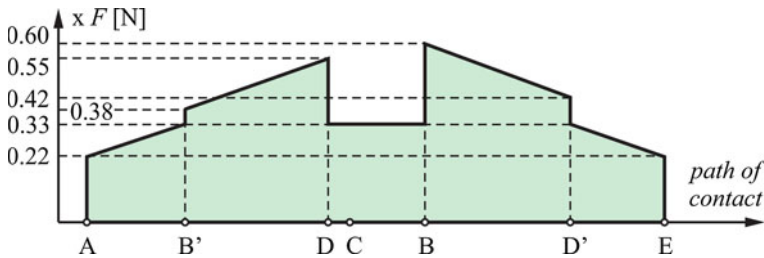


Fig. 2 Load distribution along the contact line for HCR involute gearing

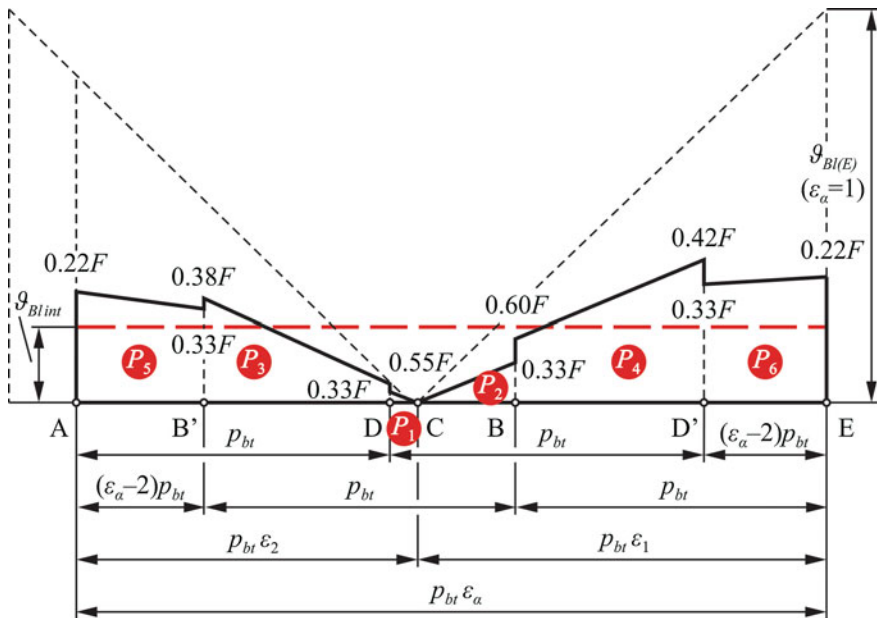


Fig. 3 Linear distribution of temperature along the path of contact for HCR involute gearing

linear, but a deviation between actual and linear course of considering temperature is negligible.

The overall surface ( $P$ ) under the flash temperature line during whole contact of path of action can be replaced with the surface of a rectangle. The width of this rectangle is the same value of contact line and the height represents the integral temperature ( $\vartheta_{Bl(E)}$ ) [1, 10, 15, 16]:

$$\vartheta_{Bl} = P = \overline{AE} \cdot \vartheta_{Bl(int)} = \vartheta_{Bl(E)} \cdot X_e \cdot X_G \cdot X_M \tag{11}$$

According to Fig. 3, it is possible to derive the relationship for factor of load distribution ( $X_\epsilon$ ) for HCR involute gearing. Overall surface will be divided into six separate parts, calculated in [10]. Equation for factor of load distribution can be written in the following form:

$$X_\epsilon = \frac{P}{l \cdot \vartheta_{Bl(E) \epsilon_\alpha = 1}} \tag{12}$$

Considering  $l = AE = \epsilon_\alpha p_{bt}$ , it follows:

$$X_\epsilon = \frac{1}{2\epsilon_1\epsilon_\alpha} [0.123\epsilon_1^2 + 0.204\epsilon_2^2 + 1.001\epsilon_1 + 0.759\epsilon_2 - 0.543\epsilon_1\epsilon_2 - 0.539] \tag{13}$$

For comparison, Winter and Michaelis derived for LCR gearing that [13, 14, 16]:

$$X_\epsilon = \frac{1}{2 \epsilon_1 \epsilon_\alpha} [0.18(\epsilon_1^2 + 0.7\epsilon_2^2) + 0.82\epsilon_1 - 0.52\epsilon_2 - 0.33\epsilon_1\epsilon_2] \tag{14}$$

## 5 Conclusions

Gear pair has high contact ratio (HCR) only in the case when there are at least two pairs of teeth in contact between gears. Addendum height of high contact ratio gears is increased, so it is larger than in standard gearing and therefore the meshing contact is longer. Geometry of HCR gearings is much complicated, since there is larger possibility of occurring meshing and production interference during the operation and it is much larger than interference occurring in LCR involute profiles. There is also higher risk of reduced thickness of a tooth tip and significantly higher values of specific slipping can occur into the flanks.

Contact ratio is increased since the tooth height is larger. Having at least two pairs of teeth in contact, dynamic loads and noise are reduced. Measuring different results of gear pair, noise reduction proved to be the best using HCR gearing with the value  $\epsilon_\alpha = 2$  for contact ratio. Noise decreasing is also the best for  $\epsilon_\alpha = 2$  since there are always two pairs of teeth in contact. So, when one pair of teeth goes out from the contact, another pair of teeth comes in contact and applied force is considerably smaller since it is always divided on two pairs of teeth. Therefore, gears from automotive industry should be done in such a way to reduce the noise and dynamic forces, with contact ratio  $\epsilon_\alpha = 2$ .

Therefore it was made a detailed theoretical analysis of the HCR geometry and impact of the shape of the involute HCR teeth on its scuffing resistance using the criterion of integral temperature. Evaluating the impact of gearing geometry to its scuffing resistance from the point of integral temperature, it can be concluded that it is possible to achieve smaller flash temperature and thus increase the resistance to

scuffing. Of course, beside this condition, type of transmission oil has very important influence on scuffing occurrence. This means that scuffing occurrence can be reduced using oils for extra pressure. Experimental verification should confirm if using this type of oil is necessary or not.

The main contribution of this paper is a generalization of the integral temperature criterion for involute HCR gearing. It is shown here that the factor of load distribution should need to be calculated for integral temperature criterion for involute HCR gearing for a case  $\varepsilon_\alpha \geq 2$ . Since factor of load distribution ( $X_e$ ) and factor of gear geometry ( $X_G$ ) were known only for LCR gearing, this paper offers deriving and equations for the case of involute HCR gearing. In the continuation of this researching, the criterion for integral temperature of involute HCR gearing can be optimized and the minimal flash temperature could be obtained.

## References

1. Vereš M, Krajčovič A, Nemčeková M (2014) Analysis of the HCR gearing from warm scuffing point of view. *FME Trans* 42(3):224–228
2. Ristojević M, Lazović T, Vencl A (2013) Studying the load carrying capacity of spur gear tooth flanks. *Mech Mach Theory* 59:125–137
3. Kopiláková B, Bošanský M, Zápotočný J (2014) Influence of the type of gearing to pitting damage. In: Ševčík L, Lepšík P, Petrů M, Mašín I, Martonka R (eds) *Modern methods of construction design: ICMD 2013*. LNME. Springer, pp 349–355
4. Michaelis K Gear failures—scuffing (Course at the University of Ljubljana), Forschungsstelle für Zahnräder und Getriebbau Gear Research Centre, FZG TU München
5. Gears—wears and damage to gear teeth—terminology, International Organization for Standardization, ISO 10825 (1995)
6. Muhs D, Wittel H, Jannasch D, Vošiek J (2007) *Roloff/Matek Maschinenelemente – Normung. Berechnung, Gestaltung, Viewegs Fachbücher der Technik*, Wiesbaden
7. Burián M, Trochta M, Havlík J (2016) HCR gears in the industrial gearbox. In: Dynybyl V, Berka O, Petr K, Lopot F, Dub M (eds) *The latest methods of construction design: ICMD 2014*. Springer, pp 7–14
8. Kasuba R (1981) Dynamic loads in normal and high contact ratio spur gearing. In: *Proceedings of the international symposium on gearing and power transmissions*, Tokyo, pp 49–55
9. Sato T, Umezawa K, Ishikawa J (1983) Effect of contact ratio and profile correction of spur gears on the rotational vibrations. *Bull JSME* 26(221):2010–2016
10. Kahraman A, Blankenship GW (1999) Effect of involute contact ratio on spur gear dynamics. *ASME J Mech Des* 121:112–118
11. Rackov M, Vereš M, Kanović Ž, Kuzmanović S (2013) HCR gearing and optimization of its geometry. *Adv Mater Res* 633:117–132
12. Blok H (1937) Theoretical study of the temperature rise at surfaces of actual contact under oiliness conditions. *Inst Mech Eng General Discus Lubr* 2:222–235
13. Vereš M, Bošanský M, Rackov M (2011) Theoretical and experimental research of the HCR gear's contact strength. *Mach Des* 3(2):105–108
14. Vereš M (1987) *Odolnost ozubenja voči zadieranju z hladiska jeho tvaru*. Kandidatska dizertačna praca, Slovenska vysoká škola technická v Bratislave, Strojnícka fakulta, Bratislava
15. *Tragfähigkeitsberechnung von Stirnrädern – Berechnung des Freßtragfähigkeit, DIN 3990-4*

16. Rackov M (2014) Optimization of HCR gearing geometry from scuffing point of view. Ph.D. thesis (in English), Slovak University of Technology in Bratislava, Faculty of Mechanical Engineering
17. Winter H, Michaelis K (1984) Scoring load capacity of gears lubricated with EP-Oils, Technical University of Munich, Gear Technology, Oct/Nov



# Erratum to: Increasing the Resistance of Scuffing for HCR External Helical Gearing



M. Rackov, M. Čavić, M. Penčić and M. Vereš

**Erratum to:**  
**Chapter “Increasing the Resistance of Scuffing for HCR External Helical Gearing” in: I. Doroftei et al. (eds.), *New Advances in Mechanism and Machine Science*, Mechanisms and Machine Science 57,**  
[https://doi.org/10.1007/978-3-319-79111-1\\_52](https://doi.org/10.1007/978-3-319-79111-1_52)

In the original version of the book, greek letter “ $\rho$ ” at the end of Equation 7 has to be removed in Chapter 52. The erratum chapter and the book have been updated with the change.

---

The updated online version of this chapter can be found at  
[https://doi.org/10.1007/978-3-319-79111-1\\_52](https://doi.org/10.1007/978-3-319-79111-1_52)

© Springer International Publishing AG, part of Springer Nature 2018  
I. Doroftei et al. (eds.), *New Advances in Mechanism and Machine Science*,  
Mechanisms and Machine Science 57,  
[https://doi.org/10.1007/978-3-319-79111-1\\_53](https://doi.org/10.1007/978-3-319-79111-1_53)

# Author Index

## A

Adouane, L., 253  
Alaci, S., 341, 349, 467  
Alexandru, C., 57  
Alexandru, E.-V., 341  
Antonescu, D., 75, 87, 99  
Antonescu, O., 75, 87  
Antonescu, P., 99  
Antonya, C., 201

## B

Balbayev, G., 211  
Banica, A., 147  
Besoiu, S., 427  
Boanta, C., 427  
Boborelu, C., 127  
Borovac, B., 37, 47  
Bouzgarrou, B.C., 253  
Brezeanu, C., 75  
Brisan, C., 427  
Budescu, E., 367  
Buium, F., 349  
Buium, Fl., 67, 455  
Butnariu, S., 201

## C

Cărăbaș, I., 273  
Carbone, G., 147, 155, 243, 283, 413  
Čavić, M., 37, 47, 523  
Ceccarelli, M., 147, 181, 211, 283, 379, 413  
Ciornei, F.-C., 341, 349, 467  
Cirebea, C.I., 291  
Ciupe, V., 137  
Ciureanu, I.-A., 331

Ciurezu-Gherghe, L., 263  
Comsit, M., 3  
Condurache, D., 331  
Copilusi, C., 171, 263  
Craciunoiu, N., 477  
Crivoi, O., 357

## D

Demirel, M., 283  
Didu, A., 191  
Dobincă, D.-I., 349  
Doroftei, I., 223, 233, 357  
Dragut, E., 477  
Drewniak, J., 311  
Duca, C.D., 67, 455  
Dumitru, N., 171, 191, 263, 477

## F

Fauroux, J.C., 253  
Filote, C., 341

## G

Gaspar, F., 99  
Gavrilă, C.C., 497  
Geonea, I., 191, 477, 487  
Gherman, B., 147  
Girbacia, T.M., 301  
Grigorescu, S.M., 273, 401  
Gruescu, C.M., 137

## I

Iacob, R.M., 367  
Inel, F., 413

**J**

Jaliu, C., 321  
Jurj, L., 507, 515

**K**

Kiper, G., 283  
Kopeć, J., 311  
Kuts, E., 27

**L**

Lateş, M.-T., 497  
Leohchi, D., 455  
Lovasz, E.-C., 137, 165, 273, 401  
Lu, Z., 37, 47

**M**

Maniu, I., 165  
Mansouri, Z., 413  
Maraje, S., 253  
Margine, A., 171  
Marszałek, J., 311  
Merticaru, E., 367  
Mogan, G.L., 301, 437, 445  
Moldovan, C., 165  
Moldovan, M., 3  
Muscă, I., 467  
Mussina, A., 211

**N**

Nawratil, G., 387  
Neagoe, M., 3, 321  
Nguyen, Hong-Nguyen, 13

**P**

Papuc, R., 497  
Penčić, M., 37, 47, 523  
Pisla, D., 147, 155  
Plitea, N., 147, 155  
Popa, D., 127  
Pop, C., 273, 401  
Popescu, I., 87  
Pop, F., 273  
Pozhbelko, V., 27

**Q**

Qiang, H., 113

**R**

Rackov, M., 37, 47, 523  
Racu (Cazacu), C.M., 223, 233  
Rasoulzadeh, A., 387  
Rinderu, P., 487  
Rosca, A., 191, 487  
Russo, Matteo, 379

**S**

Saulescu, R., 321, 515  
Sbanca, M.P., 437, 445  
Shen, H., 113  
Shen, Y., 113  
Shieh, W.-B., 13  
Siretean, S.T., 467  
Stańco, K., 311  
Stoian, Ana-Maria, 165

**T**

Tarnita, D., 127  
Tarnita, D.-N., 127  
Tătar, M.O., 291

**U**

Ulinici, I., 155

**V**

Vaida, C., 155  
Velicu, R., 507, 515  
Vereş, M., 523  
Visa, I., 3  
Vutan, A.-M., 137

**Y**

Yang, Ting-li, 113  
Yao, Shuangji, 181

**Z**

Zawiślak, S., 311